Spatio-temporal characteristics of the visual interhemispheric integration via the corpus callosum : computational modeling & optical imaging approaches

Luc Foubert

Université Paris VI – Pierre et Marie Curie
Graduate school, ED3C

Ph.D. in Neuroscience

SPATIO-TEMPORAL CHARACTERISTICS OF THE VISUAL INTERHEMISPHERIC INTEGRATION VIA THE CORPUS CALLOSUM

COMPUTATIONAL MODELLING
&
OPTICAL IMAGING APPROACHES

Presented by LUC FOUBERT

Ph.D. defense on september 27th, 2007.

Ph.D. committee:

Dr. Chantal Milleret	PhD supervisor
Dr. Jacques Droulez	PhD supervisor
Dr. Zoltan Kisvarday	Referee
Dr. Dominique Debanne	Referee
Dr. Shigeru Tanaka	committee member
Pr. Didier Orsal	committee member
Pr. Alain Berthoz	committee member

Résumé

Le cerveau des mammifères est composé de deux hémisphères. Bien qu'anatomiquement séparés, ceux-ci coopèrent l'un avec l'autre par l'intermédiaire de faisceaux de fibres qui constituent les commissures cérébrales. Parmi ces commissures, le corps calleux est la plus importante, tout au moins par le nombre de fibres qui la constitue (200 à 800 millions suivant les espèces). Bien que le rôle de cette commissure soit resté longtemps inconnu, il est maintenant bien établi qu'elle transporte des messages aussi divers que des messages visuels, limbiques, auditifs, somesthésiques et moteurs d'un hémisphère à l'autre. En conséquence, le corps calleux s'est révélé être impliqué dans des fonctions cognitives supérieures telles la perception sensorielle, l'apprentissage, la mémoire et la motricité. En dépit de l'établissement de ces concepts importants, la connaissance du corps calleux et de son rôle dans les fonctions cognitives supérieures restent encore extrêmement incomplètes que ce soit au cours du développement ou chez l'adulte. Or, ces questions sont essentielles puisqu'elles posent directement le problème du rôle de l'intégration interhémisphérique dans l'élaboration des fonctions cognitives dans les conditions normales; elles touchent également le problème du rôle de cette même intégration dans les processus de réorganisation et de compensation qui peuvent se développer dans les conditions pathologiques, conduisant à une restructuration des fonctions cognitives.

Ce travail de thèse a été réalisé dans le contexte expérimental de C. Milleret et de ses collaborateurs qui étudient les caractéristiques anatomo-fonctionnelles et topographiques des cartes corticales calleuses localisées au niveau des aires visuelles corticales *primaires* 17 et 18 de chaque hémisphère chez le mammifère et qui sont associées au traitement de la région médiane verticale centrale du champ visuel. Cette région centrale du champ visuel est des plus stratégiques d'un point de vue perceptif puisqu'elle participe à la fusion des deux hémichamps visuels. En utilisant les techniques électrophysiologies *in vivo* (enregistrements extracellulaires unitaires) et anatomiques (reconstructions 3D d'axones marqués à la biocytine), il a déjà été montré que ces connexions interhémisphériques sont presque exclusivement limitées à la bordure de transition entre les aires visuelle primaires A17 et A18. De plus, les neurones des aires visuels primaires qui sont activés par les axones interhémisphériques présentent des caractéristiques fonctionnelles bien précises. Certaines caractéristiques anatomo-fonctionnelles et topographiques des cartes corticales calleuses sont déjà bien identifiées mais elle se révèlent encore insuffisantes pour préciser le rôle du corps calleux dans les processus d'intégration visuelle interhémisphérique, en particulier en l'absence de données précises des caractéristiques dans les domaines temporels et spatiaux et la façon dont elles sont modifiées dans des conditions de développent visuel asymétriques. Ceci résulte aussi du faible nombre de travaux faisant appel à une approche computationnelle et la modélisation pour aborder ces questions. En particulier, les relations entre les caractéristiques morphologiques des axones calleux et les propriétés spatiales (cartes fonctionnelles) et temporelles (latences de transfert et propriétés spectrales) des populations neurales qu'elle mettent en relation sont encore très imprécises.

Caractérisation quantitative des distributions des terminaisons d'axones calleux.

Dans sa première partie, notre étude propose de préciser les extensions spatiales et les caractéristiques morphologiques des arborisations d'axones calleux obtenus dans les conditions de développement visuel normal (NR) et dans les conditions de déprivation monoculaire précoces (MD) afin de les différentier quantitativement. Dans cet objectif, deux groupes d'axones reconstruits en 3D sont tout d'abord décrits qualitativement par les méthodes conventionnelles d'anatomie. Cette méthode rencontre néanmoins des difficultés pour caractériser précisément les morphologies des axones, en particulier l'extension de leur terminaisons sur la surface du cortex, leur orientation et leur degré de fragmentation. Pour répondre à ces questions, deux méthodes computationnelles complémentaires et de complexité croissante ont été développées pour caractériser les distributions de terminaison axonales calleuses et mettre en évidences les différences entre les deux groupes. Celles-ci nous ont permis de montrer les plus grandes extensions spatiales ainsi que le plus grand degré de fragmentation des distributions des terminaisons des axones calleux du groupe MD.

Dans un dernier chapitre, la simulation de propagation de potentiel d'action dans les structures axonales a permis de montrer que les différences morphologiques constatées dans le groupe MD, ne semblent pas se répercuter sur la dispersion temporelle du signal entre les terminaisons. Ainsi, la distribution temporelle du signal controlatéral demeure pour la grande majorité confinée dans un intervalle inférieur à 2ms, dispersion compatible avec des hypothèses de synchronisation.

Développement de la technique d'imagerie optique par colorant sensibles au potentiels

Avec la perspective d'explorer expérimentalement les propriétés spatio-temporelles de l'intégration visuelle interhémisphérique et afin de corroborer les résultats présenté dans la première partie de la thèse, la mise en place d'un poste expérimental d'imagerie optique au sein de notre laboratoire est présentée dans la deuxième partie. Cette méthode permet de visualiser *in vivo* les domaines d'activation spécifique à différents attributs au sein des cartes corticales calleuses et d'approcher certaines caractéristiques temporelles de l'activité neuronale. Réalisé en parallèle avec les travaux de modélisation des axones calleux, le montage complet du poste a montré d'abord permis de cerner les limitations du système initial. Dans un deuxième temps l'adaptation du système à la problématique interhémisphérique, réalisée au fils des mois, a montré d'importants progrès après plusieurs modifications spécifiques.

La mise en place du poste expérimental a pu bénéficier de l'expertise en imagerie optique de l'équipe de recherche du Dr. S. Tanaka au RIKEN Brain Science Institute au Japon, où l'auteur a effectué plusieurs séjours au cours desquelles ont pu être initiées un certain nombres d'adaptation importantes comme le développement du protocole d'enregistrement en Voltage Sensitive Dye (VSD), permettant l'enregistrement de l'activité neurale avec un grande précision temporelle, ainsi que le développement de techniques de traitement des signaux appropriées. La mise en place du poste expérimental dans les locaux parisiens a pu être achevée fin 2006 avec l'obtention de données prometteuses pour la poursuite du programme expérimental, comme l'enregistrement à 3 ms/image de l'activation corticale bilatérale et ainsi que celle du transfert interhémisphérique. Ces résultats ouvrent les perspectives de recherche visant la combinaison des données anatomiques morphologiques avec les données d'enregistrement d'activations spatio-temporelles *in vivo* de l'intégration visuelle hémisphérique au sein des cortex visuels primaires.

Table of content

List of principal abbreviations

A17/A18:	Primary visual areas 17 and 18 of the cat neocortex
CC :	Corpus Callosum
LGNd:	Lateral Geniculate Nucleus (dorsal)
LH:	Left Hemisphere
MD:	Monocular Deprivation group
NR:	Normally Reared group
OI:	Optical Imaging
OI-IS:	Optical Imaging of Intrinsic Signal
OI-VSD:	Optical Imaging of Voltage Sensitive Dyes
RGC:	Retino-Geniculo-Cortical pathway
RH:	Right Hemisphere
ROI:	Region of Interest
TC:	TransCallosal activated neurons
TZ:	Transition Zone between the areas A17 and A18

Acknoledgements

To my Masters…

GENERAL INTRODUCTION

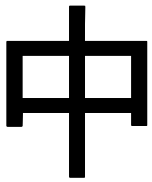

« Chû »

(the middle)

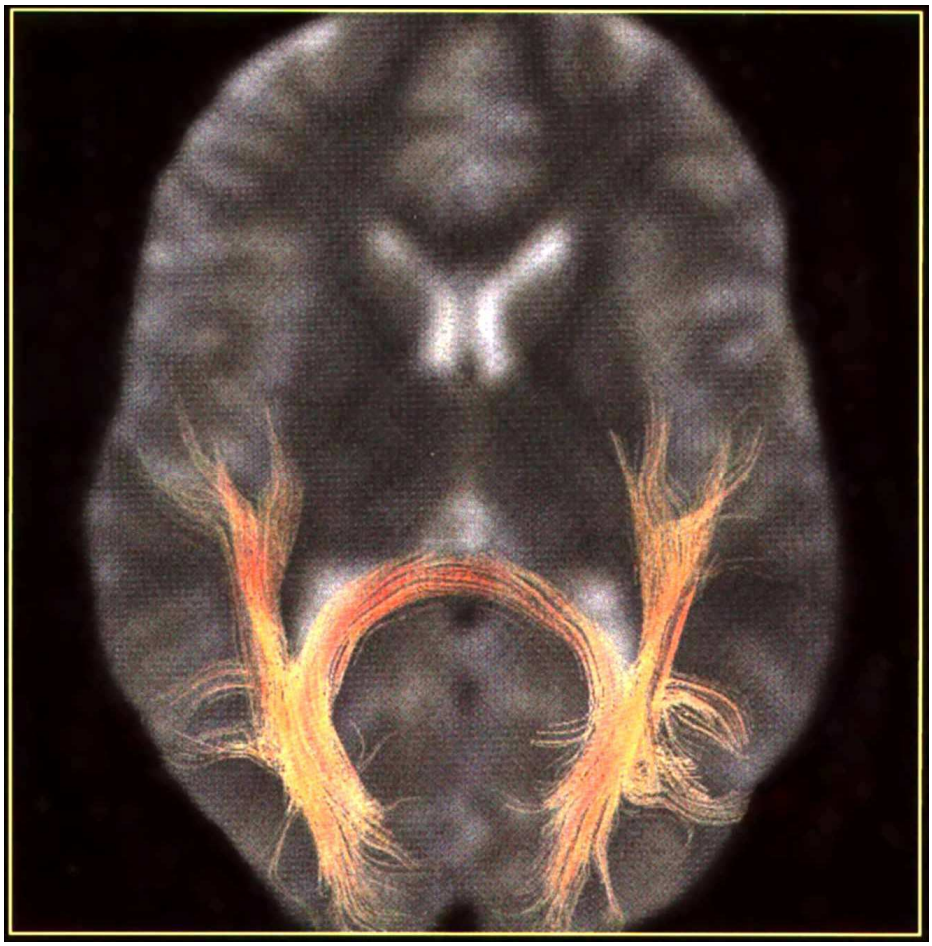

Fig. 1/ Diffusion Tensor Imaging (DTI) applied to the human brain revealing (orange tracks) both the optic radiations projecting from the thalamus to the primary visual cortex and the interhemispheric fibers connecting them through the corpus callosum; horizontal section (From Cabanis & al., 2004).

Diffusion tensor imaging (**DTI**) is a magnetic resonance imaging (MRI) technique that enables the measurement of the restricted diffusion of water in tissue. The principal application is in the imaging of white matter where the location, orientation, and anisotropy of the tracts can be measured. The architecture of the axons in parallel bundles, and their myelin sheaths, facilitate the diffusion of the water molecules preferentially along their main direction. Such preferentially oriented diffusion is called ***anisotropic diffusion*.**

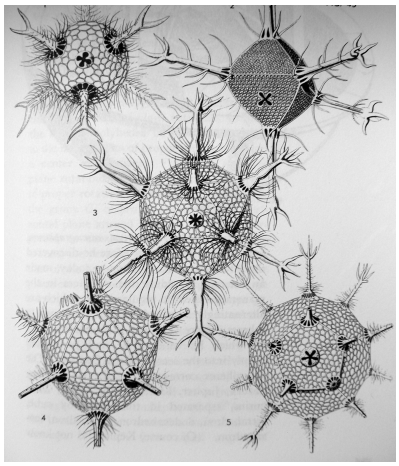

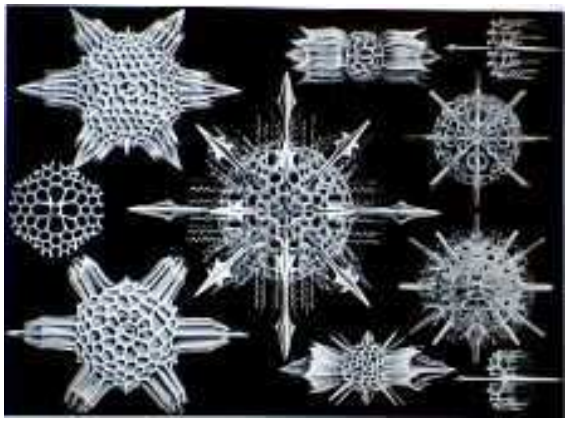

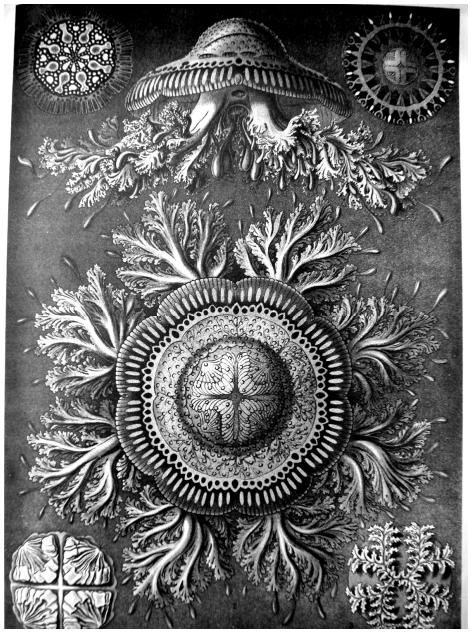

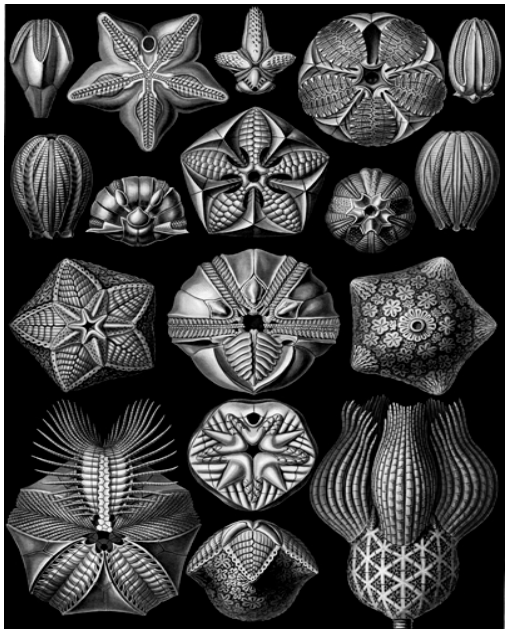

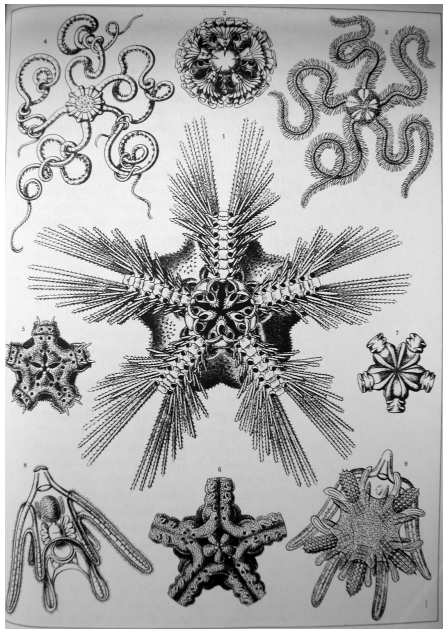

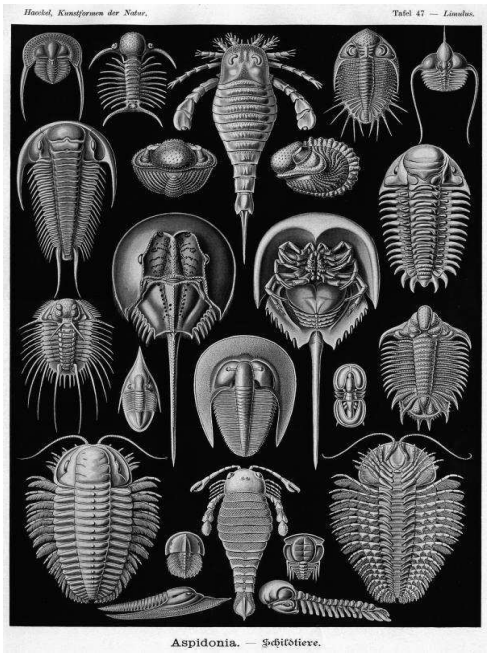

Fig. 2/ **Diversity of the symmetric organization of the body scheme in the living kingdom.** Drawings from Ernst Haeckel (*Kunstformen der Natur*, 1904) illustrating the evolutions of protoforms of life from high degree of symmetry to the reduction to the bilateral symmetry. Bottom-right: Similarities between the developments of the vertebrates' embryos. Although controversial, this draw illustrates vertebrates all share the common bilateral (mirror) symmetry (Romanes, 1901).

I " 2 hands, 2 eyes, …and 2 brains? "

On the origin of the Left & the Right

Phylogenesis and ontogenesis sciences both raise the fundamental question of the origin of forms of the living things but they involve different scales of times. While every creature's life begins with the quasi spherical shape of the primitive cell, the infinite diversity of living specimen it can create has always been fascinating as much as puzzling (see Fig. 2). The existence of elements of symmetry among them however should provide interesting clue and reflect some important characteristics of the morphogenesis rules.

The emergence of the group theory in mathematics (Galois, 1830) and the application of its principles have been particularly efficient to propose systematic classifications of shapes in many disciplines. From the concept of "group of transformations keeping globally invariant a particular form" it led to a universal definition of symmetry. The degree of symmetry of an object is thus related to the number of transformations (or dimension of this group in Lie theory) that does not change the global aspect of the original object. In the Euclidian space, a sphere has by this way the highest degree of symmetry and reflects when found in matter, a fundamental equilibrium state of its inner structure. Any other compact forms should be underlied by breaks of symmetry present either in the environment structure, in the initial conditions or in the internal organization. These breaks unbalance the original equilibrium of the constitutive forces and lead to a reduction of the degrees of symmetry. In particular, forms presenting the bilateral symmetry keep just one degree of freedom through the well known mirror inversion to stay "globally invariant" when all other directions are polarized. Considering the evolution of biological forms towards the bilateral symmetry as for many species including vertebrates, the original 3D space should have been initially structured by 2 orthogonal polarization axis presenting variations along them, to break the original spherical symmetry and reduce it to Left/Right contingency.

As suggested by H. Weil (1952), the presence of a gravitational axis in the primitive ocean and the later emergence of the self-movement abilities produce two directional fields that might have played a role in the organization of vertebrates, inducing a dorso-ventral and a rostro-caudal axis respectively to the body scheme. Care should be taken however with the pentagonal shape of the star fish for example: the appearance of these echinoderms is somehow misleading as surprisingly their larvae are also organized according to the bilateral symmetry like almost invertebrates. Interestingly, the planarian is the simplest living animal having a body plan of bilateral symmetry and cephalization. The brain of

these free-living flatworms is a bilobed structure with a cortex of nerve cells and a core of nerve fibres including some that decussate to form commissures (Sarnat and Netsky1985).

From phylogenesis to ontogenesis very interesting questions concern the polarization of the first cell and are still under debate. These questions involve different possible origins to determine the plane of the first division but also heterogeneities of morphogenetic fields to rule the construction of the embryo. In the last few years, an understanding has emerged on the developmental mechanism for the consistent internal left-right structure, termed “situs”, that characterizes vertebrates anatomy. This involves largely vertebrate-conserved gene expression cascades that encode “leftness” and “rightness” in appropriate tissues either side of the embryo's midline soon after gastrulation. This stage of development is also of particular interest as it changes the topology of the body from those of the sphere to those of the torus. Recent evidences indicate that the initial, directional symmetry breaking that initiates these genetic cascades utilises mechanisms that are conserved or at least closely related in different vertebrate types (Cooke, 2004). A scenario whereby the capacity for directional modification of an otherwise bilateral body plan can be viewed as an adaptive innovation rather closely connected with vertebrate origins, enabling optimal design for very active lifestyles and thus closely related to the emergence of neural structures.

Whatever the precise origins of the initial symmetry breaks, they lead all vertebrates to develop according to the bilateral symmetry with 2 hands (or else), 2 eyes, and two cerebral hemispheres. Regarding to this organization, any unbalanced condition occurring during the construction of the body should be considered with particular attention as a potential source of unevenness of the achieved form.

The mysteries of the interhemispheric integration

The origins of the work on the interhemispheric relations arise from partly philosophical and partly medical concerns with the explanation of the unity of the perception or consciousness. The various theories and speculations especially focused on two principal structures in the brain and have been reported as followed by I.S. Russell (Russell & Russell, 1979). In the periphery, the optic chiasm was early considered as a mechanism of visual integration. On the other hand, the unity of consciousness was believe to be a product of central integration which was originally thought to occur in the ventricular system and much later assigned to the interhemispheric fibers.

The earliest written description of the optic chiasm and its connections with the brain in fish was provided by Aristotle (384-322 B.C.). Believing that the brain was little more than an accessory to the heart, he attached no particular significance to the chiasm. Herophilus (300 B.C.) and Erasistratus (260 B.C.), the pioneers of the Alexandrian school of anatomy and medicine, correctly identified the visual role of the optic chiasm. The optic nerves, believed to be hollow tubes were described as emerging from the base of the brain and meeting in the optic chiasm and then bifurcating laterally to enter both eyes. The influence of Galen (129-199) in physiology and anatomy and in particular concerning brain functions was a very deep. His treatment and interpretation of the visual system were the first attempt to provide a coherent mechanistic explanation of visual perception in anatomical terms. Morphologically, he regarded each optic tract not as nerves but as tubular extension of the brain itself, originating from the lateral ventricles which he termed *thalami* or cavities.

The optic nerves were considered to extent from the brain separately to come together without any decussation and to end inside the eyes. There each nerve thins out to form the retina which extends as far as the lens. The function of this system was to provide a hydraulic exchange circuit in the eye to permit the transfer of information from the environment to the brain. Galen believed the ventricles contained luminous air which circulated via the channels of the optic nerves to the eye, and from there to the outside where, in presence of light, it altered or stressed the surrounding air. Galen regarded the lens as the principal organ of vision, where the photoreception should occur. The lens was supposed to act as an exchange membrane where a fluid so called pneuma could be “charged” with the images located there by visual rays. Visual perception was completed only when the pneuma conveyed these images back to the brain, which was though to be the ultimate site of consciousness.

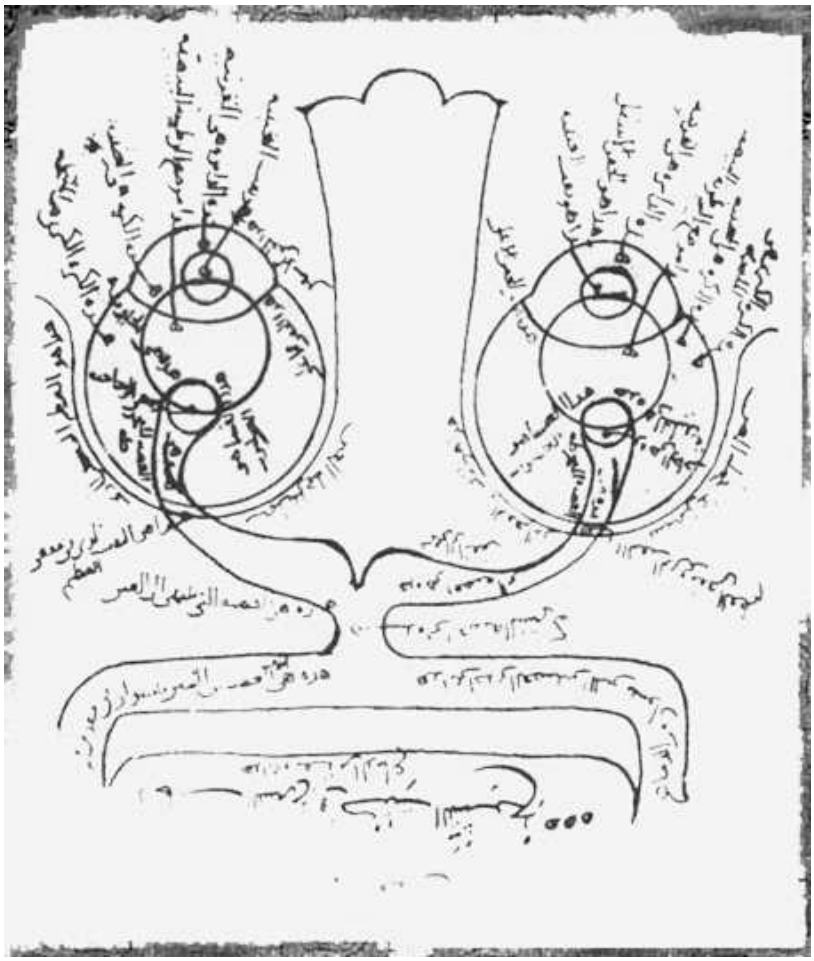

Fig. 3/ Schematic representation of the visual system from the oldest existing copy of the *Book of Optics* by Ibn Al-Haitham, written in the XIth century.

The most comprehensive and systematic alternative to classical optical theories was formulated by the mathematician and physicist Ibn al-Haytham (965-1039), known as the father of the ophthalmology. He is also the first mathematician to try to elaborate a theory of geometrical transformations. The essential feature of Ibn al-Haytham's system is his theory of direct vision and his uncompromising rejection of Galen emanation theory. His statement that "the act of vision" is accomplished by means of light rays coming from external object and entering both eyes and transferred to each ventricle through the optic chiasm (See Fig. 3). During the same period, Avicenna (980-1037), the great savant from Bukhara in Turkistan suggested, as opposed to Galen and Ibn al-Haytham, the optic nerves to be completely crossed in the chiasm such that separate images from each eye are conveyed to the opposite lateral ventricle. He provided the answer to the problem of the unity of consciousness by proposing the third and fourth ventricles acting as association chambers to unite the separate images.

Thus by the end of the eleventh century both a peripheral and a central theory of the unity of consciousness had been promulgated in terms that were to remain essentially unchanged for the next 600 years. It was not until Descartes published his *Traité de l'Homme* in 1686 that a neural alternative was proposed to the ventricular hydraulic model. With the advantage of the new knowledge in optics and mathematics Descartes was able to write former ideas of projection of light in a modern form. The pineal gland then became the neural site where binocular integration occurred during vision. It was not until 1903 that the central integrating role of the corpus callosum was discovered (Imamura, 1903).

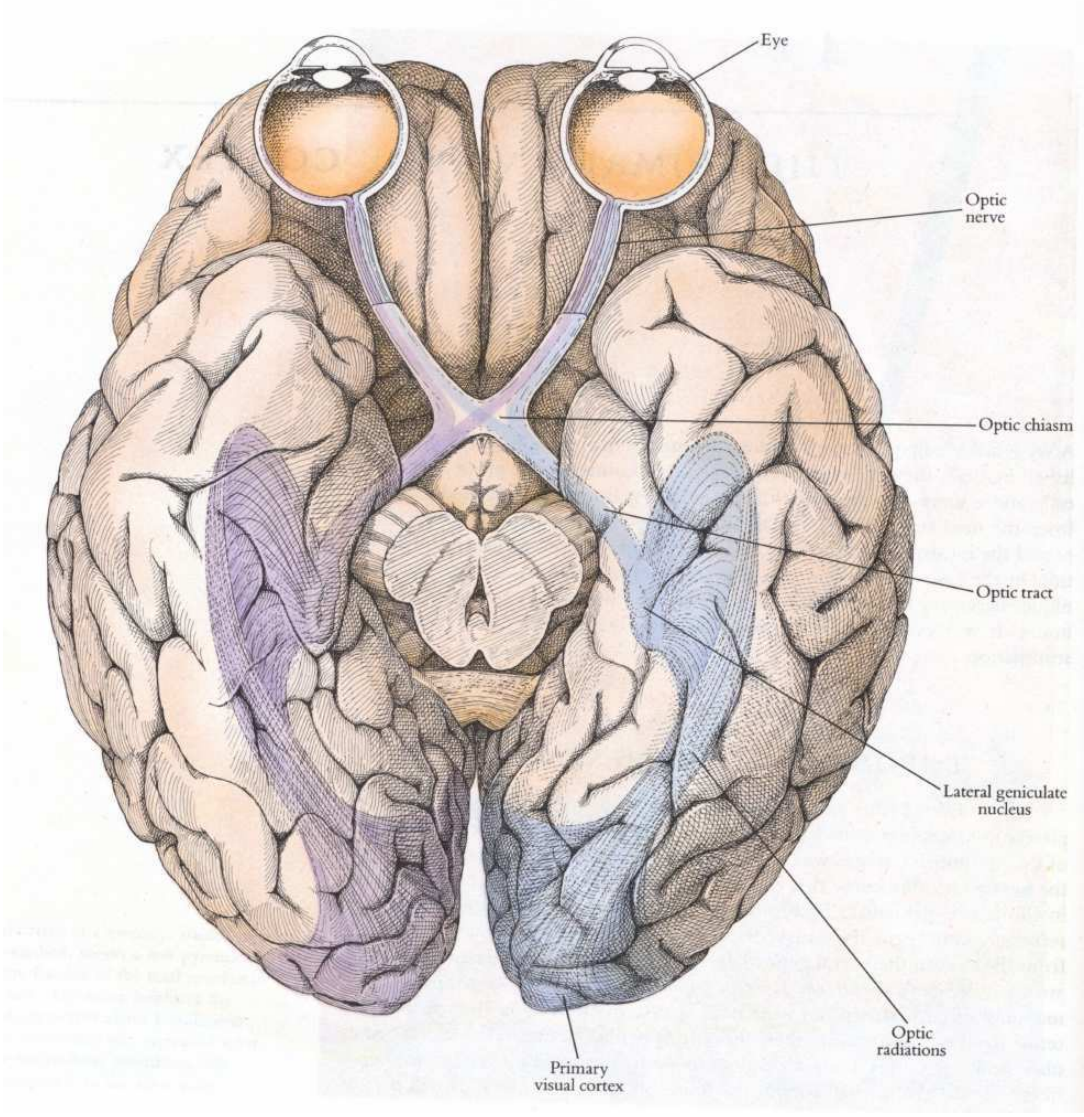

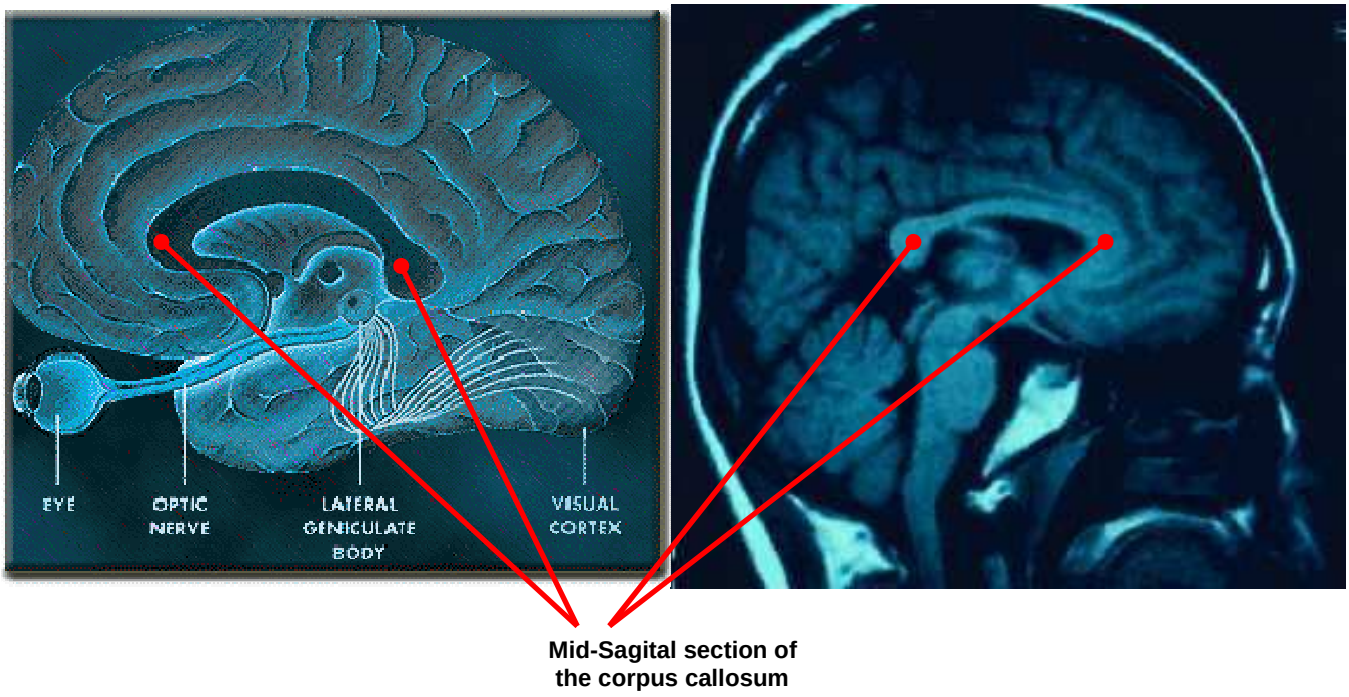

Fig. 4/ Top : visual pathways of the human brain (from Hubel, 1988).Bottom-left: schematic representation of the visual pathways on a mid-sagittal sections. Bottom-right: Anatomical MRI image of the human brain. Antero-posterior extension of the corpus callosum is visible in the middle of both figures.

Fusion of the Left and the Right: from symmetry to asymmetries

The mammalian brain is composed of two hemispheres. Although anatomically separated, they cooperate with each other through fibres bundles called cerebral commissures. Among those, the corpus callosum is the most important, at least by the number of fibres it constitutes (200 to 800 millions regarding to species). Human corpus callosum is estimated to contain about 200 millions of axons, much greater than the 1,5 million of each optic nerve and the 32 000 axons of each auditory nerve (See Fig. 1, Fig. 4 and Fig. 5). The section of the entire corpus callosum reveals about 700 mm^2 whereas the optic nerve shows few mm^2. Although the role of this commissure has been for a long time unknown, it is well established it transfer various signals such as visual, auditory, somesthesic, multisensorial, limbic and motor from one hemisphere to the other. The corpus callosum has been thus described for its implication in cognitive functions such as perception, learning, memory and movement generation (Lomber & al, 1994)

The topographic "mapping" of the dynamic of the external world onto sensory cortical areas (a property known as *visuotopy or retinotopy* for primary visual areas), induces, by a crossed organization, each left and right side of the world to be projected and analyzed in the contralateral hemisphere (see Fig. 6). This retinotopic organization helps to reduce the length of wiring between neural units by keeping close together those in relation with close parts of the visual world. It is important to notice that at the level of the primary visual cortex the organization is hugely symmetric regarding to the body scheme. As shown below, the retinotopic properties of the callosal connections are related to the vertical region of the visual field which is represented into both hemispheres. They link by this way two cortical regions whose activity during the waking time is driven or at least modulated by sensory inputs coming from the same part of the world. This means that some part of the external world is analyzed twice, once in each hemisphere but linked by the corpus callosum. The focalization of the corpus callosum fibers only close to the projection of the vertical meridian suggests the fusion of both sides as its major capability, assuming the continuity of visual analysis between the left and the right side around the vertical meridian where our daily experience never report any perceptual edge.

These disparities led to the well known asymmetries of the human brain such as the language lateralization in Broca area or the specialization for face recognition in the right fusiform gyrus. Whereas the bilateral cortical organization at low perceptive level of primary sensory areas seems to remain balanced, the elevation in the cognitive hierarchy interestingly implies, at least for humans, an uneven organization.

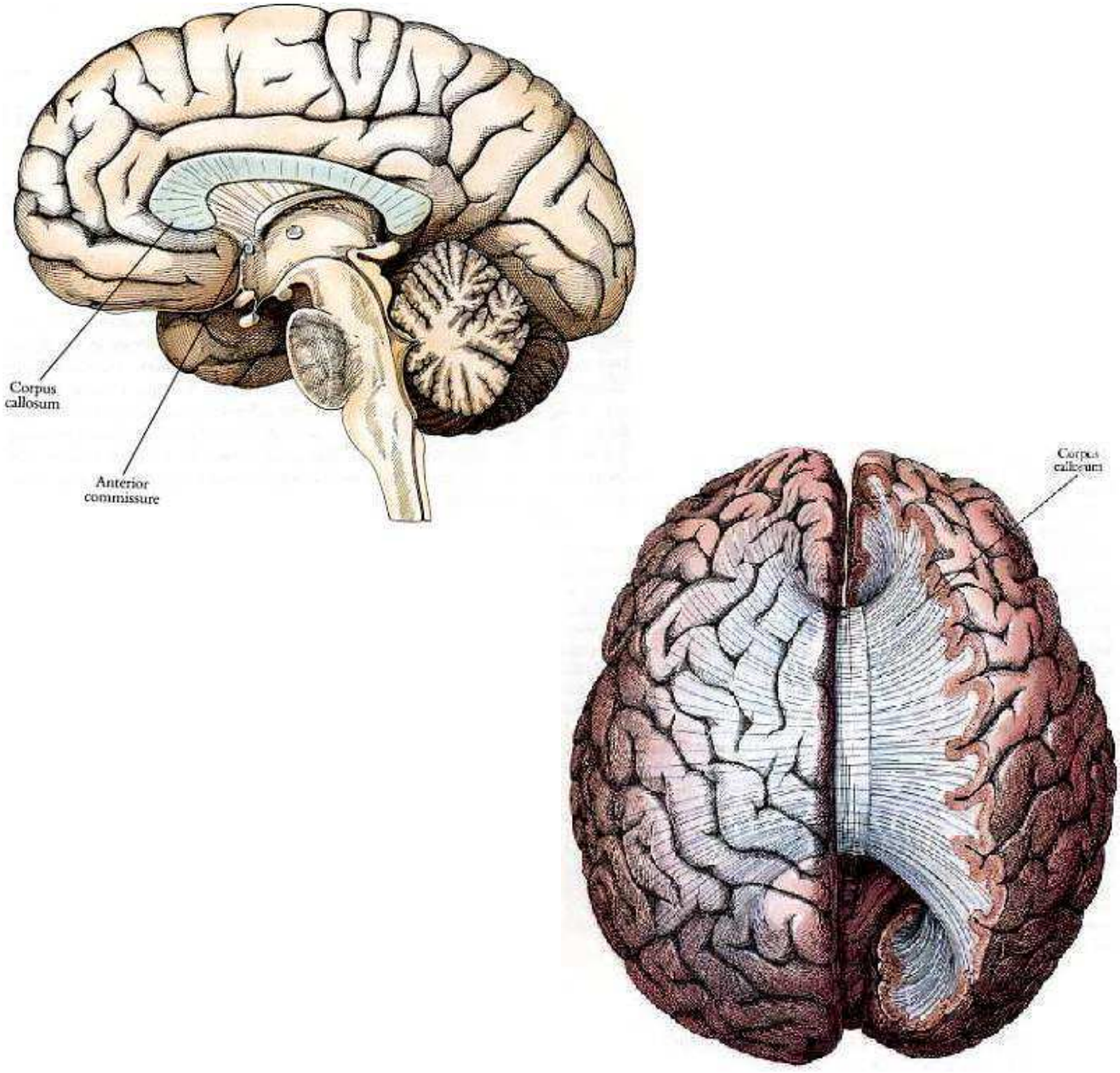

Fig. 5/ Illustration of the human brain showing the communication between the cerebral hemispheres through the bundle of fibers of the corpus callosum (From Hubel, 1988).

Despite the establishment of these important concepts, the knowledge on the corpus callosum and its role for cognitive processes remains incomplete for adult as well as during development. These questions are essential as they reflect the role of the interhemispheric integration in the emergence of cognitive function in normal condition as well as this role in the reorganization or compensation processes occurring during pathologic conditions or leading to different organization of the cognitive functions. The collection of precise information on spatial and temporal characteristics of the interhemispheric integration, on the way they emerge with age and on the way this characteristic are modified after pathologic alteration may provide interesting cue to answer these questions.

In order to precise the role of the interhemispheric connectivity in visual perception, let’s have a comprehensive description of the state of knowledge on the organization of the main visual pathways in the cat and the primary cortical areas they target.

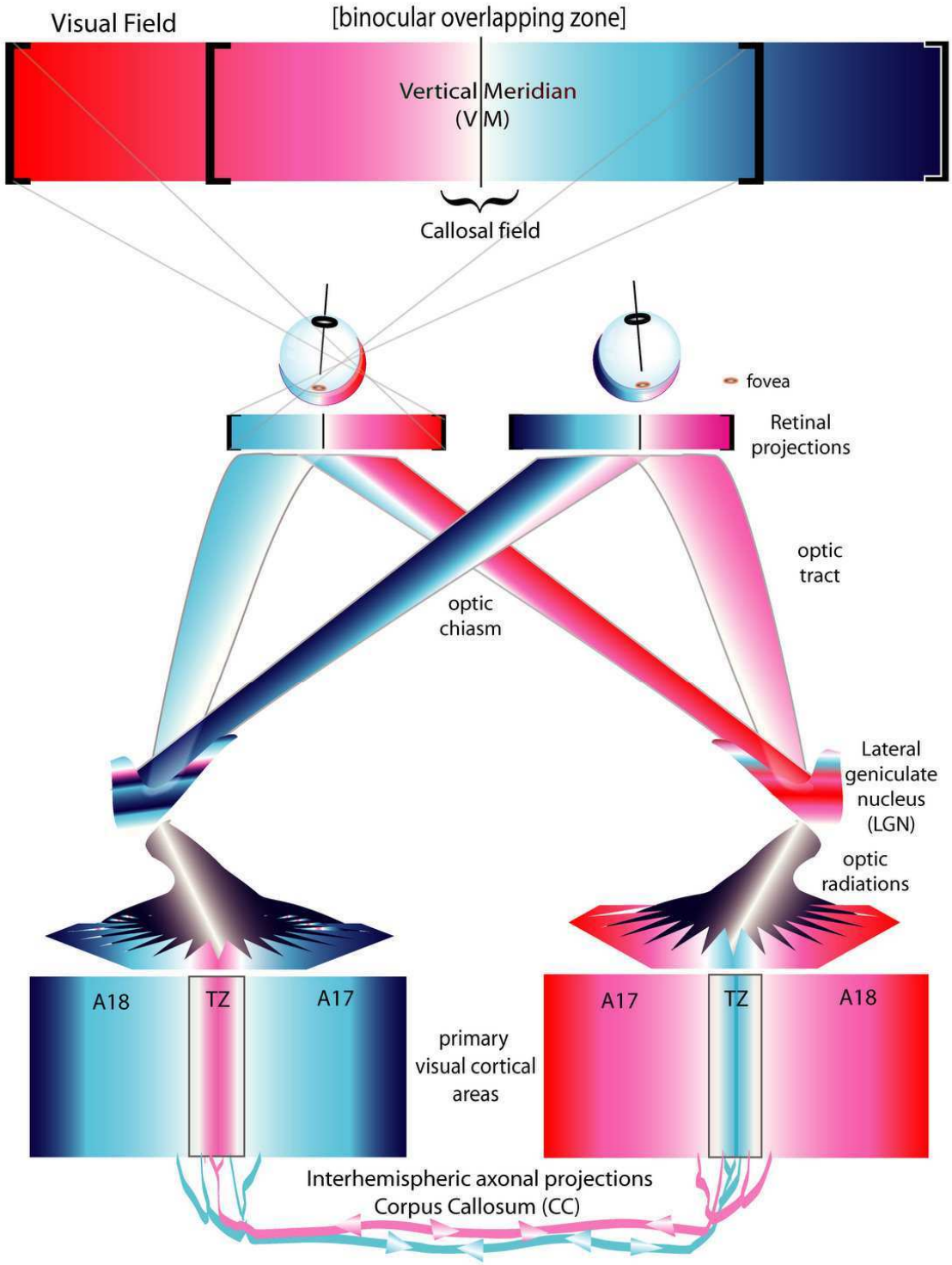

the retinotopic organization of visual connections of higher mammals

Fig. 6 (See text)

II Retinotopic organization of the primary visual pathways

As the model for this study, the architecture of the cat visual system displays an anatomical organization that is very similar to those of primate and human, at least until the primary visual cortices. Its characteristics for binocular vision make it the appropriate model to study the fundamental processes of the first stages of visual perception. Before reaching the primary visual areas, the visual information flow run through different pathways organized as follow (Cf. Fig. 6):

Luminance variations, contrasts and cues from the visual environment are projected and imaged by the optic system of the eyes and imprint photoreceptors of the retina. Information from peripheral part of the visual field is collected by the lateral part of the nasal and temporal of the retina whereas the central parts are projected onto a vertical band including the area centralis. In the inner surface of the eye, transduction by photoreceptors, local contrast detection, spatial filtering and compression are processed by the laminar organization of retinal neurons (Marr, 1982). The neural messages coming from nasal retina cross the midline through the optic chiasm to be sent into the contralateral hemisphere. This crossed route is the former one along phylogenetic history and it is the first to develop during the ontogenetic period. In contrast, the ipsilateral pathway does not cross the optic chiasm and conveys messages from temporal retinas. This route occurs lately during the evolution and is related to the emergence of binocular vision with the progressive fusion of the binocular overlapping zone coming along the drift of the eyes axis from lateral to frontal position. Both routes converge into the visual thalamus formation referred as the dorsal lateral geniculate nucleus (LGNd) for a more subtle spatiotemporal analysis (Hubel & Wiesel 1961; Sherman & Koch, 1991). Moreover, a naso-temporal overlap in the retina allows messages from the vertical meridian and its vicinities to reach both visual cortex through the thalamus (Stone, 1966; Sanderson & Sherman, 1971). The spatial organization of the LGNd keeps a retinotopic organization conjugated to a multi-layered segregation between contralateral (nasal) and ipsilateral (temporal) inputs (Bishop et al., 1962; Sanderson, 1971). At the level of the LGNd the separation between each visual hemifield is almost complete and this separation is kept until the projection to the primary visual areas A17 and A18 through the optic radiations.

Both primary visual areas A17 and A18 follow a retinotopic organization in a mirror symmetric way regarding to each other (Tusa, 1978 ; 1979) The projections of the vertical meridian region of the visual field including a narrow part of the ipsilateral field fall into the transition zone between these areas (Payne, 1990, see Fig. 7). This transition zone (TZ) is defined by progressive changes in the cytoarchitecture and thicknesses of cortical layers (Otsuka & Hassler, 1962; Milleret et al., 1994)

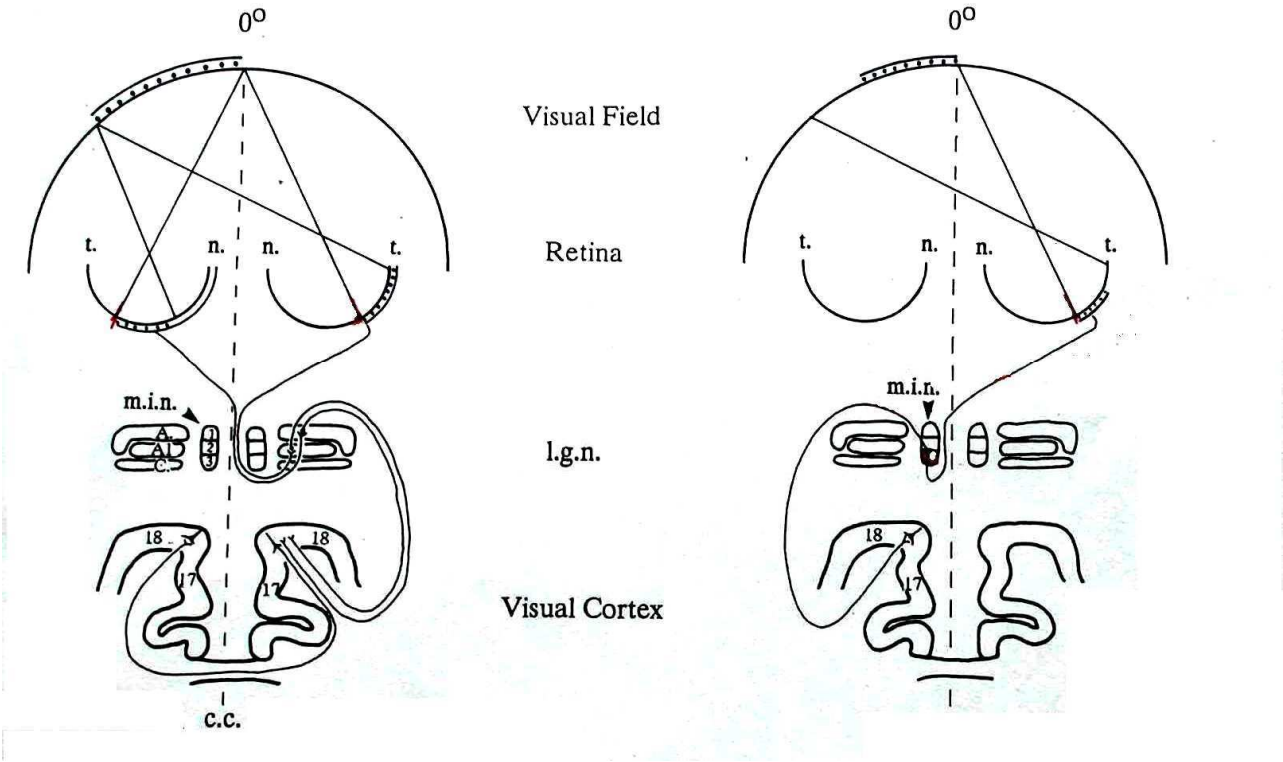

Fig. 7: **Schematic diagram showing the main routes for the representation of the ipsilateral visual field.**
Left**:** Ganglion cells in nasal retina (n.) project axons to the contralateral LGNd and ganglion cells in temporal retina (t.) project axons to the ipsilateral LGNd. Contralaterally projecting retinal axons terminate in mainly in layer A of the LGNd. Ipsilaterally projecting axons terminate mainly in layer A1. The retino-thalamo-cortical pathway is completed by neurons in the LGNd projecting axons to area A17 and A18. In areas A17 and A18, callosal neurons whose retinotopic location is close to the representation of the vertical meridian project axons through the corpus callosum and target the contralateral TZ. By this way, a part of the contralateral field map of one hemisphere is converted into an ipsilateral field representation in the opposite hemisphere. In other words, a part of the ipsilateral visual field is represented by this way in each hemisphere. Right: Another route, weaker than the former one conveys this ipsilateral visual field to the same cortical target. It originates from the temporal retina and crosses the optic chiasm and relayed by the medial interlaminar nucleus (m.i.n.); (from Payne, 1990).

occurring across 1 mm in average on the cortex. The region of the transition zone is known to concentrate the efferent and afferent fibres of the corpus callosum for which the organization of the connectivity is in correspondence with the retinotopy of the direct retino-geniculo-cortical inputs in the cortex (Payne 1990; Olavaria, 1996) . This organization follows a reciprocal TZ-convergent <=> TZ-divergent principle connecting cortical site in retinotopic correspondence between the hemispheres as shown in Fig. 6. In other words, following a "reentrant principle" for cortical connectivity (Edelman, 1993), the callosal efferent coming from areas 17 and A18 tend to project into the contralateral TZ (convergence from A17 and A18 into the contralateral TZ) and reciprocally (divergence from TZ). As a global characteristic, this retinotopic organization is submitted to local variations occurring with the constraints of the micro-functional structures of the cortex (columns) and as the "point to point" connectivity is a non-sens for cortical computation (Cowan, 1978; Edelman, 1993).

Distribution of interhemispheric connectivity of the primary visual cortex

In A17 and A18, callosal efferent cells i.e. neurons whose axons project through the corpus callosum are located in a stripe of cortex centered on the transition zone between A17 and A18 (Innocenti and Fiore, 1976). The distribution of callosal neurons varies along the rostro-caudal axis of TZ with higher density in posterior regions where their distribution can reach 3mm in both A17 & A18. The width of the distribution and the density of callsosal efferent neurons decrease in the anteriors regions of the visual cortex (see Fig. 8).

Cells projecting which axons projects through the corpus callosum are mainly located in the lower part of the layer II/III, the upper part of layer IV and layer VI (Innocenti and Fiore, 1976; Voigt et al. 1988; Boire et al., 1995). The vast majority of these callosal neurons are large pyramidal cells as revealed by many studies based on the retrograde transport of horseradish-peroxidase (Inocenti, 1980; Segraves and Rosenquist, 1982). These cells are larger than the neighboring non-callosal cells (Innocenti, 1980). The callosal pyramidal cells are localized in layer II/III and VI. In addition, non-pyramidal stellate cells in layer II and IV, and fusiform cells in layer VI also send callosal projections (Voigt et al. 1988). Nevertheless, these cells represent about only 20% of callosal efferent neurons and might have been revealed by trans-synaptic contamination of the tracer (Hughes and Peters, 1990). The great majority of callosal efferent neurons shows morphology of excitatory neurons. This was confirmed confirmed by electrophysiology and histochemistry revealing the glutamate as their neurotransmitter. Inhibitory callosal efferent neurons have not been observed yet.

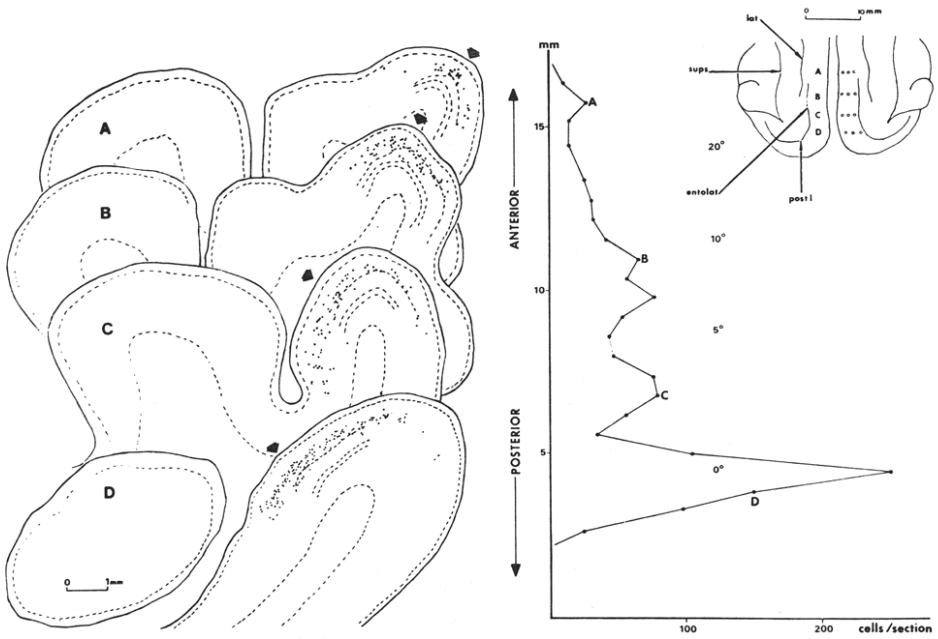

Fig. 8/ **Distribution along the lateral gyrus of neurons projecting into the corpus callosum**. Left: computer microscope reconstruction (80µm sections) indicating positions of HRP-positive neurons at different coronal levels of lateral gyrus. Only cells found in A17 and A18 are shown. In each section broken lines indicate the lower border of layer I, III, IV, V and V respectively. Arrows point onto TZ location. Letters relate each section to its lateral gyrus and in the plot. Right: number of HRP positive cell bodies per section at different antero-posterior levels (from Innocenti & Fiore, 1976).

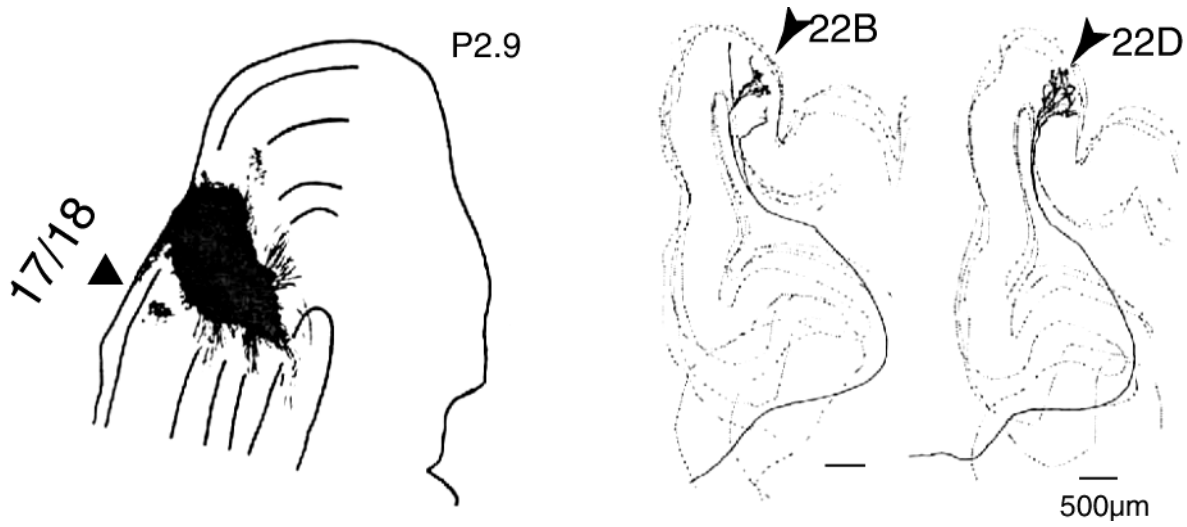

Fig. 9/ **Convergence of callosal terminals into the transition zome revealed by anteroragrade tracer injection (biocytin)**
Left: camera lucida drawing of the tracer injection site. The A17/A18 transition border is located by the arrow.
Right: Tridimensional reconstruction of the anterogradelly labeled axons showing the projection of callosal terminals into the transition zone (from Houzel et al, 1994).

Regarding to callosal terminals, their density is highest within a stripe of about 1 mm wide on the cortex coinciding with the transition zone revealed by cytoarchitectonic differentiation of A17 and A18 layers (Innocenti, 1980) (see Fig.9). This stripe has a much smaller width than the callosal efferent zone but follows a similar rostro-caudal shrinkage, narrower in the anterior region (Payne, 1986, Payne and Siwek, 1991). Callosal axons terminate in all cortical layers but with a higher density in layer II/III (Innocenti, 1980, Payne and Sywek, 1991, Houzel et al 1994). Most callosal terminals form asymmetric excitatory synapses on the spines of apical and basal dendrites of pyramidal cells (layers II/III and IV) or on dendrites of non-pyramidal cells (layer IV) (Voigt et al. 1988). Physiological experiments indicate that the excitatory callosal signal mainly target excitatory cells (Payne et al, 1991) but inhibitory transcallosal effect have been also described (Harvey, 1980; Innocenti, 1980, Payne et al., 1991) suggesting that callosal terminals may also target inhibitory neurons.

NR	A17		17-18		A18	
	TC+	TC-	TC+	TC-	TC+	TC-
	1	124	70	55	0	51
adultes	n= 125 1 ± 0.1%		n=125 56 ± 0.1%		n=51 0%	

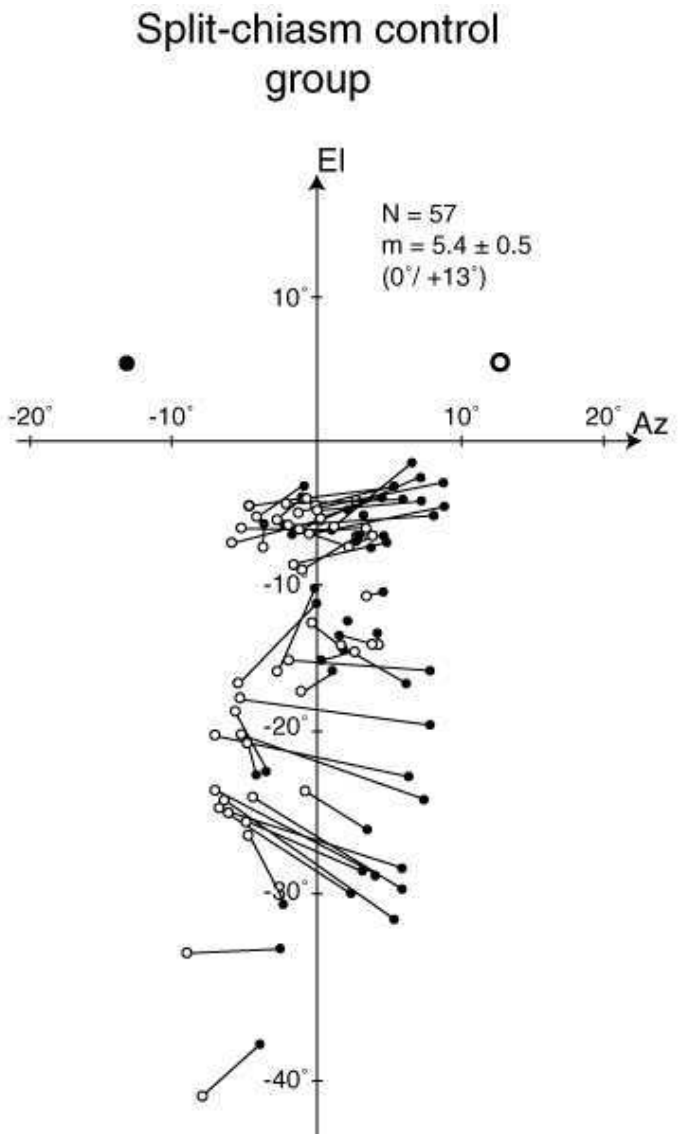

Fig. 10/ **Areal distribution and crossed binocular disparities of transcallosally activated unit**.
Top: number of cortical units responding to visual stimulation through callosal transfer inputs (TC+) or through the direct geniculocortical GC pathway (TC-) in primary visual areas bounding the transition zone. Direct GC and callosal TC pathways are experimentally segregated by split chiasm preparation. 56 +/- 0.1 % of cells recorded into the transition zone can be activated by callosal inputs (from Milleret et al. 1994). Bottom: Spatial distribution of pairs of receptive fields for binocular TC/GC units. Open circles stand for receptive field centres mapped through a GC units whereas filled circles stand for transcallosally activated units. Cells are recorded in the right hemisphere and TC/GC pathways are segregated by split chiasm preparation. Remark the disparities almost all cross the vertical meridian (cross disparities) and thus TC receptive fields generally fall into the ipsilateral visual field (from Milleret & al., 2005).

Physiological characterizations of transcallosal targeted cells

The first fine characterisation of cells driven by callosal input was performed thanks to a preparation with sagittal section of the optic chiasm (Berlucchi & Rizzolatti in 1968), depriving both visual thalamus of their contralateral retinal inputs. In this preparation, in combination with the occlusion of the ipsilateral eye, any responding cell recorded in TZ region would be activated exclusively by callosal input (TC cell). Properties of the TC cells can thus be explored by comparing physiological responses driven either by callosal input or by the direct retino-geniculo-cortical (RGC) pathway and induced by stimulations of the contralateral or ipsilateral eye respectively. Berlucchi and Rizzolatti observed by this way that corresponding pairs of receptive fields spanned the vertical midline and display similar orientation preferences. Transcallosally activated units were shown to be orientation selective with all orientations being globally represented (Leporé & Guillemot, 1982; Milleret et al., 1994).

The split chiasm preparation allows the evaluation of the proportion of visual cells activated by callosal input (cf. Fig. 10) confirming the denser transcallosal connectivity into the transition zone (Milleret et al. 1994). The major contribution of the transcallosal pathway to the representation of the ipsilateral visual field was thus reported (Milleret & Buser 1993; Milleret et al, 1994; Milleret et al, 2005). All studies confirmed that the receptive fields of neurons activated by the corpus callosum are centred on the vertical meridian or on its flanking regions. The lateral extents of these receptive fields go up to 13° in the ipsilateral field and 6° contralateral field with centre positions at 9° and 4° respectively, with a mean surface corresponding to 16.4 +/- 2.8 deg^2 (Milleret & Houzel, 2001; Milleret et al. 2005). The positions and the lateral extents of these receptive fields vary according to the elevation with shrinkage when crossing the horizontal meridian corresponding to the region of projection on the area centralis (Hourglass shape). Moreover, binocular TC units were reported to be more strongly activated by the RGC pathway than by the transcallosal pathway.

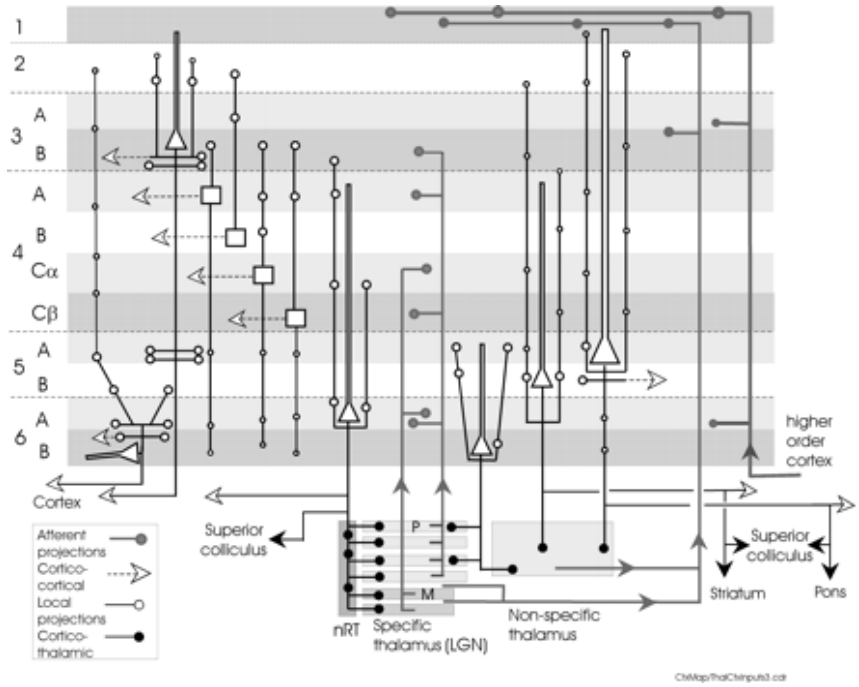

Fig. 11/ **Layered organization of mammalian primary sensory cortex**. Some of the major afferent inputs to, efferent projection from, and local intralaminar excitatory connections are represented in a idealized mammalian primary sensory region. Pyramidal cells are depicted by triangles with only the length and the termination layer of the main apical dendrite indicated. Layer 4 spiny excitatory cells, which includes pyramidal cells and spiny stellates, are depicted by squares without dendrites. Two size of axon terminals (circles) are used to indicate the relative anatomical strength of intracortical connections. Local intralaminar connections typically arise from all spiny neurons and only some are indicated. Longer distance, intra and interareal horizontal projections are indicated by open arrows those traveling via the white matter drawn below layer 6. Corticothalamic terminals are represented by filled circles and other subcortical projection by filled arrows (From Thomson and Bannister, 2003).

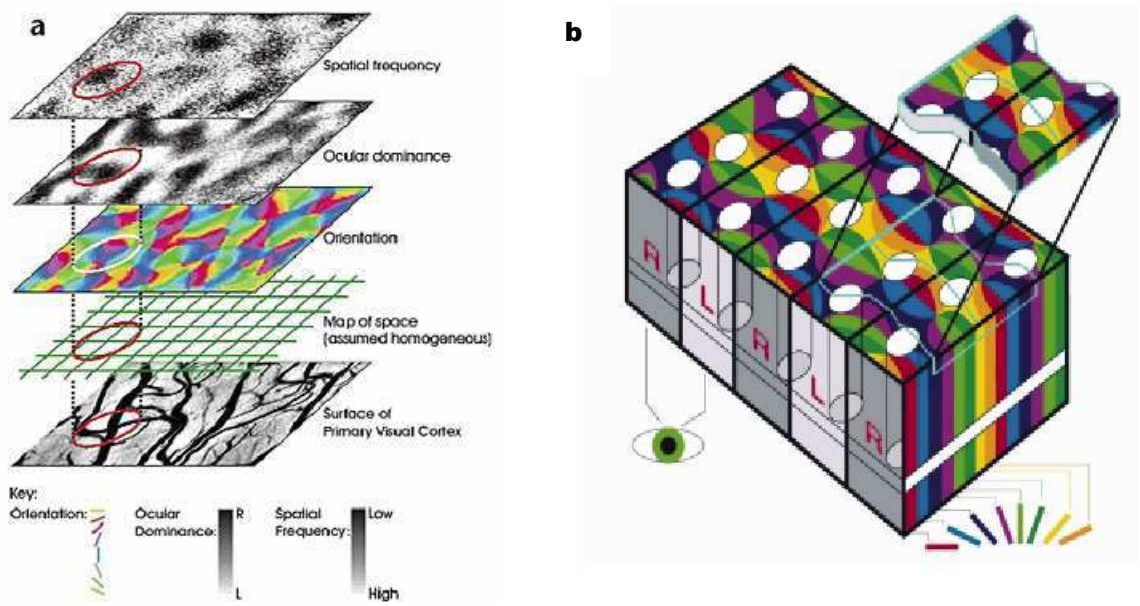

Fig. 12 (a) **The cortical sheet as a superposition of functional maps**, including preferred orientation, ocular dominance and spatial frequencies. (b) schematic map showing the relationships between ocular dominance and orientation preference maps and the cytochrome oxidase blobs. Black lines mark the borders between columns of neurons that receive signals from different eyes. This segregation is partially responsible for depth perception. White ovals represent groups of neurons responsible for color perception (blobs). The 'pinwheels' are formed by neurons involved in the perception of shape, with each color marking a column of neurons responding selectively to a particular orientation in space. The iso-orientation lines (appearing as a border between two colours) tend to cross borders of ocular dominance columns (black lines) at right angles. The top "slice" above the "ice cube" model depicts two adjacent fundamental modules (400 micron to 800 micron). Each module contains a complete set of about 60,000 neurons, processing all three features of orientation, depth and colour and is referred as an hypercolumn. This scheme is simplified in that clockwise and counter clockwise pinwheels are perfectly interconnected. In reality this simple relationship does not exist (Modified from Bartfeld and Grinvald, 1992).

III Functionnal architecture of primary visual cortices A17 and A18

Like the others primary sensory areas, the visual cortex shows a dual organization with layers and columns. The intense interlayer communication of cortical cells favors neural cells arranged along these vertical pathways to respond to similar stimulations (see Fig. 11). From the functional point of view, this microcolumnar organization was first observed by Mountcastle in the somato-senrory cortex (Mountcaslte, 1957). Soon after, Hubel & Wiesel demonstrate a microcolumnar organization in the cat visual cortex by recording neurons responding to similar orientation preferences when the electrode penetrate radialy into the cortex whereas the orientation preference vary almost continuously when moving over the surface (Hubel and Wiesel, 1962). Many other specific responses have been attributed to neurons of the primary visual cortices regarding to the parameter used to define the stimulation. Thus neurons of the primary visual cortex are known to respond specifically to oriented contrasts, but also to spatial and temporal frequencies, to the directions of movement and with a preference for one or the other eye (ocular dominance columns) particularly pronounced for the cat in the layer IV receiving mainly the efferences from the thalamus. All these local attributes of the visual scene combined with their positions in the visual filed can modulate the strength of response of neurons and give rise to a modular description of the visual cortex with a superposition of functional maps (see Fig. 12).

Initially reported with single and multiunit electrophysiological recordings, the exploration of these parameters over wide population of neurons took great advantages of the optical imaging techniques. In its intrinsic version, this methods allows to record simultaneously physiological responses correlated with neural activity with matrix of thousands photodectors (pixels of a CCD camera) with a high spatial precision (~50µm/pixel) (Salzberg et al. 1973; Grinvald, 1986). Its Application to the visual cortex in cat and monkey allows to characterize the organization of its functional maps such as orientation maps (Swindale et al. 1987), direction selectivity maps (Swindale et al. 1987; Shmuel and Grinvald, 1996), spatial frequencies maps (Huang et al, 2004) and ocular dominance maps (Obermayer and Blasdel 1993), principally. It confirms among others that iso-orientation contours within orientation maps converge onto singularities referred as pinwheels centres (Bonhoeffer and Grinvald 1991; 1993) having two types of clockwise and counter clockwise for chirality . As the responses of cells are very dependent regarding to the different parameters of description of stimuli, the relationships between these cortical maps have been explored (Bartfeld & Grinvald 1992; Hubener et al, 1997). Nevertheless it was suggested recently that the response of neurons of the visual cortex might rather characterize rather the detection of particular spatiotemporal combinations of these “canonical” parameters (Basole et al. 2003).

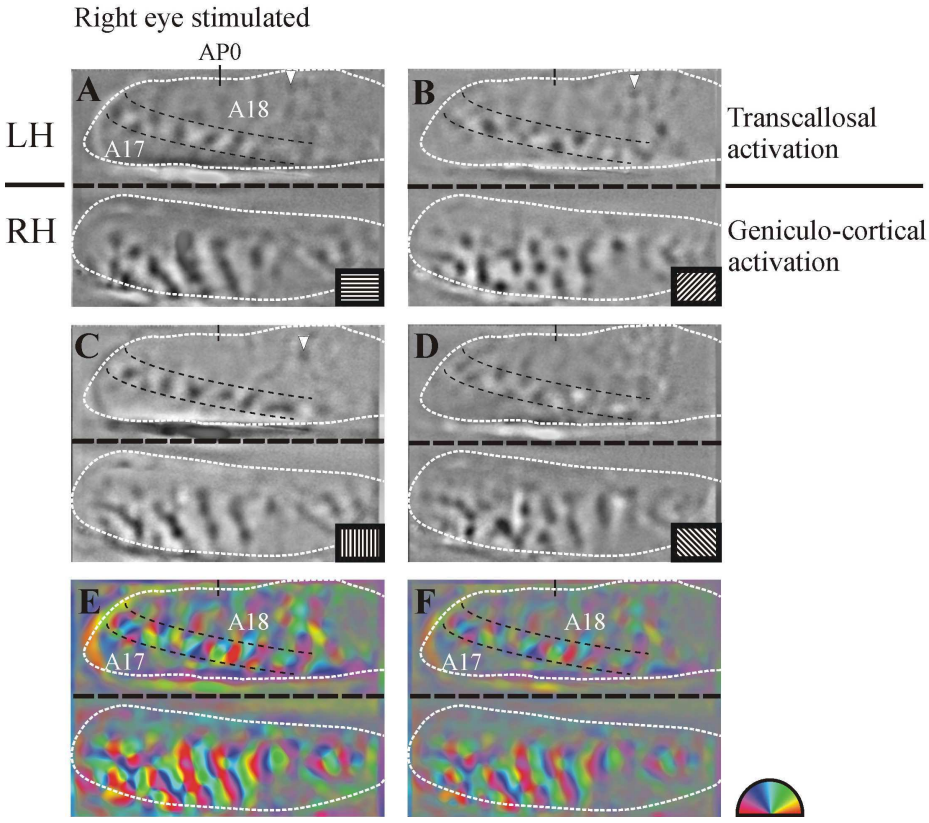

Fig. 13: **Layout of the transcallosal activity in areas A17 and A18 of the cat visual cortex revealed by optical imaging of intrinsic signal in a split chiasm preparation**. The right eye of the cat was stimulated with gratings of 4 different orientations (lower right corner of panels A-D). A-D: Single conditions maps showing by darker nuances the neural activity evoqued by visual stimulation through the direct RGC pathway (RH) and via a pure callosal transfer (LH). E-F: Polar map reporting the vectorial summation of the 4 single condition maps and normalized by cocktail blanck (E) or blanck condition (F); the preferred orientation is coded by colour index and brightness indicates relative strength of the orientation tuning (from Rochefort et al. 2007).

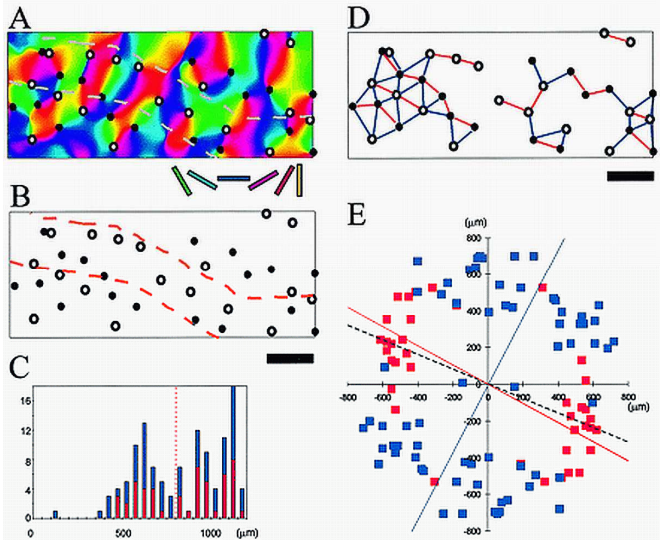

Fig. 14/ **Arrangement of orientation pinwheel centres along the transition zone**. (A) Orientation preference map and orientation pinwheel centres. Filled and open circles represent clockwise and counter-clockwise pinwheel centres. Dashed line shows the location of TZ. (B) Only pinwheel and TZ locations are shown.(C) distribution of distances among all the pairs of pinwheel. Red and Blue bars indicates the number of pinwheel pairs of the same type and opposite types respectively. (D) definition of neighbouring pairs of pinwheel. There are 19 pairs of the same type and 29 pairs of opposite types. (E). Scatter plot of the relative position of neighbouring pinwheel centres. The abscissa and ordinate show the distance between neighbouring pinwheels along antero-posterior and latero-medial axis respectively. The red and blue squares represent pinwheel pairs of the same and opposite types respectively. Red and Blue solid line indicates the direction of the first principal component for each group. The dashed line represents the average direction of TZ (From Ohki et al. 2001).

As we shall see in the second part of this thesis, continuing the development of optical imaging techniques with higher temporal resolutions with the use of extrinsic voltage sensitive dyes (Tasaki et al. 1968; Grinvald and Hildesheim, 2004) might greatly contribute to the exploration the spatiotemporal dynamics of the visual cortex

The optical imaging of intrinsic signal allowed to precise the characteristics of the transition zone. Images of the location of the A17/A18 transition border in the primary visual cortex of the cat were obtained by use of differential optimal response to spatial frequencies between A17 and A18 (Bonhoeffer et al. 1995). The orientation selectivity into the transition zone has also explored (see Fig. 13 and Fig. 14). Whereas Bosking and collaborators reported that callosal connections appear to terminate without regard to the map of orientation preference in the tree shrew striate cortex (Bosking et al, 2000), Rochefort and colleagues reported by contrast in the cat that callosal connections tend to connect similar orientation domains between each hemispheres (in preparation) . Moreover, Ohki and collaborators reported a particular organization of pinwheel centres in the transition zone, with pinwheels centres of the same types arranged in rows parallel to the transition zone alternatively (Ohki et al., 2001, see Fig. 14). The characterization of cortical functional maps in the transition zone combined with anatomical 3D reconstructions of callosal efferent is of great interest to understand the contribution of callosal linkage to the perception of the region of the vertical meridian.

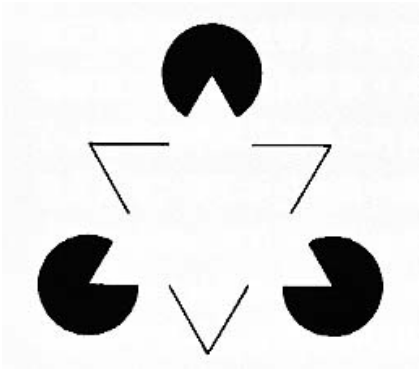

Fig. 15/ The famous Kaniza triangle illustrating the faculty of construction of amodal contour by the visual perception and raising the question of the "binding problem". The primary visual cortex can perform the detection of local orientations (edges of the "pacmans") as element of forms contours but these local attributes can likely belong to one or another perceived form in a typical figure/background situation, in case of object superposition, or in such case of ambiguous figure. The binding problem raises the question of the processes allowing separate cells responding to local attributes, to be gathered and create the coherence of single perceived object.

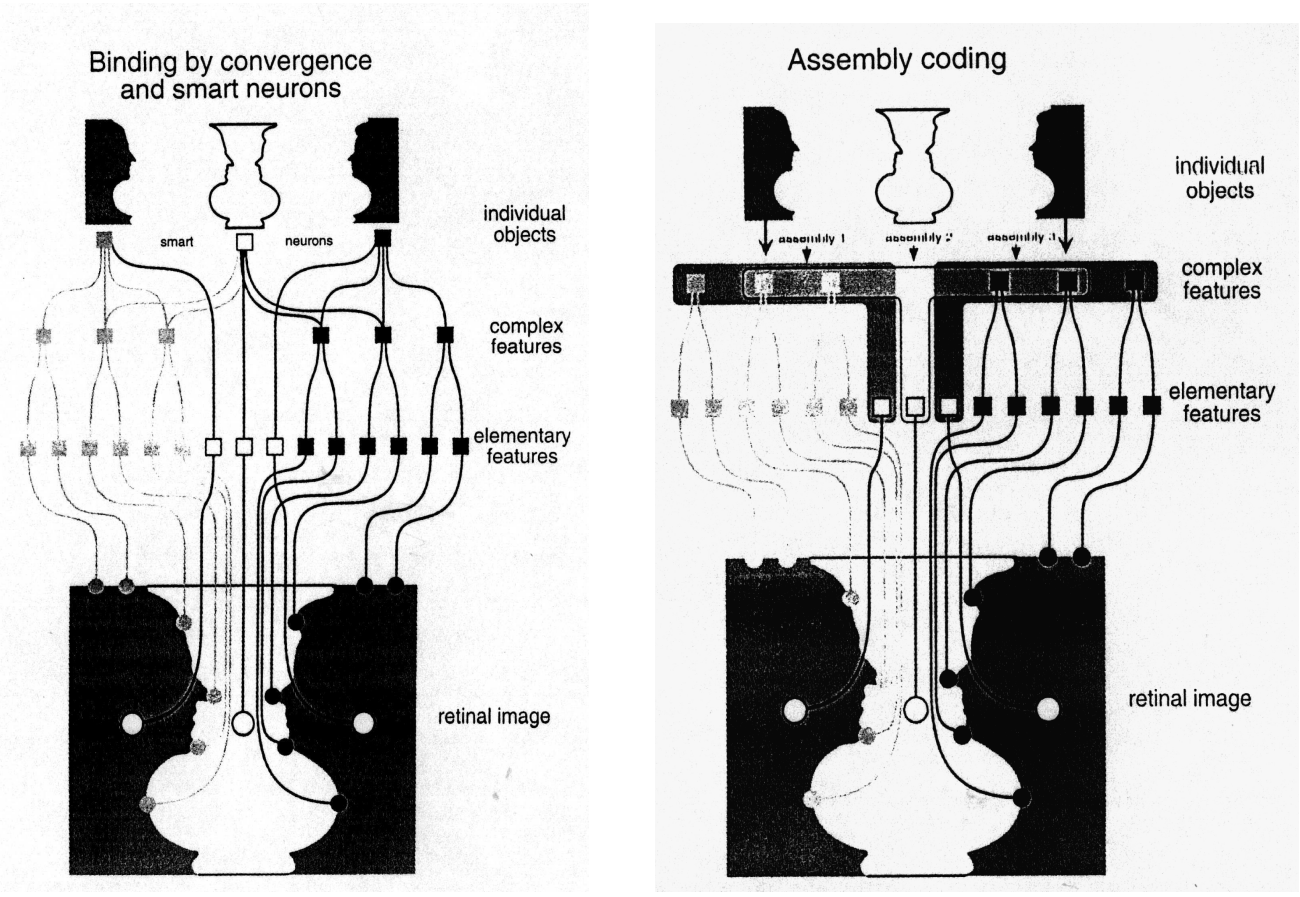

(a) (b)

Fig. 16/ **Two theoretical frameworks aiming to answer to the "perceptive binding problem"** (a)Schematic wiring diagram of a hierarchically organized feed forward network binding features by convergence on smart neurons that responds selectively to different perceptual objects. (B) Wiring diagram of neuronal architectures allowing the emergence of a unified perception by synchronized assemblies (From Singer, 2002)

IV Cortical dynamics

Possible roles for synchronizations

During the last two decades, the improvements of spatial and temporal resolutions of different *in-vivo* recording devices (i.e. f-MRI, MEG, multiunit recording and optical imaging) combined to the exponential increase of computational resources allowed to perform precise measurements and fine simulations of the cortical dynamics over large neural populations. This enables the exploration of hypothesis proposed by theoretical models on the brain dynamics.

The perceptive "binding" problem raises the puzzling question of the association of different neural populations which activities can be related to different features, to create a unique perceived "object" (See Fig. 15). When different visual features such as contours, colors, movements or any attributes from other modalities are known to be detected and analyzed by different cortical areas, the question of the communication processes underlying their association altogether into a unified coherent percept is still deeply tricky. Moreover, the general extension of the perceptual binding problem to all modalities and faculties of the brain (such as perceptive, mnesic, emotional, or motor faculties) naturally lead to wonder about the unity of consciousness considered in this framework as a global dynamic state embracing more or less intimate relationships with the environment and allowing to unify them all in a coherent self-organization. A former hypothesis exposed by Barlow suggested a strong hierarchical organization of the neural connectivity as a substrate for a stage convergent coding of the perceptual features onto "Grand Mother cells" or "smart neurons". These high level cells were assumed to be specialized in the detection of a single or restricted combination of attributes correlating the presence of a particular contingency of the environnement as a perceived object (Barlow, 1972) (see Fig. 16 (a)). Although satisfying for several points, this convergent coding hypothesis raises two major problems referred as the "combinatory explosion" and the "superposition problem".

The first problem reports the too important numbers of specialized cells required treat the diversity of the environment to associate the particular combination of features of any object to a unique detection cell. The second one relates the difficulty of the convergent model to treat correctly the uncertainties concerning the attribution of local features. In some ambiguous conditions, some local features can belong to one form or another when they are present at the same place and time in the perceptive field. In other words this problem traduces the incapacity of the convergent model to discriminate superposed forms.

(a)

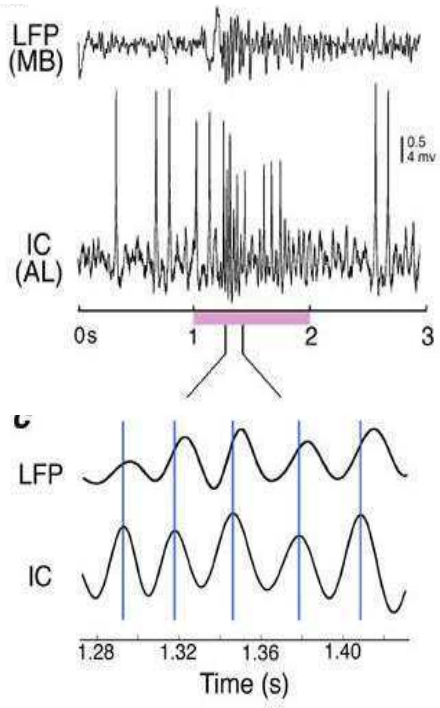

(b)

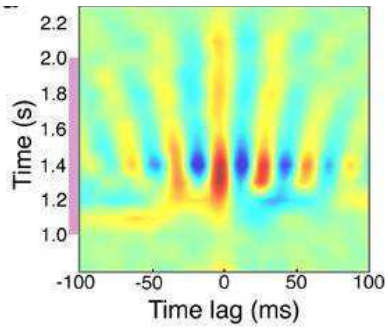

Fig. 17/ **High synchronization in the gamma band of the neural activity in the locust antennal lobe of the bee**. (a) Local field potential (LFP) and intracellular (IC) recording during olfactive stimulation (stimulation duration 1.0 s; purple bar) (b) Cross correlogram between previous traces showing the high 40 Hz synchronization correlating with odor discrimination. (from Laurent et al, 2001).

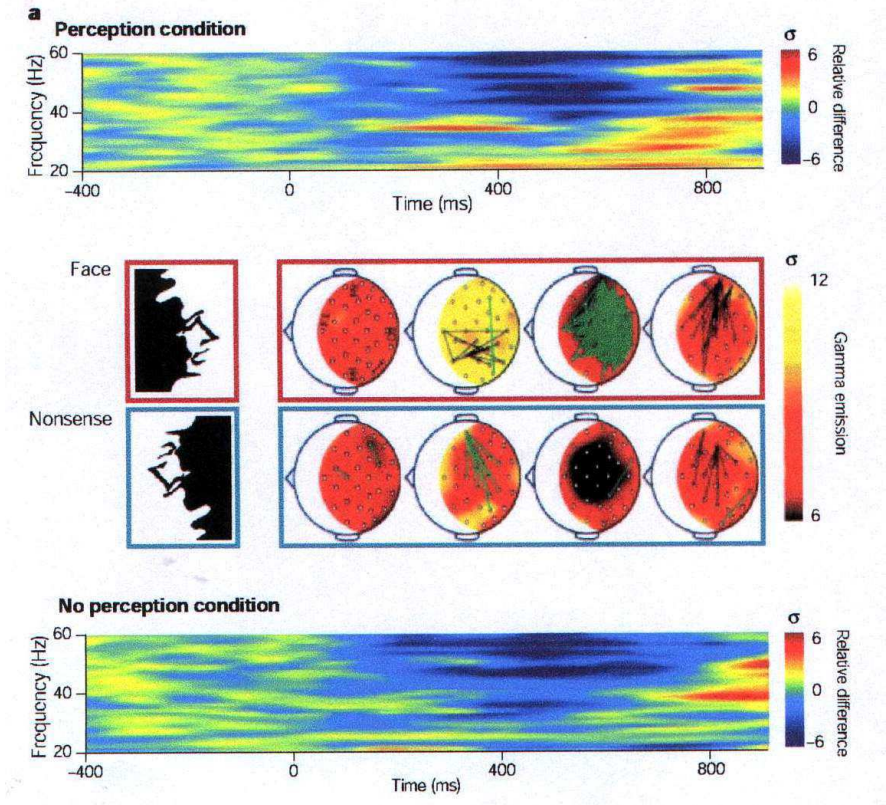

Fig. 18/ **Measurement of transient coherent dynamics on large scale of the cortex.**
Long distance synchronisation of the electroencephalographic signal during a face recognition task. The recognition of a high-contrast face lead to a highly selective increase in phase locking values (upper part) in the 40Hz range 200 ms after the stimulus presentation (at t = 0ms) which is absent when no face is recognized (lower part). The colour code indicates the degree of deviation from the from a reference period before stimulation. . In the middle panels, the perception condition is mapped onto surface electrodes. Here the colour code corresponds to the gamma emission (40 hz) over the scalp. Black lines indicate significant level of synchrony over successive moment of time. Green lines indicate a marked phase scattering between electrodes (From Varela et al, 2001).

Von der Marlsbourg first proposed a “correlation theory of brain functions” based on the hypothesis of synchronization coding to answer the question of the binding problem (von der Marlsburg, 1981, von der Marlsburg and Singer 1988). In this model, the neural units in charge of the analysis of local features of forms are bound together by synchronization of their activities providing by this way an identification of the neural assembly they belong to and giving the coherence of the perceived object (see Fig. 16(b)). This hypothesis provides satisfying answers to both combinatory explosion and superposition problems. Experimental results indicate that coherently active populations of cells are meaningful entities of information processing, rather than single "grandmother cell” neurons as suggested Barlow. In contrast to “grand-mother” neurons, for which experimental proof is still lacking, dynamic linkage of cells into assemblies has now been directly observed. The interest for the gamma frequencies band, ranging into 30-70 Hz regarding to authors, has increased since the emergence of coherent dynamics has been be correlated experimentally with discrimination or recognition tasks in various species from insects (Laurent et al. 2001; see Fig. 17) to vertebrates including human (see Varela et al, 2001; see Fig. 18) . Using simultaneous recordings with multiple electrodes, it has been shown that spatially separate cells in the visual cortex can synchronize their firing in the gamma band in response to a certain configuration of stimuli in the visual field (Gray et al, 1989; Engel et al, 1990).

By response synchronization, assemblies can be formed even across different visual areas and across the two cerebral hemispheres (Engel et al., 1991). It is currently assumed that highly distributed representational states can be established in a dynamic and flexible manner. This "binding" of distributed neurons into assemblies, which is controlled by local interactions, provides an example for the self-organization of ordered patterns in neuronal networks. From here the concept of *synchrony* should be extended to those of *coherence* defined by a particular spatiotemporal organization of the activity, stable and reproducible, with for example constant phase lags (so “off” synchrony), understood in the general framework of waves propagation. In this framework, information processing is not described as algorithmic sequences, but as a spread of activity through cortical areas leading to self-organization of highly distributed spatiotemporal patterns whose dynamic states represent the computational “result”. These patterns are determined by the nature of the cells, the topology of the cortical network and by its history, during which learning has induced adaptive structural changes. Interestingly, these arguments echo the former insights of the Gestalt psychologists. The holistic distributed processing proposed by means of synchronizations suggests the brain dynamics to have a *gestalt-like* organization, since the "meaning" of the activity of individual neurons depends on which other cells are active and with whom they fire in synchrony.

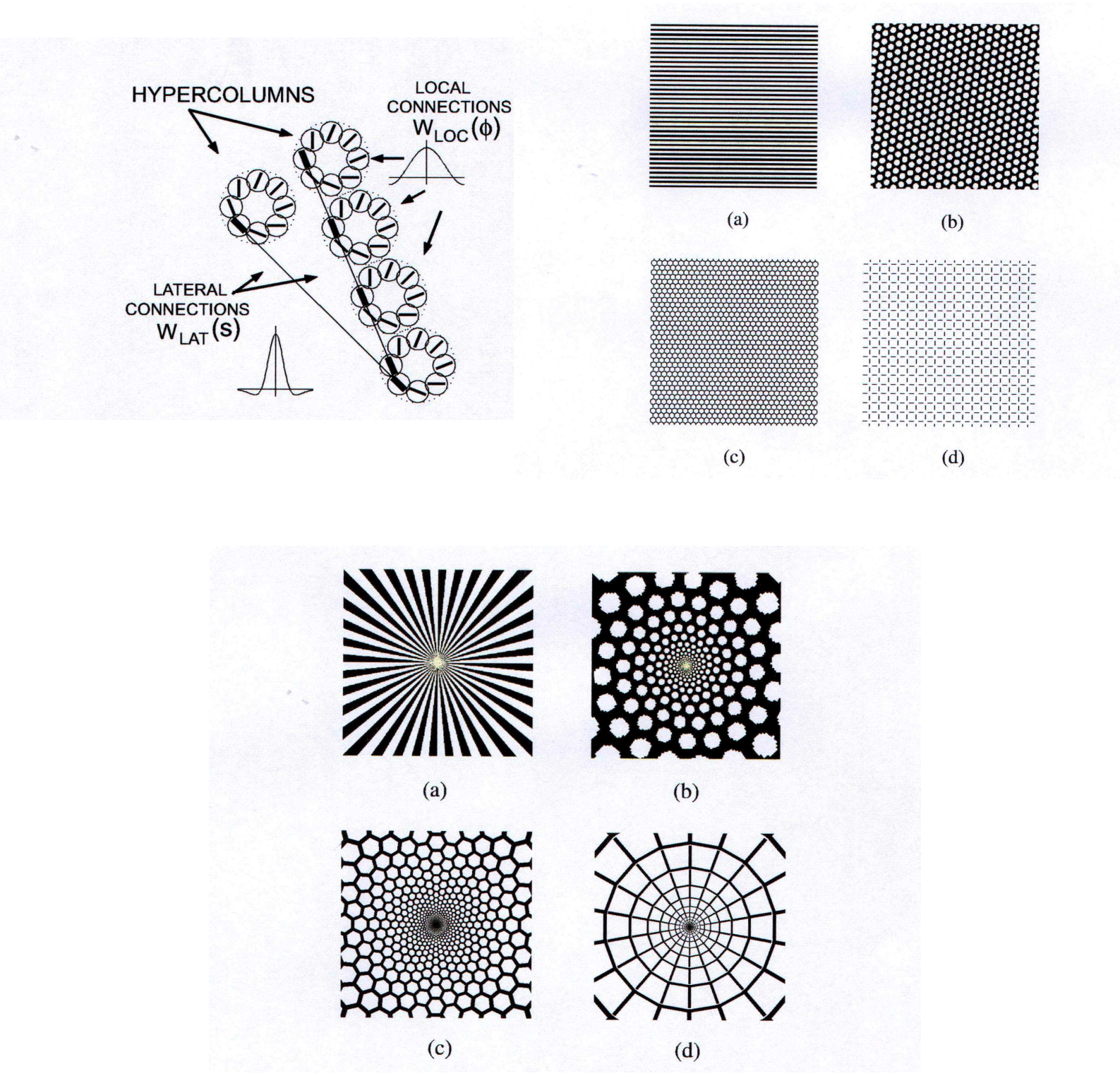

Fig. 19/ **Simulation of stationary states of the dynamic of the primary visual cortex.**
Top-Left: Outline of the architecture of the primary visual cortex. The local connections between iso-orientation patches within a hypercolum are assumed to be isotropic. The lateral connections between iso-orientation patches in different hypercolumns are assumed to be anisotropic; Top-Right: Different mode of stationary waves obtained by simulation in the cortical coordinates; Bottom: Same planform obtain for different mode of activities after application of the reverse logarithmic retino-cortical transformation, from the cortical to the visual field coordinate. (From Bressloff et al. 2002)

Because of the dense columnar organization of excitatory pyramidal cells in the cortex, the synchronization of cell firing is often reported to be tightly coupled with oscillations of the local field potentials (LFPs) indicating a strong local coherence of the neural activity (the coherence implying both oscillations and synchronizations). Characterized by spatio-temporal particular couplings, these electric waves can propagate and spread over the cortical surface (Varela et al, 2001; Cosmelli et al, 2001) and give rise in pathologic case to epileptic seizure. Recently, extensive works dealing with theoretical models and computational simulations based on oscillations and synchrony was elaborated to explore new hypothesis on the cortical dynamics. For example, the way that synaptic strength affects the phase lag between oscillators has been explored (Ermentrout & Kopell, 1994). Studies on the condition of emergence of coherent states but also desynchronization processes and phase scattering were reported in continuous and discrete time model (Tonnelier et al, 1999). Other studies reported “Correlated fluctuations” over large scale in the brain to be relevant for cortical processes that control the flow of information in the brain such as attention (Salinas & Sejnowski, 2001). Multiple “rythms” also can interact together to built complex functional assemblies by combining neural oscillators of different types. The stability of concurrent synchronizations between neural assemblies regarding to external perturbations can be evaluated (Pham & Slotine, 2007; Slotine & Lohmiller, 2001). Interesting results have been obtained concerning the oscillatory dynamic of the visual cortex combining knowledge on the synaptic organization of orientation columns and spatiotemporal computer simulations of the cortical dynamics (Bressloff et al, 2002). Oscillatory stationary states obtained by simulation of wave propagations in computational model of the visual cortex produced different modes of activities strikingly similar to form constants reported during visual hallucinations (See Fig. 19).

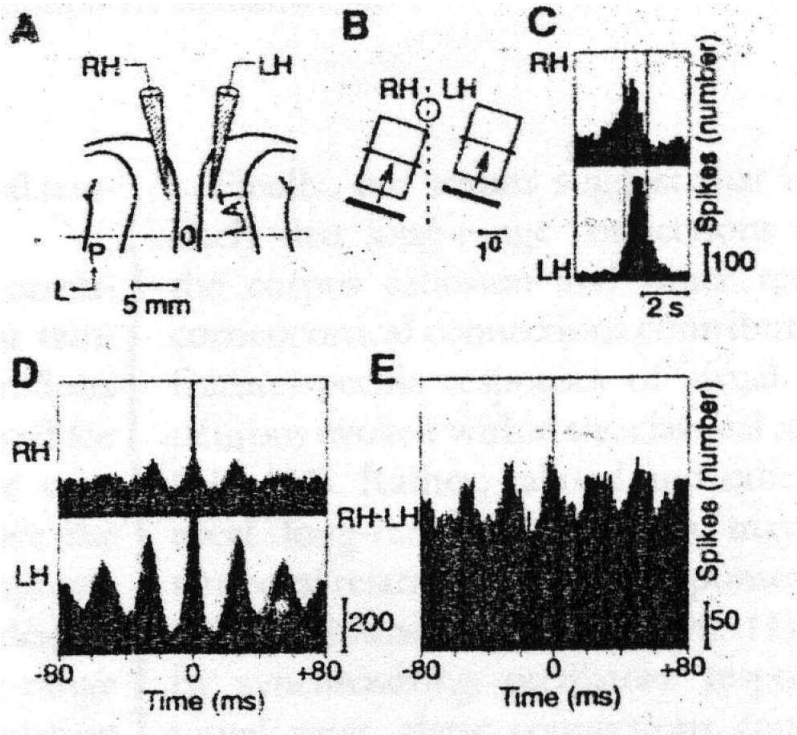

Fig. 20/ **Detection of interhemispheric oscillations and phase synchronizations between the primary visual cortices of the cat.** (A) The electrode were located in area 17 of the right hemisphere (RH) and left hemisphere (LH) close to the representation of the vertical meridian. (B) Receptive fields (RF) of the two recorded units. The cells had the same orientation preference and the RF were located in the respective contralateral hemifield within 4° of the vertical meridian (dashed line); Circle: centre of the visual field. (C) Histograms of the responses evoqued simultaneously with two ligh bars of optimal orientation. (D) Autocorrelograms computed for the two responses showing oscillatory response. (E) Cross-correlogram of the two responses showing the important gamma (40Hz) oscillatory activity of the cells and their synchronization (from Engel et al. 1991).

Interhemispheric timing, oscillations, synchronisations

Electron microscopy studies have shown that approximately two third of the visual callosal axons in cat are unmyelininated fibers with diameters of 0.08 to 0.4 µm. The remaining fibers are myelinated with diameters ranging from 0.25 to 4.0 µm (Berbel and Innocenti, 1988). Nevertheless only fibres in the splenium of the corpus callosum reach the primary visual areas and the diameters of callosal axons interconnecting A17 and A18 range from 0.25 to 2.25 µm (Houzel et al, 1994) indicating that the great majority of them are myelinated. Conduction velocities have been estimated ranging from 1.4 to 30.0 m/s (mean 13m/s) (Toyama et al. 1974; Harvey, 1980). Electrical stimulation applied into the corpus callosum or contralateral cortex have shown that most orthodromically excitated cells have latencies less than 3.0 ms (Harvey 1979). Transcallosal stimulations reported mean latency of antidromic responses of 2.73 +/- 2.3 ms near the transition zones (Innocenti, 1980) and 1.22 +/- 0.44 ms for commissural efferent cells in area A18 (Toyama et al, 1969). Similar Antidromic latencies were reported by McCourt et al 1990. Regarding to time dispersion within terminal arbors, work on simulation of spikes propagation performed in three-dimensional reconstruction of callosal axons reported dispersions of arrivals ranging from 0.3 to 2.7 ms (Innocenti et al. 1994).

On the other hand, important results were obtained by W. Singer's group about the interhemispheric dynamics of primary visual cortex in the region of the representation of the vertical meridian (Engel et al, 1991). Electrophysiological recordings revealed that not only coherent gamma oscillation patterns can occur within each hemisphere but they can also synchronize (nul phase lag) as revealed by cross-correlogram. Synchronizations were observed especially when receptive fields were on both sides of the vertical meridian and had similar orientation preferences (See Fig. 20). It was also showed that these interhemispheric synchronizations disappear after section of the corpus callosum while intra-hemispheric oscillations remain, demonstrating the necessary implication of the corpus callosum for the emergence of these coherent dynamics (Engel et al, 1991).

Moreover, regarding to synchronized activity only, Nowak et al. reported by performing multi-units recordings in TZ, three types of interhemispheric coupling modes for synchronization. They distinguished namely T-peak, C-peak and H-peak modes whose cross-correlograms have increasing mean widths of 3, 30 and 400 ms respectively (Nowak et al. 1995). The widths of the cross-correlograms give an estimation of the time windows within spiking activity of both recorded cells keeps being synchronized for each coupling mode. The narrows width T-peak mode is of important interest for us as the time windows for synchronization in this mode as of the same magnitude of the

mean interhemispheric transfer latency. So, whether these interhemispheric synchronizations could be driven or modulated by cortico-cortical connections (CC) promoting a coherent activity (in the LFP) or by a common source (i.e. a local stimulation in the central visual field, or in the same retina) whose signal is conveyed by divergent outputs targeting different cortical hemispheres, the latencies reported for the callosal transfer is compatible with the occurrence of short width T-peak synchronization. This support the hypothesis that the corpus callosum transfer could bring additional synaptic inputs to induce, enhance or sustain a synchronized activity between cortical sites in different hemispheres. This is much likely to occur that theses cortical sites are concerned by treatment of the same part of the environnement, like for example within the bilaterally represented vertical meridian. Moreover, dealing with the emergence of coherent activity, simulations of neural oscillators with reciprocal inhibitory connections have shown that the synchronization of fluctuations can be kept if the conduction time between two units do not exceed one third of the oscillation period (König et al. 1995). In case of the interhemispheric gamma oscillation (T~25 ms) recoded between primary visual areas of the cat (Engel et al., 1991), the 8 ms upper limit is compatible once again with the callosal mean latencies. Additionally, simulations of large neural networks reports effects of propagation delays on the dynamics of the network, and report them as a parameter allowing phase transition between a wide diversity of dynamical patterns including oscillatory bumps, traveling waves, lurching waves and standing waves (Brunel 2005). The interhemispheric communication seems to play an important role to enhance if not to induce synchronized bilateral activity as for the emergence of a coherent interhemispheric cortical dynamics, but it thus should be constraint by precise temporal characteristics.

At last, the convergence of synchronized input onto particular neural site might play an important role also during the development of the callosal connections in the framework of a Hebbian reinforcement hypothesis for the selection and the stabilization of the callosal connectivity. During these last two decades, the role of neuronal activity in the development of the retino-geniculo-cortical pathways in mammals has been extensively analyzed (Stryker & Harris, 1986; Galli & Maffei, 1988; Shatz & Stryker, 1988; Antonini & Stryker, 1993). The role of this activity in the development of callosal connections, and thus of the callosal cortical maps, is less understood (cf. Olavarria, 1996; 2001; Stryker & Antonini, 2001). One hypothesis is that the callosal reciprocal connections put in correspondence cortical sites having similar retinotopy and activated by input coming from the same eye (reffered as the “uniocular hypothesis”; Olavarria, 2001). However, it is clear that the developments of pathways from both eyes are tightly coupled (Striker and Antonini, 2001).

V Aims of the thesis

The knowledge of the corpus callosum and its contribution in cognitive functions remain quite incomplete both in adult and during development, whether conditions are normal or impaired. This results at least in part from the failure to have precise and complete data on some major aspects of the interhemispheric integration of neural messages including its characteristics both in spatial and temporal domains, the way they emerge or they are modified in case of sensory deprivation. As shown above, some important data about these aspects are available in the literature already, more especially about the visual system, but they are sparse because of some limitations imposed by technical approaches. We propose here a multidisciplinary approach including anatomical descriptions, 3D reconstructions and computational characterization of the synaptic spatial dispersion, and simulations of spike propagation to clarify the spatiotemporal characteristics induced by callosal axons morphology. Moreover, in order to collect comparable experimental data, we developed optical imaging technique (IO-VSD) to record the interhemispheric communication on large populations of cortical cells, with both spatial and temporal high resolutions.

For higher mammals, the vertical meridian region of the visual field is a very strategic place for perception. It merges both visual fields together and thus allows integrating continuity in the visual field. It might be also particularly implicated in the perception of lines, movements and depth in the central region of the visual field (Milleret et al, 2005). For all these faculties to be achieved properly, the visual system implicates a vertical stripe in each retina including the naso-temporal overlap region which projects directly to the retino-geniculo-cortical (RGC) pathway, and the splenium of the corpus callosum forming a set of interhemispheric connections in reciprocal retinotopic correspondence. In the primary visual cortex of each hemisphere, both of these projections converge onto a specific cortical region which is located at the transition zone (TZ) between areas 17 and 18. Because of its privileged implication in the visual perception of the vertical meridian region, TZ is of particular interest and it has been investigated both anatomically and functionally by different authors already *(Payne, 1990, Diao et al. 1990; Milleret et al.* 1994; Bonhoeffer et al. 1995; Ohki et al. 2000; Shmuel and Grinvald 2000, Rochefort & al,2007*)*. Although important, these data are nevertheless not complete enough to understand the exact contribution of TZ neural population in the visual perception of the vertical central region. Especially, the quantitative estimation of the spatial extensions of the callosal inputs into or close to TZ and their organization regarding to the cortical functional maps remains to be clarified to understand the role of the interhemispheric connections into the perception on the vertical meridian.

In the part I.1 of the thesis, we describe anatomically callosal axons observed after early monocular deprivation and characterize their particular spatial organization contrasting with those obtained under normal development. In order to quantify the morphological differences between these two populations we developed two original computational methods presented in the following chapters. The first method (Ch. I.2) is based on the ellipsoid approximation of the synaptic cloud and allows characterizing its global extension and orientation in particular with respect to TZ. For the second method (Ch. I.3) we developed a new clustering algorithm aiming to characterize the scattering and non-homogeneity of the distribution of axons terminals. With the development of these original computational methods we demonstrate the wider extensions and the much clustered aspects of the impaired callosal axons compared to the reference axons.

Moreover, the temporal profiles of activation of these connections are almost unknown. The timing of the interhemispheric information transfer might play an important role for two fundamental and complementary processes. First the convergence of synchronized signals onto a neural site might play an important role for the selection and the stabilization of neural connectivity during development. Besides, this developmental constraint may underlie particular dynamics processes inherent to perceptive faculties, such as the emergence of a coherent activity among wide neural population. The way the spatiotemporal characteristics are modified after early visual unbalanced impairment is of great interest to understand the organization and the role of interhemispheric connectivity. This may also clarify its role in the reorganization or compensation processes occurring during pathologic conditions or leading to different lateral organization of cognitive functions.

In Ch. I.4, we developed simulations of spike propagation within impaired callosal arborescences performed in order to check whether their unusually wider morphologies might induce important temporal dispersion of the contralateral neural message. As a main result we report that, although callosal axons reared under early monocular deprivation exhibit wider spatial extensions of their terminals, the spikes propagation in these structures keeps them in a close synchrony and we conclude that this temporal property remains very similar to those of normal structures.

In the second part of the thesis, we aim the compare these morphological characteristics and their spatio-temporal coupling with functional imaging data revealing also functional cortical maps. We introduce the experimental and analysis techniques related to optical imaging in its Voltage Sensitive Dye version (IO-VSD) developed to record *in vivo* the spatiotemporal dynamics of the interhemispheric connectivity with high precision both in spatial and temporal domains. Then we expose the limitation of the original system and describe some adaptations we developed for our purpose and show the primary results and latest advances of this experimental project.

As a conclusion, we discuss in the light of our findings the developmental and functional properties of callosal connections resulting from early monocular deprivation and the role of these properties in the construction of a coherent visual perception. At last we discuss the implication of the corpus callosum in the perception of the central visual field with a particular attention to the detection of the vertical bilateral symmetry.

PART I

Development of the callosal cortical maps in cat visual cortex

Comparing early monocularly deprived axons (MD) and normal adult axons (NR)

A multidisciplinary approach combining anatomy, models, and simulations

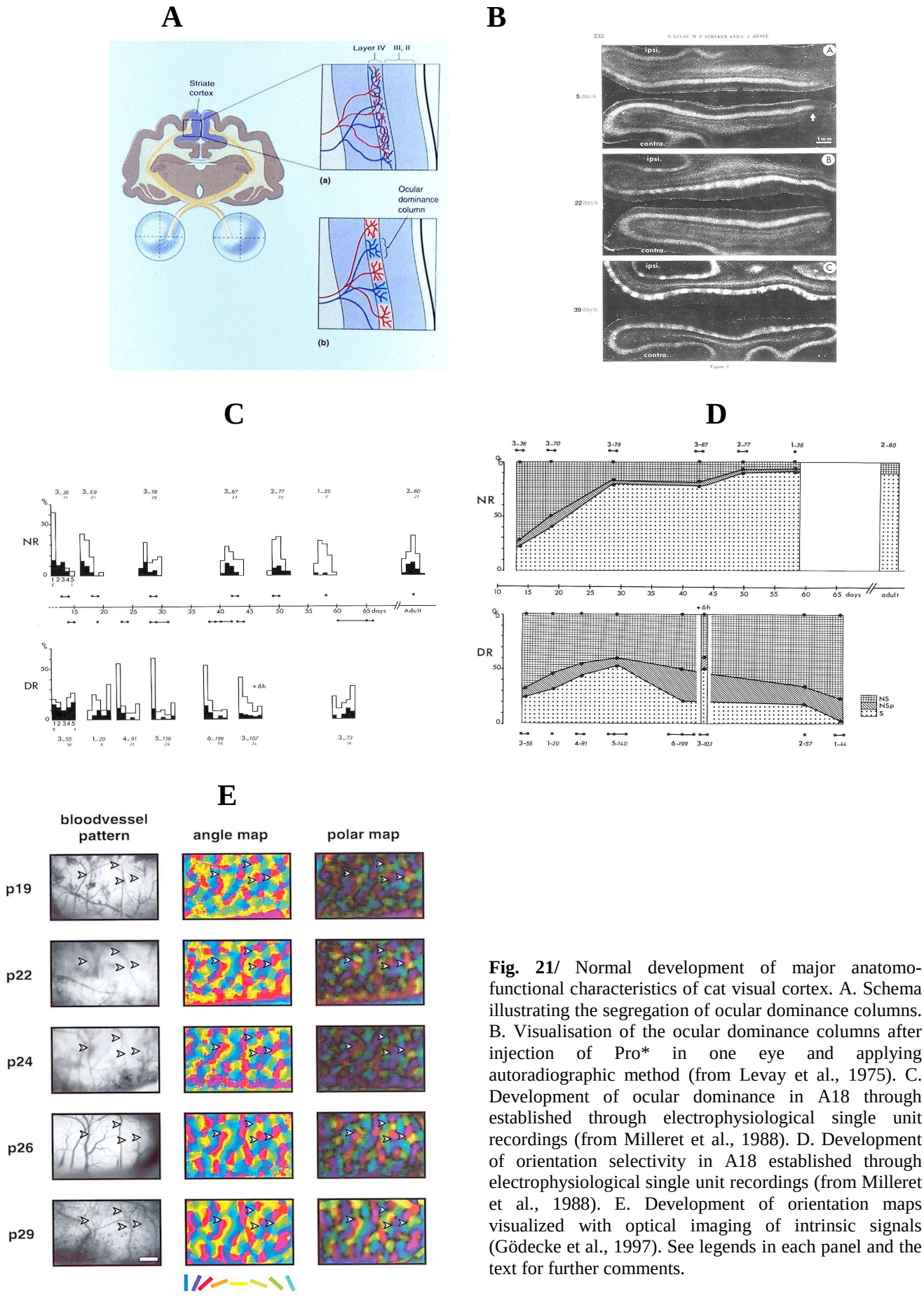

Fig. 21/ Normal development of major anatomo-functional characteristics of cat visual cortex. A. Schema illustrating the segregation of ocular dominance columns. B. Visualisation of the ocular dominance columns after injection of Pro* in one eye and applying autoradiographic method (from Levay et al., 1975). C. Development of ocular dominance in A18 through established through electrophysiological single unit recordings (from Milleret et al., 1988). D. Development of orientation selectivity in A18 established through electrophysiological single unit recordings (from Milleret et al., 1988). E. Development of orientation maps visualized with optical imaging of intrinsic signals (Gödecke et al., 1997). See legends in each panel and the text for further comments.

INTRODUCTION

During the course of development, structures in the brain undergo transformations according to sequentially implemented rules. In order to achieve the fine connectivity leading to the construction of cortical mapping of sensory inputs, developmental rules include routing of migrating neurones and growing axons by chemotropism and diffusion gradients of molecular cues, axo-axonal competition and hebbian-like synaptic potentiation. A general strategy employed by many developing intracortical pathways in many species is the initial overproduction of axons followed by selective elimination of some of them to yield the mature patters of connectivity (Price et al., 2006). The exuberant development of connections (that is the overproduction of axons, axonal branches and synaptic) followed by selection is one of the main process that underlies the development of many biological neural networks (Innocenti and Price, 2005)

This applies to the visual cortex in mammals. To summarize, for example in kittens, initially the inputs from the dorsal lateral geniculate nucleus serving the two eyes are intermingled in layer IV, with exuberant axonal branches. Then, over the course of foetal and early postnatal development, the inputs from the two eyes segregate into ocular dominance columns in layer IV through an *elimination* of some axonal branches and the *selective stabilisation* of other ones (see Fig. 21 A and B). In parallel, single units acquire progressively their functional properties such as ocular dominance and orientation selectivity, and are organized into *columns*. This has been established initially using electrophysiology (initially by Hubel and Wiesel). More recently, the imaging techniques have confirmed and extended these electrophysiological data (see also Part II).

At eye opening, ocular dominance of single units in cat visual cortex is strongly biased toward the contralateral eye. This is because, phylogenetically, the crossed retinal fibres correspond to the oldest visual pathway in mammals. Then binocularity develops progressively with age, during the 4 first postnatal months: each unit in cat visual cortex becomes progressively activated through both eyes, with however the cells displaying the same ocular dominance being regrouped into columns throughout the whole thickness of the cortex (Fig. 21 C). The corresponding functional maps of ocular dominance have been visualized a few years ago using optical imaging of intrinsic signals (Crair et al., 1998; 2001).

At the same time, each neuron in the cat visual cortex becomes selective for the orientation of the stimulus. Initially, i.e. at 2 postnatal weeks, when the eyes open, most of neurones (~80%) are not selective for the orientation: all the orientations of the visual stimulus (such as a slit) are effective to activate them; the others (~20%) are selective already, with however a wide angle of selectivity. Then, progressively with age, they become almost all orientation selective, with a rather small angle of selectivity, and are grouped for each orientation into columns across the whole 6 cortical layers. The whole process again terminates at ~4 postnatal months (see Fig. 21 D). This has been confirmed recently by using the optical imaging technique which allows visualizing the whole orientation map over extended portions of the visual cortex (see for example Fig. 21 E, from Gödecke et al., 1997).

A

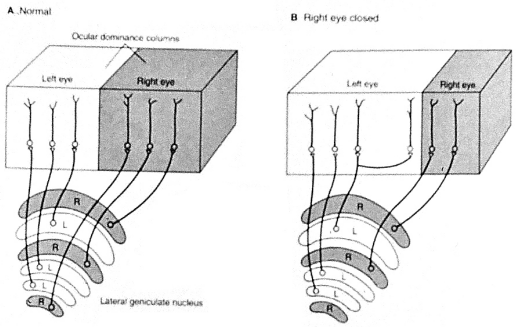

FIGURE 60- 7
This drawing illustrates how lack of vision in one eye might affect development of the ocular dominance columns.

A. Ocular dominance columns are normally equal in size for each eye.

B. Without vision in the right eye, the columns devoted to the right eye become narrow compared to those of the left eye.

According to the hypothesis illustrated here, deprivation of one eye changes the normal balance between eyes so that the geniculate cells receiving input from the nonfunctional (right) eye regress and lose some of their connections with cortical cells, whereas the geniculate cells receiving input from the left eye sprout and connect to cortical cells previously occupied by geniculate neurons from the right eye.

E. R. Kandel and J. Schwartz
Principles of Neural Science
Eds. Third edition 1991

B

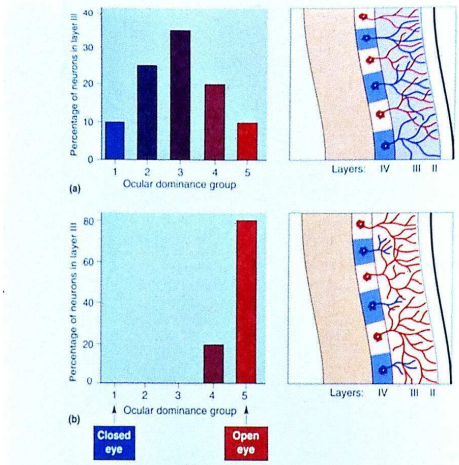

Figure 18.16
The ocular dominance shift. Shown here are ocular dominance histograms constructed after electrophysiological recording from neurons in the striate cortex of **(a)** normal cats and **(b)** cats that had been monocularly deprived early in life. The bars show the percentage of neurons in layer III in each of five ocular dominance categories. Cells in groups 1 and 5 are activated by stimulation of either the left or the right eye, respectively, but not both. Cells in group 3 are activated equally well by either eye. Cells in groups 2 and 4 are binocularly activated but show a preference for either the left or the right eye, respectively. The histogram in part a reveals that the majority of neurons in the visual cortex of a normal animal are driven binocularly. The histogram in part b shows that a period of monocular deprivation leaves few neurons responsive to the deprived eye. The illustrations to the right of the histograms show the likely anatomical basis for this change in physiology.

M. F. Bear, B. W. Connors and M. A. Paradiso
Neuroscience: Exploring the Brain
Eds. W.&W. 1996

C

WIESEL

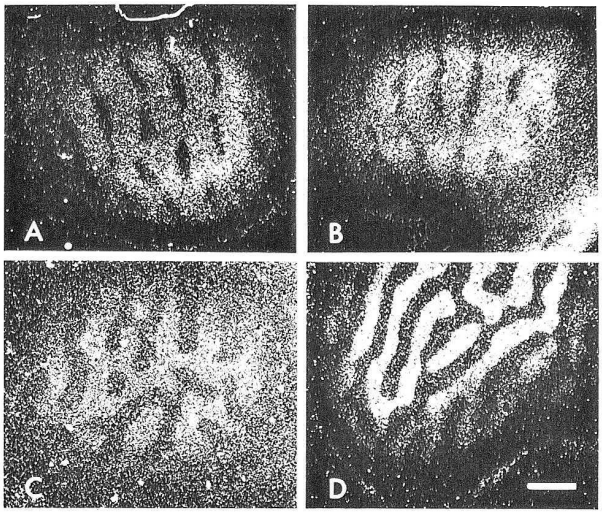

Fig. 6. Autoradiographic labelling patterns from the striate cortex of four monocularly deprived monkeys illustrating the distribution of geniculate terminals in layer IVC after closures at different ages. In all cases the normal (left) eye was injected with ^{3}H Proline thereby labelling the non-deprived geniculate terminals.[15]
A: Right eye closed at 2 weeks for 18 months. Same animal as in Fig. 1 (right), Fig. 4 (middle) and Fig. 5 (upper left).
B: Right eye closed at $5^1/_2$ weeks for 16 months.
C: Right eye closed at 10 weeks for 4 months. Same animal as in Fig. 5 (upper right).
D: Right eye closed at 14 months for 14 months. The unlabelled bar is 1 mm.

D

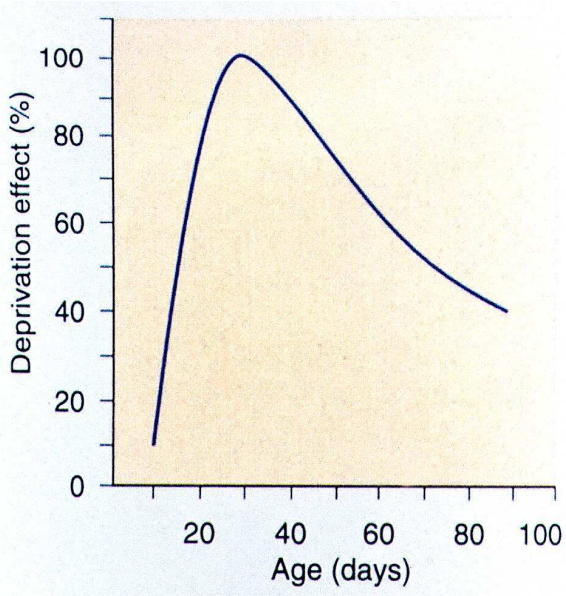

Figure 18.17
The critical period for plasticity of binocular connections in the kitten. Plotted here is the sensitivity of binocular connections in cat striate cortex to monocular deprivation at different postnatal ages. The deprivation effect is the percentage of neurons in area 17 whose responses are dominated by stimulation of the nondeprived eye. The critical period in cats begins at about 3 weeks and ends at about 3 months. (Source: Adapted from Olson and Freeman, 1980.)

M. F. Bear, B. W. Connors and M. A. Paradiso
Neuroscience: Exploring the brain
Eds. W.&W. 1996

Fig. 22/ Effects of monocular occlusion (MD) on the development of visual cortex. Definition of the *critical period*. A. Sketch summarizing how the columns of ocular dominance are modified after MD. B. Ocular dominance of the cells in cat visual cortex after MD. C. Changes of the ocular dominance columns depending on the age of induction of the MD. D. The critical period of plasticity of binocular connections in kittens. See the different legends in A, B, C and D for further details.

This normal development of anatomo-functional properties of cat visual cortex may be altered by an abnormal postnatal visual experience such as a lack of vision of one eye through monocular occlusion (MD). Again, this has been demonstrated by Hubel and Wiesel (see for example Wiesel and Hubel, 1963; 1965; Hubel and Wiesel, 1970).

While, at the end, the ocular dominance columns are equal for both eyes after a normal postnatal vision through both eyes, after MD, the columns devoted to the occluded eye become smaller compared to those of the normal eye (see Fig. 22 A). According to the hypothesis that is illustrated on the figure, deprivation of one eye changes the initial balance between eyes so that the geniculate cells receiving inputs from the non functional eye regresses and lose some of their connections with cortical cells, whereas the geniculate cells receiving inputs from the viewing eye sprout and connect to cortical cells previously occupied by geniculate neurones from the other eye. In agreement with this, neurones in the visual cortex become activated almost strictly by the viewing eye, and become not activated (or almost so) through the deprived eye (Fig. 22 B): the ocular dominance distribution becomes very strongly biased toward the eye that has been remained open.

Interestingly, this effect on ocular dominance columns and ocular dominance of cortical neurones is more or less effective depending on the age at which the monocular occlusion has been induced: a deprivation during a short duration (a few hours) may not be effective at some ages, while it may induce dramatic effects at some other ages (see Fig. 22 C and D). In kitten, if MD is induced at 2 post-natal weeks, it has a poor effect (if any). Between 2 and 4 weeks, the effect of MD increases progressively. Between 4 and 6 postnatal weeks, MD has the more dramatic effect: at that period, only a few hours of MD are sufficient to induce great anatomo-functional changes. Later on, the effect of MD decreases progressively. Such observations led Hubel and Wiesel (1970) to introduce a very important concept: that of the *critical period* (also called *sensitive period*) which corresponds in fact to a postnatal period of plasticity. During this period, the ability of the cortex to change, both anatomically and functionally, varies with age: in cat visual cortex, it displays a maximum at 4-6 postnatal weeks; in some other species, it also exist but with a differential time course. Of interest, this applies both to normal and abnormal viewing conditions.

Panel 1

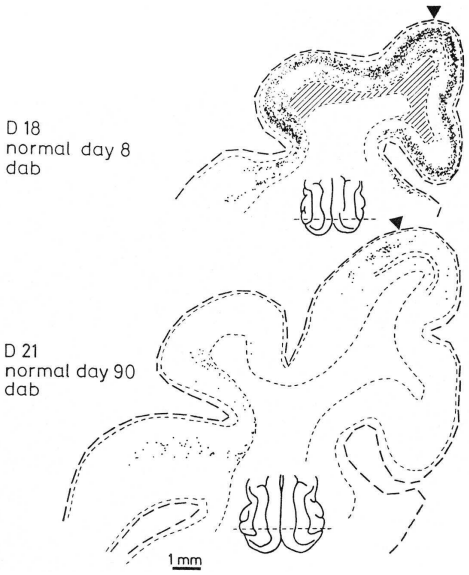

Panel 2

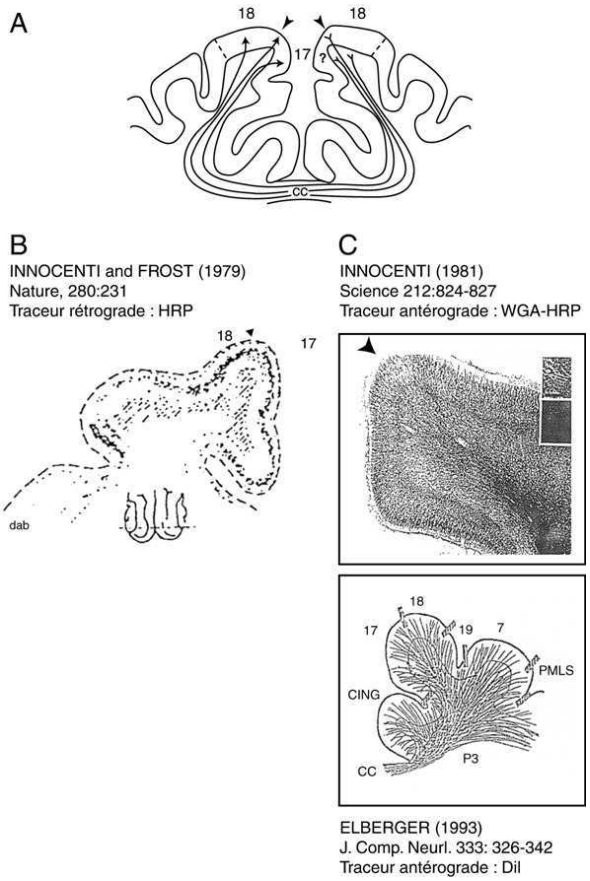

Fig. 23/ Normal development of callosal connections in cat visual cortex. *Panel 1* : Comparative distribution of cell bodies of callosal neurones in a 2 week-old kitten and an adult cat after retrograde labelling through HRP injection in the other hemisphere (from Innocenti, 1986). *Panel 2*: A. Illustration of the visual callosal connections in a young kitten soon after birth. B. Efferent callosal zone: widespread distribution of callosal neurons labelled after injection of HRP in the other hemisphere. C. Terminal callosal zone: illustration of the debate between Innocenti (1981) who demonstrated that callosal terminal were concentrated in the 17-18 transition zone from birth, and Elberger (1993) who demonstrated that callosal terminals penetrate widely the visual cortex early on.

As for many other cortical connections, the concepts described above apply to the fibres of the corpus callosum (CC) that transfer visual information at the level of primary visual cortex between the hemispheres. As a consequence, they also applied to callosal cortical maps that are defined by such connections, including both their anatomical and functional properties.

Development of callosal connections in cat visual cortex in normal viewing conditions (NR group)

At birth, perikarya of callosal neurones in cat visual cortex, which distribution corresponds to the "efferent callosal zone" (or "callosal efferent map"), occupy portions of both A17 and A18 including the transition zone (TZ) between both areas that are much larger than in the adult (Innocenti et al., 1977; Fig. 23, panel 1.). Consequently, callosal axons are more numerous at that age than at adulthood (Berbel and Innocenti, 1988). The callosal projections from one hemisphere to the other are thus "*exuberant*" in early life. However, within the contralateral hemisphere, they do not yet display any synaptic boutons in the cortical plate (Aggoun-Zouaoui and Innocenti, 1994; Aggoun-Zouaoui et al., 1996). No functional connection may thus be established at that time. The "callosal terminal map" is thus not formed yet.

Within the two first postnatal weeks (i.e. before eye opening), an *elimination* process of juvenile exuberant callosal projections occurs, reducing both the number and the distribution of the perikaria of the callosal neurones (Innocenti et al., 1977; see also Fig. 23, panel B). In parallel, the number of callosal axons evidently decreases with age (Berbel and Innocenti, 1988). Within the callosal terminal zone, the callosal axons continue to grow to finally penetrate the cortical plate. Some boutons within the visual cortex even become apparent, and their number increases progressively with age (Aggoun-Zouaoui and Innocenti, 1994; Aggoun-Zouaoui et al., 1996). The "callosal terminal map" thus begins to elaborate. Notice that some disagreements still remain upon the extent to which the exuberant callosal axons penetrate the cortex early on (Fig. 23, panel 2C). For some authors, they penetrate the visual cortex only at the 17-18 TZ, as in the adult (Innocenti, 1981; Innocenti and Assal, 1991). For others, callosal terminals invade initially large portions of cortex to regress later on (Kennedy et al., 1987; Elberger, 1993). The question presently still remains open although functional data may give some indications (see below).

Providing the postnatal viewing conditions are normal, the *elimination* process of callosal projections continues to occur from 2 weeks onwards. At the end, the perikaria of callosal neurones only occupy the 17-18 TZ and proximal portions of A17 and A18. Within the callosal terminal zone, both an *elimination* and a *stabilisation* processes likely take place. The exuberant callosal branches are eliminated, while the "pertinent" ones are stabilised almost strictly at the 17-18 TZ (Aggoun-Zouaoui and Innocenti, 1994; Houzel et al. 1994; Aggoun-Zouaoui et al., 1996). Not surprisingly, this maturational process occurs during the 4 first postnatal months i.e. during the whole critical period (see above).

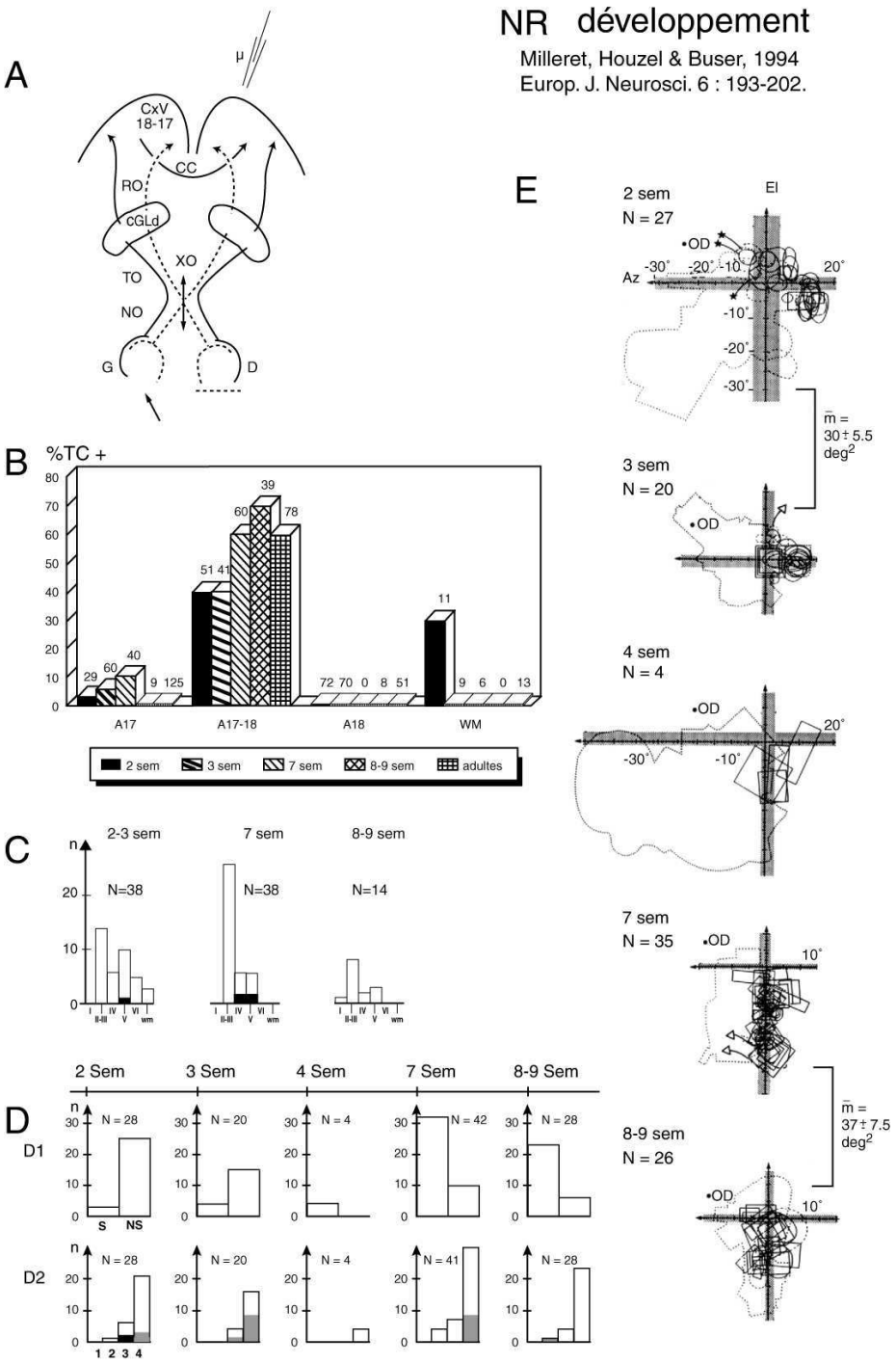

Fig. 24/ Pattern of development of the callosal transfer of visual information in cat visual cortex. A. Experimental protocol: the optic chiasm has been sectioned, permitting to activate selectively the corpus callosum by stimulating the eye contralateral to the explored cortex. B. Location of the transcallosal (TC) activated units as a function of age (from 2 weeks to adulthood). A17, area 17, A18, area 18; A17-18, transition zone between both areas; WM, white matter. C. Laminar distribution of the TC units as a function of age. D. Evolution of orientation selectivity (D1) and ocular dominance (D2) with age. S and NS, selective and non selective cells for orientation. 1, 2, 3, 4: ocular dominance of the transcallosally activated units, with 1 corresponding to those activated only through the contralateral eye, and 4 those which are binocular with a strongest activation through the direct retino-geniculo-cortical pathway. E. Spatial distribution of the receptive fields of the TC units (from Milleret et al., 1994).

Studying the functional characteristic of the transcallosally activated units (TC cells) as a function of age, Dr. Milleret and collaborators demonstrated that these cells properties also evolve during development, in parallel to anatomical changes, to reach stable characteristics again at ~4 postnatal months (Milleret et al., 1994; see also Fig. 24).

It has been first demonstrated that TC cells are almost located around TZ as soon as 2 weeks age birth, when eye lid opens in kittens (Fig. 24B). This is in agreement with anatomical data from Innocenti and collaborators showing that the callosal axons penetrate the visual cortex only with the 17-18 TZ early on, as in the adult (Innocenti, 1981; Innocenti and Assal, 1991 Aggoun-Zouaoui and Innocenti, 1994; Aggoun-Zouaoui et al., 1996).

While callosal axons originate mainly from cortical layers II-III and VI (Innocenti and Fiore, 1976), it has been also showed that the laminar distribution of their projections in the other hemisphere gets finer progressively with age: initially, they are distributed in all cortical layers, they finally reach almost only supragranular layer II-III from the 2 first post native months (Fig. 24, C).

Milleret et al. also established that the TC units: a) become selective for the orientation of the stimulus progressively with age, as the other cells do in general in the visual cortex; b) are mostly binocular early on, with a dual activation from both the corpus callosum and the direct ipsilateral retino-geniculo-cortical pathway (see Fig. 24, D1 and D2).

Finally, these authors demonstrated that the spatial distribution of the receptive fields of these TC in the visual field decreases with age, in parallel to the decrease of their size: at 2 weeks, these receptive fields are quite large and are distributed from the central vertical meridian to ~20° within the ipsilateral hemifield to the explored cortex; afterwards, the size of their receptive field decreases and the lateral extension of their spatial distribution also decreases progressively to reach ~8° in the adult (see Fig. 24, E).

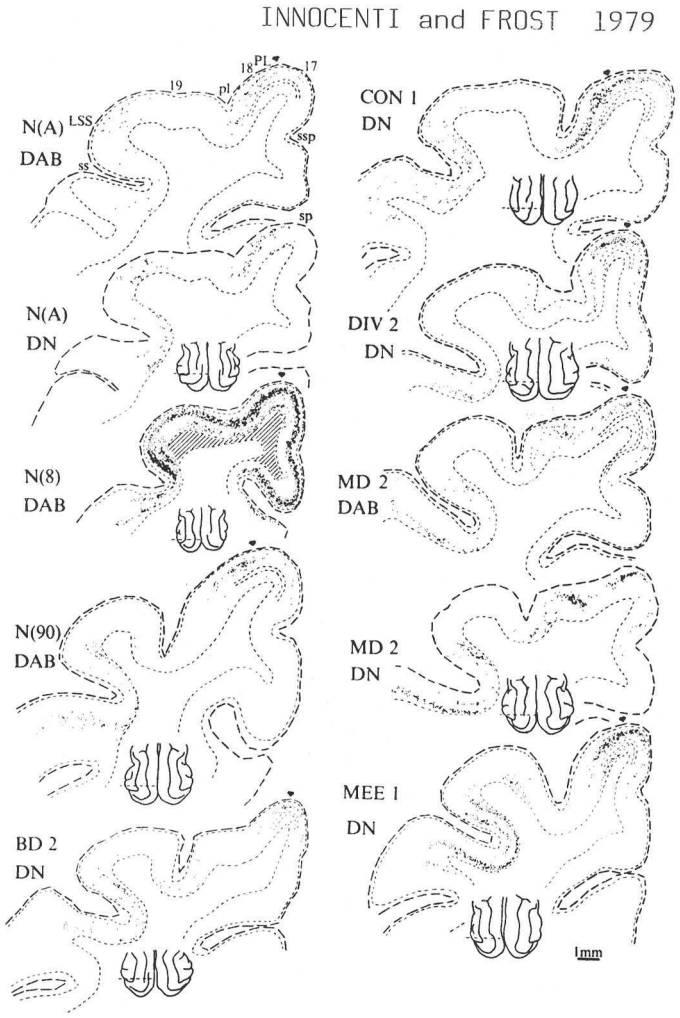

Fig. 1 Computer microscope[26] charts of the distribution of HRP-labelled callosal neurones in 80-μm thick coronal sections at comparable rostrocaudal levels of the visual cortex in different animals. Multiple, 0.5-μl injections of HRP (Boehringer grade I, 33% in sterile saline) were placed in the contralateral cortex. After a 2-day survival time, adjacent, 1-in-4 series of 80-μm sections of each brain were processed with diaminobenzidine (DAB)[1,4] and *O*-dianisidine (DN)[27]. Adjacent sections were reacted with the two substrates as shown for the normal adult, N(A), and for MD 2. In all animals, the injected postlateral and lateral gyri (areas 17, 18, 19) were invaded almost completely by dark HRP precipitate; HRP-filled neurones were found over most of the mediolateral extent of the ipsilateral lateral geniculate nucleus. Each HRP-labelled neurone is represented by a black dot. The level of each section is indicated on the inset drawn from a dorsal view photograph of the corresponding brain. In each section the thin, interrupted lines mark the lower boundaries of layers I, IV, V and VI (in N(8), lower boundaries of layers IV and V are not shown). In the DN sections from N(A) and MD 2 only the lower boundary of layer VI is marked. Cross hatching in N(8) indicates a region of displaced (migrating?) neuronal somata. The two kittens N(8) and N(90) come from a different study[5,6]. Their ages at the time of HRP injection were 8 and 90 days, respectively. Abbreviations: ss, pl, ssp and sp: suprasylvian, postlateral, suprasplenial and splenial sulci, respectively. PL: postlateral gyrus. LSS, 19, 18 and 17 indicate the lateral suprasylvian visual areas, and areas 19, 18 and 17, respectively. The arrow indicates the boundary between the latter two areas.

Fig. 25/ Distribution of the callosal neurones after labelling with HRP in different developmental conditions. See legend above for further details (from Innocenti and Frost, 1979).

Development of callosal connections after early monocular deprivation (MD group).

After an early monocular deprivation (MD), it is well established that exuberant juvenile callosal projections within the callosal efferent zone are not eliminated with age. In other words, they are stabilized. The perikaria of callosal neurons keep distributed in large portions of both A17 and A18 until adulthood. Their distribution in the adult in fact looks like that of kittens just after birth (Fig. 25; Innocenti and Frost, 1979). Although this has not been investigated, likely, the number of callosal fibres accordingly remains quite high in spite of age.

By contrast, what happens really within the callosal terminal zone remains to be characterized. Until the present thesis, no complete anatomical data, whether qualitative or quantitative, were available yet (but see below). Only functional data established from our team are presently available (Milleret et al., in preparation). And they give only some indications on what may occur in this region after visual deprivation. Notice that such latter data have been established after section of the optic chiasm at different ages, by stimulating the eye that remained open postnatally, and by exploring electrophysiologically the contralateral hemisphere through extracellular single unit recordings (Fig. 26).

Such functional data may be summarized as fellows:

(a) The callosal terminals in MD animals may establish functional connections within the visual cortex;
(b) At adulthood, they are distributed within the 17-18 TZ, but also in A17 and A18.
(c) In the MD adult, the percentages of the transcallosally activated units vary as a function of the recording site: A17, 30%; 17-18 TZ, 76%; A18, 42%, white matter 13%.
(d) If analyse as a function of development, it appears that the 17-18 TZ is the first to be activated through the corpus callosum; A17 and A18 are functionally connected only later on;
(e) The functional properties of the transcallosally activated units evolve with age, to stabilize around 4 postnatal months.

Such data clearly differ from that of NR group, in which the TC units are almost strictly located within the 17618 TZ, with a percentage of 53% (from Milleret and Houzel, 2001; Milleret et al., 1994; 2005). At least, functional data in MD animals suggest that some *sprouting* of the callosal terminals occur with age after such a deprivation, to invade widely the Lateral gyrus. See a summary of what may occur during development in normal or after MD on Fig. 27.

A

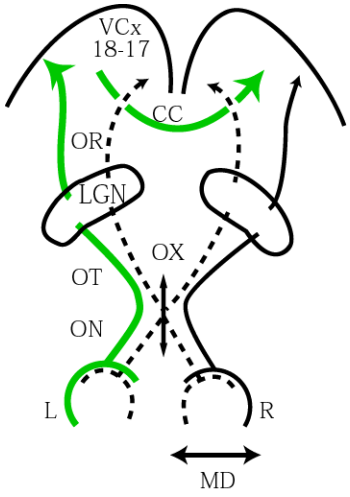

B

MD group

A17		17-18 TZ		A18		White matter	
TC+	TC-	TC+	TC-	TC+	TC-	TC+	TC-
63	146	114	35	47	63	3	19
n = 209	30 ± 6%	n = 149	76.50 ± 7%	n = 110	42.50 ± 9%	n = 22	13.5%

NR group

A17		17-18 TZ		A18		White matter	
TC+	TC-	TC+	TC-	TC+	TC-	TC+	TC-
1	124	58	51	0	49	0	0
n=125	1%	n=109	53%	n=49	0%	n=0	0%

Fig. 26/ Effect of an early monocular deprivation on the percentages of transcallosally (TC+) and non-transcallosally (TC-) activated units in the adult cat visual cortex. A. Experimental protocol. MD (of the right eye) was induced at 5-7 postnatal days. Four to seven months later, the optic chiasm (XO) of each cat was sectioned. Three days later, animals were anaesthetized and paralysed. Then, to explore functionally the transcallosal activation of the cells within the visual cortex (A17 and A18), single units were recorded extracellularly within the right hemisphere, after stimulation of the contralateral (left) "viewing" eye. B. Percentages of TC+ units in MD group. *First row*, different cortical regions of the visual cortex that have been explored electrophysiologically (after section of the optic chiasm). *Second row*, TC+ and TC-. *Third row*, number of each cell type within each explored cortical region. *Forth row*, n= total number of cells recorded and percentage (%) of TC+ units in each explored cortical region (Milleret et al., in preparation). Data from NR animals are reported for comparison (from Milleret and Houzel, 2001).

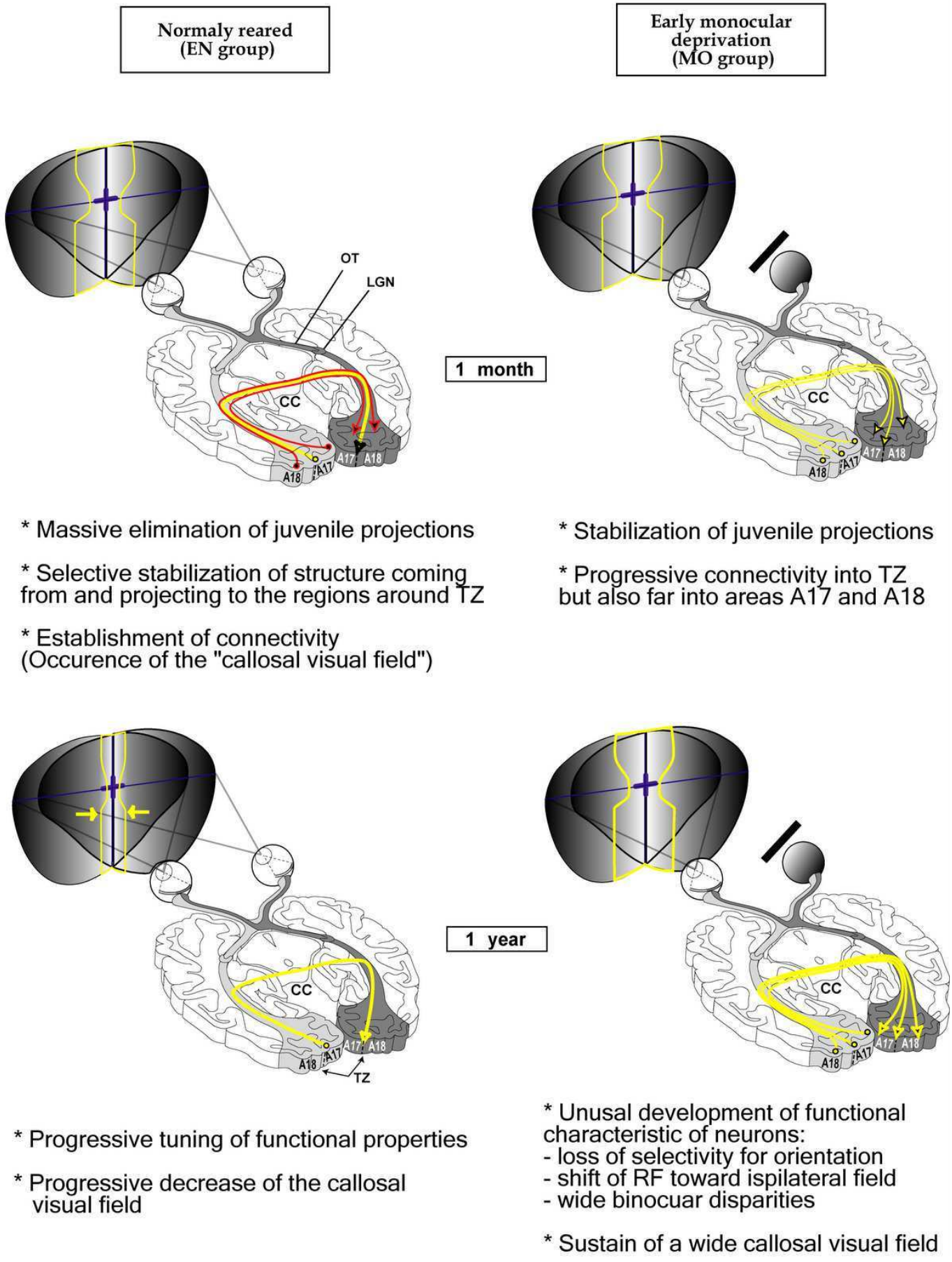

Fig. 27/ Comparison of the development of the callosal connections in cat visual cortex in normal conditions (NR, at left) and after an early monocular deprivation (MD, at right). See commentaries below each panel (and Text) for further explanations.

Aims of Part I of the thesis

The work described in this Part I of the thesis aimed at increasing our understanding of the neural networks that determine the spatio-temporal characteristics of the sensory cortical maps. This was achieved by investigating the "callosal cortical maps" (as defined by callosal connections between the hemispheres) in cat visual cortex after an early monocular deprivation (MD) through a multidisciplinary approach, combining anatomy, models, mathematics and simulations.

In a first chapter, the morphology of the callosal connections of MD animals have been described *qualitatively*, This has been achieved by analysing separately 10 single callosal axons which has been first labelled with an anterograde tracer, the biocytin, and then 3D-reconstructed with the Neurolucida software. Comparing data to those obtained previously in normal adults (Houzel et al., 1994) allowed demonstrating that the morphology of these callosal axons is greatly modified after an early monocular deprivation, because of sprouting both tangentially and radially within the visual cortex.

In a second and the third chapters, these same axons have been additionally characterized *quantitatively*. Geometrical and statistic tools were developed to characterize the global 3D spatial dispersion of their terminal arbours and that of their synaptic boutons:

a) A method referred as the "Ellipsoid approximation" was first applied to both normal and abnormal callosal terminals in order to characterize them with much more precision than before and then to reveal additional differences in their respective global spatial dispersion. The *cortical surface* they occupied, the *elongation*, the *width*, and the *orientation* of their terminal arbours with respect to some precise references such as the midline or the 17-18 TZ were more particularly defined with a precision never reached before. As expected, additional effects of MD on callosal axons were thus revealed;

b) A new statistical method allowing the characterizing of the clustered organisation of cortical connectivity has been also developped. Again, it has been applied to callosal axons of both NR and MD experimental groups to allow comparison. Gaussian mixture models were used to provide a quantitative description of the dispersion of the terminal arbours for each single axon. With priors evaluated from simulation, a maximum *a posteriori* method was used to estimate the number and the weight of each cluster of branches, as well as their centres and covariance matrices. The method has been first validated on synthetic data set. It then allowed a fine description of clusters of terminal neural branches. As expected, this provided a simple but efficient technique for comparing neurons connectivity in different experimental conditions and correlating anatomy and function in the brain.

In a final chapter, a compartmental model was used to simulate the propagation of spikes within abnormal callosal arbour in order to estimate if abnormalities in the morphology of axon may induce temporal dispersion of the neural message or if it can be kept in synchrony within the structure. In fact, we demonstrate that all the branches of one single arbour activated simultaneously the terminal callosal zone in spite of their abnormal morphology. In other words, since they are also synchronized in NR group (Tettoni et al., 1996), at least in our experimental conditions, the temporal properties of the callosal cortical maps do not seem to be altered by MD.

CHAPTER I.1.

Morphology of callosal axons in cat visual cortex after an early monocular deprivation

Comparison to normal axons

Article 1:
FOUBERT, L, BENNEQUIN, D., DROULEZ, J., QUENECH'DU, N. & MILLERET C. Morphology of callosal axons interconnecting in cat visual cortex after an early monocular deprivation (in preparation).

Article 2:
MILLERET C, HOUZEL, JC, **FOUBERT, L.**, QUENECH'DU, N. & WIRTH, S. Widespread heterotopic callosal transfer in primary visual areas after early monocular deprivation (in preparation).

INTRODUCTION

If the visual experience is altered during the critical period, a widespread distribution of efferent callosal neurons throughout A17 and A18 may be retained. This was observed repeatedly in various species (Innocenti and Frost, 1979; Berman and Payne, 1983; Elberger et al., 1983; Wree et al., 1985; Olavarria et al., 1987; Murphy and Grigonis, 1988). Little is known, however, about the fate of callosal terminals and, consequently, the interhemispheric integration of visual information in such circumstances (Cynader et al., 1981; Cusick and Lund, 1982; Toldi et al., 1989; Clarke et al., 1992; Milleret and Houzel, 2001). Here, we thus analyzed the 3D morphology of single callosal arbors in 4-5 month-old cats raised under monocular deprivation (MD) from the 6-7th postnatal day on, i.e. throughout the critical period.

Comparison of the results with our previous data from normally reared (NR) cats (Houzel et al., 1994) reveals that MD led to an extensive sprouting of callosal terminals arbors within the hemisphere ipsilateral to the occluded eye. Numerous heterotopic connections formed between both hemispheres. Thus, we show that the anatomical network subserving the interhemispheric integration of visual information is profoundly modified by an early monocular deprivation.

MATERIALS AND METHODS

Four cats were used in this study. All surgical procedures conformed to institutional and governmental requirements (Direction of veterinary services and Ethical committee) and the guidelines of the European Convention for the Protection of Vertebrate Animals Used for Experimental and Other scientific Purposes (Strasbourg, 18.III, 1986).

1. Experimental groups

The axons that are described here have been obtained in 4 early monocularly deprived cats. The eyelids were sutured shut 5-7 days after birth, i.e. a few days before the natural opening of the eyes occurs (1à-12 postnatal days). Biocytin (i.e. an anterograde tracer) was injected 4-5 months later (3 animals, at 4 months; 1 animal at 5 months). Ten of these axons were 3D reconstructed. To identify possible abnormalities, they were compared to normal callosal axons whose morphology has been described previously in our group (Houzel et al., 1994).

2. Monocular occlusion

This surgery was thus performed while the kittens were 6-7 days old. Each animal was first anaesthetized with Saffan (1.2 ml/kg, im). Its temperature was monitored continuously and maintained at 38°C through a heating pad being controlled electronically.

Then the occlusion of the right eye was performed by suturing the eyelids, after sectioning the limbs being still joined. A small opening in this was maintained medially in order to permit the lachrymal outflow.

Two antibiotics (Néomycine and Rifamycine, Chibret) were applied locally as collyres and a general one (Extencilline) were finally injected.

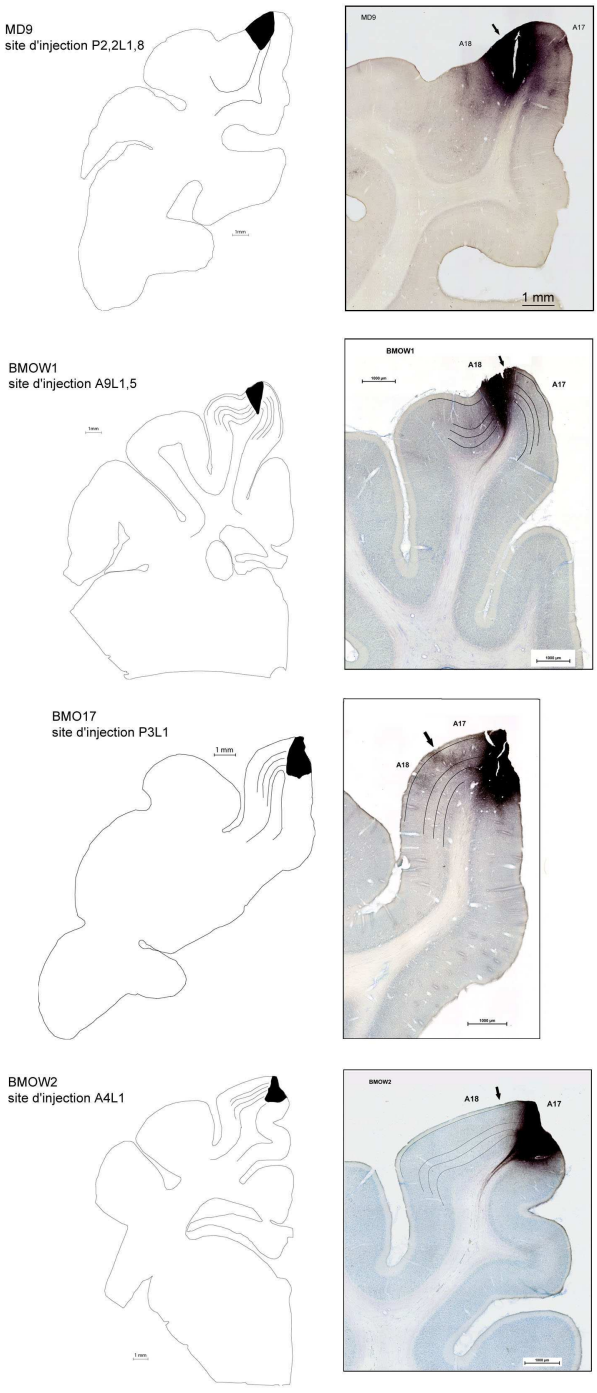

Fig. 28/ Camera lucida and photomicrographs of injection sites. Code number of the experiments and the stereotaxic levels (in mm) of the centres of injection anterior (A) or posterior (P) to the inter-aural line (= AP0) are indicated. Low and high power views of each site are shown in coronal sections of the left hemisphere. The region containing densely packed, labelled cell bodies and neuropil (the core of the injection) is drawn in solid black; axons radiating from the injection site are drawn over variable distances and the few labelled neurones clearly separated from the injection site are markedly marked by dots. The drawings represent the maximal extent of the injection sites in superposition of 21-38 adjacent sections. The core of the injection extended along the antero-posterior axis over 2850 µm in MD9 and 1575 µm in BMOW1; it aimed at labelling callosal axons originating the transition zone between A17 and A18 (TZ). The core of the injection along the same axis was 1875 µm in BMO17 and 2175 µm in BMOW2; in this case, it aimed at labelling callosal axons originating from A17. In the higher power views, continuous lines denote the limits of the different cortical layers (I to VI). Arrowheads are centred on the TZ. Notice that, in BMOW1 and BMOW2, the part of the injection site extending below layer VI consists exclusively of densely packed axons labelled from the overlying cortex.

3. Injections and perfusions

Four to five months after monocular occlusion, each animal was again anaesthetized with 1.2 ml/kf (i.m) Saffan (10.8 mg/kg Alfaloxon and 3.5 mg/kg Alfadolone acetate; Pittman-Moore, UK). Rectal temperature was maintained at 38°C and the electrocardiogram was continuously monitored. Additional anaesthetic (1:1 Saffan in saline) was delivered when needed through an i.v. catheter. Animals were positioned in a stereotaxic frame and 5% Biocytin (= Biotin + lysine, Sigma) in 0.05 M Tris buffer (pH 8.0) was injected in the left lateral gyrus (contralateral to the occluded eye) through a 20 µm (tip diameter) glass micropipette cemented to a stainless steel needle and connected to a Hamilton syringe via an oil-filled polyethylene catheter. For recall, biocytin is composed of biotin and lysine; it may be captured by cell bodies or dendrites and is transported mainly anterogradely. In each site of injection, two or three 0.2-0.5 µl pressure injections were delivered at 500-2000 µm depth (usually 800 µm apart). Generally, each animal received successively an injection in two well separated cortical sites: one posterior (P2-P3, L1-L3) and the other most anterior (A4-A9; L1). They could be within the 17/18 transition zone or in A17 (Fig. 28; see also below). Post-operatively, antibiotics were supplied (Extencilline, 200 00 U/kg i.m., Specia France).

Fifty to 60 h later, sodium pentobarbital was injected (Pentobarbital, 60 mg/kg i.p; Sanofi, France). The animal was then perfused transcardiacally with 0.1 M PBS, pH 7.4, followed by 4% paraformaldehyde in PBS (in some cases, 0.3% glutaraldehyde was added).

In two cases, in order to evaluate tissue shrinkage, electrolytic lesions were placed in the injected hemisphere before the perfusion at various depths and A/P coordinates (tungsten microelectrode; 15 µA DC for 15 s; tip negative).

4. Histological procedure

Histological procedures were similar to those published elsewhere (Assal and Innocenti, 1993; Houzel et al., 1994). Briefly, the brains were kept in cold (4°C) fixative for 4 h and stored in cold, 30% sucrose, PBS for 2 days; 75-µm-thick frontal sections were cut frozen, collected in PBS and processed according to King et al. (1989). Sections were rinsed four times in PBS with 1% Triton X-100 and incubated in avidin-peroxidase complex for one night [ABC standard or Elite kit (Vector) 1:200 in PBS-Triton]. Peroxidase was then revealed using the nickel-intensified diaminobenzidine reaction (Adams, 1981). Sections were mounted, dehydrated and cover-slipped in DPX or Eukitt medium. Every second or fourth section was counterstained with cresyl-violet or toluidine blue. Cytoarchitectonic criteria (Otsuka and

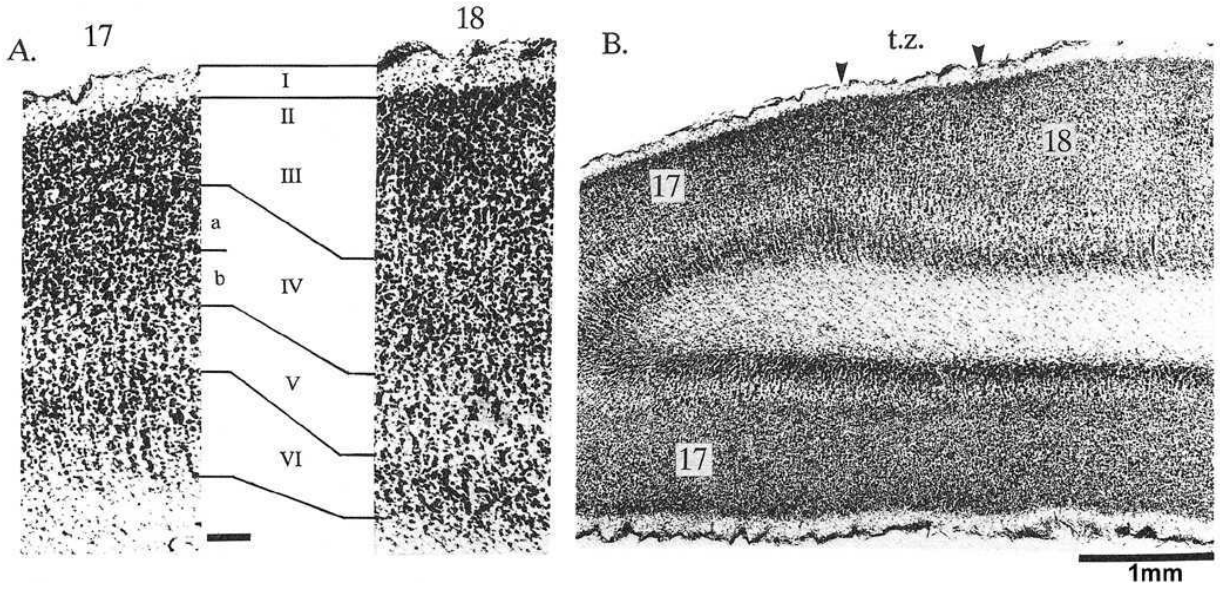

Fig. 29/ Cytoarchitectonic criteria based on Nissl staining to identify A17, A18 and the transition zone between both areas (TZ). The boundaries of cortical layers were first examined in both A17 and A18. Layer I appeared as a cell-poor region. Layers II and III were not differentiated; the lower limit of layer III was identified by its typical pyramidal cells. Layer IV was characterized by high granular cell density. Layer V contained sparse pyramidal cells. Finally, layer VI displayed a higher cell density than layer V. The transition between A17 and A18 was then analysed, using variations in the relative thickness of some cortical layers. When moving laterally from A17 to A18, layer I and layer II-III get markedly wider while layer VI gradually get thinner. In agreement with Payne's findings, the 17/18 transition zone was not sharp, but was a zone of transition. Its average extent measured at the cortical surface was ~1100 µm at 4-5 months of age (from Payne, 1990; Fig. 2)

Hassler, 1962) were used for defining areas 17 (A17) and 18 (A18) as well as the transition zone between both areas (TZ); Fig. 29.

5. Three-dimensional reconstructions

5.1. Terminal arbours

Axons that were 3D reconstructed all displayed a very good quality of filling (as judged from the intensity of staining and the presence of stained boutons. They were selected at their site of termination in the cortex or within the corpus callosum itself. Camera Lucida sketches were used to prepare the 3-D reconstruction.

Each axon was individually reconstructed using a computer-coupled microscope (Glaser and Glaser, 1990) and the Neurolucida software package (Microbrightfield Inc.). Each slide was placed on the monitored stage of the microscope and the operator could see a compound image of the preparation and of the computer-generated overlay by looking into the oculars. The contours of each section (pial surface), boundaries of cortical layers and blood vessels could be drawn at low magnification. The stained axonal processes were observed through X63 or X100 immersion objectives (final magnification of X 1000 or more) and traced as sets of connected 5- to 100-µm-long segments delimited by two points. Each point was assigned x, y and z coordinates, a diameter and one of the following structural tags: node; passing or terminal bouton; and origin or termination. The terminations were two kinds: real, or interruptions caused by sectioning. The latter was carried into the following section after the appropriate alignment of the computer overlay had been achieved. Reconstructions extended over a range of 14-98 (mean = 54) consecutive sections. Final corrections for shrinkage could be applied separately for the x, y and z dimensions. The whole set of sections enclosing an axon could then be analysed, rotated, re-scaled and plotted.

Axon diameters were estimated at X 1000 magnification or more using a graded ocular and were ascribed to classes of 0.46 or, in the second phase of the study, 0.26 µm of width. As a rule, diameters were measured near the surface of the section when the staining is often most intense.

The amount of tissue shrinkage resulting from fixation and histological processing was determined by measuring the distances between the same sets of electrolytic lesions at different stages of processing. Measurements were performed after cutting, Biocytin visualization and after dehydration and cover-slipping. Total shrinkage was 30-40%, approximately isotropic in the x, y and z axes and occurred mainly during fixation. A more severe tissue deformation (compression), perpendicular to the

cut surface of sections, was caused by dehydration-cover-slipping and reduced section thickness to ~1/3 of its value at cutting.

Shrinkage from fixation affects measurements of axon length and thickness. Since it is difficult to determine whether shrinkage is identical for every axon in grey and white matter, and for all axon dimensions, *we did not compensate for it in our measurements***.** Compression causes axons travelling along the z axis to take a characteristic wary trajectory which was followed faithfully during the reconstruction and measured as curvilinear length with the Neurolucida software. This eliminated the need for further corrections except in the 3-D visualizations for which the z axis was expanded threefold.

The definition of a "terminal column" (see Results) required the identification of one or more distinct clusters of boutons in a plane tangential to the cortical surface. This plane is seldom perpendicular to the original plane of cutting; therefore the set of sections containing the reconstruction was rotated to obtain first "standard front views" and then views perpendicular to the pial surface which separation of clusters was judged. The separation was further evaluated in a medial view. Numbers of boutons per layer and/or column were counted in the standard views described above.

Using immersion objectives, details of axonal terminations were drawn with a camera lucida and/or photographed.

5.2. Injection sites

As in previous studies (Assal and Innocenti, 1993; Houzel et al., 1994), injection sites were rather sharp and consisted in intensely stained cell bodies and neuropil. Their location and extent are shown in the following figures (Figs. 28).

All sites, when compared with the electrophysiological maps of the visual areas of Rosenquist (1985) appeared to be located clearly within the TZ (Fig. 28, cats MD9 and BMOW1) or in A17 (Fig. 28, cats BMO17 and BMOW2). This was confirmed by cytoarchitectonic criteria (Otsuka and Hassler, 1962; Payne, 1990; Milleret et al., 1994). All injections included layers I to VI. Their diameter ranged between 1400 and 1900 µm medio-laterally and 600 and 2300 µm antero-posteriorly. In all cases, they were wider in supragranular than in infragranular layers. All injections which reached layer VI also labelled axons terminating in the lateral geniculate nucleus, by respecting the retinotopic arrangement.

Although Biocytin was transported mainly anterogradely, it also labelled retrogradely a new neurones near the injection site and, occasionally, in the lateral geniculate nucleus. No labelled neurones were found in the hemisphere contralateral to the injection.

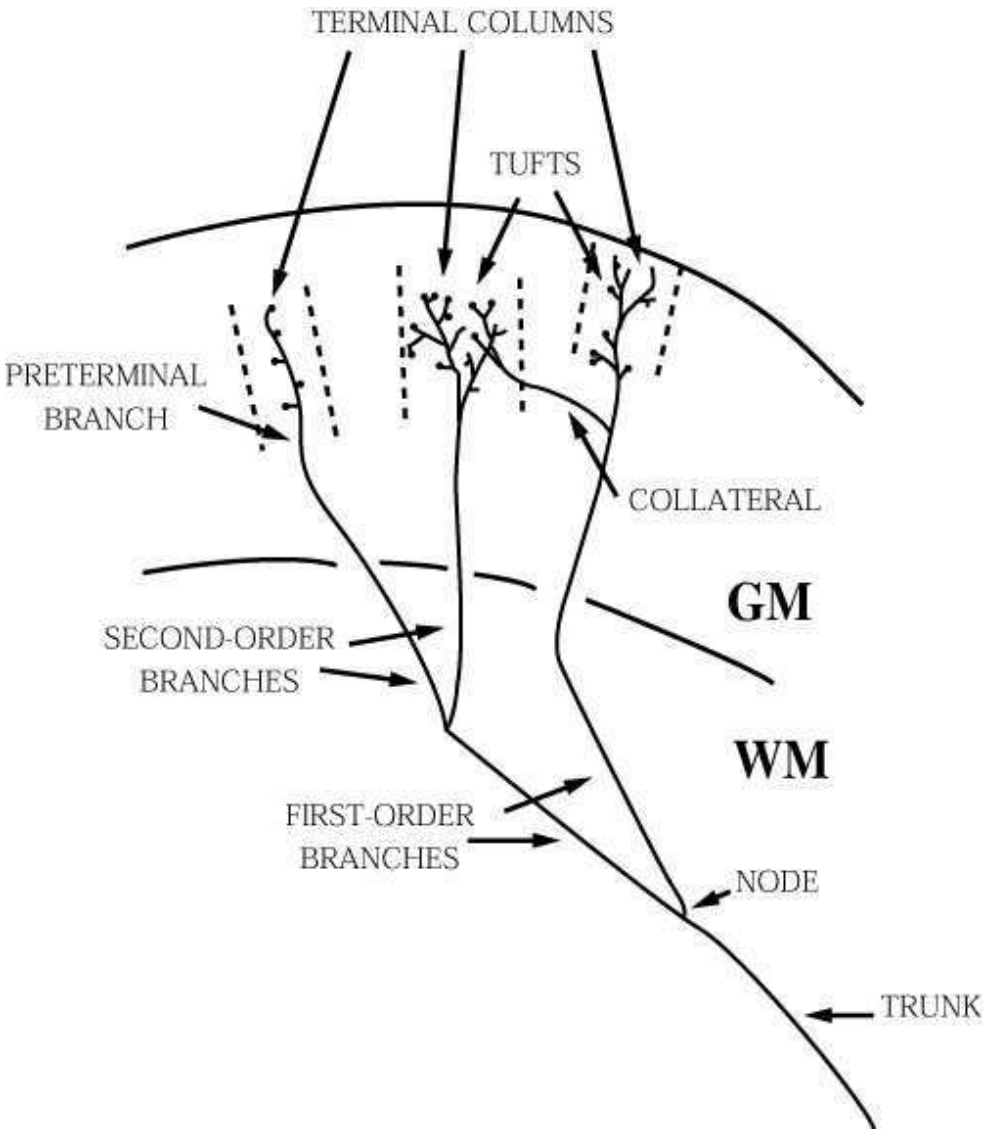

Fig. 30/ Schematic drawing of a terminal arbour ending in the cerebral cortex (VM = white matter, GM = grey matter) and illustrating the nomenclature employed. "Terminal column" refer to the volumes delineated by interrupted lines; one column is supplied by an isolated pre-terminal branch. For further details, see text (From Houzel et al., 1994, Fig. 2).

6. Terminology

As a general rule, the terms defined in Houzel et al. (1994) will be also applied here (Fig. 29). To help, they have been summarized below. This will permit comparisons later on.

6.1. Axonal morphology

The *trunk* is the part of the axon proximal to the first branching point (*node*). The part of the axon located distal to the first node is called *terminal arbour*. Axonal branches will be identified by their topological order. Thus, *first-order* (or *primary*) branches originate from the first node and give rise to *second-order* (or *secondary*) branches; the latter give rise to *third-order* (or *tertiary*) branches, etc. Branches which are particularly conspicuous by their length and/or thickness will be designated as *main branches*. *Preterminal branches* carry *boutons* (presumably synaptic boutons). The latter can be *terminal boutons*, characterized by the presence of a connecting stalk or *"en passant" boutons*, i.e. swellings along the preterminal branch (Fig. 30). A *tuft* is a part of an arbour characterized by densely ramified and tightly distributed high-order and preterminal branches originating from a common stem.

Collateral branches (*collaterals*) are first- or higher-order branches clearly distinct from the rest of the arbour and usually shorter and thinner than their parent branch. They can ramify modestly and/or carry boutons (to be verified).

6.2. **Architecture of individual terminal arbours**

Axons may vary in the complexity and spatial organisation of their terminal arbours. On the basis of data obtained previously in Dr. C. Milleret 's team, in collaboration with Dr. G.M. Innocenti from the Karolinska Institute at Stockholm in Sweden (cf. Houzel et al., 1994), at least four ones may be differentiated (Fig. 31):

- *A simple architecture:* such axon terminate with a single tuft within an approximately conical volume (not shown);
- *A parallel architecture*: the axon with such architecture usually divides in the white matter, and first- or higher-order branches of comparable length supply different columns or converge onto a same column. These branches usually run close to each other over several millimetres (Panel A in Fig. 31).
- *A serial architecture*: It is characterised by a tangentially running trunk (or else first- or higher-order branch) with roughly radial collaterals to the cortex. Usually, the tangential running also maintains a larger calibre than the collaterals (Panel B in Fig. 31).
- *A mixed serial-and parallel architecture*: Other axons may display a mixed parallel-and-serial architecture. A nice example is presented in Fig. 31 (Panel C).

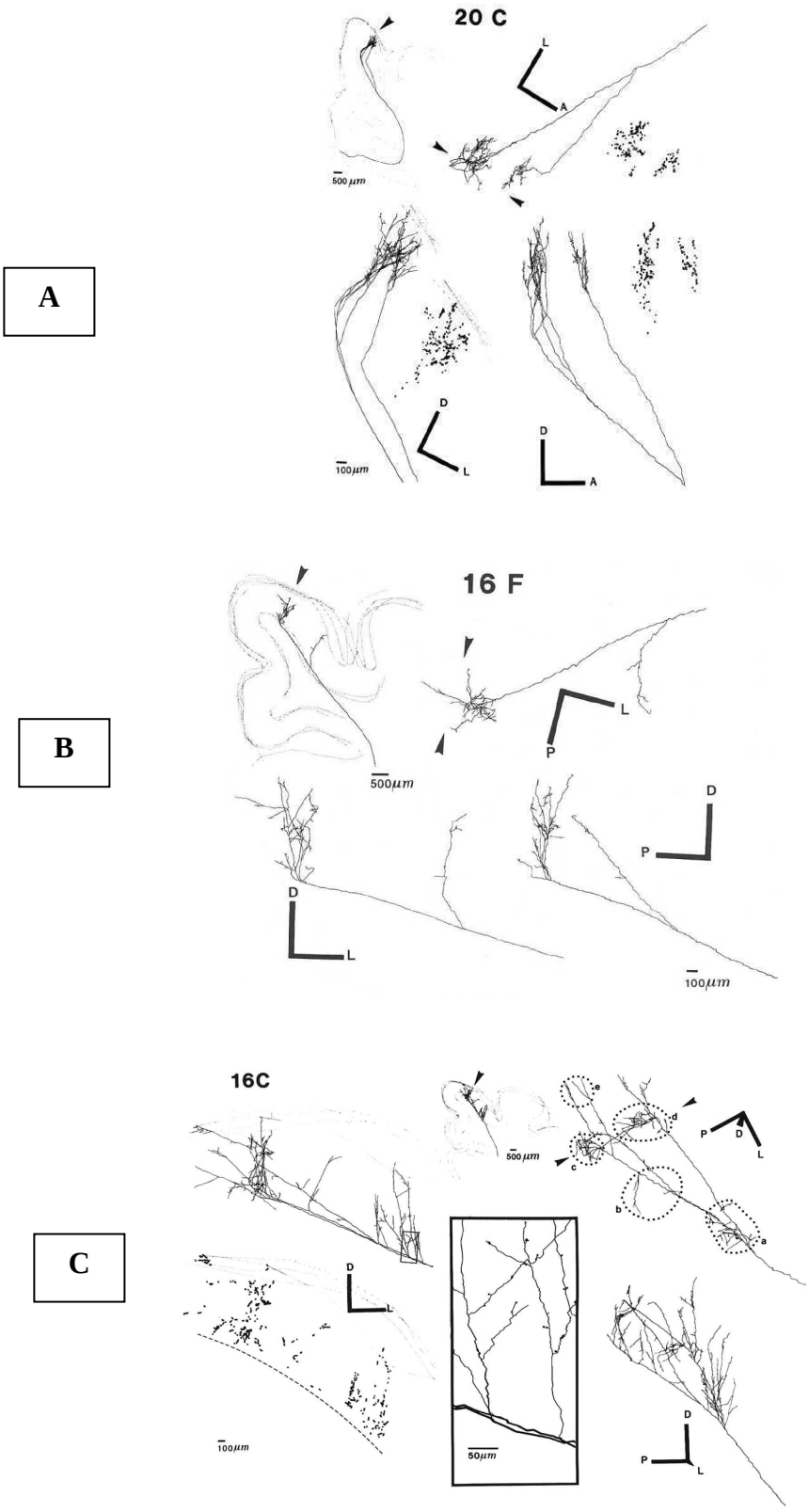

Fig. 31/ Different types of architecture of individual terminal arbours. A. Parallel architecture. B. Serial architecture. C. Mixed serial-and-parallel architecture (Normal callosal axons described in Houzel et al., 1994; Fig. 11 to 13).

6.3. Terminal structure

In the grey matter, the axons under study generally form a more or less complex arborisation. They may end with one or several *tufts*. In addition, they may have some modest *collaterals*. Tufts and/or collaterals of one axon often terminate in segregated volumes of cortex including one of several layers. In the following descriptions, these volumes will be called *terminal columns*. The characterisation of a terminal column requires the identification of distinct *clusters* of *pre-terminal branches* and *boutons* in a view **perpendicular** to the cortical surface. Columns may be supplied by only one or different separated branches originating in the white matter or grey matter.

6.4. Laminar distribution of boutons

The laminar distribution of boutons may vary across columns and axons. Four different patterns of distribution may at least in principle be identified (cf. Fig. 32): a) A *supragranular* distribution, where all the boutons are only located in layers II/III; b) In the second patter, identified as *bi-laminar*, the highest density of boutons is still in the supragranular layers, but while there is only few boutons in layer IV, numerous ones are also present in infra-granular layers; c) A third patter, complementary of the latter, displays concentrated boutons in layer IV. It is a "*granular*" distribution; d) In this fourth pattern, boutons distribute in all the cortical layers and display a *trans-granular* distribution.

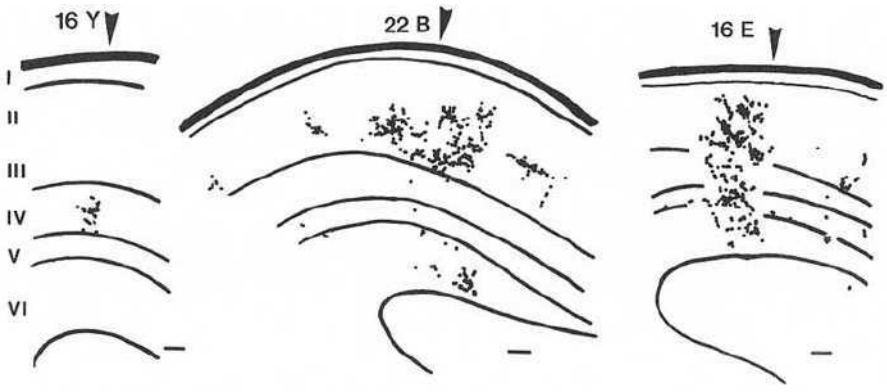

Fig. 32/ Front views of terminal columns of callosal axons showing the four patterns of laminar distribution of boutons that have been identified in normal adult cats: respectively granular (16Y), supragranular and bi-laminar (22B) and trans-granular (16E). Layers I-VI are indicated in each panel. Calibration bars are 100 µm. Area 17 is on the left and A18 on the right of the arrowheads (From Houzel et al., 1994; Fig. 8).

List of abbreviations

c.c. corpus callosum
c.g. congular gyrus
c.s. cingular sulcus
f. fimbria
h.f. hippocampal formation
h.f.g. hippocampal fusiform gyrus
d.l.g.n. dorsal lateral geniculate nucleus
l.s. lateral sulcus
m.g. marginal (or lateral) gyrus
m.i.n. medial interlaminar nucleus
m.ss.g. middle suprasylvian gyrus
p.ss.g. posterior suprasylvian gyrus
pl.g. posterolateral gyrus
pl.s. posterolateral sulcus
ps.g. parasplenial gyrus
s.c. superior colliculus
s.g. splenial gyrus
s.s. splenial sulcus
ss.s. suprasplenial sulcus
t.z. transition zone
v. ventricule

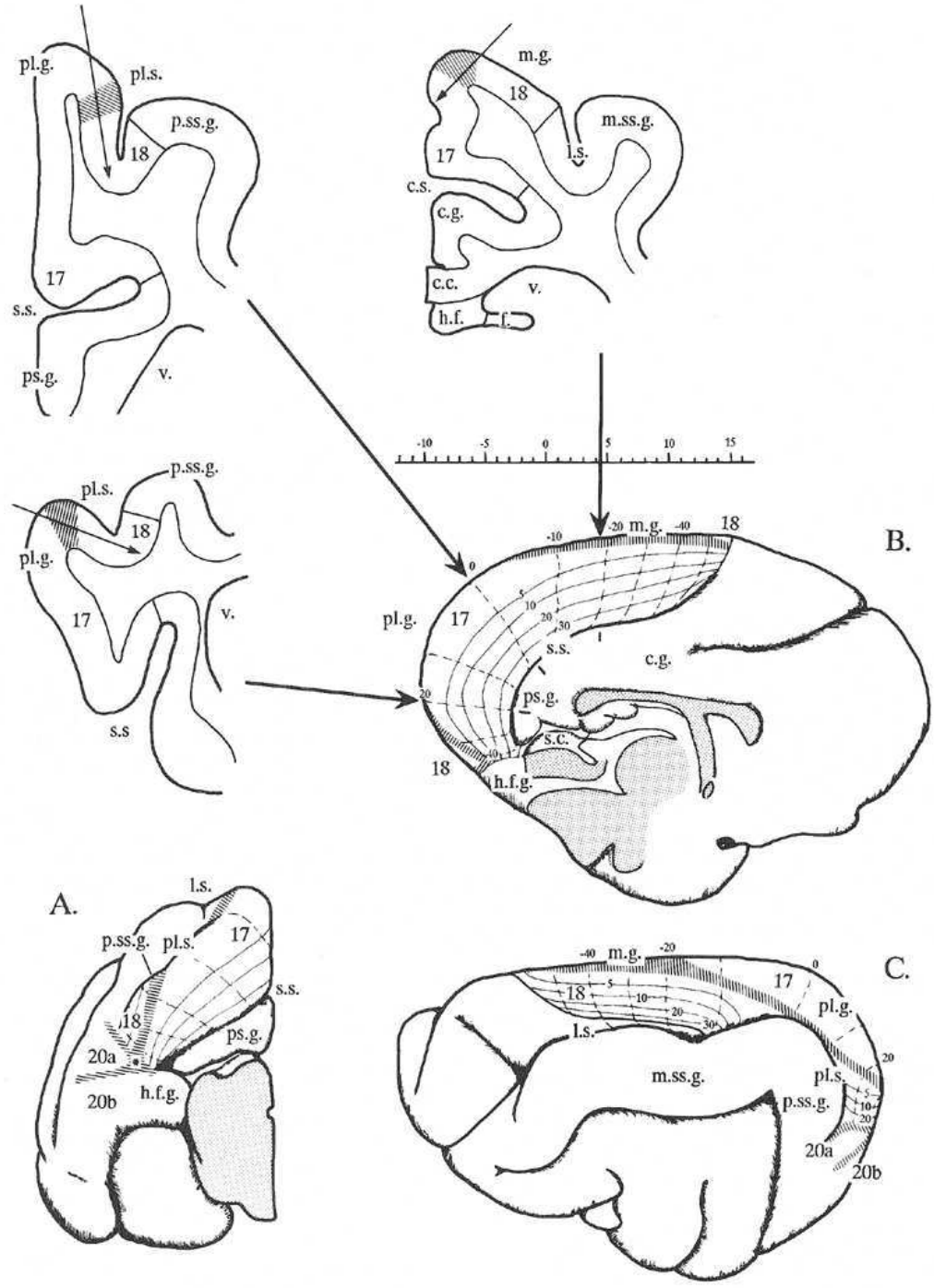

Fig. 33/ Outline drawings of the cat's cerebral hemispheres to show the positions of areas 17 and 18, and the intervening transition zone relative to named gyri and sulci. A. Posterior view of the left hemisphere. B. Medial view, including a marker of the Horsley-Clarke coronal planes. C. Dorsolateral view. In each view, the lines of elevation and azimuth in the visual field maps of areas 17 and 18 are indicated as interrupted lines and continuous lines, respectively. The hatched regions represent the position and width of the transition zone. The asterisk in part A indicates the confluence of the transition zones between areas 17, 18, 20a and 20b. The broad arrows leading to B indicate the planes of the electrode pemetrations through the marginal (=lateral) gyrus and the posterolateral gyri and the planes in which the histologic sections were cut for the recovery of the electrode tracks. Note that the planes are tipped progressively farther backwards away from the coronal plane for entry points at successively more posterior positions in areas 17 and 18. These planes pass approximately parallel to the lines of isoelevation in the visual field. Outline drawings of examples of sections in these three planes are shown. The thin arrows indicate the path of typical electrode penetrations relative to the transition zone. Electrode penetrations through the marginal gyrus were usually directed medially and downwards to cross the transition zone from area 18 to area 17. Penetrations through the posterolateral gyrus were normally inclined laterally, downwards, and forwards to cross the transition zone from area 17 to area 18. As can be seen in the subsequent figures, additional electrode penetrations are frequently made in order to obtain a more complete idea of the representation of the transition zone and the flanking cortices. Cortical maps have been redrawn with permission from Tusa et al., 11978; 1979). Abbreviations used in this and the text are given in an accompanying List of Abbreviations on the companying page). From Payne, 1990 (Fig. 1).

7. Retinotpic analysis

If a reshaping of the callosal connections occurs after MD, it seems important to make a relation between the various positions of the callosal terminals zones within the visual cortex and the retinotopic organization of the visual cortex. Even if it will be performed very briefly, this will be done here by taking data summarized in Figs. 33 and 34. as a reference (data from Tusa et al., 1978; 1979; Payne, 1990).

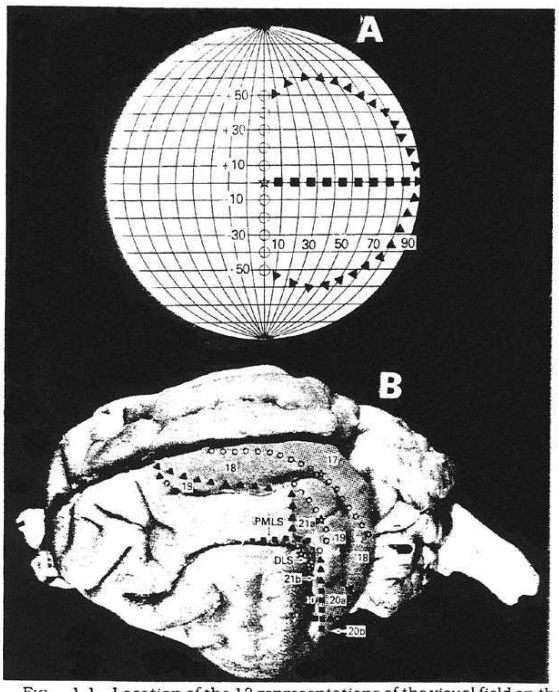

FIG. 1.1. Location of the 13 representations of the visual field on the cat's left hemisphere. A, perimeter chart of the cat's right visual hemifield. Various parts of the perimeter chart are illustrated with symbols, which are also appropriately placed onto the four views of the cat's left hemisphere (B–E) to show the location of the 13 visual areas. B, a dorsolateral view.

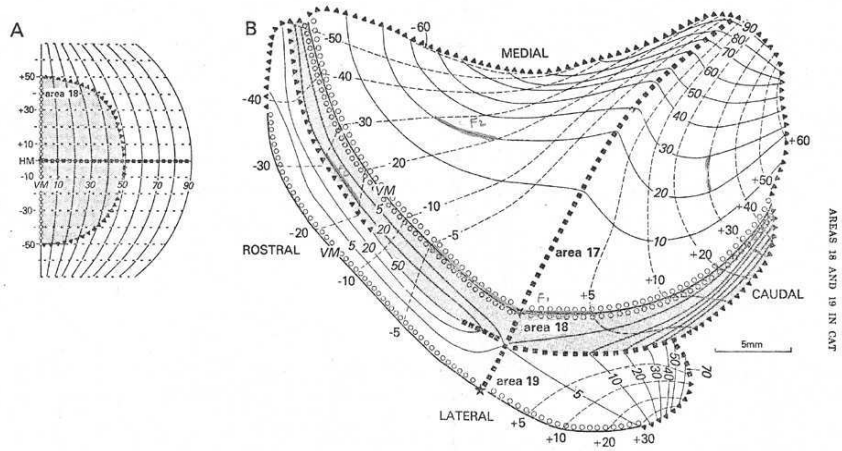

Fig. 2 Schematic representation of the visual hemifield in areas 17, 18 and 19 on the unfolded cat cortex.
A Perimeter chart showing the extent of the visual hemifield found in area 18 (shaded). The symbols used are similar to those used in figure 1. The perimeter chart is based on a world coordinate scheme in which the azimuths are illustrated as solid lines and the elevations are illustrated as dashed lines.
B A schematic representation of the visual hemifield in areas 17, 18 and 19 on the unfolded cat cortex. This figure is oriented such that the rostral and caudal edges of the cortical areas as they lie in the brain are located at the left and right edges of the figure. The lateral edge of the cortical areas is located at the bottom of the figure and the tissue located in the splenial sulcus is represented at the top of the figure. Area 18 is shaded.

AREAS 18 AND 19 IN CAT

Fig. 34/ Retinotopic organisation of cat visual cortex (From Tusa et al. 1978; 1979).

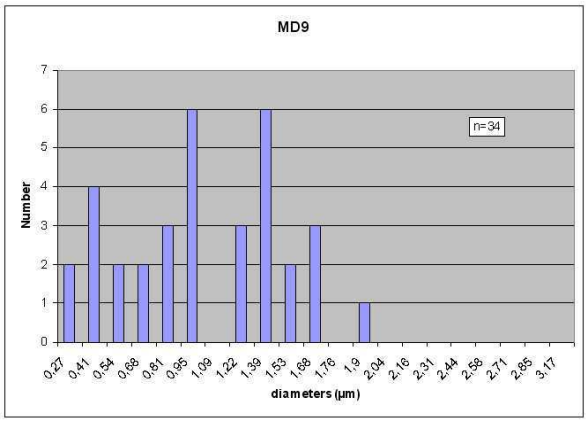

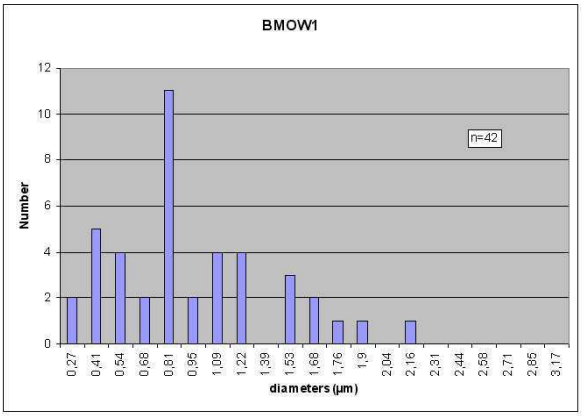

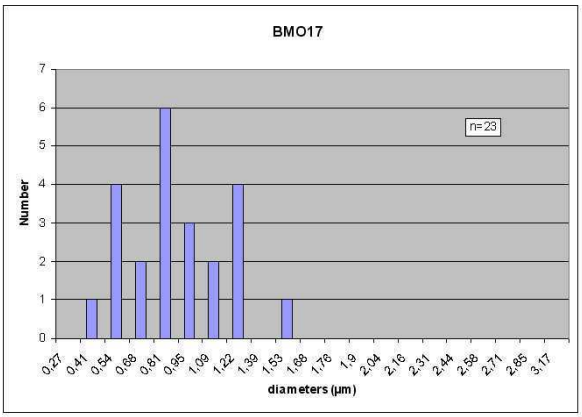

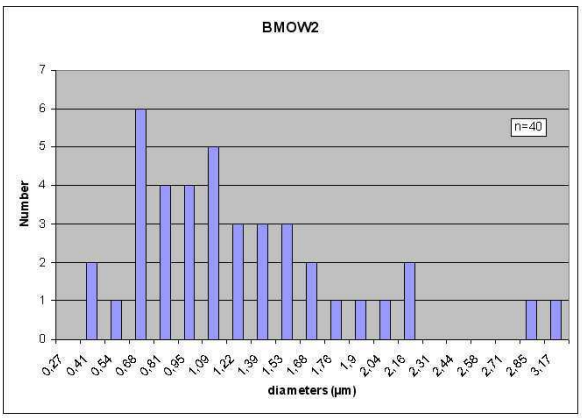

Fig. 35/ Histograms of diameters of callosal axons that have been labelled in each MD cat. The thinnest was 0.27 µm (see cats MD9 and BMOW1) while the thickest was 3.17 µm (see cat BMOW2).

RESULTS

Each injection of biocytin in each cat (see Fig. 28) allowed labelling numerous callosal axons in the corpus callosum. As illustrated in Fig. 35, at least the diameters of those which targeted the Lateral Gyrus varied greatly from one axon to another. Some were very thin with for example a diameter of 0.27 µm. Some others were rather thick, with a diameter of 3.17 µm.

The following description is based on the morphological analysis of 10 of these axons. Each has been serially 3D-reconstructed from the callosal midline to its terminal branches. Four axons originated the TZ while the 6 others clearly originated A17.

We demonstrate that individual axons in MD animals differed greatly in their morphology. They also greatly differed from those that have been found in NR adult animals.

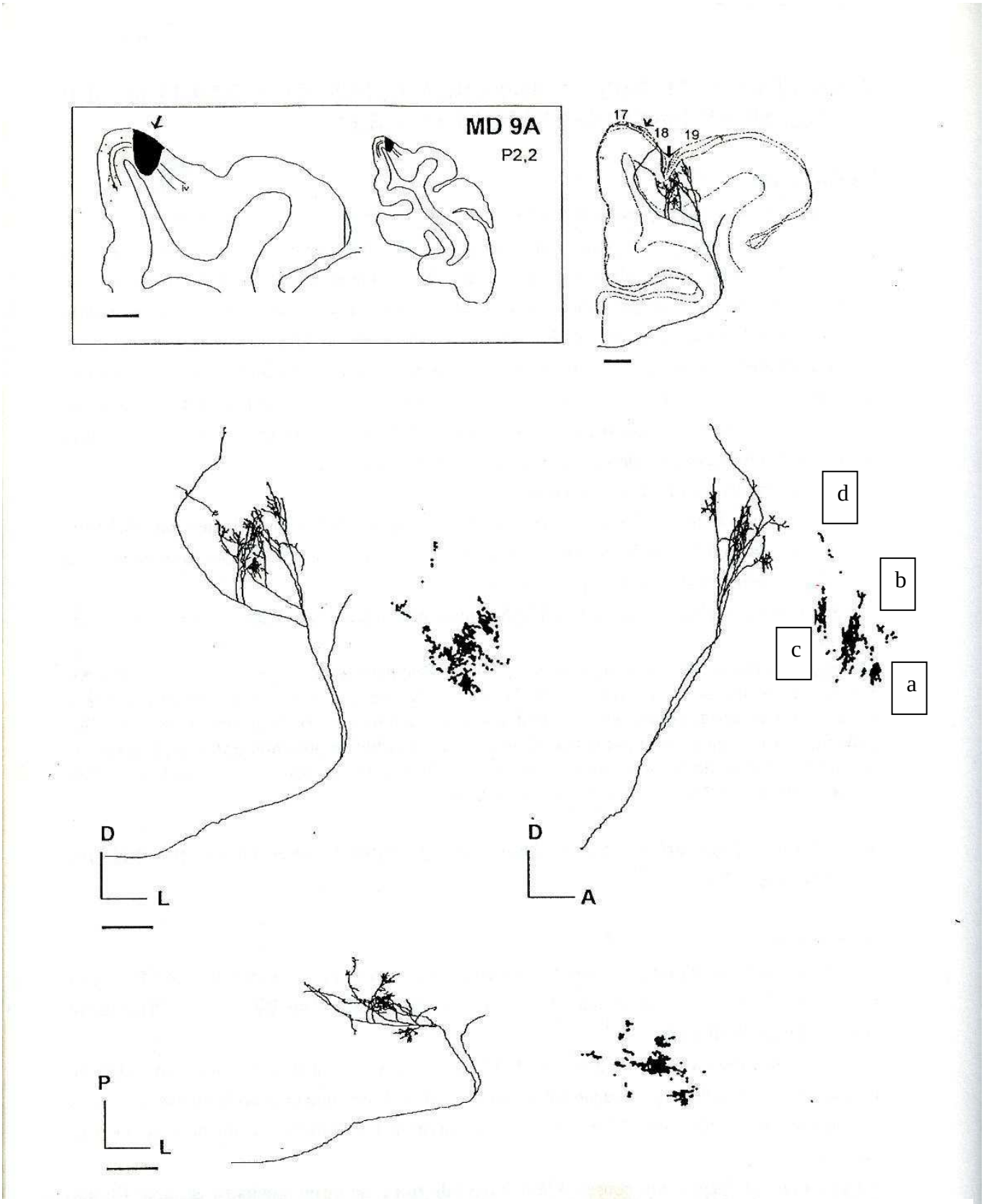

Fig. 36/ Axon MD9A, labelled anterogradely after a restricted injection of biocytine in the 17/18 transition zone of the left hemisphere which is contralateral to the eye that has been occluded 4.5 months before.
Above: on the left, injection site in the 17/18 transition zone. Lines inside the drawing: limits of layer IV; arrow: TZ centre. At right: Frontal view of the axonal terminals in the right hemisphere. Arrows: TZ centre and centre of the 18/19 transition zone. A17: area 17; A18: area 18. *In the middle:* on the left, frontal view of the axonal terminal (with a higher magnification than above) and its "en passant" boutons (dots, which have been shifted to the right for more clarity). On the right, medial views of the same arborisation and its boutons. *Below:* dorsal view of the axon. Letters indicate the different columns as defined by a viewing identification. These columns generally define clusters of boutons. Small and large scale bars: 100 and 500 µm respectively.

1. Terminal structure of individual callosal axons

1.1.1. Injections in the TZ

Two injections have been performed in the 17/18 transition zone (TZ), in two different cats.

This allowed reconstructing 4 different axons (two per site):
1) One posterior injection (P_2L_2) was performed in Cat MD9. This allowed labelling axons MD9A and MD9B;
2) One anterior one ($A_9L_{1.5}$) was performed in Cat BMOW1.2. This allowed labelling axons BMOW1.1. and BMOW1.2..

Axon MD9A

The figure 36 illustrates the injection site of biocytin in the left hemisphere, which extended over 38 adjacent 75-µm-thick frontal sections, and different views of the axon MD9A in the right hemisphere. The former is viewed from the front while the latter is viewed from the back to allow comparison between both hemispheres. The injection site, which was centred at $P_{2.2}L_{1.8}$, was located exactly in the 17/18 TZ.

This axon displayed an arborisation which was extremely bushy, with as much as 1748 boutons. Its trunk had a quite large diameter (2.7 µm) and divided as early as it goes out from the corpus callosum into 2 first-order (or primary) branches.

The thinnest primary branch (1: 0.6 µm) ran laterally towards the posterior suprasylvian gyrus (p.ss.g) and finally terminated abruptly within the white matter with no particular organisation and no bouton.

The other primary branch (2: 1.0 µm) ran more medially toward the lateral gyrus (or marginal gyrus, m.g.) over a distance of 2800 µm. After reaching the fundi of the lateral sulci (l.s), approximately 1000 µm below the grey matter, it divided into 2 second-order (or secondary) branches with a similar diameter (1.0 µm).

The most lateral of these 2 secondary branches (2.1.) divided rapidly, still below the cortex, to give 3 ascending third-order (or tertiary) branches: a) the 2 most lateral ones (0.8 et 1.0 µm) devised, providing 2 terminal columns (**a** : with 249 boutons within the medial part of A19 near A18; **b** : with 167 boutons near the 18/19 border). In both cases, the boutons displayed a trans-granular organisation by including layers I to VI (with 67% in layer II-III); b) the third ascending branch divided again before entering the cortical plate to firstly contribute to the formation of the column "**b"** (+ 606 boutons), and secondly to form a (new) granular column in the lateral part of A18, very near the 18/19 border (**c** : 96 boutons, with 81% in layer IV).

The most median of the 2 secondary branches (2.2.) ran medially until the fundus of the lateral sulcus (l.s.) where it divided to form successively 3 ascending branches. Two of these (1.6 et 1.0 µm) penetrate the grey matter at the level of the 18/19 border, contributing to the « **b** » column (+ 570 boutons); the third one (diameter 1.3 µm) ran tangentially over more than 2300 µm to reach finally the grey matter laterally to the 17/18 transition zone (TZ) and to form a bi-laminar column (**d** : 38 boutons). Notice that this last branch also gave dorsal collateral which joined the column "**c "**, providing 22 additional boutons in this region.

To summarize, this axon displayed a rather complex architecture which may be qualified of '*mixed' (parallel-and-serial) architecture*. It displayed apparently *4 columns (and thus 4 clusters of boutons)*: the largest one ("b") was located in the 18/19 transition zone and displayed the largest amount of boutons (n=1343, i.e. 72% of the total); 3 more modest columns were also identified in visual cortical areas 19 (with 249 boutons) and 18 (with 156 boutons). In total, it covered approximately 3.2 x 1.5 mm² of cortex (taking into account of its curvature) and displayed numerous (n=1748) boutons with a *trans-granular* distribution (see Table 1 for a summary).

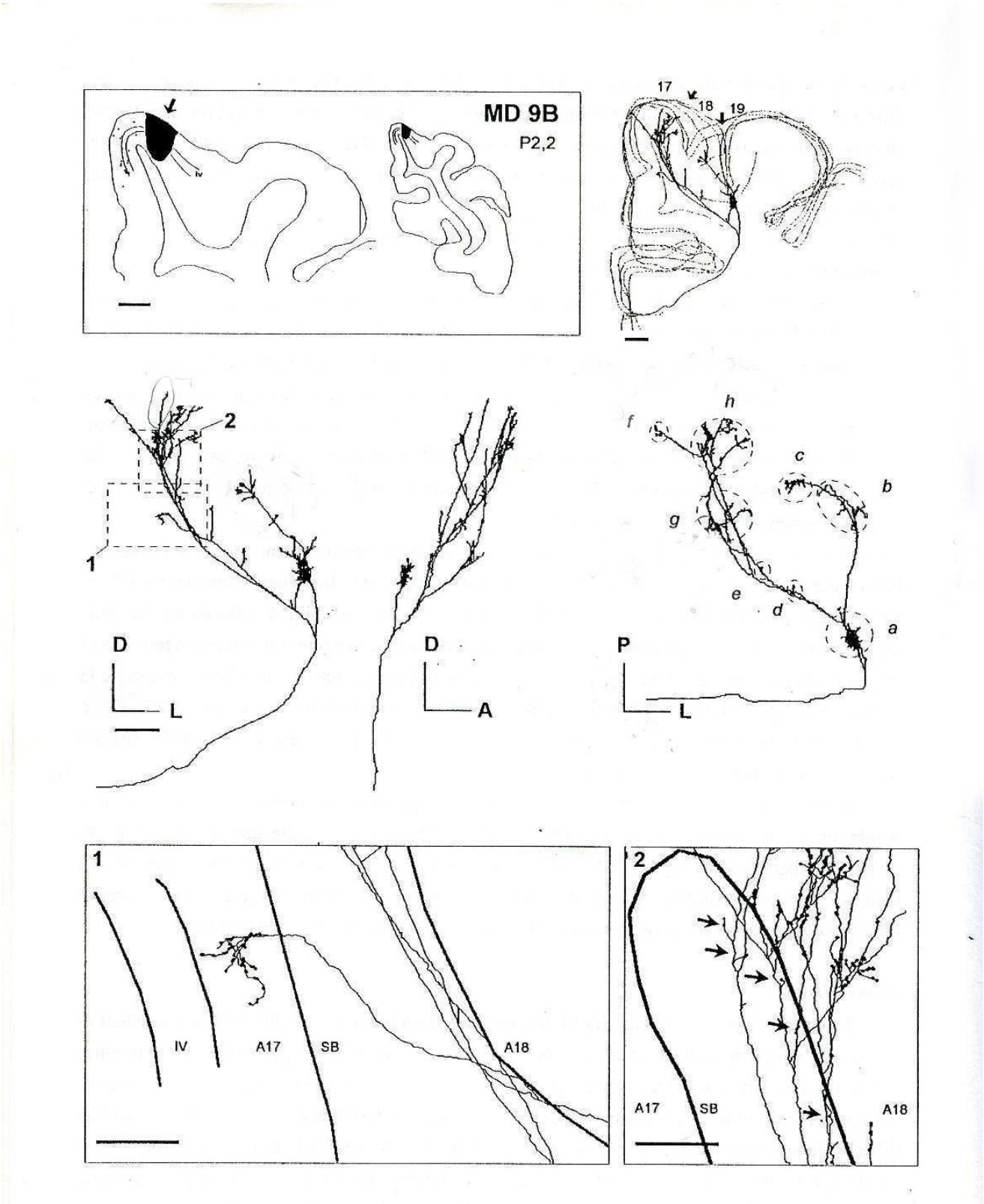

Fig. 37/ Axon MD9B, labelled anterogradely after a restricted injection of biocytine in the 17/18 transition zone of the left hemisphere which is contralateral to the eye that has been occluded 4.5 months before.
Above: on the left, injection site in the 17/18 transition zone. Lines inside the drawing: limits of layer IV; arrow: TZ centre. At right: Frontal view of the axonal terminals in the right hemisphere. Arrows: TZ centre and centre of the 18/19 transition zone. A17 and A18: areas 17 and 18. *In the middle:* on the left, frontal and lateral views of the axonal terminal (with a higher magnification than above); on the right, dorsal view of the same arborisation. The letters indicate its terminal columns and thus its clusters of boutons after identification by sight. *Below:* Frontal views of the axon after zooming onto the two portions delimited just above: (1) terminal bouquet in the median bank of A17; the thick lines indicate the limits of layer IV and of the white matter. (2) Terminal boutons and "en passant" boutons located in the white matter, below the TZ and A18 (arrows); the thick line indicates the limit of the white matter. Scale bars: 250 µm.

Axon MD9B

The figure 37 illustrates axon MD9B. It has been labelled though the same injection of biocytin as axon MD9A. Thus, it also originated from the TZ in the left hemisphere (contralateral of the occluded eye). Although the important curvature of the cortex prevented to represent globally this axon (as it was the case for the previous one), a detailed observation of its different portions has revealed that most of the terminal territories had always a cylindrical or conic shape, which main axis was perpendicular to the cortical surface.

This axon also displayed a quite complex architecture, with 1279 boutons. Its trunk had a calibre of 1.3 µm, which divided in the white matter into 2 primary branches (still very deep below the cortex) at the level of the intersection of the splenial sulcus (s.s.) and the lateral sulcus (l.s.).

The thinnest primary branch (1: 0.8) had immediately an ascendant trajectory and formed an extremely bushy and dense bouquet, with 655 boutons (column **a**, diameter: 350 µm) in the deep layers of the 18/19 border.

The other primary branch i.e. the so called "principal" one (2: diameter: 1.0 µm) ran more medially and divided several times. In a first step, it divided *"serially"*:

(1) A first oblique collateral terminated into 2 different sites. First, it fed column **b** (37 boutons) located in the 18/19 transition zone. This column **b** was more posterior and much more modest than the column **a**. Second, it ran medially before terminating as a conic bouquet (including 100 boutons) in the middle of A18 (column **c**; diameter 450 µm).
(2) Another small branch (diameter: 0.3 µm) then terminated abruptly in the white matter by giving no boutons;
(3) A third branch (diameter: 0.8 µm) ran first laterally below the cortex, distributing "serially" 2 small ascendant collaterals which distributed 4 boutons in the white matter and a few others in the deepest layers of A18 (column **d,** 25 boutons; column **e**, 31 boutons). Second, this same secondary branch (2.3) changed its trajectory, crossed obliquely the optic radiations, to finally penetrate the cortex at the level of the median flank of A17 where it formed a small bunch (column **f**: 47 boutons in the infragranular layers, diameter: 220 µm); see Fig. G, panel 1 below.

This same primary branch additionally ran posterior and medially over a distance of 2.3 mm, keeping its calibre (2: diameter: 1.0 µm), before to divide this time in a *"parallel"* fashion, to give 2 important columns in the TZ (column **g**: 123 boutons; column **h**: 251 boutons). Before entering the cortex, these 2 branches which feed these 2 columns distributed 6 boutons (3 terminal ones and 3 "en passant" ones) in the white matter (Fig. G, panel 2 below).

To summarize, this axon also displayed a very complex architecture with some branches running in very different directions. Similar to axon MD9A, it displayed clearly a *"mixed" (serial-and-parallel) architecture*. It terminated apparently by *8 columns (and thus 8 clusters of boutons*): the largest one (column **a**) was again located in the 18/19 transition zone and displayed the largest amount of boutons (692 boutons); 7 more modest columns were also identified in A18 (with 156 boutons), the 17-18 transition zone (with 374 boutons) and in A17 (with 47 boutons). Ten boutons were additionally found in the white matter, below the TZ (n= 6) and below A18 (n = 4). In total, this axon covered an extended portion of cortex. Along the postero-anterior axis, it covered more than 5 mm. On the other hand, it tangential extension was at least 7.5 mm (by following the curvature of the cortex at the level of layer IV). See Table 1 for a summary.

Panel 1

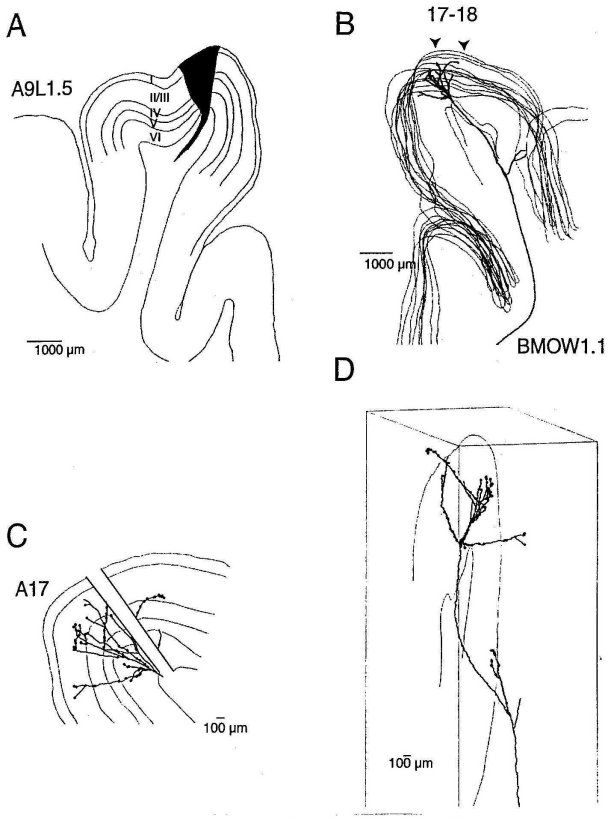

Panel 2

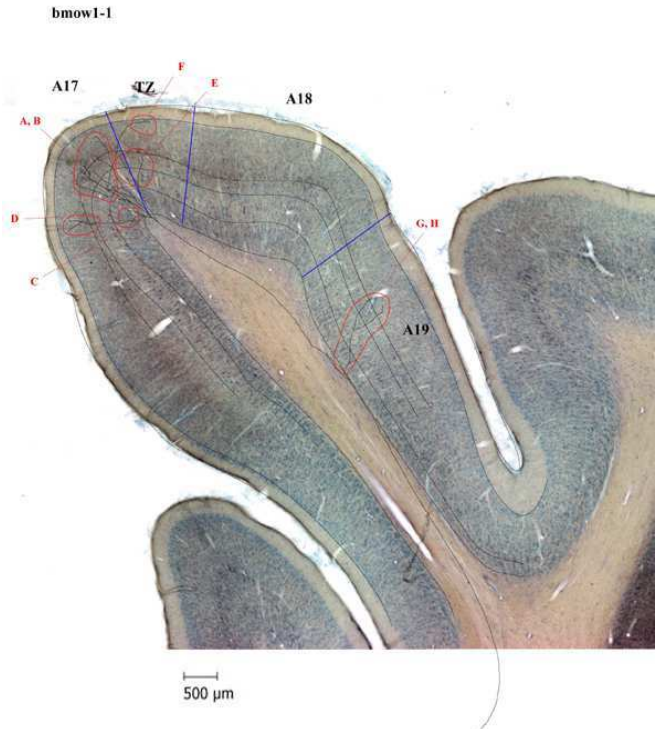

Fig. 38/ Axon BMOW1.1. labelled anterogradely after a restricted injection of biocytine in the 17/18 transition zone of the left hemisphere which is contralateral to the eye that has been occluded 4 months before. *Panel 1:* A, injection site in the 17/18 transition zone. Lines inside the drawing: limits of the different cortical layers.. B. Frontal view of the axonal terminals in the right hemisphere. Arrows: 17-18 transition zone. C. Laminar distribution of the terminal boutons in the cortex. The terminal arborisation of the axon is split because the different branches were not in the same plane and did not terminate in the same area (A17, 17-18). D. Representation of the axon after rotation of +74 degrees along the y axis and -174 degrees along the x axis, with respect to the frontal plane. The limits of the cortex and the white matter are represented. *Panel 2:* Superposition of the axon and a frontal section of the visual cortex (at the same AP) after Nissl labelling. Letters in red indicates each terminal branch.

Axone BMOW1.1.

The figures 38 and 39 illustrates the axon BMOW1.1. It has been also labelled after an injection of biocytin in the TZ, but this time at rather anterior coordinates (A_9-$L_{1.5}$; Fig. 28, panel 1).

Compared to the 2 previous ones, the arborisation of this axon was rather simple and displayed only 146 boutons. Its trunk (diameter: 1.68 µm) has been reconstructed over a distance of 33.5 mm from the corpus callosum. It ran directly toward the lateral gyrus, with an ascending trajectory (in parallel to layer VI of A17). This one divided rather highly in the white matter to give 2 primary branches at the level of the lateral sulcus (l.s., Fig. 38, 29 and 31 in panel 1). Altogether, it has been 3D-reconstructed from 39 sections (i.e. 39 x 75 µm).

The thinnest primary branch (1: 0.54 µm) was very short, and did not display any bouton.

The other primary branch (2) had a diameter of 1.10 µm and divided immediately after the first node to give 2 secondary branches (Fig. 38, 31 in panel 1; panel 2; Fig. 39). The thinnest branch (2.1; diameter 0.28 µm) ran toward A19, delivered very rapidly 12 "en passant" boutons in the white matter and entered in A19 without delivering any terminal bouton. The other secondary branch (2.2; diameter 1.10 µm) continued its ascending trajectory and ended by an extremely bushy intracortical bouquet both in A17 and TZ (see details in Fig. 38, 30 in panel 1; Fig. 39). This latter branch displayed as much as 27 intracortical nodes, included 134 boutons and covered ~6.75 mm² at the pial surface (2.5 mm along the antero-posterior axis after correction of the compression of the tissue; 2.7 mm along the medio-lateral thus frontal axis). Most of the collaterals of this branch converged onto A17 (near the TZ) to form the terminal column **a,** with 113 boutons mainly located in the supra- and the infragranular layers (Layer II/III: 42 boutons; layer IV: 18 boutons; layer V: 4 boutons; layer VI: 49 boutons). The other collaterals reached the TZ to form the terminal column **b** with 21 boutons which were mainly located in the supragranular layers (layer V: 15 boutons; layer IV: 5 boutons). Notice that this latter column was fed through 2 different branches which converged toward the TZ: one projected directly to the TZ and the other originating from the branch which ran mainly toward A17 (see Fig. 38, 31 in Panel 1).

In summary, this axon displayed a *"serial" architecture*, with a trunk giving 2 branches terminating in two separate territories. It displayed only *2 terminal columns* (and thus *2 intracortical clusters of boutons*): the largest one ("a") was located in A17 and displayed the largest amount of boutons (n = 113, i.e. 77% of the total); the other one ("b") was located in the TZ and was much more modest, with only 21 boutons. Twelve "en passant" boutons were additionally found in the white matter, below A19. Taking into account the distribution of the boutons in the cortex, it may be considered as a *trans-granular* in A17 and as a *supragranular one* in the TZ (see Table 1 for a summary).

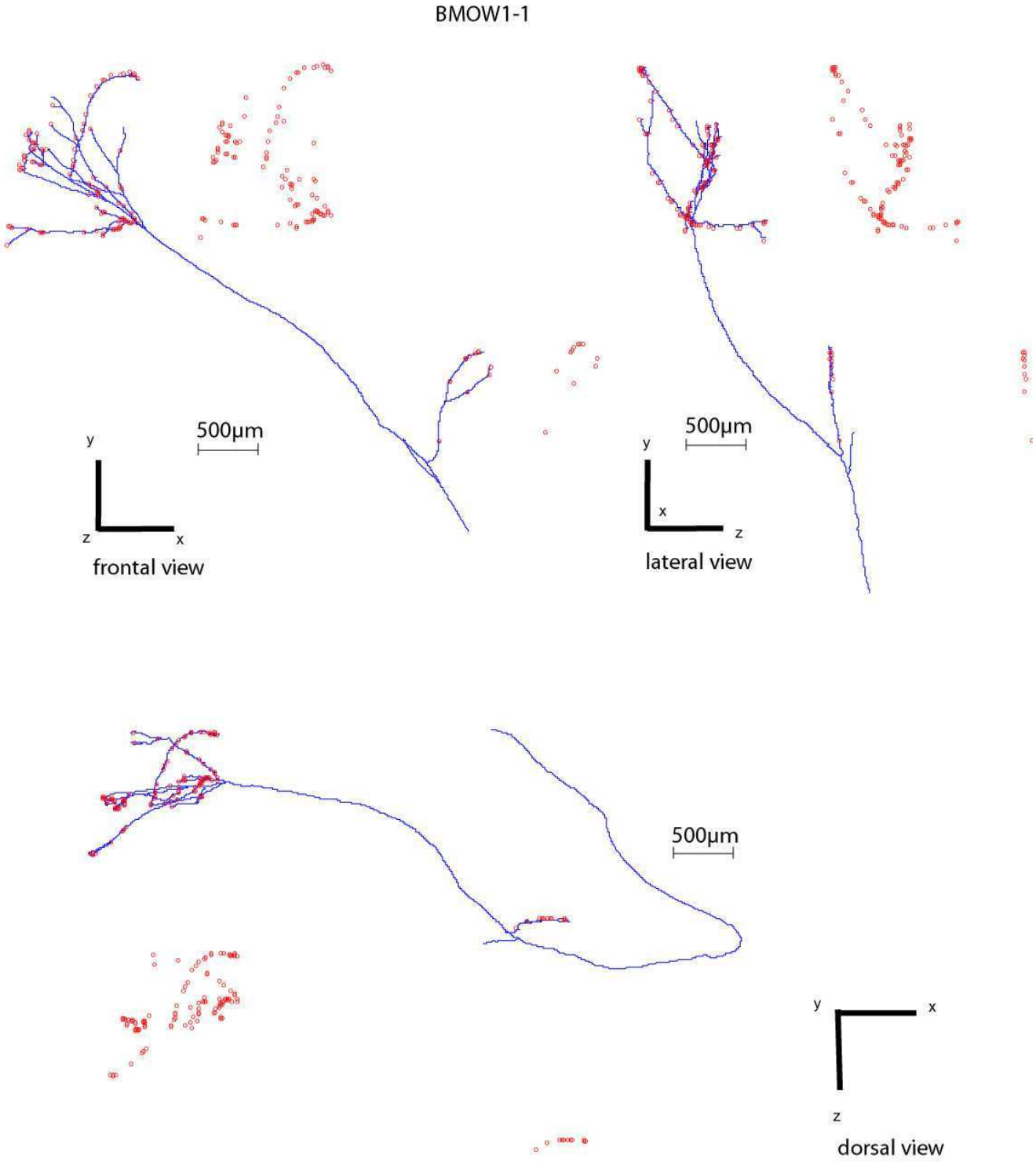

Fig. 39/ Frontal, lateral and dorsal views of axon BMOW1.1, with its boutons (which have displaced laterally or below the axon for a better view).

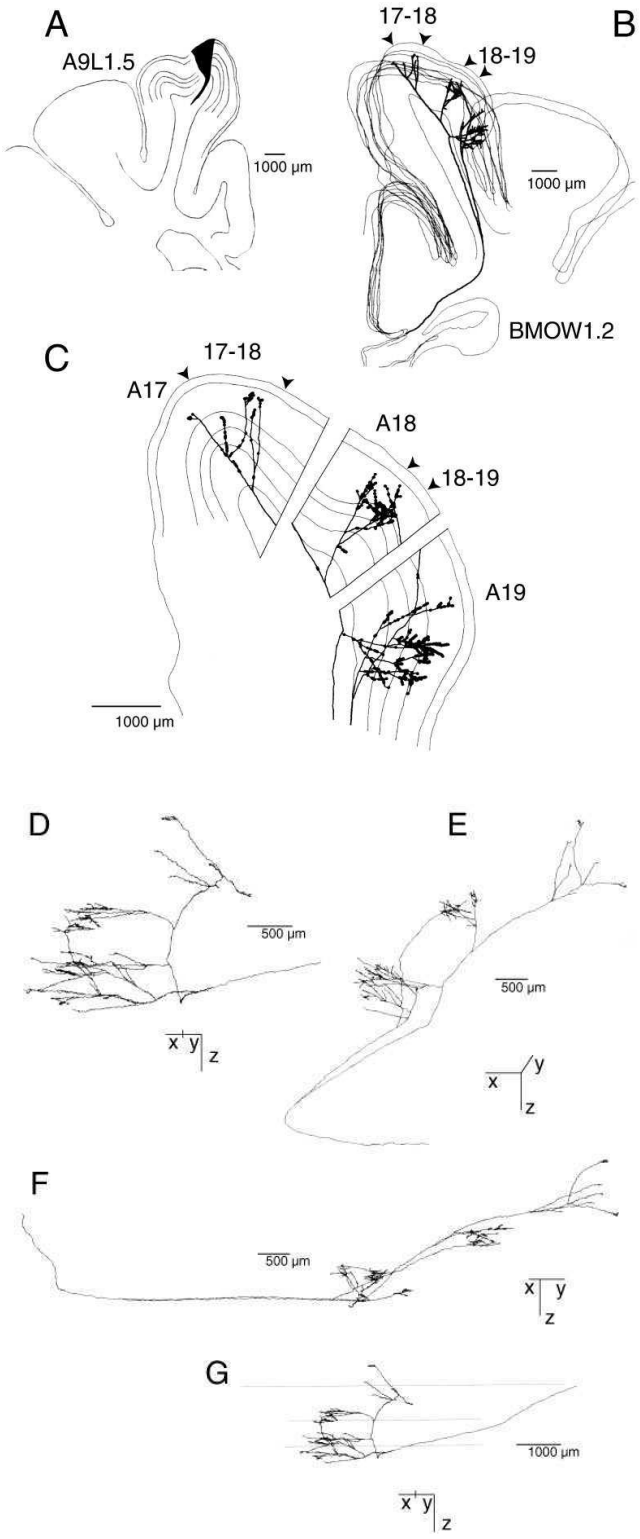

Fig. 40/ Computer-aided 3-D reconstruction of one individual labelled callosal axon (BMOW1.2) from a 4 months old cat reared with a monocular occlusion of the right eye as early as 5 or 7 post-natal days. An anterograde tracer (biocytin) was injected in the left hemisphere rather rostrally, at stereotaxic Horsley-Clarke coordinates $A_9L_{1.5}$ where the transition zone between the visual cortical areas 17 and 18 (panel A). Its terminals were 3D reconstructed within the contralateral (right) hemisphere (ipsilateral to the occluded eye) using the Neurolucida Software (panels B to G). B and C, the terminals are shown in the frontal plane, within the outlines of a few of the serial sections used for the reconstruction ; pial surface and bottom of grey matter are indicated by interrupted lines. Dorsal is upwards, medial to the left. Calibration bars are 1000 µm. A17, A18, A19, visual cortical areas 17 and 18 and 19; A17-A18, transition zone between A17 and A18 ; A18-A19, transition zone between A18 and A19. D to G, same axonal terminal but after changing the view angle (X, lateral); Y, anterior; Z, dorsal). For example, the axon in panel E is seen from the top (see text for further details). Calibration bars are here 500 or 1000 µm.

Axon BMOW1.2.

The axon BMOW1.2 has been labelled anterogradelly after injection of biocytin in the left hemisphere, at Horsley-Clarke stereotaxic coordinates $A_9L_{1.5}$ (Fig. 28; Fig. 40, panel A). In cat visual cortex, this corresponds to a rather anterior portion of the transition zone (TZ) between A17 and A18, where the inferior portion of the visual field is represented (Tusa et al., 1978; 1979). Then, its terminal arbour has been 3D reconstructed from the right hemisphere (Fig. 40, panels A to G, Figs. 41 to 43). It has been reconstructed over a distance of 66.6 mm (from the corpus callosum to the cortical plate), from 42 sections (42 x 75 µm) and displayed a trunk which diameter was 1.68 µm. At the level of the first node, this main trunk divided in the white matter at the level of the cingular sulcus (c.s), thus again very far from the cortical plate. This gave two first order (or primary) branches running in "*parallel*" and vertically toward the cortical plate (Figs. 40, panel B; Figs. 41 to 43).

The most lateral of these two primary branches (diameter 1,68 µm) turned gradually to the right, penetrated the visual cortex at the level of A19 and divided again (at the level of the second node) in the inferior part of layer VI (Fig. 40, panels B and C; Fig. 41 and 42). One of these two second-order (or secondary) branches ramified, giving 194 boutons in the different layers of A19 (see Fig. 40, panel C; Fig. 41 and 42). The other second-order branch also terminated in A19 (188 boutons). But, additionally, after distributing a few "en passant" boutons (n=3), it gave a branch terminating in the 18/19 transition zone as well as in A18 including 77 boutons.

In contrast to the former primary branch, the latter one (diameter 1,68 µm as well) continued to run in the white matter vertically toward the lateral gyrus, with a medial trajectory, distributing three second-order branches following a "*serial*" pattern (Fig. 40, panels B-C; Figs. 41 to 43). The first one gave 89 boutons in A19, at the same place as those provided by the other first-order branch. The second one terminated at the 18/19 TZ (72 boutons) and A18 (78 boutons). The third branch terminated in the 17/18 TZ (77 boutons) and in A17 (15 boutons).

In total, such individual terminal arbour displayed a *"mixed" parallel-and-serial architecture*, thus a complex architecture (see Fig. 40, panels B and C; Figs. 41 and 42). It seemed to include *4-5 terminal columns (thus 4-5 clusters of terminal boutons)* which were rather difficult to identify by sight. Such a complexity is further illustrated by the global distribution of the terminals across both the cortical areas and the different cortical layers, and the numerous boutons they included (795 boutons in total):

a) From the top of the brain, taking the midline as a reference i.e. the antero-posterior orientation, such axon was oriented obliquely and extended over ~3 mm in the visual cortex (Fig. 40, panel E);
b) Tangentially, it displayed different terminal sites, with a variable number of boutons. Most of them were however located in A19 (with 473 boutons distributed in the various cortical layers). Others were located at the 18/19 TZ (149 boutons), in A18 (78 boutons) or more medially in TZ (77 boutons) or A17 (15 boutons). The number of boutons thus decreased from the most lateral column to the most medial one. The column including the larger number of boutons was also the larger one at the level of the pial surface: 0.69 mm², with 1.4 mm of extension along the antero-posterior axis (Fig. 1E). But the column located in the 18/19 TZ and A18 had the smallest extension, while it had not the smallest amount of boutons (0.37 mm² with an extension of 0.8 mm; Fig. 40, panel E).

Radially, i.e. across the different cortical layers, the laminar distribution of the boutons was mostly "*supra-granular*". Thus, in A19, most of the boutons were located in II-III layers (n=198) and in layer IV (n=173), with however a lot of them also in layers V and VI (n=54 and n=48 respectively). Within 18-19 TZ, the layers including a majority of boutons were the II-III ones (n=71) and IV (n=64), while the layers V and VI included only few boutons (layer V, n=5; layer VI, n = 9). In A18, more than half of the boutons were located in layer II-III (n=55), but some were also located in layer IV (n=19), in layer V (n=1) and layer VI (n=3). In the 17-18 TZ, the layer II-III included 33 boutons, while the other cortical layers (except layer I) included a similar number of boutons (layer IV, n=11; layer V, n= 14; layer VI, n=19). In A17, almost all the boutons were located in layer II-III (n=12), while the others were located in layer VI (n=3). Thus, layers II-III and IV included most of the boutons while layer I did not include any. Finally, notice that 3 boutons were found in the white matter, below the 18-19 TZ (n=2) and A19 (n=1). See Table 1 for a summary.

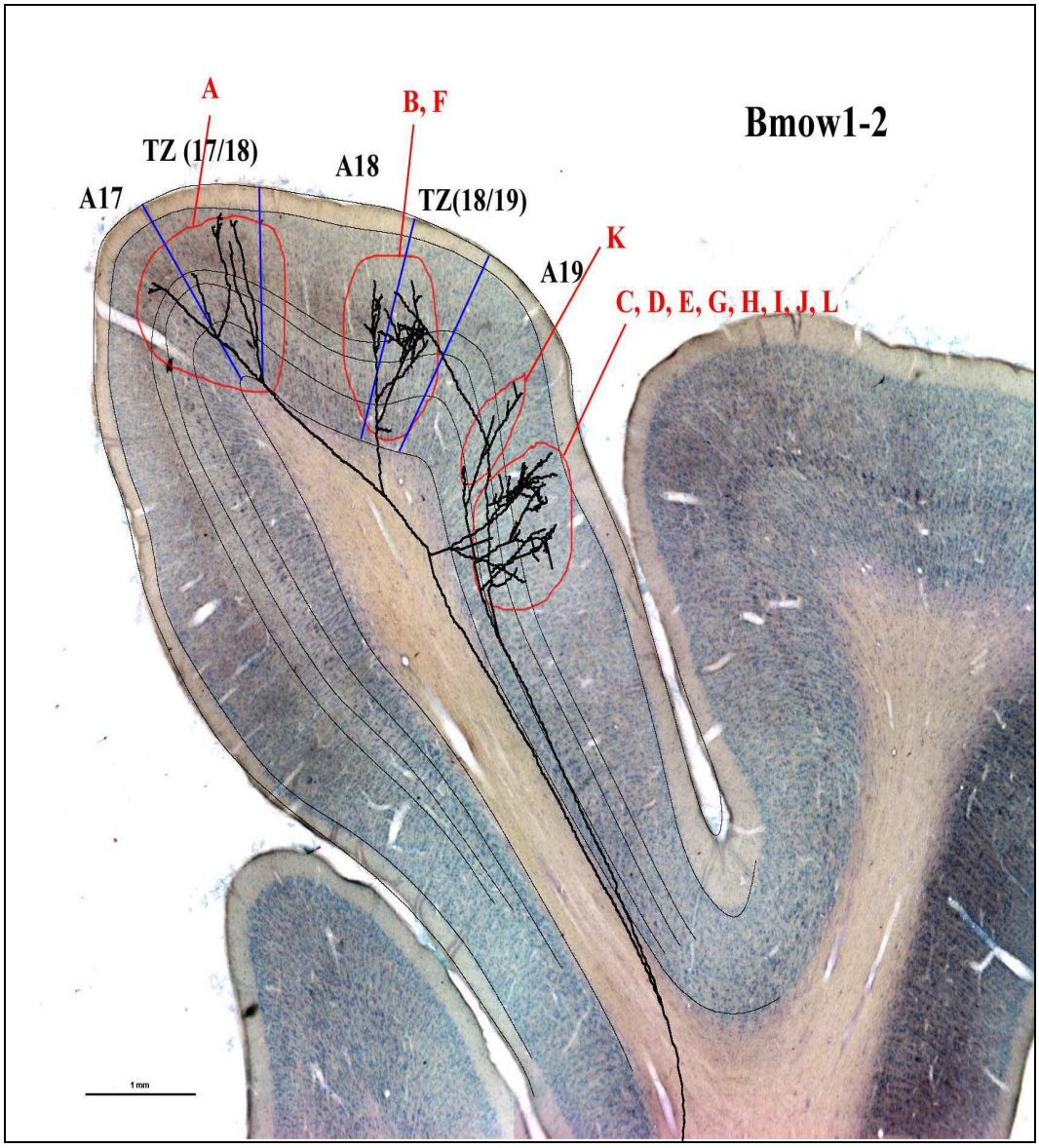

Fig. 41/ Axon BMOW1.2. labelled anterogradely after an anterior injection of biocytin in the TZ (at $A_9L_{1.5}$) of the left hemisphere which is contralateral to the eye that has been occluded 4 months before. Superposition of the 3D reconstructed axon and a frontal section of the visual cortex (at the same AP) after Nissl labelling. A17, TZ (17-18), A18, same significations as before. A19, area 19; TZ (18-19): transition zone between A18 and A19. Letters in red indicates each terminal branch.

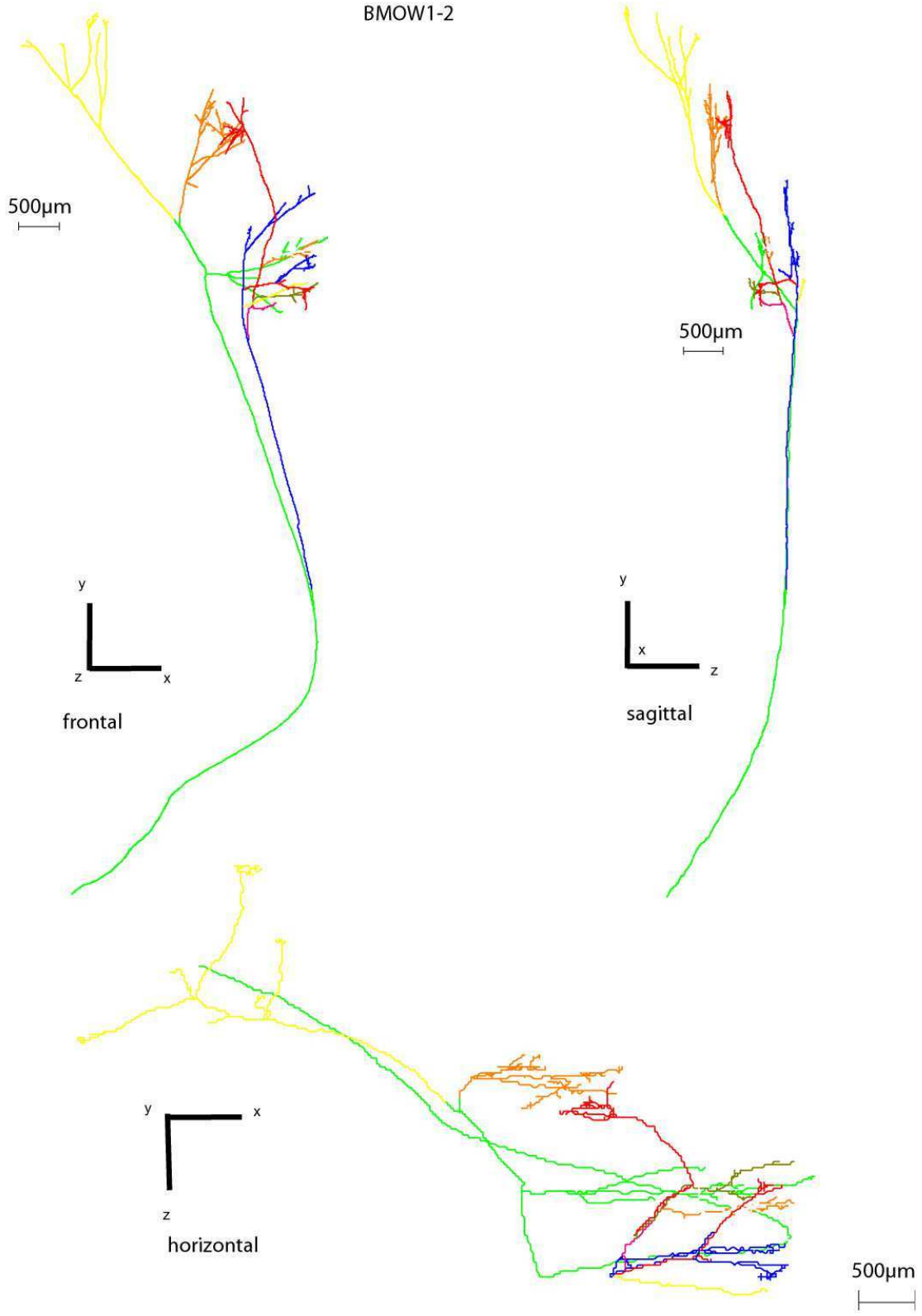

Fig. 42/ Frontal, sagittal and horizontal views of axon BMOW1.2. with each branch with a different colour.

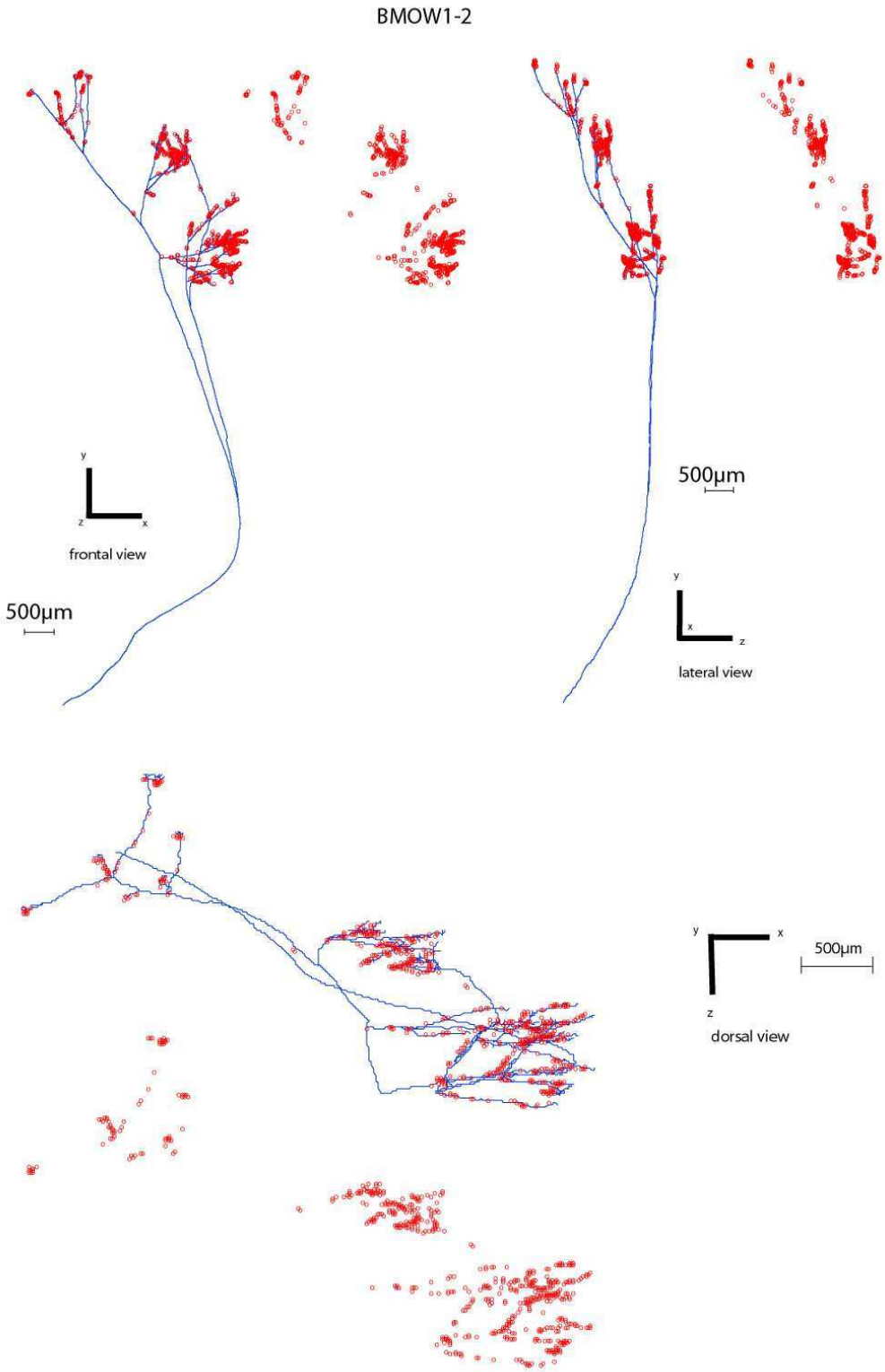

Fig. 43/ Axon BMOW1.2. and its boutons (in red). Same representation as before.

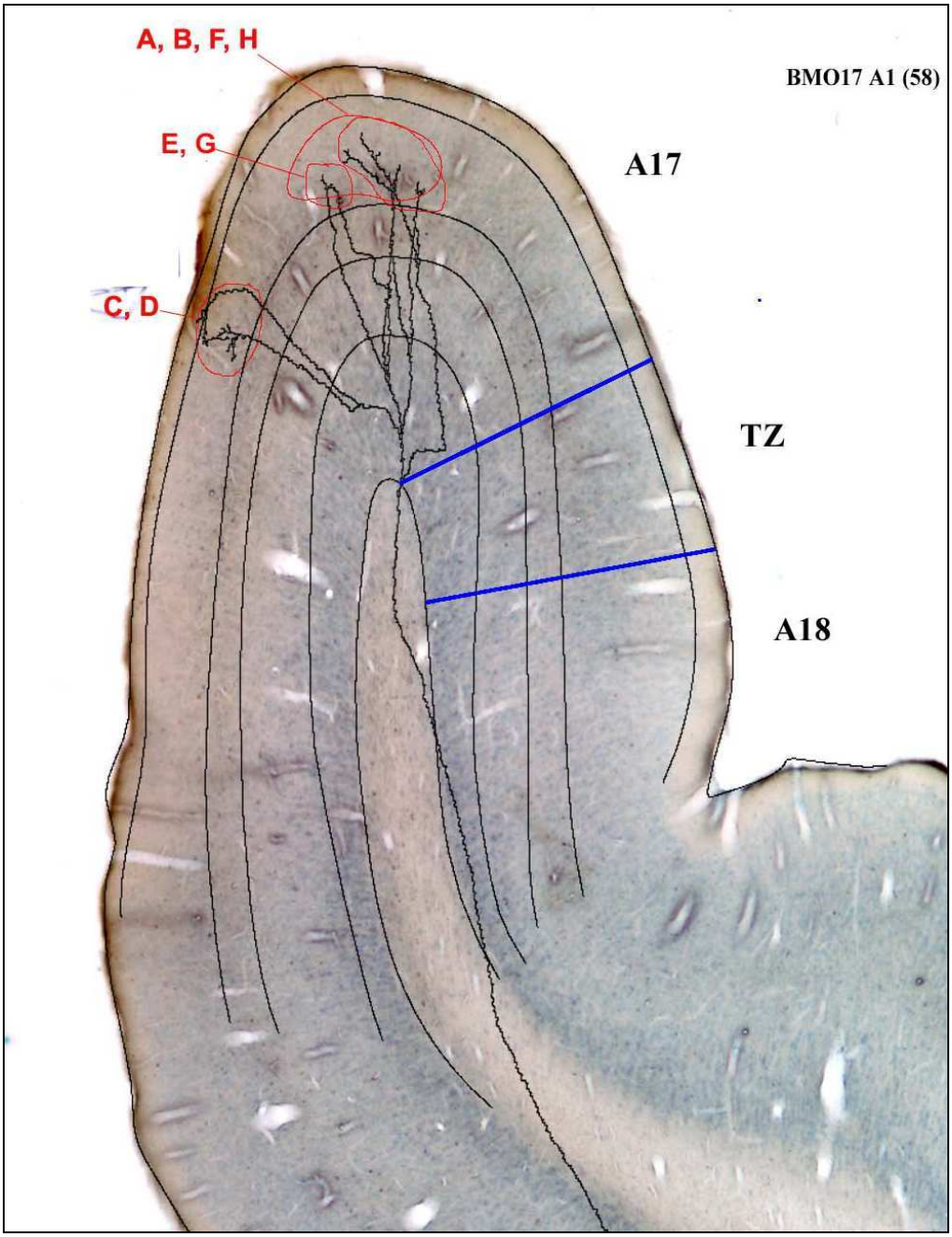

Fig. 44/ Axon BMO17.A1. labelled anterogradely after a posterior injection of biocytin in A17 (at P_3L_1) of the left hemisphere which is contralateral to the eye that has been occluded 4 months before. .Superposition of the 3D reconstructed axon and a frontal section of the visual cortex (at the same AP) after Nissl labelling. A17, TZ, A18, same significations as before. Letters in red indicates each terminal branch.

1.2. **Injections in A17**

Six additional callosal axons have been labelled in the right hemisphere (ipsilateral to the occluded eye). But this time, it was after injection of biocytin in A17 of the left hemisphere.

Three of these axons were labelled after a *posterior* injection of biocytin (P_3L_1). They were labelled in the cat BMO17 and were thus called BMO17.A1, BMO17.A2 and BMO17.A3 respectively.

Three others were labelled after a more *anterior* injection of biocytin (A_4L_1) in the cat BMOW2. They were called BMOW2.1, BMOW2.2. and BMOW2.3 respectively.

Axon BMO17.A1

This axon, which is illustrated in Figs. 44, 45 and 46 has thus been labelled after injection of biocytin in a rather posterior and medial portion of A17 (P_3L_1). This injection site extended over 25 adjacent 75-µm-thick frontal sections. The axon has been 3D-reconstructed from 98 successive sections (i.e. 98 x 75 µm).

Its trunk had a diameter of 1.53 µm and it has been reconstructed over a total distance of 30.3 mm. It ran first over 15.3 mm in the white matter to give its primary branches only immediately when entering in the cortex, in A17. Two primary branches were thus identified. The first one reached directly the more superficial cortical layers without any further division (branch H). In contrast, the second one divided (very near the first node) several times to give 7 secondary branches (branches A to G) which diameters were between 0.28 and 0.56 µm. Altogether, this axon displayed 48 nodes; terminal branches grouped apparently into 2 separate terminal columns ("**a"** and "**b"**) which all ended in A17, rather far from the TZ. It covered ~2 mm along the medio-lateral axis while it covered less than 1 mm along the antero-posterior one.

While it displayed globally 218 boutons, 90% of them (n=198) were located in layer II-III. Others were located in layer V (n=5) or in the white matter, below A17 (n=4) or below the TZ (n=11). One hundred and twenty-five of these boutons were included in column "a" while 89 others formed column "b".

Globally, this axon thus displayed a rather *simple* arborisation with however *2 terminal columns* being *restricted to A17.* It displayed only *218 boutons*, thus apparently distributed into *2 clusters*, with a *supragranular* distribution (See Table 1 for a summary).

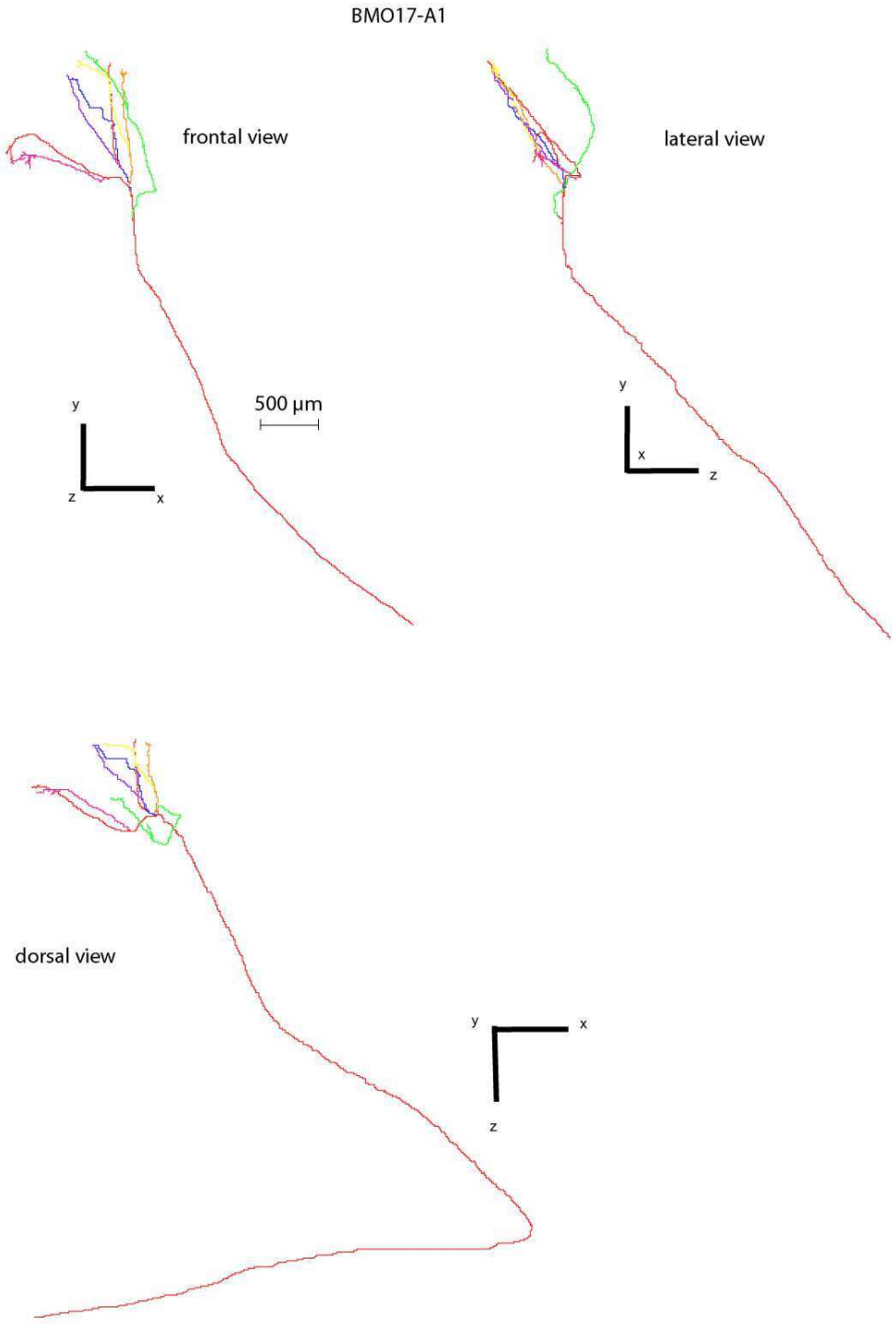

Fig. 45/ Axon BMO17-A1 with its different branches in colour.

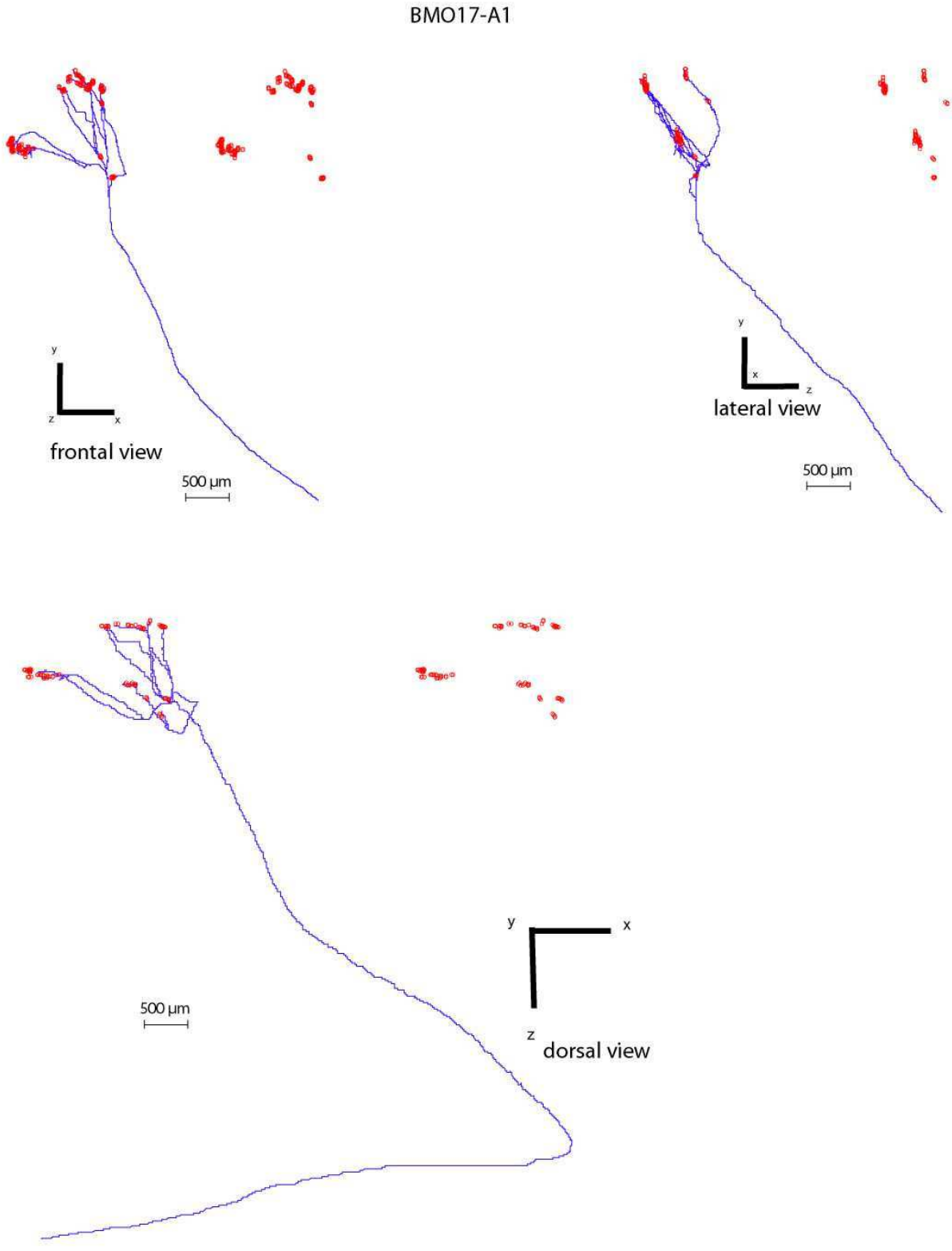

Fig. 46/ Axon BMO17-A1 with its boutons (in red). Same representation as before.

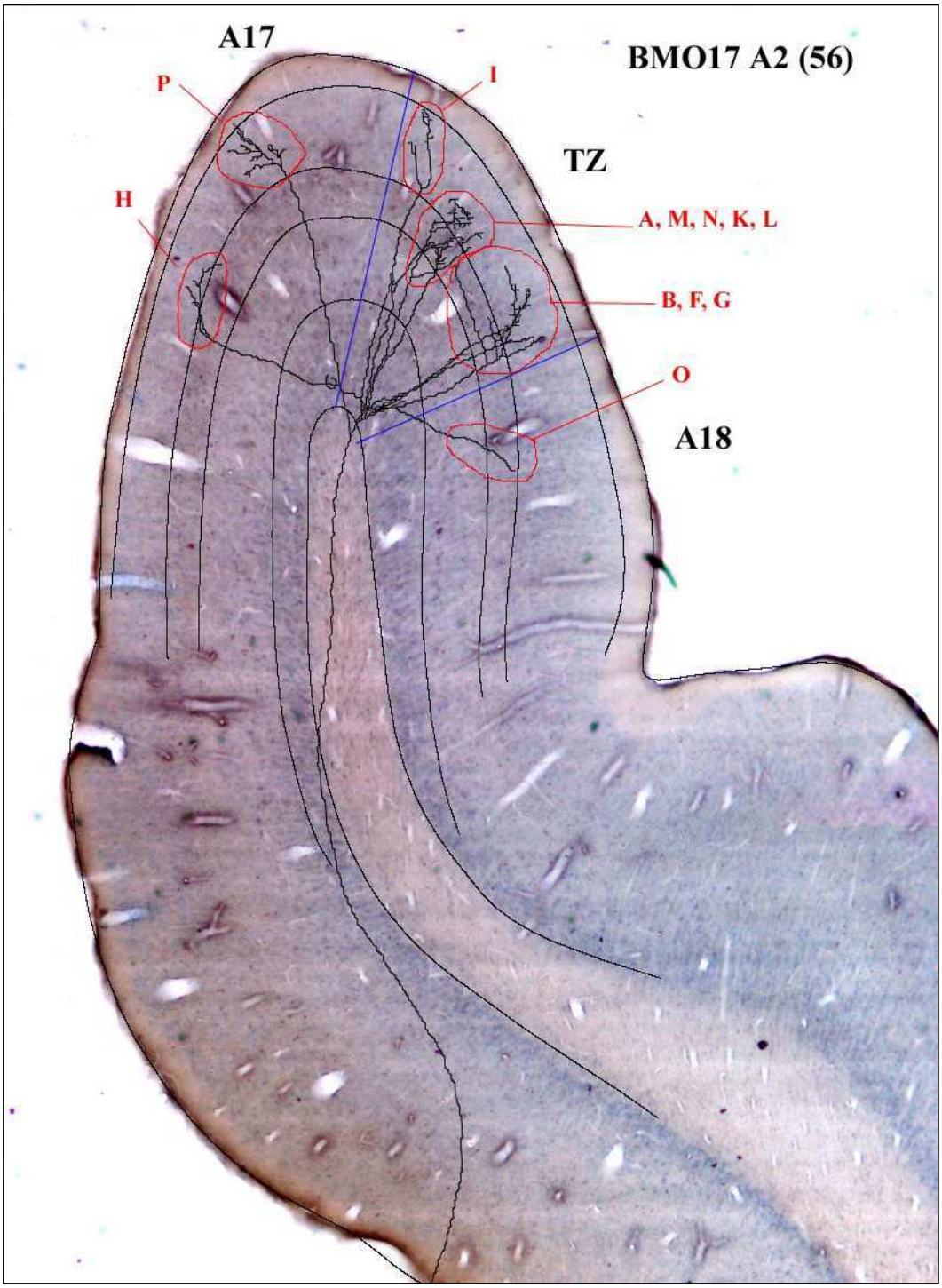

Fig. 47/ Axon BMO17-A2. labelled anterogradely after a restricted posterior injection of biocytin in A17 (at P_3L_1) of the left hemisphere which is contralateral to the eye that has been occluded 4 months before. .Superposition of the 3D reconstructed axon and a frontal section of the visual cortex (at the same AP) after Nissl labelling. A17, TZ, A18, same significations as before. Letters in red indicates each terminal branch.

Axon BMO17.A2

The Figures 47 to 49 illustrate this axon which has been labelled from the same injection site as axon BMO17.A1 (in A17, at P_3L_1, extending over 25 adjacent 75-µm-thick frontal sections).

This axon, which extended over 85 successive frontal sections (85 x 25 µm) displayed an arborisation which was rather bushy, with 671 boutons. Its trunk had a diameter of 1.39 µm, running over a total distance of 45.2 mm. It ran first in the white matter over 15.21 mm from the midline. Then, after forming a first node just below the TZ, it entered the cortex in this transition zone between A17 and A18.

After entering in the visual cortex, it divided numerous times, leading to the formation of a bouquet including 10 branches:

- 2 of these (H and P) terminated medially in A17, with 62 and 128 boutons respectively;
- 7 others ended in the TZ, with most of the boutons (n = 454);
- 1 last one in A18 (branch O), which gave 27 boutons.

In A17 and A18, all the boutons were located in the supragranular layers (n=190). In the transition zone between both areas, most of them were also located in layers II-III (n=423); others were located in layer IV (n=3) or layer V (n=28).

Altogether, this axon displayed a *simple* architecture. The number of *terminal columns* was rather difficult to appreciate even when viewing the axon from different angles. Thus the *number of clusters of boutons* itself was also difficult to determine: 1 or 2 were located in A17; at least 2 were located in the TZ, and likely a last one was located in A18. In total, it covered ~5.3 mm along the medio-lateral axis, including a medial part of A17, the TZ and a part of A18. Radially, while most of its boutons were located in layers II-III, it displayed clearly a *supragranular* distribution for that.

See Table 1 for a summary.

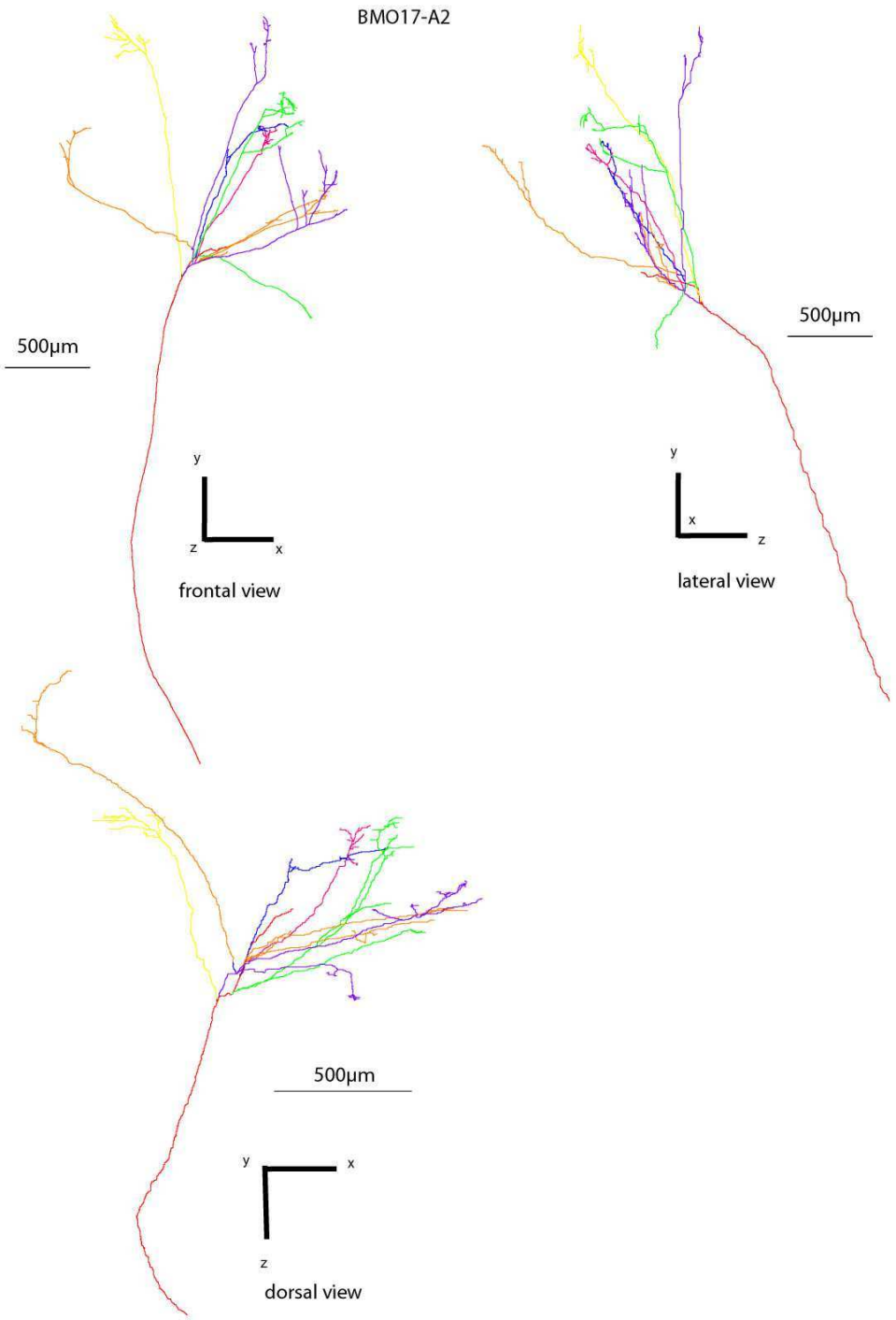

Fig. 48/ Axon BMO17-A2, with its different branches in colour.

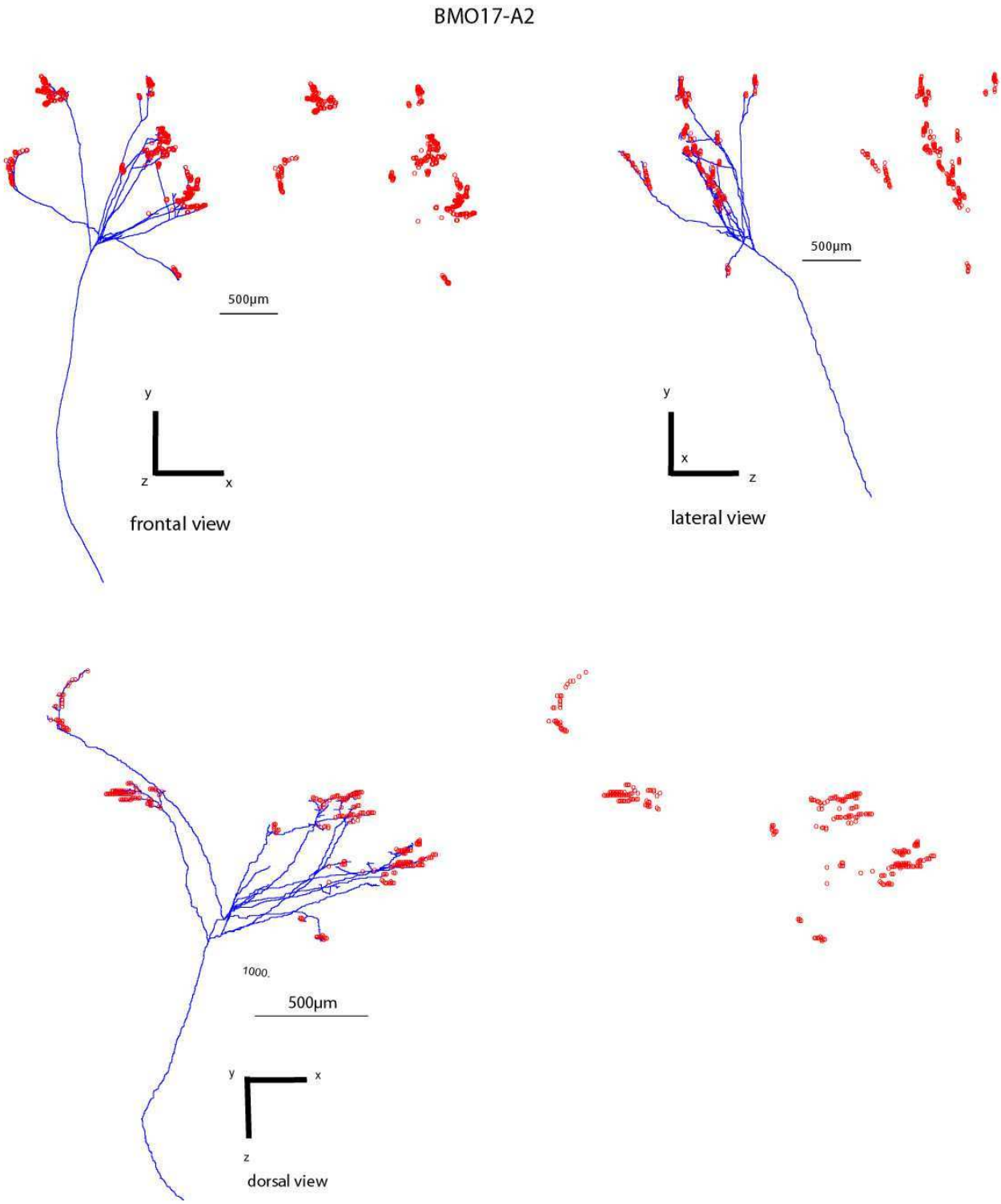

Fig. 49/ Axon BMO17-A2, with its boutons (in red).

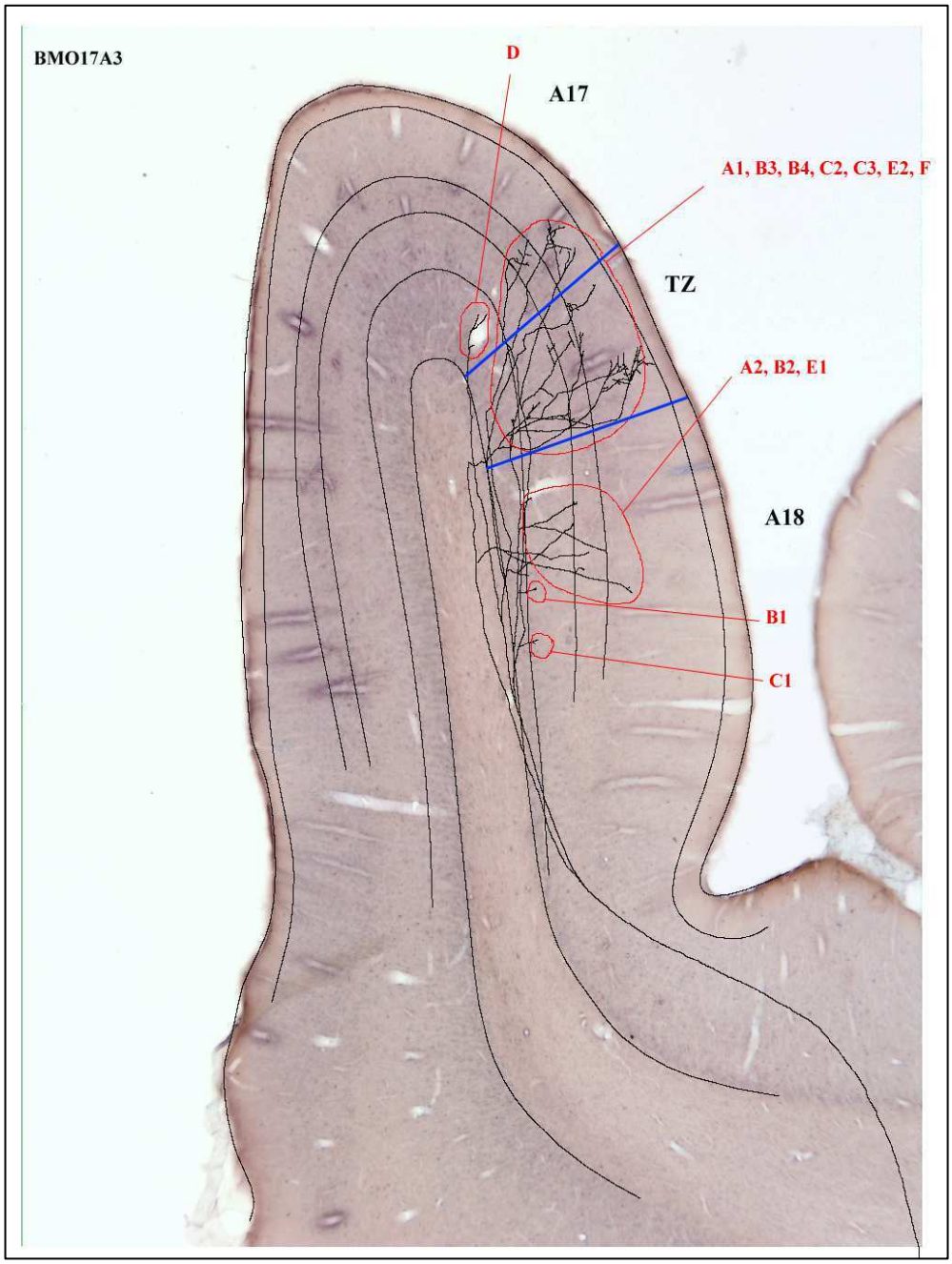

Fig. 50/ Axon BMO17-A3. labelled anterogradely after a restricted posterior injection of biocytin in A17 (at P_3L_1) of the left hemisphere which is contralateral to the eye that has been occluded 4 months before. .Superposition of the 3D reconstructed axon and a frontal section of the visual cortex (at the same AP) after Nissl labelling. A17, TZ, A18, same significations as before. Letters in red indicates each terminal branch.

The Figures 50 to 52 illustrate this axon which has been labelled from the same injection site as axons BMO17.A1 and BMO17.A2 (in A17, at P_3L_1). It has been 3D-reconstructed from 84 successive frontal sections (i.e. 84 x 75 µm).

This axon displayed an arborisation which was extremely bushy: it had as much as 103 nodes. It also displayed 510 boutons as a total.

It trunk (diameter: 1.53 µm) divided into 2 primary branches approximately at the level of the postero-lateral sulcus (pl.s), within the white matter. At that time, ~12.1 mm of the axon was 3D reconstruction. These two primary branches continued running in the while matter in *parallel*.

The most medial primary branch (1, diameter: 0.97) ran toward the cortex with an ascending trajectory, giving very rapidly different secondary branches organized *serially*. A first secondary branch (1.1, diameter: 0.56 µm), which turned left, entered into the middle of A18, distributing 20 synaptic boutons in different cortical layers (branch A2; 7 boutons in layer II-III, 12 in layer IV and 1 in layer V). Continuing its ascending trajectory, this same primary branch then gave a second secondary branch (1.2., diameter: 0.4 µm) which entered in the TZ (branch A1), distributing 210 boutons in layers II-III (n=175), IV (n=12), V (n=6) and VI (n=17).

The second primary branch (2, diameter: 1.0 µm), a little bit more lateral than the first one, also distributed different branches along its ascending trajectory toward the cortex. It divided first into 3 tertiary branches (branches B, C and d), still rather deep in the white matter, which themselves divided several times serially:

- Branch B (diameter: 0.4 µm) gave a first short branch in A18 (branch B1), with 2 boutons in layer VI. Then, running upwards, it delivered another branch (branch B2) in the same area, with 8 boutons in layer II-III and 14 boutons in layer VI. It also gave a very short branch (branch B3) in the TZ, with only 9 boutons in layer VI. Then finally, it gave another branch (branch B4) terminating in A17 with 46 boutons in layer II-III.
- Branch C (diameter: 0.4 µm) gave first a very short branch in A18 (branch C1), with 8 boutons in layer VI. A second one ended in the TZ (branch C2), with 16 boutons in layer II-II and 23 ones in layer IV. A third one (branch C3) ended in A17 (branch C3), with 20 boutons in both layers II-III and IV.
- Branch D (diameter: 0.9 µm) terminated in A17 to give 19 boutons in layer VI. It also gave 2 branches (E and F). Branch E ended first in A18 (branch E1), giving out 7 boutons in layer IV and 5 boutons in layer VI. It also gave branch E2 terminating in A17 with 41 boutons in layer II-III. Branch F ended finally in the TZ, with 42 boutons in layer II-III.

Globally, this axon clearly displayed a *"mixed"* parallel-and-serial architecture. The *number of its columns* and thus the *number of clusters* were impossible to determine through a single observation by sight. It extended over ~2.4 mm along the medio-lateral axis and ~1.5 mm along the antero-posterior axis (after correction of the shrinkage), thus covering apparently a surface of 3.6 mm². It terminated in A18, in A17 and in the TZ, with numerous boutons in each region. Such boutons were however more numerous in the TZ: 146 boutons in A17, 300 in the TZ and 64 in A18. Their distribution was mostly *supragranular* both in the TZ and A17; in A18, they rather displayed a *trans-granular* distribution.

See Table 1 for a summary.

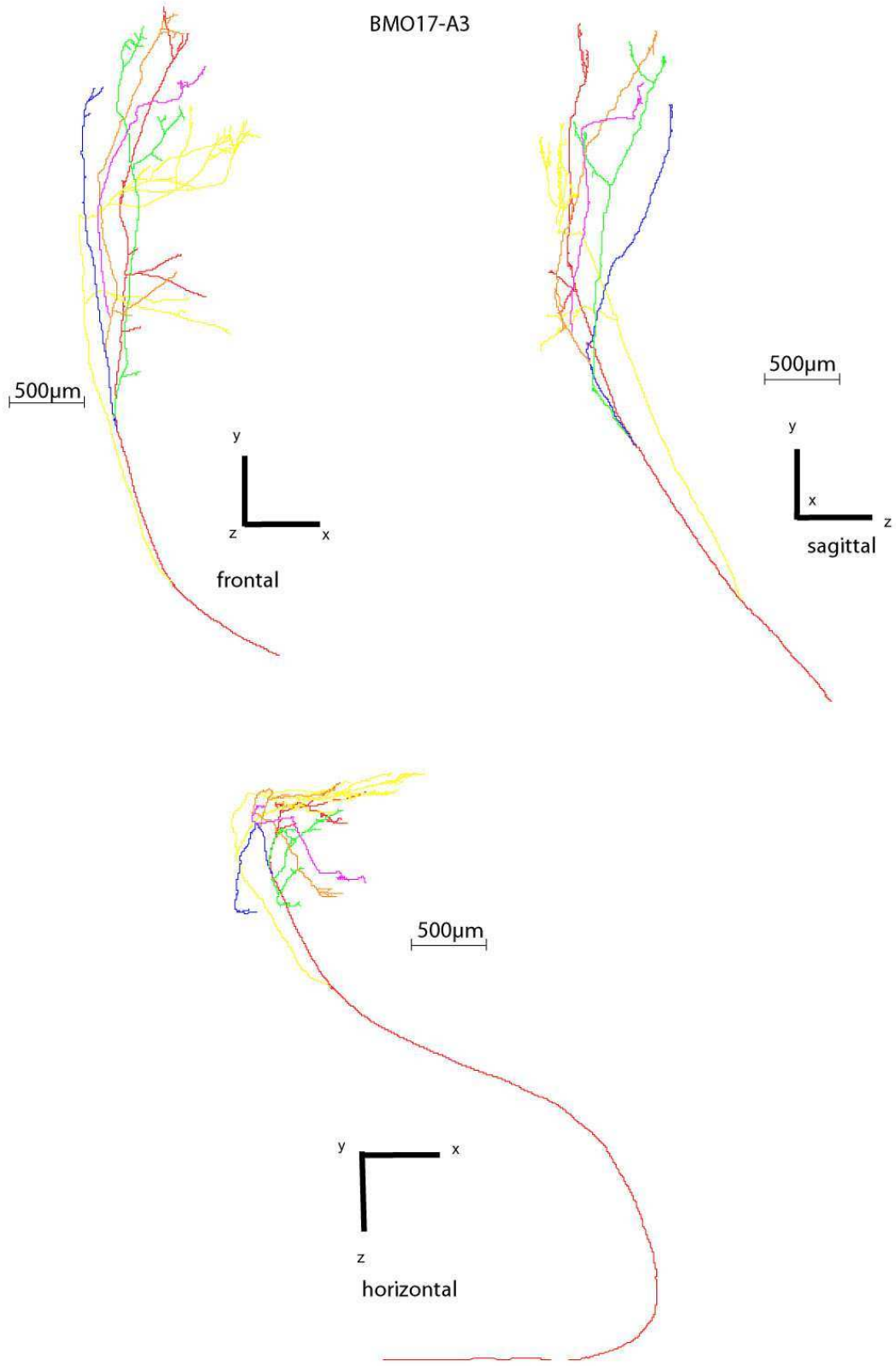

Fig. 51/ Axon BMO17-A3, with its different branches in colour.

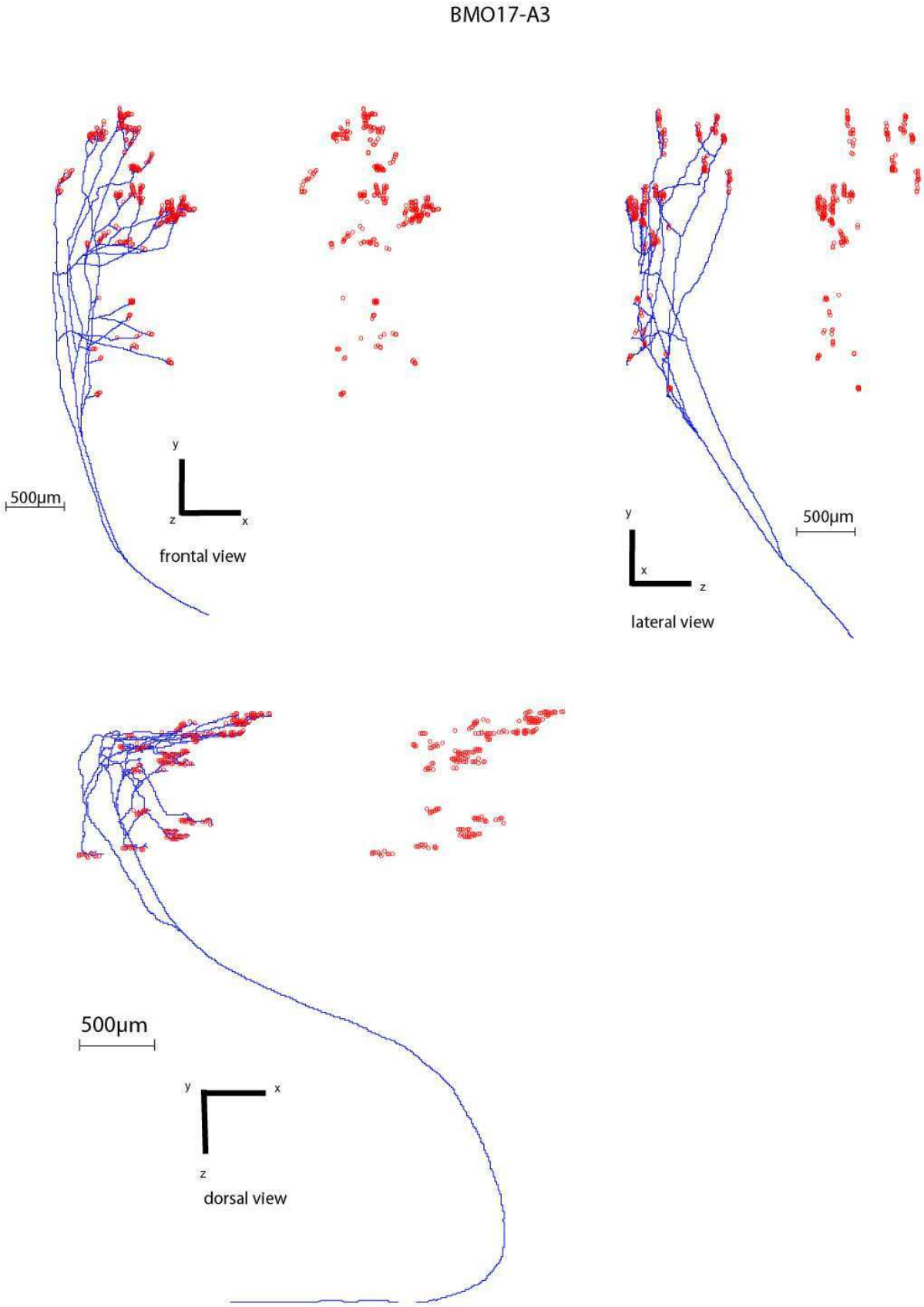

Fig. 52/ Axon BMO17-A3, with its boutons (in red). Same representation as before.

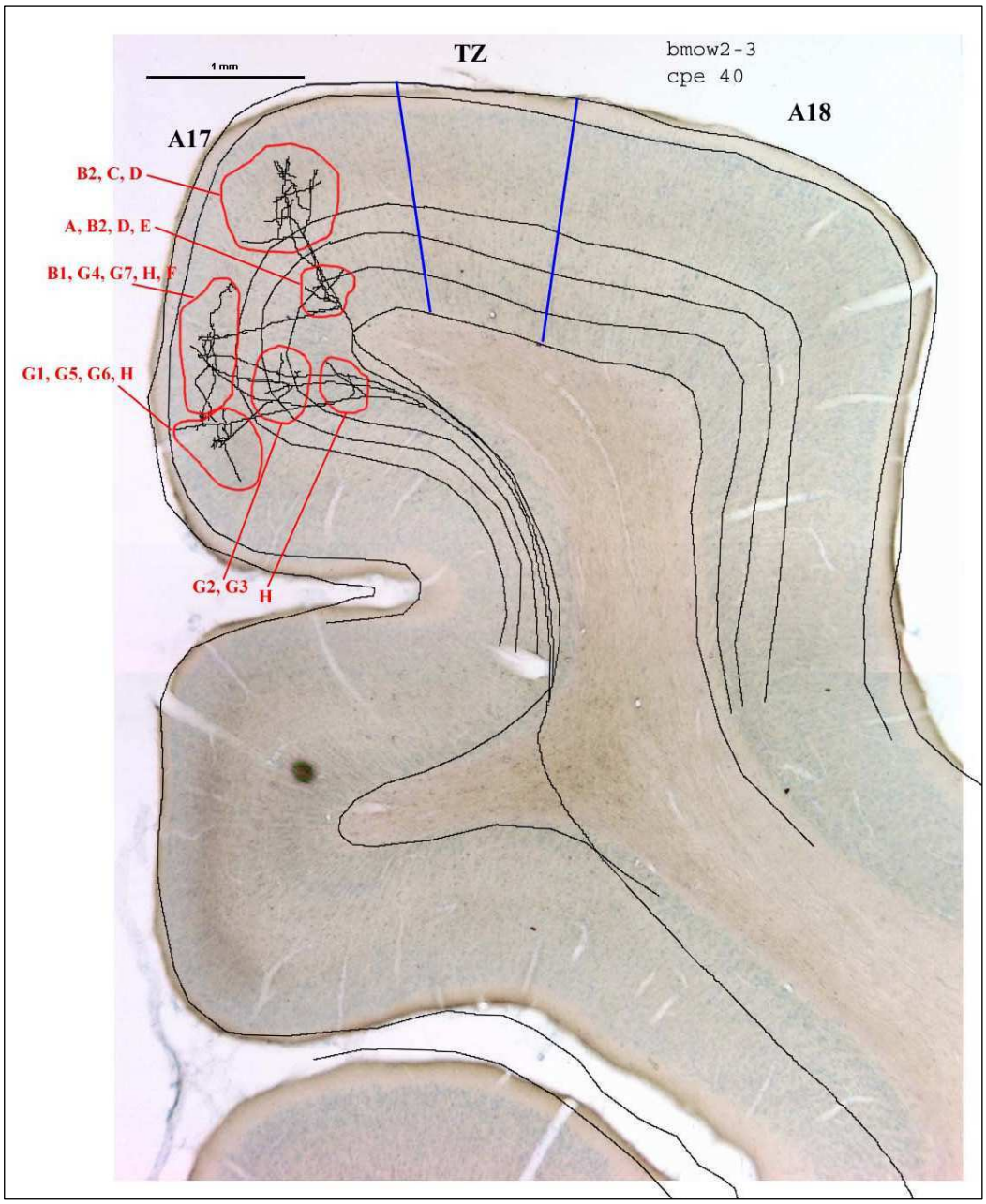

Fig. 53/ Axon BMOW2.1. labelled anterogradely after a restricted posterior injection of biocytin in A17 (at A_4L_1) of the left hemisphere which is contralateral to the eye that has been occluded 4 months before. .Superposition of the 3D reconstructed axon and a frontal section of the visual cortex (at the same AP) after Nissl labelling. A17, TZ, A18, same significations as before. Letters in red indicates each terminal branch (see Text for further details).

Axon BMOW2.1.

This axon is illustrated in Figures 53 to 55. It has been labelled after an injection of biocytin performed in A17 rather anteriorly (A_4L_1). The injection site extended over 29 sections along the antero-posterior axis. The whole axon has been 3D-reconstructed from 28 consecutive frontal sections (28 x 75 µm).

It displayed a rather small arborisation which included 84 nodes and only 356 boutons. It was reconstructed over a distance of 40.8 mm. Its trunk had a rather large diameter (2.16 µm) which divided into 2 primary branches rather deep in the white matter, 11.1 mm away from the midline, at the level of th cinglular sulcus (c.s.). These 2 primary branches ran in *parallel* towards A17.

The most lateral primary branch (1, diameter: 1.08 µm) continued to ran toward the cortex without performing any further division before to reach A17. Most of its branches entered near the TZ, but at more than 1 mm from it. It gave a bouquet including various branches A, B2, C, D and E). One additional one (branch B1) ran toward the medial part of A17, very far from the TZ.

The other primary branch (2, diameter: 1.44 µm) progressively turned left toward the medial part of A17, where the branch B2 of the other primary branch was located already. It divided several times, giving various branches of superior order (branches F to H).

To summarize, this axon displayed a *parallel* architecture, with a first node again very deep in the white matter. Globally, it extended over 3.31 mm along the antero-posterior axis and 1.2 mm along the antero-posterior one. Although it was difficult to appreciate, it seemed to display at least 2 *columns*, and thus *2 clusters of boutons.* The distribution of the boutons was mostly *supragranular*: layer II-III, n=225; layer IV, n=25; layer V, n=48, layer VI, n=58.

See Table 1 for a summary.

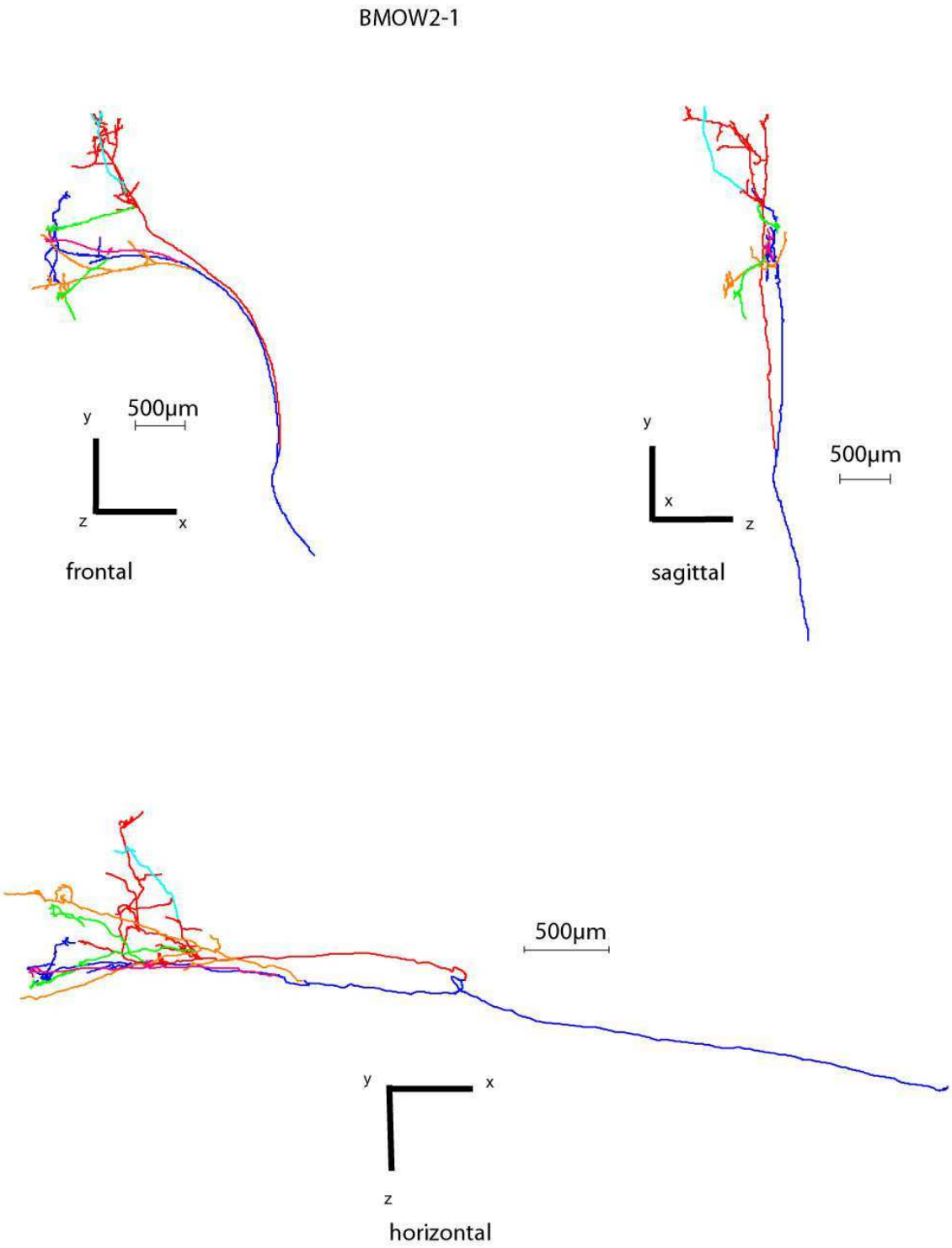

Fig. 54/ Axon BMOW2.1. with its different branches in colour.

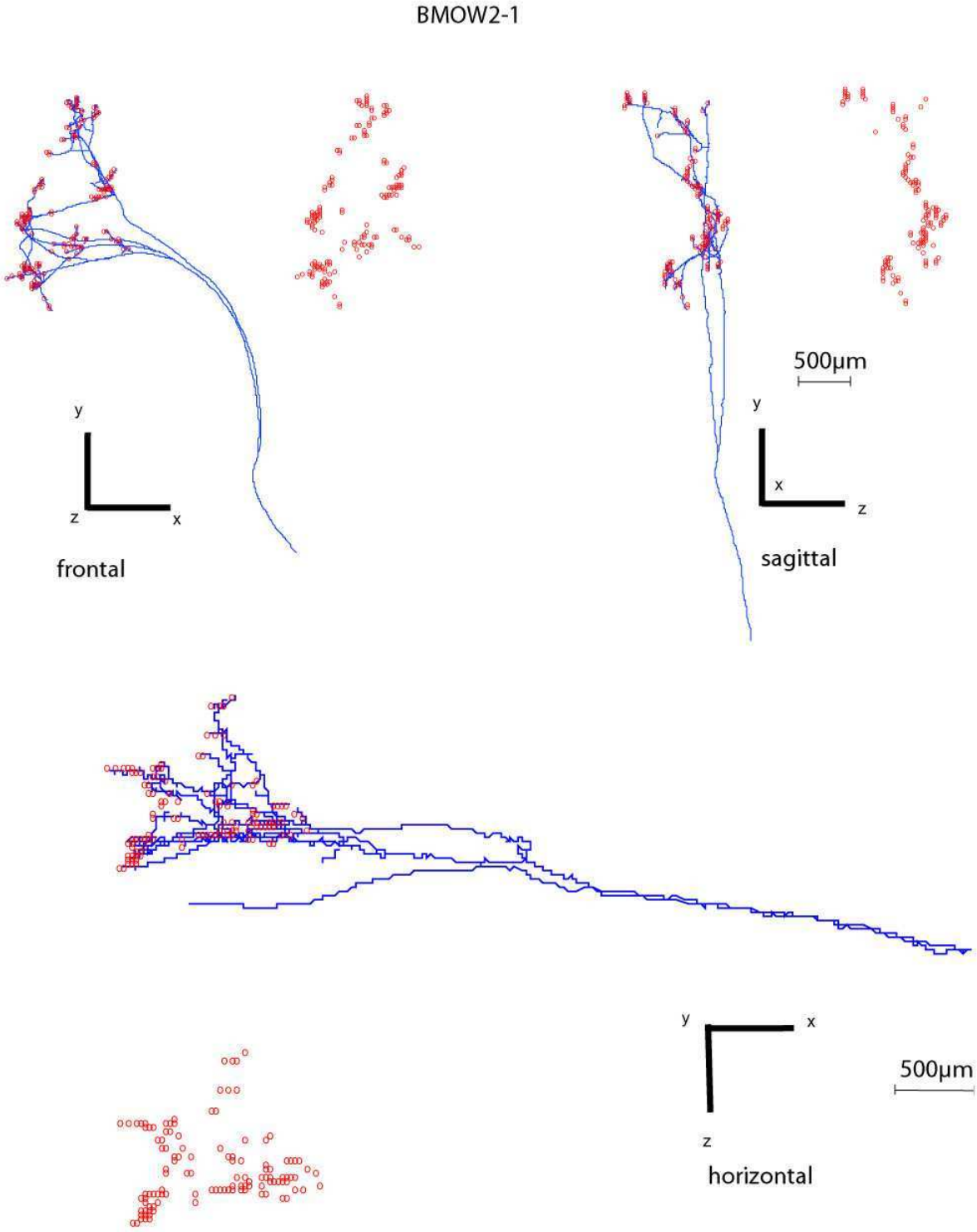

Fig. 55/ Axon BMOW2.1. with its boutons (in red).

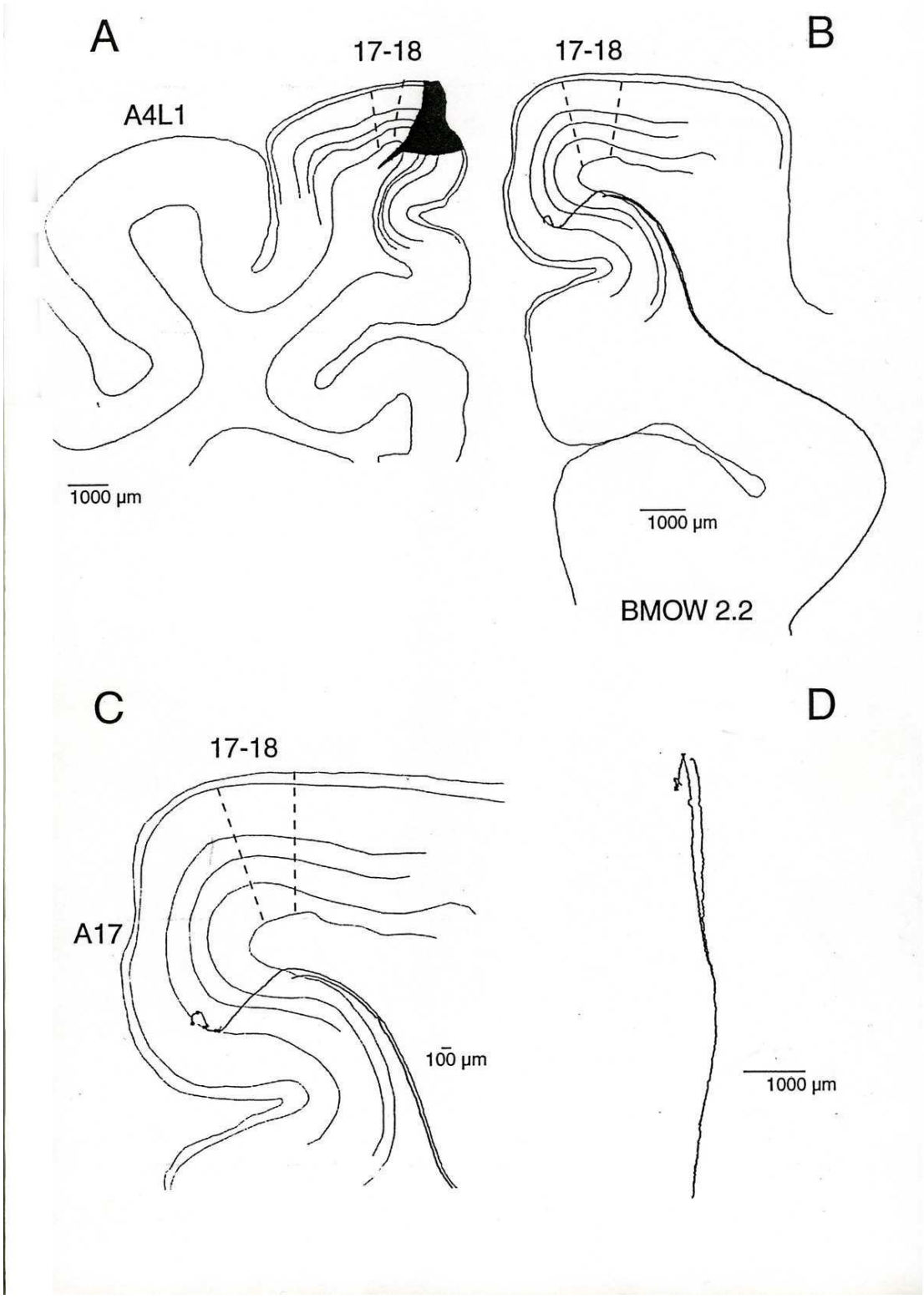

Fig. 56/ Axon BMOW2.2. labelled in a 4 month-old cat after an injection of biocytin in A17 of the left hemisphere (contralateral to the occluded eye), rather anteriorly (A_4L_1).
A. Injection site in the left hemisphere. The different cortical layers (I to VI) are visible; B. (and C): Frontal view of the axon, in the right hemisphere. C. Dorsal view of the axon.

Axon BMOW2.2

This axon (illustrated in Figs. 56 to 58) has been reconstructed over a distance of 19.1 mm, from 43 consecutive frontal sections (43 x 75 µm). Its trunk had a diameter of 1.68 µm. It formed a first node in the white matter, at the level of cingular sulcus (c.s.) i.e. very deep below the lateral gyrus, giving 2 primary branches with diameters which were very similar to the one of the trunk. These 2 primary branches ran in parallel until a very medial part of A17.

One of them stopped abruptly after entering within the cortex, delivering not any synaptic bouton.

The other primary branch also penetrated the cortex, ramified within layer IV, to reach finally layer II-III. Six and 2 boutons were delivered in these 2 cortical layers respectively.

In summary, this axon was very *simple*. Its architecture was *parallel*. Its number of boutons was very low (n=8) and they rather displayed a *granular* distribution. In agreement with its configuration, it occupied a very restricted portion of the cortex, with 367 µm along the medio-lateral axis, and 100 µm along the antero-posterior one.

See Table 1 for a summary.

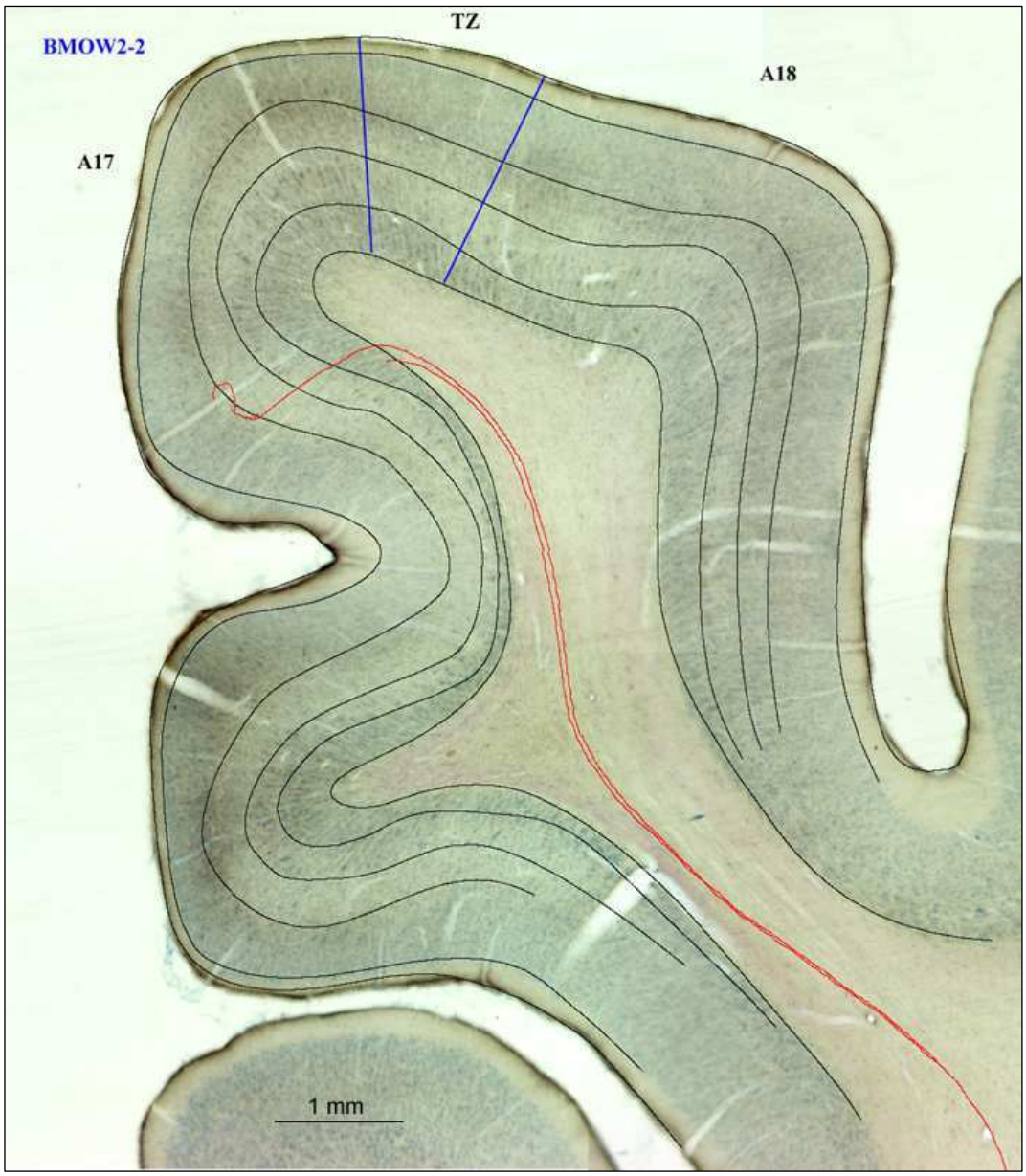

Fig. 57/ Axon BMOW2.2. Superposition of the 3D reconstructed axon and a frontal section of the visual cortex (at the same AP) after Nissl labelling. A17, TZ, A18, same significations as before. Letters in red indicates each terminal branch (see Text for further details).

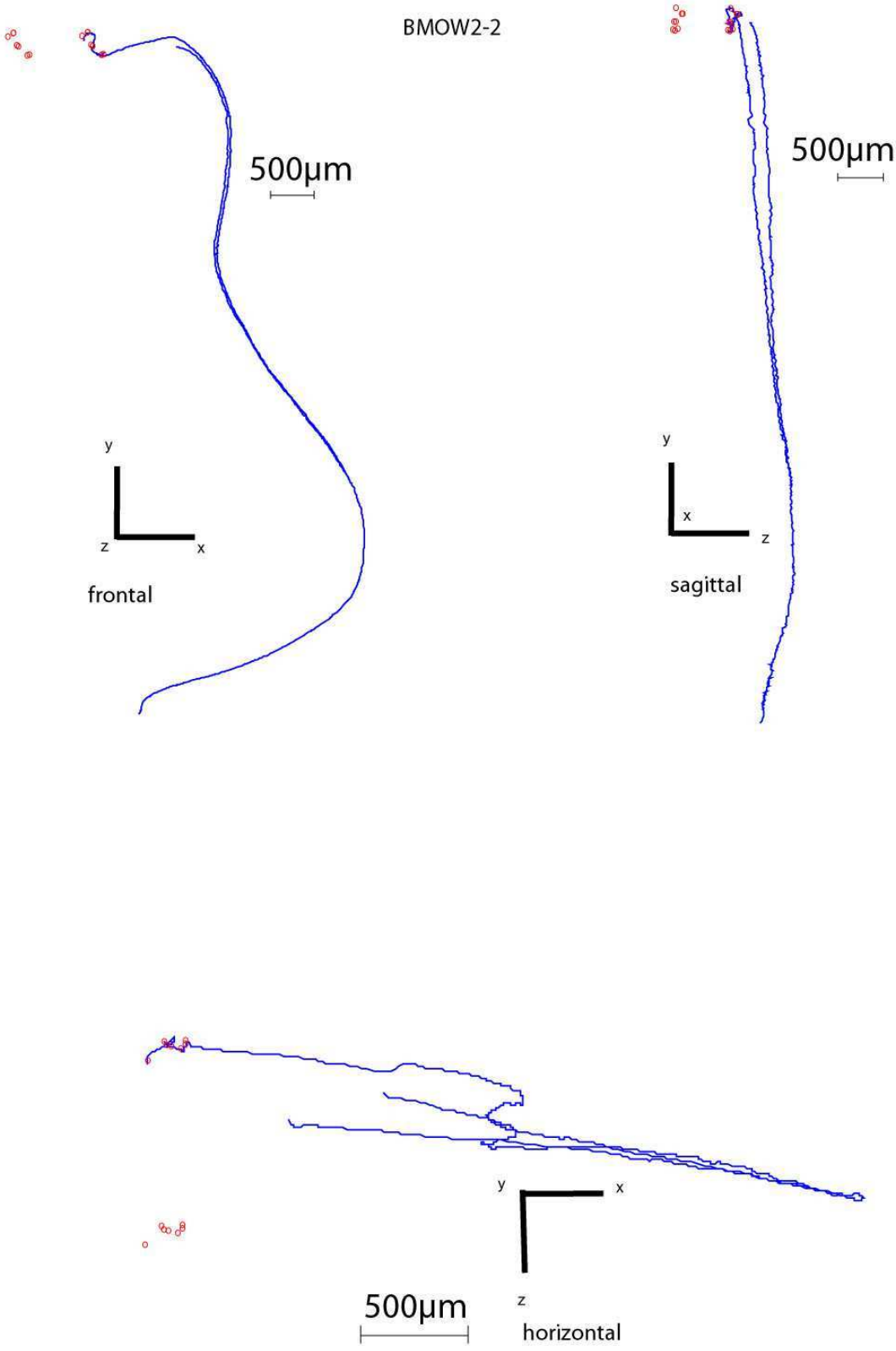

Fig. 58/ Axon BMOW2.2. with its boutons (in red).

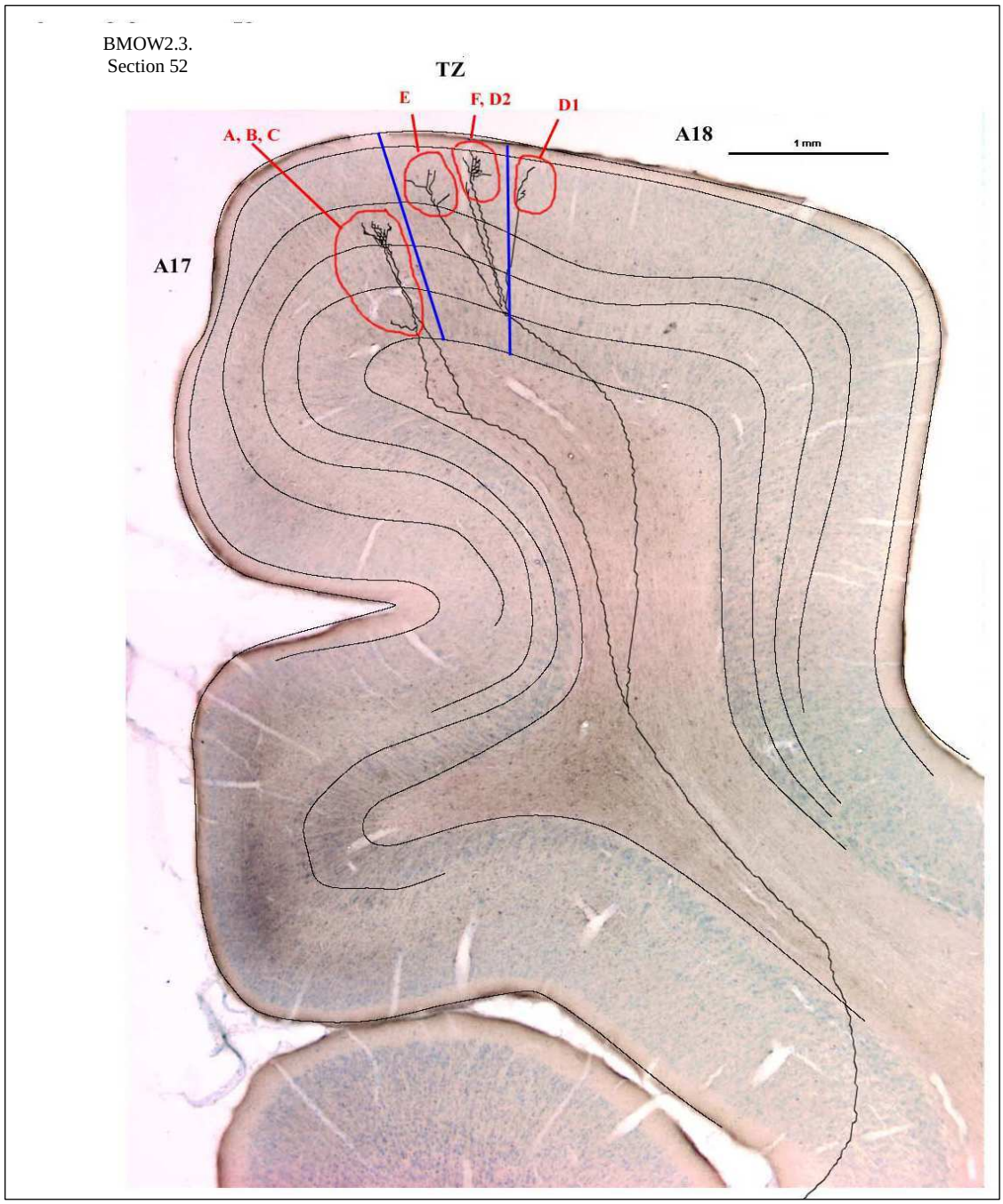

Fig. 59/ Axon BMOW2.3. Similar to axons BMOW2.1. and BMOW2.2., it was labelled after injection of biocytin in A17, at A_4L_1, in the left hemisphere. Superposition of the 3D reconstructed axon and a frontal section of the visual cortex (at the same AP) after Nissl labelling. A17, TZ, A18, same significations as before. Letters in red indicates each terminal branch (see Text for further details). Letters in red indicates each terminal branch.

Axon BMOW2.3

This axon, which has been 3D reconstructed over a distance of 35.7 mm, from 43 consecutive frontal sections (i.e. 43 x 75 µm), displayed 72 nodes and 306 synaptic boutons within the lateral gyrus (or marginal gyrus, m.g.). Its arborisation encompassed different distinct (but neighbouring) regions of the visual cortex (Fig. 59, 60 and 61).

Its trunk was 1.53 µm and ran over a distance of 10.7 mm before dividing very deep below the lateral gyrus, at the level of the cingular gyrus (c.g.). It gave 2 primary branches which ran in *parallel*.

The most medial of these 2 primary branches (1; diameter: 1.25 µm) continued to run within the white matter over a distance of 3.1 mm after the first node. There, it divided again, still in the white matter, to give 2 secondary branches which still ran in parallel (A+B and C). Both penetrated the visual cortex, within A17, with branch A+B giving 4 boutons in layer V and 78 boutons in layer II-III while branch C gave 67 boutons in layer II-III.

The most lateral primary branch (2) had the same diameter as the trunk (1.53 µm). It ran in the white matter until entering the lateral gyrus to reach both the TZ (tertiary branches E, F, D2) and A18 (tertiary branch D1). Each tertiary branch delivered synaptic boutons: branch E, 40 boutons in layer II-III; branch F, 11 boutons in layer I and 70 in layer II-III; branch D2, 13 boutons in layer II-III; branch D1 delivered 6 synaptic boutons in layer I and 17 in layer II-III.

Altogether, this axon displayed a *parallel* architecture. It seemed to display *2 or 3 terminal columns*, and thus terminated by *2-3 clusters of boutons* within A17, A18 and the TZ. Globally, it thus covered 2.5 mm along the medio-lateral axis while it covered 1.9 mm along the antero-posterior axis. Whatever the cortical region, it terminal boutons displayed a *supragranular* distribution. They were mostly located in A17 (n=149) and in the TZ (n=134); in contrast, they were much less numerous in A18 (n=23).

See Table 1 for a summary.

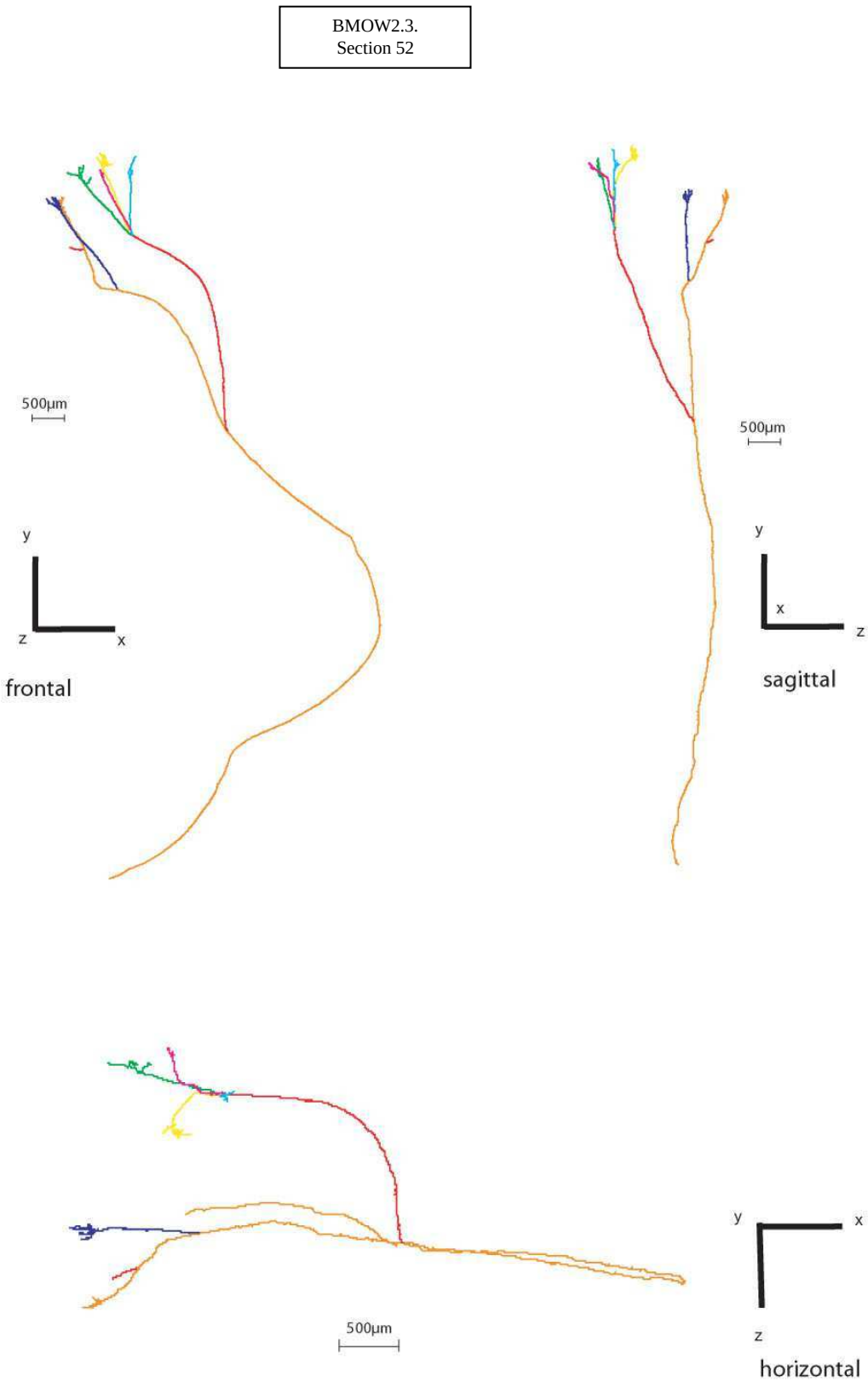

Fig. 60/ Axon BMOW2.3, with its different branches with various colours.

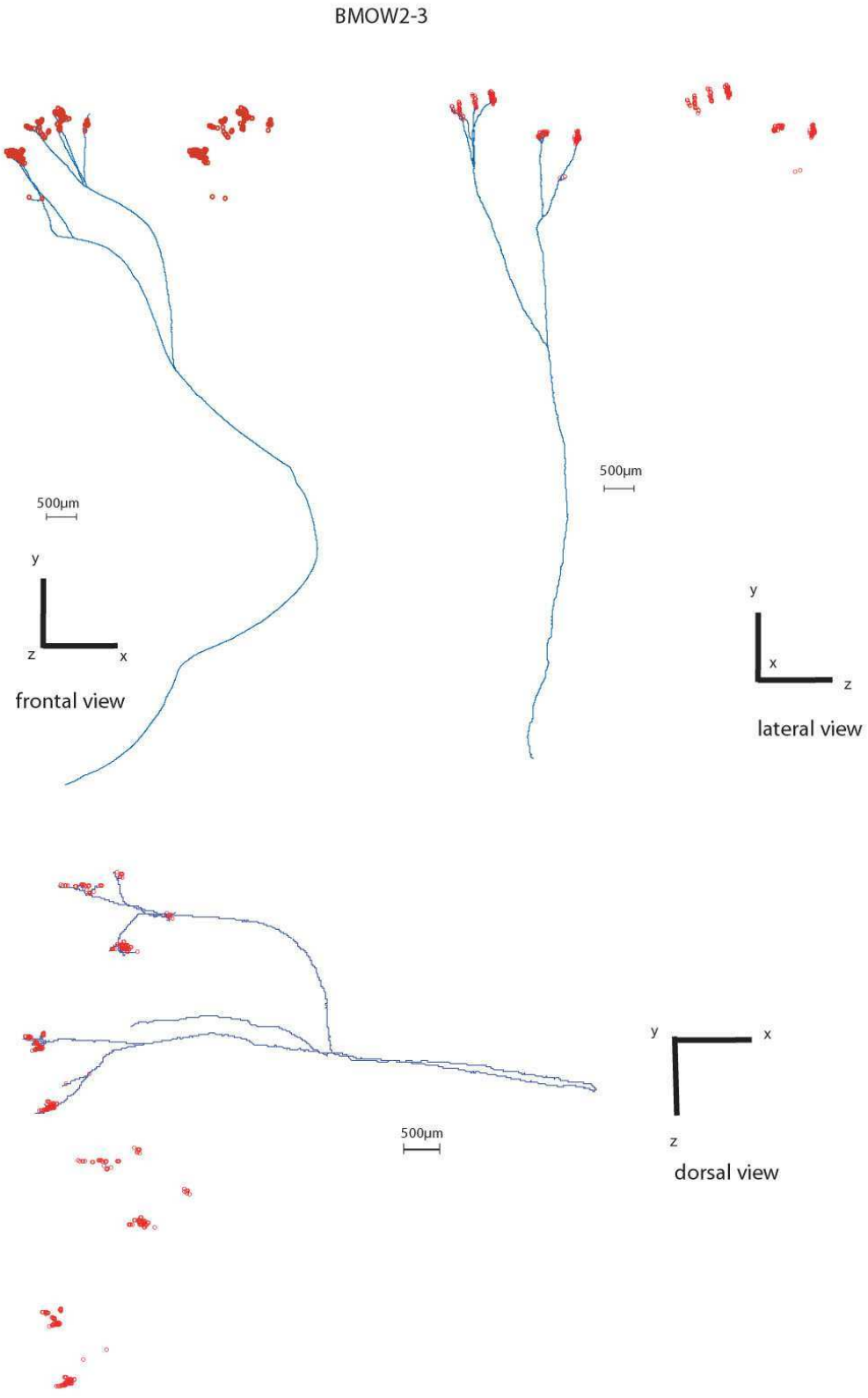

Fig. 61/ Axon BMOW2.3. with its boutons (in red).

EARLY MONOCULARLY DEPRIVAED ADULT CATS (MD)

axon name	Origin	Trunk diameter (µ)	Total length (mm)	architecture	Number of columns	Location of terminals	Cortical layers						Nb term boutons (cx)	Total Nb of boutons	Type of distribution
							I	II/III	IV	V	VI	WM			
INJECTION IN THE TZ															
MD9A	TZ 17-18 P2L2	2.7	88.6	mixed	4?	TZ 17/18							38	1748	TG
						A18			96				118		
						TZ18/19							1343		
						A19		279					249		
MD9B	TZ 17-18 P2L2	1.3	55.2	mixed	8?	A17							47	1279	-
						TZ 17/18						6	374		
						A18						4	156		
						TZ 18/19						_	692		
BMOW1-1	TZ 17/18 A9L1,5	1.68	33.5	serial	2-3?	A17	_	42	18	4	49	_	113	146	TG
						TZ 17/18	_	15	5	_	1	_	21		SG
						A19	_	_	_	_	_	12			-
BMOW1-2	TZ 17/18 A9L1,5	1.68	66.6	mixed	4-5?	A17	_	12	_	_	3	_	15	795	SG
						TZ 17/18	_	33	11	14	19	_	77		
						A18	_	55	19	1	3	_	78		
						TZ18/19	_	71	64	5	9	3	149		
						A19	_	198	173	54	48	_	473		
INJECTION IN A17															
BMO17-A1	A17 post P3L1	1.53	30.3	simple	2	A17	_	198	_	5	_	4	203	218	SG
						TZ 17/18	_	_	_	_	_	11	0		
BMO17-A2	A17 post P3L1	1.39	45.4	simple	5?	A17	_	190	_	_	_	_	190	671	SG
						TZ 17/18	_	423	3	28	_	_	454		
						A18	_	27	_	_	_	_	27		
BMO17-A3	A17 post P3L1	1.53	48.9	mixed	?	A17	_	107	20	_	19	_	146	510	SG
						TZ 17/18	_	233	35	6	26	_	300		SG
						A18	_	15	33	1	15	_	64		TG
BMOW2-1	A17 A4L1	2.16	40.8	parallel	2?	A17	_	225	25	48	58	_	356	356	SG
BMOW2-2	A17 A4L1	1.68	19	parallel	_	A17	_	2	6	_	_	_	8	8	G
BMOW2-3	A17 A4L1	1.53	35.7	parallel	2-3?	A17	_	145	_	4	_	_	149	306	SG
						TZ 17/18	11	123	_	_	_	_	134		
						A18	6	17	_	_	_	_	23		

TABLE 1. Synthesis of data about callosal axons in early monocularly deprived adult cats. For each reconstructed axon (identified by the name of the animal and a number) the following features are reported: area of injection (origin area: 17, 17/18 transition zone), with the stereotaxic coordinates of the injection; trunk diameter (in µm); total length to their site of entry in the grey matter (in µm); architecture (see text for definitions; "simple" refers to axons with single tufts); evaluation of the number of terminal columns by sight; columns location (termination area); number of boutons per layer; total number of boutons per axon; type of distribution of terminal boutons: SG, supragranular, G, granular; TG, transgranular (see Text for definitions). Notice that the values of axon length and diameter are *uncorrected* for tissue shrinkage.

NORMAL ADULT CATS (NR)

axon code	origin area	trunk diameter (µm)	total length (µm)	architecture	column	number of tufts	termination area	number of boutons					
								cortical layers				total	
								I	II-III	IV	V-VI	column	axon
16C	18	0.90-1.35 <1.12>	3940	*mixed*	a	2	18	8	21	27	249	305	864
					b	2	18		25		48	73	
					c	3	17/18		103		43	146	
					d	>3	17/18	8	188		94	290	
					e	2	17/18	41	9			50	
16D	18	1.35-1.80 <1.58>	3550	*mixed*	a	2	18		15	16	28	59	706
					b	1	18		55			55	
					c	3	18		471		55	526	
					d	2	17/18		21		45	66	
16E	18	0.90-1.35 <1.12>	5580	*parallel*	a	1	17/18	8	292	87	7	394	529
					b	2	17/18	9	66	7	7	89	
					c	1	17/18		46			46	
16F	18	0.90-1.35 <1.12>	4580	*serial*	a	1	18	4	56	3		63	332
					b	1	17/18		178	65	26	269	
16H	18	0.90-1.35 <1.12>	4600	*parallel*	a	2	17/18		111		130	241	245
					b	1pt	18				4	4	
16T	18	1.04-1.30 <1.17>	1100	*serial*	a	1	17/18	29	70			99	347
					b	2	17/18		165		83	248	
16V	18	1.04-1.30 <1.17>	2600	*parallel*	a	1pt	17/18		30			30	194
					b	1	17/18		131	25	8	164	
16W	18	1.30-1.56 <1.43>	500	-	-	-	17/18	8	130	76	31	245	245
16Y	18	0.78-1.04 <0.91>	1600	*simple*	a	1	17/18			56		56	56
19A	17/18	0.90-1.35 <1.12>	5600	*incomplete*	a	1	17/18	7	280			287	322
					b	2	17/18		35			35	
20B	17/18	1.35-1.80 <1.57>	* 12200	*parallel*	a	1	17	2				2	33
					b	2	17/18		11	5	6	22	
					c	1	17/18		8		1	9	
20C	17/18	1.80-2.25 <2.02>	* 12000	*parallel*	a	2	17/18	16	176	4	6	202	282
					b	1	17/18	2	78			80	
21B	17/18	0.52-0.78 <0.65>	* 13490	*parallel*	a	2	17/18	32	56	4		92	92
21C	17/18	1.04-1.30 <1.17>	* 12800	*parallel*	a	1	17/18	3	26			29	51
					b	2	17/18		12	2	8	22	
22B	17	0.52-0.78 <0.65>	* 12070	*mixed*	a	1	18		65			65	501
					b	2	17/18		180	1	41	222	
					c	1	17/18		72			72	
					d	>2	17/18		99	1	15	115	
					e	1	17/18		15			15	
					f	-	17		4			4	
					g	1pt	17		8			8	
22D	17	1.56-1.82 <1.69>	* 11700	*mixed*	a	>2	17/18		66			66	401
					b	2	17/18	23	77		6	106	
					c+d	4	17/18		111		38	149	
					e	3	17/18	3	77			80	
22E	17	1.30-1.56 <1.43>	* 12900	*simple*	a	1	17/18		10	24		34	34

TABLE 2. Synthesis of data about callosal axons in normal adult cats. For each reconstructed axon (identified by number of the animal and a letter) the following features are reported: area of injection (origin area: 17, 18, 17/18 transition zone); class of trunk diameter (in µm; median value of the class in brackets); total length to their site of entry in the grey matter (in µm; asterisk refer to axons fully reconstructed from the midline); architecture (see text for definitions; "simple" refers to axons with single tufts); terminal columns (identified by small letters); number of tufts or isolated □reterminal branches (pt) per column; column location (termination area); number of boutons per layer; column and arbour. Notice that the values of axon length and diameter are *uncorrected* for tissue shrinkage (From Houzel et al., 1994).

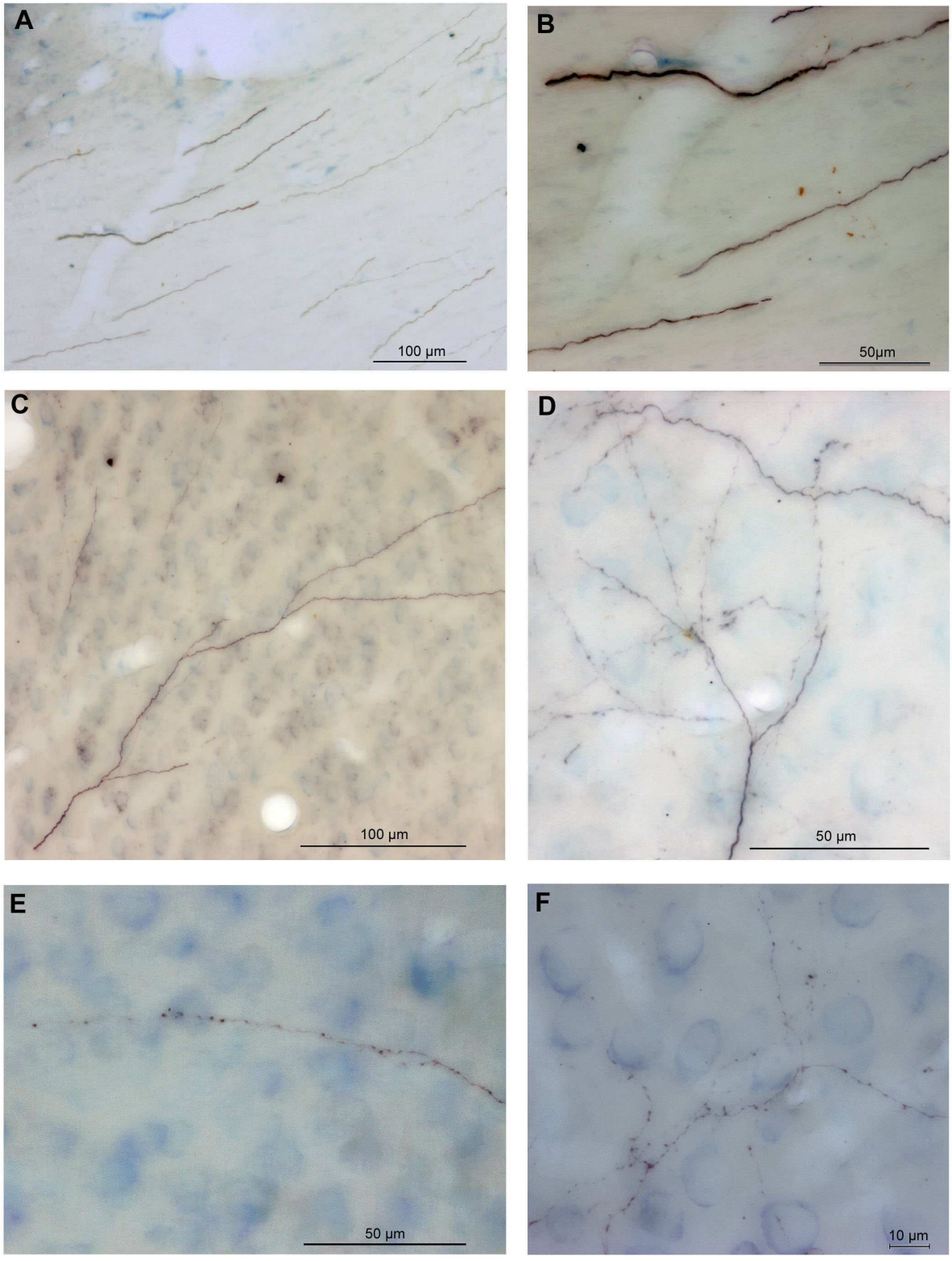

Fig. 62/ Photomicrographs (collages) of details of biocytin-labelled callosal axons in MD adult cats. (A) Axons of various diameters in the corpus callosum of BMO17. (B) Same axons as in A, with a higher magnification. (C) Three nodes within the visual cortex of BMO17A3. (D) Example of boutons that have been found in the visual cortex of BMO17 (including some of those of the axon BMO17A3). (E) Examples of boutons in visual cortex of BMOW2. (F) Examples of other boutons in visual cortex of BMO17. In all panels, dorsal is upwards.

2. Synthesis of the data obtained in MD animals. Comparison with NR adult cats.

All these data that have been obtained about the terminal structure of individual callosal axons in early monocularly deprived adult cats have been synthesized here. In order to identify possible abnormalities because of the visual deprivation, they have been also compared systematically to those which have been obtained previously by C. Milleret 's team in the NR adults (From Houzel et al., 1994). A summary of these data, when obtained for single callosal axons in both experimental conditions, are presented in Table 1 and Table 2 respectively.

2.1. Diameters and trajectories of callosal axons directed to areas 17 and 18

Location of the labelled axons in the corpus callosum

Labelled axons (see Fig. 62) were routed unbundled through the dorsal half of the splenium of the corpus callosum. After entering the medial wall of the hemisphere they coursed below the bottom of the splenial cortex and then laterally and dorsally in the optic radiations. The average length of the trunk of the 3D-reconstructed callosal axons measured from one given start point in the corpus callosum (generally the midline) and the bottom of layer VI ranged between 19 and 88.6 mm (see Table 1). This did not differ significantly from the NR adults.

Diameters of the trunks of the callosal axons

The trunk of the reconstructed axons in MD animals ranged between 1.3 and 2.7 µm in diameter (see Table 1). As a mean, these diameters did not seem to vary greatly depending on whether they originate of the TZ (cats MD9 and BMOW1; m = 1.84 µm) or A17 (cats BMO17 and BMOW2; m=1.63 µm). In order to determine whether the values for reconstructed axons were representative of the full range of axons originating near the TZ or from A17, 139 labelled axons were measured when the callosal axons ran towards the Lateral Gyrus, when getting out of the corpus callosum. They were distributed as fellows according to the animal: MD9, n = 34; BMOW1, n= 42; BMO17, n=23; BMOW2, n=40. Globally, the axons ranged between 0.27 µm and 3.17 µm in diameter, with a majority between 0.41 and 1.68 µm in diameter (Fig. 63A and B). Those we have 3D-reconstructed ranging between 1.39 and 2.17 µm in diameter, this indicates that they were among the largest axons within the total population (see Fig. 63B). Notice that, in general, the diameter remained constant right up to the first node, although occasionally the axons appeared to taper before reaching a node.

All these characteristics were very similar to those reported previously in NR animals, except that largest axons were favoured in MD animals for 3D-reconstruction while there were not (at least apparently) in the NR ones (Fig. 63C).

A

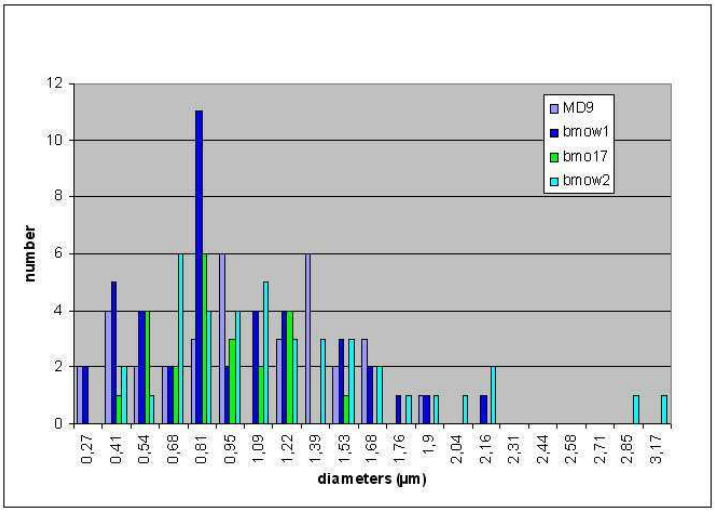

B

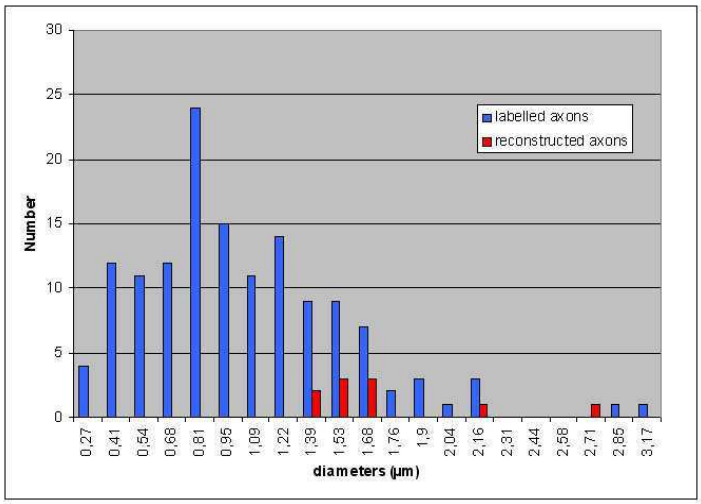

C

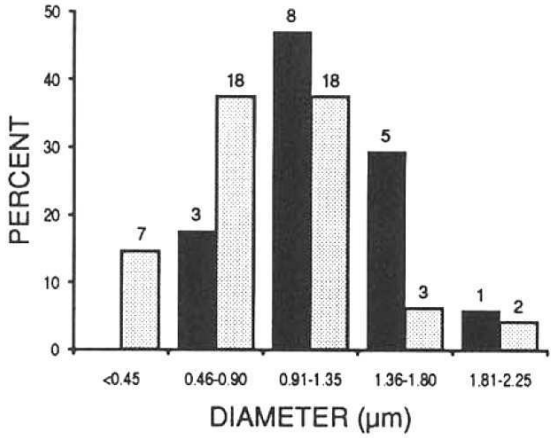

Fig. 63/ Global histograms of the diameters that have been measured in the four MD cats (MD9, BMOW1, BMO17 and BMOW2). A. The 4 histograms, with one per cat, have been superimposed. B. Compiled histogram for the whole four MD cats, with the diameters of 139 axons that have been measured in total. In red are indicated the 10 axons that have been 3D reconstructed in the present study (MD9A, MD9B, BMOW1.1., BMOW1.2., BMO17.1, BMO17.2, BMO17.3, BMOW2.1., BMOW2.2., BMOW2.3.). C. Diameters of axons that have been measured (in grey) and 3D-reconstructed (in black) in the NR adult cats (from Houzel et al., 1994, Fig. 5)

Branches vs. unbranched callosal axons

Although two axons in MD animals remained unbranched until they entered the grey matter or almost so (axons BMOW17A1 and BMOW17A2, labelled after injection in A17), all the others branched *very deep* in the white matter. Most often, this even occurred as far as the level of the fundus of the splenial sulcus (s.s.) or that of the cingular sulcus (c.s.), depending of the antero-posteriority (see for examples axons MD9A, MD9B, BMOW1.2., BMOW2.3.).

In the NR adults, a few axons remained unbranched until they entered the grey matter. Others branched in the white matter, invariably between the fundus of the lateral sulcus and the convexity of the lateral and postlateral gyri, often beneath A18. This is fundamentally different in MD animals, whose callosal axons branched very deep in the white matter, only a few millimetres beyond the midline. This is a first element indicating that the morphology of the callosal axons is rather different in MD and NR animals.

Diameters of the primary branches of the callosal axons

First-order branches were generally only two. They maintained the size of their trunk of origin in only 3 out of the 10 cases (axons BMOW1.2, BMOW2.2. and BMOW2.3.). In all the other cases, the diameter of both first-order branches decreased by ~30% of the trunk diameter. Conservation or decrease of diameter could occur at any other level of the arbour but the diameter of preterminal branches invariably ranged near the limit of optical resolution at ~ 0.26 µm.

In the NR adults, both first-order branches maintained the size of their trunk of origin in four out 13 cases. More frequently, the diameter of one (five cases) or both (four cases) decreased 10% of the trunk diameter. Globally, this indicates that the primary branches of callosal axons in MD animals were ~3 times thinner than the ones in the NR animals with respect to the trunk.

Notice that variations in axon diameter in an arbour are interesting because they contribute to its computational properties (see Chapter 1.4 in Part I).

NR animals

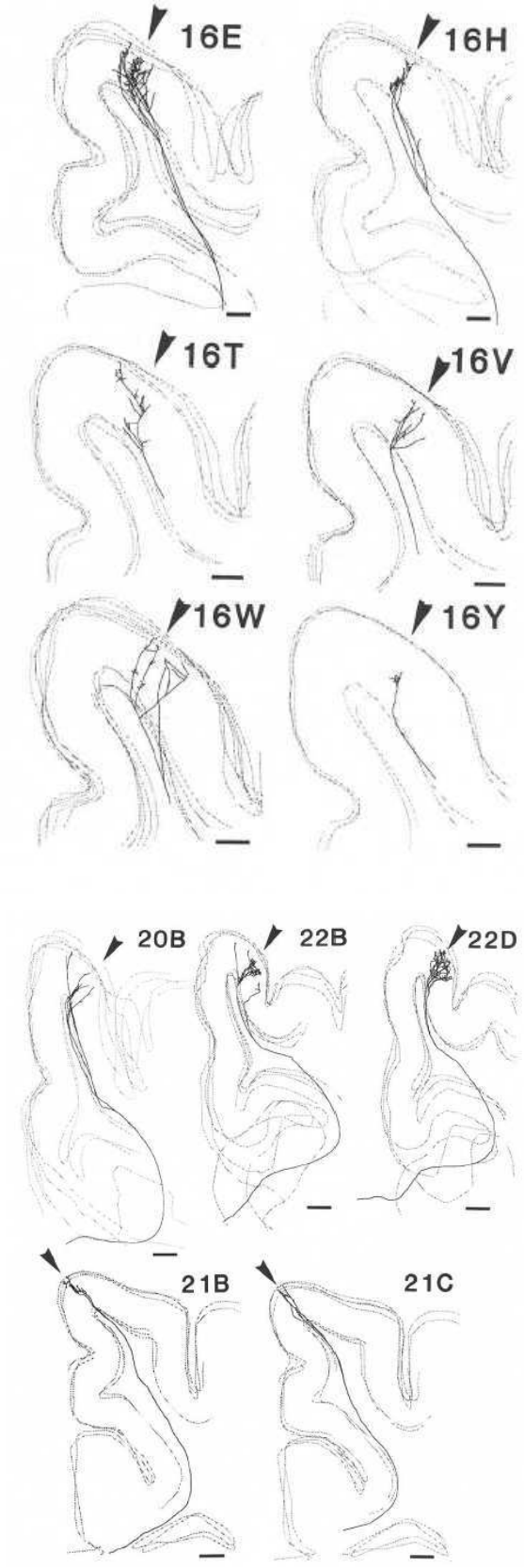

Fig. 64/ Computed-aided 3-D reconstructions of individual labelled callosal axons in NR animals. Codes numbers refer to each cat. Each panel shows an axon within the outlines of a few of the serial sections (coronal sections of the right hemisphere seen from the back) used for the reconstruction; pial surface and bottom of grey matter are indicated by interrupted lines. Dosal is upwards, medial to the left. Calibration bars are 500 µm. Arrowheads are centred on the transition zone between A17 and A18. For quantitative data on the axons, see Table 2.

MD animals

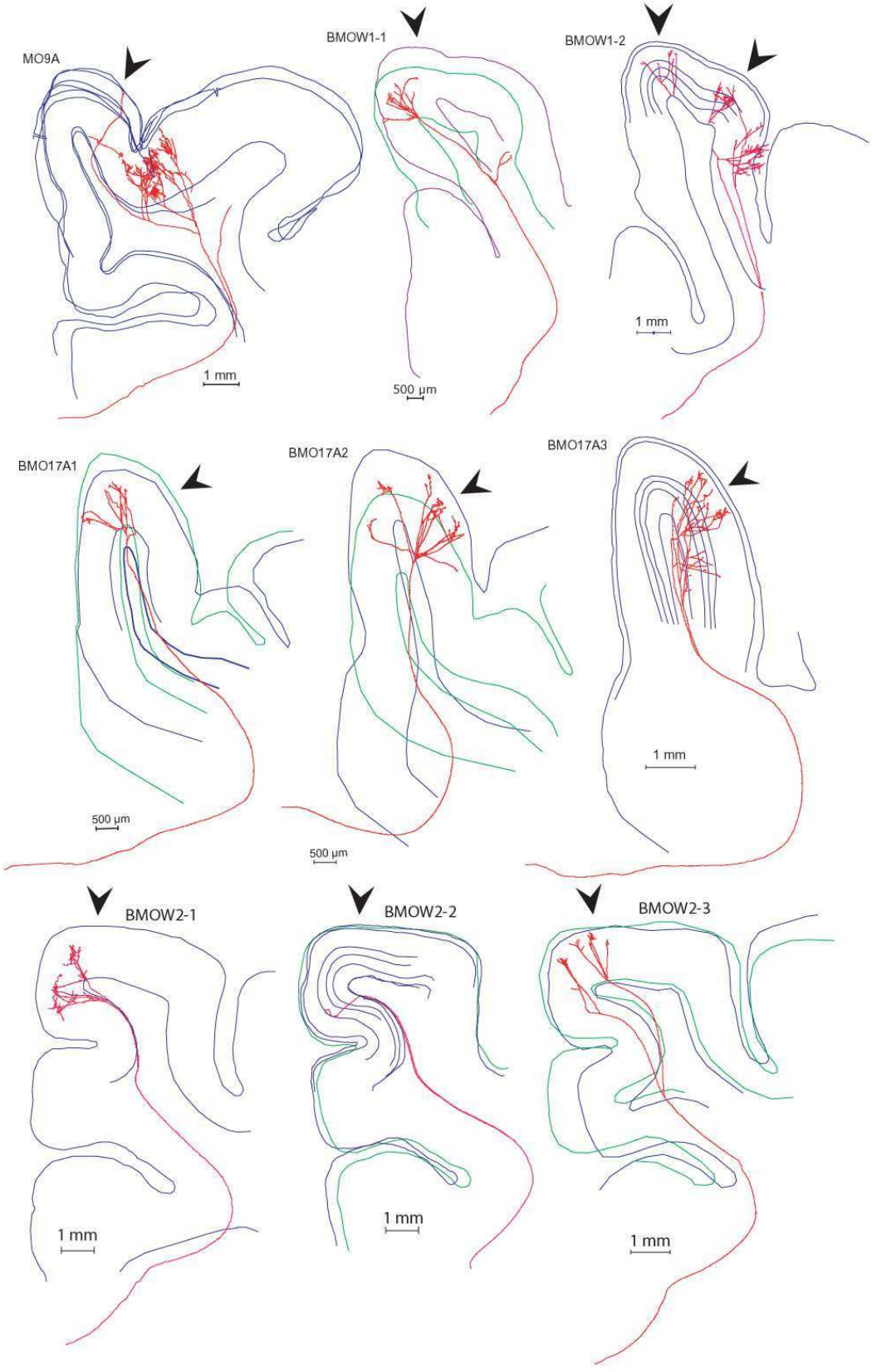

Fig. 65/ Computed-aided 3-D reconstructions of individual labelled callosal axons in MD animals. Same legend as in Fig. 64 (see Table 1 for further details).

2.2. **Architecture of callosal terminal axons**

On the basis of our classification (cf. “Materials and Methods”), out of the 10 MD callosal axons: 2 axons displayed a *simple* architecture (20%), 3 displayed a *parallel* one (30%), 1 displayed a *serial* organisation (10%) and the 4 others displayed a *mixed* architecture (40%); cf. Table 1. In the NR adults, out of the 15 callosal axons that have been 3D-reconstructed and which architecture has been defined: 2 had a *simple* architecture (13%), 7 displayed a *parallel* one (47%), 2 showed a *serial* one (13%) and the 4 remaining ones displayed a *mixed* organisation (27%); cf. Table 2.

Although the number of callosal axons is rather low in both experimental groups, it can be at least concluded that:

- The 4 architectures of the callosal terminal axons that have been found in NR animals are still present in MD animals;
- The percentages of callosal axons with a *simple* or a *serial* architecture seem very similar in both experimental groups: *simple*: 20% vs. 13%; *serial:* 10% vs. 13%;
- By contrast, the percentages of callosal axons with a *parallel* or a *mixed* architecture seemed to change significantly with the former percentage decreasing and the latter increasing with MD: *parallel*: 30% vs. 47%; *mixed*: 40% vs. 27%.

This indicates that MD modifies the architecture of callosal axons, by increasing their complexity.

All these callosal axons terminated by *tufts* and *columns.* These latter structures might be supplied by only one or different separated pre-terminal branches originating in the white matter or the grey matter. To identify such terminal columns required the identification of distinct *clusters* of preterminal branches and boutons in a view perpendicular to the cortical surface (cf. “Materials and Methods” for further details; see also below). In MD animals, when an evaluation was possible, the *number of terminal columns* ranged between 2 and 8 according to the axon (see Table 1). In NR animals, their number ranged between 1 and 7 (see Table 2). Thus, the number of columns was in the same range in both experimental groups. However, the number of axons with numerous terminal columns was significantly higher in MD animals than in NR ones (Compare Table 1 and Table 2). Again this indicates that the MD callosal axons are more complex than the NR ones. Although this has not been done here, such conclusion is likely confirmed by counting the total number of nodes, the number of n order branches per axon and the total length of branches within one given terminal arbour.

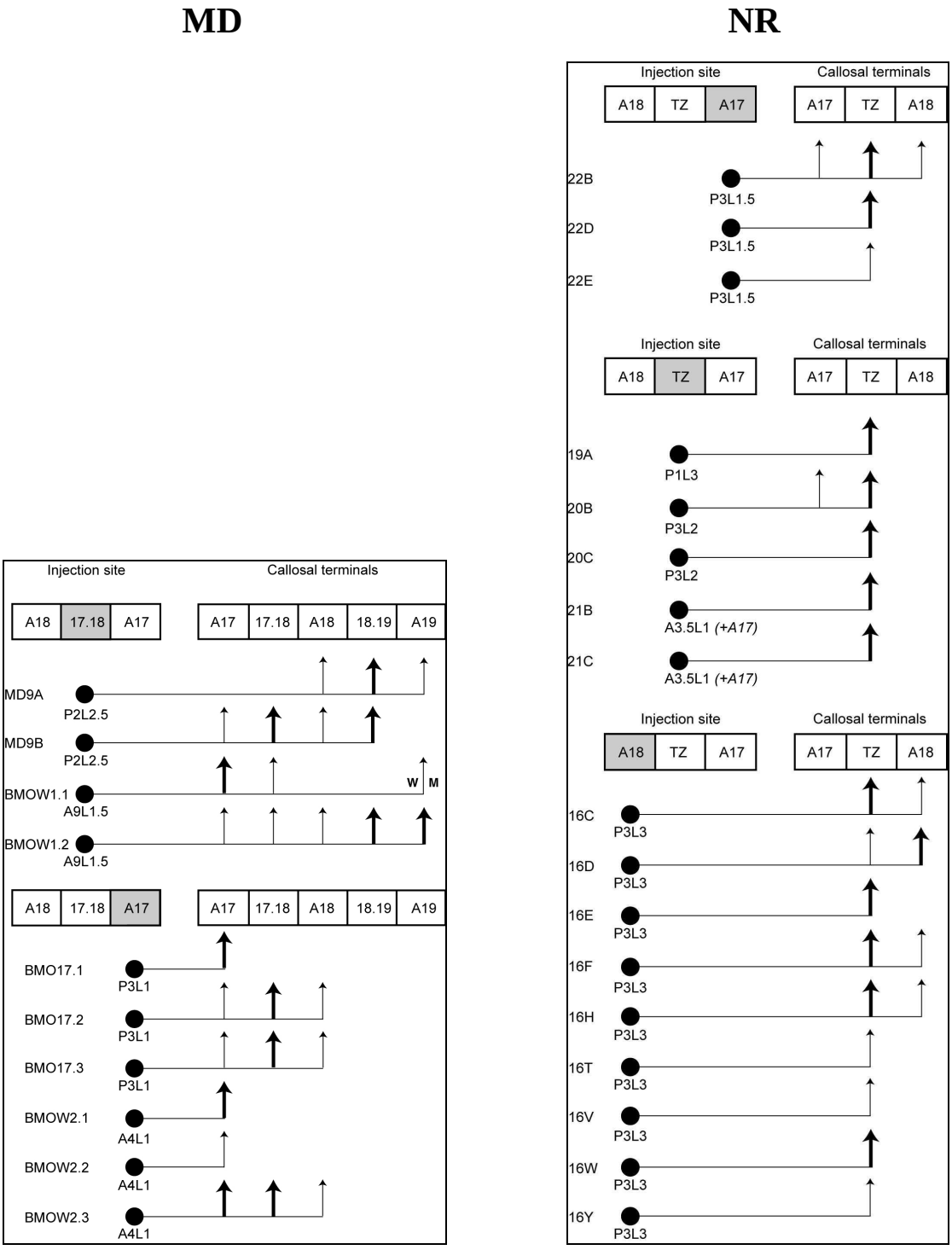

Fig. 66/ Architecture and areal distribution of callosal terminal arbours. These 2 drawings summarize the general morphologies of the different callosal axons (names indicated at left) that have been 3D-reconstructed in adult cats with an early monocular deprivation (MD) and in normally-reared (NR) adult cats respectively. In each sketch, the injection site (black circles) and their respective stereotaxic coordinates are indicated on the left; the terminal sites of the different terminal columns for each 3D-reconstructed axon are represented on the right. A17, area 17; A18, area 18; A19, area 19; 17-18, transition zone between A17 and A18; 18-19: transition zone between A18 and A19; WM, white matter.

2.3. **Areal distribution of callosal terminal arbours**

After MD, the terminal columns of the different callosal axons might be located in A17, in A18, in A19 and within the transitions zones between these different cortical areas (17-18 and 18-19). A few ones also terminated in the white matter. One give axon might terminate in each these different cortical areas (see for example axon MD9B). *In other words, the callosal terminals in MD animals generally occupied very extensive portions of the visual cortex* (see MD group in Fig. 66). This was particularly visible when the callosal axons originated from the 17-18 transition zone: they might terminate in as much as 5 very separated cortical sites. This held also true when the callosal axons originated from A17, although the number of terminal columns, and thus the number of terminal sites in the cortex, was more limited (3 as a maximum). Such data strongly contrast with those obtained in NR animals, whose callosal axons mostly terminate in the 17-18 TZ, with only 1 to 3 terminal columns, whatever their origin (see NR group in Fig. 66). *This indicates that MD may induce a great heterotopy between the site of origin of the callosal axons and their terminal sites.*

In correlation with such data, most of the callosal terminal arbours encompassed large portions of visual cortex in MD animals. Tangentially, each might cover a few tens of mm^2 of cortex, at the level of the pia surface. Again such data differed greatly from those obtained in NR animals whose callosal arbours implicated rather restricted portions of the cortex in most cases. Notice that, in all cases, the *surface* that occupied the terminal arbour was often rather difficult to estimate because of the curvature of the cortex and the complex shape which was determined by the different terminal branches of the callosal axon. Thus, for each axon, the only reliable dimensions that could be estimated here were the *lengths of the terminal arbour* along the antero-posterior axis and the one along the medio-lateral one (in mm). For similar reasons, the *orientation* of the terminal arbour with respect to the midline or the TZ was also difficult to quantify. Also the cortical *volume* which was occupied by each axon was impossible to quantify. This is unfortunate because such data may help to establish a direct relation with functional data (but see below).

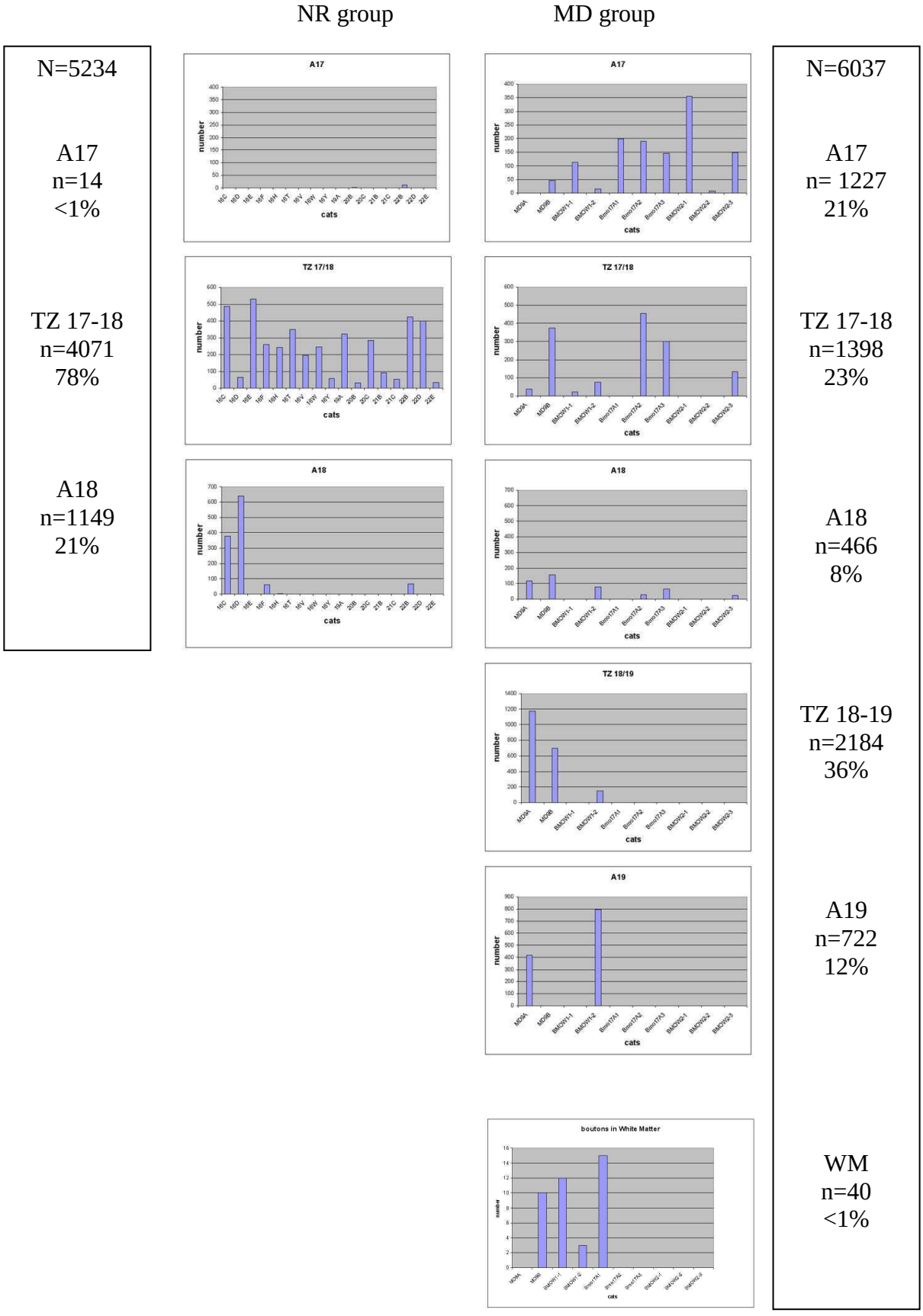

Fig. 67/ Total numbers of boutons per cat, both in MD and NR groups, as the function of the different terminal sites (same abbreviations as before). On the left and on the right, total number and percentage of boutons in each cortical areas.

2.4. Number and distribution of boutons of callosal axons

Global numbers of boutons

In MD animals, the total number of boutons per callosal axon greatly varied from one axon to the other (see Table 1). It ranged between 8 (axon BMOW2.2.) and 1748 boutons (mean = 604). In NR animals, this number of boutons per callosal axon also varied, but to a lesser extent than the MD group (see Table 2): it ranged between 33 and 864 (mean = 308) In spite of the great variability in both experimental groups, *the number of boutons per axon was significantly higher in MD animals than in NR ones*: as a mean, it was twice in MD group compared to the NR one.

Tangential distribution of synaptic boutons

In the 10 axons that have been 3D reconstructed in MD animals, most synaptic boutons were "terminal" boutons; a few "en passant" ones were however also encountered (Fig. 62). In most cases, they were located within the cortical plate (n=5997); a few additional ones (N=40) were however found in the white matter (see Table 1, Figs. 67 and 68A). Not surprisingly, in the cortical plane, they displayed the same distribution as the terminal branches: they might be distributed in A17, A18 and A19 as well as in the transition zones 17-18 and 18-19. In the white matter, boutons were found just below A17 (axon BMO17-A1), the TZ 17-18 (axon MD9B and axon BMO17-A1), A18 (axon MD9B), A19 (axon BMOW1.1.), the TZ 18-19 (axon BMOW1.2.). This distribution also clearly differs from that of the NR group since, in this group, all the (terminal and "en passant") boutons were found within the cortical plate and they were located either in the 17-18 TZ or in A17 or in A18 (see Table 2).

The number, and thus the percentage, of boutons varied as the function of their location (Table 1; Fig. 67). Thus, in MD animals, they were distributed as fellows: A17, n= 1227 (21%); TZ 17-18, n= 1398 (23%), A18, n= 466 (8%), TZ 18-19, n= 2184 (36%), A19, n= 722 (12%), white matter n = 40 (1%). In the NR group, it was quite different since out of the 5234 identified boutons (see Table 2; Fig. 67), the distribution was: A17, n= 14 (<1%), TZ 17-18, n= 4070 (78%), A18, n= 1149 (21%). Clearly, it emerges from this analysis, that MD: a) increases the percentage of boutons in A17 (<1% to 21%), the TZ 18-19 (0% to 36%), A19 (0% to 12%) and the white matter (0 to 1%); b) by contrast decreases the percentage of boutons in the TZ 17-18 (78% to 23%) as well as in A18 (21% to 8%). *Thus, the MD clearly allows some new cortical regions to be connected with the contralateral lateral gyrus through the corpus callosum.*

Concerning the number of clusters of boutons, and thus the number of boutons per column, we have decided not to treat this question here, even in NR adults. This is because the terminal columns (which allow defining clusters) were quite difficult to identify (but see below).

A

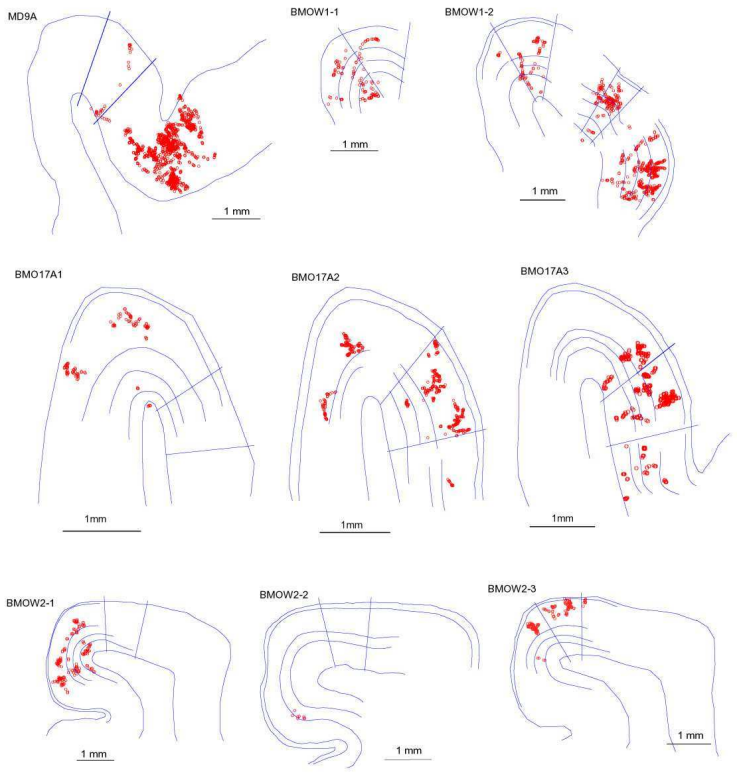

B

NR **MD**

N= 5234 **N= 3010**

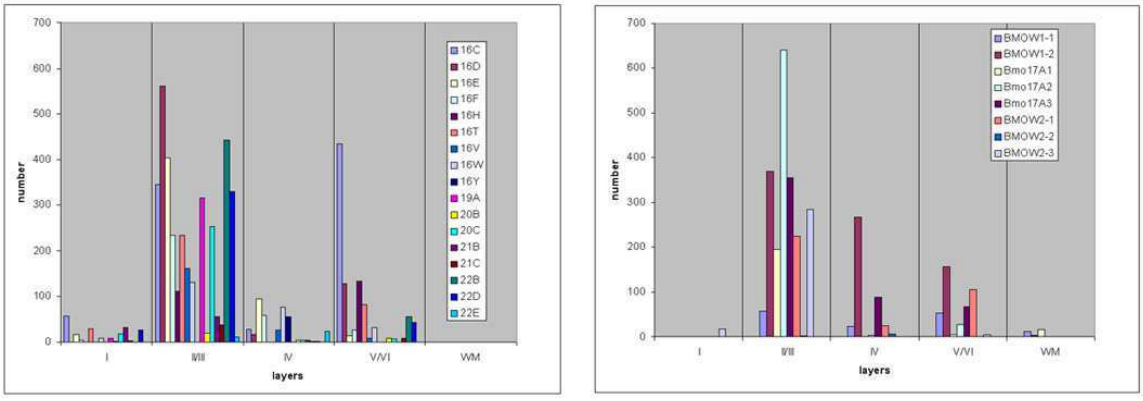

%	4	70	8	18	0	1%	71	13	14	1
n	203	3650	402	979	0	17	2131	412	420	30

Fig. 68/ Radial distribution of the synaptic boutons. A. Tangential and radial laminar distribution of boutons (in red) in the different MD callosal axons. B. Radial (= laminar) distribution of all the synaptic boutons (whatever their location) per cat, in the NR and the MD groups. The reference of each cat is represented in the column at right in each panel. The six different cortical layers are numbered from I to VI as usual.

Radial distribution of synaptic boutons

Notice first that, in MD group, the global number of boutons has decreased compared to the one referred for the tangential analysis because the radial distributions of the terminal boutons of axons MD9A and MD9B were not available. From the 8 remaining MD axons, it appeared however that most of the synaptic boutons remained present within the cortical plate, with only a few ones in the white matter.

Focalizing onto those boutons that were located in the visual cortex, it came that they were globally distributed across the different cortical layers. However they were much more numerous in layers II-III. As a result, most of their distribution was qualified as “supragranular” (see “SG” in Table 1). It was so evident that it was even visible at the level of each single axon (see Tables 1 and 3; see also Figs. 68 and 69). Globally, i.e. without distinguishing the different areas where they were found, the 3010 boutons that could be effectively located were distributed as fellows: layer I, <1% (n=17); layer II/III, 70% (n=2131); layer IV, 14% (n=412); layer V, 6% (n=170); layer VI, 8% (n=250); white matter, 1% (n=30). In NR animals, out of the 5233 boutons, the radial distribution was as fellows: layer I, 4% (n=203); layer II/III, 70% (n=3649), layer IV, 8% (n=402); layer V-VI, 18% (n=979). *Thus, surprisingly, the global radial distributions of the intracortical synaptic boutons were very similar in both experimental groups. Of interest, this may indicate that the terminal boutons of callosal terminals are in fact redistributed within the cortical plate, by simply implicating additional cortical areas (but see below).*

Extending such analysis to the radial distribution of synaptic boutons as function of the callosal terminal zone (A17 to A19) revealed additional informations. Data are summarized both in Table 3 and in Fig. 69. In MD animals, synaptic boutons were present in all cortical layers. But a strong bias in favour of layer II-III was still visible at least in A17 and in the TZ 17-18. Again this held true for each 3D-reconstructed axon. Elsewhere, it was difficult to say because of the low total numbers of boutons (since axons MD9A and MD9B were removed). Such data is evidently reminiscent of what was found in NR group.

MD	I	II/III	IV	V	VI	Total
A17	0% (0)	78% (921)	6% (69)	5% (61)	11% (129)	40% (1180)
TZ 17-18	1% (11)	84% (827)	5% (54)	5% (48)	5% (46)	33% (986)
A18	3% (6)	60% (114)	27% (52)	1% (2)	9% (18)	7% (192)
TZ 18-19	0% (0)	48% (71)	43% (64)	3% (5)	6% (9)	5% (149)
A19	0% (0)	42% (198)	36% (173)	12% (54)	10% (48)	16% (473)
N (Cx)= 2980	<1% (17)	71% (2131)	13% (412)	6% (170)	8% (250)	99%
N (WM) = 30						1%

NR	I	II/III	IV	V-VI		Total
A17	14% (2)	86% (12)	0% (0)	0% (0)		1% (14)
TZ 17-18	4% (189)	72% (2930)	9% (357)	15% (595)		78% (4071)
A18	1% (12)	62% (708)	4% (45)	33% (384)		21% (1149)
N (Cx) = 5234	4% (203)	70% (3650)	8% (402)	18% (979)		100%

Table 3. Percentages (%) and numbers of boutons (n) as a function of the different cortical layers (I to VI), in the different callosal terminal zones (A17 to A19) in MD and NR groups respectively. N (Cx), number of boutons in the cortex; N (WM), number of boutons in the white matter.

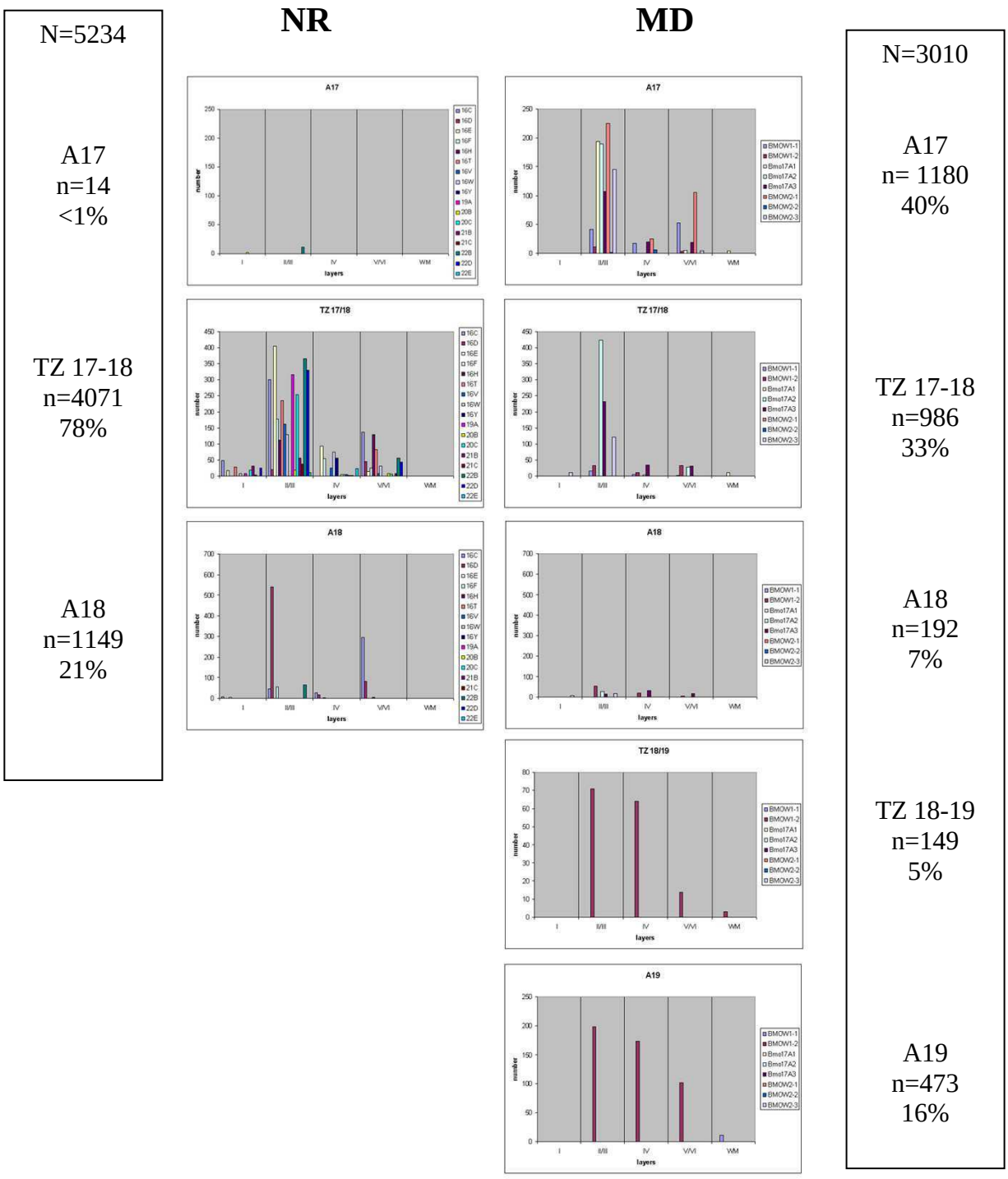

Fig. 69/ Laminar distribution of synaptic boutons in NR and MD groups, as a function of their cortical location (A17, TZ 17-18, A18, TZ 18-19, A19). Data for each cat are represented with a different colour (see at right of each panel). On the left and on the right are indicated the numbers and the percentages of boutons in each region. Notice that the white matter is not represented here: 30 boutons are also present there in MD animals, which corresponds to less than 1% of the total.

2.5. Relation of the distribution of callosal terminal arbours with retinotopy

In the MD animals, we have shown that callosal terminals could terminate in the 17-18 transition zone. But we have also shown that they could reach A17 very medially, lateral regions in A18 and A19, including the 18-19 transition zone (see above). Even if no extensive analysis of this has been performed here, taking into account of the retinotopic organisation of the visual cortex (see Figs. 33 and 34), this indicates that rather large portions of the visual field are concerned by callosal connections originating from A17 or the 17/18 transition zone after MD. This evidently contrasts greatly with the retinotopic organisation of the callosal connections in NR group, which implicates only the portions of visual cortex which are implicated in the perception of the central vertical meridian of the visual field (see for example Berlucchi and Rizzolatti, 1968; Leporé and Guillemot, 1982; Milleret et al., 1994). This confirms that MD induces the formation of heterotopic callosal connections between the hemispheres.

3. Conclusions

Altogether, it appears first that an early monocular deprivation does not prevent the callosal axons to grow during postnatal development. Instead, these axons reach the visual cortex and terminate over extensive portions of A17, TZ 17-18, A18, TZ 18-19 and A19 in the adult. They also display numerous terminal boutons. The trunk of these axons varies in diameter. The architecture of their terminal arbours, including those of terminal columns, also greatly changes from axon to axon. Although most of their terminal boutons are found within the different cortical layers, most often, they are distributed in supragranular layers where they may form clusters. Of interest, a few ones were also found in the white matter. Comparison of the results with our previous data from normally reared cats reveals that MD led to an extensive sprouting of callosal terminals arbors within the hemisphere ipsilateral to the occluded eye. Numerous heterotopic connections formed between both hemispheres. Thus, we show that the anatomical network subserving the interhemispheric integration of visual information is profoundly modified by an early monocular deprivation.

All this has been established using mostly *qualitative* analysis of the callosal axons, and this was quite effective to reveal abnormalities. But some limitations appeared concerning some important characteristics of these same axons, in particular concerning:

- The *cortical surface* that may be covered by one single axonal arborisation, in particular because of the curvature of the visual cortex. Only the antero-posterior and the latero-posterior extensions could be evaluated with reliability;
- . The *orientation of each axonal terminal* with respect for example to the midline: even by rotating the axon in different directions, it was impossible to quantify;
- The *number of terminal columns* and the *number of clusters of boutons* (see Table 1). This was quite difficult only by sight.

To tentatively solve these problems, in the next two chapters, additional *quantitative* analyses of these same axons are proposed:

- In chapter 1.2., the ellipsoid approximation give a quantitative description of the global extension and orientation of the terminals distributions regarding to TZ.
- In Chapter 1.3., a clustering method allows characterizing the scattered aspect of the terminals distributions.

Both of these methods allow characterizing morphological significant differences between NR and MD axon populations.

CHAPTER I.2

The ellipsoid approximation: a basic method to quantify the spatial extension and orientation of the distribution of synaptic boutons

An additional tool to compare callosal terminal arbours in NR and MD cats

---

Article 3:
L. FOUBERT, D. BENNEQUIN, C. MILLERET & J. DROULEZ. The ellipsoid approximation: basic methodology to characterize the spatial distribution of the synaptic connectivity (in preparation).

In the previous section, we described qualitatively the anatomy of interhemispheric axonal structures obtained after a development under monocular deprivation. With the aim to find an objective method to describe quantitatively the terminal branches and the synaptic boutons of these particularly widely spread neural structures, a set of computational tools dealing with elementary linear algebra was developed in order to get a measure of their spatial extension.

In a first part of this chapter (Part 1.2.1.), the method itself will be described (Article 3), and will be applied to callosal axons of normally-reared (NR) adult cats.

In a second part of the chapter (Part 1.2.2.), the “ellipsoid approximation” method will be applied to callosal axons from early monocularly deprived (MD) animals. A comparison of the data obtained for both NR and MD animals will be then achieved.

we demonstrate that the method is quite useful and effective to further characterize the dispersion of the callosal terminal arbors in both experimental conditions. It is also shown that the method allows identifying further differences between both groups.

PART 1.2.1.

The ellipsoid approximation: basic methodology to characterize the spatial distribution of the synaptic connectivity

L. FOUBERT[1], D. BENNEQUIN[2], C. MILLERET[1] & J. DROULEZ[1]

1. Laboratoire de Physiologie de la Perception et de l'Action, Collège de France, UMR 7152, 11 Place Marcelin Berthelot. 75005 Paris, France. 2. Équipe Géométrie et Dynamique, Institut de Mathématique de Jussieu, UMR 7586, Université Paris VII. 4 Place Jussieu. 75005 Paris, France.

Corresponding author:
Luc Foubert
Laboratoire de Physiologie de la Perception et de l'Action
Collège de France
UMR 7152
11 Place Marcelin Berthelot
75005 Paris, France.
Luc.foubert@college-de-france.fr

Abstract

Various numerical analyses are proposed here to perform a quantitative description of the spatial dispersion of the terminals arbors (and the synaptic boutons) of single neurons. They need first to be labeled with a neuronal tracer. They also need to be described in a 3D coordinates system, for example by using Neurolucida software combined with a light microscope (Glaser and Glaser, 1990). The dispersion of the branches and/or of synaptic boutons may be therefore represented in the 3D space and then analyzed in terms of a more or less widespread distribution. An "ellipsoid approximation" was used. It allowed describing quantitatively the *location, spatial extension (length, width and surface), 2D and 3D anisotropies, orientation* (for example with respect to the midline) and *volume* of each terminal arbor. When belonging to a cortical neuron, the projection of this distribution on one plane tangential (and very close) to the cortical surface may also allow visualizing the fine organization of the terminal arbor. To test the method, 15 callosal axons from cat visual cortex were used. We described them previously qualitatively (Houzel et al., 1994). Applying here the ellipsoid approximation, it came additionally to previous data that their terminal arbors most often: a) occupied each only 0.5 to 2.5 mm^2 within the 17-18 transition zone (TZ), as indicated by the surface of the ellipsoid; b) extended maximally from 0.2 to 2 mm, as indicated by the longest axis of the ellipsoid. c) displayed a rather limited 2D anisotropy, with only 6 axons showing a moderate elongation along one given direction, and only one showing a rather strong one; d) were orientated obliquely (~70°) with respect to the midline and the TZ; e) were confined in a very small cortical volume which ranged from 0.2 to 1.5 mm^3; f) displayed finally also a certain 3D anisotropy. Altogether, this method provides a simple but efficient technique to quantify terminal arbors of single neurons. These measurements may also help to compare different neuronal populations and to establish a relation between anatomy and cortical organization, in particular when obtained through imaging techniques.

Introduction

Descriptive methods have been widely used to present the diversity and to classify the various specimens of neurons with respect to their morphologies. Recently, simulation methods based on stochastic rules have been also applied to generate different shapes of neurons leading to different computational properties *(Burke & William, 2002)*. Nevertheless most of the morphological studies have been focused onto the arbor structure more than onto the spatial distribution of the connectivity. The present study aimed precisely at characterizing objectively the spatial distribution of the synaptic boutons of single neurones through a quantitative approach.

Neural populations are deeply intermingled structures. Therefore, if the dendritic or axonal processes morphologies clearly play a key role for the computational properties of communication between units (Debanne, 2004), the spatial dispersion of the connection points may also be relevant to understand the mapping properties and the distribution of information flow among populations. At the neural population level, the anatomical correlates of the physiological columnar unit remain however to be stated precisely (Rockland et al., 2004). The columnar unit concept was initially introduced to describe the radial organization of neurons in the primary visual cortices on the basis of their functional properties such as ocular dominance or orientation preference. Cortical columns were defined as functional units regrouping cells having similar functional properties. But these properties often show continuous changes running onto the cortical surface. And not any anatomical edge underlying such differentiation has been shown yet. This remains in a blur boundaries description.

At the level of their finest connectivity, rich nervous system such as those of vertebrate do not have pre-specified point to point wiring (Cowan, 1978; Merzenich et al., 1983). According to theoretical work dealing with population coding, such non point-to-point but widely overlapping connectivity is necessary for the emergence of computational properties and reliability of the brain functions. (Edelman, 1993). Thus, the widespread of single neuron connectivity is introduced as a key factor of the brain organization. Synaptic connectivity of a single neuron can be clearly identified combining immunohistological

staining methods and microscopic reconstruction to provide a collection of data with precise localization of the synaptic cloud. But numerical tools are still to be developed in order to objectively describe and quantify their spatial organization.

Another challenging aspect for a comprehensive description of the neuron morphogenesis is the study of processes of growth and reshaping of the neuronal arborescence occurring during development and underlying the functional connectivity of the networks. These morphological properties are constraint and sculpted by developmental genetic rules. But they are also reshaped and tuned through plastic changes under the influence of the environmental fluctuations traduced by the neural activity (Ghosh & Shatz, 1992). It is well known, in many species and for number of brain regions, that neural connectivity is much more spread and diffuse at birth than those observed in stable adults structures (see Innocenti & Price, 2005 for review). Thus quantitative methods to estimate the spatial dispersion of neurons connectivity may help to characterize differences between populations at different ages or developed under different post-natal environment or under pathologic conditions.

Working on the development of neural architectures of the primary cortices and their interhemispheric link through the bundle of fibres of the corpus callosum, we have to face to provide a quantitative characterization of callosal arbors at different ages, in various experimental conditions. It have been established already that the connections linking the primary visual cortices in the adult cat mainly target their axonal projections into or close to the ~1mm wide transition zone (TZ) bounding areas A17 and A18 (Payne, 1991, Houzel et al., 1994; Olavarria, 1996). Nevertheless, it has been also established that those connections are more widely projected into the contralateral cortex in the developing kittens (Innocenti et al., 1977; Innocenti, 1981, Aggoun Zaoui et al., 1994). Furthermore, after development under pathologic conditions of vision, there are good reasons to think that such kind of wide connectivity is stabilized (Lund et al., 1978; Berman & Payne, 1983; Milleret & Houzel, 2001; Milleret et al., in preparation).

In the present work, we report the development of a set of computational tools which aimed at characterizing quantitatively the spatial distribution (or dispersion) of synaptic boutons at the level of terminal arbors of single axons (and thus of single neuron). Another

goal was to locate this “synaptic field” in its cortical area context, in our case with respect the transition zone between visual cortical areas 17 and 18. Moreover, we naturally achieved the projection of the “synaptic field” onto a plane tangential cortical plane. This provided an interesting point of view to link anatomical data about the intracortical neuronal network and functional ones obtained in particular through optical imaging. This two-dimensional analysis of the connectivity is particularly interesting to get access to parameters such as the extension of the “synaptic cloud” or its orientation with respect to one given reference such as the antero-posterior axis of the brain (i.e. the midline). The method is simple but efficient. This method was applied here to the terminal arbors of 15 callosal axons that have been described previously qualitatively in visual cortex of normally reared adult cats (Houzel et al. 1994). This is in agreement with G.M. Innocenti, with whom C. Milleret coordinated the work. As expected, applying the method of the “ellipsoid approximation” provides a quantitative description of their synaptic field extension (in 3D), associated with a projective representation onto the closest cortical surface. This gives a comprehensive mapping of the spatial extension of the neuronal connectivity.

Axon EN22B

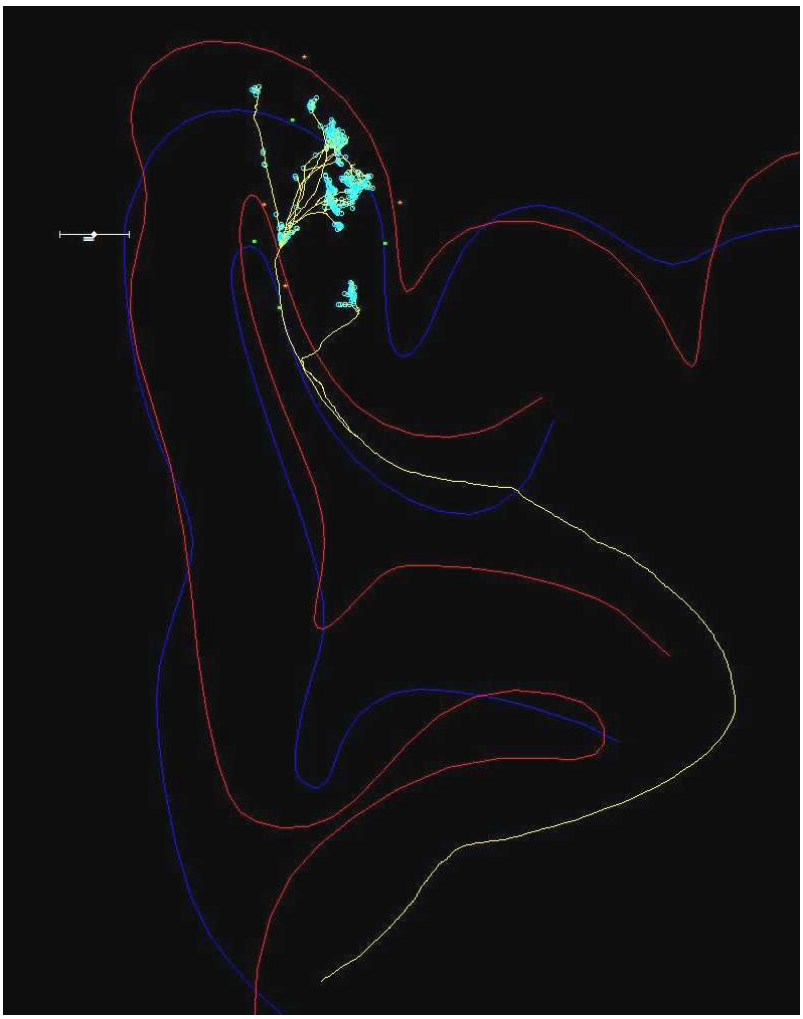

Fig. 70/ Example of axon reconstruction. Coronal projection of three-dimensional reconstruction of a callosal axon in the right hemisphere. The clusters of blue spots show the arbor terminals locations where the synaptic connectivity is concentrated. The small spots on the cortical surface lines and on limits of the white matter mark the transition zone borders location obtained by cytoarchitectonic layers differentiation (scale bar: 1mm).

Materials & Methods

1/ Three-dimensional reconstruction

Data from fifteen callosal axons that have been 3D reconstructed from cat primary visual cortex were used to demonstrate the methods we have proposed here. All these axons were obtained from adult cat developed under normal visual condition and have been previously described qualitatively (cf. Houzel et al., 1994; see Chapter 1.1. in Part I for further details). However, while no correction for shrinkage (because of histological procedure) was achieved initially, final shrinkage corrections have to be applied here to provide the correct scale of the distribution in each direction (see below).

To summary, an anterograde tracer injection (biocytin) was performed at adulthood. Axons were obtained from different sites of injection in areas A17, A18 and from TZ. Histological procedures provided 75µm thick frontal serial slices of brain after fixation and cryoprotection in a 30% sucrose solution and incubated at room temperature for 12 hours in an avidin peroxydase complex (ABC kit, 1/200 dilution into PBS solution with 1% of Trixon-X100). Second incubation was performed under di-aminobenzidin solution to stain peroxydase and amplified with nickel sulfate. One over two slices was stained with Nissl method for cortical layers identification. The observation of the cortical layers thickness allowed to perform a cytoarchitectonic differentiation of primary visual cortex areas 17, 18 and A17/A18 border as described in Milleret et al. 1994. One should notice that the 17/18 border is not localized as a sharp edge but as a transition zone (*TZ)* whose latero-medial location on the cortical surface decreases with respect to the midline from posterior to anterior parts (Payne, 1990). Optical microscopic observations of serial slices coupled with neurolucida© *(Microbrightfield Inc.)* tracing system provides three dimensional transcallosal axon morphologies reconstructed from root into the midline until their terminals in the hemisphere opposite to the injection site (see Fig. 70). Histological procedures such as fixation, cryogenation generally induce a 35-40% isotropic shrinkage that can be compensated on numerical data (Innocenti & al. 1994). Both isotropic and non anisotropic shrinkage have to be estimated and compensated for a

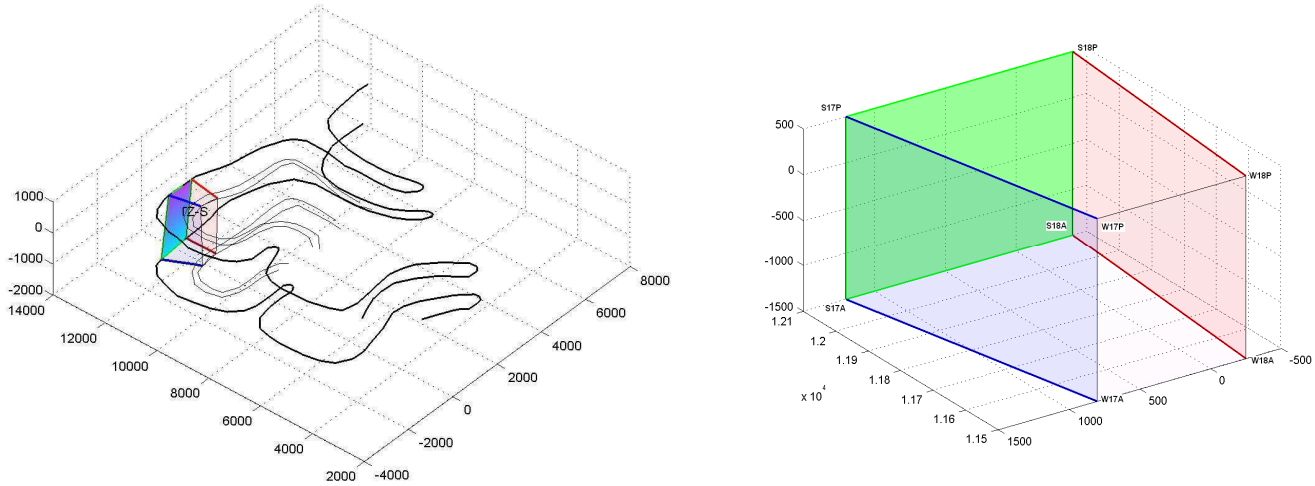

(a) (b)

Fig. 71/ Definition of the reference frame (TZ-volume). (a) Two histological sections with cortical contours and cytoarchitectonic differentiation provide the separation points between area A17, A18 and define the transition zone volume. (b) Height vertex from on these contours defines the TZ-volume reference frame to locate the synaptic distribution within a cortical context. The four barely coplanar "S" vertexes define the tangential plane that is the closest from the cortical surface (in green) for a 2-Dimensinal projection. Flanking areal vertex define separation planes (blue for A17, red for A18). These planes have been used a "within or without TZ" categorization of each synaptic points. (scales in µm)

correct spatial analysis. Anisotropic shrinkage was first compensated on data with a 3 fold expansion along z axis (orthogonal to the cutting plane) to overcome the 1/3 compression due to dehydratation and cover slipping. The mean 35 % isotropic shrinkage was also compensated by a 1.54 scaling factor.

2/ **The "*TZ-volume*" definition, an inter-areal cortical reference frame**

Data about the 3D "synaptic field" are sufficient to analyze the spatial dispersion of the synaptic boutons of a neuron with respect to its own morphology. But to position these synaptic boutons in their cortical context necessitates having a framework. This allows to link neurons morphology and functional cortical maps. Callosal axons linking the primary visual cortices are known to project onto the *Transition zone (TZ)* between visual cortical areas 17 and 18. This region can be determined by observing the cytoarchitecture and the thickness cortical layers which is specific for each area and which is visible on histological frontal sections with appropriate staining (Milleret et al. 1994). On each section of the brain, limits of the TZ can be plotted to separate A17 and A18 within a ~1mm wide region. We took advantage of such cortical specificity to provide a spatial context for the tridimensional data which characterize each distribution of synaptic boutons. Therefore, four points on the highest part of the cortical section and four on the lower one were used to define a reference frame called "TZ-volume". On each section, 2 points on the cortical surface and 2 points on the upper limits of layer IV were use to define one of the height vertex of the *TZ-volume* (see Fig. 71). Each vertex of the volume is labeled regarding to its proximity to a cortical area (-17 or -18), to its cortical depth (S- or W-) and to the antero-posterior index (-A or -P) within the section it belongs to. Areal proximity vertex (-17 or -18) was also used to define separation planes to discriminate whether a connection point from the 3D set falls into the TZ volume or remains outside of it. The superficial "S" points were at last used to define a plane tangential to the cortical surface. At this scale of observation, this plane is used to approximate the weakly curved surface of the cortex and is defined as a tangential bi-dimensional projection space, providing an equivalent "*view from the top*" of the synaptic distribution . This representation gives an interesting point of view for comparison with functional cortical maps such as ocular dominance or orientation preference maps obtained with high resolution imaging techniques such as optical imaging.

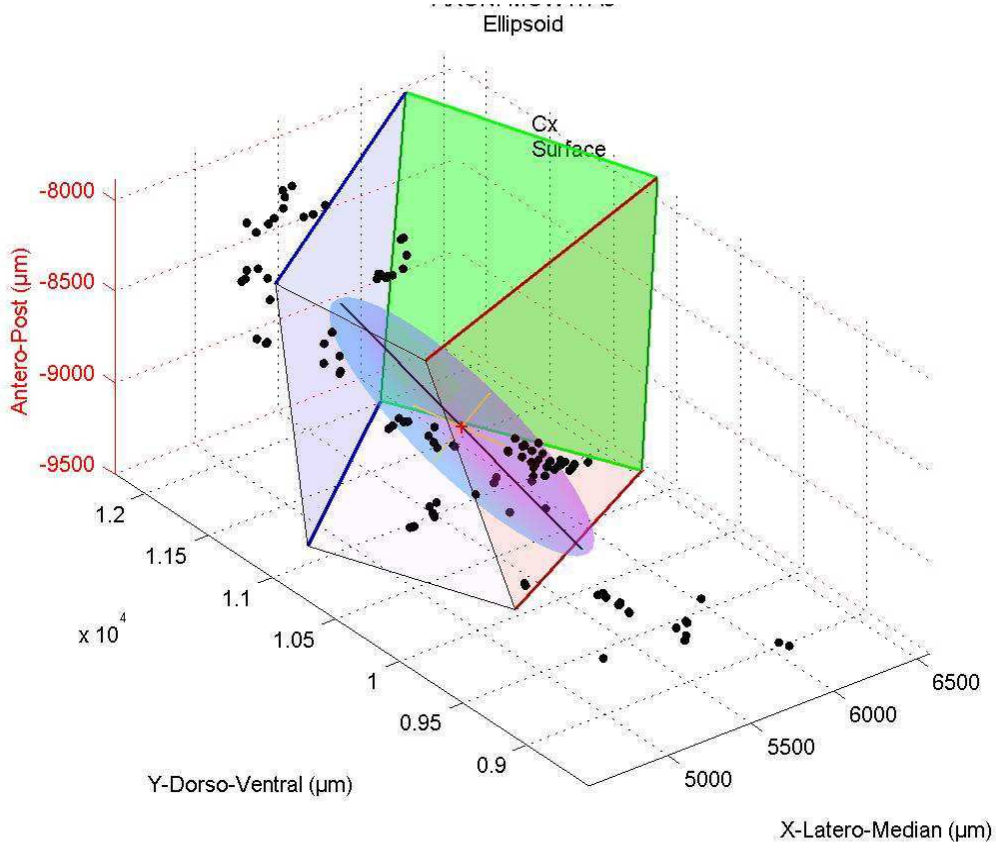

Fig. 72/ Ellipsoid approximation of the terminal arbor (without a detailed representation of each synaptic bouton) of a callosal axon into its *TZ-volume* reference frame. The greatest axis of the ellipsoid (direction along the distribution variance is maximum) is colored in black. The two others orthogonal axes are plotted with yellow. The ellipsoid surface is centered onto the center of mass of the distribution here plotted by a small red point.

3/ 3D Extension axis and elongation of the synaptic field by applying the ellipsoid approximation

Staining and histological procedures provide after reconstruction a set of data containing a morphological description of the arbor. The locations of N synaptic boutons or arbor terminals are collected within the axonal structure and give a three-dimensional description of the synaptic field as a set of 3xN values. The diagonalization of the covariance matrix of this set of data provides 3 orthogonal eigen vectors associated respectively with 3 eigen values. These vectors correspond to direction axes where variances of the distribution are maximized when data are projected onto. These three axes indicate the principal directions of elongation of the distribution with each associated eigen value related to the length of the elongation along each axis.

Let $A_{n,i} = (X_n, Y_n, Z_n)$ be the structure of the data where n[1,..N] is the index of the sample (an identified synapse or branch terminals) for each spatial coordinates. The 3x3 covariance matrix of the distribution is defined by:

$$Cov(ij) = \frac{1}{N} \sum_{1}^{N} [(A_i-\mu_i) (A_j-\mu_j)] \quad \text{where } \mu_i = \frac{1}{N} \sum_{1}^{N} (A_{n,i})$$ is the mathematical expectation and i, j [=1,2,3] stand as index for spatial coordinates [x,y,y].

Each element Cov(ij) of the covariance matrix is the covariance coefficients between N couples of spatial coordinates. The analytic solution of the diagonalization of the covariance matrix provides 3 eigen vectors associated with 3 eigen values. This set of axis can be used to create a graphic representation of the distribution as an ellipsoid volume where the lengths of the axes (two times the square root of eigen values) are proportional to the standard deviations of the distribution along each axis (see Fig. 72). As a first order model, the ellipsoid approximation of the distribution represents a trivariate Gaussian distribution which standard deviations are reported by the lengths of the ellipsoid axes and are equivalent to the standard deviations of the synaptic distribution when projected along the principal axe

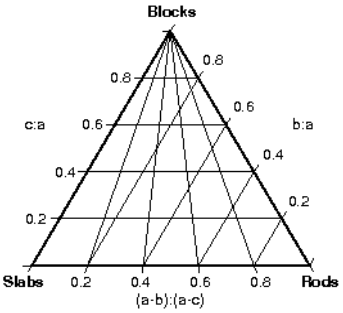

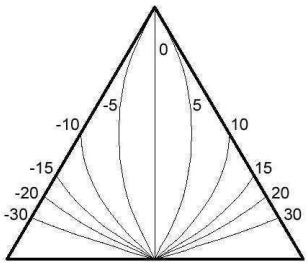

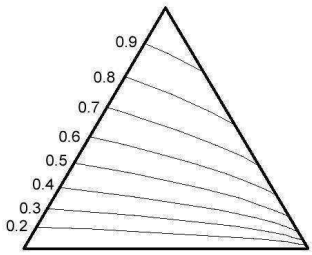

Sneed & Folk diagram | Oblate-Prolate index isolines | M.P.Sphericity index isolines

Oblate Prolate-index: O.P. i = $\frac{10(a-b/a-c - 0.5)}{c/a}$; M.P. Sphericity index: MPSi = $\sqrt[3]{\frac{c^2}{ab}}$

Fig. 73/ Triangular diagrams for anisotropy of ellipsoids. On the Sneed and Folk diagram, The 3 ratios of ellipsoid lengths are linearly plotted along the sides of a triangle. Any spheroid shape can thus be identified in this continuum space where extrema represent sphere (top), disc (bottom left) and rod (bottom right). For a precise characterization the same space can be divided with the OP index and the MPS index isolines

4/ Anisotropy

It is interesting to go further with the ellipsoid approximation by using it to measure likely anisotropies of the synaptic distribution defined by ratios of elongation values of ellipsoid. For clarity, these lengths were labeled **a**, **b** and **c** by decreasing order. When 2 of the 3 axis have the same length, the spheroid volumes are commonly referred as prolate (a>>b~c) or oblate (a~b>>c) shapes. Prolate shapes are elongated under one direction and tend to have a rod-like shape whereas oblate shapes are similar to pumpkins and tend to have disc appearance. The oblate/prolate classification of spheroids have been widely used in the field of nuclear physic for heavy nuclei or in the field of condensed matter for liquid metal clusters (see the liquid drop deformation model, Borggreen et al., 1993). By this way any trivariate distribution can be continuously indexed in a continuous way as a blend of each pure spherical, rod-like and disc shapes. Researchers in Earth sciences have also been confronted to such problem for sorting sand or sedimentary particles and developed efficient graphics methods for classification, especially the Sneed & Folk triangular diagram to sort trivariate distributions (Graham & Midgley, 2000). For this diagram the different ratios **c/a**, **b/a** and **(a-b)/(a-c)** are plotted along each sides of a triangle (see Fig. 73). The ratios vary linearly with lengths resulting in an even representation of spheroids shapes across the diagram without distortion in the shape continuum. Spheroids can thus be represented, regardless to their size, into a continuum between block (or spheres), slabs (disc, oblate) and rods (prolate) which mark each corner of the diagram. This analysis includes fine qualitative indices such as the Oblate-Prolate index (OPi) and the Maximum Projection Sphericity index (MPSi) for which isolines can be drawn into the triangular diagram.

5/ Tangential cortical surface projection for 2D cortical-map analysis.

The functional mapping framework of the cortical organization naturally leads our morphological analysis to be flattened onto the cortical surface in order to access a similar point of view. A local tangential plane of the cortical surface was chosen and associated to a unique orthogonal direction along which the distribution of the synaptic cloud is projected. One of the sides of the TZ-volume introduced above gives a good approximation of a plane

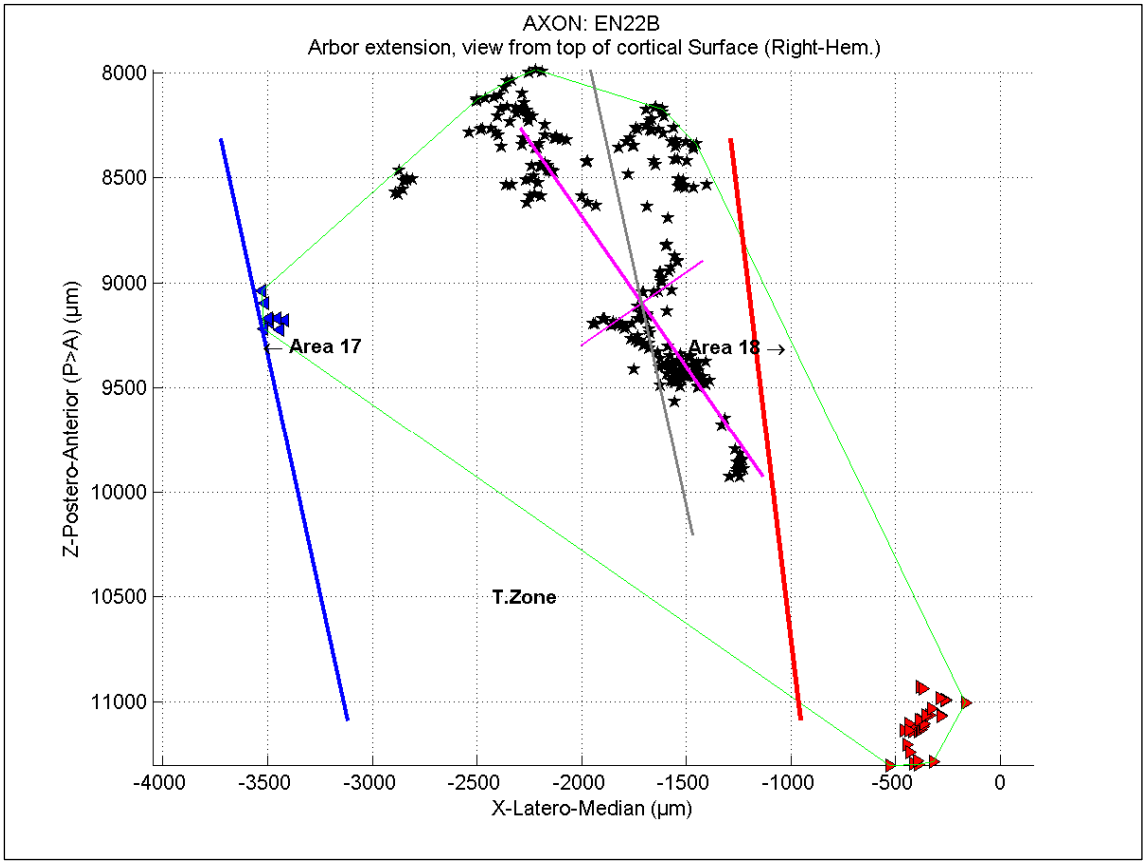

Fig. 74/ Tangential projection of the terminal arbor onto cortical surface for 2D cortical-map analysis. The 3D synaptic-cloud distribution (from axon 22B) is projected onto a plane defined by the S- vertex of the TZ-volume. The two lines of boundary between A17/TZ and TZ/A18 respectively plotted in blue and Red. The mean of these two directions provide the average direction of the course on the TZ-border onto the cortical surface (grey line). The covariance matrix of the 2D distribution provides a set of 2 orthogonal elongated axes (purple crossed lines) with associated eigen values. These lines cross onto the 2D center of mass of the distribution. The Angle between the great axis and the mean direction of the transition border is also computed. A convex hull algorithm gives the least area surrounding all point (green contour). Each point of the distribution is represented regarding to the area it falls into with A17, TZ and A18 respectively plotted with **< / * / >** symbols. The scales on axis reflect relative positions but are not consistent with stereotaxic absolute coordinates. See text for details.

tangential the closest cortical surface. The plane equation is simply given by choosing 3 among the 4 S-labeled vertex of the TZ-volume. After projection onto this tangential plane, a 2D extension analysis similar to the 3D one can be performed (cf. Fig. 74). Diagonalization of the 2x2 covariance matrix was performed to provide the couple of orthogonal axes and their respective eigen values for a quantitative description of the spatial dispersion of the synaptic cloud onto the cortical map. Two dimensional anisotropy is defined by the ratio between the square root of the 2 eigen values. Regarding to the global spatial extension onto the cortical surface, we also computed the value of the minimum area surrounding all projected points (green contour and on Fig. 74) using conventional "convex hull" algorithm (Barber et al., 1996) available in many calculation software. The definition of the TZ-volume by its 8 vortices, can easily solve the troublesome problem of counting synaptic boutons and relate the cortical area they belong to. The two flanking planes of the TZ-volume were used as a linear separator in the 3D space. Each synaptic contact of the distribution can thus be sorted within one of the 3 following categories *into-A17*, *into-TZ* and *into-A18* respectively represented by the < / * / > symbols on the cortical planar projection graphic on fig.5. The local curvature of the cortex makes the area separation planes not to be parallel so the orthogonal 2D projection of each points may not reflect the right area it belong to. The segregation performed before projection reduces mistaking the area identification due the smooth curvature of the cortex.

6/ Trigonometry

Any pronounced anisotropic 2D distribution on the cortical surface may traduce a particular orientation between the post-synaptic units in the retinotopic cortical map. In order to reach this parameter, we reported the angle between the great axis of the ellipse (purple great segment in Fig. 5) and the mean direction of TZ (grey line). This orientation is obtained by $\theta_{Ell/TZ.} = \text{acos}(\mathbf{a_{Ell.}}.\mathbf{n_{TZ}})$ where $\mathbf{a_{Ell.}}$ is the support vector of the great axis direction and $\mathbf{n_{TZ}}$ the support vector for the mean TZ direction. Because the direction of TZ is submitted to variability on the cortex, we also reported the angle with respect to the antero-posterior axis (i.e; the midline) as an alternative measure. We used circular statistics to report the mean and standard deviation of angles on a set of 15 samples and performed a circular Rayleigh test to check the non uniformity of the distributions.

Results

The Table 4 reports the means and standard deviations for all quantities that have been defined above when applied to the terminal arbors of the 15 callosal axons (and therefore to the spatial distribution of their synaptic boutons). The wide heterogeneity of the morphologies of the callosal axons led to consider these means values with caution, in particular because most standard deviations were of similar order

In fact, the population was better appreciated and specified through characteristics of histograms where values from the 15 samples were reported altogether. Relevant parameters for callosal terminal arbors are highlighted with red color in Table 4 and associated histograms are plotted in Fig. 75. The following parameters gave a relevant description of our visual interhemispheric axons:

a) For 12/15 axons, the percentage of terminations falling into the TZ-volume were superior to 80% (fig. 75(a)).

b) For a great majority (11/15), the minimum surrounding surface of the projection of the terminations onto the cortex lied into the [0.5~2.5] mm^2 interval, covering the surface of a patch of about 1mm x 3mm (Fig. 75(b)).

c) This magnitude also reflected the length of the majority of the greatest axis of the 2D ellipses falling into [0.5~2] mm for 12/15 axons (Fig. 75(c)).

d) The 2D anisotropy was smaller than 2 for more than half of the population (8/15 axons). Six others remained weakly elongated with anisotropy from 3 to 5. Surprisingly, one of the axons however showed a very strong anisotropy of 9.6 (Fig. 75 (d)).

ELLIPSOiD Analysis	MEANS	St. Dev.
Number of terminals	131	87
Number of terminals in A17	2,2	3,3
Number of terminals in TZ	107	73,5
Number of terminals in A18	22,1	43,6
Terminals % in A17	3,05	6,6
Terminals % in TZ	84,52	20,9
Terminals % in A18	12,43	21,4
Surface on the Cortex (mm^2)	2,7	2,6
ellipse Axis 1 (mm)	1,5	8,9
ellipse axis 2 (mm)	0,5	0,3
anisotropy 2D	3,0	2,1
Angle axis 1 / TZ (deg)	76,5	56,0
Angle axis 1 / Axe AP (deg)	70,6	53,7
TZ/AP axis angle difference	- 5,9	7,8
Ellipsoid Volume (mm^3)	0,83	0,98
Ellipsoid 3D Axis 1 (mm)	1,6	0,8
Ellipsoid 3D axis 2 (mm)	0,8	0,3
Ellipsoid 3D axis 3 (mm)	0,4	0,2
3D anisotropy 1 (ax1/ax2)	2,0	0,9
3D anisotropy 2 (ax2/ax3)	2,0	0,8
Oblate-Prolate index	7,5	11
M.P. Sphericity index	0,54	0,16

Table 4/ Means & standard deviations of spatial extensions parameters for 15 arbors terminals distributions of callosal axons.

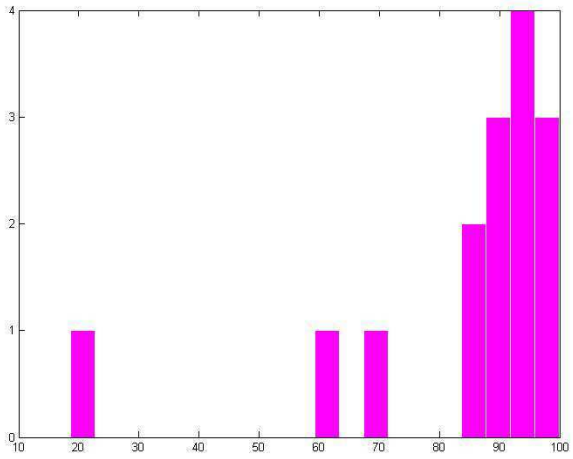

Fig. 75 (a) Histogram showing the numbers of callosal axons as a function of the percentage of terminals falling into the TZ-volume (X-axis: %).

Fig. 75 (b) Distribution of the surfaces on the cortex covered by projection for each axon (mm^2).

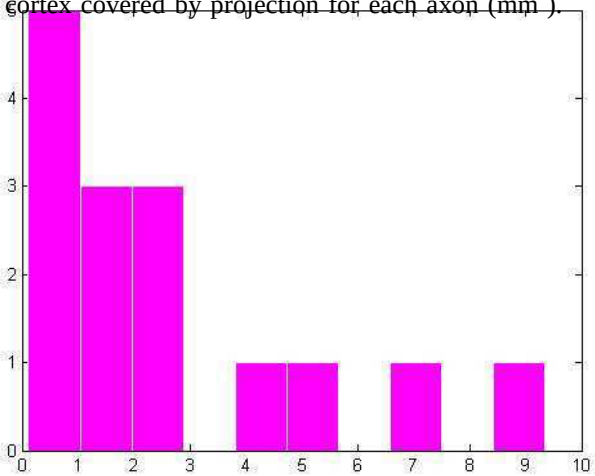

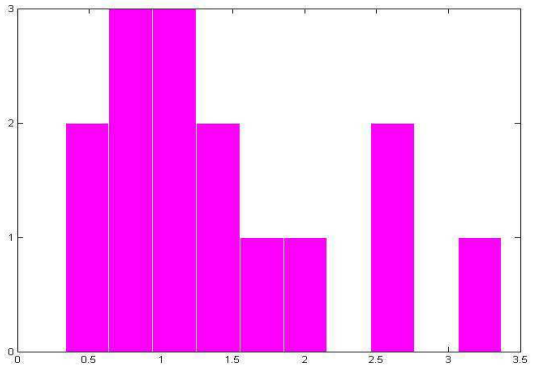

Fig. 75 (c) Lengths of the 2D greatest elongation axis (mm)

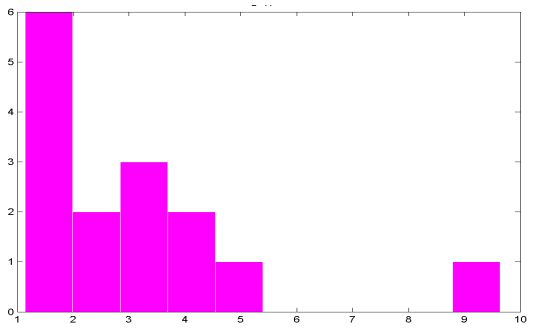

Fig. 75 (d) 2D anisotropies (axis lengths ratios)

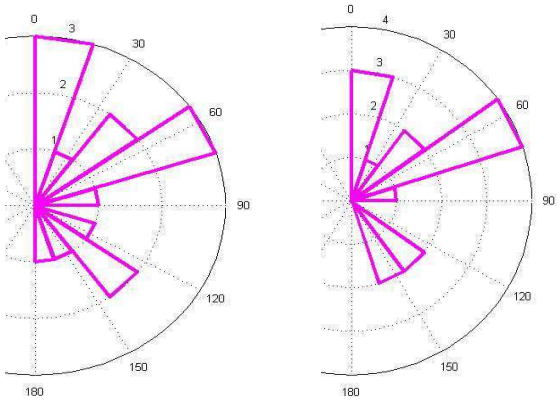

Fig. 75 (e) Distributions of the 2D orientations of the callosal terminals (located within a right hemisphere) with respect to the antero-posterior orientation of the transition zone between A17 and A18 (at left) and the antero-posterior axis of the brain, i.e. the midline (right) which corresponds here to the vertical.

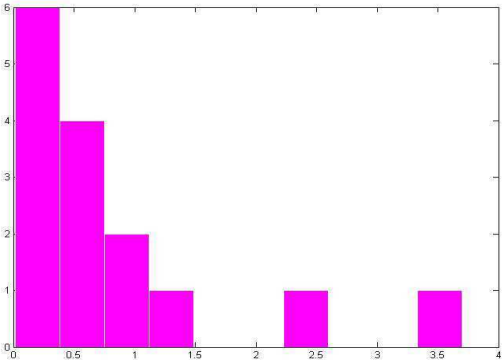

Fig. 75 (f) Distribution of Ellipsoid volumes (mm^3)

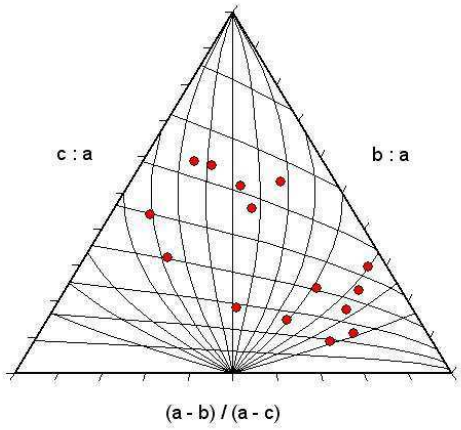

Fig. 75 (g) 3D anisotropies distribution in the Sneed & Folk diagram.

e) Circular statistics performed into [0-180°] revealed that the mean orientation of the callosal terminal arbours was 76° with respect to the TZ direction and 70° with respect to the AP direction (i.e. the midline). But these trends are submitted to important variability (Fig. 75(e)). The difference of 6° between them corresponds to the mean orientation of TZ on the cortex found for our callosal population. In order to check the relevance of this oblique bias, we additionally applied a Rayleigh circular statistic test with a null hypothesis of uniformity. This hypothesis can not be rejected on raw data (P-value>0.4) as a weak anisotropy (smaller than 1.8 for 5/15 axons) leads to meaningless angle interpretation. However, when weighted with respective anisotropy values, the hypothesis of uniformity of the angles distribution is rejected by the test with a high significance (P-values equal to $1.4\ 10^{-3}$ and $1.5\ 10^{-4}$ regarding to the TZ and AP directions respectively) conferring a relevant meaning to the angle means.

f) Dealing with the 3D analysis, the most important parameter is the ellipsoid volume. For the majority of axon (13/15), this volume was confined into the [0.2~1.5] mm^3domain (Fig. 75(f)).

g) At last the 3D systematic anisotropies of the ellipsoid were checked on triangular diagrams (Fig. 75(g)) and an important heterogeneity was found for this population. However, two subpopulations seemed to emerge from the triangular diagram. One had sphere-like shapes and a weak anisotropy (top-left half of the diagram); the other one showed rod-like shapes (bottom right of the diagram). Five axons showed a M.P.S. index > 0.65 indicating an almost spherical distribution, and five others showed a high O.P. index > 15 combined with low (<0.5) M.P.S. index indicating strongly elongated shapes, but any boundary can be clearly seen in between.

Discussion

From a collection of precise anatomical data, we proposed here a set of geometrical methods which aimed at quantifying relevant parameters to describe the spatial dispersion of the synaptic distribution into a particular cortical context. As a first step, 3D computations, volumes and elongations of distributions approximated by an ellipsoidal shape provide information on the general spatial configuration of the synaptic field.

The internal structure of the cortex is far from being isotropic. The early development sequences with the course of neurons along radial glia and the laminar organization of the cortex generally constrain neural structures to develop radial extensions and horizontal extensions through the cortical surface. Under such constraints of organization, it is likely to find unequal extensions in some directions of space instead of isotropic spherical distribution. The distribution of anisotropies reported here give an interesting characteristic of heterogeneity for callosal population. But further studies should be performed in order to distinguish the radial inter-laminar communication and the horizontal intra-laminar component of connectivity for strongly elongated distributions. Whatever the anisotropy, the callosal volume of connectivity for one axon was found to be confined under 1.5 mm^3 for most of the cases (13/15), with an important concentration around 0.5 mm^3 with almost 80% of the terminals falling into TZ. We reported superficial extensions on the cortex of the terminal distributions between 0.1 and 9.3 mm^2 with the highest concentration between 0.1 and 2.8 mm^2. Our callosal population shows heterogeneous 2D anisotropy with many of them targeting a focused spot on the cortex but oblique relevant mean angle with TZ or AP directions was demonstrated when angles distributions are weighted by anisotropy values.

The use of 8 reference points on histological sections to build the TZ-volume reference frame has been particularly useful to locate the distribution of terminal branches and synaptic boutons into its cortical inter-areal context especially in the case of the callosal axons targeting this narrow cortical region. This simple technique allows the computer automation of the “area related counting” procedure usually hardly performed by a human operator, and provides data which are in an excellent agreement with the relative areal distribution between A17/TZ/A18 already reported for these axons (Houzel et al, 1994). Other landmarks related to

cortical layer boundaries could be inserted to the TZ-volume. This would allow performing a laminar analysis by use of separation planes. But particular care has to be taken in case of important curvature of the cortex. The precise tridimensional, multi-layered organization of connectivity of the cerebral sensory cortex is still under intense discussions (Thomson & Bannister 2003, Raizada & Grossberg 2003). However the wide two-dimensional topology of the cortical sheet and its columnar organization lead to a mapping description of its capabilities. Once projected onto a cortical tangential surface, a synaptic or terminals distribution can thus be reinterpreted in terms of columns and functional mapping. The 2D ellipse approximation computed into a tangential cortical surface provides the elongation and its orientation regarding to the direction of the transition border or to the antero-posterior axis. Whereas any neural network can be functionally structured regardless to any particular spatial configuration of its elements, the specificity of the visual cortex combining a retinotopic organization with the detection of local orientations strongly constraints the spatial relationship of connected neurons. Especially it was demonstrated that long range horizontal connections are much more likely to occur when both units are tuned to detect a similar orientation, together with this orientation similar to the direction bounding the two units in the retinotopic space (Das & Gilbert, 1995). These observations provide important substrate to the “association field” models of the visual cortex (Chavane et al., 2000).

Moreover, the transition zone between visual area A17 and A18 is known to follow the representation of the vertical meridian and include a part of the ipsilateral field confined into an about 1mm wide band running onto the cortical surface from its posterior to its anterior part (Payne, 1990; Milleret al., 1994). In the many cases we found superficial terminals distributions to be quite elongated and anisotropic, one could ask whether the information provided by this cell is distributed along the TZ border direction or across. Wide distribution of directions was found but a bias toward the TZ-crossing with a mean 76° (or 70° with the AP axis) was observed. Combined together with the cortical areas association of the terminals, this directional information complete physiological data reporting the organization of receptive fields and binocular disparities of transcallosally activated units on both sides of the vertical meridian (Milleret et al. 2005).

The core of these methods is based on the ellipsoid approximation of the synaptic distribution. The trivariate Gaussian is taken as a first order model of the distribution

geometrically represented with an ellipsoid volume. Higher order analysis such as clustering methods would provide a finer representation of the heterogeneities of the synaptic cloud but they require much more computational procedures and calculation time. The most important need for this method to work properly is a set of synaptic data and to assume having a precise idea of the shrinkage correction to apply before performing the spatial dispersion analysis. Isotropic and anisotropic shrinkage depends on the histological procedures that are used to stain the tissues, to dry and to maintain slices onto the microscopic glass plate. The second key point is to precisely mark the transition zone location indexes onto the first and latest cortical slices as described in Milleret et al., 1994. Since theses points are used to define the TZ-volume reference frame, much of the precision of the different analysis proposed here depends on the precision obtained for the location of the 8 vertex as also on good estimations of the shrinkage correction.

Lastly, the curvature of cortex is another source of disturbance of the analysis: strong curvatures induce distorted cortical projections and generate irrelevant results. The problem of curvature of the cortex for functional imaging led to the development of linearization algorithms to obtain a flatten representation of the cortical sheet. These techniques are particularly interesting for global mapping such as f-MRI technique. But the local scale of the projection method proposed here produced satisfying results for the morphological analysis of a single neuron. In most cases, the local aspect of the analysis and the little dimension of the synaptic extension reduce the distortion effects of the cortical curvature. This makes the planar approximation of the cortical surface quite good enough to avoid strong distortions after projection. This also provides satisfying bi-dimensional results. In future studies, it would be particularly interesting to merge the planar projection analysis presented here with data obtained with superficial functional imaging such as optical imaging techniques. The superimposition of functional maps obtained with optical physiology with planar cortical view of synaptic stained contact may reveal interesting organization of callosal structures.

PART 1.2.2.

Characterization of the spatial extensions of terminal arbors of visual callosal axons by using 2D and 3D ellipsoid approximations

Comparison between the NR reference group and the MD group

The following pages report the detailed results of the ellipsoid analysis after application onto the set of the 15 callosal axons obtained in NR group (see also Part 1.2.1.) and 6 additional callosal axons originating from cats with an early monocular deprivation (MD group). As we saw in the Chapter 1.1., the complexity of the structures of the callosal axons and their heterogeneity make difficult their complete description. Their qualitative description is far being sufficient to obtain a general characterization of their morphology. The aim of this study is to collect additionally, through the ellipsoid method, a set of parameters that allows describing quantitatively the spatial extensions of the terminal arbours being found for each population. The goal is also showing that relevant spatial characteristics of the callosal terminal arbours can significantly allow distinguishing these two populations, demonstrating in particular that early monocular deprivation induces the stabilization of wider interhemispheric axonal structures than normal.

Presentation of the results

Each of the following pages reports the data that have been obtained for each axon. They include each:

1) The 3D reconstruction of the axon (when available, from Chapter 1.1.);
2) The related spatial parameters that have been obtained after applying the ellipsoid method (in a Table);
3) A 3D representation of the callosal terminal arbour and its ellipsoidal model into the TZ-volume cortical context. For this illustration, the AP axis (expressed in µm) runs from bottom to the top of the figure, with the anterior direction oriented toward the bottom of the figure (axis in red). The dorso-lateral and latero-medial axes are also represented in an orthogonal plane.
4) By a third figure that reports the projection of the callosal terminal arbour under study onto the cortical tangential plane (green plane in 3D). This is equivalent to a “view from the top” of the distribution of the terminal branches (and the terminal synaptic boutons), with the anterior direction again oriented toward the top of the Figure (y axis). As described in the methodology, this latter graphic illustrates the spatial configuration and the extensions of the terminal arbour. It allows showing the 2D ellipse axis lengths (purple cross), the TZ mean direction (grey line) and their relative orientation, and the distribution of the terminals throughout the different cortical areas that may be obtained from a planar separation in 3D.

Notice that the above text will be used as a legend for all of the following figures.

A.

Characterization of the callosal terminal arbors in the NR group

(Reference group)

AXON EN16C

Ellipsoid analysis

	ORIGIN AREA	A18
counts	**Number of terminals**	**263**
	Number of terminals in A17	0
	Number of terminals in TZ	162
	Number of terminals in A18	101
	Terminals % in A17	0
	Terminals % in TZ	61,6
	Terminals % in A18	38,4
2D	**Surface on the Cortex (mm^2)**	**9,35**
	ellipse Axis 1 (mm)	**3,37**
	ellipse axis 2 (mm)	1,17
	anisotropy 2D	**2,87**
	Angle axis 1 / TZ (deg)	61,0
	Angle axis 1 / Axe AP (deg)	57,3
	TZ/AP axis angle difference	-3,7
3D	**Ellipsoid Volume (mm^3)**	**3,70**
	Ellipsoid 3D Axis 1 (mm)	**3,65**
	Ellipsoid 3D axis 2 (mm)	1,20
	Ellipsoid 3D axis 3 (mm)	0,84
	anisotropy 3D (1/2)	3,0
	anisotropy 3D (2/3)	1,4
	Oblate-Prolate index	16,1
	M.P. Sphericity index	0,54

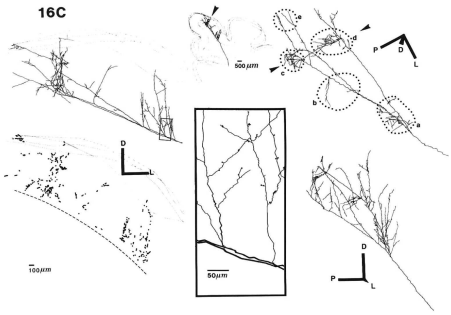

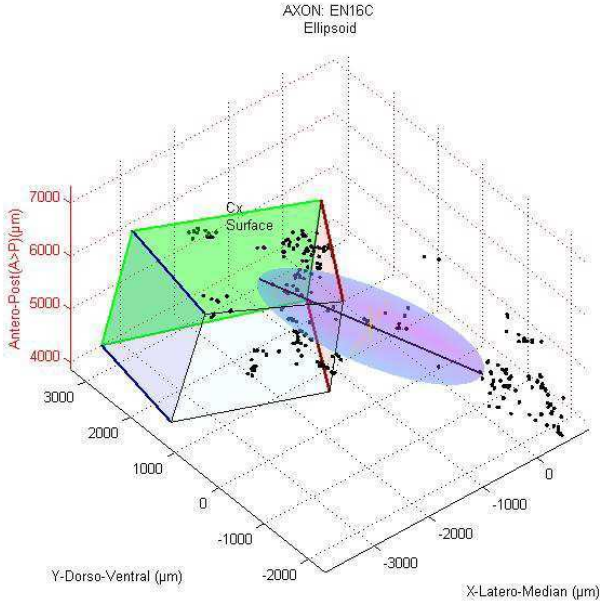

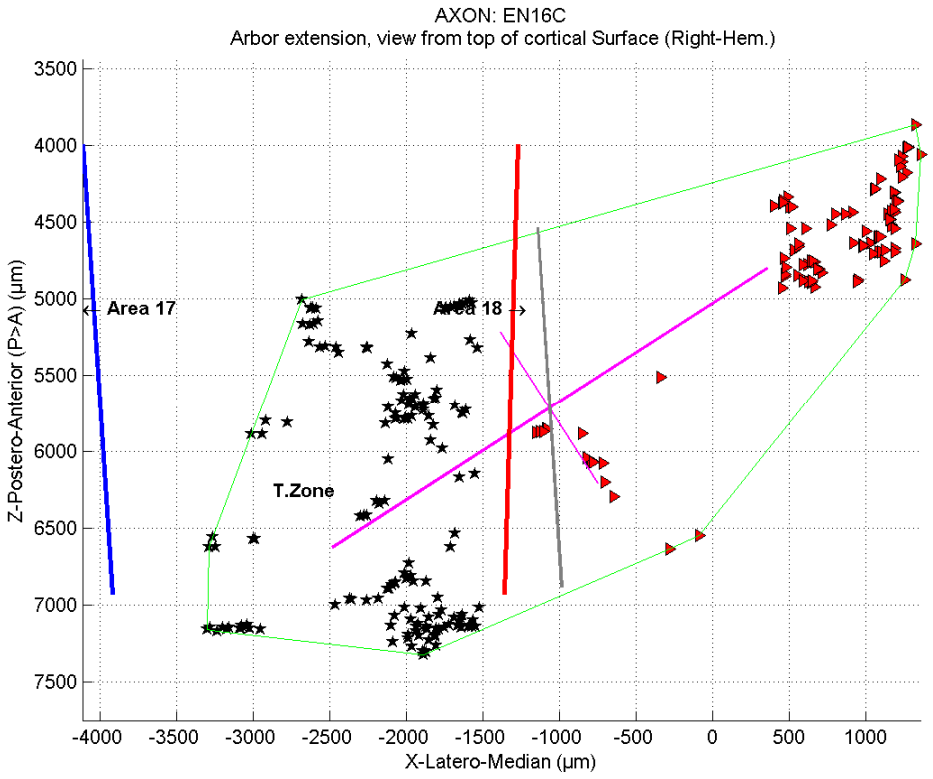

Fig. 76/ 2D & 3D ellipsoid analysis results for axon EN16C.

AXON EN16D

Ellipsoid analysis

	ORIGIN AREA	A18
Counts	**Number of terminals**	**183**
	Number of terminals in A17	0
	Number of terminals in TZ	34
	Number of terminals in A18	149
	Terminals % in A17	0
	Terminals % in TZ	18,6
	Terminals % in A18	81,4
2D	**Surface on the Cortex (mm^2)**	**6,98**
	ellipse Axis 1 (mm)	**2,71**
	ellipse axis 2 (mm)	0,56
	anisotropy 2D	**4,8**
	Angle axis 1 / TZ (deg)	67,0
	Angle axis 1 / Axe AP (deg)	59,8
	TZ/AP axis angle difference	- 7,2
3D	**Ellipsoid Volume (mm^3)**	**2,33**
	Ellipsoid 3D Axis 1 (mm)	**2,80**
	Ellipsoid 3D axis 2 (mm)	1,63
	Ellipsoid 3D axis 3 (mm)	0,51
	anisotropy 3D (1/2)	1,7
	anisotropy 3D (2/3)	3,2
	Oblate-Prolate index	0,7
	M.P. Sphericity index	0,38

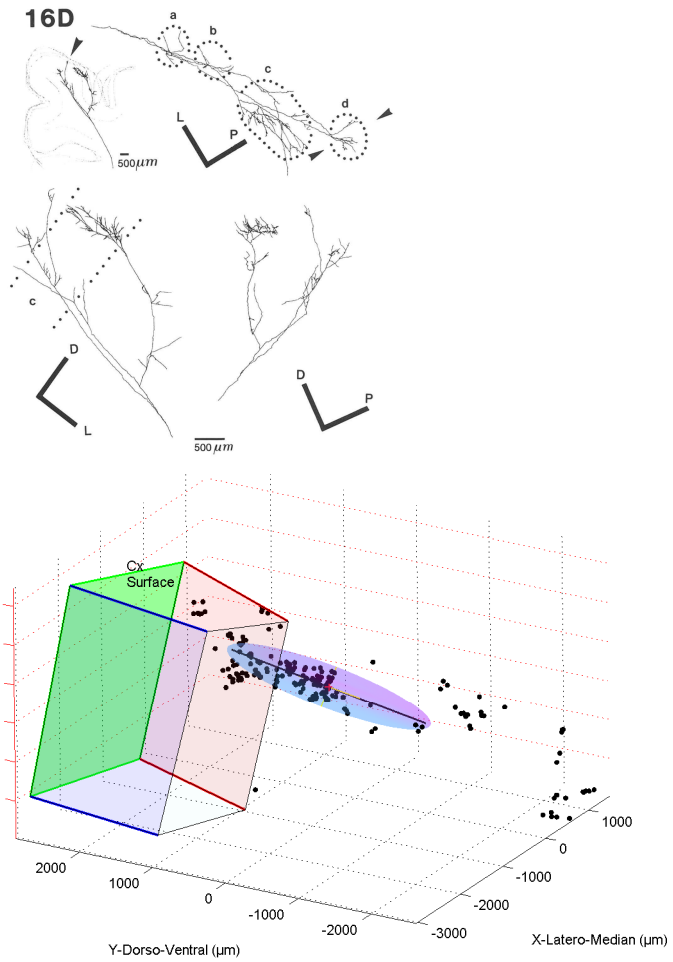

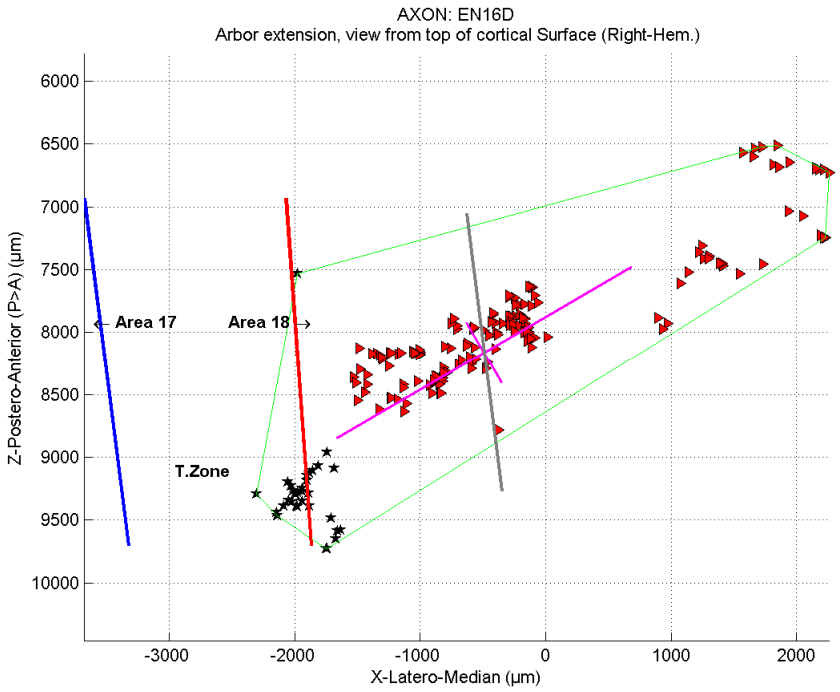

Fig. 77/ 2D & 3D ellipsoid analysis results for axon EN16D.

AXON EN16E

Ellipsoid analysis

	ORIGIN AREA	A18
Counts	**Number of terminals**	**138**
	Number of terminals in A17	6
	Number of terminals in TZ	132
	Number of terminals in A18	0
	Terminals % in A17	4,3
	Terminals % in TZ	95,7
	Terminals % in A18	0
2D	**Surface on the Cortex (mm^2)**	**4,18**
	ellipse Axis 1 (mm)	**1,39**
	ellipse axis 2 (mm)	0,81
	Anisotropy 2D	**1,72**
	Angle axis 1 / TZ (deg)	11,3
	Angle axis 1 / Axe AP (deg)	0,1
	TZ/AP axis angle difference	-11,2
3D	**Ellipsoid Volume (mm^3)**	**0,88**
	Ellipsoid 3D Axis 1 (mm)	**1,40**
	Ellipsoid 3D axis 2 (mm)	0,98
	Ellipsoid 3D axis 3 (mm)	0,64
	Anisotropy 3D (1/2)	1,46
	Anisotropy 3D (2/3)	1,50
	Oblate-Prolate index	1,69
	M.P. Sphericity index	0,67

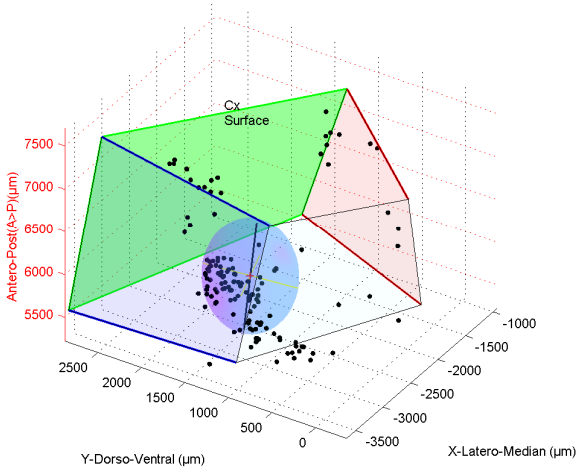

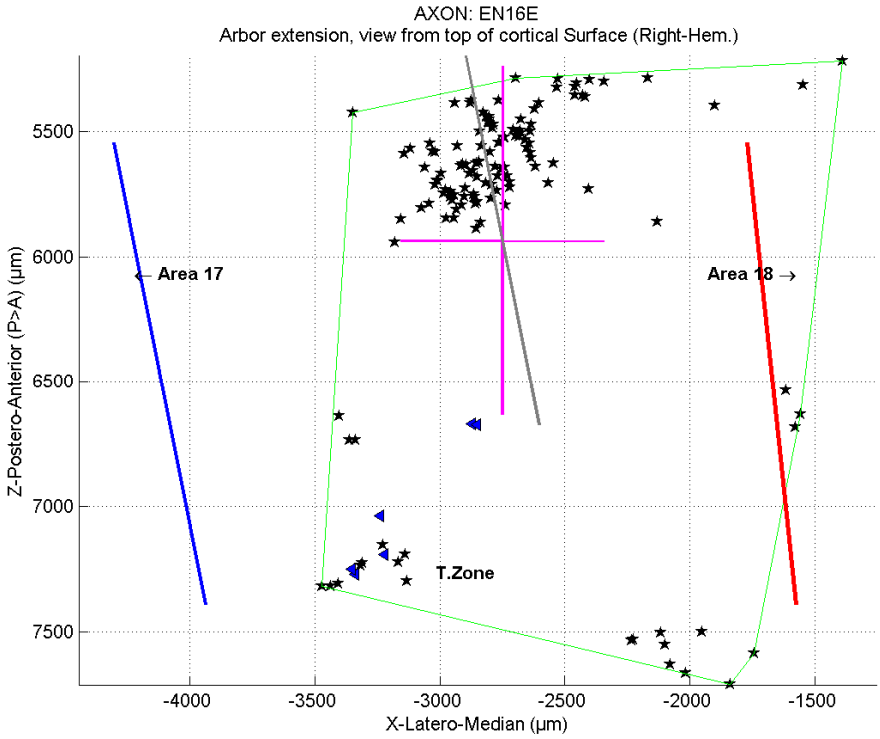

Fig. 78/ 2D & 3D ellipsoid analysis results for axon EN16E.

AXON EN16F

Ellipsoid analysis

	ORIGIN AREA	A18
Counts	**Number of terminals**	**94**
	Number of terminals in A17	0
	Number of terminals in TZ	85
	Number of terminals in A18	9
	Terminals % in A17	0
	Terminals % in TZ	90,4
	Terminals % in A18	9,6
2D	**Surface on the Cortex (mm^2)**	**2,82**
	ellipse Axis 1 (mm)	**1,68**
	ellipse axis 2 (mm)	0,41
	Anisotropy 2D	**4,0**
	Angle axis 1 / TZ (deg)	65,9
	Angle axis 1 / Axe AP (deg)	64,9
	TZ/AP axis angle difference	-1,0
3D	**Ellipsoid Volume (mm^3)**	**0,56**
	Ellipsoid 3D Axis 1 (mm)	**1,77**
	Ellipsoid 3D axis 2 (mm)	0,76
	Ellipsoid 3D axis 3 (mm)	0,41
	Anisotropy 3D (1/2)	2,3
	Anisotropy 3D (2/3)	1,82
	Oblate-Prolate index	10,6
	M.P. Sphericity index	0,5

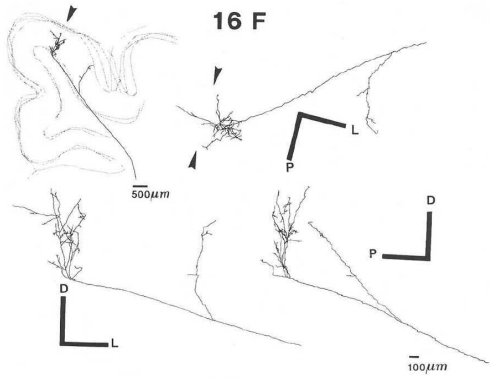

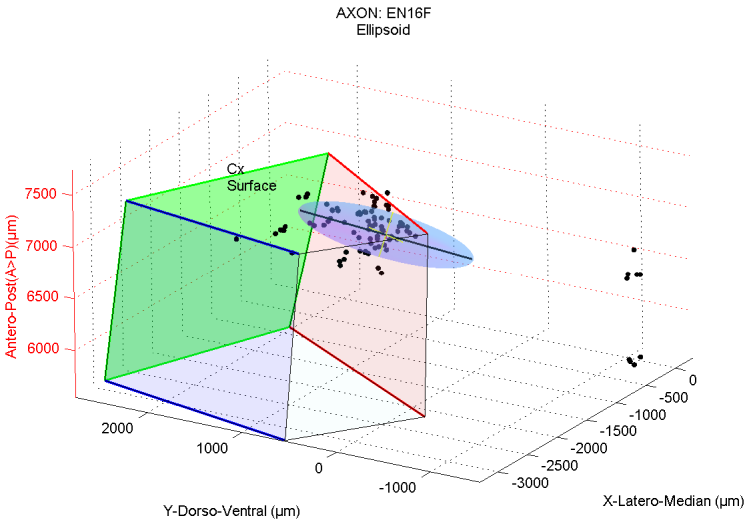

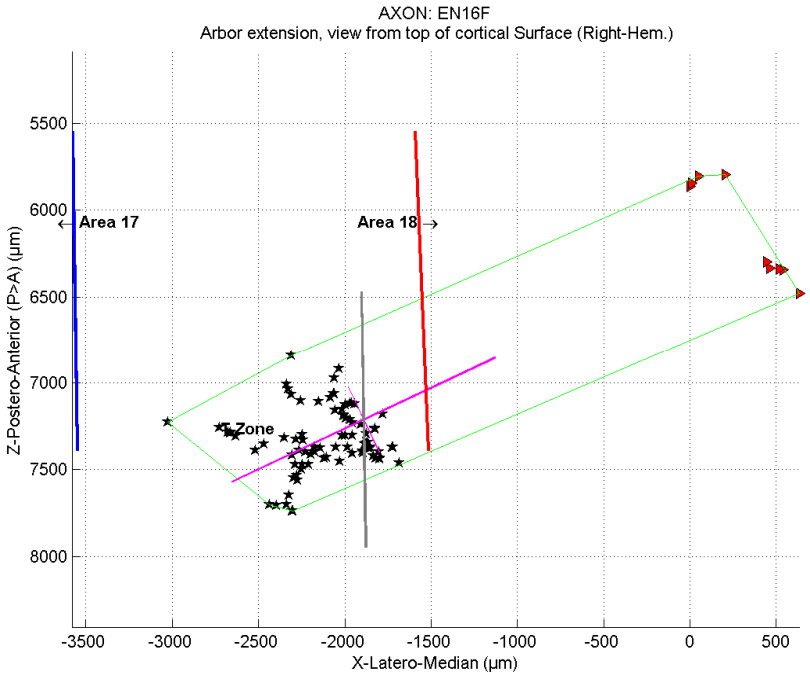

Fig. 79/ 2D & 3D ellipsoid analysis results for axon EN16F.

AXON EN16H

Ellipsoid analysis

	ORIGIN AREA	A18
counts	**Number of terminals**	**97**
	Number of terminals in A17	0
	Number of terminals in TZ	94
	Number of terminals in A18	3
	Terminals % in A17	0
	Terminals % in TZ	96,9
	Terminals % in A18	3,1
2D	**Surface on the Cortex (mm^2)**	**1,96**
	ellipse Axis 1 (mm)	**0,90**
	ellipse axis 2 (mm)	0,53
	Anisotropy 2D	**1,71**
	Angle axis 1 / TZ (deg)	29,3
	Angle axis 1 / Axe AP (deg)	21,0
	TZ/AP axis angle difference	- 8,3
3D	**Ellipsoid Volume (mm^3)**	**0,48**
	Ellipsoid 3D Axis 1 (mm)	**1,11**
	Ellipsoid 3D axis 2 (mm)	0,73
	Ellipsoid 3D axis 3 (mm)	0,59
	Anisotropy 3D (1/2)	1,52
	Anisotropy 3D (2/3)	1,23
	Oblate-Prolate index	4,42
	M.P. Sphericity index	0,75

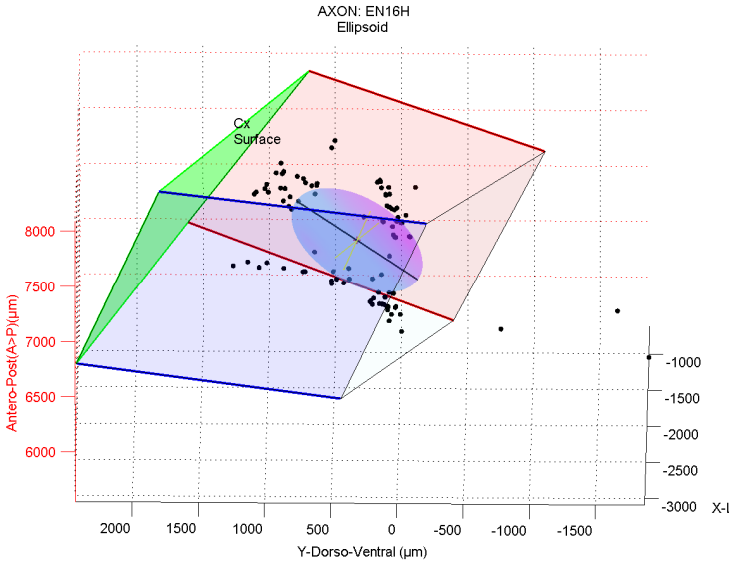

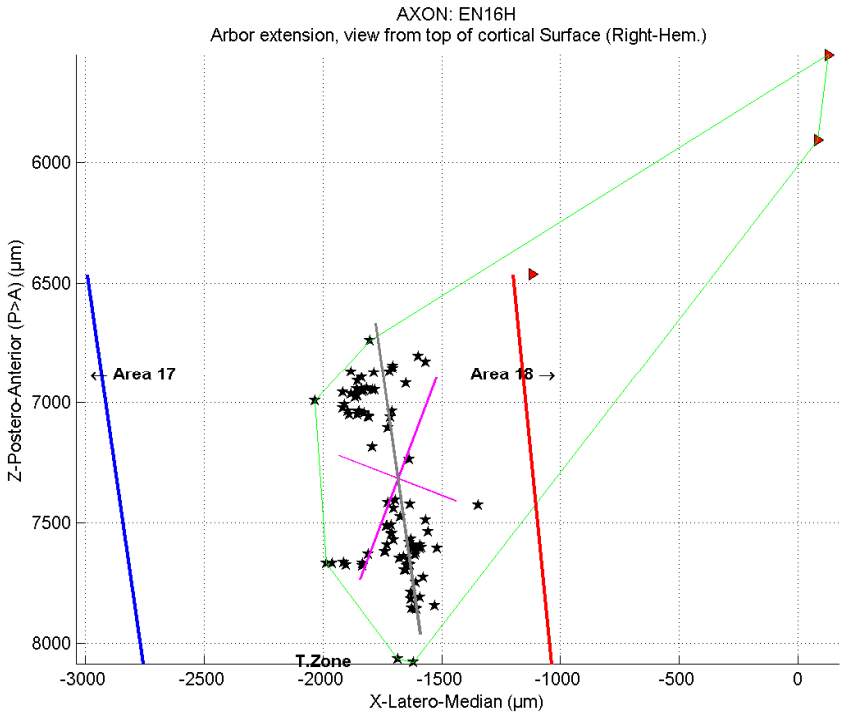

Fig. 80/ 2D & 3D ellipsoid analysis results for axon EN16H.

AXON EN16T

Ellipsoid analysis

	ORIGIN AREA	A18
counts	**Number of terminals**	**96**
	Number of terminals in A17	0
	Number of terminals in TZ	90
	Number of terminals in A18	6
	Terminals % in A17	0
	Terminals % in TZ	93,7
	Terminals % in A18	6,3
2D	**Surface on the Cortex (mm^2)**	**1,12**
	ellipse Axis 1 (mm)	**1,05**
	ellipse axis 2 (mm)	0,54
	Anisotropy 2D	**1,95**
	Angle axis 1 / TZ (deg)	76,9
	Angle axis 1 / Axe AP (deg)	67,2
	TZ/AP axis angle difference	-9,7
3D	**Ellipsoid Volume (mm^3)**	**0,26**
	Ellipsoid 3D Axis 1 (mm)	**1,58**
	Ellipsoid 3D axis 2 (mm)	0,71
	Ellipsoid 3D axis 3 (mm)	0,23
	Anisotropy 3D (1/2)	2,21
	Anisotropy 3D (2/3)	3,0
	Oblate-Prolate index	9,7
	M.P. Sphericity index	0,36

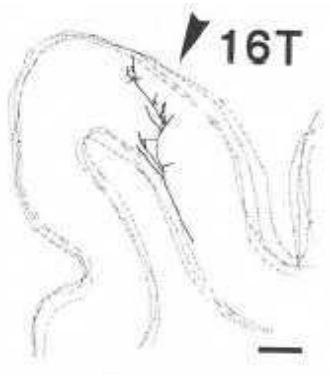

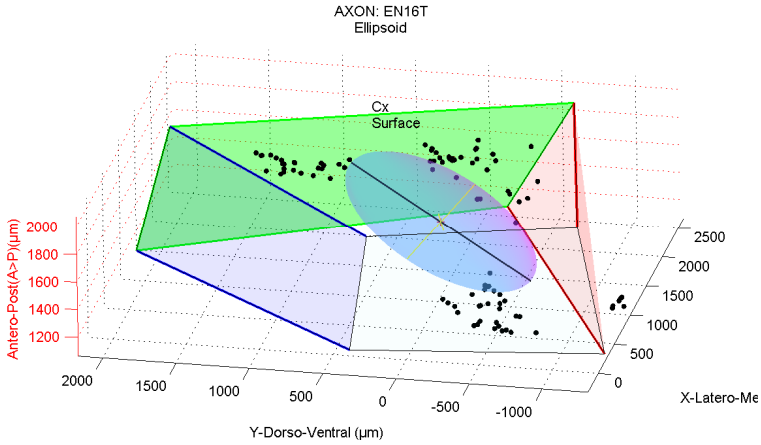

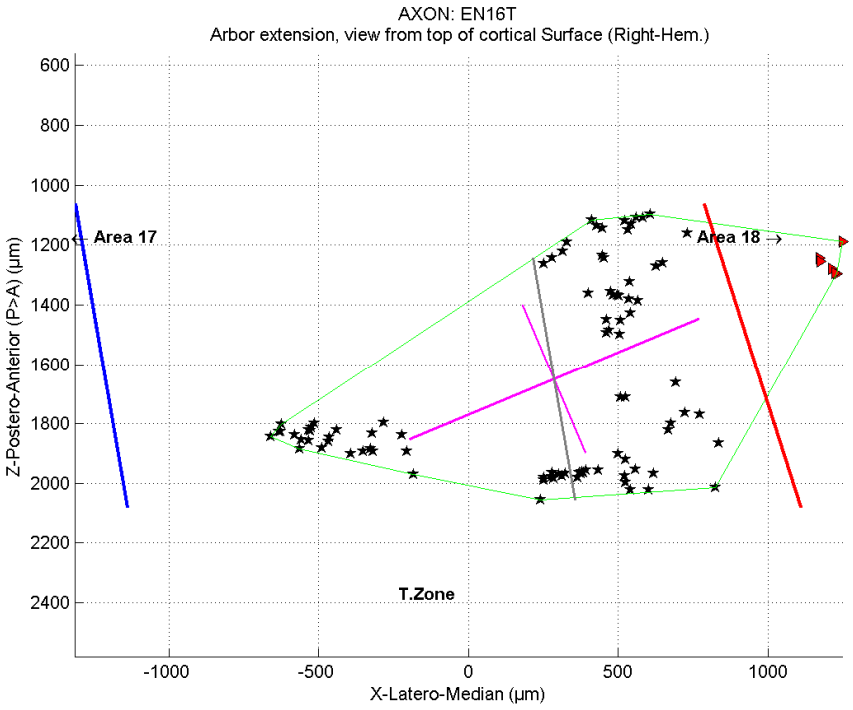

Fig. 81/ 2D & 3D ellipsoid analysis results for axon EN16T.

AXON EN16V

Ellipsoid analysis

	ORIGIN AREA	A18
counts	**Number of terminals**	**52**
	Number of terminals in A17	0
	Number of terminals in TZ	49
	Number of terminals in A18	3
	Terminals % in A17	0
	Terminals % in TZ	94,2
	Terminals % in A18	5,8
2D	**Surface on the Cortex (mm^2)**	**0,87**
	ellipse Axis 1 (mm)	**0,87**
	ellipse axis 2 (mm)	0,40
	Anisotropy 2D	**2,1**
	Angle axis 1 / TZ (deg)	143,2
	Angle axis 1 / Axe AP (deg)	140,8
	TZ/AP axis angle difference	-2,4
3D	**Ellipsoid Volume (mm^3)**	**0,32**
	Ellipsoid 3D Axis 1 (mm)	**1,07**
	Ellipsoid 3D axis 2 (mm)	0,87
	Ellipsoid 3D axis 3 (mm)	0,34
	Anisotropy 3D (1/2)	1,2
	Anisotropy 3D (2/3)	2,5
	Oblate-Prolate index	-7,01
	M.P. Sphericity index	0,5

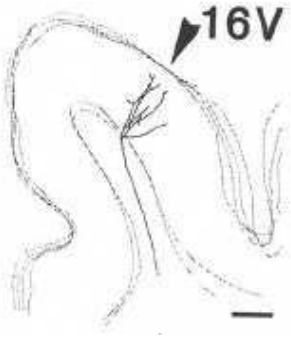

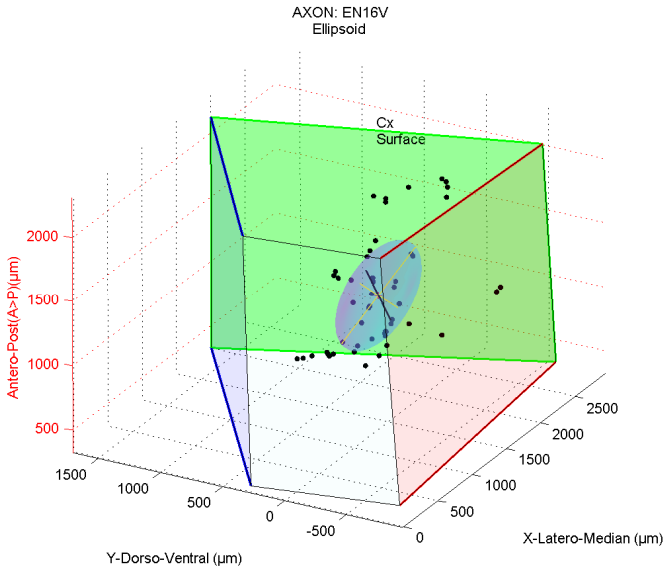

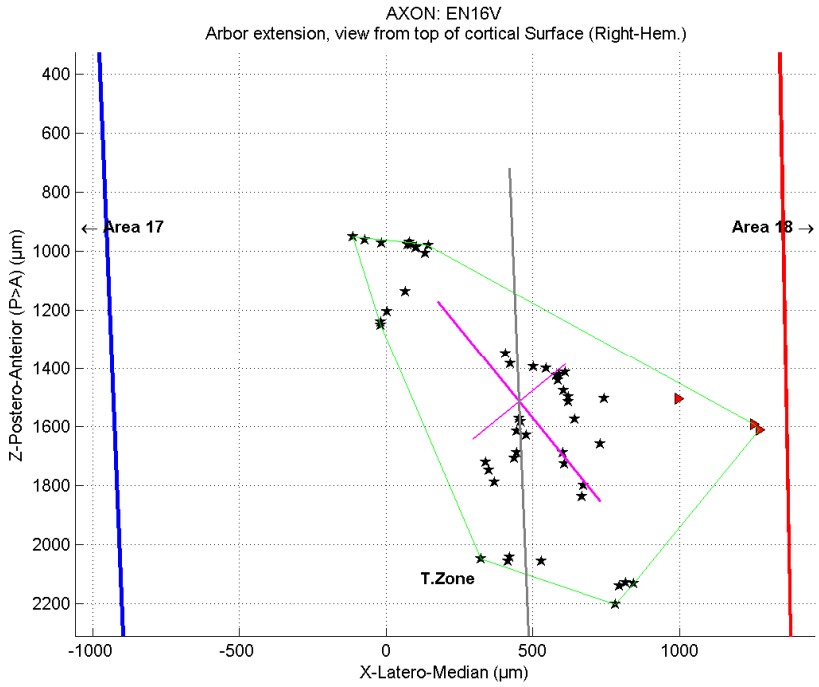

Fig. 82/ 2D & 3D ellipsoid analysis results for axon EN16V.

AXON EN16W

Ellipsoid analysis

	ORIGIN AREA	A18
Counts	**Number of terminals**	**91**
	Number of terminals in A17	0
	Number of terminals in TZ	88
	Number of terminals in A18	3
	Terminals % in A17	0
	Terminals % in TZ	96,7
	Terminals % in A18	3,3
2D	**Surface on the Cortex (mm^2)**	**1,92**
	ellipse Axis 1 (mm)	**1,13**
	ellipse axis 2 (mm)	0,51
	Anisotropy 2D	**2,20**
	Angle axis 1 / TZ (deg)	42,6
	Angle axis 1 / Axe AP (deg)	42,8
	TZ/AP axis angle difference	0,2
3D	**Ellipsoid Volume (mm^3)**	**0,67**
	Ellipsoid 3D Axis 1 (mm)	**1 ,19**
	Ellipsoid 3D axis 2 (mm)	1,08
	Ellipsoid 3D axis 3 (mm)	0,52
	Anisotropy 3D (1/2)	1,1
	Anisotropy 3D (2/3)	2,0
	Oblate-Prolate index	-7,7
	M.P. Sphericity index	0,59

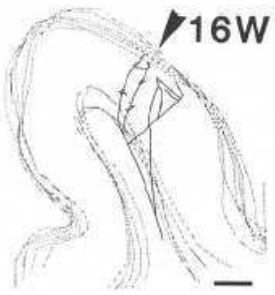

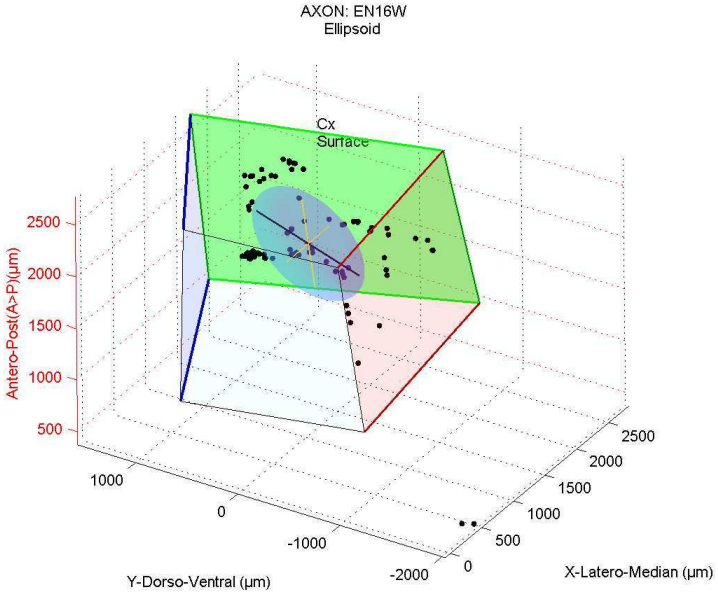

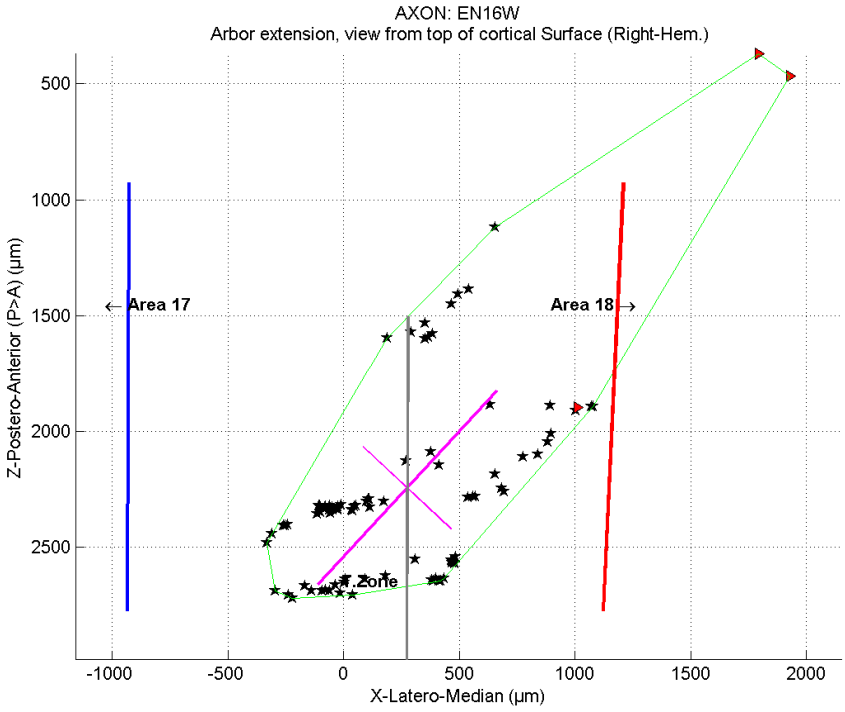

Fig. 83/ 2D & 3D ellipsoid analysis results for axon EN16W.

AXON EN20B

Ellipsoid analysis

	ORIGIN AREA	TZ
counts	**Number of terminals**	**28**
	Number of terminals in A17	7
	Number of terminals in TZ	20
	Number of terminals in A18	1
	Terminals % in A17	25
	Terminals % in TZ	71,4
	Terminals % in A18	3,6
2D	**Surface on the Cortex (mm^2)**	**2,26**
	ellipse Axis 1 (mm)	**2,71**
	ellipse axis 2 (mm)	0,62
	Anisotropy 2D	**4,35**
	Angle axis 1 / TZ (deg)	136,3
	Angle axis 1 / Axe AP (deg)	140,5
	TZ/AP axis angle difference	4,2
3D	**Ellipsoid Volume (mm^3)**	**1,22**
	Ellipsoid 3D Axis 1 (mm)	**2,78**
	Ellipsoid 3D axis 2 (mm)	0,91
	Ellipsoid 3D axis 3 (mm)	0,48
	Anisotropy 3D (1/2)	3,0
	Anisotropy 3D (2/3)	1,8
	Oblate-Prolate index	18,1
	M.P. Sphericity index	0,45

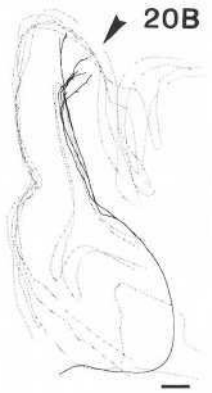

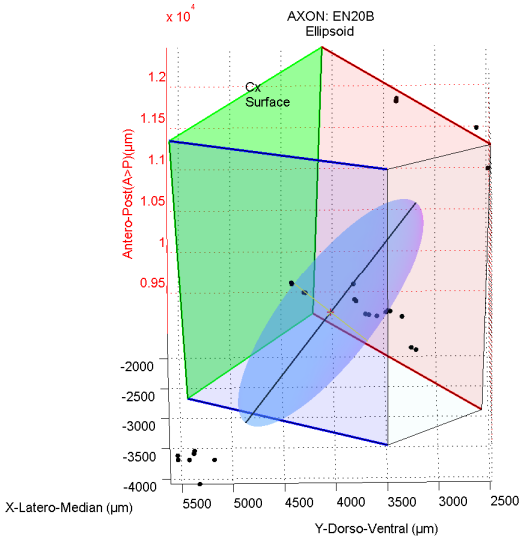

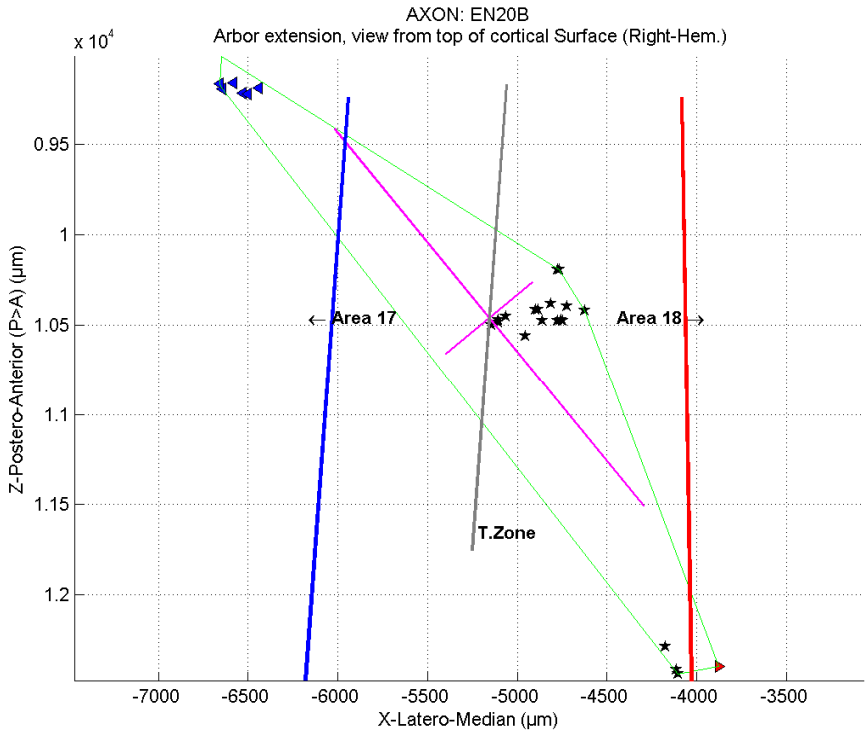

Fig. 84/ 2D & 3D ellipsoid analysis results for axon EN20B.

AXON EN20C

Ellipsoid analysis

	ORIGIN AREA	TZ
Counts	**Number of terminals**	**172**
	Number of terminals in A17	0
	Number of terminals in TZ	172
	Number of terminals in A18	0
	Terminals % in A17	0
	Terminals % in TZ	100
	Terminals % in A18	0
2D	**Surface on the Cortex (mm^2)**	**0,88**
	ellipse Axis 1 (mm)	**0,74**
	ellipse axis 2 (mm)	0,50
	Anisotropy 2D	**1,49**
	Angle axis 1 / TZ (deg)	7,1
	Angle axis 1 / Axe AP (deg)	8,3
	TZ/AP axis angle difference	1,2
3D	**Ellipsoid Volume (mm^3)**	**0,20**
	Ellipsoid 3D Axis 1 (mm)	**0,74**
	Ellipsoid 3D axis 2 (mm)	0,62
	Ellipsoid 3D axis 3 (mm)	0,42
	Anisotropy 3D (1/2)	1,1
	Anisotropy 3D (2/3)	1,4
	Oblate-Prolate index	-2,0
	M.P. Sphericity index	0,73

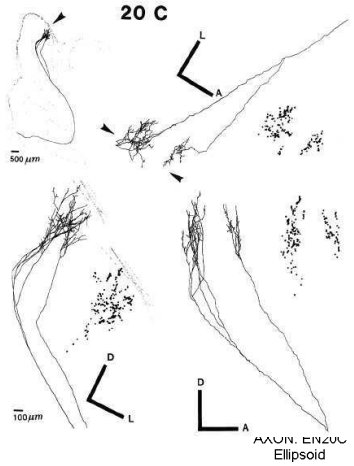

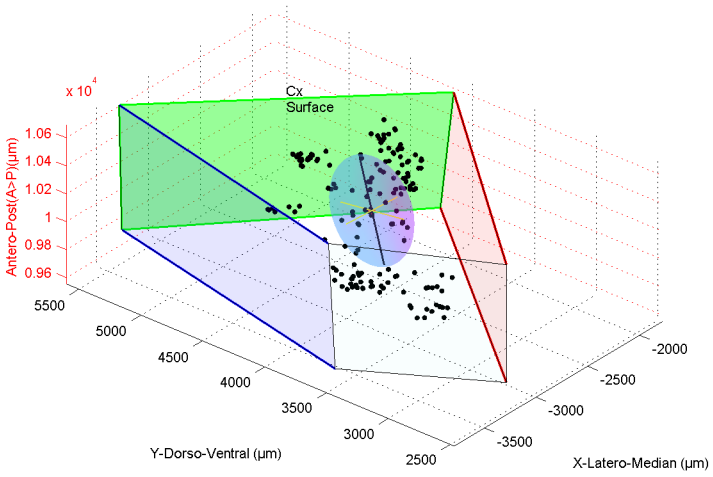

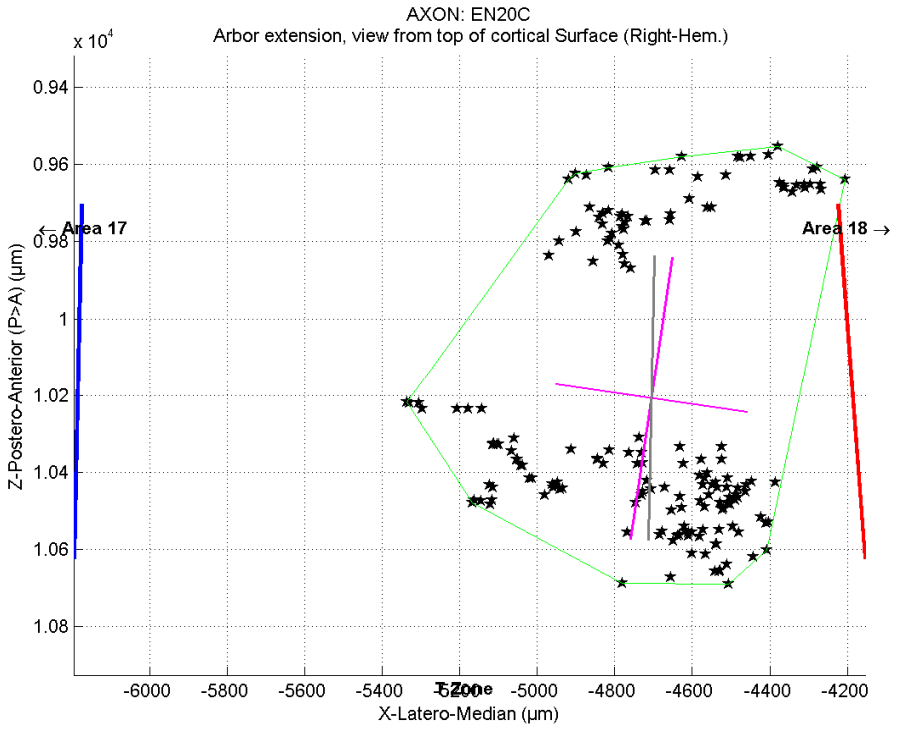

Fig. 85/ 2D & 3D ellipsoid analysis results for axon EN20C.

AXON EN21B

Ellipsoid analysis

	ORIGIN AREA	TZ
counts	**Number of terminals**	**120**
	Number of terminals in A17	6
	Number of terminals in TZ	114
	Number of terminals in A18	0
	Terminals % in A17	5
	Terminals % in TZ	95
	Terminals % in A18	0
2D	**Surface on the Cortex (mm^2)**	**0,11**
	ellipse Axis 1 (mm)	**0,33**
	ellipse axis 2 (mm)	0,93
	Anisotropy 2D	**3,56**
	Angle axis 1 / TZ (deg)	112,3
	Angle axis 1 / Axe AP (deg)	89,5
	TZ/AP axis angle difference	- 22,8
3D	**Ellipsoid Volume (mm^3)**	**0,017**
	Ellipsoid 3D Axis 1 (mm)	**0,82**
	Ellipsoid 3D axis 2 (mm)	0,23
	Ellipsoid 3D axis 3 (mm)	0,09
	Anisotropy 3D (1/2)	3,5
	Anisotropy 3D (2/3)	2,5
	Oblate-Prolate index	27,8
	M.P. Sphericity index	0,35

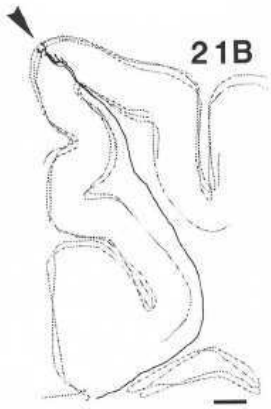

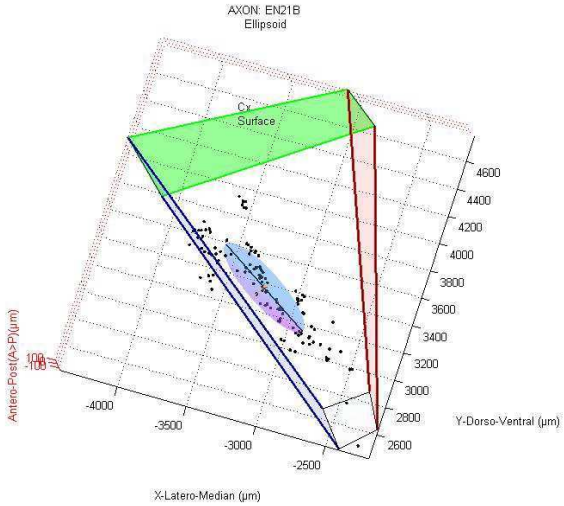

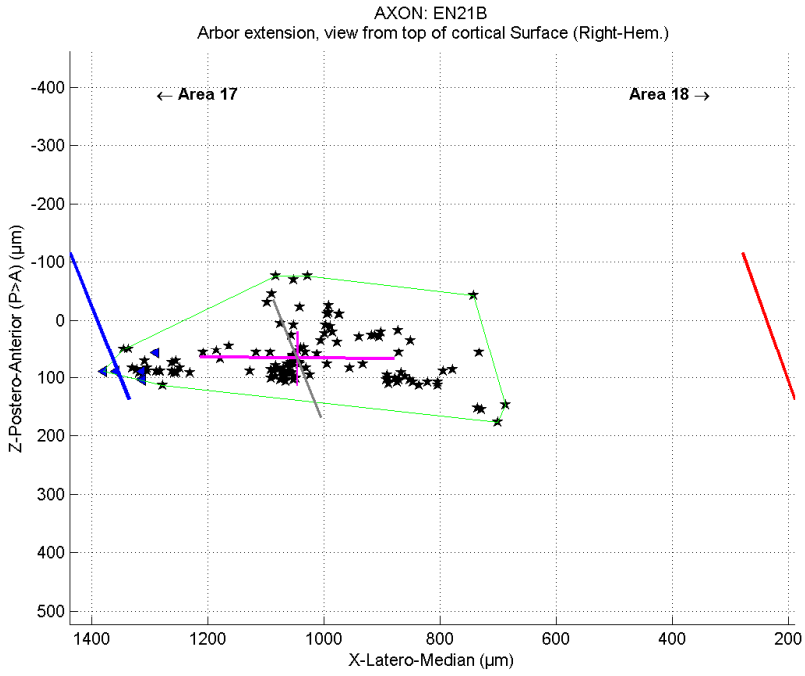

Fig. 86/ 2D & 3D ellipsoid analysis results for axon EN21B.

AXON EN21C

Ellipsoid analysis

	ORIGIN AREA	TZ
counts	**Number of terminals**	**60**
	Number of terminals in A17	5
	Number of terminals in TZ	55
	Number of terminals in A18	0
	Terminals % in A17	8,3
	Terminals % in TZ	91,7
	Terminals % in A18	0
2D	**Surface on the Cortex (mm^2)**	**0,49**
	ellipse Axis 1 (mm)	**1,51**
	ellipse axis 2 (mm)	0,15
	Anisotropy 2D	**9,6**
	Angle axis 1 / TZ (deg)	10,2
	Angle axis 1 / Axe AP (deg)	7,6
	TZ/AP axis angle difference	-2.6
3D	**Ellipsoid Volume (mm^3)**	**0,16**
	Ellipsoid 3D Axis 1 (mm)	**1,78**
	Ellipsoid 3D axis 2 (mm)	0,57
	Ellipsoid 3D axis 3 (mm)	0,15
	Anisotropy 3D (1/2)	3,1
	Anisotropy 3D (2/3)	3,7
	Oblate-Prolate index	27,9
	M.P. Sphericity index	0,29

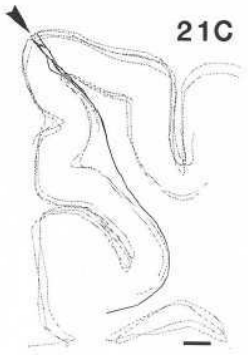

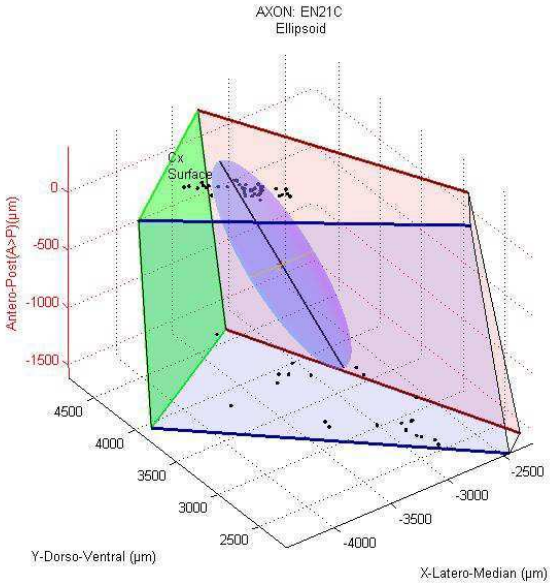

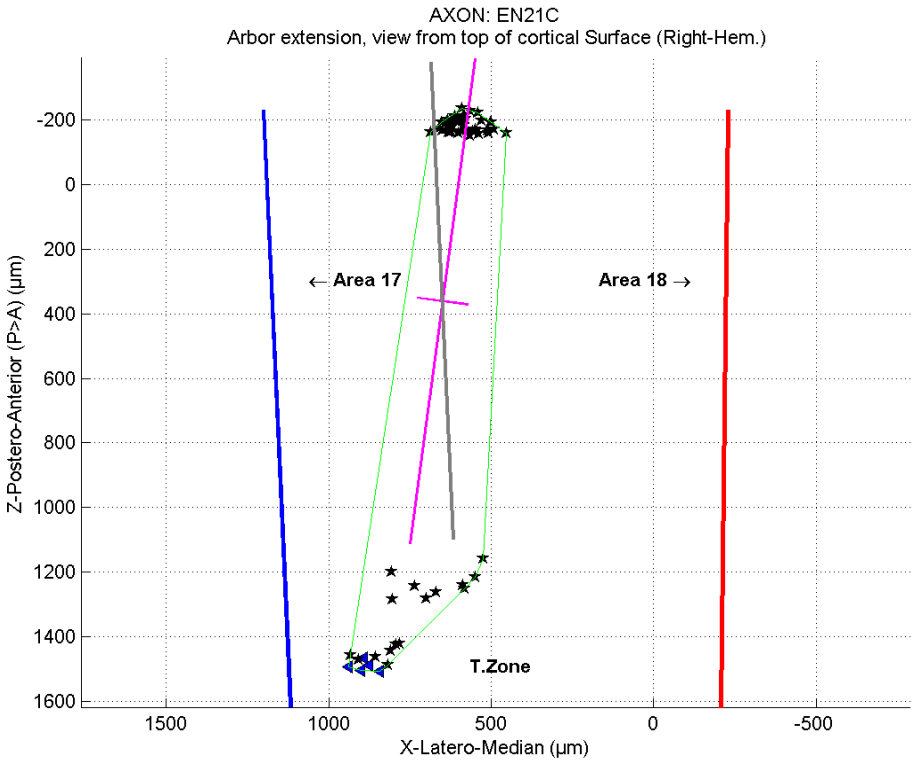

Fig. 87/ 2D & 3D ellipsoid analysis results for axon EN21C.

AXON EN22B

Ellipsoid analysis

	ORIGIN AREA	A17
counts	**Number of terminals**	**300**
	Number of terminals in A17	9
	Number of terminals in TZ	260
	Number of terminals in A18	31
	Terminals % in A17	3
	Terminals % in TZ	86,7
	Terminals % in A18	10,3
2D	**Surface on the Cortex (mm^2)**	**5,09**
	ellipse Axis 1 (mm)	**2,02**
	ellipse axis 2 (mm)	0,70
	Anisotropy 2D	**2,86**
	Angle axis 1 / TZ (deg)	157,5
	Angle axis 1 / Axe AP (deg)	145,1
	TZ/AP axis angle difference	-12,4
3D	**Ellipsoid Volume (mm^3)**	**0,98**
	Ellipsoid 3D Axis 1 (mm)	**2,14**
	Ellipsoid 3D axis 2 (mm)	0,72
	Ellipsoid 3D axis 3 (mm)	0,63
	Anisotropy 3D (1/2)	2,9
	Anisotropy 3D (2/3)	1,1
	Oblate-Prolate index	14,8
	M.P. Sphericity index	0,63

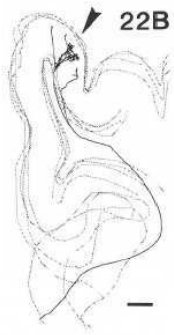

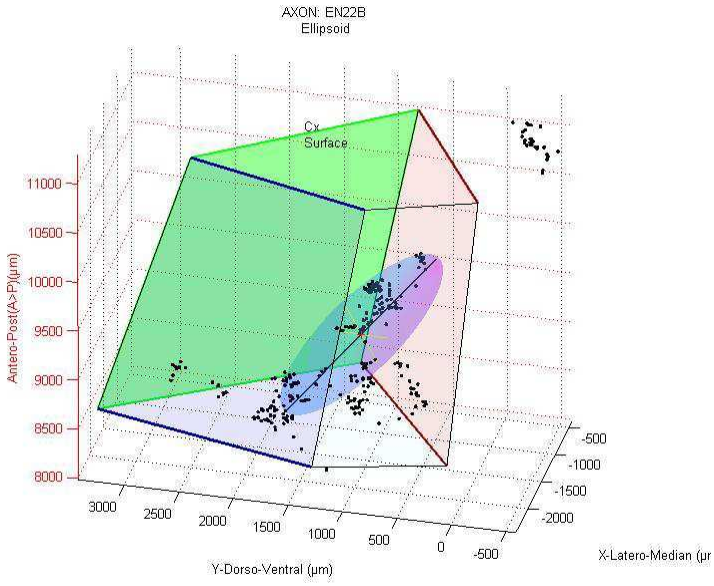

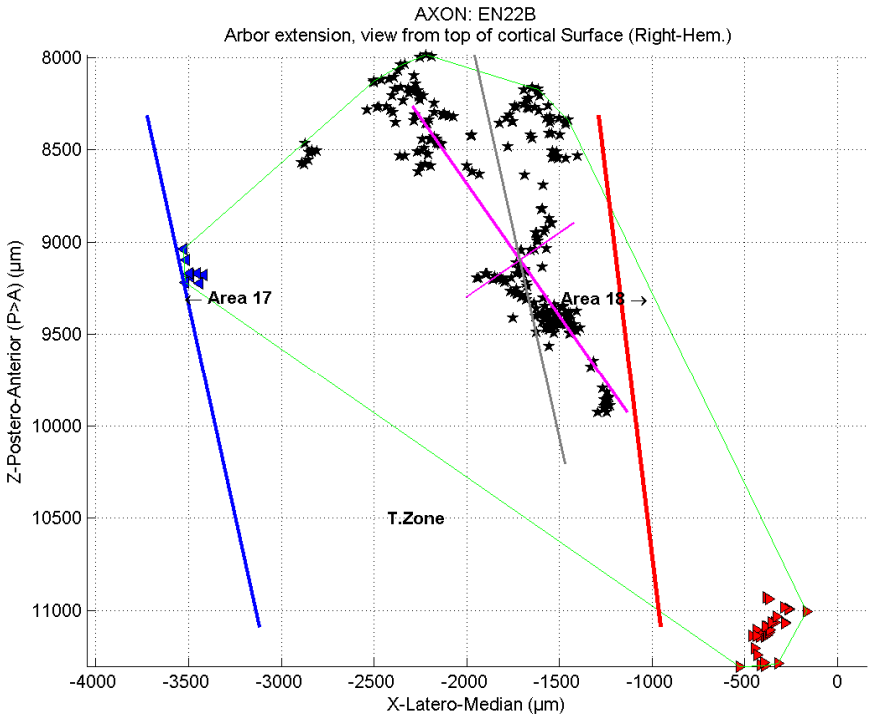

Fig. 88/ 2D & 3D ellipsoid analysis results for axon EN22B.

AXON EN22D

Ellipsoid analysis

	ORIGIN AREA	A17
counts	**Number of terminals**	**256**
	Number of terminals in A17	0
	Number of terminals in TZ	233
	Number of terminals in A18	23
	Terminals % in A17	0
	Terminals % in TZ	91,0
	Terminals % in A18	9,0
2D	**Surface on the Cortex (mm^2)**	**2,68**
	ellipse Axis 1 (mm)	**1 ,02**
	ellipse axis 2 (mm)	0,89
	Anisotropy 2D	**1,14**
	Angle axis 1 / TZ (deg)	176,9
	Angle axis 1 / Axe AP (deg)	159,7
	TZ/AP axis angle difference	-17,2
3D	**Ellipsoid Volume (mm^3)**	**0,69**
	Ellipsoid 3D Axis 1 (mm)	**1,10**
	Ellipsoid 3D axis 2 (mm)	0,97
	Ellipsoid 3D axis 3 (mm)	0,64
	Anisotropy 3D (1/2)	1,13
	Anisotropy 3D (2/3)	1,50
	Oblate-Prolate index	-3,66
	M.P. Sphericity index	0,73

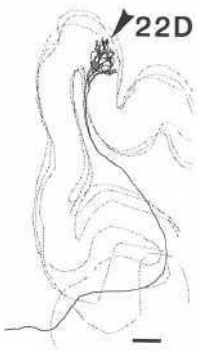

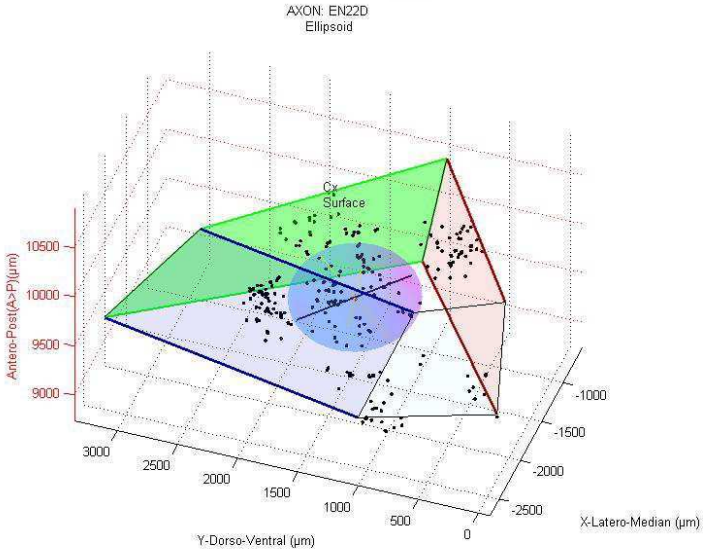

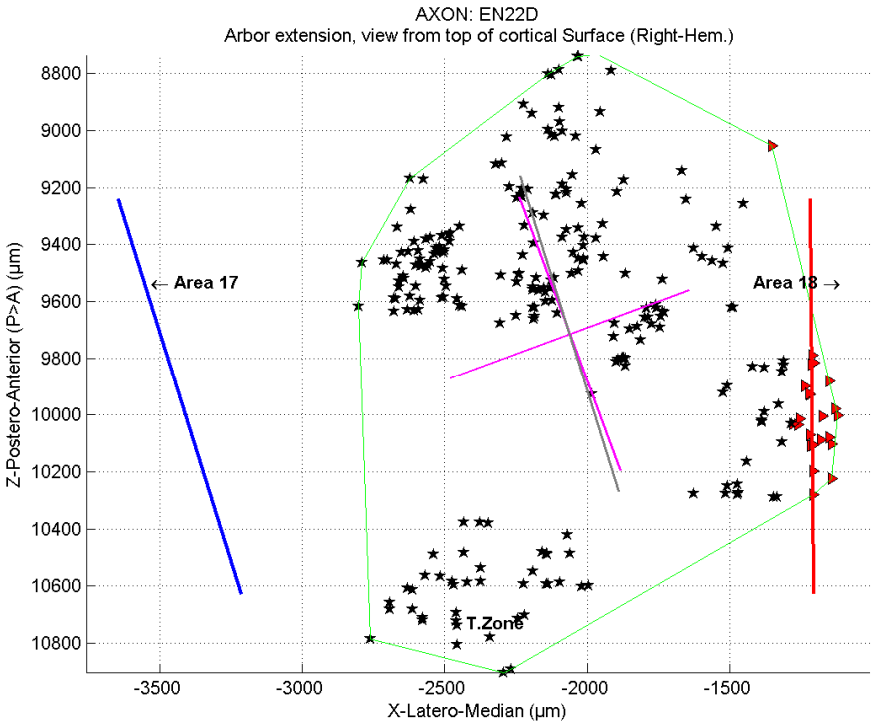

Fig. 89/ 2D & 3D ellipsoid analysis results for axon EN22D.

AXON EN22E

Ellipsoid analysis

	ORIGIN AREA	A17
Counts	**Number of terminals**	**19**
	Number of terminals in A17	0
	Number of terminals in TZ	16
	Number of terminals in A18	3
	Terminals % in A17	0
	Terminals % in TZ	84,2
	Terminals % in A18	15,8
2D	**Surface on the Cortex (mm^2)**	**0,185**
	ellipse Axis 1 (mm)	**0,37**
	ellipse axis 2 (mm)	0,28
	Anisotropy 2D	**1,36**
	Angle axis 1 / TZ (deg)	49,7
	Angle axis 1 / Axe AP (deg)	53,8
	TZ/AP axis angle difference	4,1
3D	**Ellipsoid Volume (mm^3)**	**0,05**
	Ellipsoid 3D Axis 1 (mm)	**0,50**
	Ellipsoid 3D axis 2 (mm)	0,37
	Ellipsoid 3D axis 3 (mm)	0,26
	Anisotropy 3D (1/2)	1,34
	Anisotropy 3D (2/3)	1,42
	Oblate-Prolate index	0,73
	M.P. Sphericity index	0,71

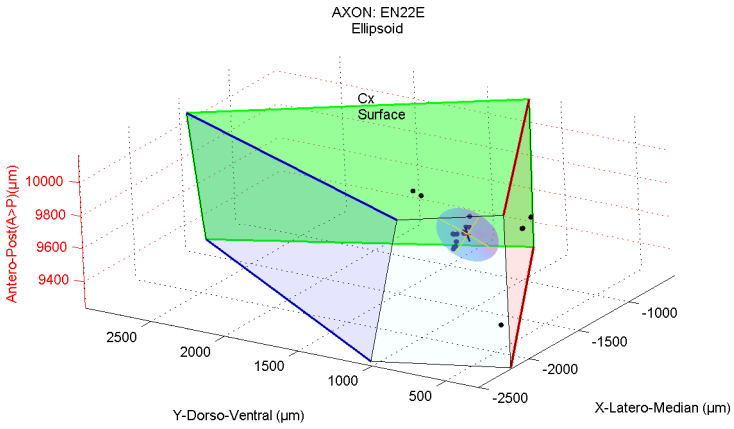

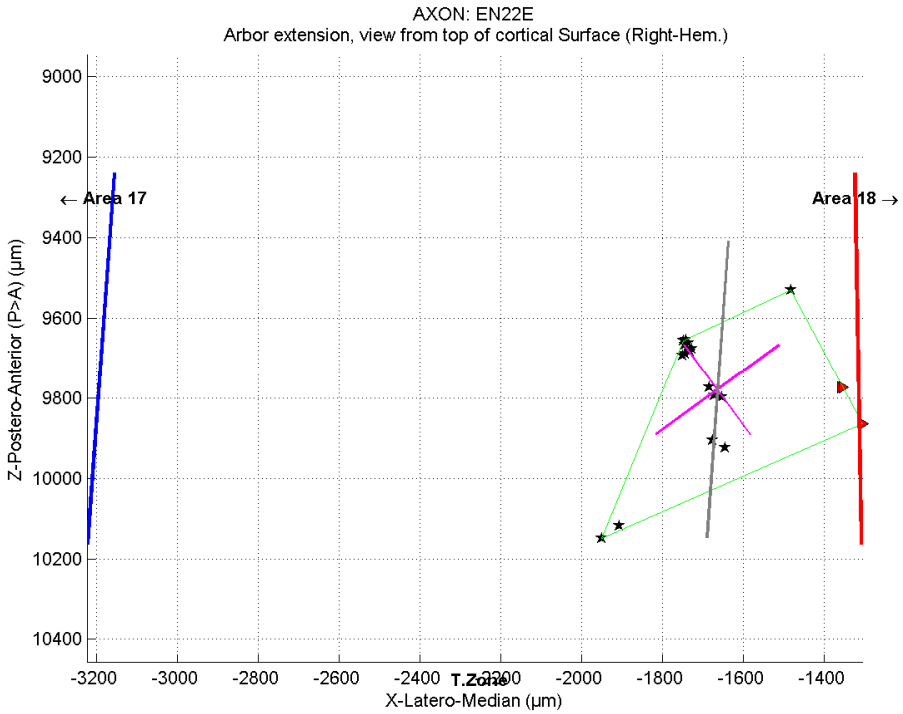

Fig. 90/ 2D & 3D ellipsoid analysis results for axon EN22E.

B.

Characterization of the callosal terminal arbors in the MD group

AXON BMOW12

Ellipsoid analysis

	ORIGIN AREA	TZ
counts	**Number of terminals**	**241**
	Number of terminals in A17	3
	Number of terminals in TZ	24
	Number of terminals in A18	214
	Terminals % in A17	1,2
	Terminals % in TZ	10,0
	Terminals % in A18	88,8
2D	**Surface on the Cortex (mm^2)**	**11,9**
	Ellipse Axis 1 (mm)	**3,31**
	Ellipse axis 2 (mm)	0,89
	anisotropy 2D	**3,72**
	Angle axis 1 / TZ (deg)	43,7
	Angle axis 1 / Axe AP (deg)	50,1
	TZ/AP axis angle difference	6,4
3D	**Ellipsoid Volume (mm^3)**	**4,15**
	Ellipsoid 3D Axis 1 (mm)	**4,51**
	Ellipsoid 3D axis 2 (mm)	1,06
	Ellipsoid 3D axis 3 (mm)	0,86
	anisotropy 3D (1/2)	4,23
	anisotropy 3D (2/3)	1,23
	Oblate-Prolate index	23,21
	M.P. Sphericity index	0,54

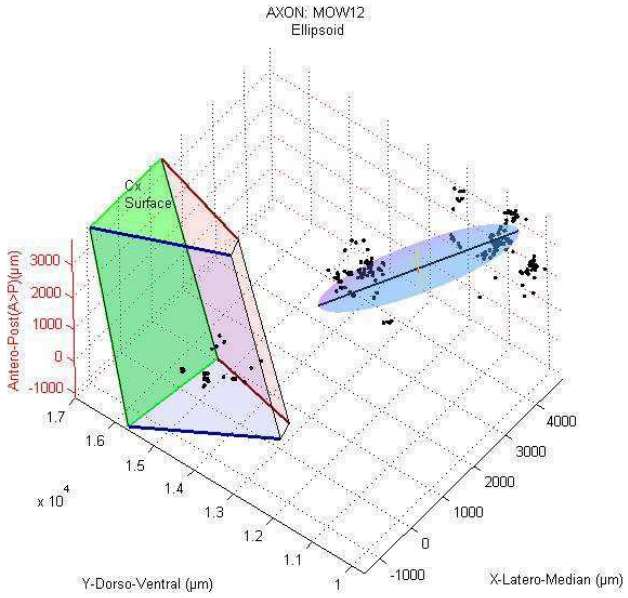

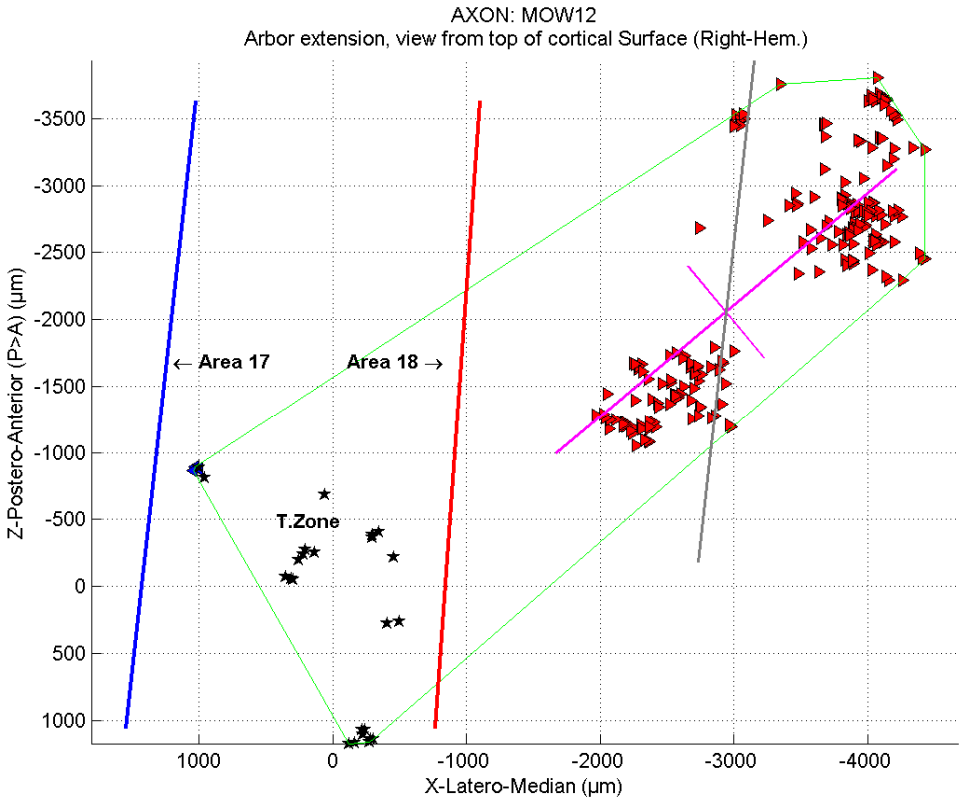

Fig. 91/ 2D & 3D ellipsoid analysis results for axon BMOW12.

AXON BMOW21

Ellipsoid analysis

	ORIGIN AREA	A17
counts	**Number of terminals**	**87**
	Number of terminals in A17	87
	Number of terminals in TZ	0
	Number of terminals in A18	0
	Terminals % in A17	100
	Terminals % in TZ	0
	Terminals % in A18	0
2D	**Surface on the Cortex (mm^2)**	**2,10**
	ellipse Axis 1 (mm)	**1,13**
	ellipse axis 2 (mm)	0,71
	anisotropy 2D	**1,58**
	Angle axis 1 / TZ (deg)	2,9
	Angle axis 1 / Axe AP (deg)	5,3
	TZ/AP axis angle difference	2,3
3D	**Ellipsoid Volume (mm^3)**	**1,31**
	Ellipsoid 3D Axis 1 (mm)	**1,95**
	Ellipsoid 3D axis 2 (mm)	1,02
	Ellipsoid 3D axis 3 (mm)	0,66
	anisotropy 3D (1/2)	1,9
	anisotropy 3D (2/3)	1,5
	Oblate-Prolate index	6,56
	M.P. Sphericity index	0,60

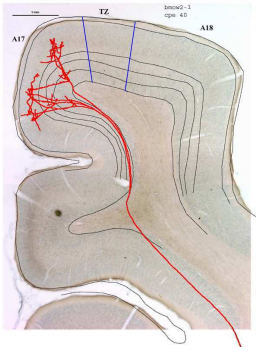

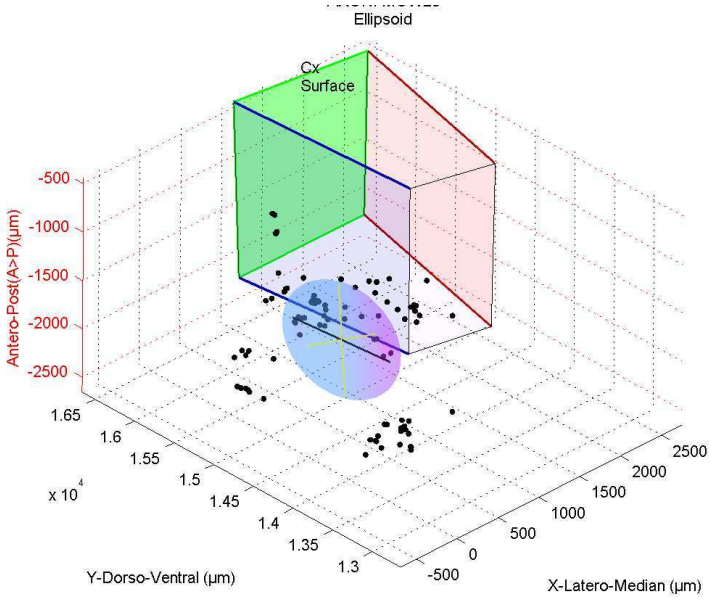

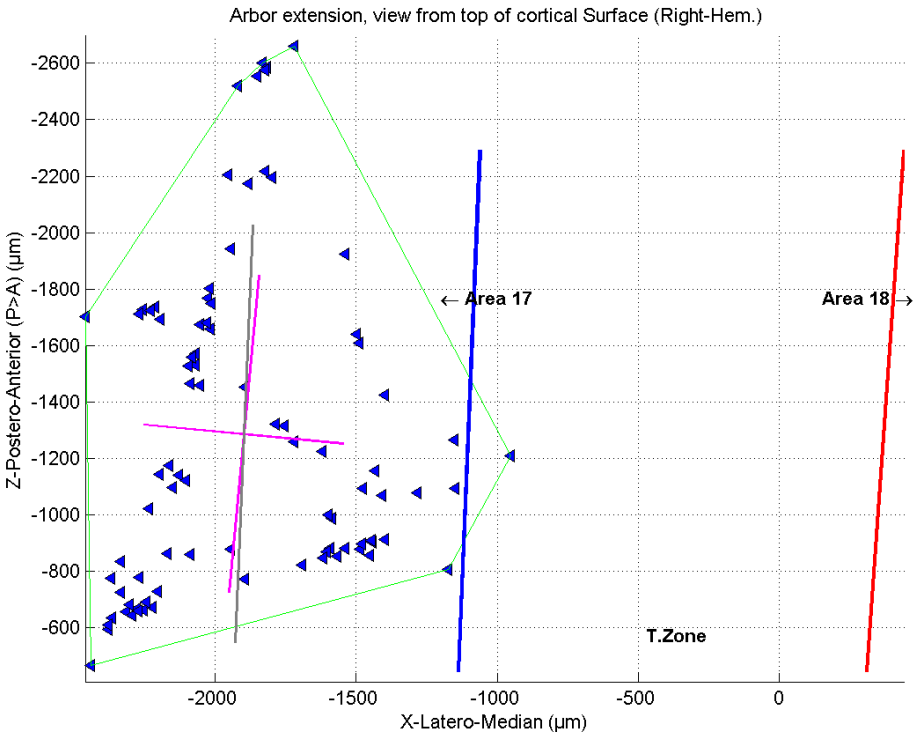

Fig. 92/ 2D & 3D ellipsoid analysis results for axon BMOW21.

AXON BMOW23

Ellipsoid analysis

	ORIGIN AREA	A17
counts	**Number of terminals**	**81**
	Number of terminals in A17	46
	Number of terminals in TZ	31
	Number of terminals in A18	4
	Terminals % in A17	56,8
	Terminals % in TZ	38,3
	Terminals % in A18	4,9
2D	**Surface on the Cortex (mm^2)**	**5,08**
	ellipse Axis 1 (mm)	**3,50**
	ellipse axis 2 (mm)	0,78
	anisotropy 2D	**4,51**
	Angle axis 1 / TZ (deg)	19,6
	Angle axis 1 / Axe AP (deg)	18,4
	TZ/AP axis angle difference	-1,2
3D	**Ellipsoid Volume (mm^3)**	**1,58**
	Ellipsoid 3D Axis 1 (mm)	**3,54**
	Ellipsoid 3D axis 2 (mm)	0,78
	Ellipsoid 3D axis 3 (mm)	0,57
	anisotropy 3D (1/2)	4,53
	anisotropy 3D (2/3)	1,37
	Oblate-Prolate index	26,68
	M.P. Sphericity index	0,49

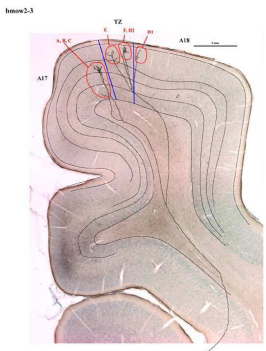

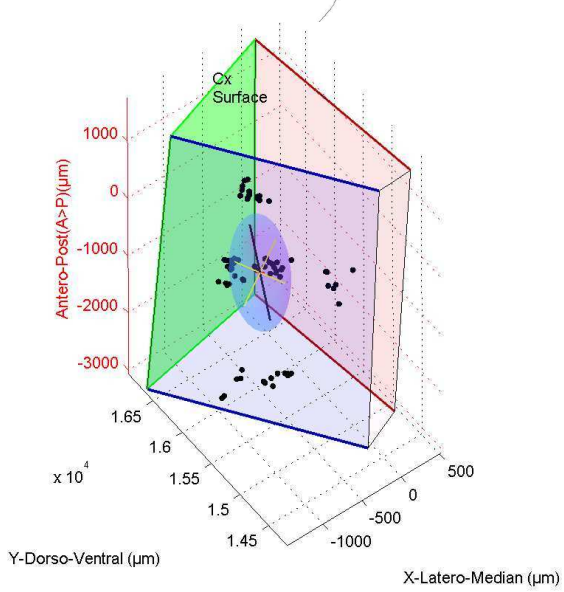

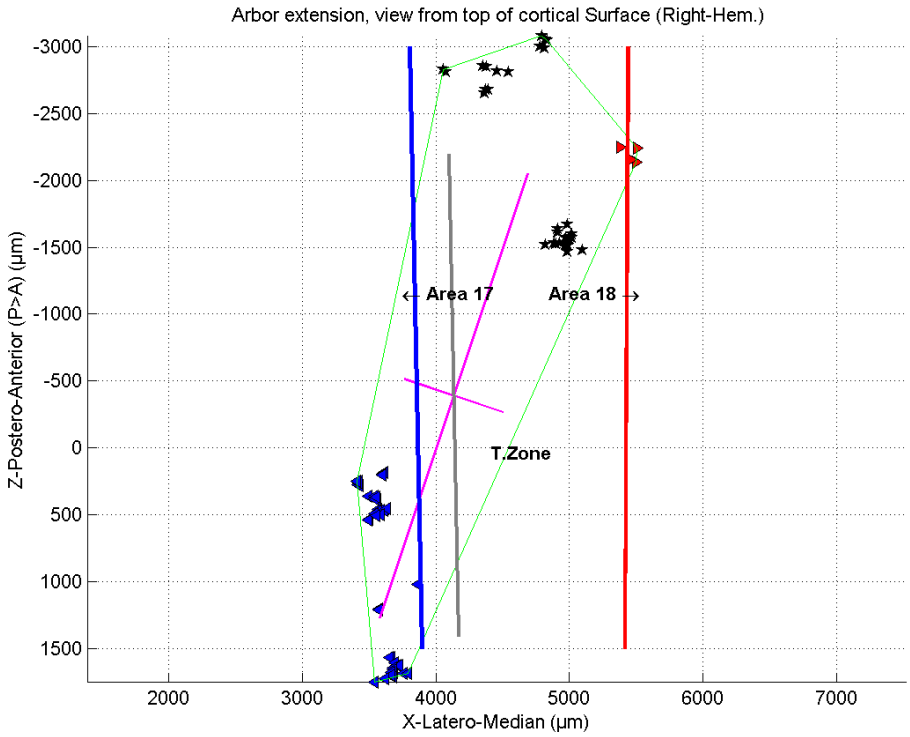

Fig. 93/ 2D & 3D ellipsoid analysis results for axon BMOW23.

AXON BMO17A1

Ellipsoid analysis

	ORIGIN AREA	A17
counts	**Number of terminals**	**49**
	Number of terminals in A17	49
	Number of terminals in TZ	0
	Number of terminals in A18	0
	Terminals % in A17	100
	Terminals % in TZ	0
	Terminals % in A18	0
2D	**Surface on the Cortex (mm^2)**	**0,89**
	ellipse Axis 1 (mm)	**1,00**
	ellipse axis 2 (mm)	0,39
	anisotropy 2D	**2,56**
	Angle axis 1 / TZ (deg)	12,5
	Angle axis 1 / Axe AP (deg)	15,3
	TZ/AP axis angle difference	2,8
3D	**Ellipsoid Volume (mm^3)**	**0,41**
	Ellipsoid 3D Axis 1 (mm)	**1,72**
	Ellipsoid 3D axis 2 (mm)	0,66
	Ellipsoid 3D axis 3 (mm)	0,36
	anisotropy 3D (1/2)	2,62
	anisotropy 3D (2/3)	1,81
	Oblate-Prolate index	13,47
	M.P. Sphericity index	0,48

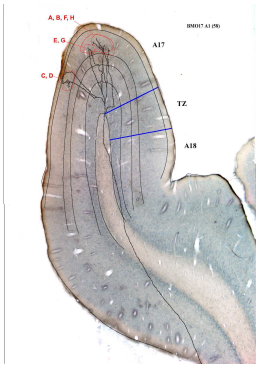

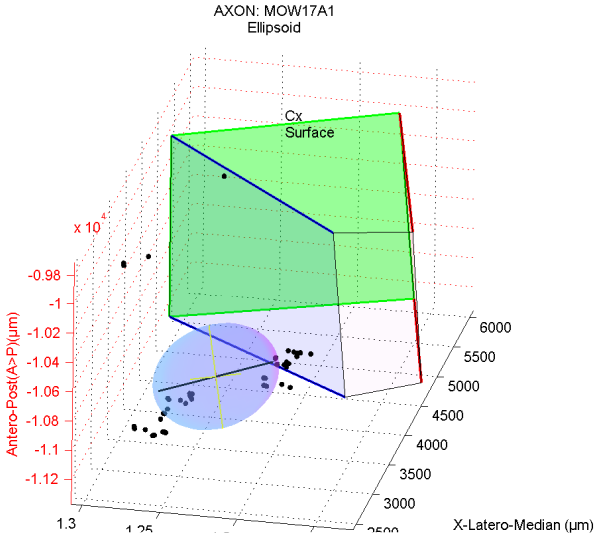

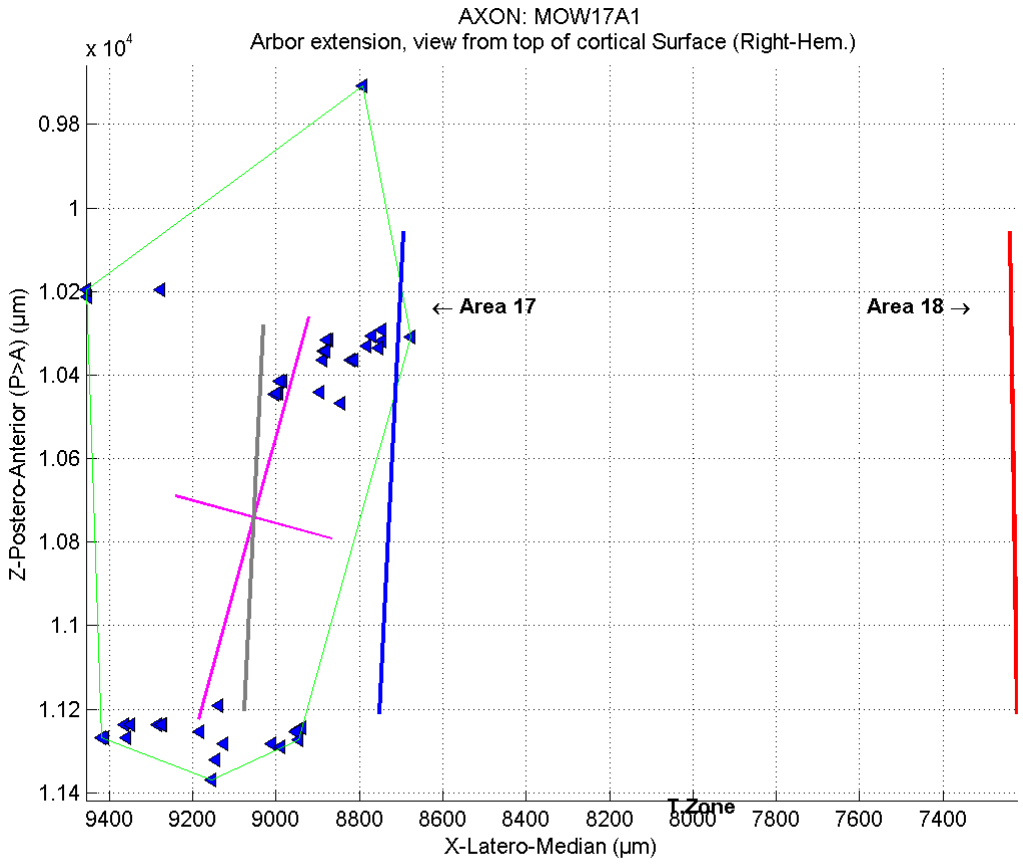

Fig. 94/ 2D & 3D ellipsoid analysis results for axon BMO17A1.

AXON BMO17A2

Ellipsoid analysis

	ORINGIN AREA	A17
counts	**Number of terminals**	**261**
	Number of terminals in A17	63
	Number of terminals in TZ	172
	Number of terminals in A18	26
	Terminals % in A17	24,1
	Terminals % in TZ	65,9
	Terminals % in A18	10,0
2D	**Surface on the Cortex (mm^2)**	**7,28**
	ellipse Axis 1 (mm)	**2,07**
	ellipse axis 2 (mm)	1,09
	anisotropy 2D	**1,89**
	Angle axis 1 / TZ (deg)	80,0
	Angle axis 1 / Axe AP (deg)	66,6
	TZ/AP axis angle difference	-33,4
3D	**Ellipsoid Volume (mm^3)**	**2,48**
	Ellipsoid 3D Axis 1 (mm)	**2,31**
	Ellipsoid 3D axis 2 (mm)	1,33
	Ellipsoid 3D axis 3 (mm)	0,81
	anisotropy 3D (1/2)	1,75
	anisotropy 3D (2/3)	1,64
	Oblate-Prolate index	4,48
	M.P. Sphericity index	0,59

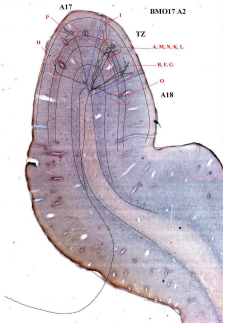

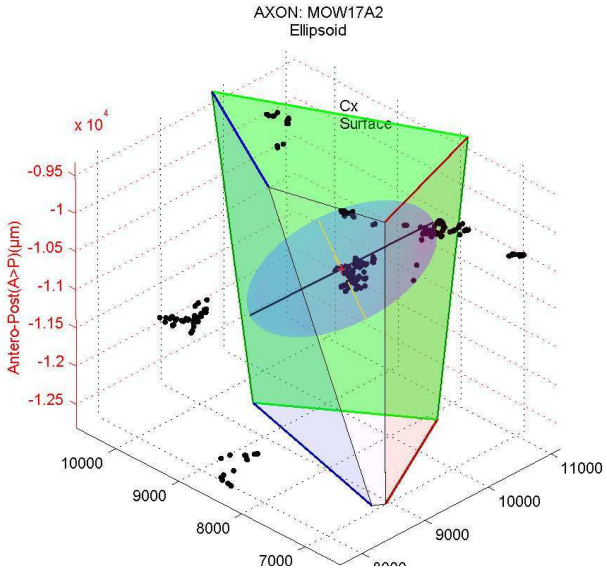

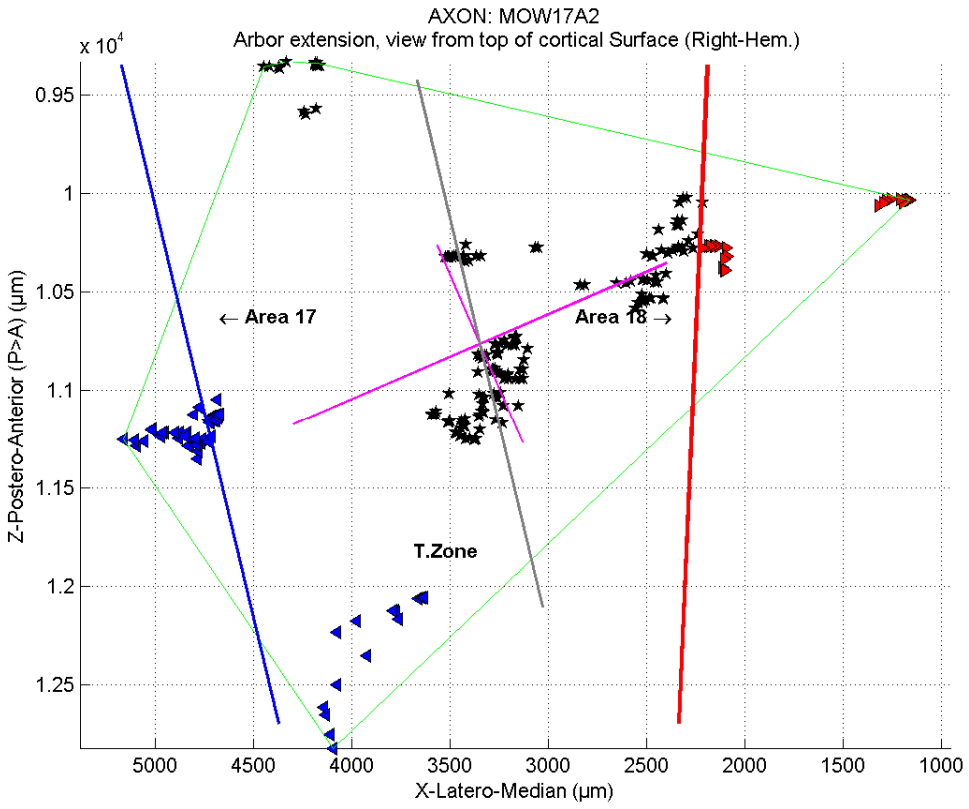

Fig. 95/ 2D & 3D ellipsoid analysis results for axon BMO17A2.

AXON BMO17A3

Ellipsoid analysis

ORIGIN AREA

counts	**Number of terminals**	**106**
	Number of terminals in A17	18
	Number of terminals in TZ	58
	Number of terminals in A18	30
	Terminals % in A17	17,0
	Terminals % in TZ	54,7
	Terminals % in A18	28,3
2D	**Surface on the Cortex (mm^2)**	**4,69**
	ellipse Axis 1 (mm)	**1,94**
	ellipse axis 2 (mm)	0,86
	anisotropy 2D	**2,25**
	Angle axis 1 / TZ (deg)	118,8
	Angle axis 1 / Axe AP (deg)	119,9
	TZ/AP axis angle difference	1,1
3D	**Ellipsoid Volume (mm^3)**	**1,09**
	Ellipsoid 3D Axis 1 (mm)	**1,98**
	Ellipsoid 3D axis 2 (mm)	1,11
	Ellipsoid 3D axis 3 (mm)	0,49
	anisotropy 3D (1/2)	1,77
	anisotropy 3D (2/3)	2,26
	Oblate-Prolate index	3,18
	M.P. Sphericity index	0,48

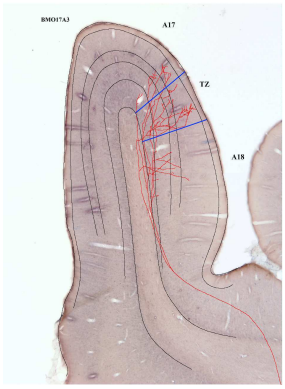

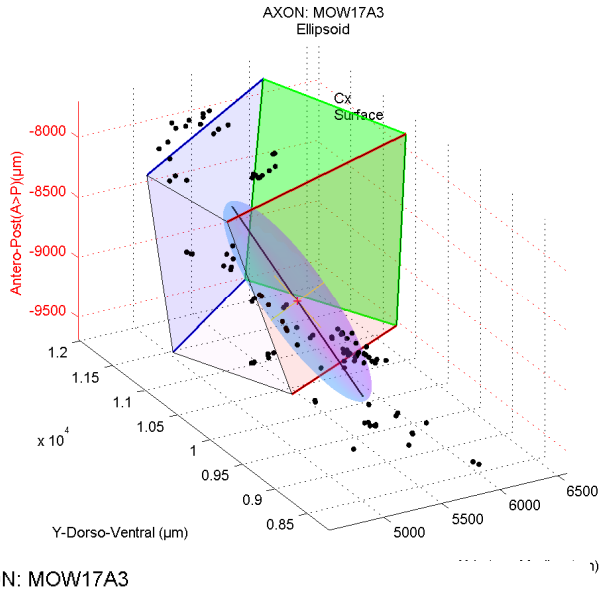

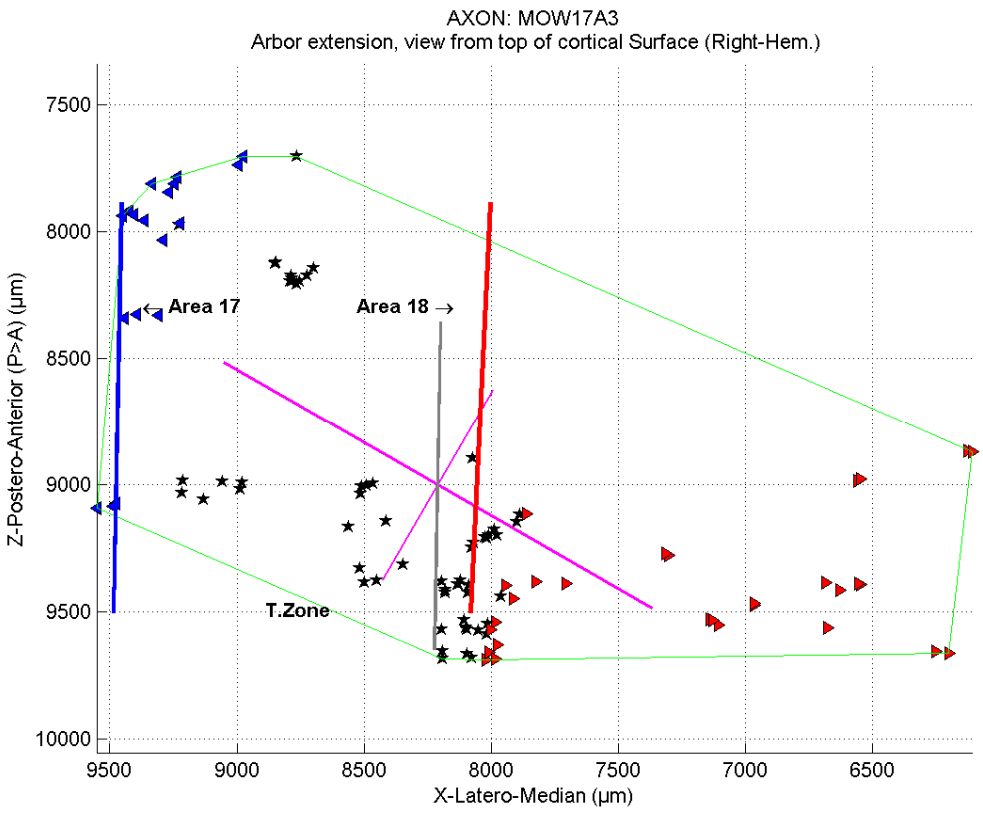

Fig. 96/ 2D & 3D ellipsoid analysis results for axon BMO17A3.

C.

Characterization of the callosal terminal arbors

Comparison of both NR and MD group

	Ellipsoid analysis	NR group		MD group		means MD/NR		Modified Student T-test H0: equal means + unequal variance + left tailed : (mean MD > mean NR)	
Idx		MEANs	Std	MEANs	Std		≠ ?	Test	Significance
1	**Number of terminals**	**131,27**	87,0	**137,50**	90,0	1,05			
2	Number of terminals in A17	2,20	3,3	44,33	30,3	20,15			
3	Number of terminals in TZ	106,93	73,5	47,50	64,7	0,44			
4	Number of terminals in A18	22,13	43,6	45,67	83,5	2,06			
5	**Terminals % in A17**	**3,05**	6,5	**49,86**	42,8	16,37	**Y**	**1**	**2,19E-02**
6	**Terminals % in TZ**	**84,52**	20,9	**28,14**	28,8	**0,33**	**Y**	**1**	**(right tailed) 1,55E-03**
7	Terminals % in A18	12,43	21,4	22,00	34,3	1,77	n	0	2,74E-01
8	**Surface on the Cortex (mm^2)**	**2,73**	2,6	**5,82**	3,5	**2,13**	**Y**	**1**	**4,53E-02**
9	**ellipse Axis 1 (mm)**	**1,46**	0,9	**2,39**	0,8	**1,64**	**Y**	**1**	**2,20E-02**
10	**ellipse axis 2 (mm)**	**0,55**	0,3	**0,88**	0,2	**1,61**	**Y**	**1**	**2,54E-02**
11	**Anisotropy 2D**	**3,06**	2,1	**2,79**	1,1	**0,91**	**N**	**0**	**6,48E-01**
12	Angle axis 1 / TZ (deg)	76,5	56	46,3	45	0,60	**n**	0	8,89E-01
13	Angle axis 1 / Axe AP (deg)	70,6	53	45,9	43	0,65	**n**	**0**	**8,54E-01**
14	TZ/AP axis angle difference	-5,9	8	-0,3	15	0,62			
15	**Ellipsoid Volume (mm^3)**	**0,83**	0,9	**1,84**	1,3	**2,20**	**X**	0	**6,71E-02**
16	**Ellipsoid 3D Axis 1 (mm)**	**1,63**	0,8	**2,67**	1,1	**1,64**	**Y**	**1**	**3,83E-02**
17	Ellipsoid 3D axis 2 (mm)	0,82	0,3	0,99	0,2	1,21			
18	Ellipsoid 3D axis 3 (mm)	0,45	0,2	0,63	0,2	1,38			
19	anisotropy 3D (1/2)	2,07	0,8	2,80	1,3	1,36			
20	anisotropy 3D (2/3)	2,03	0,7	1,64	0,3	0,81			
21	Oblate-Prolate index	**7,48**	11	**12,9**	10,0	1,73	**n**	0	1,53E-01
22	M.P. Sphericity index	**0,55**	0,15	**0,53**	0,06	0,97	**n**	0	6,31E-01

Table 5/ Means of the spatial parameters obtained with the ellipsoid approximation methods for 2 different callosal populations and result of statistic test aiming to show population separability (see text for details).

Results

The Table 5 reports the mean values of the different parameters that have been obtained from the ellipsoid analysis when applied to the callosal terminal arbours of both the MD and the NR groups. It also reports comparison between groups. The ratios of the mean values (MD/NR) have been first calculated (represented in coloured when particularly relevant). Data were also compared statistically, with the data being reported in the last three columns of the Table. The chosen test is a derivative of the Student's T-test, known as the Welch's test. It is recommended to compare two samples having unknown and unequal variances. As for the original T-test, both populations are assumed to display a normal distribution and it aims at rejecting the null hypothesis of equal means. Moreover, the test was tailed toward one direction in order to favour the hypothesis of a chosen mean greater than the other. Especially, with the aim to demonstrate the wider extensions of the MD group, the test was left tailed favouring the hypothesis $\mu_{MD} > \mu_{NR}$. These adaptations give results equivalent to the original T-test but provide better significances. In one case, the tail was reverse for the terminal percentage falling into TZ where the trend is opposite (index 6 in 1st column of table 5). In all other cases of trend inversion, such as for the angle distribution, the inversion of tail direction does not change the results of the test for which the null hypothesis could no be rejected (results of tail inversion not shown). In the 4 Last columns of the Table, values are coloured in red when the statistical test could reject the null hypothesis (i.e. equal means), with a significance better than 0.05; in contrast, values are coloured with blue when the parameter could not be taken as a discriminating criteria for the two population on the basis of our samples set.

The figures then show dual histograms for both NR and MD populations for each relevant parameter of the spatial extension analysis in order to provide a better estimation of the variability of the populations and their differences.

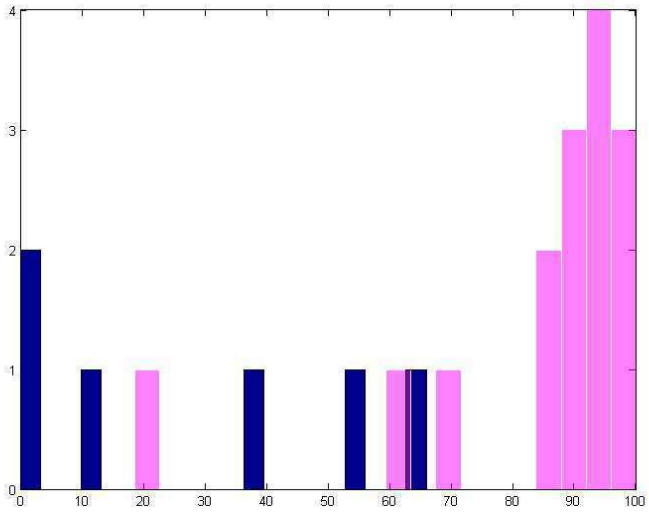

Fig. 97/ Histograms showing the number of callosal axons as a function of the percentage of their terminals falling within the TZ-volume; (purple: EN group, blue: MD group).

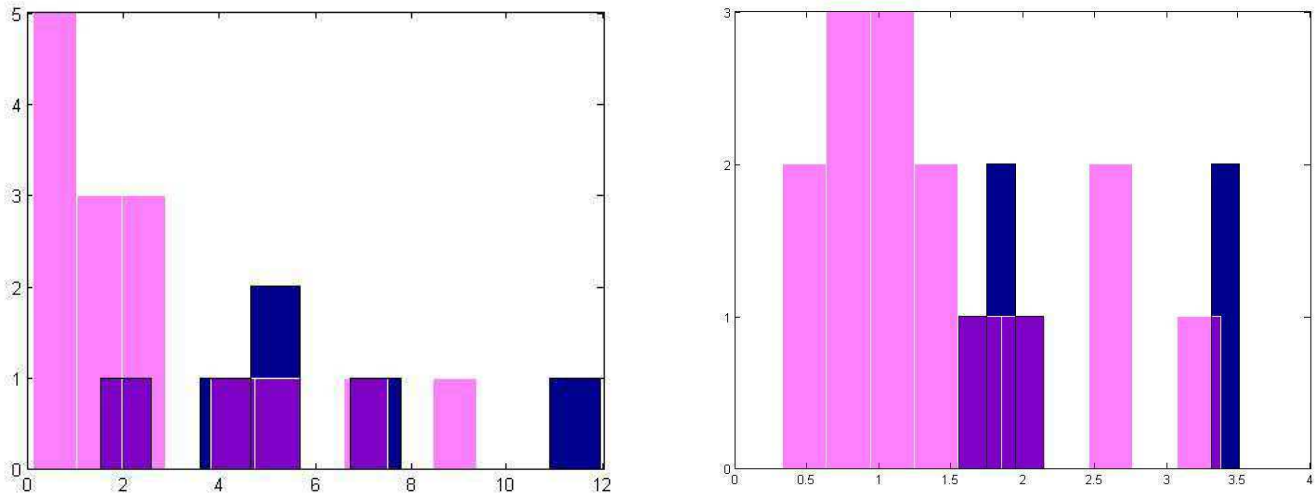

(a) (b)

Fig. 98/ (a) Distribution of the surfaces on the cortex covered by projection for each axon (mm^2); (b) Lengths of 2D greatest elongation axis (mm); (purple: EN group, blue: MD group).

Characterization of the 2D dispersion of the callosal terminal arbours in the MD group

Dispersion of the terminal arbours onto the cortical surface (= areal distribution)

As shown on Fig. 97, the first characteristic of the 2D spatial distribution of the callosal terminal arbours in the MD group is the *dispersion* of the terminal branches and of the synaptic boutons around the TZ-volume. Whereas most of axons from NR group target more than 80% of their branches into the TZ volume, branches of MD axons only focus less than 70% of their terminals in the best case, leaving the counterpart in the flanking cortical areas.

Global cortical area being concerned per axon

The most important specificity of the MD group is the *widespread projection of the callosal terminal branches* onto the cortical surface: their callosal axons occupied 1.5 mm^2 to 11.9 mm^2 (with a mean of 5.8 mm^2) whereas those from the NR group almost all focus onto cortical surfaces smaller than 2.5 mm^2 (Fig 98 (a)). Thus, they vary by a factor 2. As revealed by the ellipsoids, this wide extension onto the cortical surface is related to the elongation of the greatest axis of the ellipse ranging from 1.5 mm to 3.5 mm (mean: 2.4 mm) when the NG group ellipses great axis lie between 0.5mm and 2mm for most of the samples (Fig. 98(b)).

2D anisotropy of the callosal terminal arbours

While the NR and MD populations were found to be statistically different (with a good significance) as far as the areal dispersion of the callosal terminal arbours were concerned, in contrast the *2D anisotropy indexes* remained similar to those observed for the NR group with values confined between 1.9 and 4.5 (Fig. 99(a). Nevertheless, it is shown that a smaller dispersion range is present in the NR group, with half of the callosal terminal arbours showing an anisotropy smaller than 2. One axon in the NR group also showed an extreme value of 9.6, which may conduct the statistical test to give a negative result.

Orientation of the callosal terminal arbours

Associated with this anisotropy, the distributions of the orientations of the great axes of the ellipses with respect to the TZ or the AP direction (i.e. the midline) showed important heterogeneities, with a mean of 46° in both cases (Fig. 99(b)). As for the NR group, this mean direction was irrelevant regarding to the Rayleigh circular statistic test of uniformity when performed onto raw values. But it became highly significant when the angles were weighted with respective anisotropy values (p-value$< 2.3\ 10^{-5}$). The callosal terminal arbours thus

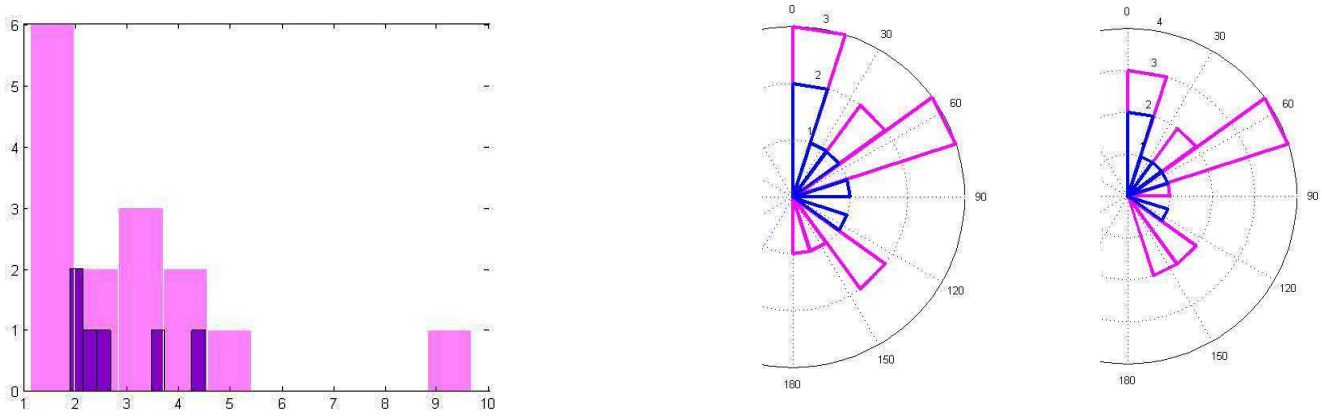

(a) (b)

Fig.99/ (a) 2D anisotropies (axis lengths ratios); (b) Distributions of 2D orientations of terminals distributions with TZ (left) and AP (right) directions; (purple: EN group, blue: MD group).

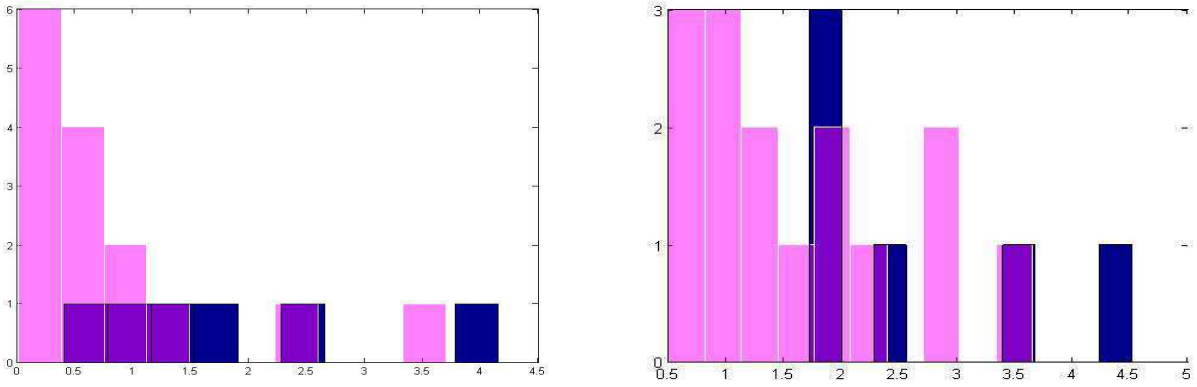

(a) (b)

Fig.100/ Distributions of ellipsoids volumes (mm^3) (a) and great axis lengths (mm) (b); (purple: EN group, blue: MD group)

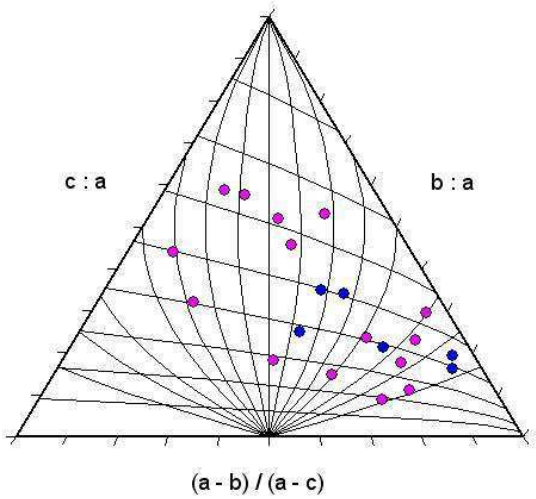

Fig. 101/ Anisotropies indexes reported in the Sneed & Folk diagram; (purple: EN group, blue: MD group).

appeared as being biased for one given oblique orientation. These anisotropies and angles distributions were not found to be statistically different between the NR and the MD groups.

3D extensions of the callosal axons terminals in the MD group.

Cortical volumes occupied by callosal terminal arbours

The MD group was also characterized by a wide extension of the terminals within the whole thickness of the cortex. This wide extension was revealed by the important volume of the ellipsoids embracing the distribution of the callosal terminal arbours and the important lengths of their great axis (cf. Fig 100). Ellipsoid volumes of the MD group varied from 0.4 to 4.1 mm^3 (with a mean of 1.8 mm^3), while most of the NR group ellipsoid volumes were smaller than 1.5 mm^3. In spite of these important differences, the T-test could not reject the null hypothesis (meaning equal means). But it reported a significant value for disparity being close to the threshold for significant difference (p=0.067 instead of 0.05; cf. index 15 in Table 5). On the other hand, regarding the great axis lengths, the two populations show a significant difference. The lengths of the great axes in the MD group ranged from 1.7 to 4.5 mm (mean 2.7mm), while 11/15 values of the NR group kept smaller than 2 mm (cf. fig 100(b)).

3D anisotropy of the callosal terminal arbours

At last, the 3D anisotropy indexes did not reflect significant differences between the two populations. However, when plotted into the Sneed & Folk diagram, the MD group showed a trend toward the prolate shapes (bottom-right of the diagram). This indicates that an elongation toward the great axis is much more important than for the two others (cf Fig. 101).

Discussion

The 2D and 3D ellipsoid approximation allows characterizing the spatial extensions of the callosal axons terminals in terms of volume, elongations and cortical projection surface. Most of these parameters allow not only the characterization of both the NR and MD groups, but also allows reporting significant difference between them. Especially, the cortical surfaces of the distributions from the MD group were found as a mean to be twice greater than those of the NR group. Moreover, means ratio between population for the great and small axis of the 2D ellipses showed equivalent values (1.6) whereas anisotropies remained similar (mean ratio: 0.9). These observations lead to the interpretation of a homothetic expansion of the spatial dispersion for the MD group. But this hypothesis should be confirmed with additional samples.

As a first order approximation, the ellipsoid model thus provides interesting results about the global organisation of the callosal terminals distributions. But finer morphological description could be achieved with higher order analysis such as clustering method in order to reveal intrinsic organization.

CHAPTER I.3.

Morphological characterization of the synaptic dispersion of the callosal terminal arbours by clustering analysis.

Article 4 :

L. FOUBERT, D. BENNEQUIN, C. MILLERET & J. DROULEZ. A quantitative analysis of 3D synaptic dispersion. Submitted to Journal of Neurophysiology (May 2007).

In the last chapter, the spatial extensions of axons terminals distribution have been characterized by 2D and 3D ellipsoid methods. It allowed characterizing and quantifying the wider extension of the callosal terminal arbours in the MD group with respect to the NR one.

In order to go further into the morphological characterization of these callosal axons and to reveal additional differences between the control and the impaired groups, a clustering analysis for 3D distributions has been developed in the present chapter and it has been applied it to the two groups:

- In its first part (Part 1.3.1.), the article that has been submitted to Journal of Neurophysiology is presented. It includes an extensive description of the method which allows identifying objectively (and thus counting) the clusters within a synaptic distribution in general. As a first application, it also includes a characterisation of the synaptic dispersion that is present at the level of callosal terminal arbours in NR adult cats;
- In its second part of this chapter (Part 1.3.2.) this method of clustering is also applied to callosal terminal arbours that have been found in MD animals. And a comparison with those of NR animals has been finally achieved.

By this way, a quantitative description of the 3D intrinsic organization was reached and a the scattered structure of the axons terminals resulting from development under unbalanced conditions of vision has been demonstrated as opposed to the more compact distributions of normal callosal projections.

Part 1.3.1

A quantitative analysis of 3D synaptic dispersion

Luc FOUBERT[1], Daniel BENNEQUIN[2], Chantal MILLERET[1], Jacques DROULEZ[1]

1 Laboratoire de Physiologie de la Perception et de l'Action, UMR CNRS 7152,

Collège de France, 11 place Marcelin Berthelot, 75005 Paris, France.

2 Institut de Mathématiques de Jussieu- UMR CNRS 7586

Université Paris 7 Denis Diderot, 2 Place Jussieu, 75005 Paris, France

Abbreviated title: Identification of clusters from a 3D synaptic dispersion

Corresponding author:

Luc Foubert

luc.foubert@college-de-france.fr

Laboratoire de Physiologie de la Perception et de l'Action, UMR CNRS 7152, Collège de France, 11 place Marcelin Berthelot, 75005 Paris, France.

ABSTRACT

We propose here a new statistical method to characterize the clustered organisation of cortical connectivity. This is to compare later on different neuronal populations on the basis of the spatial organization of their respective connectivity or to relate the spatial dispersion of synaptic boutons to functional cortical maps. To test this method, terminal arbours from single neurones whose axon interconnect both hemispheres through the corpus callosum were used. They were anterogradely labelled with biocytin and 3D reconstructed from serial sections within areas 17 and 18 of cat visual cortex. Most of them (n=13) were normal ones and their terminal arborisation has been described qualitatively already (cf. Houzel et al., 1994). One abnormal callosal terminal that has been identified in an early monocular deprived adult cat, within the hemisphere ipsilateral to the occluded eye, has been also presented to test our method on complex or extended terminal arbour (Milleret et al., in preparation). Here, these different callosal neurones have been described by the 3D coordinates of their respective terminal branches. Gaussian mixture models were used to provide a quantitative description of the dispersion of the terminal arbours for each single axon. With priors evaluated from simulation, a maximum *a posteriori* method was used to estimate the number and the weight of each cluster of branches, as well as their centres and covariance matrices. The method has been first validated on synthetic data set. It then allowed a fine description of clusters of terminal neural branches. As expected, this provides a simple but efficient technique for comparing neurons connectivity in different experimental conditions and correlating anatomy and function in the brain.

KEYWORDS

Cat visual cortex - Callosal connections - 3D distribution of terminal arbours - Clusters analysis - Gaussian mixture models –

INTRODUCTION

The spatial distribution of the terminal arbours in the central nervous system of mammals is usually described qualitatively. This is achieved at the level of the dendritic or the axonal arborisation of one single neuron or from a larger population of neurones. According to the structure under study, this analysis can be detailed specifically. For example, in the cortex, these distributions might be additionally described according to the different cortical layers (namely I to VI). To characterise such distributions, a retrograde or an anterograde tracer (for example HRP or biocytin) is usually injected in the brain. Then, the distribution of the terminal branches and/or the synaptic boutons around labelled cell body(ies) or at their terminal arbour(s) are 2D or 3D reconstructed; their number might be additionally evaluated. Although providing interesting informations, these data remain however rather imprecise. For example, if terminal branches or synaptic boutons form *"clusters"*, these clusters are most often rather difficult to identify with accuracy either because terminal branches or synaptic boutons are too sparse or because the variations in their density are difficult to evaluate. Instead, this is fundamental to compare different populations of neurons. This is also important to understand the functioning brain since anatomy and function are closely related. Precisely, this study aimed at describing into details the geometry of this particular axonal dispersion by using a new statistical (thus quantitative) method.

Focusing onto visual cortical areas in the adult mammal, studies have often described or suggested non-random and discontinuous distributions of neuronal terminals already. This has been reported both at the level of connections between distant structures and at the level of single cortical neurones. This has also been described in and across different cortical layers. For example, it has been found that the thalamic afferents and their synaptic boutons in the cat primary visual cortex are clustered, in particular in layer IV (Ferster & LeVay, 1978; Gilbert & Wiesel, 1979). The same has been observed at the level of intracortical connections, in particular in the supragranular layers (see for example Gilbert & Wiesel, 1983; Somogyi et al., 1983; Ferrer et al., 1988). The clustering of terminal arbours and of synaptic boutons is thus a main feature in the organisation of the visual cortex in the normal adult mammal.

Previous data have also reported that the expression of such periodic "clusters" of axonal branches and synaptic boutons is age and experience-dependent. Typically, it emerges by implicating the "elimination" of some early supernumerary projections (including synaptic boutons) and the selective "stabilization" of some others. Thus, for example, in normally-reared kittens,

horizontal intrinsic connections in cat striate cortex (A17) are first unclustered: terminal arbours and boutons display a diffusely organized pattern. Second, “clusters” of both terminal branches and synaptic boutons form but they are difficult to distinguish. In other words, during these two first steps, they display an “exuberant” form. Finally, from 4-6 weeks of age, isolated “clusters” form through classical developmental processes recalled above (Luhmann et al., 1986; Callaway and Katz, 1990; Galuske and Singer, 1996). The formation of distinct clusters formed by the cortico-cortical projections from A17 to A18 in cat visual cortex also occurs postnatally (Price, 1986). After an abnormal postnatal visual experience, the development of clusters of terminal branches and of synaptic boutons is most often altered in both cases. Thus, in the former case described above, the “clustering” process has been demonstrated to be modified after a long-term binocular deprivation (Callaway and Katz, 1991). In the latter one, it has been shown to be altered after monocular deprivation because the terminal arbours innervated by the deprived eye have become much smaller than normal (Price, 1986). Altogether, this indicates that the clustering organisation in the cortex is a very good index to follow what happens in the brain during normal development, and what happens in case of abnormalities.

Of interest, it has also been established that this specific “clustered” organisation is closely related to the functional organisation of the cortex. Thus, for example, it has been known from a long time that the clustering of the thalamic afferents (and their synaptic boutons) in cat visual cortex is responsible for ocular dominance columns (Ferster and LeVay, 1978). More recently, from optical imaging experiments, it also appeared that the “clustered” organisation of the synaptic boutons in visual cortex, and thus of the terminal arbours, may be spatially organized in relation to retinotopic map (see for example Shmuel et al., 2005) and is closely related to the various functional domains implicated in visual perception (see for example Malach et al., 1993; Kisvárday et al., 1994; 1996; Bosking et al., 1997; Buzás et al., 2001).

Although interesting, these data on intracortical neuronal clusters remain rather imprecise. As indicated above already, this is because most of them are qualitative ones. Thus, important questions can not be solved properly. For example, any abnormalities in the spatial distribution of synaptic boutons remain difficult to identify and to characterize. The exact relation between the axonal clusters and the functionality of the brain is also not totally resolved. This may be solved however by using an objective and reliable method. To date, at least from our knowledge, only a few recent studies have addressed this question, measuring some quantitative morphometric features such as the distribution of synaptic boutons (Buzás et al., 2006) or the densities of

branching points and boutons, segments length, branching angles and terminal field areas (Rocha et al., 2007). But they do not solve totally the problem (cf. Discussion for further details).

The present study aimed precisely at solving such problem of identification of clusters of terminal branches (and thus of synaptic boutons) through a new statistical method using the 3D coordinates of each termination from single arborisations. This has been achieved on the basis of interhemispheric connections through the corpus callosum in cat visual cortex (A17 and A18). First, this is because, similar to other intracortical connections, they are clustered (Voigt et al., 1988; Boyd and Matsubara, 1994; Houzel et al., 1994; Boyd and Matsubara, 1996; Rocherfort et al., 2005). This clustered organisation emerges progressively with age in normal conditions (Aggoun-Zouaoui and Innocenti, 1994; Aggoun-Zouaoui et al., 1996), and it might be altered by an abnormal postnatal visual experience (Innocenti and Frost, 1979; Milleret et al., in preparation). Their distribution is also closely related to the functional organisation of the visual cortical maps, in particular the distribution of the ocular dominance and the orientation domains (Olavarria, 2001; Rochefort et al., 2005). Second, our group is quite familiar with such connections, as far as both their anatomical and functional properties are concerned. Among other studies, of interest in the context of the present study, we have already described qualitatively the fine terminal architecture of single callosal neurones originating near the TZ in cat visual cortex, after their anterograde labelling with biocytin and reconstruction in 3D from serial sections of the brain (Houzel et al., 1994). We also showed that most of the axons terminated in multiple terminal clusters (or columns) scattered over several square millimetres of cortex. In agreement with G.M. Innocenti (with whom C. Milleret coordinated such study), we re-investigated here some of these callosal terminals from normal adult cats. A direct comparison has thus been possible between the data that have been obtained previously after a pure qualitative analysis and those that may be obtained after application of the new statistical method we propose here. In addition, a callosal terminal that has been identified (in similar experimental conditions than before) in an early monocular deprived adult cat has been also presented here (from Milleret et al., in preparation) to test our method in case of great complexity and abnormalities of the terminal arbour.

We demonstrate here that the statistical method we propose is simple but is quite efficient for identifying clusters from a tri-dimensional distribution of terminal branches. It allows characterizing and comparing neuronal connectivity with precision in different experimental conditions. In the future, it will also allow a pretty good correlation between the anatomy and the functional organisation in the brain, whether it is functioning normally or not.

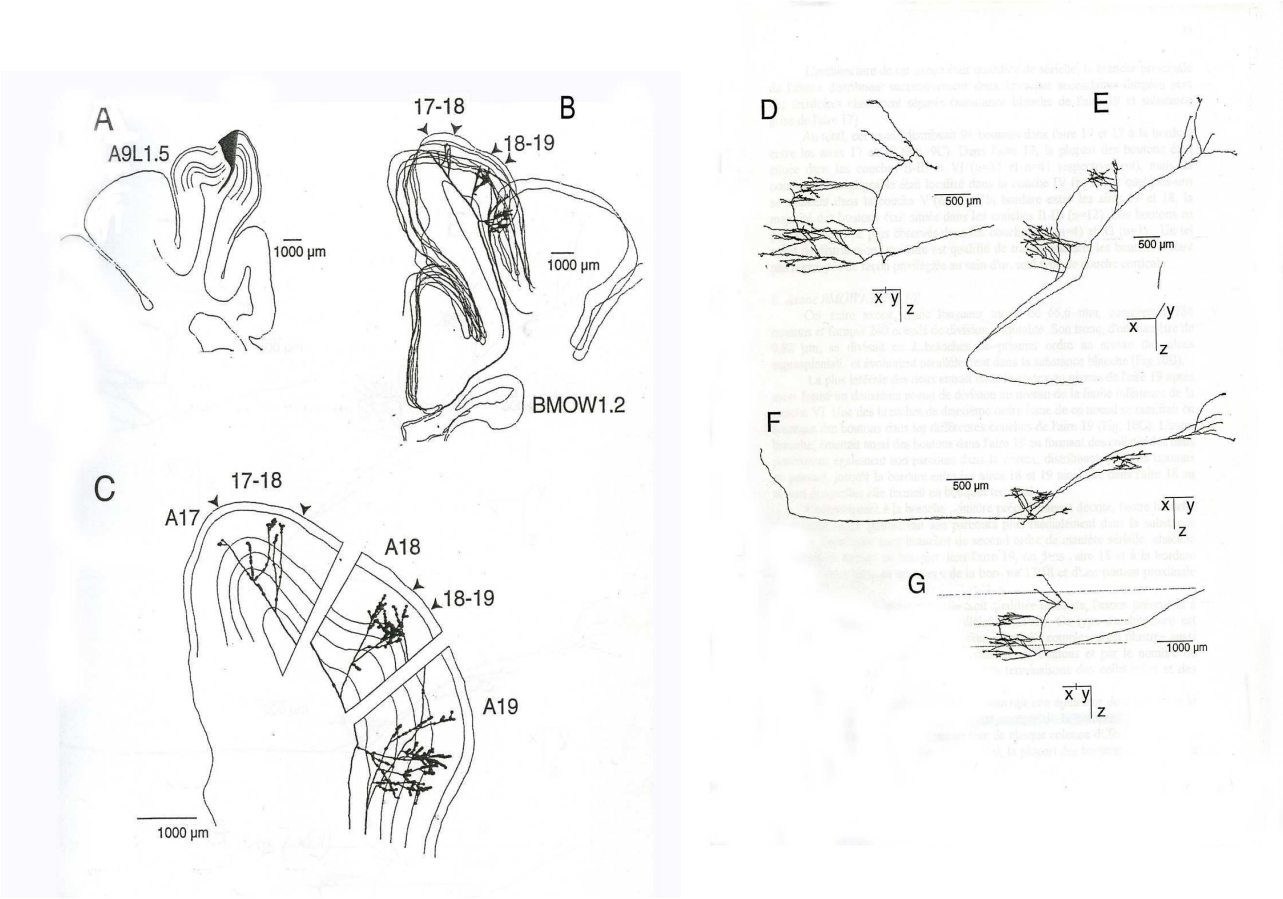

Fig. 102/ Computer-assisted 3-D reconstruction of one individual labelled callosal axon (BMOW1.2) from a 4 months old cat reared with a monocular occlusion of the right eye as early as 5 or 7 post-natal days. An anterograde tracer (biocytin) was injected in the left hemisphere rather rostrally, at stereotaxic Horsley-Clarke coordinates $A_9L_{1.5}$ where the transition zone between the visual cortical areas 17 and 18 (panel A). Its terminals were 3D reconstructed within the contralateral (right) hemisphere (ipsilateral to the occluded eye) using the Neurolucida Software (panels B to G). B and C, the terminals are shown in the frontal plane, within the outlines of a few of the serial sections used for the reconstruction ; pial surface and bottom of grey matter are indicated by interrupted lines. Dorsal is upwards, medial to the left. Calibration bars are 1000 µm. A17, A18, A19, visual cortical areas 17 and 18 and 19 ; A17-A18, transition zone between A17 and A18 ; A18-A19, transition zone between A18 and A19. D to G, same axonal terminal but while changing the view angle (X, horizontal plane; Y, vertical plane; Z, sagittal plane). For example, the axon in panel E is seen from the top (see text for further details). Calibration bars are here 500 or 1000 µm.

MATERIALS AND METHODS

Three-dimensional reconstruction of single callosal terminal arbours

Fourteen callosal axons terminating in cat visual cortex, which were labelled anterogradely with biocytin and then 3D-reconstructed (see below for further details of the technique), were used to test the efficacy of the method we propose here. They were all obtained while the surgical procedures were conformed to institutional and governmental requirements (Direction of Veterinary Services and Ethic comity) and the guidelines of the European Convention for the Protection of Vertebrate animals used for experimental and Other Scientific purposes (Strasbourg, 18.III, 1986).

Thirteen “normal” terminal callosal arbours come from normal adult cats. We have described qualitatively their fine architecture in great details already (Houzel et al, 1994). Thus, with respect to the present purpose, this is lucky because they represent a very good reference. An additional one comes from a 4 month-old cat that has been reared with an early monocular deprivation from 6 postnatal days (Fig. 102). It has been added to others because, on the basis of its qualitative description, it displays an obvious abnormal spatial dispersion of callosal terminals, with a complex clustering of synaptic boutons (Milleret et al., in preparation).

The labelling method of these callosal terminal arbours has been described in great details in Assal and Innocenti (1993). To summary, an anterograde tracer (biocytin) was injected very locally at specific stereotaxic Horsley-Clarke coordinates. Specific histological procedures were then applied. Briefly, the brains were kept in cold (4°C) fixative for 4 h and stored in cold, 30% sucrose, PBS for 2 days; 75-µm-thick frontal sections were then cut frozen, collected in PBS and processed according to King et al. (1989). Section were rinsed four times in PBS with 1% Triton X-100 and incubated in avidin-peroxidase complex for one night [ABC Standard or Elite Kit (Vector) 1:200 in PBS-Triton]. Peroxidase was then revealed using the nickel-intensified diaminobenzidine reaction (Adams, 1981). Sections were mounted, dehydrated and cover-slipped in DPX or Eukitt medium.

Every second or fourth section was counterstained with cresyl-violet or toluidine blue to identify cortical layers. The stained axons were then individually reconstructed using a computer-coupled microscope (Glaser and Glaser, 1990) and the Neurolucida software package *(Microbrightfield Inc.)*. The contours of each section (pial surface), boundaries of cortical layers

and blood vessels were drawn at low magnification. The stained axonal processes were observed through x 63 or x 100 immersion objectives (final magnification of x 1000 or more) and traced as sets of connected 5- to 100-µm-long segments delimited by two points. Each point was assigned *x*, *y* and *z* coordinates, a distance and one of the following tags: node; passing or terminal bouton; origin or termination. Generally, reconstructions extended over a range of 3-62 (mean = 32) consecutive sections. Final corrections for shrinkage were applied separately for the *x*, *y* and *z* dimensions. In the context of the present analysis of spatial dispersion of synaptic boutons, both isotropic and non anisotropic shrinkages have to be estimated and compensated for a correct spatial analysis. Anisotropic linear shrinkage was first compensated with a 3 fold expansion along *z* axis (orthogonal to the cutting plan) to overcome the 1/3 compression due to dehydration and cover slipping (Houzel et al, 1994(1)). A final shrinkage correction had to be done to provide the correct scale of the distribution of synaptic boutons in each direction, so that the mean 35 % isotropic shrinkage was also compensated by a 1.5 scaling factor. Staining and histological procedures provide after reconstruction a set of data containing morphological parameters of the axonal tree. The locations of the very ends of the terminal branches were collected within the axonal structure and provide a three-dimensional description of the synaptic connection field. In agreement with Houzel et al. (1994), this topographic distribution is assimilated here to the one of the synaptic boutons themselves. This allows comparing easily our statistical clustering with the qualitative description of terminal columns that has been performed previously.

Quantitative analysis of 3D reconstructed single terminal arbours

To describe quantitatively each callosal terminal arbour, we developed a specific algorithm. This one allowed extracting a particular set of parameters from the 3D coordinates of the very most terminal branches of each of these terminal arbours. One of these parameters was the *number of clusters* as an objective evaluation of a dense terminal arbour, which is in some respect the characteristic of order zero. The next parameters were: 1) the *proportions* of points in each “cluster”, corresponding to the number of branches terminating in one given dense terminal area; 2) the *mean position* of such “cluster”, constituting the order 1; 3) the *ellipsoid of inertia* of each “cluster”, as elements of order 2, giving a measure of dispersion, flatness, and orientation.

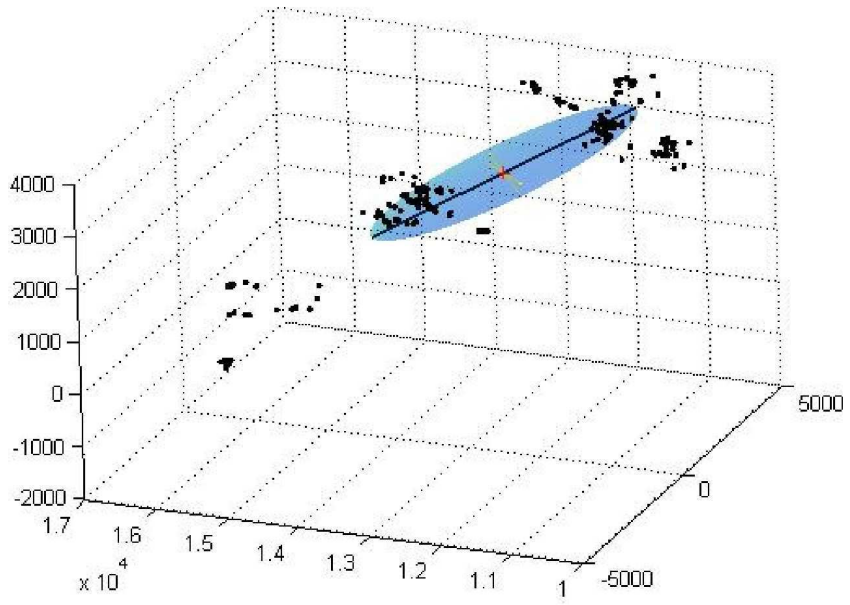

Fig. 103/ Gaussian approximation of the synaptic distribution of callosal axon shown in Fig.102. The ellipsoid greatest axis (direction along which the variance is maximum) is in black. The ellipsoid volume in blue is centred onto the centre of mass of the distribution here plotted by a small red dot. The global dispersion of the synaptic cloud is well represented but the finer structure is not captured by this simple Gaussian approximation.

Tri-dimensional elongations and ellipsoid approximation

To describe the global organisation of the reconstructed distribution of the terminal branches of callosal axons, a first simple analysis can be performed based on a multivariate Gaussian model defined by the mean and the covariance matrix Σ of the empirical distribution of boutons. The centre μ and the 3 by 3 covariance matrix Σ are estimated from data set as follows:

Let $\mathbf{r}_n$ be the 3D location of the n^{th} sample (an identified synapse) where $n \in \{1,..N\}$

$$\mu = \frac{1}{N} \sum_{1}^{N} \mathbf{r}_n$$

$$\Sigma = \frac{1}{N} \sum_{n=1}^{N} (\mathbf{r}_n - \mu)^{\mathbf{T}} (\mathbf{r}_n - \mu)$$

where the symbol $^{\mathbf{T}}$ stands for transpose.

The diagonalization of the symmetric definite positive covariance matrix Σ provides 3 orthogonal directions (along the 3 eigenvectors) associated with their respective positive eigenvalues. The square root of each eigenvalue defines the standard deviation of the Gaussian distribution along the associated direction. The largest one corresponds to the direction along which the synaptic field is maximally elongated. On the opposite, the smallest one corresponds to the direction along which the synaptic field is maximally concentrated. Therefore, the set of 3 eigenvectors with their associated eigenvalues could be used to create a graphic representation with an ellipsoid where axes lengths are proportional to standard deviation.

The Gaussian approximation is a simple, fast and robust method that provides a global view of a spatial distribution However, it cannot account for a finer spatial organization, such as the existence of dense clusters well visible on the example shown in Fig. 103. The precise locations and extents of these clusters with respect to the functional organization of the visual cortex might be of primary relevance. Moreover, well established criteria for a distribution to be Gaussian such as kurtosis and skewness remain far from the accepted range [-2 ; 2]. Thus the spatial distribution of the terminal branches of one single neuron connectivity cannot be approximated by a simple Gaussian model. A clusterization method based on a Gaussian mixture model has then been developed. The gain obtained by mixtures compared to simple Gaussian will be computed, in the form of difference of log-likelihood.

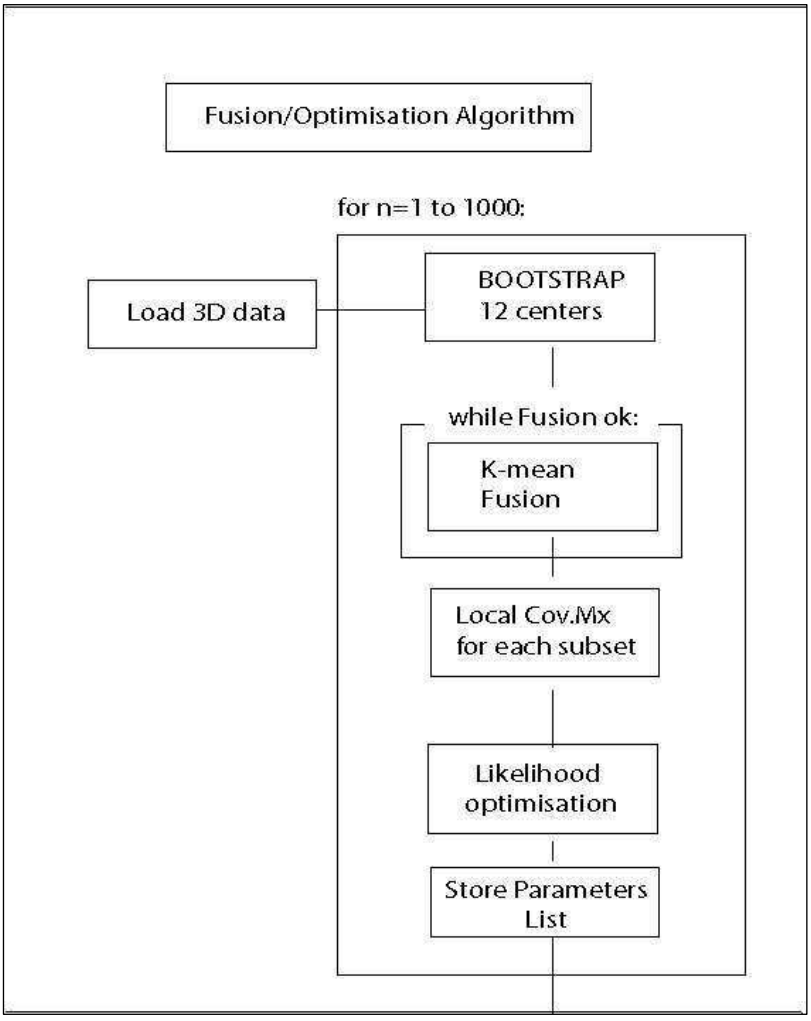

Fig. 104/ Algorithm main sequence fixing the number of clusters and initializing the parameters list. See text for details.

Clustering, fusion & optimisation methods for a Gaussian mixture model

In order to provide a more accurate description of the 3D distribution of the terminal branches, we propose here a Gaussian mixture model. According to this model, each cluster is characterized by a weight (somehow related to the number of synapses per *cluster*) and a single 3D Gaussian distribution (centre and covariance matrix). This Gaussian mixture model is a logical extension of the previously described Gaussian model. The choice of normal mixture results from a minimum of *prior information* (or equivalently maximal entropy) for a given variance and mean. It allows a compact and meaningful description to characterize the spatial organisation of clusters (position, elongation, orientation, density). McLachlan and Peel (2000) gives an extensive treatment of the mixture approach to statistical modelling, with component distributions possibly non-Gaussian. On the other hand, a summary of the case of Gaussian mixture can be found in McLachlan (1982). The state of the art in clustering and the link with data mining can be found in Kogan et al. (2006) as well as in Everitt et al. (2001).

The parameters to be identified are therefore: the number of Gaussians NG (i.e. the number of clusters), and for each cluster its weight A_i, its centre μ_i and its covariance matrix Σ_i. In the following paragraphs, the symbol θ stands for the full set of parameters; each Gaussian subset θ_i (i = 1 to NG) includes A_i, μ_i and Σ_i. One of the goal is to find the best estimate of θ, i.e. the maximum *a posteriori* (MAP) of the distribution $P(\theta \mid R)$, when NG is fixed. The main problem is that, except for NG = 1 (single Gaussian model), there is no analytical solution for the best parameter estimation, given the data set R. The function to maximize is known to have several local maxima when the number of Gaussians is bigger than 1 (McLachlan ,1982), part of the art is then to prepare a starting point for an optimization method, sufficiently well to quickly detect a large maximum.

To solve this problem, we adopted an iterative scheme summarized in Fig. 104. In summary, we first applied an initialization procedure by randomly drawing a subset of samples used as initial centres (***bootstrap***). We then applied the ***K-mean method*** to segregate the full set of data into convex subsets (Seber, 1984; Spath, 1985). A ***Ward cost function*** is used to reduce the number of convex subsets. Each subset is associated to Gaussian model as described above. The number of points within each subset and the Gaussian centre and covariance matrix are used as a first approximation of the best parameter choice. Starting from this initial guess, we finally applied a simplex optimization algorithm to find the MAP (maximum a posteriori). Maximum a posteriori is

obtained by applying a penalization (to be described below) to the maximum likelihood. This penalisation comes from an a priori of smallest possible number of cluster (or complexity of the mixture); it is empirically obtain from an artificial chosen set of data, i.e. from model parallel distributions where the result of our wishes is known. The whole sequence (bootstrap/K-mean/fusion/MAP) was repeated for about 1000 initial random drawings and the overall best model was retained. A similar model is described in McLachlan and Peel (1998). It also chooses the number of clusters by re-sampling and K-mean after random start but uses an alternative penalization by comparing ratios of likelihoods between n and n+1 clusters given by data and by bootstrapping on the distribution with n clusters (McLachlan, 1987), referred as the MIXFIT algorithm. Several other algorithms in the same spirit are proposed in the literature such as for example EMMIX or MULTIMIX, from the Wolfe's method in 1970. See also Celeux and Soromenho (1996). The originality of our method (detailed below) resides in the specific combination of computational techniques to provide not only the most likely numbers of subunits NG but also supplementary quantitative descriptors (amplitude, position, orientation of each clusters and entropy of the distributions).

More importantly, we verified that the algorithm is valid on simulated data. Such data were generated by drawing artificial 3D points from a known distribution, in order to set key parameters and check the relevance of the obtained results on the basis of a penalized maximum likelihood.

For tri-dimensional data, 10 independent parameters have to be estimated to describe a particular cluster: the first concerns the relative weight of each cluster assuming their sum equal to unity and the nine others are related to the construction of an ellipsoid for this cluster: 3 values for the coordinates of its centre (mean of the local subset), 3 for the orientation of orthogonal principal axis and 3 for the elongation of the distribution along each axis (standard deviation). The last 6 ones are given by the eigenvalues and eigenvectors of the covariance matrix of the local distribution. When NG is the number of Gaussian clusters used to fit the data, the total number of free parameters for our model is 10xNG - 1. The initial number of cluster NG has been fixed to 12 as a reasonable upper limit latter decreased by fusion of subunits. This upper limit has to be adapted to the specific anatomical data set. The ***bootstrap initialization*** consists in random drawing 12 points among the data set. These points are used as initial candidates for clusters centres. The ***K-mean(2; 3)*** method applied afterwards leads to divide the 3D space into volumes around each centre with equal distance separation plans thus associating each sample of the data to the closest centre. The cluster centres are then redefined as the X, Y, Z means of all sample of each subset. Mean positions

for new centres are evaluated for the each whole subset after all samples have been associated with a given cluster. We excluded coplanar subset or subset with less than 4 points whose determinant of covariance matrix is null. Very few iterations of this sequence (stable convergence for less than 20 iterations for 12 centres) quickly lead to a relevant partition of the data set. The following ***fusion*** step has been designed to combine adjacent clusters together when a specific condition is fulfilled, thus reducing the number of clusters engaged for optimization. The fusion criterion known as the ***Ward rule*** is tested by calculating a cost function W applied on the unified whole subset compared with the sum of the cost function when evaluated for each of the two subunits.

The Ward cost function for a subset of N points $\mathbf{r}_n$ (x,y,z) is:

$$W(\text{subset}) = \frac{1}{N} \sum_{n=1}^{N} (\mathbf{r}_n - \boldsymbol{\mu})^2$$

$$\text{where } \boldsymbol{\mu} = \frac{1}{N} \sum_{1}^{N} \mathbf{r}_n$$

For two A and B subsets grouping respectively N_A and N_B synapses positions, the fusion is applied when $W(A \cup B) < W(A) + W(B)$. Under this condition, the fusion of a subset consists in re-indexing all related samples to a unique cluster centred on its mean. Evaluated for each couple, the fusion is processed only for the couple of clusters showing the greater difference between the two cost values then fusion estimation is iterated again until the fusion criterion is valid for at least one couple of clusters. A power N^{α} in place of N in denominators can control the sensitivity of the fusion criterion but, in our case, best results were obtained for $\alpha = 1$. As low as the power α is, as often fusions occur.

Maximum a posteriori of the Gaussian mixture model

Let G be a trivariate Gaussian distribution with a density of probability for **r** = (x,y,z)

$$G(\mathbf{r} \mid \mu\, \Sigma) = \frac{1}{(2\pi)^{3/2} \det(\Sigma)^{1/2}}\, e^{\frac{1}{2}(r-\mu)^T \Sigma^{-1}(r-\mu)}$$

We aim to model the distribution of a set of point within space with a weighted sum of Gaussians which density of probability is given by:

$$P(\mathbf{r} \mid \theta) = \sum_{k=1}^{NG} A_k . G_k(\mathbf{r} \mid \mu_k\, \Sigma_{\mathbf{k}}) \text{ with } \sum_{k=1}^{NG} A_k = 1$$

Under the usual hypothesis of conditional independence of individual data samples, the probability density for having any set of N data R = [$\mathbf{r}_1$, … ,$\mathbf{r}_N$] is given by:

$$P(\mathbf{R} \mid \theta) = \prod_{n=1}^{N} P(\mathbf{r_n} \mid \theta)$$

Finally, according to Bayes formula, the posterior distribution of parameters given the data set is:

$$P(\theta \mid \mathbf{R}) = P(\theta).P(\mathbf{R} \mid \theta) / P(\mathbf{R})$$

where P(**R**) is a constant used for normalization and P(θ) is the prior

The prior distribution for weights, centres and covariance matrix is supposed to be uniform. However, the prior distribution on the number of clusters cannot be uniform, otherwise the maximum a posteriori reduces to the maximum likelihood. As extensively discussed by McKay (2004), model comparison based on maximum likelihood suffers from the problem of over-fitting.

Given the data, the maximum likelihood increases with NG. An extreme case could be for instance a Gaussian mixture with as many Gaussians as data points: considering that each bouton is a cluster clearly yields a perfect model from the likelihood point of view. More generally, the class of models with k Gaussians is enclosed into the class with k+1 Gaussians; therefore the maximum likelihood increased monotonically with NG. A popular way to compare models of various complexities has been proposed by Akaike (1974). His criterion (AIC) has been later refined and theoretically grounded by various authors (see Burnham & Anderson, 2004 for a review). Basically, it consists to penalize complex models with a “savvy” prior which is an exponentially decreasing function of the number of parameters. Accordingly, we choose to bias the choice of the number of clusters in order to balance the natural increase of likelihood with an exponential decreasing prior of the form:

$$P(NG)= 2^{-\beta.NG}$$

where β is a key parameter to be evaluated with simulated data

To maximize the posterior probability, we then have to find θ which maximizes the following function:

$$F(\theta|\mathbf{R}) = \sum_{n=1}^{N} \text{Log}_2 \left(\sum_{k=1}^{NG} A_k.G_k (\mathbf{r}| \theta_k) \right) - \beta.NG$$

Developed under *Matlab 7.r14* programming environment, an optimisation routine based on the simplex method was written to maximise this function Constraint on amplitude was applied to keep each of them and their sum into the [0, 1] interval. The simplex optimisation method was applied over ten thousands iterations and shows a rapid progression of the likelihood. Optimisation from one configuration set θ was stopped when relative difference of consecutive values of the likelihood was less than 10^{-6}. An example of results is shown in Fig. 105.

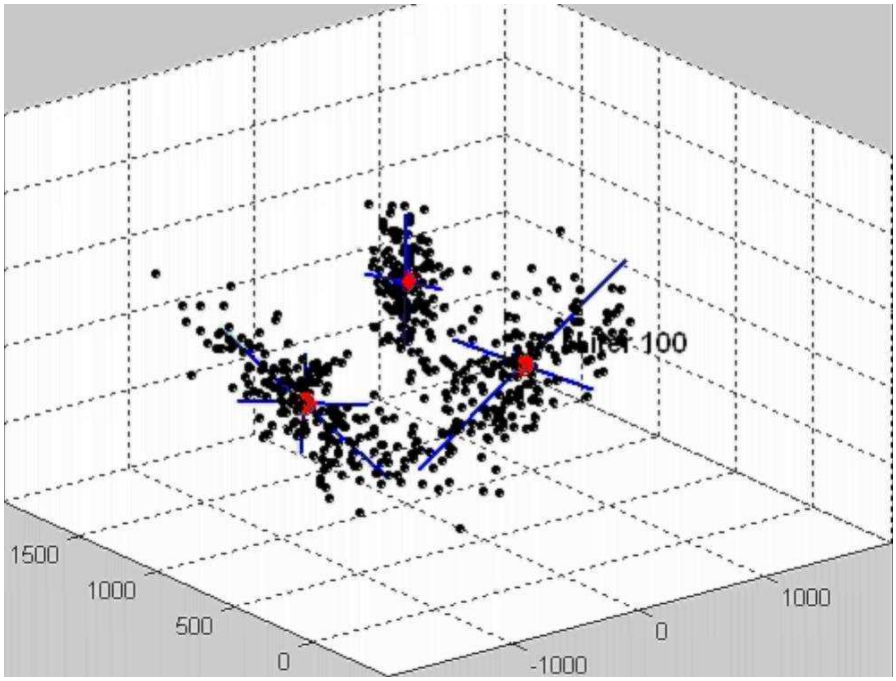

Fig. 105/ Example of optimisation result on simulated data. The output of an optimisation session is shown by setting for each identified cluster a centre (red) and 3 orthogonal axis (blue) with length relative to the variance in this direction (synapse positions are shown with black dots).

Simulated 3D data to validate the fusion/clustering method

In order to validate the method and obtain a convenient value for β, we used it on different simulated data set obtained by generating random mixture of trivariate Gaussian distributions, as follow. The number of clusters (NG) and the total number of points (N) to be generated are fixed by user, as the mean radius (Rc) and possibly an anisotropy factor to elongate distribution toward one or two directions. From this, a simulation algorithm randomly draws NG centres within a sphere (Rs) and draws, associated to each one, a given fraction of N points from tri-variate Gaussian distribution. In about half of the simulated trials the fractions were balanced for all Gaussians whereas for the remaining half of the trials the fractions varied in the range [6.25%, 75%]. Variances of all distributions are also randomly fluctuating around the radius (Rc) to provide more diversity. Moreover, to generate non-isotropic distribution, every subset of points was oriented with random rotation matrix. The compactness of distributions or instead their *overlapping* can be controlled by changing the ratio Rc/Rs. At last, the procedure provides a mean of N points randomly distributed among NG subset whose centres, covariance matrix elements and relative amplitudes are known and labelled as a θ_{sim} parameters list.

The main sequence of the method (e.g Boostrap/K-mean/Fusion/Optimisation) ran on thousand initializations, each of them providing an initial configuration set θ_{init} and its likelihood optimisation set θ_{optim}. Different types of simulated data were tested, changing the total number of points, the number of initial clusters and their compactness, in order to check the stability and the robustness of the method.

For a given simulated trial i where all the parameters are known, in particular the simulated number of Gaussians denoted by NGsim and for a given fixed value of β we choose the value of θ giving the highest value of F(θ|Ri). For each of these results we retained the corresponding optimal number of Gaussian Qi. In order to evaluate the performance of the algorithm associated to β we calculate the following relative error measure:

$$\text{Err} = \frac{1}{Ntrials} \sum_{i=1}^{Ntrials} \frac{|Qi - NGsim|}{NGsim}$$

We also calculated the mean and the standard error of the difference between Qi given by the criterion and the original NGsim in order to estimate any bias for overestimation or

underestimation of NG and its dispersion. A good value of β is one which minimizes the quantity Err.

Another criterion to select the number of clusters

Before optimization, the simple sequence (Bootstrap/K-mean/Fusion) produced the histogram NG which gives an idea of the frequency over thousand trials on how any random initialization converges after fusion on a particular number of clusters. This histogram in itself is rich of information and might be considered as part of the result. However this information has to be used with care because it is strongly "algorithm dependant". To evaluate the gain we got with optimization of F with respect to the simple sequence (Bootstrap/K-mean/Fusion), we also computed Err (and mean and standard deviation) for the number NGalg corresponding to the maximum frequency given by the histogram.

Fitness quality and gain of the method

To evaluate the gain of this method with respect to a simple construction of inertia ellipsoid, we calculated an absolute distance between the empirical distribution **R** and the one associated to θ_{optim}. We compared this distance with the one obtained with simple Gaussian approximation. We also compared it with the distance from **R** to the known $\theta_{sim.}$

A well adapted quantity to compare distributions is the Information distance of Kullback-Leibler (Kullback, 1959). When applied (in the right order) between a Gaussian mixture distribution parameterized with θ and one sampled distribution (or real data) R, it yields:

$$D_{KL}(R \mid \theta) = - \text{Log}(N) - (1/N) \sum n=1,N \text{Log}(P(r_{\mathbf{n}} \mid \theta)) = - \text{Log}(N) - (1/N) \text{Log}(P(R \mid \theta))$$

For a given sample size (N), this distance is negatively related to likelihood $P(R \mid \theta)$, allowing to take the likelihood values to evaluate the quality of fit of a given theoretical model. According to Kullback (1959), D_{KL} represents the mean information for discrimination in favour of the empirical distribution against the one associated to θ.

Application to real anatomical data.

The hypothesis we will use is that anatomical data follow the probabilistic law in form of Gaussian mixture. After a good value for β has been chosen, we applied our method to real data **R'** to find the best parameter set θ', that is the one which maximizes F(θ'| **R'**). The quantity D_{KL}(R' | θ') was used to estimate the fitness quality of the model. Finally we compared the obtained results with the ones described before in Houzel et al. (1994).

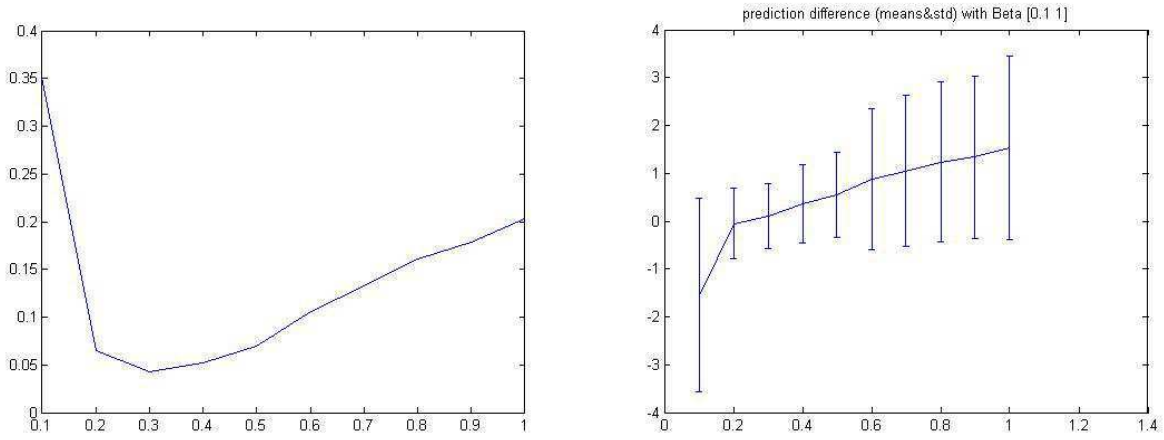

(a) **(b)**

Fig. 106/ Error on the number of Gaussians as a function of β. (A) Mean of relative error (Err) in ordinate as a function of β (abscissa) for the 38 simulated data set. (B) Mean and standard deviation of the signed error (ordinate) as a function of β (abscissa) on the same data.

RESULTS

The new statistical method we propose here to characterize the clustered organisation of single neuronal terminal arbours has been first applied to various simulated distributions of points. As defined above, several types of Gaussian mixtures were explored. Then this method has been applied to real anatomical data. Terminal arbours from single callosal neurones that were 3D reconstructed from normal or early monocularly deprived adult cats were used. This allowed testing our method in case of various degrees of complexity in the spatial organisation of terminal arbours.

Simulations

The following results have been obtained from 38 simulated distributions, while each one has been evaluated with thousand initialisations (bootstrap) followed by the K-mean-fusion-optimisation sequence. The first 10 were obtained with 80 points drawn from balanced Gaussians mixture with an *overlapping ratio* Rc/Rg (see Methods) equal to 10 or 15. The next 10 ones were obtained with the same characteristics but with 150 points. The last 18 ones were obtained with an *overlapping ratio* equal to 15 (half with 80 and half with 160 points) but with non-uniform repartition of points between Gaussians. Mixtures of 3, 5, 7 or 9 Gaussians were generated in equal proportion except the last 18 ones where only 3, 5 or 7 Gaussians were generated.

Influence of β on the number of Gaussians

As expected, increasing β tends to decrease the optimal number of Gaussians. As shown in Fig. 106A the difference “simulated minus optimal” Gaussians number increases as a function of β. The first result is the existence of unique minimum of Err for β = 0.3 as shown in Fig. 106B. This choice is confirmed by the mean crossing zero and the minimal standard deviation (see Fig.106A). It should be stressed that this optimal value (β = 0.3) was obtained for the described set of simulations. Changing the set of data could yield a range of optimal values from 0.25 to 0.4 (data not shown). Notice that jumps of likelihood were often observed onto or close to the number of clusters used for simulations. However this step transition was not always well contrasted in the natural progression of the likelihood. Thus the transition step could not be used as a general criterion for the choice of the best number of clusters.

Fitness quality and gain measured by Kullback-Leibler distances

The simulated data were drawn from Gaussians mixtures and we evaluated the fitness quality of the simulated distribution against simulated data with Kullback-Leibler distance: D_{KL}sim. This value was used as a reference for sake of comparison with optimal Gaussians mixture (D_{KL}optim) and single Gaussian distribution (D_{KL}ellipsoid). Fig. 107 plots the two last ones as a function of the former one. This figure shows first that the optimal model explained the data as accurately as the simulated distribution. There is no significant difference between D_{KL}optim and D_{KL}sim whereas the number of Gaussians and the parameter values may differ. Secondly, on the opposite, the distance obtained with the single Gaussian (D_{KL}ellipsoid) is clearly much higher, from 2 to 8 bits of information.

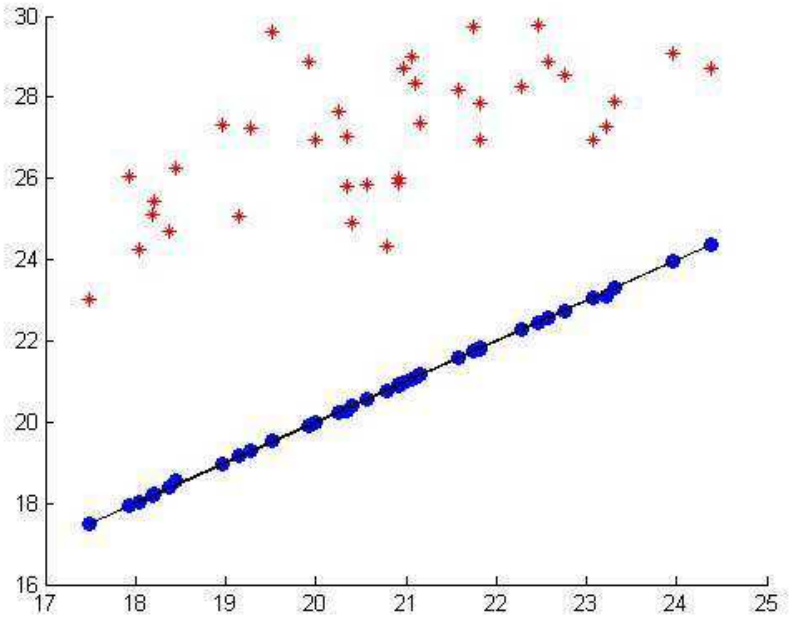

Fig. 107/ Kullback-Leibler Distances for simulated data. The Kullback-Leibler Distances (D_{KL}) between the samples and the simulated distribution are reported on X axis. Blue dot ordinates report the D_{KL} between samples and the optimized model. Red star ordinates report D_{KL} between samples and for the single Gaussian model. Distances between blue dots and red stars give an indication of the D_{KL} gain obtained from single Gaussian distributions to Gaussian mixture distributions. (β=0.3). Blue dots are aligned onto the diagonal (black line) showing a perfect agreement of the optimized model with respect to the simulated distribution. (units: bit of information).

Table 6/ Optimisation results for clustering (see text for details)

Axon name	Column	NG model	DKL	N. points	InfraG F.
Mean	3.071	3.9231	21.6583		
standard Dev.	1.979	2.0191	2.2546		
EN16C	5	2	23.679	263	0.534
EN16D	4	5	22.525	183	0.204
EN16E	3	3	23.1	138	0.204
EN16F	2	5	21.686	94	0.283
EN16H	2	1	24.224	97	0.547
EN16T	2	8	19.384	96	0.239
EN16V	2	5	21.943	52	0.170
EN16W	1	1	25.734	91	0.437
EN20C	2	3	20.782	172	0.035
EN21B	1	3	18.321	120	0.043
EN21C	2	5	18.374	60	0.196
EN22B	7	6	19.953	300	0.136
EN22D	7	4	21.853	256	0.105
BMOW1.2	3	4	24.113	241	

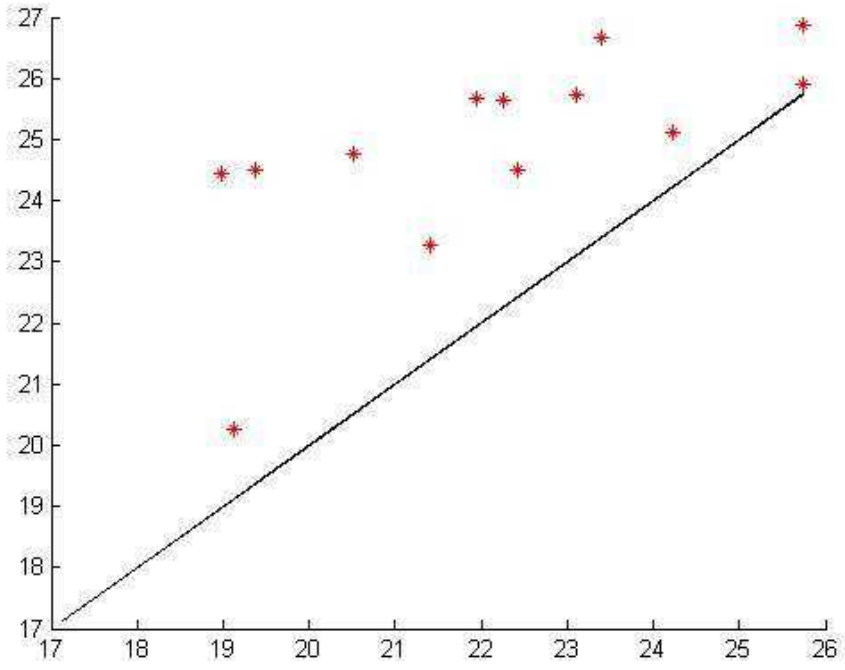

Fig.108/ Kullback-Leibler Distances for real data. X axis report D_{KL} values obtained from optimized model (β=0.3) on real data. Y axis report the D_{KL} values obtained for single Gaussian model. The vertical distance from the diagonal (black line) gives an estimation of the D_{KL} gain from single to multiple Gaussian models.

Results on real anatomical data

The method we proposed here has thus been tested on 14 callosal terminal arbours terminating in the cat visual cortex. Thirteen ones come from normal adult cats. Of interest, the architecture of their various branches has been described qualitatively in great details after 3D reconstruction already (cf. Houzel et al, 1994 (1)). In the present context, they will be further quantitatively analysed on the basis of the 3D coordinates of their respective terminal boutons. Obviously, we expect that the quantitative method will allow going further the previous qualitative observations, in particular concerning the clustered organisation of the terminal boutons. An additional (new) callosal terminal arbour has been 3D-reconstructed from an adult cat reared with an abnormal postnatal experience (BMOW1.2, Fig. 102). To illustrate data that may be obtained after a qualitative analysis and a quantitative one, both from this neuron have been presented here. This allowed testing the efficacy of our new statistical method in case of a very complex arborisation. This also allowed showing how our method may identify abnormalities.

Normal reared animals

The data obtained applying our algorithm onto real data are shown in Table 6. As indicated above (from results on simulated data), the value $\beta = 0.3$ has been used. The number of clusters identified varied from 1 to 8 (Table 6, 3rd column). In most cases, these numbers are different compared to the ones that have been reported previously from qualitative analysis. Notice that the choice of β has an influence for many axons on the number of clusters (but not on the quality of fitness). For instance, means of cluster numbers (NG) obtained for $\beta = 0.25, 0.3, 0.4, 0.5$ were 5.6923, 3.9231, 3.3846, and 2.8462 respectively, whereas the mean value of clusters obtained from visual inspection is 3.07. Nevertheless, not any β value provides the same number of clusters for individual axons as compared to visual inspection. In term of fitness quality, as revealed by the DKL values, we obtained the same range than the one for simulated data (from about 19 to 26 bits). Of course, there is no reference value in this case. However, one can compare the optimal DKL obtained with our method to the one obtained with a single Gaussian approximation (see Fig. 108). In the real case also, the gain is important (about 4) and comparable to the one obtained in the simulations.

Monocularly deprived animal, an example of qualitative versus quantitative analysis

The axon BMOW1.2 has been labelled anterogradelly after injection of biocytin in the left hemisphere, at Horsley-Clarke stereotaxic coordinates $A_9L_{1.5}$ (Fig. 102A). In cat visual cortex, this corresponds to a rather anterior portion of the transition zone (TZ) between A17 and A18, where the inferior portion of the visual field is represented (Tusa et al., 1978; 1979). Then, its terminal arbour has been 3D reconstructed from the right hemisphere (Fig. 102A-G). It has been reconstructed over a distance of 66.6 mm (from the corpus callosum to the cortical plate) and displayed a trunk which diameter was 1,68 µm. At the level of the first node, this main trunk divided in the white matter at the level of the Sulcus Suprasplenialis, thus very far from the cortical plate. This gave two first order (or primary) branches running in "parallel" and vertically toward the cortical plate.

The most lateral of these two primary branches (diameter 1,68 µm) turned gradually to the right, penetrated the visual cortex at the level of A19 and divided again (at the level of the second node) in the inferior part of layer VI (Fig. 102B-C). One of these two second-order (or secondary) branches ramified, giving 194 boutons in the different layers of A19 (see Fig. 102C). The other second-order branch also terminated in A19 (188 boutons). But, additionally, after distributing two "en passant" boutons, it gave a branch terminating in the 18/19 transition zone as well as in A18 including 77 boutons.

In contrast to the former primary branch, the latter one (diameter 1,68 µm as well) continued to run in the white matter vertically toward the lateral gyrus, with a medial trajectory, distributing three second-order branches following a "serial" pattern (Fig. 102B-C). The first one gave 89 boutons in A19, at the same place as those provided by the other first-order branch. The second one terminated at the 18/19 TZ (72 boutons) and A18 (78 boutons). The third branch terminated in the 17/18 TZ (77 boutons) and in A17 (15 boutons).

In total, such individual terminal arbour displayed a "mixed parallel-and-serial" architecture (see Houzel et al., 1994 for details), thus a complex architecture (see Fig. 102B-C). Such a complexity is further illustrated by the global distribution of the terminals across both the cortical areas and the different cortical layers, and the numerous boutons they included (792 boutons in total):

a) From the top of the brain, taking the midline as a reference i.e. the antero-posterior orientation, such axon was oriented obliquely and extended over ~3 mm in the visual cortex (Fig. 102E);

b) Tangentially, it displayed different terminal sites, with a variable number of boutons. Most of them were however located in A19 (with 473 boutons distributed in the various cortical layers). Others were located at the 18/19 TZ (149 boutons), in A18 (78 boutons) or more medially in TZ (77 boutons) or A17 (15 boutons). The number of boutons thus decreased from the most lateral column to the most medial one. The column including the larger number of boutons was also the larger one at the level of the pial surface: 0.69 mm^2, with 1.4 mm of extension along the antero-posterior axis (Fig. 102E). But the column located in the 18/19 TZ and A18 had the smallest extension, while it had not the smallest amount of boutons (0.37 mm^2 with an extension of 0.8 mm; Fig. 102E);

c) Radially, i.e. across the different cortical layers, the laminar distribution of the boutons was “transgranullar” within each area (see Houzel et al., 1994 for details) although the majority of the boutons was always located in the supragranular layers. Thus, in A19, most of the boutons were located in II-III layers (n=198) and in layer IV (n=173), with however a lot of them also in layers V and VI (n=54 and n=48 respectively). Within 18-19 TZ, the layers including a majority of boutons were the II-III ones (n=71) and IV (n=64), while the layers V and VI included only few boutons (layer V, n=5; layer VI, n = 9). In A18, more than half of the boutons were located in layer II-III (n=55), but some were also located in layer IV (n=19), in layer V (n=1) and layer VI (n=3). In the 17-18 TZ, the layer II-III included 33 boutons, while the other cortical layers (except layer I) included a similar number of boutons (layer IV, n=11; layer V, n= 14; layer VI, n=19). In A17, almost all the boutons were located in layer II-III (n=12), while the others were located in layer VI (n=3). Thus, layers II-III and IV included most of the boutons while layer I did not include any. Finally, notice that 3 boutons were found in the white matter, below the 18-19 TZ (n=2) and A19 (n=1).

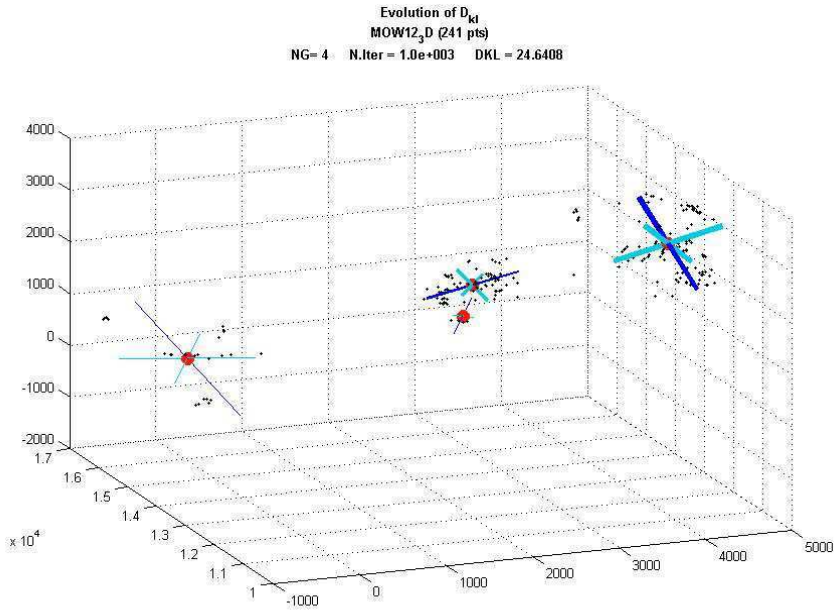

Fig.109/ Tri-dimensional representation of the best model obtained from the axon BMOW1.2 shown in Fig.102. Each identified cluster is represented on its centre of mass (red point) and a set a 3 orthogonal axis showing the elongation of the local distribution (darker one is the longest one, showing direction of possible anisotropy). Relative amplitudes of each local distribution are indicated with the thickness of the axis. For this axon the highly clustered distribution is clearly visible (unit: µm).

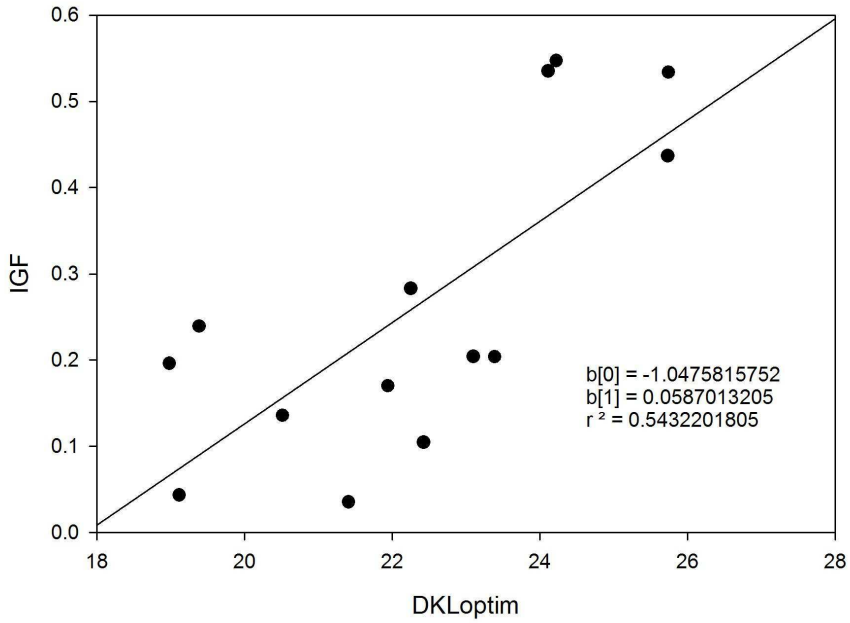

Fig. 110/ Linear regression of the layer dispersion of synaptic boutons, characterized by the granular and infragranular fraction (IGF) with respect to the fitness quality, characterized by the optimal DKL. Insert: numerical regression results.

In term of cluster number, our method yields values ranging from 3 to 6 according to the β value. For the optimal choice β = 0.3, the estimated cluster number is 4, as compared to 3 clusters from visual inspection. From this particular neuron, the visual inspection is therefore more in agreement with a slightly higher β value. On the opposite, changing the β value has little influence on the fitness quality, as revealed by the DKL which ranges from 24.113 (β = 0.25) to 24.97 (β = 0.5). As compared to other axons (normally reared animals), the optimal DKL value is relatively high but within the overall range. The remark is also true for the number of clusters. The main particularity of this axon, from the point of view of the terminal arbour dispersion, is the wide scattering of the cluster centres (see Fig. 109) contrasting with the nearly normal radius of individual clusters.

Correlation between layer dispersion and morphology given by our quantitative method

For each analyzed axons, we calculated the proportion of synaptic boutons located in layers IV, V and VI (granular and infragranular). This proportion (InfraGF) is reported in the last column of Table 6. It has also been plotted in Fig. 110 on the Y axis as a function of the optimal DKL obtained with β = 0.3. There is a clear correlation (r^2 = 0.543). This result indicates that the synaptic distribution in the granular and infragranular layers is relatively less captured by a Gaussian mixture model than the supragranular layer. This new result has to be confirmed by further analysis. It is mentioned here to exemplify the interest of our quantitative statistical analysis.

DISCUSSION

In the present study, we propose a new statistical method which allows describing quantitatively and objectively the clustered organisation of terminal arbours of single cortical neurones. Gaussian mixture models were used to provide a quantitative description of the dispersion of terminal arbours of single axons. A maximum *a priori* method was used to estimate the number and the weight of each cluster, as well as their centres and covariance matrices. The method has been validated first by using synthetic data. Then, it has been applied to real data, namely terminals arbours of single callosal neurones displaying various amounts of complexity. As expected, this allowed an accurate identification of the various clusters formed by the very most terminal branches within each terminal arbour.

Comparison with quantitative methods described previously in the literature.

Since the discovery of repeated patchy structures formed by intrinsic lateral connections in V1 in the Tree shrew (Rockland and Lund, 1982), many studies, models and computer simulations have tried to elucidate some rules of formation of horizontal connectivity. For example, Mitchison and Crick (1982) affirmed their relation to orientation maps. Gilbert and Wiesel (1983) insisted on the presence of clusters. More recently, Bosking et al. (1997) described a specific arrangement between the clusters formed by the horizontal connections and the orientation domains in the Tree Shrew striate cortex. Although some quantifications have been done (see for example Kisvarday et al., 1994; 1996), only few studies have elaborated explicit quantified analysis of clusters. And, in fact, either they complement ours, or they have been elaborated on completely different principles compared to the ones we applied here.

Buzás et al. (2006) are likely the first authors attempting to solve the problem. Combining optical imaging of intrinsic signal and anatomical tracing, they have re-examined the relationship between the orientation map and the intrinsic excitatory lateral connections in the cat primary visual cortex. They confirmed the standard assumption on rules of connectivity at the level of one given population, but not at the level of single neuron. More precisely, they tested a quantitative parametric model of (surface-view) distribution of boutons originated from a neuron in V1, constituted by the sum of products of circular symmetric Gaussians with von Mises distributions for

preferred orientations. This is an assumption of clustering distribution, with a restricted mixture of Gaussians (where Bernoulli weights are correlated to a preferred orientation and Gaussian are symmetric). They fitted the parameters by least mean square error, and conclude that the composite of neurons agrees with the model, but individual neurons do not. If applied to their data, our method can additionally measure which parameters individualized distributions of boutons of single axons.

A statistical method has also been used for another rodent species and another sensorial primary cortex in Rocha et al, (2007). Quantitative morphometric features of callosal axon arbours projecting from and to the hind- or forelimb representations in S1, such as densities of branching points and boutons, segment length, branching angles and terminal field areas were measured. A cluster analysis, using all these criteria, was conducted and revealed the existence of two types of axon terminals: one less branched and much more widespread and another one more branched and compact. A relation was made with function because both types are unequally distributed between fore- and hind-limb regions. Their statistical analysis of “clusters” followed however a different line than ours. It is an agglomerative hierarchical method of clustering, constructing a dendrogram, along the line of Schweitzer and Renehan (1997). In this latter study, the authors have developed one of the few exposed algorithms of clustering for neurons, which is dedicated to classification of cells: 1) select features, described by numerical values, 2) assemble them in related groups, 3) choose as distance between groups of features (for example here “the average linkage between groups” related to Ward rule), 4) this construct a rooted tree by proximity, 5) cut the branches of this tree to obtain clusters, and finally 6) use analysis of variance to confirm the utility of the cluster solution. This algorithm is made to define different types of forms. More than an alternative to our algorithm, it might be complementary. Taking into account the parameters of spatial clustering we propose, we add other features to get a classification. Thus, for example, while the method used in Rocha et al. (2007) does not permit to deduce automatically a model, our method is contrastingly “model-based”: by using *a priori* multivariate normal mixture as reference distributions, it automatically produces a model with possible variances. This allows getting information by quantifying the departure from the family of models, and we can use data as input in computational integrative study by using the parameters at different order of approximation.

Advantages of our method.

In addition to previously enounced advantages, the presented algorithm is also simple, objective and clear. From the distribution of one given terminal arbour through an hundred of points, the pertinent parameters we determined here are unambiguously and can be defined in a relatively short time. Secondly, the method belongs to a well investigated branch in probabilistic clustering theory. Indeed, even if some other approaches of clustering are permanently developed, and that some are much more involved (cf. McLachlan & Peel, 1998 for example), our method mixes efficient tools. Third, our method is in relative agreement with expert visual inspection. But, it is more objective and is really three dimensional. Above all, it provides additional parameters describing the synaptic dispersion, as shown in Fig. 8 and 9. These additional parameters allow to quantitatively investigate functional connectivity in the cortex. Finally, the kind of algorithm that is developed here can be applied to any sets of spatially identified points, so it can concern other 3D data.

Altogether, this allowed re-investigating the “clustered” organisation of 13 reconstructed axons of normally reared adult cats that were described qualitatively already (cf. Houzel et al., 1994; Table 2).

Limits of our method of analysis.

The present algorithm has been elaborated from the combination of three partitioning methods (bootstrapping, K-mean plus Ward fusion rule) and a maximisation of a penalized likelihood. It allowed constructing an approximate normal mixture model. Thus, the final selected mixture is not the optimal solution. Rather, it is a compromise between the maximum likelihood and the minimum number of “clusters” within each terminal arbour, which maximizes the difference F between likelihood of the model distribution and a multiple of cluster number: $F = \text{Log}(P) - \beta NG$. An empirical justification of this last formula is given in the “Materials and methods”. It also results from its ability to recover the right number of Gaussians in synthetic data. The algorithm was however tested on artificially chosen mixtures of normal distributions, for NG less than 9: it gave the good value of NG in 86% of the cases, and reconstructed the distribution with good agreement.

One may also evoke some other additional limitations, although most of them are unavailable: a) the time for 3D reconstructing each terminal arbour and extracting pertinent parameters (~one month for each). It is not the easiest way to obtain geometric informations on neuronal networks. But to obtain real and precise data makes such an approach unavoidable; b) the possibility to miss some terminal branches, in particular the finest ones. This creates some incertitude. Notice that these two first points explain the reason why such anatomical studies remain relatively rare. One may expect that better methods of analysis and exploitation of data in the future may motivate researchers to use such a direct approach of real neural networks, which is indispensable to understand their diversity; c) The algorithm is certainly biased, favouring separated "clusters" of terminal branches. Thus, functionally distinct connexions might be confounded in the results. It can be underlined however that modularity is frequent in the regarded neocortical areas. Many functions are localized and vary continuously. Thus, such functional separation of "clusters" has a special meaning. The present algorithm may provide supplementary information coming from the reconstruction of the total axonal tree, and could thus tell if several "clusters" (in the sense of arborescence) are mixed. Note that, to be useful, the identification of "clusters" has to be conjugated with identification of layers in the cortex and position into the given functional areas; d) as any purely anatomical study, our method of analysis (which is finally a statistical one) needs to be completed by other methods such as optical Imaging or physiological recordings. This needs to be absolutely applied for understanding functionalities. Ideally, anatomy of neurones might be available first; e) as Clustering Analysis is a world in pure and applied mathematics; we limit ourselves to description of the distributions of axonal terminals.

Potential applications

The output of the fusion/optimisation program we propose here provides a set of pertinent parameters that allows various applications. Among these: 1) it makes possible describing quantitatively one given terminal arbour from its 3D coordinates. The set of parameters being provided contains elements that may characterize both its spatial extension and its "clustered" organisation. This evidently applies whatever the cell type being considered (for example pyramidal cell vs. basket cell); 2) by extension, the present method permits to analyse the relationships between the pre- and the post-synaptic connectivity; 3) of interest, it also allows comparing statistically different neural populations, for categorisation or diagnostics. For that, our method may

provide as much as five different parameters: a) the *average number of clusters NG*, obtained for one given population; b) the *distribution of volumes of clusters*; c) the *global spatial dispersion of the weighted centres*. This method should be much finer than the direct calculation on samples; d) the *averaged orientations* of the "clusters" formed by each terminal arbour along or across the cortical layers; e) the *total entropy of one given terminal arbour*. This may provide an interesting criterion to categorise the complexity of the spatial organisation of the distribution of the information throughout the synaptic neuronal network. This will greatly help when callosal terminal arbours from both normal and early monocularly deprived adult cats will be compared (Milleret et al., in preparation). More generally, our quantitative analysis may allow following all types of plasticity, whether it is during development or whether it is in the adult, in normal or pathological conditions.

The new statistical method we propose here may also greatly help to establish a relation between the spatial dispersion of intracortical neuronal terminals and the functional cortical maps. As underlined already, both the clustered organisation of terminal arbours and the functional organisation of the cortex are indeed closely related (cf. Introduction). When functional domains exist, such as orientation or ocular dominance ones in the visual cortex, its application is obvious. Clustering of boutons of lateral connections in the cortex is not always associated with known modular functional maps. For example, there is no orientation map in rodents but "there is a well-developed network of clustered intrinsic lateral interconnections within Oc1" (Burkhalter, 1989). But it is likely that these clustered connections underlie the dynamic structure of cortical receptive fields. Also, a nice qualitative and quantitative analysis of patches for intra- and inter-areal connections of V1 of rats with neighbour areas (Oc2LM) has been achieved by Rumberger et al. (2001). But, unfortunately, each cluster was assigned by hand, which likely eliminates some important information in relation with their distribution and their functionality.

Finally, one may briefly recall that our method may greatly help to establish models, in particular because it is "model-based": by using *a priori* multivariate normal mixture as reference distributions, it automatically produces a model with possible variances (see also above).

ACKNOWLEDGMENTS

The authors would like to thank G.M. Innocenti for having accepted that the data from normal adult cats may be used here to test the new proposed method. We are also grateful to DR. S. Wiener for useful comments on the manuscript and N. Quenech'Du and N. Lebas for their technical contribution. This work was supported: by the ANR (ACI "Neurosciences integrative et Computationnelles" to C. Milleret, J. Droulez & D. Bennequin & ACI "Nouvelles interfaces avec les Mathématiques" to D. Bennequin, J. Droulez and C. Milleret); by the CNRS; by the MENSER and the Collège de France to LF.

Reference List

1. **Houzel JC, Milleret C and Innocenti G**. Morphology of callosal axons interconnecting areas 17 and 18 of the cat. *Eur J Neurosci* 6: 898-917, 1994.

2. Seber. Multivariate Observations. Wiley, New York . 1984.

   Ref Type: Generic

3. Spath, H. Cluster Dissection and Analysis: Theory, FORTRAN Programs, Examples. translated by J.Goldschmidt. 1985. Halsted Press, New York.

   Ref Type: Generic

Part 1.3.2.

Characterization of the callosal terminal arbours of the NR and MD groups through clustering analysis.

This section gives a detailed presentation of the results obtained with the clustering analysis when applied to both EN and MD axons populations. As for the ellipsoid approximation analysis, the results concerning each experimental group are shown for each axon. They report the interesting characteristics that the clustering method can extract to describe the spatial organization of each callosal terminal arbours. They are presented in different panels as follow:

- The global parameters such as the number of clusters, the total volume of all clusters, and the characteristics of the spatial distribution of the weighted centres are reported in the first Table (titled "*clusters analysis*"on the top on left).
- Individual clusters attributes are detailed in the second Table (middle panel of each page, titled "*individual clusters*").
- The 3 lengths of the ellipsoid axis of each individual cluster were also used to calculate the anisotropy indexes of the local distribution (Oblate-Prolate index and MPS index) so it can also be represented in the triangular diagram of shapes (right-top panel, see Ch2, p. for details).
- In the lowest panel, we show a 3D representation of all clusters identified by the clustering procedure with a likelihood penalty value sets to its optimal value $\beta=0.3$ as determined from synthetic data.
- The small panel on the bottom-left of each page report an anatomical figure for seek of comparison.

The first Table reports the total volume as the sum each individual cluster volume. Another measure of the total volume of clusters is proposed with the weighted sum related to the statistical importance of each cluster as reveal by its relative amplitude from the mixture model. This alternative measure of volume is much more relevant as it doesn't take excessive contribution from large but less representative clusters. When the number of identified clusters is greater than 3, an ellipsoid approximation of the centres distribution weighted by relative amplitudes can be performed. This procedure provides volume, 3D spatial elongations, anisotropies and orientation with the AP direction reported as global features in the first table. When some of these attributes are not unavailable, i.e. when NG model is smaller than 4, making impossible to calculate some ellipsoid features, a green "0" is indicated in the Table and the sample was dismissed from the final means and statistics calculation related to this field. At last, the volume ratio between global extensions and local extensions is indicated. It reports the ratio between the volume of the ellipsoid embracing all terminals (the ellipsoid volume reported in Ch2.) and the weighted sum of the local counter part.

In the second Table, the relative amplitude of each cluster originating from the weight of its respective trivariate Gaussian distribution from the Gaussian mixture model (first attribute in the second table, sorted by decreasing order) is reported for each identified cluster. Every local trivariate Gaussian distribution can also be characterized by a set of spatial extension parameters (axis lengths) using the same method as for the 3D ellipsoid analysis (cf. Chapter 1.2.). The volume of each cluster is estimated by the product of these 3 lengths used also for the calculation of individual anisotropy indexes (reported in the triangular diagram). The orientation between the direction of the great axis of the local ellipsoid and the antero-posterior direction is also reported in this Table.

The 3 characteristics lengths of each local cluster are used to produce graphical representations of the optimal model shown in the bottom-right panel. In this panel, centres of clusters are shown with red dots and elongation axis thicknesses are related to the amplitudes of the clusters (great axis shown in dark blue). As for the ellipsoid method (see Chapter 1.2., Part 1.2.1., the antero-posterior axis runs from the bottom to the top of the 3D graphic representation (vertical axis). This allows comparison between data obtained with both methods.

After the clustering method has been applied to each axon, a synthesis of the data, for each experimental group, is presented. Finally, data from both groups are compared. Without going into details here, the clustering method reveals quite pertinent parameters to further describe quantitatively the callosal terminals arbours of both NR and MD animals. It also allows identifying differences between these groups that could not be identified another way.

PART A

Clustering analysis of callosal terminal arbours of the NR (reference) group

Clusters Analysis	**EN16C**
ORIGIN AREA	**A18**
NG model	**2**
Sum of volumes of all Clusters (mm^3)	1,94
Sum vol. All Clusters (Amp) (mm^3)	**1,23**
Vol. Ellips.Centres (NG>3) (mm^3)	**0**
Ell_C Axis 1 (mm)	**1,82**
Ell_C Axis 2 (mm)	0
Ell_C Axis 3 (mm)	0
Ell_C Obl-Prol. Idx	0
Ell_C MP Sphericity idx	0
Ell_C Angle Axis 1 / AP (deg)	61,9
Vol. Ellipsoid/Sum Vol. Clust(amp)	3,0

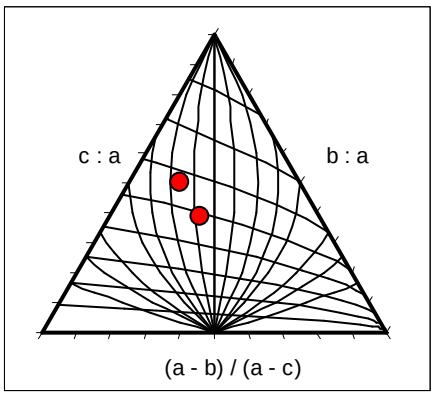

anisotropy indexes
of individual clusters

INDIVIDUAL CLUSTERS	**MEAN**	**Std**	**Clust 1**	**Clust 2**
Amplitudes	**0,5**	**0,25**	**0,68**	**0,32**
Volume Cluster (mm3)	**0,97**	**1,05**	**1,72**	**0,22**
Clust. Axis 1 (mm) (a)	**1,260**	**471.10^{-3}**	**1,590**	**925.10^{-3}**
Clust. Axis 2 (mm) (b)	1,013	473.10^{-3}	1,348	678.10^{-3}
Clust. Axis 3 (mm) (c)	577.10^{-3}	311.10^{-3}	797.10^{-3}	357.10^{-3}
Clust. MPSphericity idx	0,62	0,05	0,67	0,59
Clust. Obl-Prol. Idx	-2,80	1,52	-3,88	-1,72
Clust. Angle Axis1 / AP (deg)	68,5	59,8	26,1	110,8

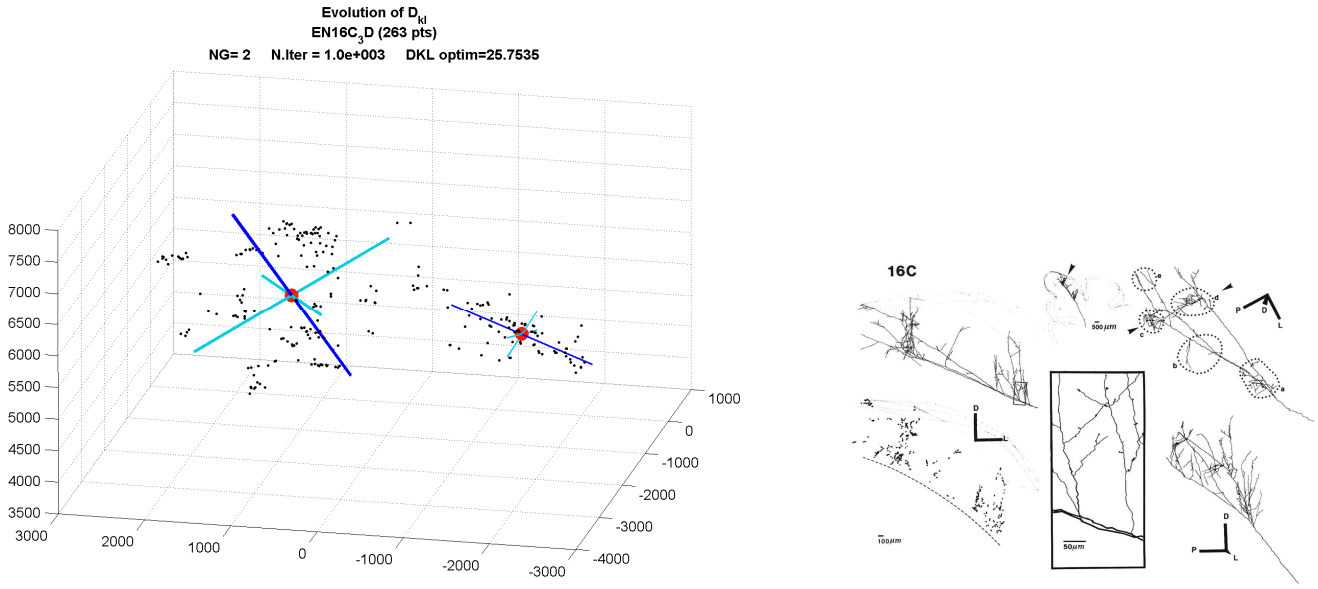

Fig. 111/ Clustering analysis results for axon EN16C.

Clusters Analysis — EN16D

ORIGIN AREA A18

NG model	5
Sum of volumes of all Clusters (mm^3)	0,290
Sum vol. All Clusters (Amp) (mm^3)	**0,066**
Vol. Ellips.Centres (NG>3) (mm^3)	**1,48**
Ell_C Axis 1 (mm)	**1,45**
Ell_C Axis 2 (mm)	0,80
Ell_C Axis 3 (mm)	0,15
Ell_C Obl-Prol. Idx	-1,73
Ell_C MP Sphericity idx	0,26
Ell_C Angle Axis 1 / AP (deg)	117,4
Vol. Ellipsoid/Sum Vol. Clust(amp)	34

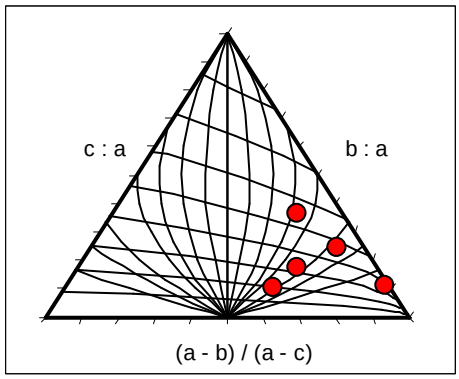

anisotropy indexes
of individual clusters

INDIVIDUAL CLUSTERS	MEAN	Std	Clust 1	Clust 2	Clust 3	Clust 4	Clust 5
Amplitudes	0,2	0,18	0,52	0,18	0,11	0,10	0,08
Volume Cluster (mm3)	0,057	0,033	0,068	0,109	0,052	0,024	0,032
Clust. Axis 1 (mm) (a)	**1,020**	**370.10^{-3}**	**1,000**	**1,130**	**1,573**	**818.10^{-3}**	**565.10^{-3}**
Clust. Axis 2 (mm) (b)	312.10^{-3}	81.10^{-3}	393.10^{-3}	355.10^{-3}	188.10^{-3}	348.10^{-3}	276.10^{-3}
Clust. Axis 3 (mm) (c)	182.10^{-3}	66.10^{-3}	174.10^{-3}	271.10^{-3}	176.10^{-3}	86.10^{-3}	204.10^{-3}
Clust. MPSphericity idx	0,48	0,13	0,42	0,57	0,47	0,29	0,64
Clust. Obl-Prol. Idx	19,1	14,0	13,4	16,705	43,765	13,529	8,285
Clust. Angle Axis1 / AP (deg)	62,9	13,3	67,9	83,6	59,2	53,3	50,6

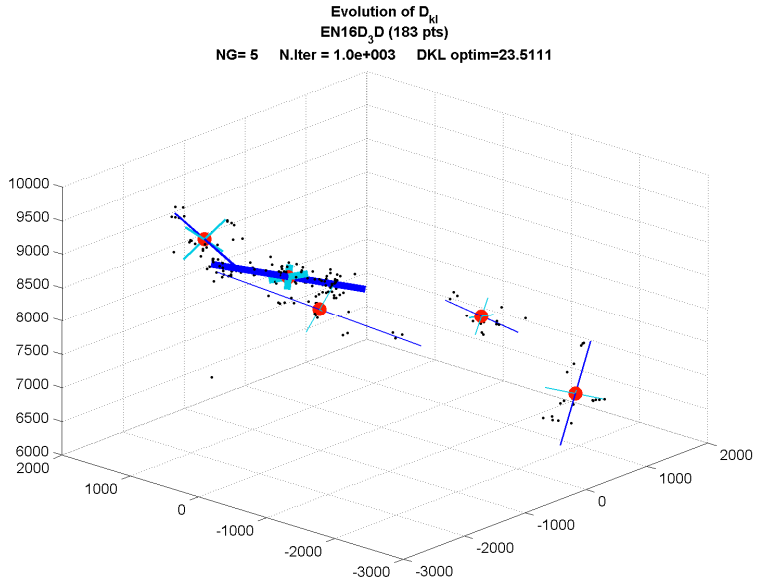

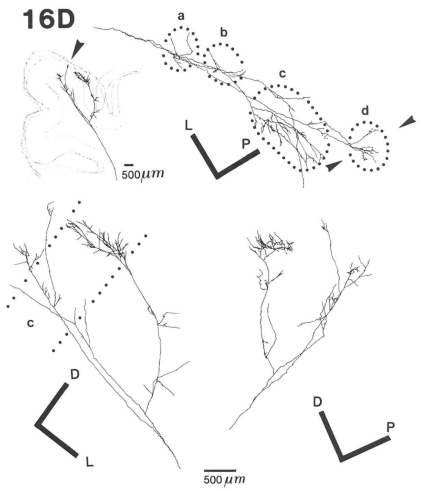

Fig. 112/ Clustering analysis results for axon EN16D.

Clusters Analysis — EN16E

ORIGIN AREA	A18
NG model	**3**
Sum of volumes of all Clusters (mm^3)	0,220
Sum vol. All Clusters (Amp) (mm^3)	**0,062**
Vol. Ellips.Centres (NG>3) (mm^3)	**0**
Ell_C Axis 1 (mm)	**1,02**
Ell_C Axis 2 (mm)	0
Ell_C Axis 3 (mm)	0
Ell_C Obl-Prol. Idx	0
Ell_C MP Sphericity idx	0
Ell_C Angle Axis 1 / AP (deg)	16,2
Vol. Ellipsoid/Sum Vol. Clust(amp)	14

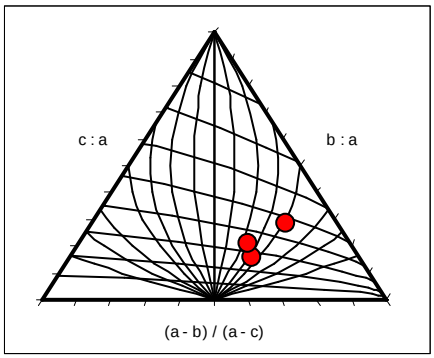

anisotropy indexes
of individual clusters

INDIVIDUAL CLUSTERS	MEAN	Std	Clust 1	Clust 2	Clust 3
Amplitudes	**0,33**	**0,38**	**0,78**	**0,13**	**0,08**
Volume Cluster (mm3)	**0,073**	**0,038**	**0,059**	**0,043**	**0,117**
Clust. Axis 1 (mm) (a)	**884.10^{-3}**	**80.10^{-3}**	**820.10^{-3}**	**840.10^{-3}**	**980.10^{-3}**
Clust. Axis 2 (mm) (b)	412.10^{-3}	17.10^{-3}	415.10^{-3}	393.10^{-3}	427.10^{-3}
Clust. Axis 3 (mm) (c)	194.10^{-3}	75.10^{-3}	173.10^{-3}	131.10^{-3}	279.10^{-3}
Clust. MPSphericity idx	0,46	0,09	0,44	0,37	0,57
Clust. Obl-Prol. Idx	8,2	2,0	6,1	8,5	10,2
Clust. Angle Axis1 / AP (deg)	69,3	38,3	109,7	64,9	33,3

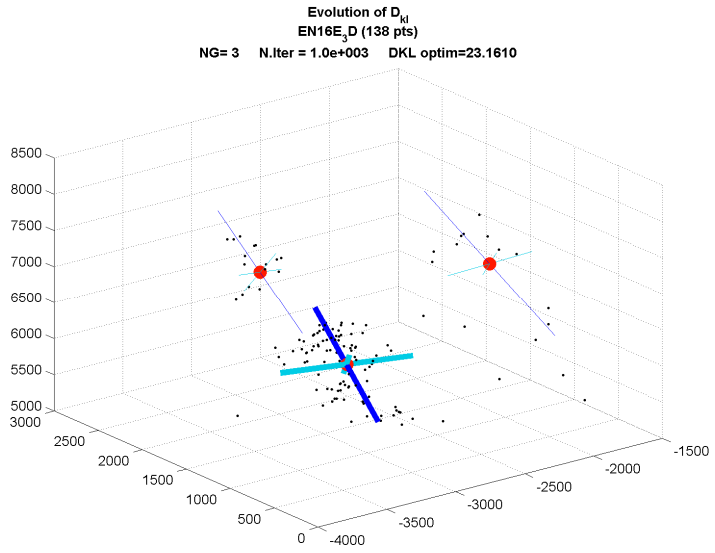

Fig. 113/ Clustering analysis results for axon EN16E.

Clusters Analysis — EN16F

ORIGIN AREA A18

NG model	5
Sum of volumes of all Clusters (mm^3)	0,070
Sum vol. All Clusters (Amp) (mm^3)	**0,018**
Vol. Ellips.Centres (NG>3) (mm^3)	**0,230**
Ell_C Axis 1 (mm)	**0,91**
Ell_C Axis 2 (mm)	0,30
Ell_C Axis 3 (mm)	0,10
Ell_C Obl-Prol. Idx	21,8
Ell_C MP Sphericity idx	0,33
Ell_C Angle Axis 1 / AP (deg)	66,6
Vol. Ellipsoid/Sum Vol. Clust(amp)	31

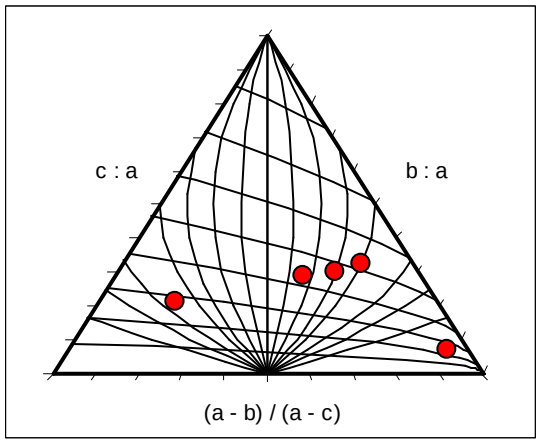

anisotropy indexes
of individual clusters

INDIVIDUAL CLUSTERS	MEAN	Std	Clust 1	Clust 2	Clust 3	Clust 4	Clust 5
Amplitudes	**0,20**	**0,12**	**0,41**	**0,21**	**0,14**	**0,12**	**0,09**
Volume Cluster (mm3)	0,014	0,012	0,023	0,030	0,003	0,004	0,009
Clust. Axis 1 (mm) (a)	**549.10^{-3}**	**311.10^{-3}**	**540.10^{-3}**	**560.10^{-3}**	**270.10^{-3}**	**310.10^{-3}**	**1,050**
Clust. Axis 2 (mm) (b)	227.10^{-3}	140.10^{-3}	265.10^{-3}	458.10^{-3}	155.10^{-3}	138.10^{-3}	120.10^{-3}
Clust. Axis 3 (mm) (c)	106.10^{-3}	35.10^{-3}	160.10^{-3}	117.10^{-3}	80.10^{-3}	102.10^{-3}	70.10^{-3}
Clust. MPSphericity idx	0,48	0,12	0,56	0,37	0,53	0,62	0,34
Clust. Obl-Prol. Idx	15,1	30,4	7,5	-12,8	3,4	10,0	67,2
Clust. Angle Axis1 / AP (deg)	58,5	22,1	65,5	82,8	22,4	61,4	60,5

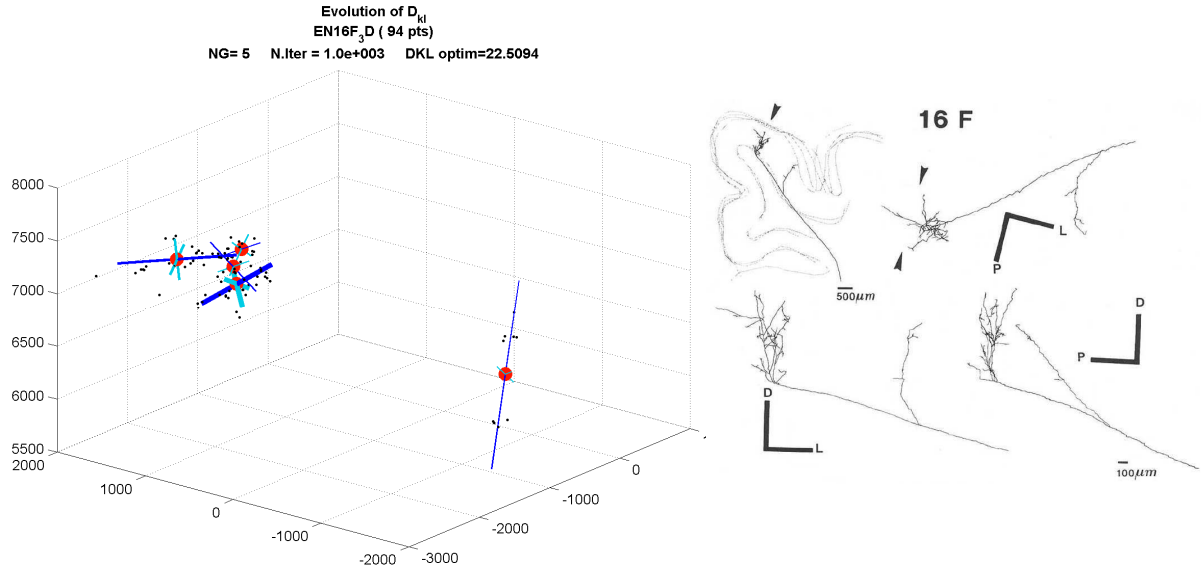

Fig. 114/ Clustering analysis results for axon EN16F.

Clusters Analysis	EN16H
ORIGIN AREA	A18
NG model	1
Sum of volumes of all Clusters (mm^3)	0,48
Sum vol. All Clusters (Amp) (mm^3)	**0,48**
Vol. Ellips.Centres (NG>3) (mm^3)	0
Ell_C Axis 1 (mm)	0
Ell_C Axis 2 (mm)	0
Ell_C Axis 3 (mm)	0
Ell_C Obl-Prol. Idx	0
Ell_C MP Sphericity idx	0
Ell_C Angle Axis 1 / AP (deg)	0
Vol. Ellipsoid/Sum Vol. Clust(amp)	3,1

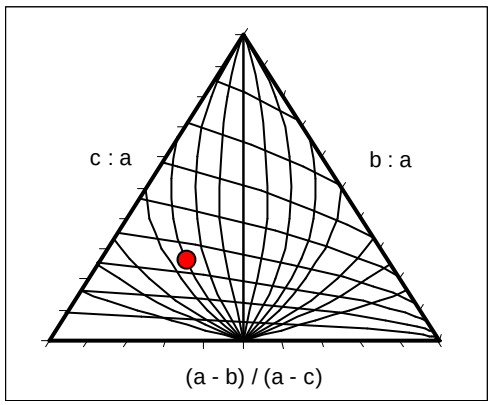

anisotropy indexes
of individual cluster

INDIVIDUAL CLUSTER	MEAN
Amplitude	1
Volume Cluster (mm3)	0,48
Clust. Axis 1 (mm) (a)	**1,110**
Clust. Axis 2 (mm) (b)	729.10^{-3}
Clust. Axis 3 (mm) (c)	589.10^{-3}
Clust. MPSphericity idx	0,75
Clust. Obl-Prol. Idx	4,4
Clust. Angle Axis1 / AP (deg)	55,2

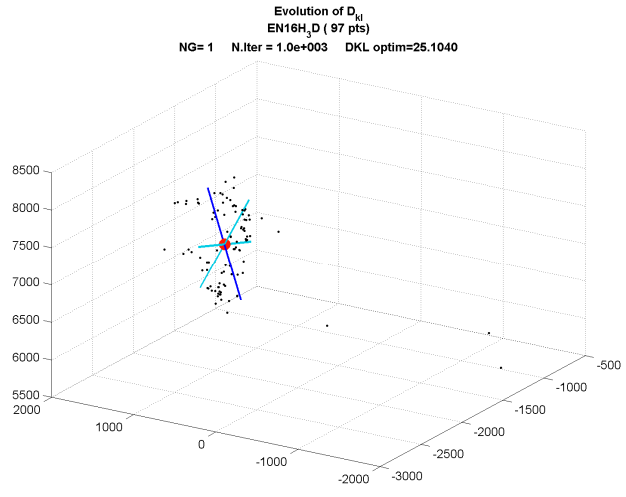

Fig. 115/ Clustering analysis results for axon EN16H.

Clusters Analysis — EN16T

ORIGIN AREA A18

NG model	8
Sum of volumes of all Clusters (mm^3)	0,021
Sum vol. All Clusters (Amp) (mm^3)	**0,003**
Vol. Ellips.Centres (NG>3) (mm^3)	**0,197**
Ell_C Axis 1 (mm)	**0,84**
Ell_C Axis 2 (mm)	0,34
Ell_C Axis 3 (mm)	0,08
Ell_C Obl-Prol. Idx	16,0
Ell_C MP Sphericity idx	0,29
Ell_C Angle Axis 1 / AP (deg)	70,4
Vol. Ellipsoid/Sum Vol. Clust(amp)	72

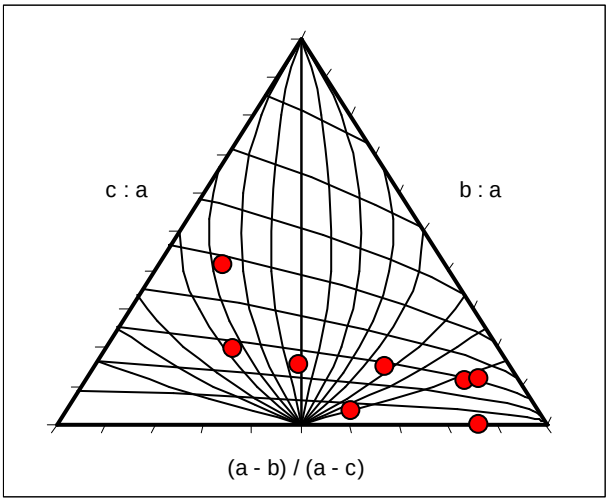

anisotropy indexes
of individual clusters

INDIVIDUAL CLUSTERS	MEAN	Std	Clust 1	Clust 2	Clust 3	Clust 4	Clust 5	Clust 6	Clust 7	Clust 8
Amplitudes	0,12	0,07	0,26	0,22	0,12	0,12	0,09	0,07	0,06	0,04
Volume Cluster (mm3)	0,003	0,004	0,004	0,003	$0,6.10^{-3}$	0,011	$0,1.10^{-3}$	$0,6.10^{-3}$	$0,05.10^{-3}$	$0,002.10^{-3}$
Clust. Axis 1 (mm) (a)	**246.10^{-3}**	**107.10^{-3}**	**431.10^{-3}**	**291.10^{-3}**	**292.10^{-3}**	**316.10^{-3}**	**184.10^{-3}**	**195.10^{-3}**	**151.10^{-3}**	**102.10^{-3}**
Clust. Axis 2 (mm) (b)	119.10^{-3}	92.10^{-3}	174.10^{-3}	215.10^{-3}	64.10^{-3}	274.10^{-3}	36.10^{-3}	113.10^{-3}	63.10^{-3}	14.10^{-3}
Clust. Axis 3 (mm) (c)	42.10^{-3}	41.10^{-3}	64.10^{-3}	57.10^{-3}	32.10^{-3}	130.10^{-3}	21.10^{-3}	30.10^{-3}	5.10^{-3}	$0,1.10^{-3}$
Clust. MPSphericity idx	0,33	0,17	0,38	0,37	0,38	0,58	0,41	0,34	0,14	0,03
Clust. Obl-Prol. Idx	246	659	13,4	-8,8	33,8	-6,6	35,2	-0,3	28,7	1878
Clust. Angle Axis1 / AP (deg)	62,5	25,5	96,3	86,2	46,0	48,3	83,7	18,7	62,2	58,7

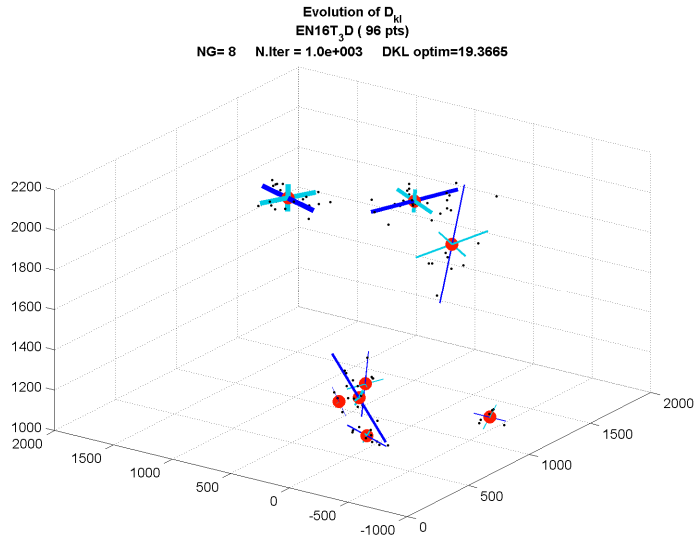

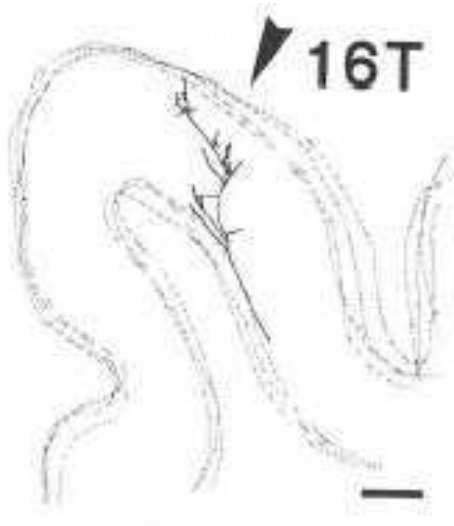

Fig. 116/ Clustering analysis results for axon EN16T.

Clusters Analysis — EN16V

ORIGIN AREA A18

NG model	5
Sum of volumes of all Clusters (mm^3)	0,080
Sum vol. All Clusters (Amp) (mm^3)	**0,022**
Vol. Ellips.Centres (NG>3) (mm^3)	**0,041**
Ell_C Axis 1 (mm)	**0,55**
Ell_C Axis 2 (mm)	0,42
Ell_C Axis 3 (mm)	0,02
Ell_C Obl-Prol. Idx	-62,5
Ell_C MP Sphericity idx	0,12
Ell_C Angle Axis 1 / AP (deg)	79,5
Vol. Ellipsoid/Sum Vol. Clust(amp)	14

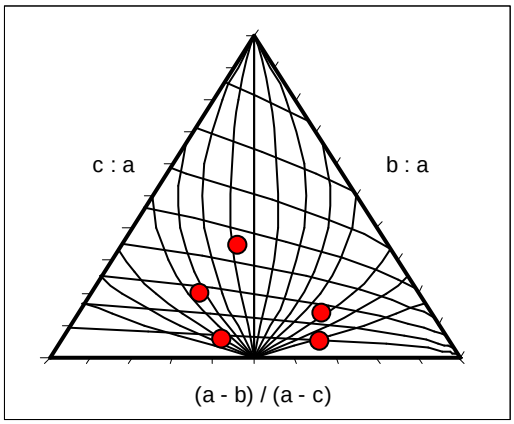

anisotropy indexes
of individual clusters

INDIVIDUAL CLUSTERS	MEAN	Std	Clust 1	Clust 2	Clust 3	Clust 4	Clust 5
Amplitudes	0,2	0,08	0,28	0,28	0,17	0,15	0,09
Volume Cluster (mm3)	0,016	0,021	0,048	0,025	$0,3.10^{-3}$	0,005	$0,2.10^{-3}$
Clust. Axis 1 (mm) (a)	**417.10^{-3}**	**197.10^{-3}**	**698.10^{-3}**	**471.10^{-3}**	**215.10^{-3}**	**459.10^{-3}**	**239.10^{-3}**
Clust. Axis 2 (mm) (b)	249.10^{-3}	173.10^{-3}	510.10^{-3}	335.10^{-3}	131.10^{-3}	185.10^{-3}	87.10^{-3}
Clust. Axis 3 (mm) (c)	77.10^{-3}	69.10^{-3}	137.10^{-3}	162.10^{-3}	11.10^{-3}	63.10^{-3}	12.10^{-3}
Clust. MPSphericity idx	0,32	0,15	0,37	0,55	0,16	0,36	0,19
Clust. Obl-Prol. Idx	4,3	19,7	-8,4	-1,7	-15,5	13,9	33,7
Clust. Angle Axis1 / AP (deg)	67,3	23,0	69,1	82,1	94,6	54,8	35,8

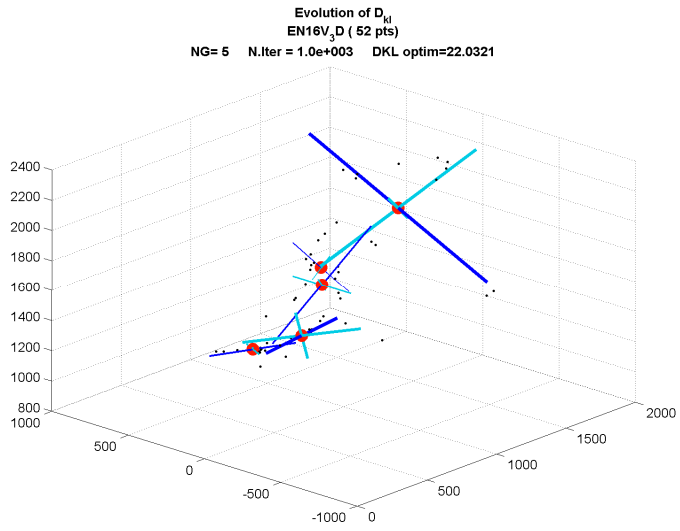

Fig. 117/ Clustering analysis results for axon EN16V.

Clusters Analysis	**EN16W**
ORIGIN AREA	**A18**
NG model	**1**
Sum of volumes of all Clusters (mm^3)	0,67
Sum vol. All Clusters (Amp) (mm^3)	0,67
Vol. Ellips.Centres (NG>3) (mm^3)	0
Ell_C Axis 1 (mm)	0
Ell_C Axis 2 (mm)	0
Ell_C Axis 3 (mm)	0
Ell_C Obl-Prol. Idx	0
Ell_C MP Sphericity idx	0
Ell_C Angle Axis 1 / AP (deg)	0
Vol. Ellipsoid/Sum Vol. Clust(amp)	1,4

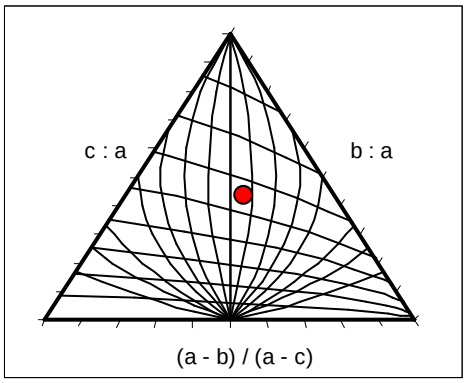

anisotropy indexes
of individual cluster

INDIVIDUAL CLUSTER	**Clust 1**
Amplitudes	1
Volume Cluster (mm3)	0,67
Clust. Axis 1 (mm) (a)	1,19E+03
Clust. Axis 2 (mm) (b)	1,08E+03
Clust. Axis 3 (mm) (c)	5,21E+02
Clust. MPSphericity idx	0,59
Clust. Obl-Prol. Idx	-7,7
Clust. Angle Axis1 / AP (deg)	48,4

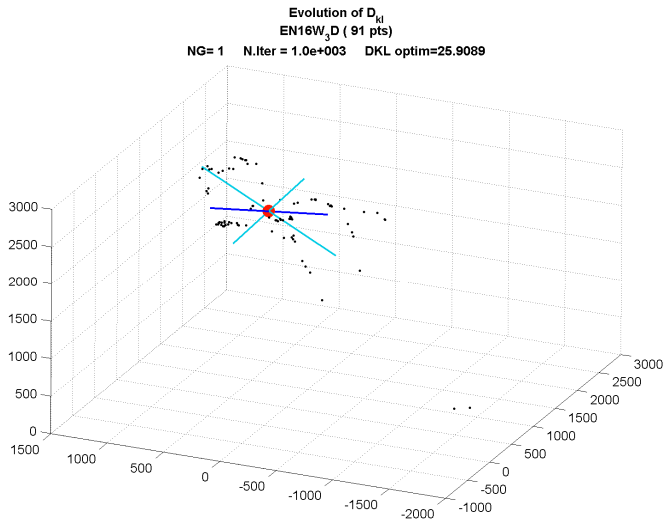

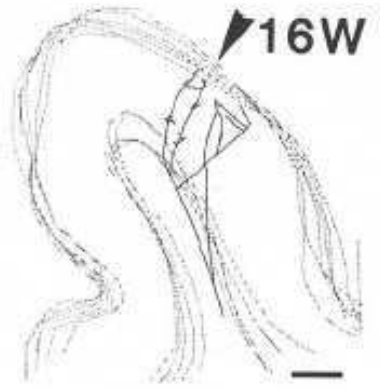

Fig. 118/ Clustering analysis results for axon EN16W.

Clusters Analysis	EN20B
ORIGIN AREA	TZ
NG model	4
Sum of volumes of all Clusters (mm^3)	0,013
Sum vol. All Clusters (Amp) (mm^3)	**0,004**
Vol. Ellips.Centres (NG>3) (mm^3)	**0,785**
Ell_C Axis 1 (mm)	**1,36**
Ell_C Axis 2 (mm)	0,38
Ell_C Axis 3 (mm)	0,19
Ell_C Obl-Prol. Idx	24,4
Ell_C MP Sphericity idx	0,41
Ell_C Angle Axis 1 / AP (deg)	41,0
Vol. Ellipsoid/Sum Vol. Clust(amp)	309

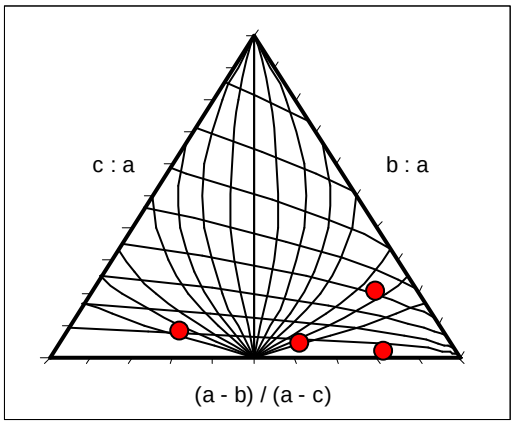

anisotropy indexes
of individual clusters

INDIVIDUAL CLUSTERS	MEAN	Std	Clust 1	Clust 2	Clust 3	Clust 4
Amplitudes	**0,25**	**0,10**	**0,39**	**0,25**	**0,18**	**0,18**
Volume Cluster (mm3)	**0,0033**	**0,003**	**0,007**	**0,001**	**0,002**	**0,004**
Clust. Axis 1 (mm) (a)	**571.10^{-3}**	**365.10^{-3}**	**482.10^{-3}**	**251.10^{-3}**	**456.10^{-3}**	**1,095**
Clust. Axis 2 (mm) (b)	181.10^{-3}	25.10^{-3}	146.10^{-3}	180.10^{-3}	187.10^{-3}	208.10^{-3}
Clust. Axis 3 (mm) (c)	38.10^{-3}	40.10^{-3}	99.10^{-3}	19.10^{-3}	20.10^{-3}	16.10^{-3}
Clust. MPSphericity idx	0,24	0,18	0,51	0,20	0,17	0,10
Clust. Obl-Prol. Idx	58	107	18,3	-25,4	25,9	215
Clust. Angle Axis1 / AP (deg)	80,5	12,3	68,0	73,4	95,5	85,1

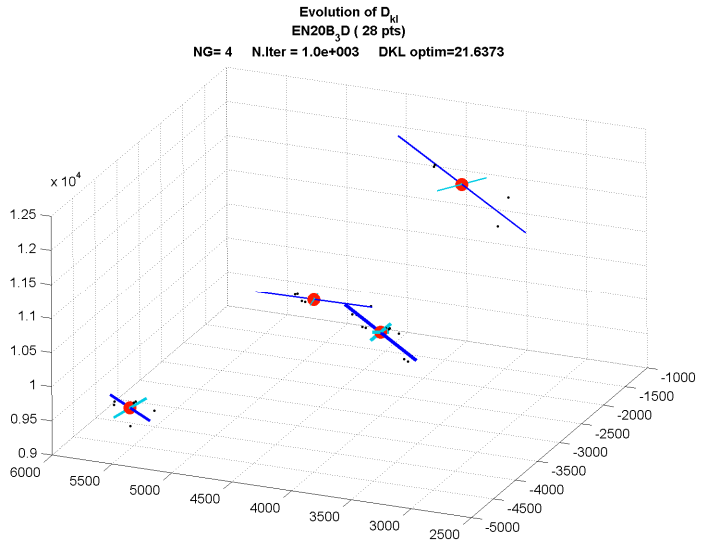

Fig. 119/ Clustering analysis results for axon EN20B.

Clusters Analysis	**EN20C**
ORIGIN AREA	**TZ**
NG model	**3**
Sum of volumes of all Clusters (mm^3)	0,055
Sum vol. All Clusters (Amp) (mm^3)	**0,022**
Vol. Ellips.Centres (NG>3) (mm^3)	**0**
Ell_C Axis 1 (mm)	**0,36**
Ell_C Axis 2 (mm)	0
Ell_C Axis 3 (mm)	0
Ell_C Obl-Prol. Idx	0
Ell_C MP Sphericity idx	0
Ell_C Angle Axis 1 / AP (deg)	5,8
Vol. Ellipsoid/Sum Vol. Clust(amp)	8,9

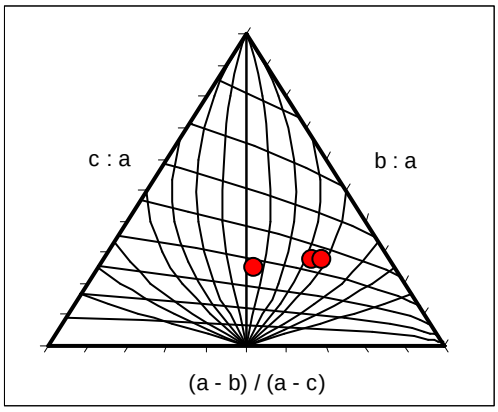

anisotropy indexes
of individual clusters

INDIVIDUAL CLUSTERS	MEAN	Std	Clust 1	Clust 2	Clust 3
Amplitudes	**0,33**	**0,16**	**0,5**	**0,33**	**0,17**
Volume Cluster (mm3)	**0,018**	**0,011**	**0,029**	**0,019**	**0,006**
Clust. Axis 1 (mm) (a)	**496.10^{-3}**	**116.10^{-3}**	**610.10^{-3}**	**501.10^{-3}**	**378.10^{-3}**
Clust. Axis 2 (mm) (b)	253.10^{-3}	74.10^{-3}	288.10^{-3}	303.10^{-3}	168.10^{-3}
Clust. Axis 3 (mm) (c)	132.10^{-3}	33.10^{-3}	168.10^{-3}	125.10^{-3}	102.10^{-3}
Clust. MPSphericity idx	0,52	0,04	0,54	0,47	0,55
Clust. Obl-Prol. Idx	6,3	4,6	8,2	1,0	9,6
Clust. Angle Axis1 / AP (deg)	89,9	13,3	92,8	101,6	75,4

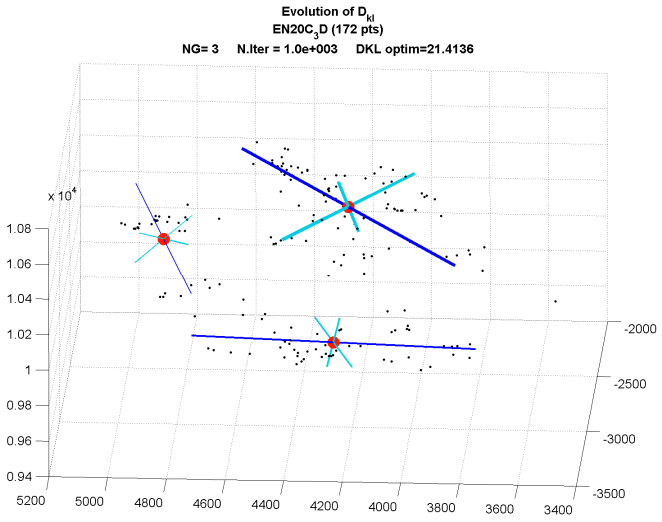

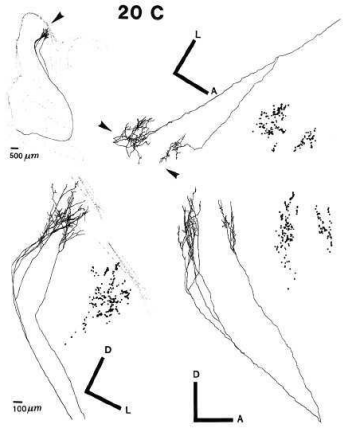

Fig. 120/ Clustering analysis results for axon EN20C.

Clusters Analysis	**EN21B**
ORIGIN AREA	**TZ**
NG model	**3**
Sum of volumes of all Clusters (mm^3)	0,009
Sum vol. All Clusters (Amp) (mm^3)	**0,003**
Vol. Ellips.Centres (NG>3) (mm^3)	**0**
Ell_C Axis 1 (mm)	**0,32**
Ell_C Axis 2 (mm)	0
Ell_C Axis 3 (mm)	0
Ell_C Obl-Prol. Idx	0
Ell_C MP Sphericity idx	0
Ell_C Angle Axis 1 / AP (deg)	92,3
Vol. Ellipsoid/Sum Vol. Clust(amp)	5,1

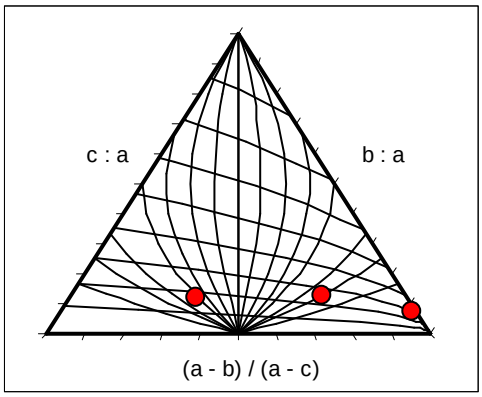

anisotropy indexes
of individual clusters

INDIVIDUAL CLUSTERS	MEAN	Std	Clust 1	Clust 2	Clust 3
Amplitudes	**0,33**	**0,04**	**0,37**	**0,33**	**0,30**
Volume Cluster (mm3)	**0,003**	**0,003**	**0,007**	**0,8.10-3**	**0,0016**
Clust. Axis 1 (mm) (a)	**448.10^{-3}**	**152.10^{-3}**	**542.10^{-3}**	**528.10^{-3}**	**272.10^{-3}**
Clust. Axis 2 (mm) (b)	137.10^{-3}	82.10^{-3}	187.10^{-3}	42.10^{-3}	183.10^{-3}
Clust. Axis 3 (mm) (c)	46.10^{-3}	19.10^{-3}	68.10^{-3}	36.10^{-3}	32.10^{-3}
Clust. MPSphericity idx	0,34	0,05	0,36	0,39	0,27
Clust. Obl-Prol. Idx	26,4	40,7	19,6	70,1	-10,5
Clust. Angle Axis1 / AP (deg)	90,7	4,8	96,3	88,2	87,6

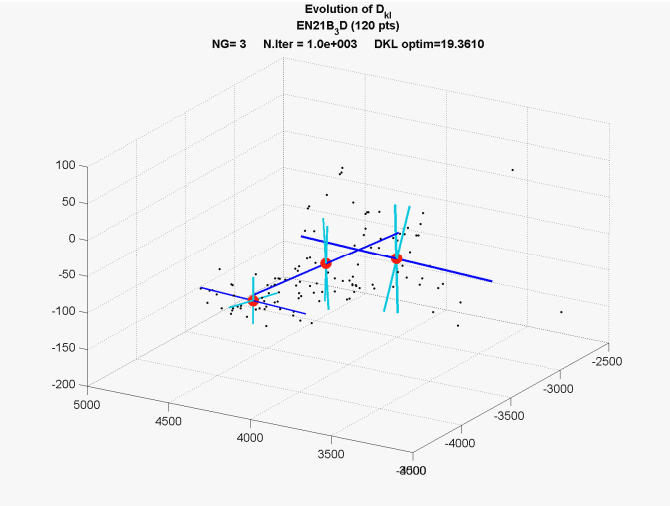

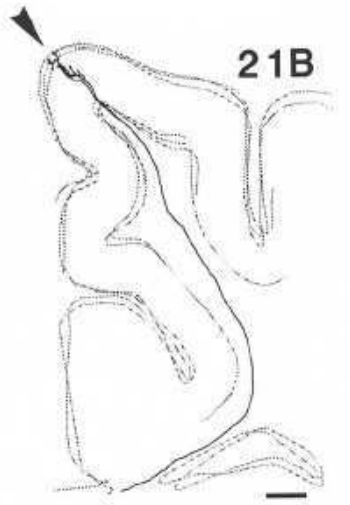

Fig. 121/ Clustering analysis results for axon EN21B.

Clusters Analysis — EN21C

ORIGIN AREA — **TZ**

NG model	5
Sum of volumes of all Clusters (mm^3)	0,019
Sum vol. All Clusters (Amp) (mm^3)	**0,003**
Vol. Ellips.Centres (NG>3) (mm^3)	**0,058**
Ell_C Axis 1 (mm)	**0,90**
Ell_C Axis 2 (mm)	0,23
Ell_C Axis 3 (mm)	0,03
Ell_C Obl-Prol. Idx	69,8
Ell_C MP Sphericity idx	0,18
Ell_C Angle Axis 1 / AP (deg)	34,6
Vol. Ellipsoid/Sum Vol. Clust(amp)	45

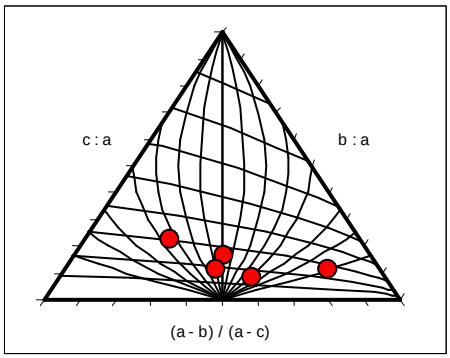

anisotropy indexes
of individual clusters

INDIVIDUAL CLUSTERS	MEAN	Std	Clust 1	Clust 2	Clust 3	Clust 4	Clust 5
Amplitudes	0,2	0,04	0,24	0,23	0,18	0,16	0,16
Volume Cluster (mm3)	0,004	0,007	$0,3.10^{-3}$	$0,3.10^{-3}$	0,016	0,002	$0,2.10^{-3}$
Clust. Axis 1 (mm) (a)	**298.10^{-3}**	**258.10^{-3}**	**154.10^{-3}**	**21610^{-3}**	**754.10^{-3}**	**227.10^{-3}**	**139.10^{-3}**
Clust. Axis 2 (mm) (b)	148.10^{-3}	118.10^{-3}	88.10^{-3}	55.10^{-3}	344.10^{-3}	171.10^{-3}	79.10^{-3}
Clust. Axis 3 (mm) (c)	35.10^{-3}	20.10^{-3}	25.10^{-3}	23.10^{-3}	63.10^{-3}	50.10^{-3}	15.10^{-3}
Clust. MPSphericity idx	0,33	0,06	0,36	0,36	0,25	0,40	0,27
Clust. Obl-Prol. Idx	6,3	15,0	0,3	30,1	11,1	-8,4	-1,6
Clust. Angle Axis1 / AP (deg)	81,7	11,5	84,4	90,4	82,8	61,9	89,2

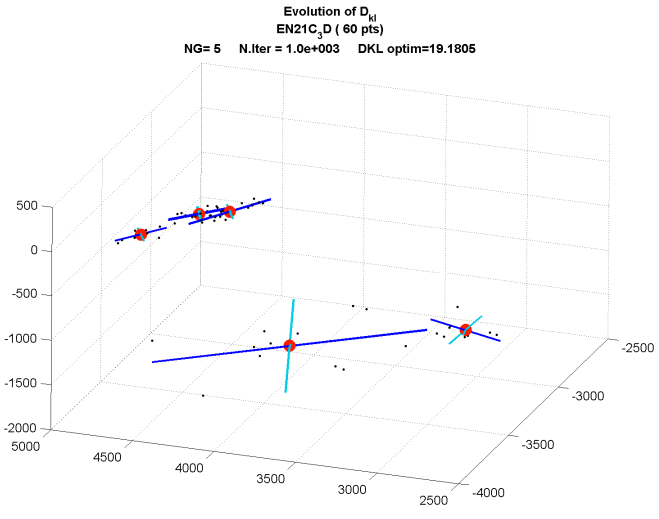

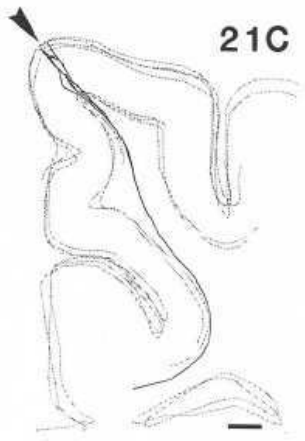

Fig. 122/ Clustering analysis results for axon EN21C.

Clusters Analysis — EN22B

ORIGIN AREA A17

NG model	6
Sum of volumes of all Clusters (mm^3)	0,063
Sum vol. All Clusters (Amp) (mm^3)	**0,021**
Vol. Ellips.Centres (NG>3) (mm^3)	**1,00**
Ell_C Axis 1 (mm)	**1,08**
Ell_C Axis 2 (mm)	0,40
Ell_C Axis 3 (mm)	0,28
Ell_C Obl-Prol. Idx	13,3
Ell_C MP Sphericity idx	0,56
Ell_C Angle Axis 1 / AP (deg)	36,2
Vol. Ellipsoid/Sum Vol. Clust(amp)	45

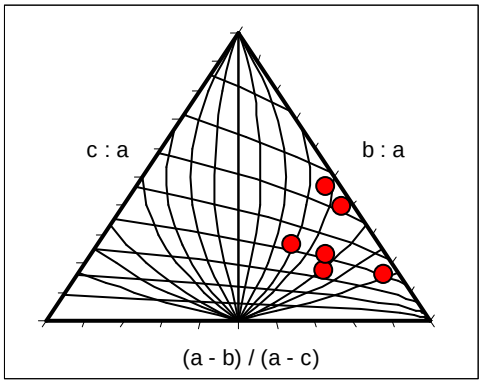

anisotropy indexes
of individual clusters

INDIVIDUAL CLUSTERS	MEAN	Std	Clust 1	Clust 2	Clust 3	Clust 4	Clust 5	Clust 6
Amplitudes	**0,16**	**0,14**	**0,41**	**0,24**	**0,12**	**0,10**	**0,09**	**0,03**
Volume Cluster (mm3)	**0,01**	**0,01**	**0,045**	**0,006**	**0,003**	**0,003**	**0,005**	**0,4.10-3**
Clust. Axis 1 (mm) (a)	**412.10^{-3}**	**241.10^{-3}**	**798.10^{-3}**	**582.10^{-3}**	**371.10^{-3}**	**252.10^{-3}**	**340.10^{-3}**	**126.10^{-3}**
Clust. Axis 2 (mm) (b)	149.10^{-3}	85.10^{-3}	309.10^{-3}	116.10^{-3}	133.10^{-3}	107.10^{-3}	167.10^{-3}	63.10^{-3}
Clust. Axis 3 (mm) (c)	98.10^{-3}	45.10^{-3}	185.10^{-3}	92.10^{-3}	64.10^{-3}	99.10^{-3}	89.10^{-3}	58.10^{-3}
Clust. MPSphericity idx	0,57	0,12	0,52	0,50	0,43	0,71	0,52	0,75
Clust. Obl-Prol. Idx	14,1	7,5	12,7	28,3	15,7	11,3	7,2	9,2
Clust. Angle Axis1 / AP (deg)	45,8	25,4	88,3	49,8	55,3	38,8	15,2	27,5

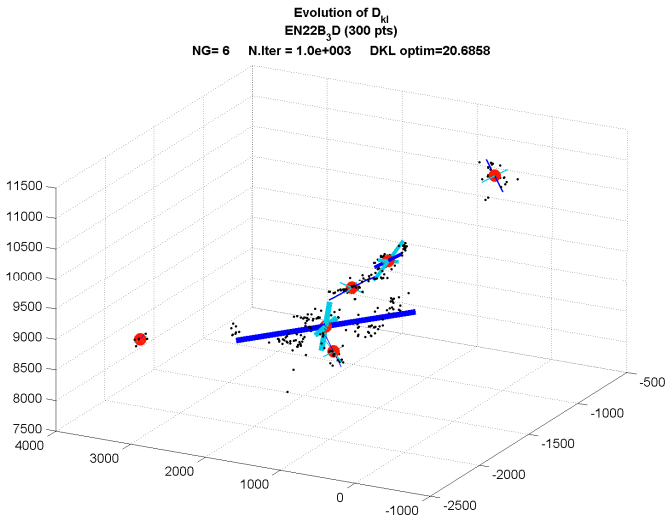

Fig. 123/ Clustering analysis results for axon EN22B.

Clusters Analysis — EN22D

ORIGIN AREA A17

NG model	4
Sum of volumes of all Clusters (mm^3)	0,188
Sum vol. All Clusters (Amp) (mm^3)	**0,049**
Vol. Ellips.Centres (NG>3) (mm^3)	**0,498**
Ell_C Axis 1 (mm)	**0,50**
Ell_C Axis 2 (mm)	0,43
Ell_C Axis 3 (mm)	0,28
Ell_C Obl-Prol. Idx	-36,0
Ell_C MP Sphericity idx	0,72
Ell_C Angle Axis 1 / AP (deg)	35,0
Vol. Ellipsoid/Sum Vol. Clust(amp)	14

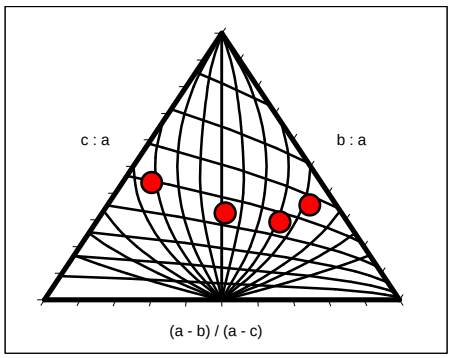

anisotropy indexes
of individual clusters

INDIVIDUAL CLUSTERS	MEAN	Std	Clust 1	Clust 2	Clust 3	Clust 4
Amplitudes	**0,25**	**0,13**	**0,44**	**0,22**	**0,16**	**0,16**
Volume Cluster (mm3)	**0,047**	**0,023**	**0,054**	**0,042**	**0,074**	**0,017**
Clust. Axis 1 (mm) (a)	**605.10^{-3}**	**181.10^{-3}**	**709.10^{-3}**	**474.10^{-3}**	**806.10^{-3}**	**431.10^{-3}**
Clust. Axis 2 (mm) (b)	352.10^{-3}	71.10^{-3}	304.10^{-3}	434.10^{-3}	388.10^{-3}	281.10^{-3}
Clust. Axis 3 (mm) (c)	208.10^{-3}	49.10^{-3}	251.10^{-3}	207.10^{-3}	235.10^{-3}	140.10^{-3}
Clust. MPSphericity idx	0,59	0,05	0,66	0,59	0,56	0,54
Clust. Obl-Prol. Idx	2,8	8,4	10,8	-8,0	7,9	0,4
Clust. Angle Axis1 / AP (deg)	68,8	15,1	81,3	46,9	71,1	75,9

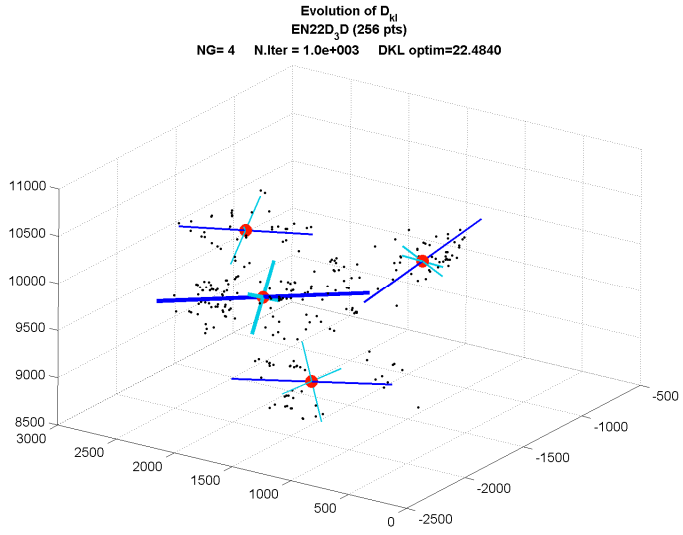

Fig. 124/ Clustering analysis results for axon EN22D.

Clusters Analysis — EN22E

ORIGIN AREA **A17**

NG model	1
Sum of volumes of all Clusters (mm^3)	0,051
Sum vol. All Clusters (Amp) (mm^3)	**0,051**
Vol. Ellips.Centres (NG>3) (mm^3)	0
Ell_C Axis 1 (mm)	0
Ell_C Axis 2 (mm)	0
Ell_C Axis 3 (mm)	0
Ell_C Obl-Prol. Idx	0
Ell_C MP Sphericity idx	0
Ell_C Angle Axis 1 / AP (deg)	0
Vol. Ellipsoid/Sum Vol. Clust(amp)	1,1

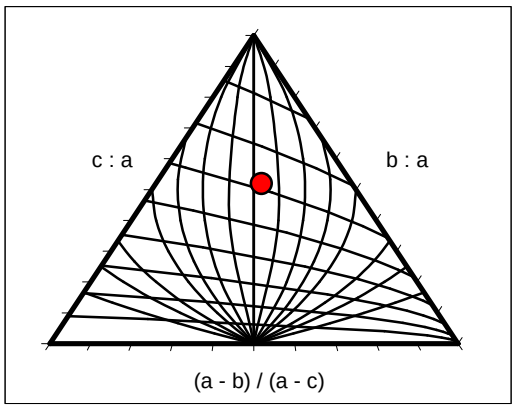

anisotropy indexes
of individual cluster

INDIVIDUAL CLUSTER	MEAN
Amplitudes	**1**
Volume Cluster (mm3)	**0,051**
Clust. Axis 1 (mm) (a)	**510.10^{-3}**
Clust. Axis 2 (mm) (b)	378.10^{-3}
Clust. Axis 3 (mm) (c)	265.10^{-3}
Clust. MPSphericity idx	0,71
Clust. Obl-Prol. Idx	0,7
Clust. Angle Axis1 / AP (deg)	78,3

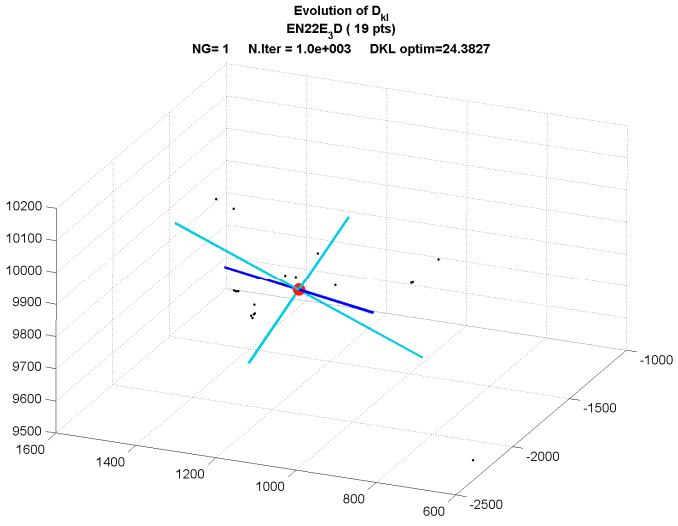

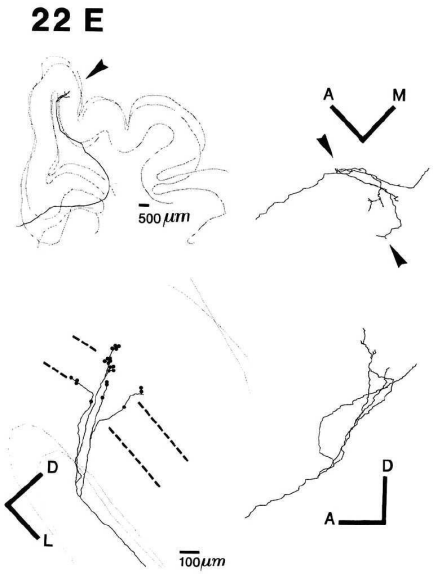

Fig. 125/ Clustering analysis results for axon EN22E.

PART B

Morphological characterization of the MD group;

Comparison with the reference NR group

Clusters Analysis	BMOW12
NG model	4
Sum of volumes of all Clusters (mm^3)	1,39
Sum vol. All Clusters (Amp) (mm^3)	**0,392**
Vol. Ellips.Centres (if NG>3) (mm^3)	**0,721**
Ell_C Axis 1 (mm)	**2,56**
Ell_C Axis 2 (mm)	0,41
Ell_C Axis 3 (mm)	0,08
Ell_C Obl-Prol. Idx	111
Ell_C MP Sphericity idx	0,19
Ell_C Angle Axis 1 / AP (deg)	61,4
Vol. Ellipsoid/Sum Vol. Clust(amp)	10,6

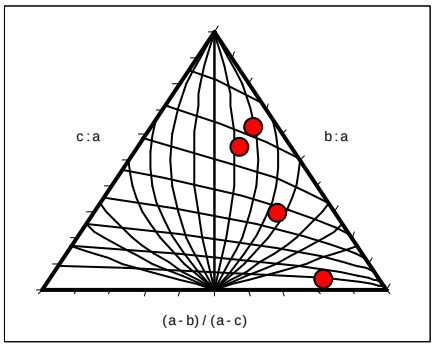

anisotropy indexes
of individual clusters

INDIVIDUAL CLUSTERS	MEAN	Std	Clust 1	Clust 2	Clust 3	Clust 4
Amplitudes	**0,25**	**0,22**	**0,52**	**0,32**	**0,11**	**0,03**
Volume Cluster (mm3)	**0,347**	**0,36**	**0,524**	**0,086**	**0,776**	**0,001**
Clust. Axis 1 (mm) (a)	**1,010**	**571.10^{-3}**	**1,060**	**609.10^{-3}**	**1,793**	**564.10^{-3}**
Clust. Axis 2 (mm) (b)	523.10^{-3}	325.10^{-3}	741.10^{-3}	423.10^{-3}	821.10^{-3}	109.10^{-3}
Clust. Axis 3 (mm) (c)	386.10^{-3}	279.10^{-3}	664.10^{-3}	334.10^{-3}	527.10^{-3}	19.10^{-3}
Clust. MPSphericity idx	0,58	0,28	0,82	0,75	0,57	0,18
Clust. Obl-Prol. Idx	29	46	4,9	3,1	9,1	99
Clust. Angle Axis1 / AP (deg)	57,9	17,6	58,8	59,8	35,0	78,0

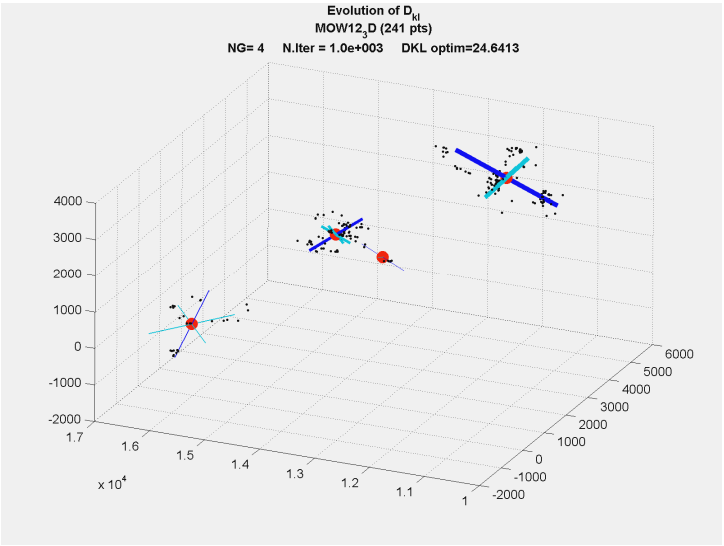

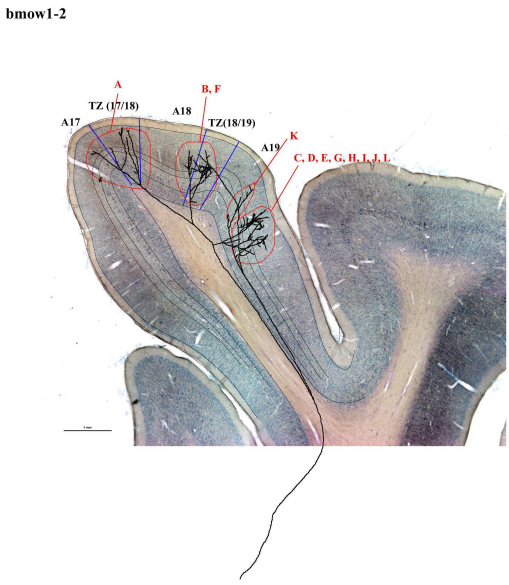

Fig. 126/ Clustering analysis results for axon BMOW12.

Clusters Analysis	BMOW21
NG model	**9**
Sum of volumes of all Clusters (mm^3)	0,110
Sum vol. All Clusters (Amp) (mm^3)	**0,013**
Vol. Ellips.Centres (if NG>3) (mm^3)	**1,18**
Ell_C Axis 1 (mm)	**0,98**
Ell_C Axis 2 (mm)	0,50
Ell_C Axis 3 (mm)	0,30
Ell_C Obl-Prol. Idx	66,6
Ell_C MP Sphericity idx	0,56
Ell_C Angle Axis 1 / AP (deg)	75,1
Vol. Ellipsoid/Sum Vol. Clust(amp)	**100**

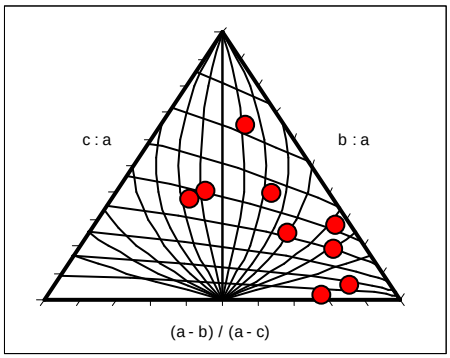

anisotropy indexes
of individual clusters

INDIVIDUAL CLUSTERS	MEAN	Std	Clust 1	Clust 2	Clust 3	Clust 4	Clust 5	Clust 6	Clust 7	Clust 8	Clust 9
Amplitudes	0,11111	0,061098	0,21	0,18	0,14	0,11	0,09	0,08	0,07	0,04	0,04
Volume Cluster (mm3)	0,012	0,015	0,014	0,006	0,014	0,005	0,048	0,019	0,002	$0,04.10^{-3}$	$0.04.10^{-3}$
Clust. Axis 1 (mm) (a)	$\mathbf{357.10^{-3}}$	$\mathbf{124.10^{-3}}$	$\mathbf{400.10^{-3}}$	$\mathbf{272.10^{-3}}$	$\mathbf{502.10^{-3}}$	$\mathbf{396.10^{-3}}$	$\mathbf{548.10^{-3}}$	$\mathbf{342.10^{-3}}$	$\mathbf{361.10^{-3}}$	$\mathbf{225.10^{-3}}$	$\mathbf{163.10^{-3}}$
Clust. Axis 2 (mm) (b)	182.10^{-3}	122.10^{-3}	223.10^{-3}	203.10^{-3}	219.10^{-3}	124.10^{-3}	426.10^{-3}	259.10^{-3}	101.10^{-3}	51.10^{-3}	27.10^{-3}
Clust. Axis 3 (mm) (c)	111.10^{-3}	77.10^{-3}	156.10^{-3}	109.10^{-3}	125.10^{-3}	108.10^{-3}	206.10^{-3}	221.10^{-3}	66.10^{-3}	4.10^{-3}	8.10^{-3}
Clust. MPSphericity idx	0,51	0,21	0,65	0,59	0,52	0,61	0,56	0,82	0,49	0,10	0,25
Clust. Obl-Prol. Idx	31	55	5,7	-1,9	9,9	16,2	-3,8	2,8	20	167	70
Clust. Angle Axis1 / AP (deg)	52,3	35,3	58,4	56,6	108,1	8,3	6,0	65,3	96,9	32,3	38,8

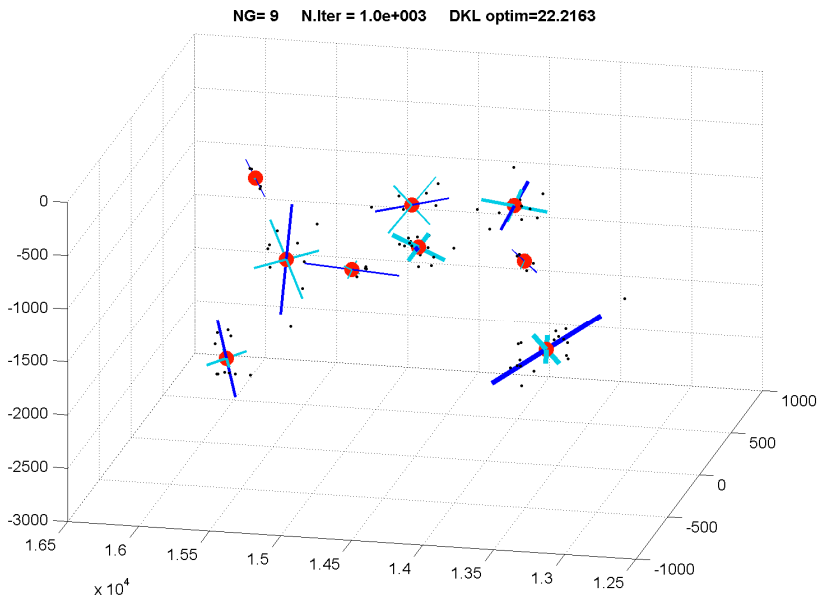

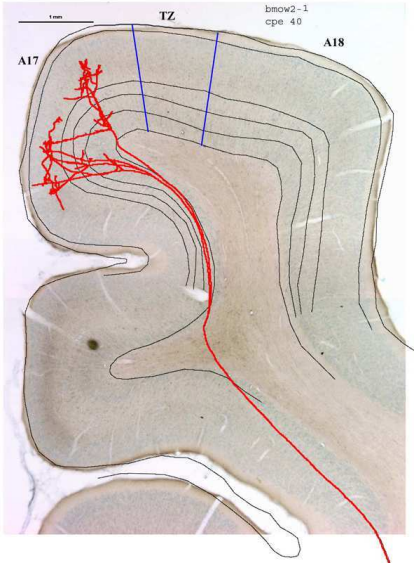

Fig. 127/ Clustering analysis results for axon BMOW21.

Clusters Analysis	BMOW23
NG model	**9**
Sum of volumes of all Clusters (mm^3)	0,006
Sum vol. All Clusters (Amp) (mm^3)	**0,001**
Vol. Ellips.Centres (if NG>3) (mm^3)	**1,74**
Ell_C Axis 1 (mm)	**1,85**
Ell_C Axis 2 (mm)	0,39
Ell_C Axis 3 (mm)	0,29
Ell_C Obl-Prol. Idx	27,2
Ell_C MP Sphericity idx	0,49
Ell_C Angle Axis 1 / AP (deg)	19,1
Vol. Ellipsoid/Sum Vol. Clust(amp)	1395

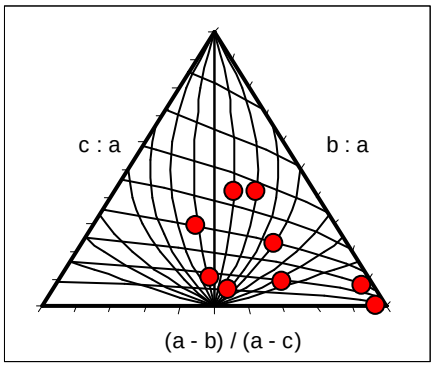

anisotropy indexes
of individual clusters

INDIVIDUAL CLUSTERS	MEAN	Std	Clust 1	Clust 2	Clust 3	Clust 4	Clust 5	Clust 6	Clust 7	Clust 8	Clust 9
Amplitudes	**0,11111**	**0,072688**	**0,22**	**0,20**	**0,17**	**0,12**	**0,06**	**0,06**	**0,05**	**0,05**	**0,05**
Volume Cluster (mm3)	$0,7.10^{-3}$	$0,8.10^{-3}$	$1,7.10^{-3}$	$2,4.10^{-3}$	$0,3.10^{-3}$	$0,8.10^{-3}$	$0,07.10^{-3}$	$0,3.10^{-3}$	$0,5.10^{-3}$	$0,2.10^{-3}$	$0,004.10^{-3}$
Clust. Axis 1 (mm) (a)	**213.10^{-3}**	**73.10^{-3}**	**188.10^{-3}**	**214.10^{-3}**	**121.10^{-3}**	**204.10^{-3}**	**129.10^{-3}**	**333.10^{-3}**	**207.10^{-3}**	**193.10^{-3}**	**322.10^{-3}**
Clust. Axis 2 (mm) (b)	80.10^{-3}	41.10^{-3}	121.10^{-3}	125.10^{-3}	84.10^{-3}	89.10^{-3}	45.10^{-3}	36.10^{-3}	117.10^{-3}	94.10^{-3}	9.10^{-3}
Clust. Axis 3 (mm) (c)	35.10^{-3}	30.10^{-3}	78.10^{-3}	89.10^{-3}	35.10^{-3}	46.10^{-3}	11.10^{-3}	25.10^{-3}	21.10^{-3}	11.10^{-3}	1.10^{-3}
Clust. MPSphericity idx	0,38	0,20	0,64	0,66	0,50	0,48	0,28	0,37	0,26	0,19	0,08
Clust. Obl-Prol. Idx	150	410	2,4	5,1	-2,4	9,9	24,1	61,5	-1,3	7,3	1243
Clust. Angle Axis1 / AP (deg)	71,0	29,8	107,4	108,1	13,0	71,3	57,8	87,9	82,1	51,9	59,3

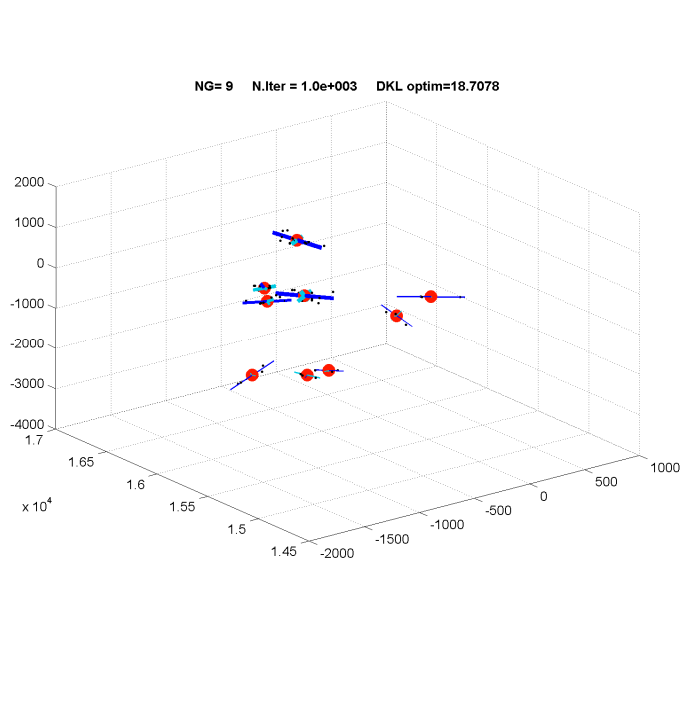

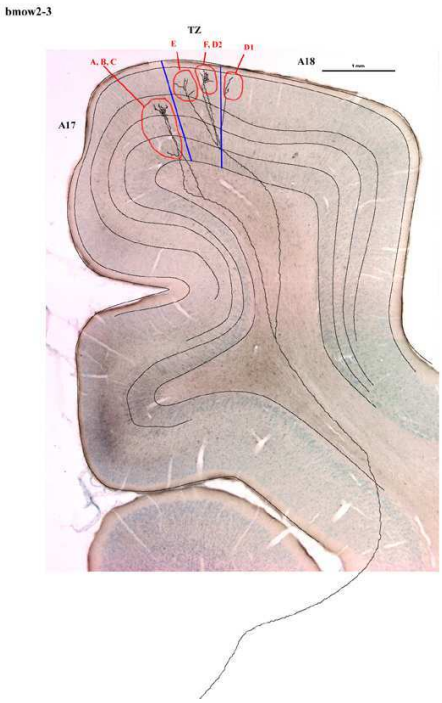

Fig. 128/ Clustering analysis results for axon BMOW23.

Clusters Analysis	BMO17A1
NG model	**6**
Sum of volumes of all Clusters (mm^3)	0,002
Sum vol. All Clusters (Amp) (mm^3)	**0,0004**
Vol. Ellips.Centres (if NG>3) (mm^3)	**0,325**
Ell_C Axis 1 (mm)	**0,86**
Ell_C Axis 2 (mm)	0,32
Ell_C Axis 3 (mm)	0,14
Ell_C Obl-Prol. Idx	14,9
Ell_C MP Sphericity idx	0,42
Ell_C Angle Axis 1 / AP (deg)	62,8
Vol. Ellipsoid/Sum Vol. Clust(amp)	928

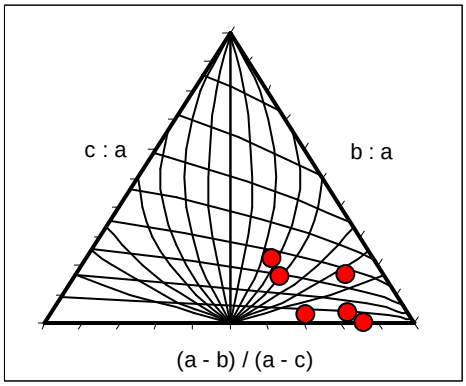

anisotropy indexes
of individual clusters

INDIVIDUAL CLUSTERS	MEAN	Std	Clust 1	Clust 2	Clust 3	Clust 4	Clust 5	Clust 6
Amplitudes	**0,16**	**0,07**	**0,24**	**0,24**	**0,20**	**0,12**	**0,10**	**0,08**
Volume Cluster (mm3)	$0,3.10^{-3}$	$0,4.10^{-3}$	$1,2.10^{-3}$	$0,3.10^{-3}$	$0,1.10^{-3}$	$0,002.10^{-3}$	$0,1.10^{-3}$	$0,2.10^{-3}$
Clust. Axis 1 (mm) (a)	**254.10^{-3}**	**209.10^{-3}**	**260.10^{-3}**	**150.10^{-3}**	**230.10^{-3}**	**64.10^{-3}**	**658.10^{-3}**	**162.10^{-3}**
Clust. Axis 2 (mm) (b)	68.10^{-3}	36.10^{-3}	115.10^{-3}	74.10^{-3}	70.10^{-3}	12.10^{-3}	93.10^{-3}	43.10^{-3}
Clust. Axis 3 (mm) (c)	18.10^{-3}	17.10^{-3}	41.10^{-3}	33.10^{-3}	6.10^{-3}	2.10^{-3}	2.10^{-3}	26.10^{-3}
Clust. MPSphericity idx	0,27	0,18	0,38	0,46	0,13	0,18	0,03	0,46
Clust. Obl-Prol. Idx	245	498	10,1	6,5	78	93	1259	22
Clust. Angle Axis1 / AP (deg)	64,2	33,1	88,9	76,5	97,6	63,6	53,7	4,9

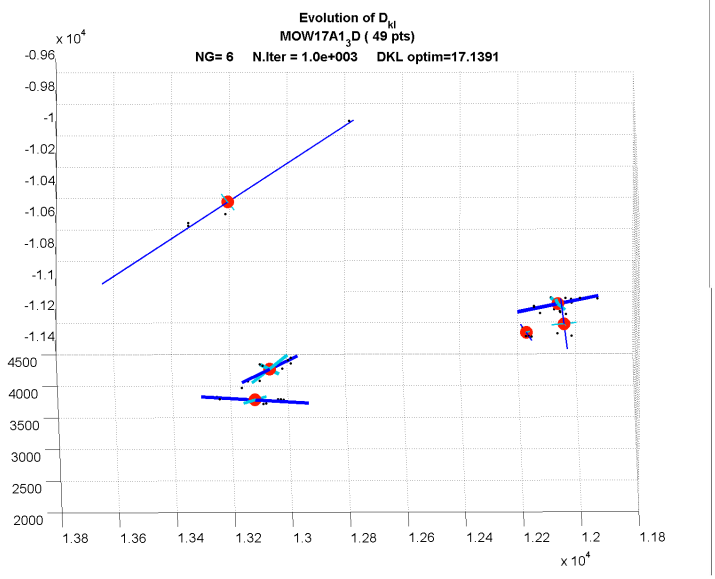

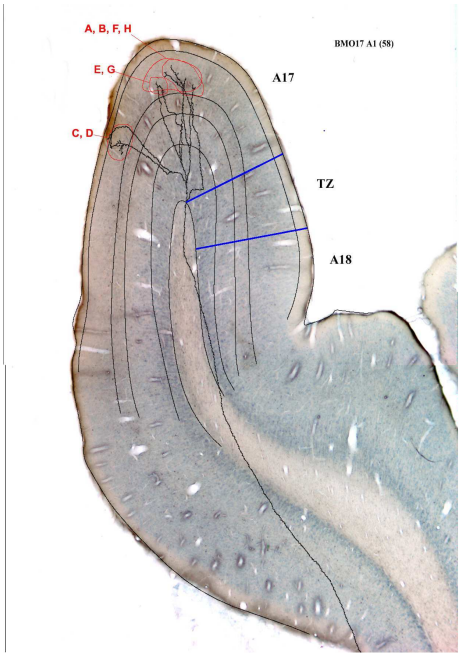

Fig. 129/ Clustering analysis results for axon BMO17A1

Clusters Analysis	BMO17A2
NG model	8
Sum of volumes of all Clusters (mm^3)	0,054
Sum vol. All Clusters (Amp) (mm^3)	**0,011**
Vol. Ellips.Centres (if NG>3) (mm^3)	**2,29**
Ell_C Axis 1 (mm)	**1,16**
Ell_C Axis 2 (mm)	0,65
Ell_C Axis 3 (mm)	0,37
Ell_C Obl-Prol. Idx	46,3
Ell_C MP Sphericity idx	0,57
Ell_C Angle Axis 1 / AP (deg)	65,6
Vol. Ellipsoid/Sum Vol. Clust(amp)	216

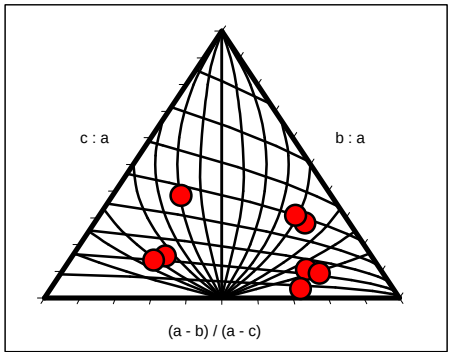

anisotropy indexes of clusters

INDIVIDUAL CLUSTERS	MEAN	Std	Clust 1	Clust 2	Clust 3	Clust 4	Clust 5	Clust 6	Clust 7	Clust 8
Amplitudes	0,12	0,09	0,33	0,18	0,14	0,09	0,06	0,06	0,06	0,05
Volume Cluster (mm3)	$7,7.10^{-3}$	$7,8.10^{-3}$	0,225	$7,1.10^{-3}$	0,129	$1,1.10^{-3}$	$0,3.10^{-3}$	$2,0.10^{-3}$	$8,0.10^{-3}$	$0.4. .10^{-3}$
Clust. Axis 1 (mm) (a)	**364.10^{-3}**	**194.10^{-3}**	**582.10^{-3}**	**285.10^{-3}**	**453.10^{-3}**	**218.10^{-3}**	**311.10^{-3}**	**260.10^{-3}**	**686.10^{-3}**	**112.10^{-3}**
Clust. Axis 2 (mm) (b)	167.10^{-3}	69.10^{-3}	236.10^{-3}	229.10^{-3}	202.10^{-3}	167.10^{-3}	92.10^{-3}	$192 .10^{-3}$	185.10^{-3}	35.10^{-3}
Clust. Axis 3 (mm) (c)	71.10^{-3}	59.10^{-3}	163.10^{-3}	109.10^{-3}	140.10^{-3}	31.10^{-3}	11.10^{-3}	40.10^{-3}	63.10^{-3}	12.10^{-3}
Clust. MPSphericity idx	0,39	0,16	0,57	0,56	0,59	0,29	0,16	0,32	0,31	0,33
Clust. Obl-Prol. Idx	13,9	26	11,6	-4,8	9,6	-15,7	65	-12,0	32,9	24,8
Clust. Angle Axis1 / AP (deg)	81,0	24,5	63,3	99,7	108,3	89,6	95,9	55,1	40,6	95,9

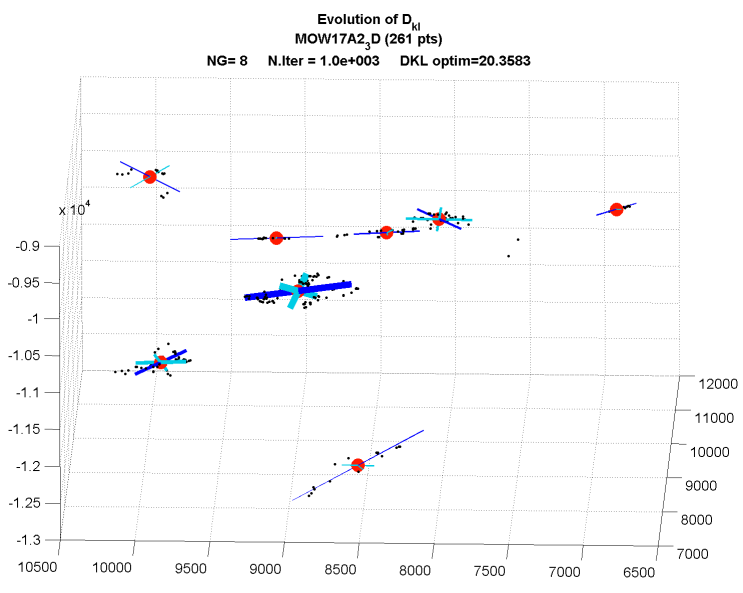

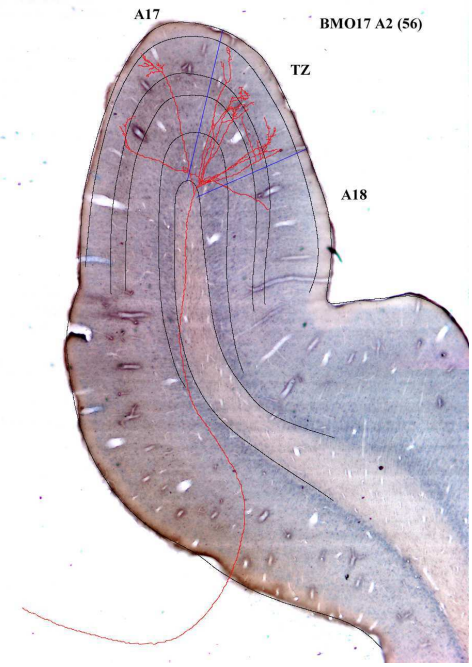

Fig. 130/ Clustering analysis results for axon BMO17A2

Clusters Analysis	BMO17A3
NG model	**10**
Sum of volumes of all Clusters (mm^3)	0,046
Sum vol. All Clusters (Amp) (mm^3)	**0,005**
Vol. Ellips.Centres (if NG>3) (mm^3)	**0,951**
Ell_C Axis 1 (mm)	**0,97**
Ell_C Axis 2 (mm)	0,57
Ell_C Axis 3 (mm)	0,21
Ell_C Obl-Prol. Idx	1,31
Ell_C MP Sphericity idx	0,43
Ell_C Angle Axis 1 / AP (deg)	61,9
Vol. Ellipsoid/Sum Vol. Clust(amp)	196

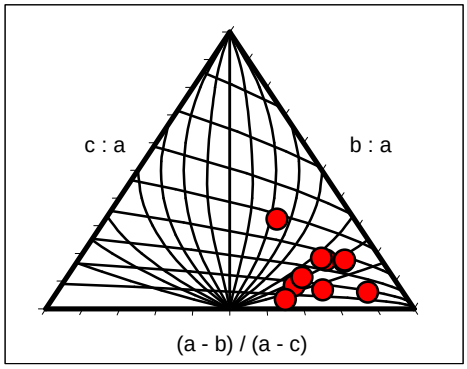

anisotropy indexes of clusters

INDIVIDUAL CLUSTERS	MEAN	Std	Clust 1	Clust 2	Clust 3	Clust 4	Clust 5	Clust 6	Clust 7	Clust 8	Clust 9	Clust 10
Amplitudes	0,1	0,06	0,26	0,13	0,09	0,09	0,09	0,08	0,06	0,06	0,05	0,04
Volume Cluster (mm3)	$4,6.10^{-3}$	$5,0.10^{-3}$	$5,2.10^{-3}$	0,181	$0,7.10^{-3}$	$3,2.10^{-3}$	$6,3.10^{-3}$	$2,3.10^{-3}$	$3,1.10^{-3}$	$0,2.10^{-3}$	$4,4.10^{-3}$	$2,5.10^{-3}$
Clust. Axis 1 (mm) (a)	457.10^{-3}	179.10^{-3}	312.10^{-3}	763.10^{-3}	250.10^{-3}	408.10^{-3}	466.10^{-3}	426.10^{-3}	694.10^{-3}	229.10^{-3}	424.10^{-3}	596.10^{-3}
Clust. Axis 2 (mm) (b)	146.10^{-3}	64.10^{-3}	166.10^{-3}	275.10^{-3}	69.10^{-3}	112.10^{-3}	159.10^{-3}	156.10^{-3}	108.10^{-3}	64.10^{-3}	139.10^{-3}	218.10^{-3}
Clust. Axis 3 (mm) (c)	57.10^{-3}	29.10^{-3}	100.10^{-3}	86.10^{-3}	43.10^{-3}	69.10^{-3}	84.10^{-3}	35.10^{-3}	41.10^{-3}	15.10^{-3}	74.10^{-3}	19.10^{-3}
Clust. MPSphericity idx	0,37	0,13	0,58	0,32	0,48	0,47	0,45	0,26	0,28	0,25	0,45	0,14
Clust. Obl-Prol. Idx	27,9	17	5,8	19	21	21	16	22	66	39	18	47
Clust. Angle Axis1 / AP (deg)	**65,7**	**22,6**	**48,7**	**101,8**	**81,3**	**42,2**	**43,0**	**81,2**	**82,1**	**83,2**	**37,9**	**55,4**

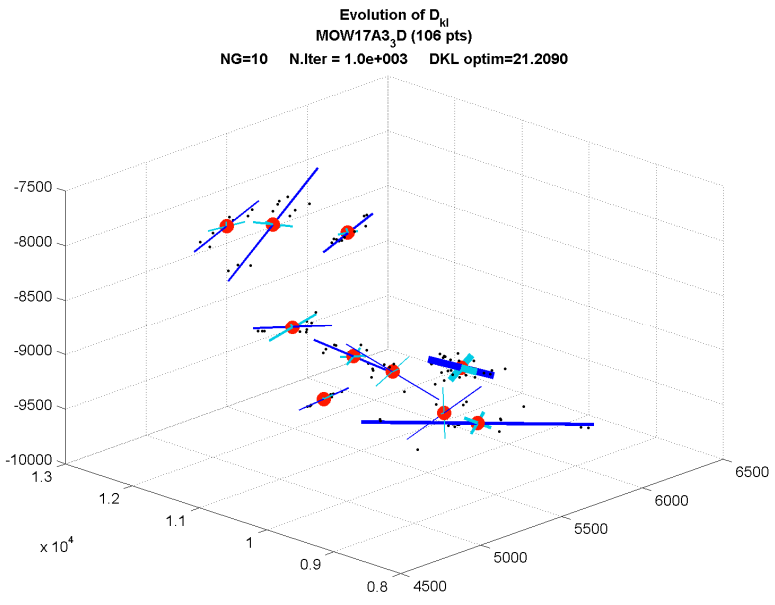

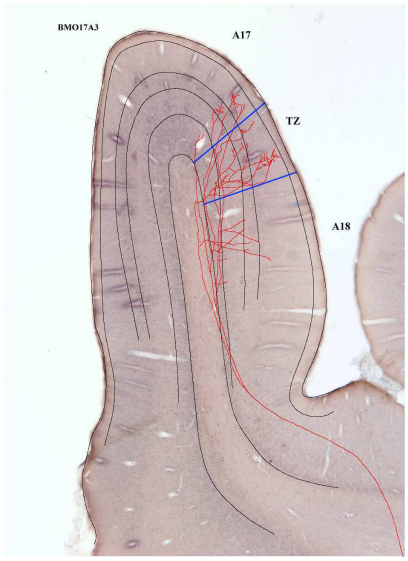

Fig. 131/ Clustering analysis results for axon BMO17A3

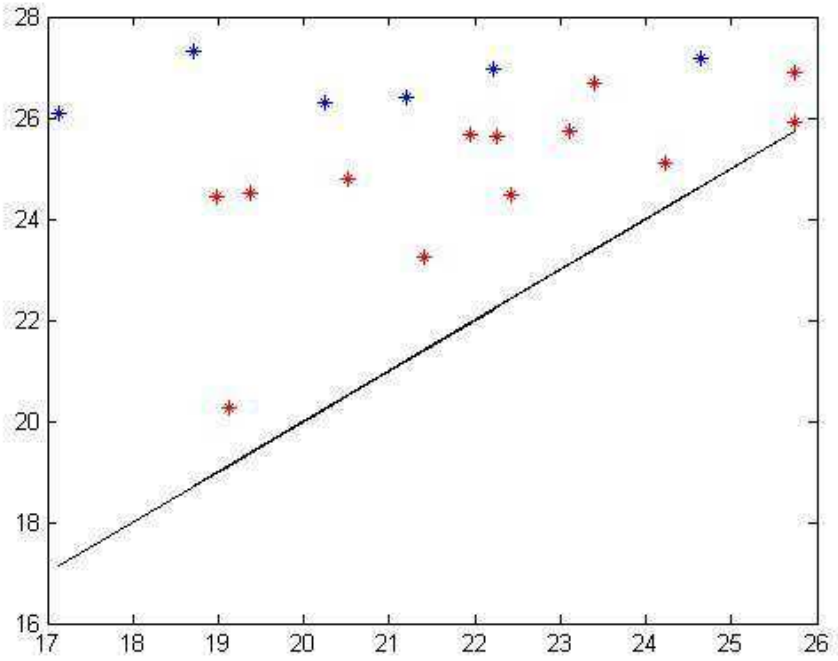

Fig. 132/. Kullback-Leibler Distances differences between single and multi-Gaussian models. X axis report D_{KL} values obtained from optimized model (β=0.3) for each distribution. Y axis report the D_{KL} values obtained for single Gaussian model. The vertical distance from the diagonal (black line) gives an estimation of the D_{KL} gain from single to multiple Gaussian models. (red star: NR group, mean difference 2.7 +/- 1.7 bits; blue stars: MD group, mean difference 5.4 +/- 2.7 bits).

Table 7: Means and standard deviations of clustering analysis for NR and MD groups; results of T-test.

Clusters Analysis	**NR**		**MD**				
	mean	Std	**Mean**	Std	**MD/NR**	T-Test	significance
NG model	**3,73**	2,02	**7,67**	2,25	**2,05**	**1**	$2,67.10^{-3}$
Sum of volumes of all Clusters (mm^3)	**0,242**	0,48	**0,268**	0,55	1,11		
Sum vol. All Clusters (Amp) (mm^3)	**0,145**	0,32	**0,070**	0,16	0,48		
Vol. Ellips.Centres (mm^3)	**0,438**	0,51	**1,20**	0,71	**2,74**	**1**	$4,28.10^{-2}$
Ell_C Axis 1 (mm)	**0,929**	0,46	**1,40**	0,67	**1,51**	**1**	$4,26.10^{-2}$
Ell_C Axis 2 (mm)	**0,421**	0,17	**0,476**	0,12	1,13		
Ell_C Axis 3 (mm)	**0,138**	0,10	**0,236**	0,11	1,71		
Ell_C Obl-Prol. Idx	**7,5**	36	**27,6**	42	3,64		
Ell_C MP Sphericity idx	**0,35**	0,20	**0,44**	0,14	1,26		
Ell_C Angle Axis 1 / AP (deg)	**54,7**	32,4	**57,7**	19,6	1,05		
Vol. Ellipsoid/Sum Vol. Clust(amp)	**40,1**	77,3	**475**	557	**11,8**	**1**	$4,73.10^{-2}$

Results and comparison

As a justification of the clustering model, the Kullback-Leibler distances gains obtained from Gaussian mixtures compared with single Gaussian models (ellipsoid approximation) are shown on fig 132. Whereas the fitness of the mixture model on the NR population were already demonstrated to be better than those of single Gaussians with a mean D_{KL} difference of 2.7 +/- 1.7 bits (cf Ch3, Fig.108), the mixture model is shown here to be much more efficient again on the MD population with a mean D_{KL} difference of 5.4 +/- 2.7 bits. This difference confirms the limitations of the single Gaussian model and the necessity of using local decomposition methods such as clustering to reach a fine description of the spatial organization of callosal terminals. This description is shown to be more relevant again for terminals distributions from the MD group revealing their more scattered organization as shown below.

The Table 7 reports the means and the values of the standard deviations of global attributes for both populations. The same statistical Welch's *T*-test as the one used to compare the parameters defined through the ellipsoid method (Cf. Ch2, Results) was applied to detect significant differences between the two populations and relevant ones are highlighted in red in the table. The MD/NR column report means ratios.

The most relevant difference concerns the numbers of clusters identified for each terminal distribution. Whereas 13/15 axons from the NR group were found with 5 clusters or less, including 7 with 3 clusters or less, the great majority (5/6) of axons from the MD group are analyzed with more than 6 clusters with 3 of them showing 9 clusters or more (Cf Fig 133). This leads to a mean value of 3.7+/- 2 clusters for the NG group and 7.7 +/- 2 clusters for the MD group. The T-test was successfully passed with very good significance ($2.7.10^{-3}$) demonstrating that axons from the MD group are clearly much more clusterized (two times by means) than those from the NR group.

Submitted to large variability, the volume of the weighted centres distribution moves however in mean from 0.44 +/0.5 mm^3 for NR axons to 1.2 +/-0.7 mm^3 for MD axons and its great elongation from 0.93 +/-0.5 mm to 1.40 +/-0.7 mm with good significance for both ($4.3\ 10^{-2}$), demonstrating again the wider global extension of axons from the MD group.

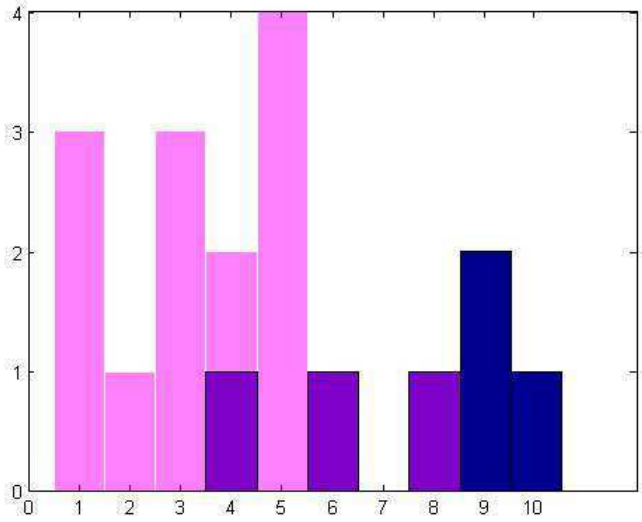

Fig. 133/ Number of Clusters identified by Gaussian mixtures models (β=0.3) for NR group (purple) and MD group (blue). The degree of clusterization is much more pronounced for axons obtained after early monocular deprivation.

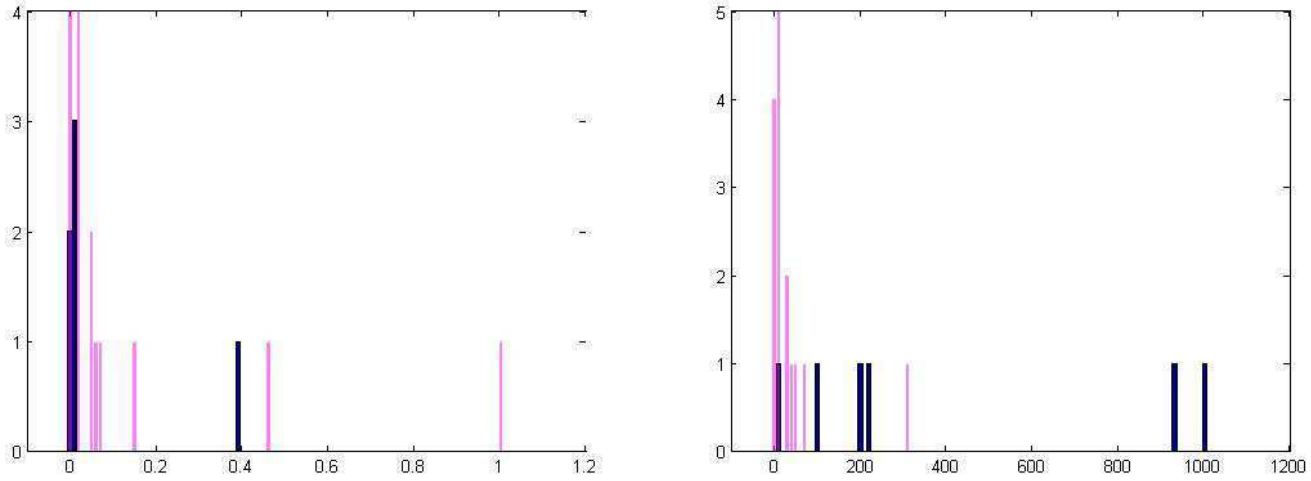

(a) (b)

Fig 134/ (a) Histogram of amplitude weighted sums of cluster volume occupied for each axons (unit:mm^3). (b) histogram of ratio between the initial ellipsoid volumes and the amplitude weighted sums of cluster volumes; (purple NR group, blue: MD group).

It is interesting to notice that the means of the overall volumes of clusters, whatever summing the full clusters volumes or the amplitude weighted volumes, do not show any significant differences. But a bias for smaller cluster is observed in mean in the MD group when the volumes as weighted by amplitudes (0.14 +/0.3 mm^3 for NR against 0.07+/0.2 mm^3 for MD) as shown also on Fig. 134(a). This bias can also be shown indirectly by looking to the ratios between the initial ellipsoid volume and the overall volume of clusters weighted by amplitudes. This measure shows a significant difference from NR to MD population indicating, if not smaller clusters, at least higher density for MD axons (see Fig. 134(b)).

In order to check these trends not only by mean but onto the overall cluster distribution, we grouped the volume and the relative density (amplitude/volume) of each cluster altogether for each population as shown onto Fig. 135. Both trends, indicating for clusters of axons from the MD group smaller volumes and a higher density, are visible on these histograms. But the differences between the NR and MD populations could not reach the significance level onto our data.

Others global attributes did not reflect significant difference and other particular spatial organization of individual clusters features has not been explored.

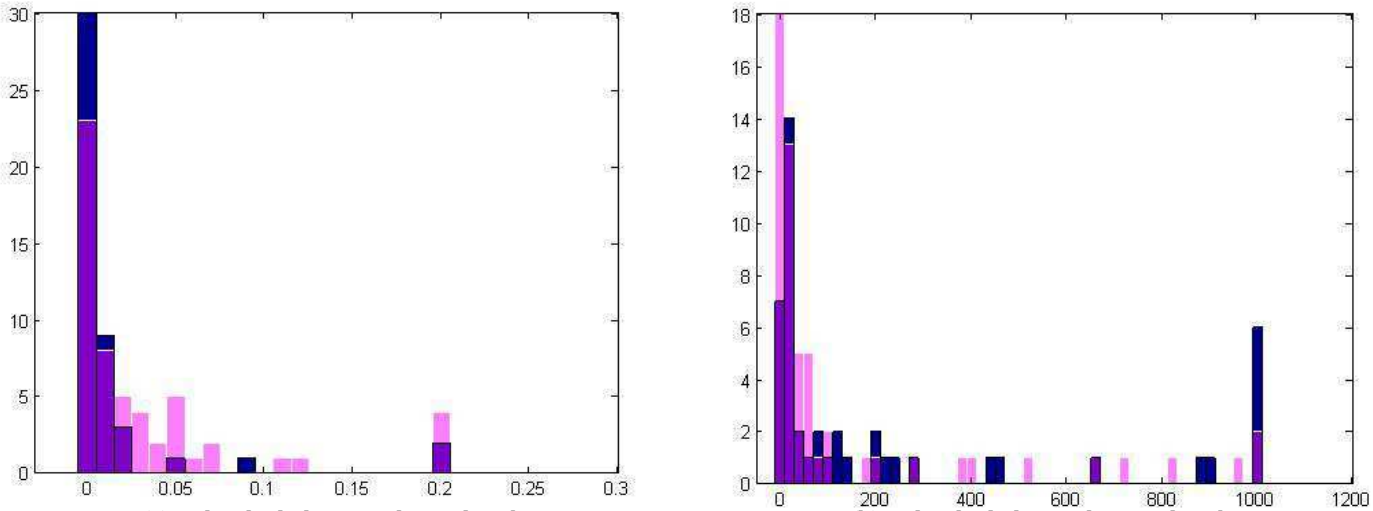

(a) individual cluster volume distribution (b) individual cluster density distribution

Fig. 135/ (a) histogram of individual cluster volumes (unit: mm^3); (b) histogram of relative density (amp/volume) of individuals clusters (unit: mm^{-3}). The histograms show the tendencies for cluster of MD axons to have smaller size and higher density than those observed from the NR group (purple NR group 56 clusters, blue: MD group, 46 cluster).

Discussion

The clustering procedure is a powerful method allowing access to many quantities used to describe the general organisation of a 3D distribution but also providing details about local organization of each subset or clusters. As every cluster is described by a local trivariate Gaussian distribution, each identified cluster could be assign geometrical quantities such as 3D elongations, volume, anisotropies and orientations allowing many rich possible descriptions of the synaptic spatial organisation. Although these attributes reflect important variability in both of our populations, further analysis need to be performed into this direction to explore the specificity of individual clusters organization such as shapes trends (as shown in triangular diagrams) or orientations trends regarding to cortical structures like TZ or the interlayer surfaces. Such kind of description may help to reveal self-organisation rules such as observed for the orientation of elongated molecules in liquid crystals. Moreover the projection of individual clusters attributes onto the cortical surface might also reveal interesting mapping properties.

As for the results obtained from the ellipsoid approximation when performed directly onto terminal distributions, the volume and the great elongation of the weighted centres distributions of the MD group showed expansions of similar magnitudes (2.5 and 1.5 respectively). As the attributes can only be extracted from NR axons having more the 3 clusters, this analysis stress the differences between the two groups even for axons reflecting highest number of clusters. Moreover, the Ellipsoid/Cluster(amp) volume ratio mean increases by more than ten times between the NR and the MD group. As the volume of the initial ellipsoid was demonstrated to double from NR to MD, the jump of the volumes ratio reveals smaller size and/or higher density (more terminals by cluster) for clusters of axons from the MD group. Although weak, both trends for clusters of axons from MD group to have smaller size and higher density are visible on overall clusters distributions (fig. 135). Altogether, these observations support the global expansion hypothesis for MD axons as suggested in the Chapter 2.

Even if clustering features were not all explored, important differences were found on main descriptors such as the number of clusters, and spatial extension of the weighted centres distribution. We should notice that the clustering procedure was run with the likelihood penalty value set at its optimal value $\beta=0.3$, but any other values would have also lead to significant difference in the number of clusters between NR and MD populations with a mean difference of 3 clusters whatever $0.25 < \beta < 0.5$ (data not shown). This observation shows the robust characteristic of the higher degree of clusterization of MD axons whatever the mixture chosen for its description. The power of this method resides in its 3D analysis capability to segregate terminal clusters whereas a direct visual inspection can only estimate this feature by projection, even through different angles of view, and remains very subjective.

Altogether, principal results from Ch2 and Ch3 demonstrate the wider spatial extension of terminals of MD axons, their higher degree of clusterization and a possible tendency for higher density of terminals. Regarding to the widely scattered organization of MD axonal structure, we may wonder if the original contralateral signal conveyed to all terminals arrives in synchrony to their post synaptic targets. To answer this question we performed spike propagation simulations through callosal axons structures with a compartmental model as shown in the following chapter.

CHAPITRE I.4

Effects of the morphology on the dispersion of temporal profiles of activation by simulations of spike propagation within 3D reconstructed callosal axons obtained after early monocular deprivation

---

Article :
L. FOUBERT, D. BENNEQUIN, J. DROULEZ and C. MILLERET. Simulation of spike propagation within 3D reconstructed abnormal callosal axons of cat visual cortex: does spatial dispersion lead to temporal dispersion?

The last chapters demonstrate the morphological differences between two populations of callosal axons obtained under normal condition of vision or after a development with early monocular deprivation. These latter ones showed not only wider tangential extension within the cortical structure but also a higher clustered organization. In order to estimate the spatio-temporal coupling between the axonal morphology and the signal transmission, we replicate the paradigm of spike propagation performed within normal callosal axons (Innocenti et al., 1994) under quite similar assumptions for seek of comparison. Even if a deeper examination of the complexity of the spike propagation properties in axons revealed the limitation of the model, our results showed that under these assumptions, the time dispersion of the callosal signal is not as large as suggested by the morphology. In particular, the implication of myelin sheet for most of callosal visual axons keeps the signal dispersion within a narrow time window, less than 2ms, compatible with functional and developmental synchronization hypothesis.

Simulation of spike propagation within 3D reconstructed abnormal callosal axons of the primary visual cortex: does spatial dispersion lead to temporal dispersion?

Luc FOUBERT[1], Daniel BENNEQUIN[2], Jacques DROULEZ[1], Chantal MILLERET[1]

1 Laboratoire de physiologie de la perception et de l'action, UMR CNRS 7124, Collège de France, 11 place Marcelin Berthelot, 75005 Paris, France.

2 Institut de Mathématiques - UMR CNRS 7586 Université Paris 7 Denis Diderot, 2 Place Jussieu, 75005 Paris

Abstract

This work provides results of numerical simulations of spike propagation within tridimensionnally reconstructed transcallosal axons obtained after early monocular deprivation in cat in order to test synchronisation hypothesis between terminations of an axonal structure. An abnormal widespread was previously reported for these structures. We imported the structural 3D reconstructed data (node's positions and axoplasm's diameters) to be interpreted under NEURON software to simulate single spike propagation. Inspite of the abnormal widespread dispersion of the axons under monocular visual experience, our results show that these morphological differences do not significantly widen the time dispersion of the initial controlateral signal between terminations in comparison with normal structures and most of the spikes distribution keeps confined within 2ms. Nevertheless, time delays imposed at ends of tiny collateral branches could not provide evidence for complete synchrony.

Keywords: Callosal connections, three-dimensional reconstruction, spike propagation, compartmental model, synchrony.

1. Introduction

The mammalian central nervous system is divided into two hemispheres. These hemispheres can communicate through neural fibres bundles and among these the corpus callosum is the most important one. The mammalian binocular visual system is organized in such a way to provide to primary cortical areas (A17 & A18) of each hemisphere, visual signals from the contralateral visual hemifield. In cats, visual information concerning the central vertical meridian is projected bilaterally around a 1mm wide strip, the transition zone (TZ) between A17 and A18 that contains a representation of the ipsilateral field (Payne, 1990). These cortical regions also receive callosal convergent inputs connected in a retinotopic correspondence with their contralateral area A17 or A18 (Olavarria, 1996). Developed under normal visual condition callosal connections terminate inside or near the transition zone and show relatively low tangential extension. Nevertheless, when developed under early monocular deprivation, the visual interhemispheric connections show wider morphologies with sometimes lateral extents far from the transition zone.

Neural time code is far being fully understood. However spike timing should play an important role during development as well as for visual processing. This study aims to answer the following question: does axon's morphology provide an important contribution to time dispersion of spikes between each end of the structure? Especially, we try to understand if the wide spatial dispersion of abnormal morphologies modifies the temporal dispersion of a single spike within a single callosal arbor. Answering this question will contribute to understand the relevance of axon's morphology for spike timing dependant activities such as axon selection and synapse stabilization during development. A retinal message initiated from one eye could be routed along two pathways, the first is projected through the direct retino-geniculo-cortical route and the second is projected to the contralateral cortex through the optic chiasm and projected back to the initial hemisphere along a callosal fibre. These two pathways finally converge into a same cortical area around the transition zone. The "uni-ocular hypothesis" (Olavarria, 2001) suggests that a developmental process tends to stabilize only circuits providing neural message in synchrony when following the two routes. It is thus necessary for each connection, including the callosal ones, to keep the coherence of the axonal message when feeding the post-synaptic units. One of our goals is to check this hypothesis on some stable abnormal morphologies.

Moreover this work aims to clarify the contribution of callosal connections for visual perceptive binding problem (von der Marlsbourg 1981; Singer 1989). Callosal reverberant circuits could generate interhemispheric synchronizations, only if the dispersion of the signal is small enough to establish and maintain stable constructive oscillations locked in phase. So, the aim of this study is to understand whether or not wider abnormal morphologies induce larger time dispersion.

This work makes echo to simulation studies performed on callosal structures obtained under normally reared visual conditions (Innocenti et al, 1994) whereas the present study is based on abnormally wider morphologies.

2. Material and methods

2.1 Experimental groups, tracer injection, staining method and 3D reconstruction

Axons reconstructed for this study were obtained from cats reared under early monocular deprivation. Eyelid suture was performed at 5 to 7 postnatal days, before natural eye opening (10 to 12 postnatal days). Anterograd tracer injection (biocytin) was performed on four months adult cats. Two sites of injection were chosen: the first was localized within the A17/A18 border (A9-L1.5). The second injection was done more medially in A17 (A4L1) where any callosal efferent have never been reported from normally reared animals. Histological procedures was performed to obtain 75µm thick frontal serial slices of brain after fixation and cryoprotection in a 30% sucrose solution and incubated at room temperature for 12 hours in an avidin peroxydase complex (ABC kit, 1/200 dilution into PBS solution with 1% of Trixon-X100). Second incubation was performed under di-aminobenzidin solution to stain peroxydase and amplified with nickel sulphate. One over two slices was stained with Nissl method for cortical layers identification. Observation of cortical layer thickness modification allowed cytoarchitectonic differentiation of primary visual cortex areas 17, 18 and A17/A18 border (Milleret et al. 1994). One should notice that the 17/18 border is not localized as a sharp edge but as a transition zone whose latero-medial extent on the cortical surface increases from posterior to anterior parts (Payne 1990). Adult cats show a 1.3 mm wide transition zone by mean. Optical microscopic observations of serial slices coupled with neurolucida© *(Microbrightfield Inc.)* tracing system provides three dimensional transcallosal axon's morphology thus reconstructed from their midline root until their terminations in the opposite to the injection site hemisphere. Histological procedures such as fixation, cryogenation and glassplates mount generally induce a 35-40% isotropic shrinkage and thus latter compensated on numerical data (Innocenti & al. 1994).

2.2 Morphological properties

Ellipsoid approximations allow characterizing the spatial extensions of the distribution of callosal terminals in terms of volume, elongations and cortical projection surface. Most of these parameters reports significant differences between normal reference population and

those grown under impaired visual experience. Especially, the cortical surfaces of the distributions were found to be two times greater in mean than those of the reference group. Moreover, clustering method based on Gaussian mixture models revealed the higher degree of clusterization of the axons terminals distribution. Regarding to this widely scattered organization of axonal structures, we wondered about its impact on the time dispersion of the contralateral signal.

2.3 *Numerical simulations*

As for the simulation method used for normally developed arbors, our simulation is based on the linear relation assumption between myelinated axon diameters and the spike velocity (Waxman and Bennett, 1972, Moore et al, 1978, Waxman and Wood, 1984, Innocenti et al, 1994 ; Tettoni et al. 1996). Note that for their study on normal callosal axons, Innocenti and collaborators assumed on each segment of the dendrogram a constant conduction speed following the linear relation V ($m.s^{-1}$) = 7.14 D (µm), where D is the axoplasm diameter. In order to perform our simulation we decide to take advantage of a compartmental model provided by NEURON software, that provides much flexibility to control biophysical parameters relevant for spike propagation and timing such as membrane capacity, axial resistance, voltage dependant channels distribution and so on. Other similar compartmental model software like GENESIS are available but we choose NEURON for its compatibility and stability on our calculation platform running under windows XP©.

Electron microscopy study revealed that callosal axons whose diameter across the brain midline is greater than 0.3 µm are myelinated in adult cats (Looney and Berbel, 1986; Berbel and Innocenti, 1988). Moreover it has been shown that monocular deprivation rearing had relatively little effect upon the development of myelinated fibres (Winfield, 1983). In the same direction, Milleret and collaborators reported that the distribution and the morphology of astrocytes cells do not show significant difference after early monocular deprivation and no difference for the timing of sequence development. So, even if we have no certitude on myelination of our axons it is natural to assume they are normally myelinated (Rochefort et al. 2002; 2005). For monkeys the similar results are shown by O'Kusky and Colonnier (1982), for astrocytes, oligodendrocytes and microglia. No difference even were found for the timing of development. So, even if we have no certitude about myelination of our axons it is natural to assume they are normally myelinated.

Presence of myelin sheath is known to change the spike propagation velocity by decreasing drastically the membrane capacity thus increasing the passive diffusion constant of the fibre and the spike velocity. Myelination is thus known to switch the propagation type from locally regenerative to saltatory conduction. In vertebrates, spike regeneration occurs at "hot spot" nodes showing high concentration of Na^+ Channel. Spike velocity is in this case described by the relation $v \sim d/\tau$ where d is the internodal length and τ is time required for spike regeneration response between two nodes. In the mammalian central nervous system the internodal lengths vary from 0.1mm to 3 mm (Ràmon y Cajal, 1952) and Na^+ Channels density ranges from 1000 to 10 000 units/μm^2 at nodes (Peres and Andreotti, 1986; Rasband and Shrager 2000). Nevertheless, the internodal spacing is far to be constant in cortical axons, particularly near bifurcations (Deschênes & Landry, 1980). The effect of branching nodes on spike propagation in myelinated axons has been first studied with computational models by Zhou & Chiu (2001). A compartmental model of the myelin sheet should contains several layers in each compartment, plus a compartment at each node (Blight,1985; Halter & Clark,1991). Remark that it is possible to construct compartmental models of realistic myelinated axons by using additional modules implemented in NEURON (McIntyre et al., 2002). However in the current literature only single segment or single branching node was studied but the implementation of this method on complete arbor has not been reported yet, maybe because of heavy complexity, more likely because of lack of details in knowledge on myeline structure, internodes and so on.

Thus, the lack of precise ultra-structural knowledge on the myelin parameters for the callosum fibres and the complexity related to the implementation of myelinated compartments on the overall arbor lead us to build the simulations onto homogeneous distribution of electrophysiological parameters as in the Hodgkin & Huxley model (HH).

Let us give justification for this procedure:

1) The system of equations describing the voltage pulse propagation in a segment of myelinated fiber is a discrete system of difference equations, coupling potentials and concentrations of various ions. The relation between membrane potentials is given by:

$$(1/\lambda)(V_{n+1}-2V_n+V_{n-1}) = C.d(V_n)/dt + I_n\,(V_n,),$$

where n is the index of nodes varying between 1 and N, the total number of nodes, and V_n stands for the value of the membrane potential on the node n at time t. The internodal distance is supposed constant here and denoted λ and C is the total capacitance of the membrane with myelin. The term $C.d(V_n)/dt$ is the capacitive current and I_n the ionic current entering the node. This dynamic system has two limits, the first one for large d is the *saltatory limit*, where potential jumps from n to n+1; the second one for small d is the *continuum limit*, where the Hodgkin-Huxley equations system well approximates the discrete system. The counterpart for speed gain with myelin sheet insulation is the propagation failure occurring when the length λ reach a critical value. On this point experimental and computational data agree on the values of λ giving maximum speed with almost no failure (cf. Scott, 2002, p147). The former assumption explains the main discovery of Moore et al. (1978) about the relative independence between the internodal length λ and the propagation in the optimal regime, a property later confirmed by Binczak et al. (2001). In other words, experimentally reported parameters are near optimal, so the values for λ in these case are not critical for propagation. Especially, λ could be fixed at relative small value which justify the use of continuous approximation.

2) The spatial and temporal evolution of the potential in the continuous system has the standard form:

$$B.V'' = C.\ d(V)/dt + I(V),$$

Where V" denotes the second derivative of the potential with respect to the space variable x, where n.λ is comparable to x. The diffusion coefficient is given by the constant B/C. We can interpret this equation as the HH equation for an axon with a diameter A, diameter of the myelin sheet. As shown in Scott (2002, p.97), C is proportional to A, and B is proportional to A^2; moreover, the conduction velocity V is proportional to the square root of B/C and thus proportional to the square root of A ($V(m.s^{-1}) \alpha A^{½}$ (mm)).

3) In the HH model, the homogeneous distribution of channels and biophysical values along the axon provides a propagation velocity that increase as the square root of the axoplasm diameter D (i.e. fibres inner diameter, without myelin) as first observed on the historical squid's giant axon. Thus squaring diameters values until quasi-extreme ends of structures, where axons keep myelinated, allowed assuming the well-known experimental linear relationship between spike velocity and axons diameters.

In order to keep a smooth transition between myelinated sections and non myelinated ones (the last micrometers of terminations) we introduced a normalisation factor ($D_{trans.}$= 0.28 µm) that corresponds to a chosen transition for axoplasm diameter beyond myelination may disappear (Innocenti et al. 1994). By this way, the transformation from the measured real axoplasm's diameter ($D_{real.}$) and the simulation parameter ($D_{eff.}$) is as follow:

Squaring relation on diameters: $D_{eff.} = D^2_{real.} / D_{trans.}$

In the framework of the HH model, this modification lead effectively to a linear relation for spike velocity and real diameters and avoid an abrupt transition between myelinated and non myelinated sections but is not enough to provide the spike velocity. A well established value for mammalian myelinated fibres was given by Waxman and Bennett in 1972 with the following relation: V ($m.s^{-1}$) = 7.14 D (µm), where D is the axoplasm diameter. Keeping in mind that for the HH-model, once a homogenous channels distribution is assumed, two main parameters fix the conduction velocity: the axial resistance and the membrane capacitance. In order to preserve the natural continuity of the inner media of the axoplasm at the myelinated/non-myelinated transition, we decided to fix the axial resistance to its standard value along all the axon and adjust the membrane capacitance on myelinated part in order to obtain the proper velocity given by the experimental linear relation.

Remark that what precedes neglects the problems of spike propagation at branching nodes. At these bifurcations, experiments and models for HH propagation have shown that failure or delay could occurs, mainly depending on a geometrical ratio GR first introduced by Rall (cf. Debanne (2004) and references inside) and defined as follows: let D_{in} , D_{out1} and D_{out2}, denote the radii of the parent fiber and the two daughters fibers respectively, then:

$$GR= (D_{out1}{}^{3/2}+ D_{out2}{}^{3/2})/ D_{in}{}^{3/2}$$

For GR=1, the characteristic impedance between segments match, so no reflection occurs and spike can propagate. A GR value greater than 1 induces a delay in the propagation at the branching point. Similarly to the callosal GRs reported by Innocenti et al. (1994), the estimation of axon diameters within our abnormal callosal arbors lead to GRs lying between

0.5 and 2.0, a range where failure almost never occurs (cf. Manor et al., 1991) whereas delays can occur. Numerical evaluation of those delays with compartmental models was computed for example by Manor and collaborators (Manor et al., 1991); they used the HH parameters for a squid axon at 20°C, and they established that delay increase non-linearly when GR grows. For GR=2 the value of the delay is approximately 0.1 ms, and in the same conditions it increases to 0.25 ms for GR=4 and 0.5 ms for GR=8. Although Manor et al. underlined that different parameters such as channel and ionic concentrations, temperatures and so on, may have an influence on delays, authorities have considered this order of magnitude is applicable to cortical axons of mammals. (see for example Segev & Schneidman, 1999). On the other hand Deschênes & Landry (1980) have experimentally studied myelinated fibers coming from thalamocortical afferents or intracortical connections in cat which are very similar to the axons we consider. On these axons they reported GR in-between 0.78 and 1.98 and they reported problems of fractionation of spike for high frequency bursts. Zhou and Chiu (2001) also showed that at branching points in myelinated axons the proper conduction is achieved for low frequency bursts but failure can appear for very high frequency (only 60% of spike propagate beyond 400Hz, at 37°C). Recall we only consider here single spike propagation so it is not surprising no failure occurs in our simulations. Note that Manor et al also proved that GR less than 1 accelerate the spike transmission at the branching point, i.e. corresponds to negative a delay.

Now we have to consider the influence of the procedure of diameter squaring, used for accounting presence of myelin sheet, onto the GR values. Changing GR values may induce artificial suppression (or addition) of delay *a priori* but they are very small in our case. Let us call GR_{real} the geometric ratio observed at a branching point given by the real axoplasm diameters, and GR_{square} the geometric ratio we obtain after squaring the diameters. First, as the daughter's diameters are always smaller than their parent one in our axons, both GR are smaller than 2 and GR_{square} is smaller than GR_{real}, with equality only if GR_{real} =2, which often occurs. It is easy to prove that the difference $E = GR_{square} - GR_{real}$ is necessarily smaller than 0.5, a value only reached when GR_{real} =1 and $D_{out1}^{3/2}$, $D_{out2}^{3/2}$ are both equals to 0.5. To prove this fact, consider the function E of the two variables $x = D_{out1}^{3/2}$, $y = D_{out2}^{3/2}$. This function is positive and strictly concave on the domain where x and y lie between 0 and 1 and reach its maximum only when x = y = 1. Moreover, when the GR lies between 0.5 and 2, like in our cases, the transmission delay vary linearly with the GR (Manor et al, 1991). Thus, the estimations of Manor et al. show that the maximum error induced by squaring diameters on

each delay is smaller than 0.05 ms. However successive branchings induce additional effects but the delays simply add when the distance between two consecutive bifurcations is large enough with respect to axoplasm radius. The examination of our axons shows that this condition is generally satisfied. In general, less than six bifurcations occur along the myelinated part of the fiber, with no more than two pairs of close consecutive bifurcations inducing non-linear delay smaller than 0.1ms. Thus we are confident with that the total error due to squaring does not exceed 0.5 ms. Note that this is certainly an overestimation because in myelinated fibers at nodes and then at bifurcations, the Na conductance is elevated, which has the effect of reducing the delays; we can even hope that an axon which takes the pain to use myeline takes also the pain to accord propagation at branching with the gain of speed.

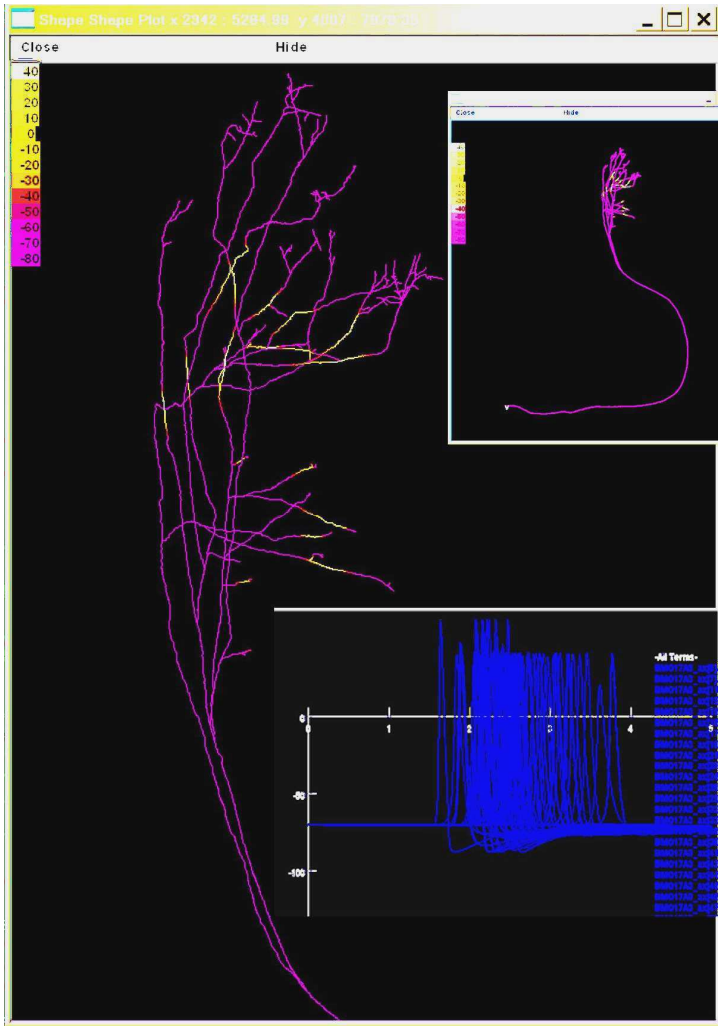

Fig. 136/ Screen capture of NEURON simulation.
Figure showing the evolution of membrane potential (mV.) along the axon morphology (axon BMO17A3); the small up-right window shows the whole axon morphology; The blue traces represent spikes arrivals timing (membrane potentials (mV)) at each ends of the arbor. The timescale is millisecond and its origin corresponds to initiation of a spike on the root of the structure.

So as a first step, according to results reported for mammalian central nervous system neurons (Spruston et al. 1992; Johnston and Wu, 1995), we assumed a standard set of electrophysiological value and HH-model ionic channel values for mammalian cortical axons thus homogeneously distributed along morphology for all sections. In a second step, in order to simulate the presence of myelin for propagation, we squared diameters for sections until the transition diameter and affect them a low membrane capacitance value. This value was obtained from “Y” shape axon tests so they reflect the well established experimental velocity value.

Finally, the simulation of current injection into a virtual soma connected to the origin of root increases the local membrane potential value until the spiking threshold and initiates the spike propagation along the morphology (See fig. 136). The timing of spike arrivals on each termination of the axon is monitored into the simulation software and events are binary transformed by threshold analysis (-40 mV.) and binned into channel (0.01 ms.) for histogram construction.

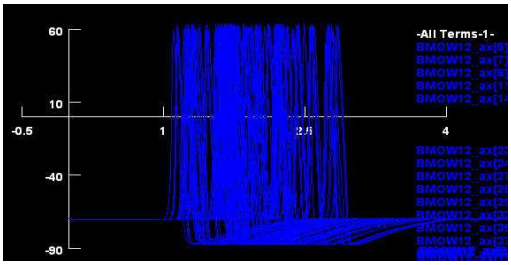

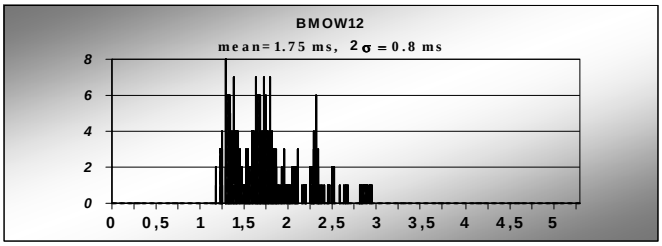

BMOW12

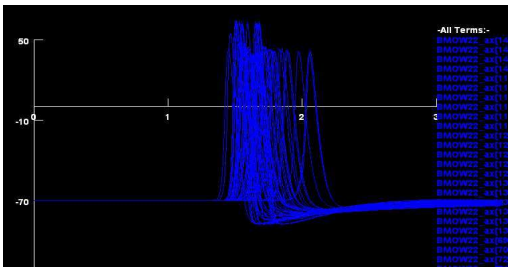

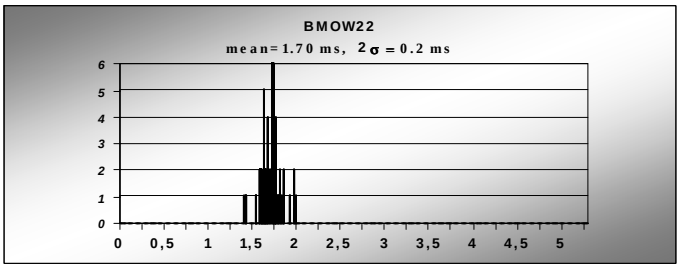

BMOW22

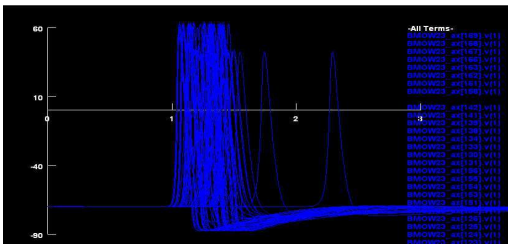

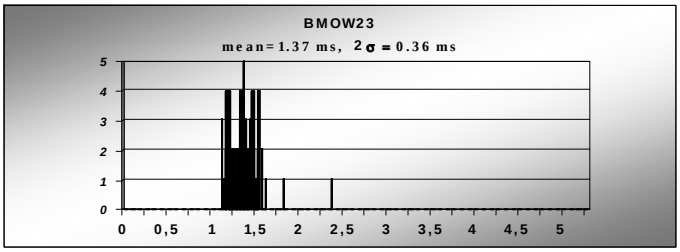

BMOW23

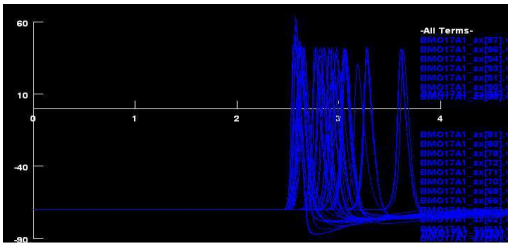

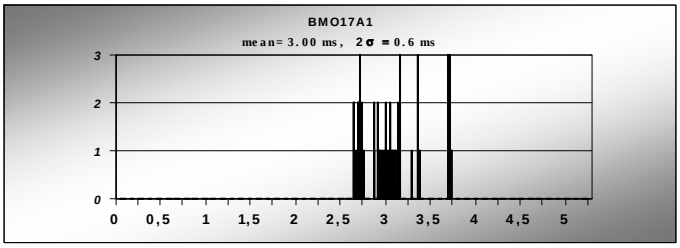

BMOW17A1

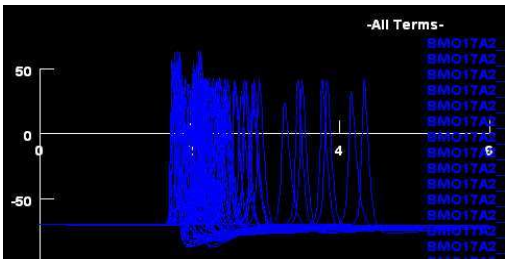

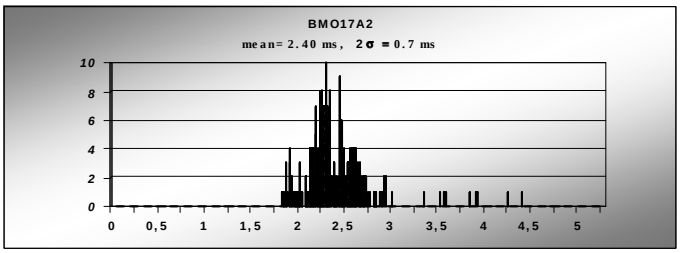

BMOW17A2

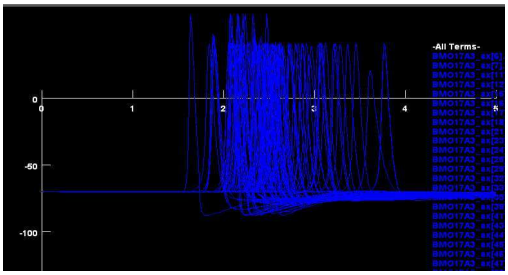

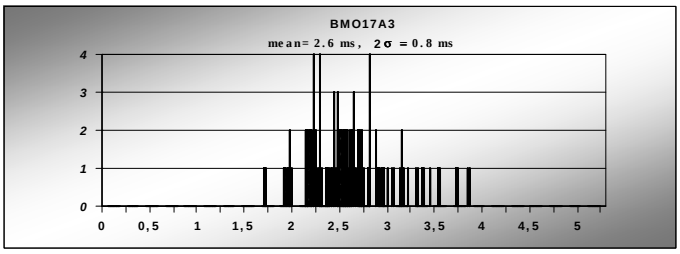

BMOW17A3

Fig 137/ Spikes arrivals on each terminal of callosal arbours and time dispersion histograms (scale: ms)

3. Results

The figure 137 shows the spike arrivals on terminals and related histograms for each axon. Each blue trace corresponds to the membrane potential at the end of a terminal segment reporting the propagation of the single spike initiated on the root segment. The evolution of the potential on each terminal was reported into histograms after thresholding (–40 mV).

Axon	ROOT				TERMINALS			TIMING		
	Length (µm)	diam (µm)	S. Veloc. (m.s-1)	I/O time (ms)	Nb term.	Ends mean diam. (µm)	End mean lenght (µm)	Mean time (ms)	Time dispersion 2*sigma	Max-Min
BMOW12	9653	1,68	12,0	0,47	252	0,30	60,00	**1,75**	**0,80**	**1,8**
BMOW22	9839	2,10	14,9	0,66	60	0,20	63,80	**1,70**	**0,20**	**0,7**
BMOW23	10532	2,16	15,4	0,68	83	0,40	99,10	**1,37**	**0,36**	**1,2**
BMO17A1	14359	0,70	5,0	2,87	49	0,15	22,76	**3,00**	**0,60**	**0,9**
BMO17A2	13759	1,39	9,9	1,39	243	0,15	18,20	**2,40**	**0,70**	**2,7**
BMO17A3	12105	1,53	10,9	1,11	106	0,16	61,54	**2,60**	**0,80**	**2,1**

Table 8: Root and terminals properties and spike timing dispersion

The Table 8 reports the spike timing arrivals on axons terminals. The root properties of the axons are such as lengths and diameters are reported to indicate the spike conduction velocity and the conduction timing from the midline to the first bifurcation. Number of terminals and means of their diameter and lengths is also shown. The means time from spike initiation is also reported. To estimate the dispersion time, the standard deviations (x2) of the difference between the first and the last arrivals time is reported. The surprising result is that for all abnormal structures the great majority of spikes distribution is kept within a submillisecond interval. Distribution ranges are similar to those reported from 0.3 to 2.7 ms for normal callosal connections (Innocenti et al., 1994). Nevertheless, very asymmetric structures such as BMOW12 and BMO17A3 or presence of tiny unmyelinated collateral like on BMO17-A2 axon, induced spike arrivals within the two following milliseconds as shown on histograms.

4. Discussion

In spite of the morphological aberrations of their interhemispheric connections monocularly deprived cats do not show any postural or behavioral abnormality. And their transcallosal postsynaptic cells also show strong activation. This demonstrates the relevance of these connections in the construction of visual perception (Milleret et al. in preparation).

Careful attention was done in this work to obtain precise data on axonal morphologies. But the lack of information on ultrastructural parameters and principally those related to myelin distribution and voltage-dependant channels distribution at nodes along mammalian visual callossal axons, did not afford us to implement them into the compartmental model. Nevertheless our discussion shows that the homogeneous distribution (HH model) associated with diameter squaring assumption is relevant enough to provide precise idea of the spikes timing distribution.

Results obtained under these assumptions lead us to conclude that the widespread of axons grown under monocular deprivation visual experience does not allow concluding to significant difference of time distribution compared with normal structures. Moreover the choice for a myelinated/unmyelinated transition diameter of 0.28 µm also provides to our simulations the worst condition for synchrony. As reported from electron microscopic study myelination has always been observed on callosal structures at least until this diameter and thus myelination until ends of arbors would provide still more synchrony.

For the role of the morphology in the spike timing distribution, our results confirm that the strong confinement of the distribution of the contralateral signal (~1-2 ms) is constraint, at least for myelinated fibers, by the high velocity imposed by myelination on overall axons. Thus morphology seems not to play a major role in the time distribution for this kind of fibres.

Concerning interhemispheric synchronizations that callosal connections could provide through reverberant circuits, a low dispersion of the signal is a key parameter to establish and maintain stable constructive oscillations. In the gamma band frequencies often related for the perceptive binding hypothesis, few milliseconds dispersion seems to be compatible with construction of oscillation within this frequency range.

Finally, we found that the spatial extension and the increase of the number of clusters found for axons obtained under early monocular deprivation do not drastically modify the temporal dispersion of the neural signal they convey. This is in agreement with the hypothesis claiming that those abnormal neural structures are nevertheless normally functional.

PART I

Conclusions

The work described in the Part I of the thesis aimed at increasing our understanding of the neural networks that provides the spatio-temporal characteristics of the sensory cortical maps. This was achieved by investigating the “callosal cortical maps”, as defined by callosal connections between the hemispheres, in cat primary visual cortex of adult cats either normally reared or after an early monocular deprivation (MD) through a multidisciplinary approach, combining anatomy, models and simulations.

In a first chapter, the morphology of the callosal connections of MD animals has been described qualitatively. This was achieved by describing single callosal axons which has been first labelled with an anterograde tracer, the biocytin, and then 3D-reconstructed with the Neurolucida software. Comparison to data obtained previously in normal adults (Houzel et al., 1994) allowed to demonstrate that the morphology of these callosal axons is greatly modified after an early monocular deprivation, because of sprouting both tangentially and radially within the visual cortex. Instead of being confined close to TZ, these axons reach the visual cortex and terminate over extensive portions of A17, TZ 17-18, A18, TZ 18-19 and A19 in the adult. The architecture of their terminal arbours, including those of terminal columns, also greatly changes from axon to axon and shows a wide diversity. Although most of their terminal boutons are found within different cortical layers, most often, they are distributed in supragranular layers where they seem to form clusters. Numerous heterotopic connections were found between hemispheres. Thus, we show that the anatomical network underlying the interhemispheric integration of visual information is profoundly modified by an early monocular deprivation. In order to quantify the morphological differences between the axon populations, we developed two original computational methods referred as the “ellipsoid approximation” and “clustering analysis” respectively.

From the collection of precise anatomical data on the axon structures, the ellipsoid approximation (Ch. I.2) propose a set of geometrical tools allowing to quantify the spatial dispersion of the synaptic distribution into the particular cortical context of TZ. This method was applied on terminals distributions of both of our NR and MD axon populations. As a first

step in 3D, the volumes and the elongations of a distributions embraced by an ellipsoidal shape provide quantitative information on the general spatial configuration of the synaptic field. In a second step, the 2D projection onto a tangential cortical surface provides interesting clue to relate the spatial synaptic distribution with functional cortical maps and especially with the retinotopic organization. The transition zone between visual area A17 and A18 is known to follow the representation of the vertical meridian and include a part of the ipsilateral field confined into an about 1mm wide band running onto the cortical surface from its posterior to its anterior part (Payne, 1990; Milleret al., 1994). In the many cases we found 2D terminals distributions to be quite elongated and anisotropic. Wide distribution of directions was found but a bias toward the TZ-crossing oblique directions was reported for both groups. Combined together with the cortical areas association of the terminals, this directional information complete physiological data reporting the organization of receptive fields and binocular disparities of transcallosally activated units on both sides of the vertical meridian (Milleret et al. 2005). Most of these parameters allow not only the characterization of both the NR and MD groups, but also allows reporting significant difference between them. Especially, the cortical surfaces of the distributions from the MD group were found as a mean to be twice greater than those of the NR group.

For the second method (Ch. I.3) we developed a new clustering algorithm aiming to characterize the scattering and non-homogeneity of the distribution of axons terminals. Gaussian mixture models were used to provide a quantitative description of the dispersion of the terminal arbours for each single axon. With priors evaluated from simulation, a maximum *a posteriori* method was used to estimate the number and the weight of each cluster of branches, as well as their centres and covariance matrices. The method has been first validated on synthetic data set. The development of this original computational method demonstrates the wider extensions and the much clustered aspects of the impaired callosal axons compared to the reference axons. This powerful method applied on 3D data allows revealing some morphological aspect of the distribution difficult to catch by expert visual inspection and especially the subjective number of clusters. This number of clusters was found to be twice higher for MD axons. Further study combining functional recording with this technique would provide very interesting information on the functional preference of these clustered connections. Especially, relating these clusters into a particular cortical map such as orientation or ocular dominance preference may contribute to the understanding of the functional constraint onto the development of callosal structure.

In a final chapter, a compartmental model was used to simulate the propagation of spikes within abnormal callosal arbour in order to estimate if abnormalities in the morphology of axon may induce temporal dispersion of the neural message. We demonstrate that all branches of a single arbour activate the terminals together in the callosal zone within a short time window, less than 2ms, in spite of their abnormal morphology. In other words, since terminal activations are also synchronized for normal callosal axons (Innocenti et al, 1994), the temporal properties of the callosal cortical maps do not seem to be altered by early monocular deprivation.

For the second coming part of the thesis, we aim the compare these morphological characteristics and the strong temporal confinement of spike dispersion reported by simulations, with functional imaging data. We introduce some experimental and analysis techniques related to optical imaging in its Voltage Sensitive Dye version (IO-VSD) developed to record *in vivo* the spatiotemporal dynamics of the interhemispheric connectivity with high precisions both in spatial and temporal domains. By revealing the functional organization of the cortex around TZ, this technique can be coupled with the anatomical reconstructions and morphological characterizations proposed in the part I . This would hopefully provide very interesting information to understand how a particular morphology obtained under particular conditions of vision, weather normal or impaired, is related to the functional activity of the local cortical map.

PART II

Optical Imaging
of the dynamic of the interhemispheric connectivity
by use of Voltage Sensitive Dye

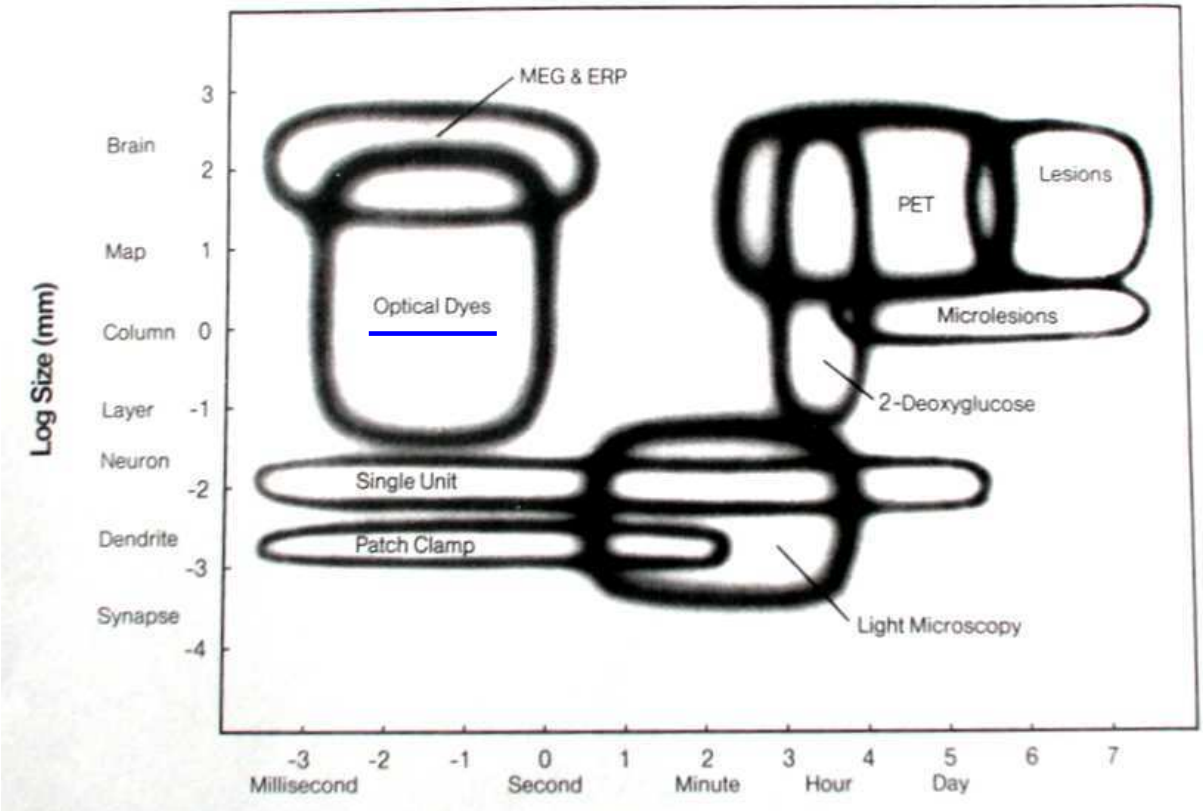

Fig. 138/ Schematic illustration of the range of spatial and temporal resolutions of various experimental techniques to explore functional organization of the brain. Note the range the "Optical Dyes" provide a very good compromise between spatial and temporal accuracies and allows recording the activity over a wide neural population.

Introduction

The interhemispheric connectivity between primary visual cortices has been explored by means of many techniques. Among them, in our team, single unit recordings and the anatomical reconstructions provide very precise information about physiological and morphological properties of single neurons respectively. Physiological recordings provide precise spatial and temporal responses of a single units evoqued by visual stimulation. This method allowed the extensive physiological characterization of transcallosally activated cells and the accurate establishment of their receptive fields. On the other hand, the anatomical reconstruction method provides very precise data about the morphology of single axons. It allowed to access their fine structures and to explore their relations with the distribution of neural information within the cortical space, as presented in the first part of this thesis.

Nevertheless, whereas powerful in their own framework, both of these methods lack of providing clear relations between the collected data and the context of the dense and wide neural population of the cortex. The use of optical imaging has been the sharpest experimental solution to integrate our results in the functional organization of the cortical network, reporting for both spatial and temporal domains the activity of a wide population of cells in response to various stimulations. The optical imaging allows the establishment of cortical functional maps, reporting optical signal correlated to physiological responses over wide cortical areas (~ cm^2); see Fig. 138. The optical imaging method is based on the recording of optical changes correlated to neural activity by 2 means principally. The *intrinsic signal* (OI-IS) reports the slow absorption components of the hemodynamic response induced by neural activity and allows functional mapping of the cortical surface with a high spatial resolution. On the other hand, the changes of fluorescence of *Voltage Sensitive Dyes* (OI-VSD) anchored in neuron membranes follows their membrane potential at higher temporal resolutions combined with an optimal spatial resolution.

In the framework of an international cooperation with our team, the recording of the transition zone between the areas A17 and A18 solely activated through the corpus callosum by mean of a preparation with sagittal section of the optic chiasm, was successfully performed using the OI-IS method (Cf, Fig. 13); (Rochefort et al, 2007). Our aim for the present work is to perform similar experiments and reach the interhemispheric cortical dynamics with the highest temporal resolution available by use of IO-VSD. Such results on the functional dynamics are aimed to be combined with data like those presented in the first part in order to obtain a more complete description of the interhemispheric integration between primary visual areas, with a particular attention on temporal aspects.

In the first chapter we will review the principles of optical imaging and some related techniques such as signal analysis. In the second chapter, we will introduce some modifications made from the original setup of OI-VSD in order to reach the highest temporal resolution in combination with the widest reachable cortical area, aiming to records the dynamics of the interhemispheric communication between primary visual cortices. The results obtained step by step along these adaptations will be presented each time.

CHAPTER II.1

Principles of optical imaging

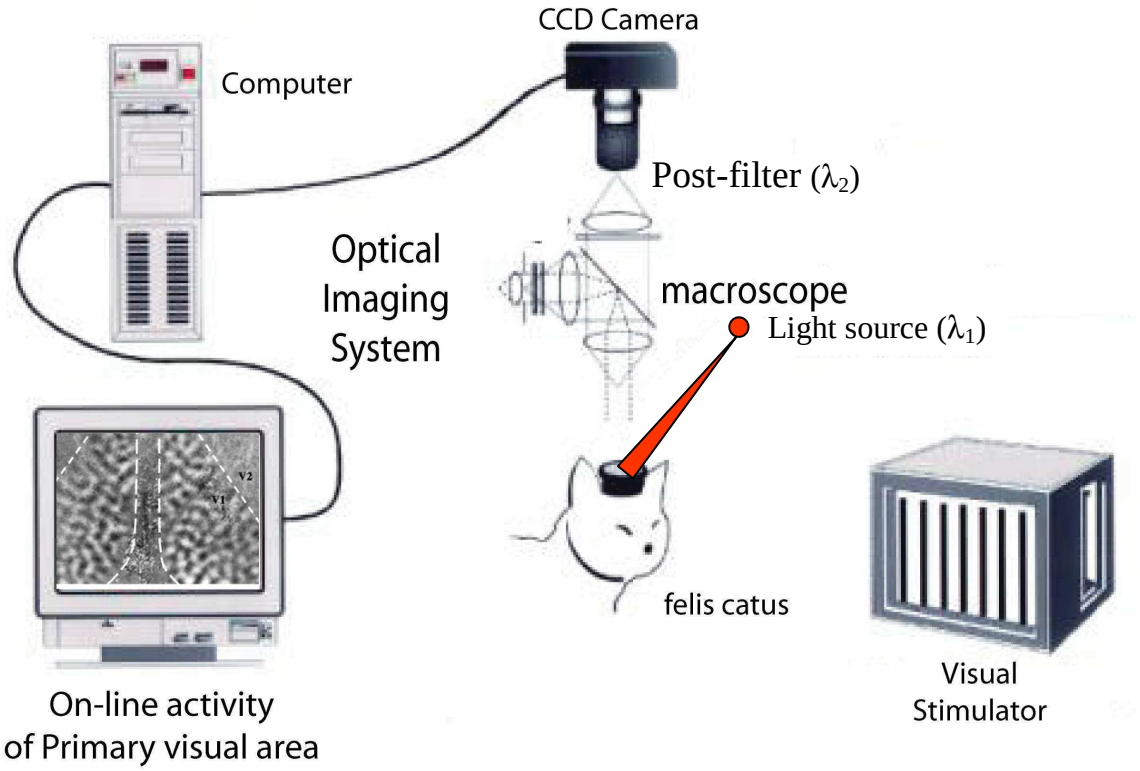

Fig. 139/ Principle of optical imaging.
A typical setup of optical imaging includes a light source to illuminate the cortical surface through the recording chamber mounted by surgical preparation. The changes on optical properties induces by the cortical activity in response to visual stimulations are collected by a CCD camera through a macroscope lens system focused ~500µm under the cortical surface. Data are monitored on-line and recorded on mass storage for finer analysis (modified for Grinvald & Bonhoeffer 1998).

Principle: modulations of optical signals induced by the neural activity on cortical surface

The principle of optical imaging technique consists in illuminating the cortical surface at a specific wavelength and to follow local modifications of optical properties induced by neural activity. These local changes of the optical properties are collected by recording the modulation of the reflected light.

Practically, the experiment requires the illumination of a cortical area exposed after proceeding the proper surgical preparations. The collection of the reflected light is done by mean of a CCD camera through a macroscope focused 500 µm under the cortical surface in order to place the cortical layer II/III in the focal plane. A macroscope is an optical system composed of two photographic lens mounted face-to-face so it combines an important numerical aperture and a minimal depth of field. The important numerical aperture allows the collection of light from a wide area at short distance from the objective. When focalized under the surface, the minimal depth of field allows blurring particularly the blood vessels on the cortical surface, and focus on the CCD detector almost only optic rays emitted from a zone confined within about 50µm of depth. The signals are transferred to the acquisition system performing on-line monitoring and recorded onto mass storage media for finer off-line analysis (see a typical experimental setup on Fig 139). This setup allows to measure the changes in optical properties occurring in the first hundreds micrometers under the cortical surface and related to neural activity by mean of two types of couplings. The first one is related to changes occurring in the concentrations of endogenous molecular probe and principally the Hb/HbO_2 couple (i.e. the Blood Oxygen Level Dependant (BOLD) or hemodynamic signal identical to the one recorded for f-MRI). This kind of coupling induces changes in absorption of light related to neural responses and is referred as optical imaging of intrinsic signal. The second method reacquires the use of extrinsic molecular probes anchored into the cellular membranes by means of a staining procedure, and whose fluorescent properties are changed due to modification of the local electric field. This later method is referred as optical imaging with “Voltage Sensitive Dyes” and allow following the neural activity at high sampling rates in order to access aspects of the cortical dynamics.

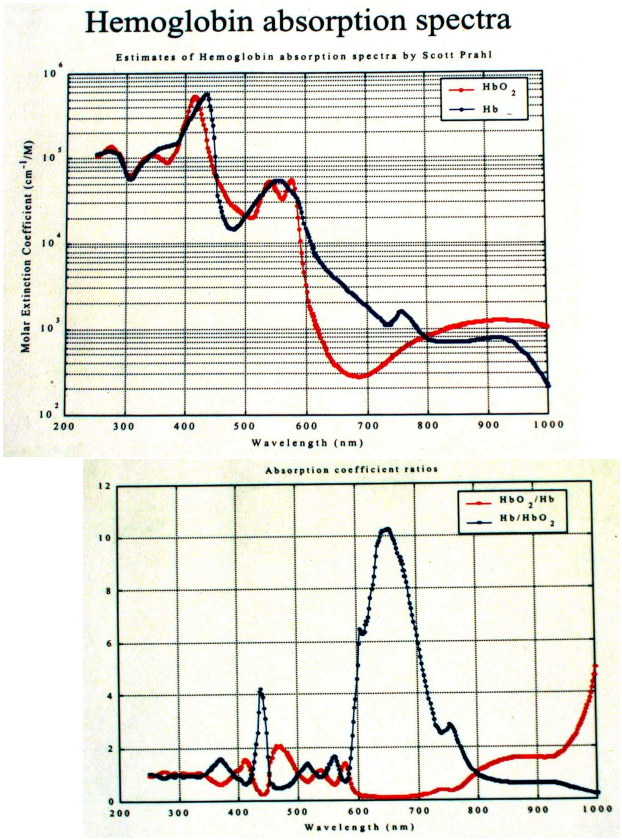

Fig. 140/ Hemoglobin absorption spectra and absorption coefficient ratios.
The highest difference in light absorption between Hb and HbO_2 is obtained at wavelengths lying between 600µm and 700 µm.

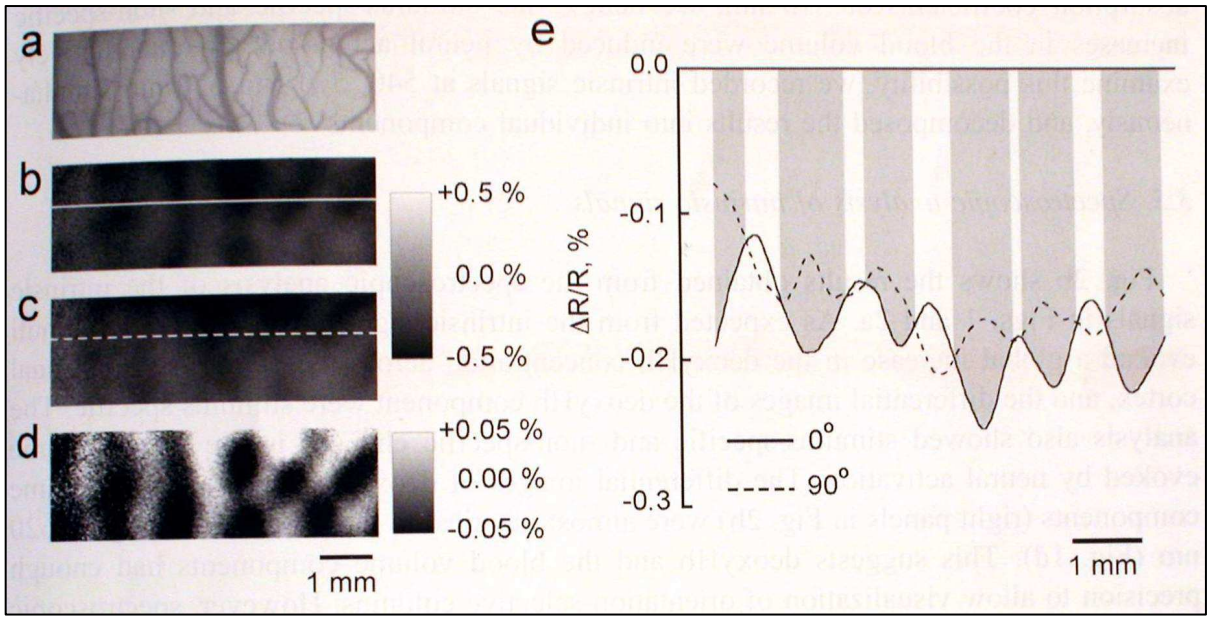

Fig. 141/ Image darkening resulting from neural activity (OI-IS)
(a) surface reference image. (b) and (c) local absorption resulting from neural activity induced by presentation of a visual stimulus (horizontal and vertical drifting gratings respectively); activated regions are darker. (d) Enhancement of functional difference by division of pixel levels between former images. (e) Cross-section of level activity from images (a) and (b) showing modulations of absorption on cortex surface. Level activity is reported by the relative absorption difference ΔR/R (from Mitsuhiro et al., 2002).

Origin intrinsic signal

The intrinsic signal originates from the local hemodynamic response dues to the metabolic consumption of activated neural cells. This response induces a local increase in the blood volume in surrounding capillaries and local changes in the oxygenation level of the blood. All together these effects modify the relative concentrations of both hemoglobin forms Hb and HbO_2 inducing local changes in absorption of light. Depending on the wavelength used for the illumination, the neural activity induce a decrease of light reflectivity related and is traduced by a darkening of active regions on resulting images (see Fig. 140 and 141). Practically, the absorption level is measured by the relative absorption difference $\Delta R/R$ varying by few tenths of percents. This weak values reacquires the use of very sensible CCD detector (dynamics>10bits) and the recording of many data blocks in order to perform signal averaging or other statistical method to reduce random fluctuations. Moreover, the relative absorption level is very dependant of the wavelength used for illumination and other sources might be involved in the signal modulation. Such modulations can occur from ionic or water movements, extracellular space expansions or neurotransmitters diffusion, all inducing changes in light absorption or scattering with their own dynamic and with different amplitudes depending on the wavelength used. Nevertheless, whatever the illumination wavelengths used, they all produce similar and reproducible spatial functional maps (Frostig et al., 1990; Bonhoeffer & Grinvald, 1991).

As for f-MRI technique, the components of hemodynamic signal are rather slow (~seconds) and do not allow monitoring the fast dynamics of cortical activity. As the intrinsic signal is related to metabolic activity it is conventionally accepted to be linked to the spiking activity of recorded sites. This method has been used extensively to explore the spatial properties of the cortical functional domains among various species (see for exemple Orbach et al., 1985; Grinvald et al., 1991; Wang et al., 1998; Vnek et al., 1999).

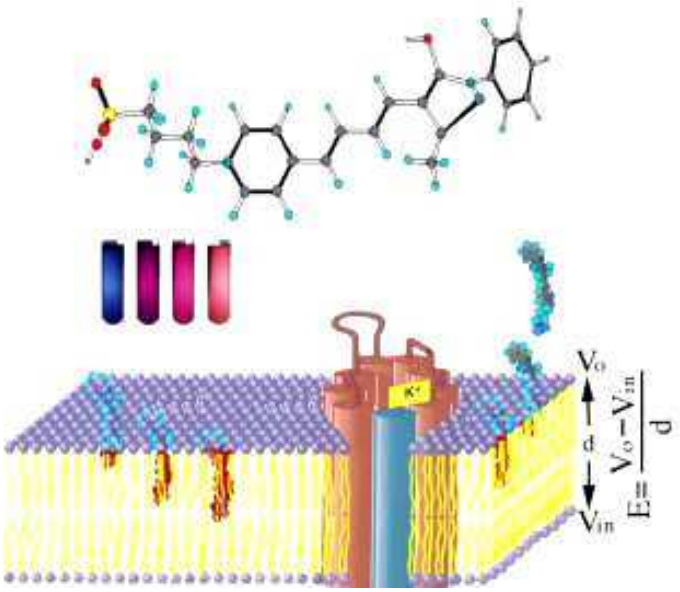

Fig. 142/ Anchoring of voltage sensitive dyes (VSD) in the neuron membrane.
Top: Molecular structure of a blue VSDye. Middle: The change in color of a VSDye into different solvents solutions indicates its optical sensibility to the electrical environment. Bottom: The anchoring of VSDyes into neuron membranes allow monitoring the fluctuations of membrane potentials by recording the following fluorescence variations (the size of a potassium channel is shown for comparison); (from Grinvald et al. 1995).

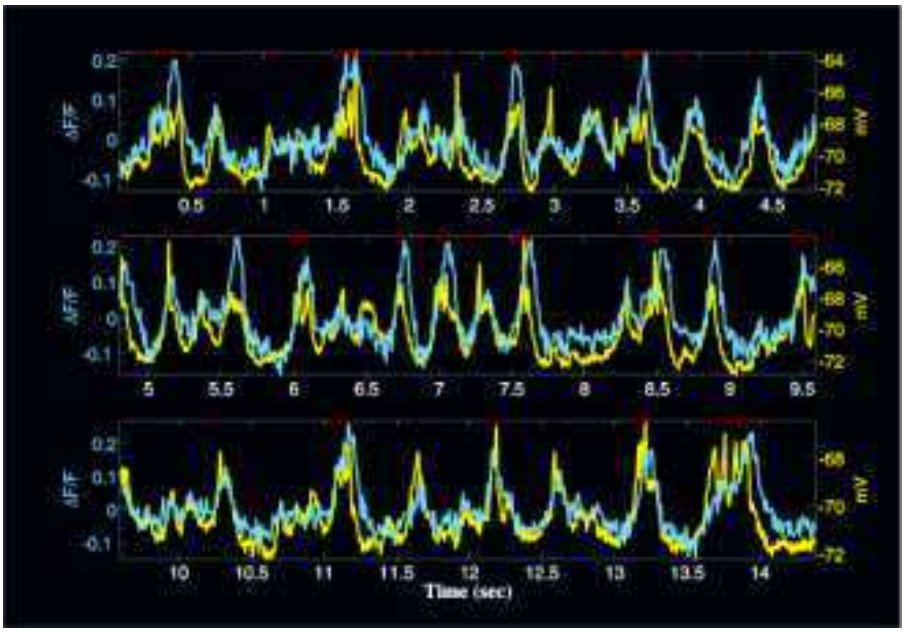

Fig. 143/ The similarity between the dye fluorescence signal from a small population of neurons and intracellular recording. The Two traces show simultaneous intracellular and optical recording for 15 seconds, performed in a deeply anesthetized cat a condition in which spontaneous changes in membrane potential are highly synchronized in a large population of neuron. The intracellular recording is depicted by the yellow traces. The optical signal from the population next to the electrode is depicted in blue. The action potentials were truncated and occurred at times marked by the red dots (Modified from Sterkin et al., 1998; unpublished results).

With a similar experimental setup, the insertion of synthesized fluorescent molecular probes into the membranes of cortical cells allows to increase the rate of the optical modulations by directly monitoring the mean membrane potentials. The specific activity of neuron is expressed by changes of their membrane potentials. When anchored in membrane of cortical cells after slow perfusion of a blue-colored solution, these chromophores follow the surrounding electric field inducing ultra-fast moves of charge densities on the chromophores molecular structure and thus modifying its fluorescence. (see Fig Fig. 142 and 143). The relative change in fluorescence induced by neural activity *in vivo* is of few tenth of percents as for the intrinsic signal, nevertheless the very weak time constant of the electro-optical coupling ($<10^{-9}$ s.) allows in theory submilisecond monitoring. Practically, the temporal resolution of the system is limited by the maximum frame rate of the camera (<500Hz) and the important random fluctuations of light. Dealing with fluorescence, the excitation and emission wavelengths are different and require the use of pre- and post filtering to eliminate the important background fluorescence from recording. It have been reported that the relative variations of fluorescence vary linearly with membrane potentials, thus following not only the spiking activity but also the summation of synaptic inputs (Sterkin et al. 1998). The use of Voltage Sensitive Dyes (VSD) for in-vivo recording suffered for decades of neural photo-toxicity until recent discovery of blue dyes (Grinvald & Hildesheim, 2004). These blue dyes not only enhance the fluorescence response but also yield the S/N ration by 30 times by having its emission wavelength out of the hemoglobin absorption spectra (Shoham et al., Neuron, 1999). However, the optically active life-time of VSDyes decreases under light exposure, its is thus necessary to strictly limit the illumination time by mean of an electronic shutter on illumination path. At last, the fluorescence signal can not be calibrated in mV as the response strength is dependant on the local density of staining of membranes. Comparison between cortical functional maps obtained with the intrinsinc signal method and VSDye recordings demonstrate that both methods produce similar results for revealing functional domains (Shoham et al., Neuron, 1999).

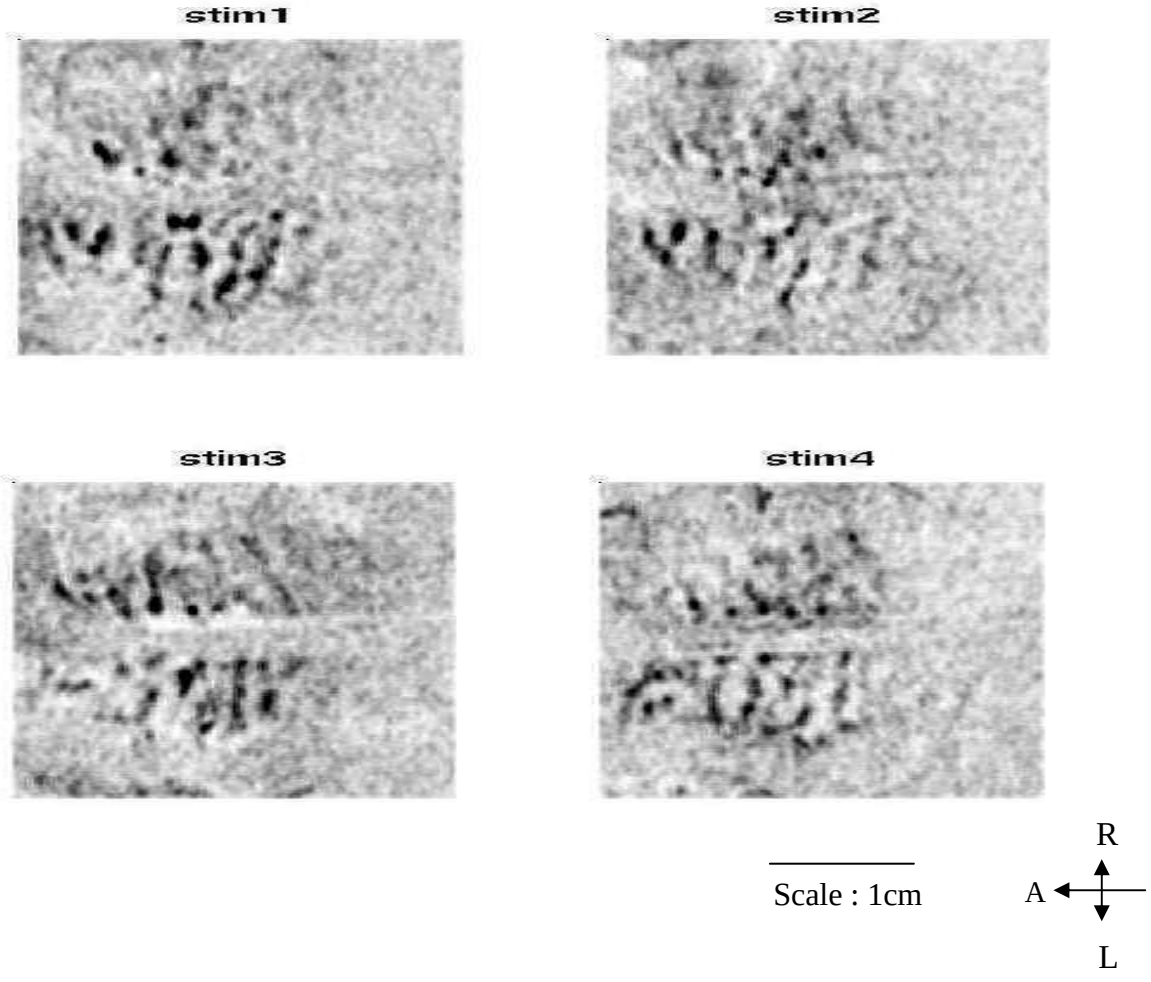

Fig 144/ Single condition maps (orientation) revealed by the "generalized indicator functions" algorithm.
These Images were obtained during a first period spent in Dr. S. Tanaka's laboratory at RIKEN B.S.I in Japan. They show the bilateral activity of the cat primary visual cortex recorded by optical imaging of intrinsic signals in response to 4 orientations (0°, 90°, 45° and 135° for stim. 1, 2, 3 and 4 respectively). Visual stimulations consist in drifting square gratings having spatial frequency enhancing activity of areas A18. The use of "generalized indicator functions" algorithm provides a strong contrast between functional orientation domains.

When experimental conditions are favourable, the on-line processing of averaging and algebraic treatment of maps might already reveal contrasted functional domains. Nevertheless, some statistical off-line treatment of data recorded over many blocks is often necessary to reveal or enhance functional contrasts.

The achievement of well contrasted “single condition maps” indicates successful experiments. The basic method consist in averaging all recorded blocks in order to enhance the signal to noise ratio and to normalize them by a blank condition (response of a neutral stimulus) or by a cocktail-blank condition (summation of every stimulus condition) providing in most cases more satisfying results. Moreover, differentiating responses from complementary stimuli condition (orthogonal orientation in case of orientation maps for example) enhances the contrast between functional domains.

Finer statistical analysis can by performed by use of Principal Component Analysis (PCA) reporting in a vectorial space defined by the orthogonal base of (m*n pixels * k stimulus conditions) vectors, the subspaces (or components) showing the strongest variances. However, as many sources of fluctuation, from physiological perturbation to random noises embed the signal correlated to neural response, its is necessary to sort and select the most relevant component describing the neural response for each condition of stimulation. Such kind of spatial decorrelation method allows removing artifacts such as the global signal, blood vessel patterns and movement artifacts (Sirovitch & Everson, 1992; Stetter et al. 2000). The problem of blind signal extraction from noisy multivariate data aim to identify the different activity patterns that are attributable to specific experimental conditions. For the particular case of optical imaging, a powerful algorithm based on PCA has been developed for applications without *a priori* knowledge about the signal or the noise characteristics. The extracted signals, referred as the “generalized indicator functions” are optimal in the sense they maximize a weighted difference between the signal variance and the noise variance (Yokoo et al. 2001); (cf Fig. 144).

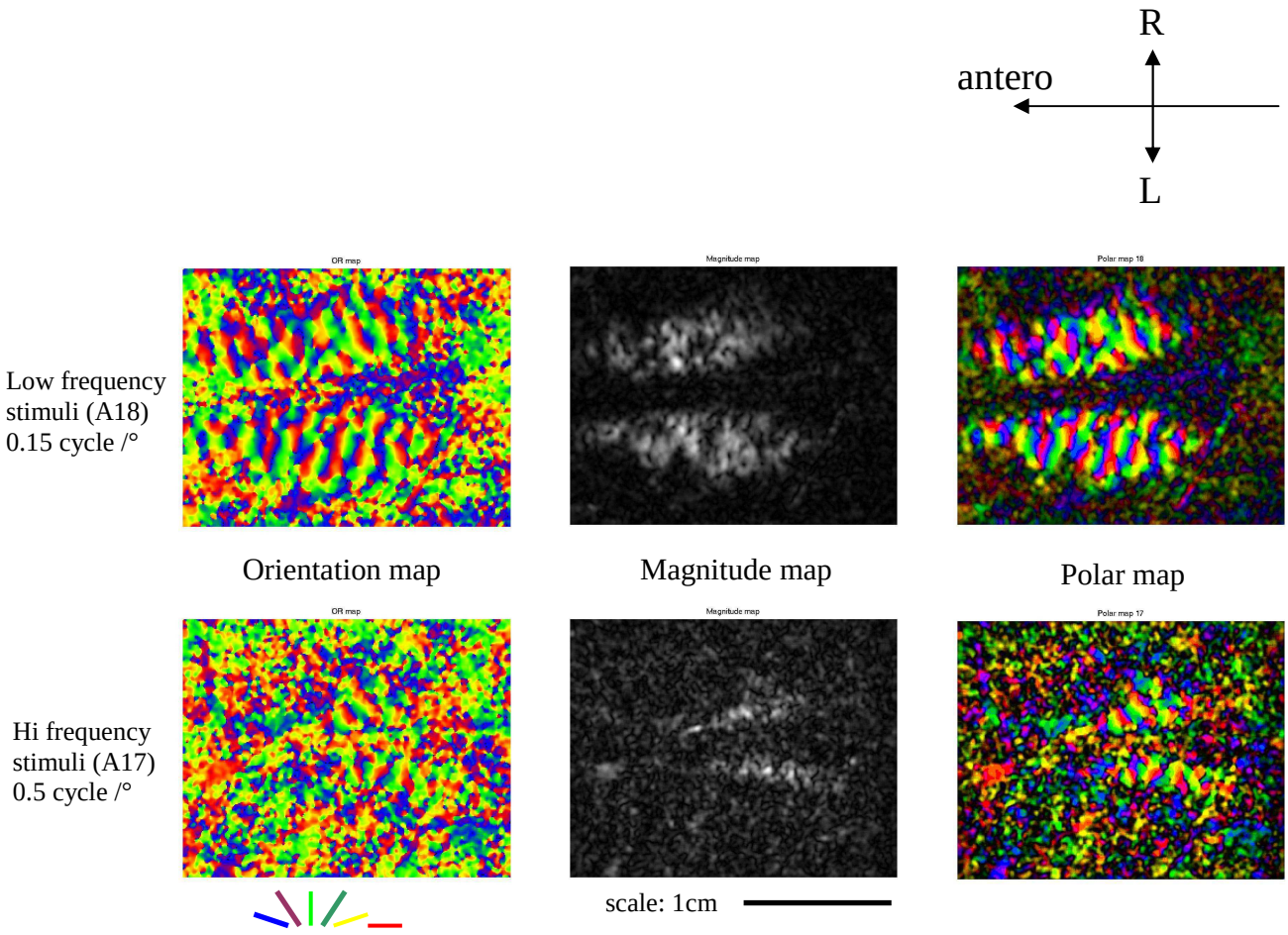

Fig 145/ Production of functional maps from single condition maps.
In the case of orientation preference, pixels from each single condition maps are vectorially summed in order to produce an orientation map (vector angle) and a magnitude map (vector length). The combination of both produces a polar map indicating functional domain and relative response strength. The use of different spatial frequencies for the visual stimuli can enhance preferential responses from A17 or A18 (top vs bottom images).

Another method proposes to explore the response dynamics to enhance source localization. This method combines principal component analysis and multitaper harmonic analysis to extract statistically significant spatial and temporal responses from sets of imaging data (Sornborger et al., 2002). Recently, promising method based on Independent Component Analysis (ICA) might reveal with enhanced accuracy the spatio-temporal dynamics signal from multivariate noisy sources (Reidl et al. 2007).

Single condition maps can be later combined to precise functional specifity of activated domains. Algebraic or vectorial operations can be performed on pixels-to-pixels values from single condition map to produce functional maps (cf Fig 145).

CHAPTER II.2

Adaptations for recording the interhemispheric cortical dynamics and first results

Fig 146/ The experiment room of the Visual Neurocomputing laboratory
directed by Dr. S. Tanaka in Riken B.S.I (Japan), during a surgical preparation session.

Aiming to reveal the interhemispheric dynamic between primary visual areas by mean of Optical imaging with voltage sensitive dyes, our experimental project greatly benefit from the fruitful collaboration with Dr. S. Tanaka and his team in the Riken B.S.I. (Japan) For this international collaboration, I had the great opportunity to spent several times for couple of months between 2004 and 2006 in the *visual neurocomputing laboratory* to develop and perform our first VSDye experiments. During these periods, Dr. T. Tani and I, supervised by Dr. S. Tanaka and Dr. C. Milleret, adapted the knowledge available in both teams on the organization of the primary visual cortices of cat and the OI-IS methodology to setup and performed IO-VSD experiments. The increasing knowledge on optical imaging techniques resulting from these collaboration periods allowed us to built an optical imaging setup in the laboratory at collège de France (Paris) designed for both IS and VSD related techniques which provided step by step accurate results.

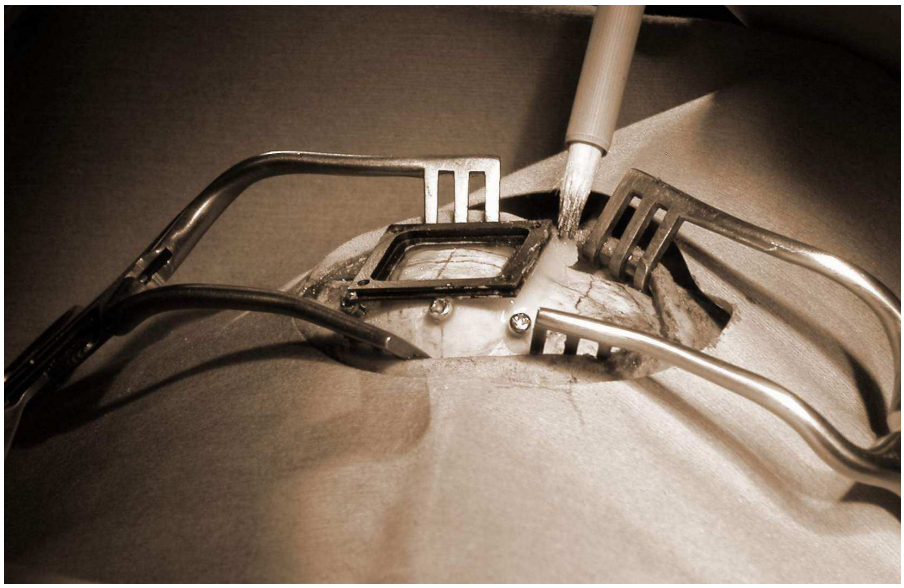

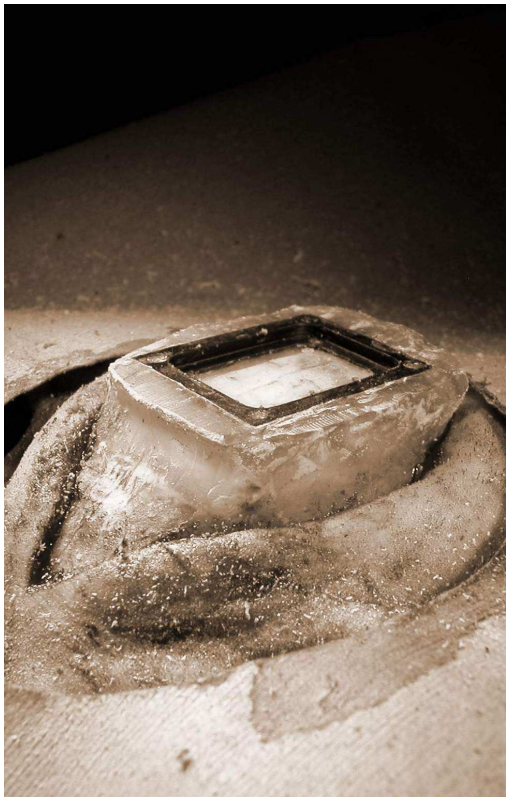

Fig. 147 & 148/ 3rd generation thin plastic chamber mount
(see text for details)

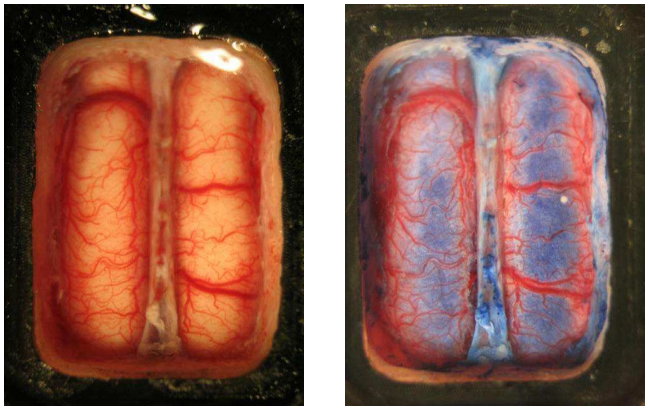

Fig. 149/ Staining of the cortical surface with blue voltage sensitive dyes (RH 1691)
The Left image shows the optical access to the cortical surface from the recording chamber. The same cortical areas after 3hours of VSD staining are shown on right (scale 2:1).

Accessing the cortical surface and VSD staining

Excepted for the modifications proposed here, materials and methods used for experiments presented here are very similar to the conventional ones needed for optical imaging sessions. Especially, surgical preparations and anesthesia induction and sustain have been proceeded on young adults cats as same described for works of our collaborators (see for example Tanaka et al. 2005; 2006 for works on development of orientation maps).

Initially developed in VNC laboratory, we took advantage of using thin square recording chambers, slightly modified for our purpose. This 3rd generation chambers is made of plastic material. It has been design to provide convenience and simplicity of use as well as an increase in sealing safety against cortical injuries when used for chronicle experiments. The 3rd generation chamber are made with black ***Delrin***© (Polyoxymethylen), a low cost thermoplastic easy to machine, therefore reducing drastically the cost and the time for manufacturing, ten times cheaper than for production of metal chambers. As made of plastic, this chamber has a low weight (3.2 g) thus lightening carriage and reducing disturbance for lasting mount allowing long period of chronic experiments. This is particularly important for young animals and to avoid chamber desanchoring damageable for animal health as for experiment results. The use of low cost plastic make the chamber a “single-use” type avoiding the procedures of unmounting, cleaning and sterilization usually need for re-use operations.

The plastic chamber keeps the advantages of the thin square shape of the metal chamber developed initially in VNC laboratory. This square frame is convenient for stereotaxic placement and very useful for chronic optical imaging experiment, providing a rectangular field for imaging and a coordinates frame for sites localization. Its very low thickness (<3mm), makes it also easier to carry for animal, but is first of all very relevant to minimize the shadows of chamber walls from illumination sources leading to a more homogeneous illumination and thus yielding the optical signal on wider cortical surface (see Fig. 147 and 148). The low thickness of the chamber also minimizes the optic pathway through the stabilization media (agar or artificial CSF), thus reducing the optical aberrations due to propagation of light through successive media of different optical indexes. Small groove within external walls enhance anchoring and sealing with dental cement. In its latest version, the plastic chamber also includes a slight curvature for best fit the cranial surface making the mounting procedure simpler and faster again.

A bath-tank made with the same plastic material was developed with high walls to maintain an important volume of VSDye solution over the cortical surface during the staining procedure. This volume prevents the rapid dilution of the VSD solution with natural CSF and maintains a weak hydrostatic pressure within the chamber to enhance the perfusion of dye molecules through the cortex. This removable element makes the wall of the chamber to be higher (~ 1cm) during the staining procedure and allows a larger amount of a solution to be in contact with the cortex for couple of hours. The periodic refuelling of the VSD solution is nevertheless necessary to keep the dye concentration at its optimal level and slow down its dilution with the flow of natural CSF on the cortical surface. The optimal concentration of dye solution is obtained at optical density of 4.0 (personal communication from A. Grinvald) measured by mean of absorption spectroscopy. The natural continuous flow of the CSF close to the surface of the cortex also prevents the dye solution to penetrate into the cortical layers, so keeping a weak hydrostatic pressure can greatly enhance the quality of the staining (see Fig. 149).

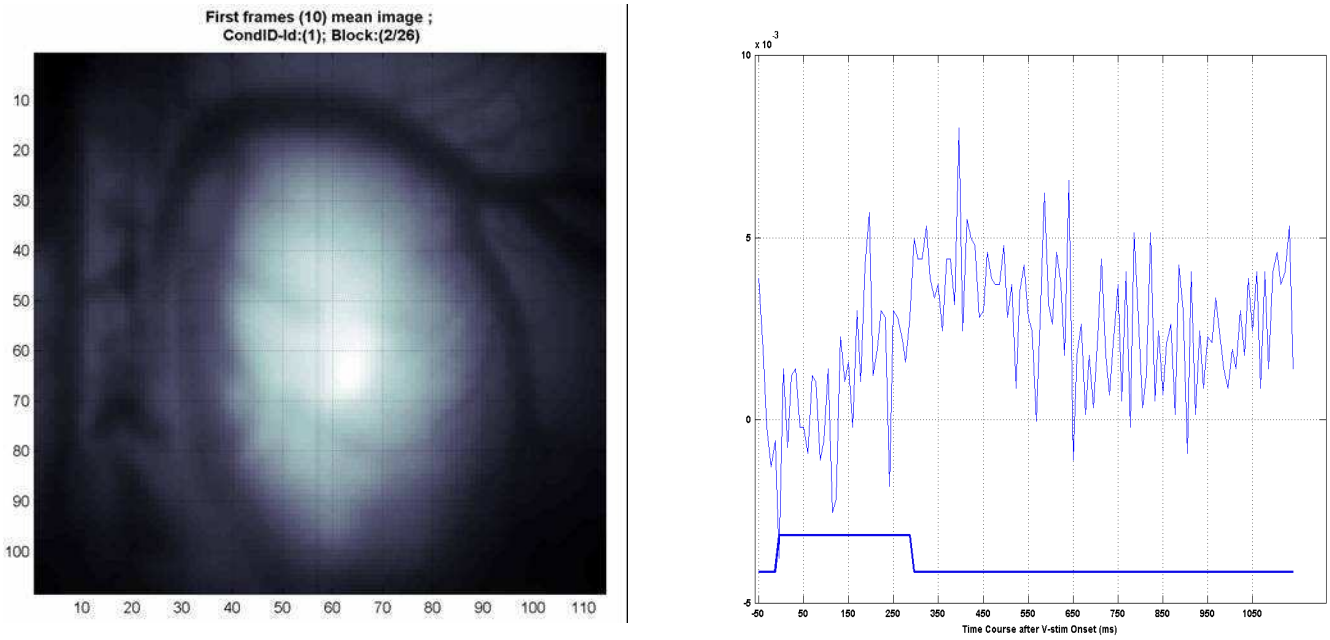

Fig. 150/ Mean fluorescence image and single pixel response time course.
Left: mean fluorescence image of a well stained cortical region (A18). An epi-illumination system conveys the illumination light through the macroscope by reflection on a dichroic mirror and focuses the light beam on the cortical surface; Scale for 1 pixel: 56µmx56µm.
Right: fluorescence time course from a single pixel after visual stimulation (bottom trace, duration 300 ms); the important fluctuations are due to the quantum nature of light; time scale: ms ; frame rate: 9.1 ms/img. (see also text for details)

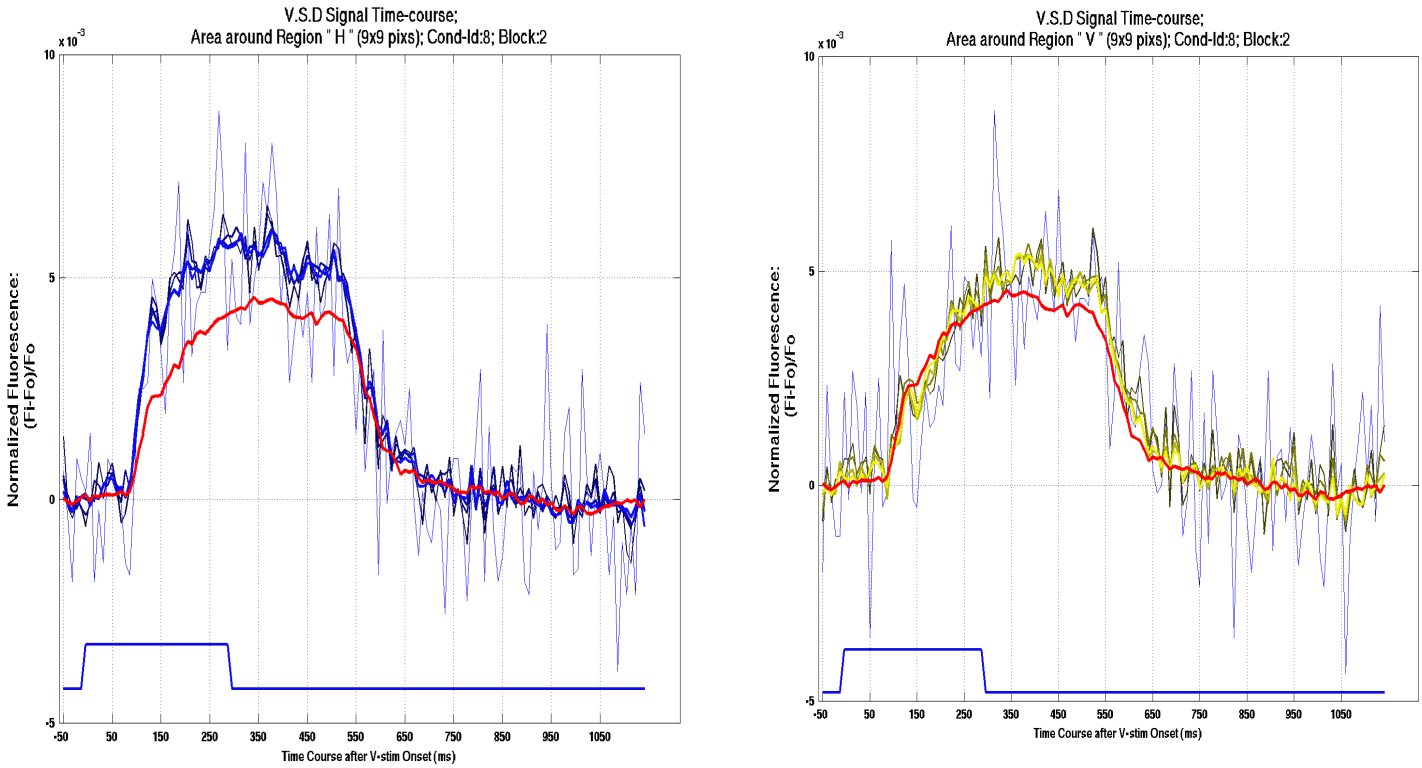

Fig. 151/ Spatial averaging of pixels response time course after visual stimulation for 2 different regions.
All traces show the time course of the mean fluorescence responses when averaged over different width of cortical areas after the same visual stimulation (horizontal drifting grating); The thin blue trace is a single pixel trace whereas 3 others having increasing thickness are averaged on 2x2, 5x5 and 9x9 pixels respectively around a single pixel. **Left** image shows the responses from a region responding preferentially to horizontal stimulation. **Righ** image shows the responses from a region responding preferentially to vertical stimulation.. The identical Red trace in both image show the fluorescence trace averaged on a wide area (50x50 pixels; 3.1 mm^2); bottom trace: stim. duration (300ms); times scale (ms); frame rate: 9.1 ms/img.

The illumination of the stained cortical surface by use of the standard epi-illumination system allows focusing a strong intensity of light on a region of interest and check the quality of staining by monitoring the mean fluorescence (see Fig. 150). An important mean fluorescence providing the best conditions for functional imaging results from a homogeneous staining combined with an even illumination of the region of interest. In order to record fast cortical response of primary visual cortices, we set the visual stimulation for short presentation (300 ms) of oriented drifting gratings (4 orientations, 8 directions, SF: 0.15 cpd optimized for A18 where usually the best staining were found). The Fig. 150 report the fluorescence time course (or “optical trace”) recorded from a single pixel in the region of good illumination. A modulation following the stimulation period is roughly observable, but the important noise resulting from the source fluctuations and the quantum nature of light requires proceeding to signal averaging to smooth its temporal evolution. This can be performed through spatial averaging (adjacent pixel binning), or by block and/or temporal meaning. Nevertheless, these signals averaging imposed by the weak signal to noise ratio available for a single pixels and obtained in our experimental conditions abolished the hope for detection of fine cortical oscillations. However spatial and block averaging demonstrated the functional preference of different cortical sites, as all site elicited a fluorescent response with different strength depending on stimulation conditions. (See Fig. 151). These experiments provide fluorescence modulations over a well stained/illuminated region of few mm^2 recorded at a frame rate of 9.1 ms/image.

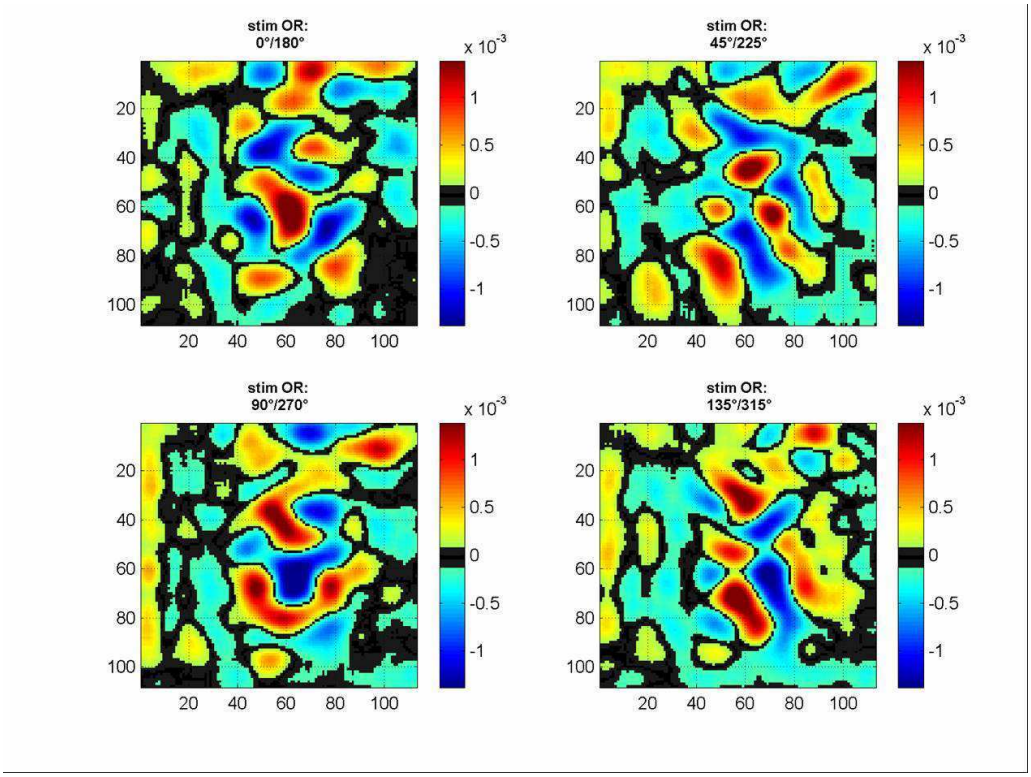

Fig. 152/ Single condition maps obtained by processing the "generalized indicator functions" algorithm.
Signals are time-averaged on the strong response period (150-450 ms after stimulus onset). Responses to stimulation with opposite directions of movement (drifting gratings) are combined to produce single condition maps for orientation.

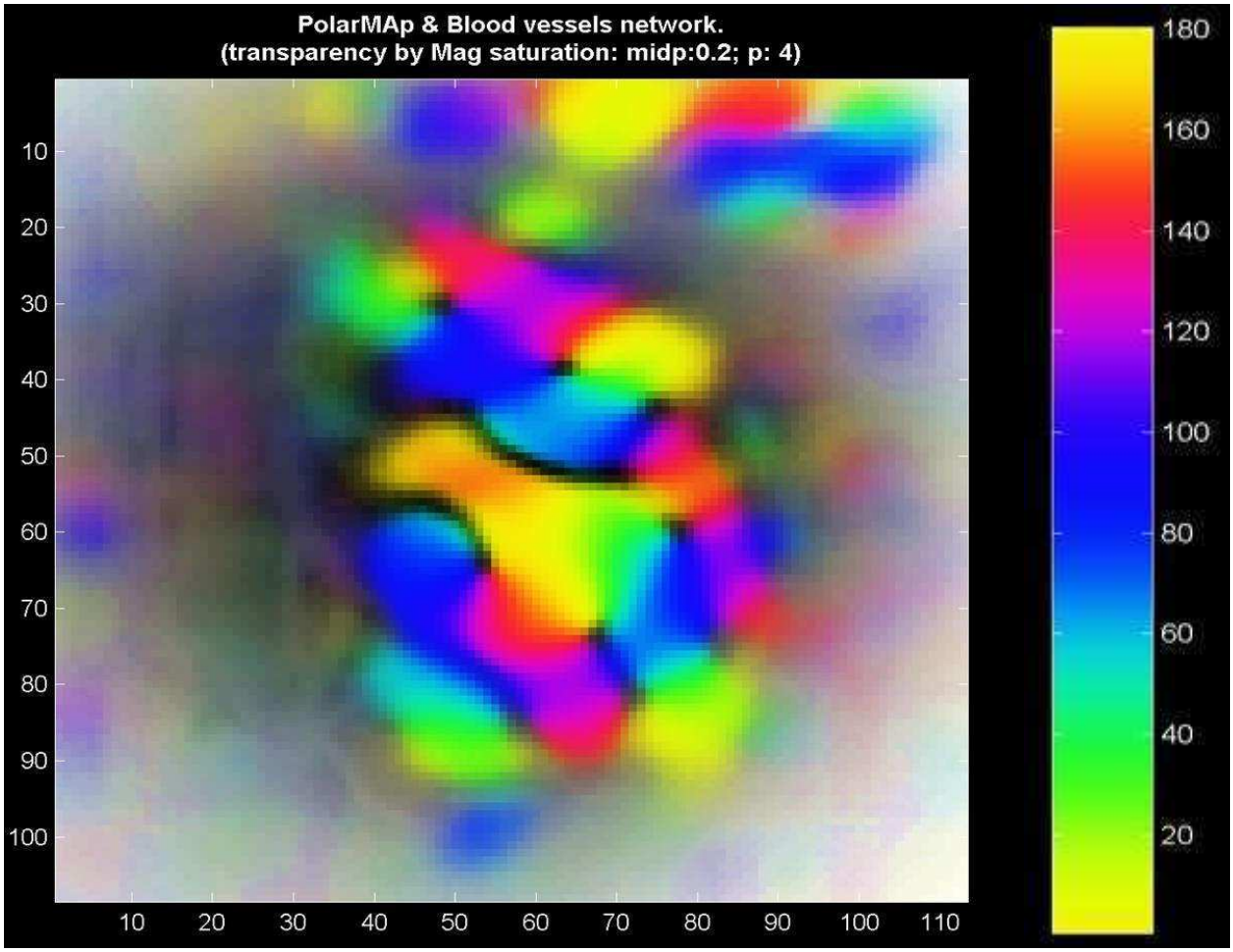

Fig. 153/ Polar map obtained with the 4 single condition maps of Fig. 152.
Colormap for orientation preferences is shown on the right side (deg°).

Functionnal imaging with VSDye signal from primary visual areas

The differential responses from site to site lead us to perform analysis to produce functional cortical maps. For this purpose, we averaged the optical signal of each pixel on a time window corresponding to the period of the sustain level or “high” mean response (150 to 450 ms after stimulus onset) and over all recorded blocks (26, one block contains data recorded for presentation of all condition of stimulation). The resulting “spatial” signal feed the generalized indicator function algorithm (see Ch. II.1, Signal and images analysis) to find optimal component of activation for each stimulus conditions (See Fig 152). The complementary aspect of patterns obtained from orthogonal stimulus conditions is clearly visible (compare top and bottom images of Fig. 152). These clear single condition maps for orientation serve for the construction of a polar map with conventional pixel-to-pixel vector summation (see Fig. 153). This demonstrated the successful use of VSDye for functional imaging of the primary visual cortices but these results lack of fine temporal resolution and they were confined into a very small cortical zone, thus remaining a major problem for interhemispheric dual recordings.

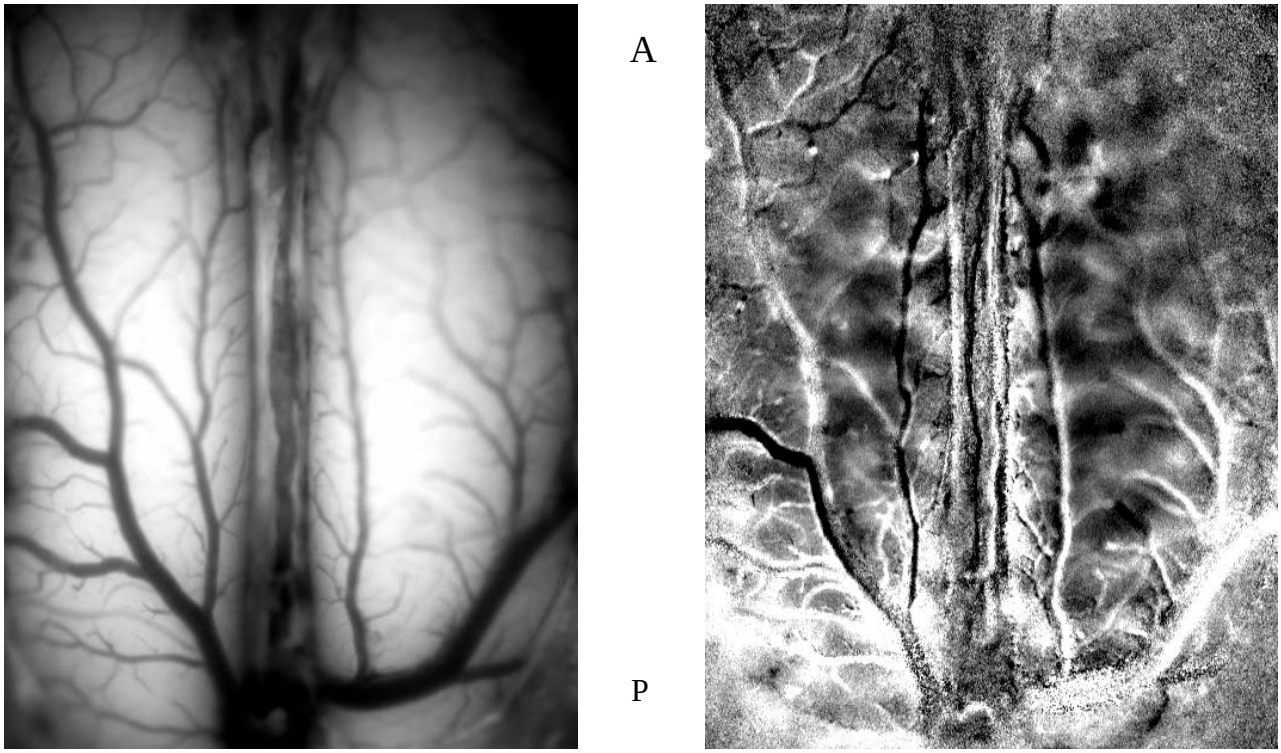

Fig. 154/ Our first bilateral activation revealed by optical imaging of intrinsic signal (LPPA, Paris, Jan 07)
Left: vascularization network of the cortical surface.
Right: Difference of responses from complementary vertical and horizontal stimulus conditions is performed to enhance the contrast of functional domains.

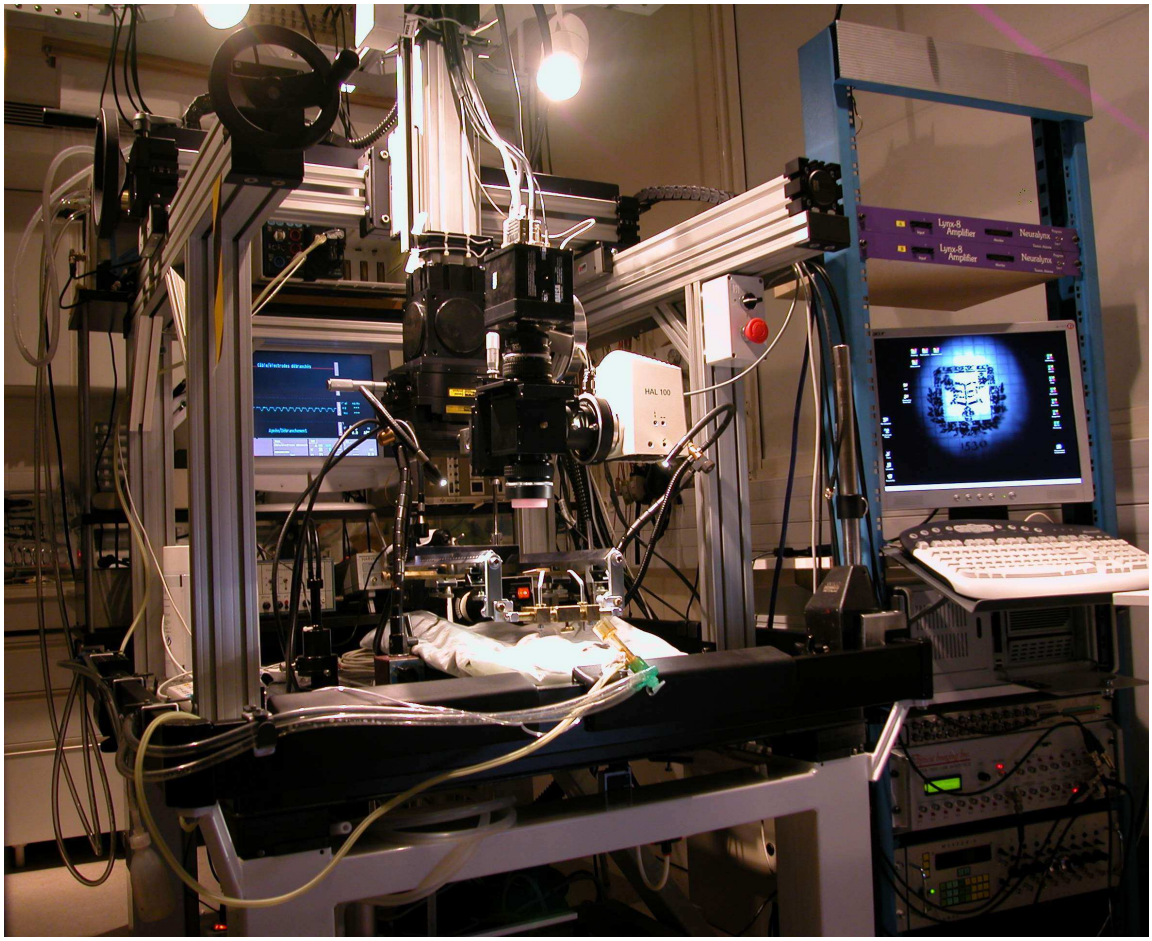

Fig. 155/ The optical imaging setup in Paris (LPPA, College de France).

Finer adaptations

All along this project, an optical imaging system has been setup in the Laboratoire de Physiology de la Perception et de l'Action (LPPA) at College de France. It benefits from the accumulated knowledge and know how developed along the thesis and from recent advances and adaptations realized in the aim of recording the cortical dynamics of both hemisphere together (see Fig. 155). This Imager can record both intrinsic signals and VSDye signals by change of the CCD camera and very little modifications. It provides its first well contrasted images of bilateral activation of primary visual cortices from OI-IS in the beginning of the year 2007 (See Fig. 154).

Both heart beats and respiration cycle are known to produce movement of the cortical surface decreasing the illumination stability. In order to enhance the signal strength by minimizing these biological perturbations, a synchronization protocol has been established between heart beat signal, the recording computer and the artificial respiration apparatus. Thus, the recording period is triggered by heart beat signal and the respiration pump is freezed at the same point in the respiration cycle during the recording period (interval < 1sec for VSDye recordings).

The illumination of the stained cortical surface by use of the standard epi-illumination system aims to focus strong intensity of light on a small region of interest, keeping in the darkness the flanking zones (see Fig. 150). Thus this kind of illumination apparatus is not satisfying to produce an even illumination over both hemispheres. In order to keep the strong illumination intensity necessary to provide enough fluorescence and to enhance the natural limitation of the signal-to-noise ratio of the light beam, we setup a high power illumination source whose light is conveyed to the cortical surface through conventional optic fibers. This allows the exposition of a wide cortical surface with an even illumination and an important light intensity.

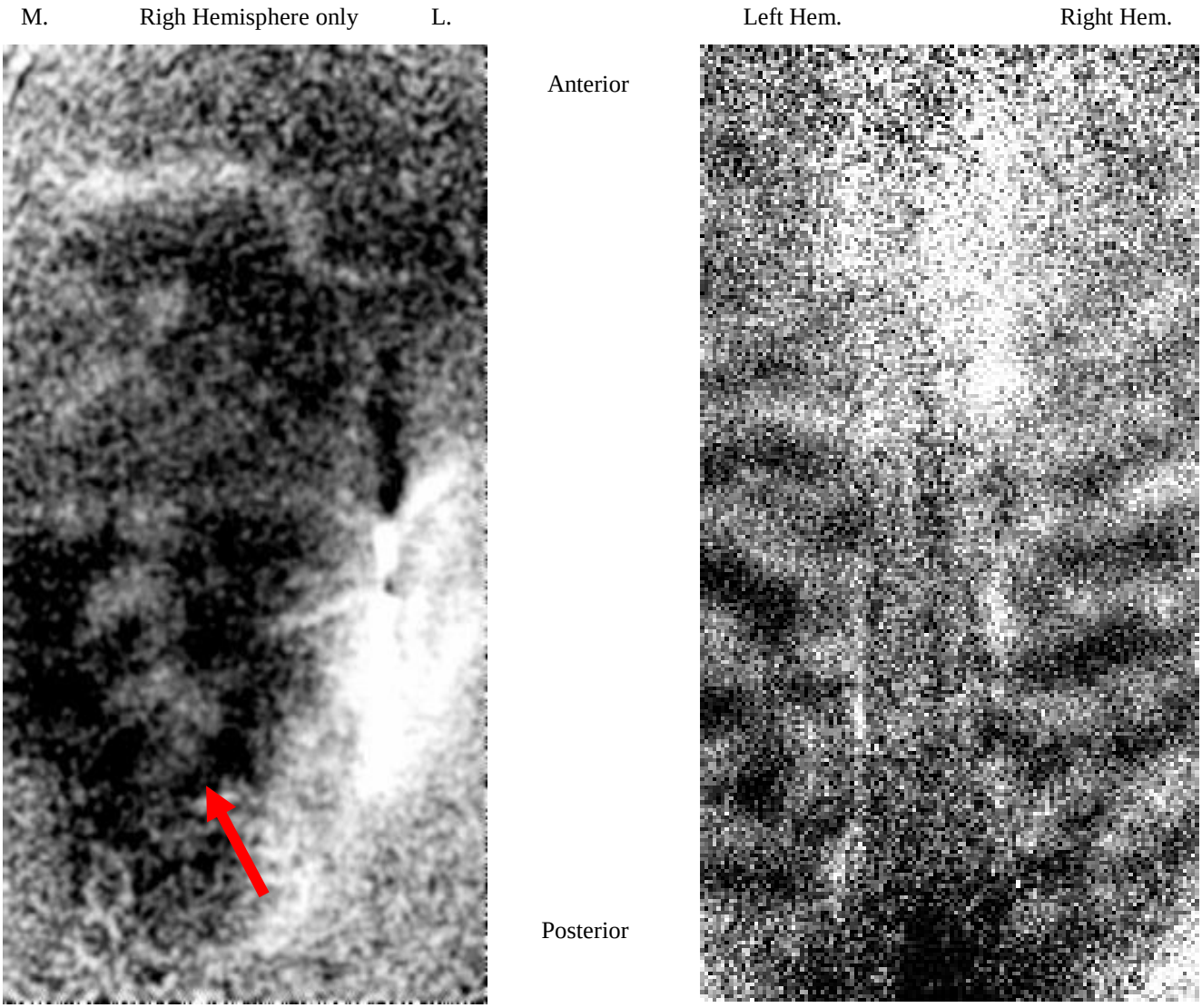

Fig 156/ Transcallosal activation (OI-VSD) (Image width: 5mm)

Fig. 157/ Wide area recording of bilateral activation by OI-VSD (width: 10 mm) at high frame rate (3ms/img).

Fig. 156/ Transcallosal activation (Right Hemisphere) along the (A17/A18) transition zone revealed by OI-VSD (clear patches along the direction of the red arrow) on a preparation with sagittal section of the optic chiasm. Visual stimulation is performed solely through the contralateral (left) eye, allowing the exclusive activation of the cortex through the corpus callosum (Stim: Horizontal grating,; frame rate 9.1 ms/ img).

Fig. 157/ Wide recording of bilateral activity by mean of OI-VSD at high frame rate (3 ms/img). The weakness of the signal still requires block averaging and complementary conditions (H-V) difference to yield contrast of functional domains.

At last, the callosal time transfer is of few ms by mean (Harvey, 1980). Thus, in order to reach the highest time resolution for our recording, compromise had to be found between the spatial and the temporal resolution of the CCD camera. By construction constraints of the CCD camera, increasing its temporal resolution decrease by the same order the available surface on the CCD detector. The best compromised was found for 3 ms per image with an image definition of 512x 128 pixels offering a band for which a well adapted lens allows to record interesting parts of each hemispheres.

The Fig. 156 shows transcallosal activation by use of VSDyes on a preparation with sagittal section of the optic chiasm. This experiment demonstrated the callosal inputs being confined onto the 1mm wide transition zone between area A17 and A18 but the signal strength was not good enough this time to explore some temporal aspects (contrast revealed by blocks and temporal averaging). The figure 157 shows a bilateral activation revealed by OI-VSD combining on both hemispheres a wide recorded area with a very high frame rate (3ms/image). All together, these latest adaptations bring promising results, making the imager almost ready to reveal some temporal aspects of the cortical integration between the primary visual cortices.

GENERAL CONCLUSION

The cerebral cortex is the largest and most intricately connected part of the mammalian brain. Its size and complexity has increased during the course of evolution allowing improvements in old functions and causing the emergence of new ones such as language. This has expanded the behavioural and cognitive repertoire of different species and has determined their competitive success. To allow the relatively rapid emergence of large evolutionary changes in a structure of such importance and complexity, the mechanisms by which cortical circuitry develops must be flexible and yet robust against changes that could disrupt the normal function of the network. Perhaps the most important function of the overproduction and selection of connections in the development is to provide a high degree of flexibility of the information flow in cortical circuits (Innocenti & Price, 2005). Thus, a part of the story of the construction of the brain and a part of its functional capabilities are hold in the architecture of its connectivity and in the morphology of the connecting structures. Moreover, the way these connecting structures grow, stabilize and connect should be somehow closely linked to the way the connected units "work" together, in normal conditions as much as under unusual conditions.

Among these structures, the callosal axon projections reflect a wide diversity and are challenging to describe. In the first part of this thesis we compared two populations obtained from normal and unbalanced conditions of vision, in order to understand the functional role of the morphology of single visual callosal axons falling into the particular environnement of the transition zone and its cortical mapping properties in close relation with the vertical meridian and its vicinity. The absence of behavioural or postural impairment and the strength of physiological response of TC cells in MD population demonstrate the relevance of the transcallosal structure as functional units after early monocular deprivation.

In the first chapter, the anatomical descriptions revealed important morphological differences between reference callosal axons and those obtained after an early monocular deprivation. The two following chapters proposed 2 original computational methods to overcome the challenge of the quantitative description of the wide diversity of the callosal axons morphology. Both the "ellipsoid approximation" and the "clustering analysis" succeeded in not only providing complementary relevant descriptions of the spatial organisation of callosal axons terminals, but also in revealing significant differences between the NR and MD two populations. It was demonstrated by this way the wider spatial extension of MD axons and their much more scattered aspect, almost both twice greater compared to NR axons. The wider extension and clustered organisation of MD population might reflect for a part the stabilization of exuberant juvenile connections combined also with axonal sprouting.

The thalamus and the cerebral cortex are interconnected in an ordered fashion such as adjacent cells in the presynaptic structure project, as a general rule, to adjacent structure in the post synaptic

structure. Recent evidence has indicated that members of the *Eph/ephrin* family of guidance molecules are required for subcortical ordering of thalamocortical growth (Dufour et al, 2003). A Phase in the thalamic development is believed to be increasingly dependant on input activity. Exactly when this phase begins is not strictly defined but it is probable that peripheral neurons first develop spontaneous activity and later start to respond to stimuli from the external environment. Peripheral sensory organs can generate patterns of spontaneous activity at the time when sensory afferents first reach the thalamus. (Galli & Maffei, 1988, Meister & at, 1991). Similar mechanisms can reach and drive the organization of the cortical connectivity (Innocenti & Price, 2005).

During axonal growth, the extracellular factors that trigger axonal retraction include molecules known to be chemorepulsive to growth cones such as *semaphorins*, *slits* and *ephrines* but the molecular mechanisms involved in the elimination of exuberant connections remains largely unknown. Once the cortex is reached, activity dependant mechanisms become increasingly important in shaping topographic and feature maps (Katz & Shatz, 1996). Axonal remodelling are likely to depend on factors that include correlated neural activity and gradient of chemoattractant and chemorepellent molecules.

The fact that callosal connections in primary visual areas are stabilized by information contained in retinal topography is implicit in the finding that the connections are restricted close to the representation of the visual midline (Innocenti & Price 2005). This induced the idea that callosal connections could be stabilized, within each hemisphere, by mean of a correlated activity that is driven by inputs from both temporal retinae, or by mean of spontaneous activity from one retina before eyes opening. However, the relationship between retinotopy and callosal connections can be modified during development (Restrepo et al., 2003). So, others factors such as axonal competition as for the *Brain Derived Neurotrophic Factors* (BDNFs) might therefore override information from the periphery (Lotto et al. 2001). The fast, vision independent stabilization and maturation of arbour of callosal axons that follows a short period of normal vision (Zufferey et al. 1999) suggest that the fast release of trophic molecules, in particular BDNF, as reported in the development of retinotectal and cortical connections, might trigger a cell-intrinsinsic programme of axonal development. It seems likely that activity still controls the fine structure of the axonal arbours by interacting with the cell-intrinsic developmental programmes, but this remains to be determined by studies of axonal morphologies combined with their functional consequences as we initiated in the work presented here. In any case, myelination, and therefore the axonal conduction properties that are crucial to the timing of cortical computation might heavily depend on cell extrinsic factors including activity (Bengtson et al., 2005).

Callosal timing and development time course of myelination

The timing of callosal propagation is heavily dependant on myelination of fibers. However the late development of its myelination during the second postnatal month, only at the end of the critical period was reported (Elberger & Smith, 1982; Looney & Elberger, 1986). As indicated by Elberger (1988): The neonatal corpus callosum is involved in the development of pathways or mechanisms that coordinate the inputs from the two eyes. Some visual functions are permanently altered by the absence of the callosum during early development. Changes in acuity and striate binocularity only result when a callosal section occurs during a critical period of the first postnatal month, and the earlier the surgery is, the greater the changes are. The lack of myelination during the first postnatal month indicates that the high velocity conduction properties of the callosum are poorly developed during this critical period. The precise temporal pattern of callosal connectivity is probably significant for its role in development, but not all callosal fibres are necessary for normal visual development.

In fact many callosal fibers are eliminated during development, as shown in particular by Innocenti and collaborators (Berbel & Innocenti, 1988): Elimination begins before the beginning of fast synaptogenesis in the cerebral cortex, but it continues throughout the phase of decrease in cortical synaptic density. This would suggest that the early eliminated callosal axons probably did not establish contacts, whereas the late eliminated axons did. The phase of rapid axonal elimination occurs before the onset of myelination, and the whole elimination seems nearly finished before an adult proportion of myelinated axons has been reached. It is therefore conceivable that most or all callosal axons are eliminated before they are myelinated. Cortical axons incapable of forming a sufficient number of synapses may fail to be sustained and therefore may be eliminated, whereas others mature, i.e., stabilize their cytoskeleton, and some increase in diameter and myelinate.

Moreover, the majority of myelinated fibers in all layers of the visual cortex occurs after the second postnatal month (Sherman & Spear, 1982), so all the network, including thalamocortical, cortico-cortical, intra and interhemispheric connectivity first develops without myelin. All the network works at slower rhythms in the kitten and consequently precise synchronization could also be detected for selection during this unmyelinated period.

All together, these data provide an interesting framework to understand some spatio-temporal characteristics of callosal connections. First of all, the MD axons were shown to be functionally relevant for visual perception at least by their strong physiological evoqued activity. The ways they grow, connect and stabilize are likely to follow the same rules as for normal rearing, with however a wider cortical spread following, interestingly in a similar fashion, what is found in the LGNd under the same

conditions of development: for the thalamocortical axons coming from the non-deprived eye it was also noticed an extension of arbors (by a factor 2) and a strong diminution of termination density with respect to NR, (Friedlander et al. 1991). Once installed, the callosal connections should develop their myelination in order to provide the highly precise synchronization necessary for an effective and coherent visual perception.

Our research perspectives are to place the spatial and temporal characteristics of callosal axons described here, in the context of the functional mapping of the primary visual cortices. Especially, the spatial extension on the cortical surface, the average orientation of the synaptic distribution and the clustered organization of axon terminals described and discussed in this work, all should be closely related to the arrangement of the retinotopic map, the orientation map and the ocular dominance map. The temporal properties, in particular delays and dispersion should also be experimentally explored by mean of population activity in the vicinities of the transition zone. The optical imaging combined with voltage sensitive dye is one of the most relevant methods for this purpose. It is available and ready to use by now in our laboratory and already gave very promising results.

Recording of spatial and temporal transcallosal activity with VSD optical imaging.

For the second part of this thesis, we aimed to record the activity of a wide population of cortical cells in the region of TZ with the development of optical imaging technique using voltage sensitive dyes in order to reveal *in vivo* their temporal characteristics and replace them in the cortical functional mapping context. Among them, the interhemispheric communication timing, the temporal dispersion of the callosal signal and the spectral contents of the related cortical dynamic is of great interest. The limitation of the signal to noise ratio induced by the nature of the illumination source and the blocks-averaging procedure necessary to enhance the recorded activity abolished for a while the hope for access the spectral content of the cortical activity. Especially, the recording of the gamma band activity to test the hypothesis of perceptive binding by synchronized oscillation had to be laid aside until technological solution afford a better signal to noise ratio. However, the challenge of recording both hemispheres with both satisfying spatial and temporal resolutions was overcome with important modifications of the original system. Among them the accurate control of the biological perturbations (principally due to movements from heart beats and respiration) with the proper synchronisation between the artificial respiration system and the record/stimulation sequence locked on heart signal improved the quality of the recorded signal. Moreover we combined the enhancement of the staining procedure, the improvement of the illumination power and its stability, the simplification of the optic pathways and the reduction of the recording chamber depth. All together, these advances allow us to improve step by step the width of the region of interest in order to embrace together both hemispheres in the callosal relevant regions, and to increase the temporal resolution of the images sequence (3 ms/frame) close to the affordable technical limit of the CCD camera (2 ms/frame). The compromise found between the spatial width and temporal accuracy finally allows us to record bilateral sequences of activity at an important sampling rate (340Hz). As this project is still in progress, we assert our efforts on the experimental program to reveal temporal properties of the interhemispheric communication between primary visual areas, focusing especially on transcallosal delays and dispersions. The clear objective is to merge such dynamics functional data with those from the first part including anatomical and physiological models.

Functional implications of the corpus callosum in the primary visual areas

At the level of the primary visual areas, the organization of callosal efferent and afferent structure in the retinotopic map, combined with the binocular disparities of transcallosally activated cells and with the oblique bias found for axons terminal extensions in both NR and MD population (ChI.2) suggest interesting functional hypothesis for the corpus callosum between primary visual areas.

First of all, assuming the connectivity between two cortical domains having both shared a representation of the vertical meridian and its vicinity in the visual field, strongly suggest the participation in the fusion of the two visual hemifield as its major role. Participating in the bilateral representation of the ipsilateral visual field in one hemisphere, the callosal inputs allow each hemisphere to assume primary visual processing continuously across the vertical meridian. The results of the visual processings concerning a local region in a receptive field were found recently to be also dependant on modulations of the external regions of this receptive field (Series et al. 2003). In other words, the response of a cortical cell concerning the dynamic of its classical receptive field is modulated by the response of some of its surrounding neighbours as demonstrated for the "association field" theory (George et al. 2002; Series et al. 2002; 2003). Thus, it is not surprising that a representation of a part of the visual field across the vertical midline (i.e. the ipsilateral visual field) is necessary to complete the local integration of a visual process as needed for the contour completion for example. It is thus likely that the callosal inputs into or around the transition zone provide "additional" information about flanking visual regions processed in the contralateral hemisphere and thus participate in the fusion of both hemifields.

At the end of the 19th century, Mach observed that vertical symmetry is more easily perceived than bilateral symmetry at other orientations and proposed this resulted from the bilateral symmetry in the visual system. This particular salience has been reported experimentally on human subjects (Wenderoth, 1994). The involvement of the callosum fibers concerned by the transmission of informations around the vertical meridian suggests a "callosal hypothesis" to enhance the detection of the vertical symmetry and this hypothesis has been explored through psychophysical experiments (Herbert and Humphrey, 1996). In particular, it was found that the vertical advantage of the symmetry detection was disrupted by presentation of patterns 1.2° from the vertical meridian (VM) while detection of symmetry at other orientations was not significantly changed out of the VM. Moreover, the detection of vertical symmetry at fixation was found to be anomalous for two subjects born without a corpus callosum as compared with controls, while remains relatively normal for presentation "off" fixation. Thus it appear that the callosal hypothesis may account for the relative advantage of vertical symmetry, but only close to the VM, in natural agreement with the retinotopic organization of the callosal connection.

The distribution of centres of the TC cells receptive fields spanned on both side of the vertical meridian and the oblique bias for the spatial extension of callosal axons reported in our work provide interesting cues on the possible role of the corpus callosum in the detection of the vertical symmetry. The disparity of TC cells could allow a comparison of visual attributes between inputs from the direct

RGC pathway on one side in the visual field, with the contralateral signal related to the other side of the visual field with stronger TC cell activation when both inputs match. On the other hand, the mediolateral extensions of callosal terminals distribution reported in this work and corresponding, in term of retinotopy, to visual sites across the vertical meridian may suggest that the callosal axons distribute information enhancing the detection of the vertical symmetry on the VM.

However, recent EEG experiments reveal strong activations correlated with the detection of vertical symmetry from random dot fields presented at fixation point in visual areas far in the hierarchy from the primary visual cortices (Norcia et al. 2002). The latency of a response significantly distinguishable for the symmetry detection, 220 ms after the stimulus onset, is consistent with the hypothesis that the vertical symmetry properties, involving wider receptive fields is extracted by processing in extra-striate cortex (Lee et al. 1998, Tyler & Baseler, 1998).

Thus Vertical symmetry on fixation point appears to be special and the salience of this kind of structure may results for a part from the particular importance of the bilateral representation of the vertical meridian in the primary visual system connected through the corpus callosum. A part of the pre-processing of the detection of bilateral symmetry on the VM might be underlied by callosal connection establishing relation between cells having receptive field on each side of the VM, however the integration of a global form seems necessary to be performed into higher cortical areas until phenomenological “detection” occurs.

Although not as detectable as vertical symmetry, non vertical symmetry is also a salient form. The callosal hypothesis may account for the salience of vertical symmetry at fixation but it cannot account for the detection of non vertical symmetry or for detection of vertical symmetry in patterns presented off fixation.

At last, the crossed disparities found for TC cells may suggest also a role played by the callosal inputs in the vision of the stereopsis in front of the fixation plane. This was demonstrated in the effects of a callosal critical period by Elberger & Smith (1982), and by the recent study on disparities of Milleret et al (2005); the interplay between ocular dominance, binocularity and interhemispheric connections is not completely understood.

On the origins of the Left and the Right, when two become one.

The two cerebral hemispheres of mammals are not completely equivalent in their information processing abilities. However, they cooperate one with the other through bundles of fibres which constitute the commissures of the brain. Being back on brain lateralisation, the classical view of cerebral dominance point out the word-blindness, the word-deaf and the silence of the human right hemispheres (for the average right handed population), as revealed by local lesions in the left hemisphere. Moreover, extensive works on commissurotomy inducing split-brain subjects revealed each brain half to have its own, largely separate, cognitive domains with its own private perceptual, learning and memory experiences as reported by R. Sperry and its colleagues (Sperry, 1981). Among them, in such particular experimental conditions, the right hemisphere surprisingly showed having language but non-verbal skills, while the contralateral speaking hemisphere could not report any content of the inner experience of the opposite mute hemisphere. Likewise, the mute hemisphere showed having developed particular skills to make intermodal spatial transformations from three dimensional to unfolded two dimensional projected forms for example (Levy, 1968; 1970). This set of spatial skills could be interestingly related to "change of point of view" ability or even "empathy" when described in the framework of social interactions. The mute hemisphere was then described having non verbal, non mathematical and non sequential skills, showing particular spatial and imaginative specialities, of a kind where a single picture is worth thousand words. From these data it was proposed that the left and the right hemispheres are characterized by inbuilt, qualitatively different and mutually antagonistic modes of cognitive processing, the left being basically sequential and analytic and the right spatial and synthetic. Nevertheless the two halves of the brain, when connected in normal conditions, work closely together as a functional unit with the leading control of a particular task being in one or the other. Recently, alteration in the morphology of callosal connections have been reported in several conditions caused by abnormal development including Attention Deficit Hyperactivity Disorder (ADHD) (Giedd et al., 1994; Magara et al., 2000), dyslexia (von Plessen et al., 2002) and schizophrenia (Innocenti et al, 2003).

The origins of brain lateralizations are mainly unknown. Whereas primary sensory areas are organized according to the bilateral symmetry in agreement with the general organization of the body scheme, higher cortical treatment in the cognitive process hierarchy shows strong asymmetries with functional localisation for human almost always found on the same side of the brain as described above. If the evolutional natural expansion of the cortical surface would have been the only reason for the division of the task repartition, with former abilities present in both hemispheres and new modules emerging in one or the other hemisphere (Gazzaniga, 2000), the hemispheric repartition

should have been found equally distributed in the left and the right hemispheres, at least in the population distribution. This specialization processes are likely to depend on local interactions between morphogenetic substrate and local neural activity modulated by the dynamic of the environnement. It is interesting to remark that the structure of the environment and its dynamic is likely to be globally unbiased regarding to the body scheme and thus would not induce any particular unbalance on one side of the brain instead of the other. Thus, the systematic bias for lateralization specialization of the human brain remains rather mysterious. In other word, a symmetry break occurring during the construction of the brain remains to be found. Very recently, researchers discovered strong correlations between the presence of genes in a population of subject and their left-handeness (Francks et al., 2007). People showing a particular set of genes in their genotype (LRRTM1 on chromosome 2p12**)** are likely to be left handed but surprisingly also to develop symptoms of schizophrenia. At the beginning of this work, this team was trying to demonstrate a correlation between left-handeness and dyslexia symptoms. Whereas left-handed subject are known to be much less lateralized as the average human population, this correlation with a genetic substrate is a very interesting advance on the quest for the symmetry break of brain lateralization. The discovery of this genetic substrate gives rise to interesting molecular hypothesis for the induction of lateral specializations of the human brain. Particularly, some well known strongly biased molecular chirality such as those found for sugar molecules in the living kingdom, for whose only one chiral form is found over two possible symmetric enantiomeres synthesized in laboratory, are of the rare candidates to explain the preference of nature for one side rather the other. Whatever the origins of differences, along the development of two twin brain entities, the corpus callosum seems to assume a harmonious communication in-between and is likely to allow the emergence of a unity.

Reference List

[1] Adams JC: Heavy metal intensification of DAB-based HRP reaction product. J Histochem Cytochem 1981;29:775.

[2] Agoun-Aouaoui D, Kiper DC, Innocenti GM: Growth of callosal terminal arbors in primary visual areas of the cat. Eur J Neurosci 1996;8:1132-1148.

[3] Agoun-Zouaoui D, Innocenti GM: Juvenile visual callosal axons in kittens display origin- and fate-related morphology and distribution of arbors. Eur J Neurosci 1-12-1994;6:1846-1863.

[4] Akaike H: A New Look at the Statistical Model Identification. IEEE Transactions on Automatic Control 1974;19:716-723.

[5] Antonini A, Stryker MP: Development of individual geniculocortical arbors in cat striate cortex and effects of binocular impulse blockade. J Neurosci 1993;13:3549-3573.

[6] Assal F, Innocenti GM: Transient intra-areal axons in developing cat visual cortex. Cereb Cortex 1993;3:290-303.

[7] Barlow HB: Single units and sensation: a neuron doctrine for perceptual psychology? Perception 1972;1:371-394.

[8] Bartfeld E, Grinvald A: Relationships between orientation-preference pinwheels, cytochrome oxidase blobs, and ocular-dominance columns in primate striate cortex. Proc Natl Acad Sci U S A 15-12-1992;89:11905-11909.

[9] Basole A, White LE, Fitzpatrick D: Mapping multiple features in the population response of visual cortex. Nature 26-6-2003;423:986-990.

[10] Berbel P, Innocenti GM: The development of the corpus callosum in cats: a light- and electron-microscopic study. J Comp Neurol 1-10-1988;276:132-156.

[11] Berlucchi G, Rizzolatti G: Binocularly driven neurons in visual cortex of split-chiasm cats. Science 19-1-1968;159:308-310.

[12] Berman NE, Payne BR: Alterations in connections of the corpus callosum following convergent and divergent strabismus. Brain Res 12-9-1983;274:201-212.

[13] Bishop PO, KOZAK W, LEVICK WR, VAKKUR GJ: The determination of the projection of the visual field on to the lateral geniculate nucleus in the cat. J Physiol 1962;163:503-539.

[14] Blight AR: Computer simulation of action potentials and afterpotentials in mammalian myelinated axons: the case for a lower resistance myelin sheath. Neuroscience 1985;15:13-31.

[15] Boire D, Morris R, Ptito M, Lepore F, Frost DO: Effects of neonatal splitting of the optic chiasm on the development of feline visual callosal connections. Exp Brain Res 1995;104:275-286.

[16] Bonhoeffer T, Grinvald A: Iso-orientation domains in cat visual cortex are arranged in pinwheel-like patterns. Nature 3-10-1991;353:429-431.

[17] Bonhoeffer T, Grinvald A: Optical imaging of the functional architecture in cat visual cortex: the layout of direction and orientation domains. Adv Exp Med Biol 1993;333:57-69.

[18] Bonhoeffer T, Kim DS, Malonek D, Shoham D, Grinvald A: Optical imaging of the layout of functional domains in area 17 and across the area 17/18 border in cat visual cortex. Eur J Neurosci 1-9-1995;7:1973-1988.

[19] Borggreen J, Chowdhury P, Kebaïli N, Lundsberg-Nielsen L, Lützenkirchen N, Nielsen MB, Pedersen J., Rasmussen H.D.: Plasma excitations in charged sodium clusters. Phys Rev B 48 1993;17507-17516.

[20] Bosking WH, Kretz R, Pucak ML, Fitzpatrick D: Functional specificity of callosal connections in tree shrew striate cortex. J Neurosci 15-3-2000;20:2346-2359.

[21] Bosking WH, Zhang Y, Schofield B, Fitzpatrick D: Orientation selectivity and the arrangement of horizontal connections in tree shrew striate cortex. J Neurosci 15-3-1997;17:2112-2127.

[22] Boyd J, Matsubara J: Tangential organization of callosal connectivity in the cat's visual cortex. J Comp Neurol 8-9-1994;347:197-210.

[23] Boyd JD, Matsubara JA: Laminar and columnar patterns of geniculocortical projections in the cat: relationship to cytochrome oxidase. J Comp Neurol 19-2-1996;365:659-682.

[24] Bressloff PC, Cowan JD, Golubitsky M, Thomas PJ, Wiener MC: What geometric visual hallucinations tell us about the visual cortex. Neural Comput 2002;14:473-491.

[25] Burke R.E., William B.M.: Some approaches to qunatitative dendritic morphology; in G.ascoli (ed): computational neuroanatomy. 2002.

[26] Burkhalter A: Intrinsic connections of rat primary visual cortex: laminar organization of axonal projections. J Comp Neurol 8-1-1989;279:171-186.

[27] Burnham KP, Anderson DR: Multimodel Inference: understanding AIC and BIC in Model Selection. Sociol Meth Res 2004;33:261-304.

[28] Buzas P, Eysel UT, Adorjan P, Kisvarday ZF: Axonal topography of cortical basket cells in relation to orientation, direction, and ocular dominance maps. J Comp Neurol 27-8-2001;437:259-285.

[29] Buzas P, Kovacs K, Ferecsko AS, Budd JM, Eysel UT, Kisvarday ZF: Model-based analysis of excitatory lateral connections in the visual cortex. J Comp Neurol 20-12-2006;499:861-881.

[30] Cabanis E.M., Iba-Zizen M., Nguyen T.H., Bellinger L., Stienvenart J.L, Yoshida M., Hamard H.: Les voies visuelles de la vision, de l'IRM anatomique à la physiologie (IRM(f)) et IRM en tenseur de diffusion (IRMTD) ou tractographie. Bull Acad Natle Méd 2004;188, n°7.

[31] Callaway EM, Katz LC: Emergence and refinement of clustered horizontal connections in cat striate cortex. J Neurosci 1990;10:1134-1153.

[32] Callaway EM, Katz LC: Effects of binocular deprivation on the development of clustered horizontal connections in cat striate cortex. Proc Natl Acad Sci U S A 1-2-1991;88:745-749.

[33] Celeux G, Soromenho G: An Entropy Criterion for Assessing the Number of Clusters in a Mixture Mode. Journal of Classification 1996;13:195-212.

[34] Chavane F, Monier C, Bringuier V, Baudot P, Borg-Graham L, Lorenceau J, Fregnac Y: The visual cortical association field: a Gestalt concept or a psychophysiological entity? J Physiol Paris 2000;94:333-342.

[35] Clarke RJ, Datskovsky BW, Grigonis AM, Murphy EH: Transcallosally evoked responses in the visual cortex of normal and monocularly enucleated rabbits. Exp Brain Res 1992;91:296-302.

[36] Cooke J: The evolutionary origins and significance of vertebrate left-right organisation. Bioessays 2004;26:413-421.

[37] Cosmelli D, David O, Lachaux JP, Martinerie J, Garnero L, Renault B, Varela F: Waves of consciousness: ongoing cortical patterns during binocular rivalry. Neuroimage 2004;23:128-140.

[38] Cowan WM: Aspects of neural development. Int Rev Physiol 1978;17:149-191.

[39] Crair MC, Horton JC, Antonini A, Stryker MP: Emergence of ocular dominance columns in cat visual cortex by 2 weeks of age. J Comp Neurol 5-2-2001;430:235-249.

[40] Cusick CG, Lund RD: Modification of visual callosal projections in rats. J Comp Neurol 20-12-1982;212:385-398.

[41] Cynader M, Lepore F, Guillemot JP: Inter-hemispheric competition during postnatal development. Nature 12-3-1981;290:139-140.

[42] Das A, Gilbert CD: Long-range horizontal connections and their role in cortical reorganization revealed by optical recording of cat primary visual cortex. Nature 29-6-1995;375:780-784.

[43] Das A, Gilbert CD: Receptive field expansion in adult visual cortex is linked to dynamic changes in strength of cortical connections. J Neurophysiol 1995;74:779-792.

[44] Debanne D: Information processing in the axon. Nat Rev Neurosci 2004;5:304-316.

[45] Deschenes M, Landry P: Axonal branch diameter and spacing of nodes in the terminal arborization of identified thalamic and cortical neurons. Brain Res 9-6-1980;191:538-544.

[46] Diao YC, Jia WG, Swindale NV, Cynader MS: Functional organization of the cortical 17/18 border region in the cat. Exp Brain Res 1990;79:271-282.

[47] Dufour A, Seibt J, Passante L, Depaepe V, Ciossek T, Frisen J, Kullander K, Flanagan JG, Polleux F, Vanderhaeghen P: Area specificity and topography of thalamocortical projections are controlled by ephrin/Eph genes. Neuron 31-7-2003;39:453-465.

[48] Edelman GM: Neural Darwinism: selection and reentrant signaling in higher brain function. Neuron 1993;10:115-125.

[49] Elberger AJ: The role of the corpus callosum in the development of interocular eye alignment and the organization of the visual field in the cat. Exp Brain Res 1-6-1979;36:71-85.

[50] Elberger AJ: Developmental interactions between the corpus callosum and the visual system in cats. Behav Brain Res 15-9-1988;30:119-134.

[51] Elberger AJ: Distribution of transitory corpus callosum axons projecting to developing cat visual cortex revealed by DiI. J Comp Neurol 15-7-1993;333:326-342.

[52] Elberger AJ, Smith EL, III, White JM: Spatial dissociation of visual inputs alters the origin of the corpus callosum. Neurosci Lett 31-1-1983;35:19-24.

[53] Engel AK, Konig P, Gray CM, Singer W: Stimulus-Dependent Neuronal Oscillations in Cat Visual Cortex: Inter-Columnar Interaction as Determined by Cross-Correlation Analysis. Eur J Neurosci 1990;2:588-606.

[54] Engel AK, Konig P, Kreiter AK, Singer W: Interhemispheric synchronization of oscillatory neuronal responses in cat visual cortex. Science 24-5-1991;252:1177-1179.

[55] Ferrer JM, Price DJ, Blakemore C: The organization of corticocortical projections from area 17 to area 18 of the cat's visual cortex. Proc R Soc Lond B Biol Sci 23-2-1988;233:77-98.

[56] Ferster D, LeVay S: The axonal arborizations of lateral geniculate neurons in the striate cortex of the cat. J Comp Neurol 15-12-1978;182:923-944.

[57] Francks C, Maegawa S, Lauren J, Abrahams BS, Velayos-Baeza A, Medland SE, Colella S, Groszer M, McAuley EZ, Caffrey TM, Timmusk T, Pruunsild P, Koppel I, Lind PA, Matsumoto-Itaba N, Nicod J, Xiong L, Joober R, Enard W, Krinsky B, Nanba E, Richardson AJ, Riley BP, Martin NG, Strittmatter SM, Moller HJ, Rujescu D, St CD, Muglia P, Roos JL, Fisher SE, Wade-Martins R, Rouleau GA, Stein JF, Karayiorgou M, Geschwind DH, Ragoussis J, Kendler KS, Airaksinen MS, Oshimura M, Delisi LE, Monaco AP: LRRTM1 on chromosome 2p12 is a maternally suppressed gene that is associated paternally with handedness and schizophrenia. Mol Psychiatry 31-7-2007.

[58] Frostig RD, Lieke EE, Ts'o DY, Grinvald A: Cortical functional architecture and local coupling between neuronal activity and the microcirculation revealed by in vivo high-resolution optical imaging of intrinsic signals. Proc Natl Acad Sci U S A 1990;87:6082-6086.

[59] Galli L, Maffei L: Spontaneous impulse activity of rat retinal ganglion cells in prenatal life. Science 7-10-1988;242:90-91.

[60] Galuske RA, Singer W: The origin and topography of long-range intrinsic projections in cat visual cortex: a developmental study. Cereb Cortex 1996;6:417-430.

[61] Gazzaniga MS: Cerebral specialization and interhemispheric communication: does the corpus callosum enable the human condition? Brain 2000;123 (Pt 7):1293-1326.

[62] Gazzaniga MS: Forty-five years of split-brain research and still going strong. Nat Rev Neurosci 2005;6:653-659.

[63] Gazzaniga MS, Bogen JE, Sperry RW: Some functional effects of sectioning the cerebral commissures in man. Proc Natl Acad Sci U S A 15-10-1962;48:1765-1769.

[64] Georges S, Series P, Fregnac Y, Lorenceau J: Orientation dependent modulation of apparent speed: psychophysical evidence. Vision Res 2002;42:2757-2772.

[65] Ghosh A, Shatz CJ: Involvement of subplate neurons in the formation of ocular dominance columns. Science 13-3-1992;255:1441-1443.

[66] Ghosh A, Shatz CJ: Pathfinding and target selection by developing geniculocortical axons. J Neurosci 1992;12:39-55.

[67] Giedd JN, Castellanos FX, Casey BJ, Kozuch P, King AC, Hamburger SD, Rapoport JL: Quantitative morphology of the corpus callosum in attention deficit hyperactivity disorder. Am J Psychiatry 1994;151:665-669.

[68] Gilbert CD, Wiesel TN: Morphology and intracortical projections of functionally characterised neurones in the cat visual cortex. Nature 12-7-1979;280:120-125.

[69] Gilbert CD, Wiesel TN: Clustered intrinsic connections in cat visual cortex. J Neurosci 1983;3:1116-1133.

[70] Glaser JR, Glaser EM: Neuron imaging with Neurolucida--a PC-based system for image combining microscopy. Comput Med Imaging Graph 1990;14:307-317.

[71] Godecke I, Kim DS, Bonhoeffer T, Singer W: Development of orientation preference maps in area 18 of kitten visual cortex. Eur J Neurosci 1997;9:1754-1762.

[72] Graham, Midgley: Graphical representation of particle shape using triangular diagrams: an excel spreadsheet method. Earth Surface & Landforms 2000;25:1473-1477.

[73] Gray CM, Singer W: Stimulus-specific neuronal oscillations in orientation columns of cat visual cortex. Proc Natl Acad Sci U S A 1989;86:1698-1702.

[74] Grinvald A, Frostig RD, Siegel RM, Bartfeld E: High-resolution optical imaging of functional brain architecture in the awake monkey. Proc Natl Acad Sci U S A 15-12-1991;88:11559-11563.

[75] Grinvald A, Hildesheim R: VSDI: a new era in functional imaging of cortical dynamics. Nat Rev Neurosci 2004;5:874-885.

[76] Grinvald A, Segal M, Kuhnt U, Hildesheim R, Manker A, Anglister L, Freeman JA: Real-time optical mapping of neuronal activity in vertebrate CNS in vitro and in vivo. Soc Gen Physiol Ser 1986;40:165-197.

[77] Halter JA, Clark JW, Jr.: A distributed-parameter model of the myelinated nerve fiber. J Theor Biol 7-2-1991;148:345-382.

[78] Harvey AR: A physiological analysis of subcortical and commissural projections of areas 17 and 18 of the cat. J Physiol 1980;302:507-534.

[79] Houzel JC, Milleret C, Innocenti G: Morphology of callosal axons interconnecting areas 17 and 18 of the cat. Eur J Neurosci 1-6-1994;6:898-917.

[80] HUBEL DH: Eye, Brain and Vision. 1988.

[81] HUBEL DH, Wiesel TN: Integrative action in the cat's lateral geniculate body. J Physiol 1961;155:385-398.

[82] HUBEL DH, Wiesel TN: Receptive fields, binocular interaction and functional architecture in the cat's visual cortex. J Physiol 1962;160:106-154.

[83] HUBEL DH, Wiesel TN: The period of susceptibility to the physiological effects of unilateral eye closure in kittens. J Physiol 1970;206:419-436.

[84] Hubener M, Shoham D, Grinvald A, Bonhoeffer T: Spatial relationships among three columnar systems in cat area 17. J Neurosci 1-12-1997;17:9270-9284.

[85] Hughes CM, Peters A: Morphological evidence for callosally projecting nonpyramidal neurons in rat visual cortex. Anat Embryol (Berl) 1990;182:591-603.

[86] Imamura A: Über die kortikalen storungen des Sehaktes und die Bedeutung des Balkens. Pflügers Arch 1903;100:495-531.

[87] Innocenti G, Fiore L., Caminiti R.: Exuberant projection into the corpus callosum from the visual cortex of newborn cat. Neuroscience Letters 1977;4:237-242.

[88] Innocenti GM: Postnatal development of interhemispheric connections of the cat visual cortex. Arch Ital Biol 1978;116:463-470.

[89] Innocenti GM: The primary visual pathway through the corpus callosum: morphological and functional aspects in the cat. Arch Ital Biol 1980;118:124-188.

[90] Innocenti GM: Growth and reshaping of axons in the establishment of visual callosal connections. Science 15-5-1981;212:824-827.

[91] Innocenti GM: Postnatal development of corticocortical connections. Ital J Neurol Sci 1986;Suppl 5:25-28.

[92] Innocenti GM, Ansermet F, Parnas J: Schizophrenia, neurodevelopment and corpus callosum. Mol Psychiatry 2003;8:261-274.

[93] Innocenti GM, Frost DO: Effects of visual experience on the maturation of the efferent system to the corpus callosum. Nature 19-7-1979;280:231-234.

[94] Innocenti GM, Lehmann P, Houzel JC: Computational structure of visual callosal axons. Eur J Neurosci 1-6-1994;6:918-935.

[95] Innocenti GM, Price DJ: Exuberance in the development of cortical networks. Nat Rev Neurosci 2005;6:955-965.

[96] Johnston D, Wu S: Foundation of cellular neurophysiology. MIT Press, Cambridge Massachusetts, 1995.

[97] Katz LC, Shatz CJ: Synaptic activity and the construction of cortical circuits. Science 15-11-1996;274:1133-1138.

[98] King MA, Louis PM, Hunter BE, Walker DW: Biocytin: a versatile anterograde neuroanatomical tract-tracing alternative. Brain Res 18-9-1989;497:361-367.

[99] kisvarday Z., Bonhoeffer T., Kim D.S., Eysel U.T: *Brain Theory - Biological Basis and Computational Principles*. Elsevier Science B.V., 1996.

[100] Kisvarday ZF, Kim DS, Eysel UT, Bonhoeffer T: Relationship between lateral inhibitory connections and the topography of the orientation map in cat visual cortex. Eur J Neurosci 1-10-1994;6:1619-1632.

[101] Konig P, Engel AK, Roelfsema PR, Singer W: How precise is neuronal synchronization? Neural Comput 1995;7:469-485.

[102] Kullback S: Information theory and statistics. John Wiley & Sons, Inc., 1959.

[103] Laurent G, Stopfer M, Friedrich RW, Rabinovich MI, Volkovskii A, Abarbanel HD: Odor encoding as an active, dynamical process: experiments, computation, and theory. Annu Rev Neurosci 2001;24:263-297.

[104] Lepore F, Phaneuf J, Samson A, Guillemot JP: Interhemispheric transfer of visual pattern discriminations: evidence for a bilateral storage of the engram. Behav Brain Res 1982;5:359-374.

[105] LeVay S, HUBEL DH, Wiesel TN: The pattern of ocular dominance columns in macaque visual cortex revealed by a reduced silver stain. J Comp Neurol 15-2-1975;159:559-576.

[106] Levy-Agresti J, Sperry RW: Differential perceptual capacities in major and minor hemospheres. Proc Nat Acad Sci U S A 1968;61:1151.

[107] Lomber SG, Payne BR, Rosenquist AC: The spatial relationship between the cerebral cortex and fiber trajectory through the corpus callosum of the cat. Behav Brain Res 20-10-1994;64:25-35.

[108] Lotto RB, Asavaritikrai P, Vali L, Price DJ: Target-derived neurotrophic factors regulate the death of developing forebrain neurons after a change in their trophic requirements. J Neurosci 1-6-2001;21:3904-3910.

[109] Luhmann HJ, Martinez ML, Singer W: Development of horizontal intrinsic connections in cat striate cortex. Exp Brain Res 1986;63:443-448.

[110] Lund RD, Mitchell DE, Henry GH: Squint-induced modification of callosal connection in cats. Brain Res 7-4-1978;144:169-172.

[111] Magara F, Ricceri L, Wolfer DP, Lipp HP: The acallosal mouse strain I/LnJ: a putative model of ADHD? Neurosci Biobehav Rev 2000;24:45-50.

[112] Malach R, Amir Y, Harel M, Grinvald A: Relationship between intrinsic connections and functional architecture revealed by optical imaging and in vivo targeted biocytin injections in primate striate cortex. Proc Natl Acad Sci U S A 15-11-1993;90:10469-10473.

[113] Manor Y, Gonczarowski J, Segev I: Propagation of action potentials along complex axonal trees. Model and implementation. Biophys J 1991;60:1411-1423.

[114] Manor Y, Koch C, Segev I: Effect of geometrical irregularities on propagation delay in axonal trees. Biophys J 1991;60:1424-1437.

[115] Marr D: Vision. W.H.Freeman & Co Ltd, 1982.

[116] McIntyre CC, Richardson AG, Grill WM: Modeling the excitability of mammalian nerve fibers: influence of afterpotentials on the recovery cycle. J Neurophysiol 2002;87:995-1006.

[117] McKay DJC: *Information Theory, Inference and Learning Algorithms*. Cambridge University Press, 2003.

[118] McLachlan G.J.: The classification and Mixture Maximum Likelihood approaches to cluster analysis. Classification, pattern Recognition and reduction of Dimensionality 1982.

[119] McLachlan G.J.: On Bootstrapping the Likelihood Ratio Test Statistic for the Number of Components in a Normal Mixture. Applied Statistics 1987;36:318-324.

[120] McLachlan G.J., Peel D: MIXFIT: An algorithm for the automatic fitting and testing of the normal mixture models. Proceedings of the 14th International Conference on Pattern Recognition 1998;1:553-557.

[121] Meister M, Wong RO, Baylor DA, Shatz CJ: Synchronous bursts of action potentials in ganglion cells of the developing mammalian retina. Science 17-5-1991;252:939-943.

[122] Merzenich MM, Kaas JH, Wall J, Nelson RJ, Sur M, Felleman D: Topographic reorganization of somatosensory cortical areas 3b and 1 in adult monkeys following restricted deafferentation. Neuroscience 1983;8:33-55.

[123] Milleret C, Buser P: Reorganization processes in the visual cortex also depend on visual experience in the adult cat. Prog Brain Res 1993;95:257-269.

[124] Milleret C, Gary-Bobo E, Buisseret P: Comparative development of cell properties in cortical area 18 of normal and dark-reared kittens. Exp Brain Res 1988;71:8-20.

[125] Milleret C, Houzel JC: Visual interhemispheric transfer to areas 17 and 18 in cats with convergent strabismus. Eur J Neurosci 2001;13:137-152.

[126] Milleret C, Houzel JC, Buser P: Pattern of development of the callosal transfer of visual information to cortical areas 17 and 18 in the cat. Eur J Neurosci 1-2-1994;6:193-202.

[127] Mitchison G, Crick F: Long axons within the striate cortex: their distribution, orientation, and patterns of connection. Proc Natl Acad Sci U S A 1982;79:3661-3665.

[128] Moore JW, Joyner RW, Brill MH, Waxman SD, Najar-Joa M: Simulations of conduction in uniform myelinated fibers. Relative sensitivity to changes in nodal and internodal parameters. Biophys J 1978;21:147-160.

[129] MOUNTCASTLE VB: Modality and topographic properties of single neurons of cat's somatic sensory cortex. J Neurophysiol 1957;20:408-434.

[130] Murphy EH, Grigonis AM: Postnatal development of the visual corpus callosum: the influence of activity of the retinofugal projections. Behav Brain Res 15-9-1988;30:151-163.

[131] Nowak LG, Munk MH, Nelson JI, James AC, Bullier J: Structural basis of cortical synchronization. I. Three types of interhemispheric coupling. J Neurophysiol 1995;74:2379-2400.

[132] O'Kusky J, Colonnier M: Postnatal changes in the number of astrocytes, oligodendrocytes, and microglia in the visual cortex (area 17) of the macaque monkey: a stereological analysis in normal and monocularly deprived animals. J Comp Neurol 20-9-1982;210:307-315.

[133] O'Kusky J, Colonnier M: Postnatal changes in the number of neurons and synapses in the visual cortex (area 17) of the macaque monkey: a stereological analysis in normal and monocularly deprived animals. J Comp Neurol 20-9-1982;210:291-306.

[134] Obermayer K, Blasdel GG: Geometry of orientation and ocular dominance columns in monkey striate cortex. J Neurosci 1993;13:4114-4129.

[135] Ohki K, Matsuda Y, Ajima A, Kim DS, Tanaka S: Arrangement of orientation pinwheel centers around area 17/18 transition zone in cat visual cortex. Cereb Cortex 2000;10:593-601.

[136] Olavarria J, Malach R, Van Sluyters RC: Development of visual callosal connections in neonatally enucleated rats. J Comp Neurol 15-6-1987;260:321-348.

[137] Olavarria JF: Non-mirror-symmetric patterns of callosal linkages in areas 17 and 18 in cat visual cortex. J Comp Neurol 18-3-1996;366:643-655.

[138] Olavarria JF: Callosal connections correlate preferentially with ipsilateral cortical domains in cat areas 17 and 18, and with contralateral domains in the 17/18 transition zone. J Comp Neurol 14-5-2001;433:441-457.

[139] OTSUKA R, HASSLER R: [On the structure and segmentation of the cortical center of vision in the cat.]. Arch Psychiatr Nervenkr Z Gesamte Neurol Psychiatr 1962;203:212-234.

[140] Payne BR: Function of the corpus callosum in the representation of the visual field in cat visual cortex. Vis Neurosci 1990;5:205-211.

[141] Payne BR, Siwek DF: Visual-field map in the callosal recipient zone at the border between areas 17 and 18 in the cat. Vis Neurosci 1991;7:221-236.

[142] Peres A, Andrietti F: Computer reconstruction of the spread of excitation in nerve terminals with inhomogeneous channel distribution. Eur Biophys J 1986;13:235-243.

[143] Pham QC, Slotine JJ: Stable concurrent synchronization in dynamic system networks. Neural Netw 2007;20:62-77.

[144] Polyak S: in The vertebrate visual system: University of Chicago Press, 1957.

[145] Price DJ: The postnatal development of clustered intrinsic connections in area 18 of the visual cortex in kittens. Brain Res 1986;389:31-38.

[146] Price DJ, Kennedy H, Dehay C, Zhou L, Mercier M, Jossin Y, Goffinet AM, Tissir F, Blakey D, Molnar Z: The development of cortical connections. Eur J Neurosci 2006;23:910-920.

[147] Raizada RD, Grossberg S: Towards a theory of the laminar architecture of cerebral cortex: computational clues from the visual system. Cereb Cortex 2003;13:100-113.

[148] RAMON YC: Structure and connections of neurons. Bull Los Angel Neuro Soc 1952;17:5-46.

[149] Rasband MN, Shrager P: Ion channel sequestration in central nervous system axons. J Physiol 15-5-2000;525 Pt 1:63-73.

[150] Reidl J, Starke J, Omer DB, Grinvald A, Spors H: Independent component analysis of high-resolution imaging data identifies distinct functional domains. Neuroimage 1-1-2007;34:94-108.

[151] Restrepo CE, Manger PR, Spenger C, Innocenti GM: Immature cortex lesions alter retinotopic maps and interhemispheric connections. Ann Neurol 2003;54:51-65.

[152] Rocha EG, Santiago LF, Freire MA, Gomes-Leal W, Dias IA, Lent R, Houzel JC, Franca JG, Pereira A, Jr., Picanco-Diniz CW: Callosal axon arbors in the limb representations of the somatosensory cortex (SI) in the agouti (Dasyprocta primnolopha). J Comp Neurol 10-1-2007;500:255-266.

[153] Rochefort N, Quenech'du N, Ezan P, Giaume C, Milleret C: Postnatal development of GFAP, connexin43 and connexin30 in cat visual cortex. Brain Res Dev Brain Res 7-12-2005;160:252-264.

[154] Rochefort N, Quenech'du N, Watroba L, Mallat M, Giaume C, Milleret C: Microglia and astrocytes may participate in the shaping of visual callosal projections during postnatal development. J Physiol Paris 2002;96:183-192.

[155] Rochefort NL, Buzas P, Kisvarday ZF, Eysel UT, Milleret C: Layout of transcallosal activity in cat visual cortex revealed by optical imaging. Neuroimage 1-7-2007;36:804-821.

[156] Rockland KS, Ichinohe N: Some thoughts on cortical minicolumns. Exp Brain Res 2004;158:265-277.

[157] Rockland KS, Lund JS: Widespread periodic intrinsic connections in the tree shrew visual cortex. Science 19-3-1982;215:1532-1534.

[158] Rumberger A, Tyler CJ, Lund JS: Intra- and inter-areal connections between the primary visual cortex V1 and the area immediately surrounding V1 in the rat. Neuroscience 2001;102:35-52.

[159] Salinas E, Sejnowski TJ: Correlated neuronal activity and the flow of neural information. Nat Rev Neurosci 2001;2:539-550.

[160] Salzberg BM, Davila HV, Cohen LB: Optical recording of impulses in individual neurones of an invertebrate central nervous system. Nature 21-12-1973;246:508-509.

[161] Sanderson KJ: The projection of the visual field to the lateral geniculate and medial interlaminar nuclei in the cat. J Comp Neurol 1971;143:101-108.

[162] Sanderson KJ, Sherman SM: Nasotemporal overlap in visual field projected to lateral geniculate nucleus in the cat. J Neurophysiol 1971;34:453-466.

[163] Sarnat HB, Netsky MG: The brain of the planarian as the ancestor of the human brain. Can J Neurol Sci 1985;12:296-302.

[164] Schweitzer L, Renehan WE: The use of cluster analysis for cell typing. Brain Res Brain Res Protoc 1997;1:100-108.

[165] Scott A: Neuroscience, a mathematical primer. Springer, 2002.

[166] Seber. Multivariate Observations. Wiley, New York . 1984.
Ref Type: Generic

[167] Segev I, Schneidman E: Axons as computing devices: basic insights gained from models. J Physiol Paris 1999;93:263-270.

[168] Segraves MA, Rosenquist AC: The afferent and efferent callosal connections of retinotopically defined areas in cat cortex. J Neurosci 1982;2:1090-1107.

[169] Series P, Georges S, Lorenceau J, Fregnac Y: Orientation dependent modulation of apparent speed: a model based on the dynamics of feed-forward and horizontal connectivity in V1 cortex. Vision Res 2002;42:2781-2797.

[170] Series P, Lorenceau J, Fregnac Y: The "silent" surround of V1 receptive fields: theory and experiments. J Physiol Paris 2003;97:453-474.

[171] Shatz CJ, Stryker MP: Prenatal tetrodotoxin infusion blocks segregation of retinogeniculate afferents. Science 7-10-1988;242:87-89.

[172] Sherman S.M, Koch C.: Thalamus; in Shepherd (ed): The synaptic organization of the brain. Oxford University Press, 2004.

[173] Shmuel A, Grinvald A: Functional organization for direction of motion and its relationship to orientation maps in cat area 18. J Neurosci 1-11-1996;16:6945-6964.

[174] Shmuel A, Grinvald A: Coexistence of linear zones and pinwheels within orientation maps in cat visual cortex. Proc Natl Acad Sci U S A 9-5-2000;97:5568-5573.

[175] Shmuel A, Korman M, Sterkin A, Harel M, Ullman S, Malach R, Grinvald A: Retinotopic axis specificity and selective clustering of feedback projections from V2 to V1 in the owl monkey. J Neurosci 23-2-2005;25:2117-2131.

[176] Shoham D, Glaser DE, Arieli A, Kenet T, Wijnbergen C, Toledo Y, Hildesheim R, Grinvald A: Imaging cortical dynamics at high spatial and temporal resolution with novel blue voltage-sensitive dyes. Neuron 1999;24:791-802.

[177] Sirovitch L., Everson R.: Management and analysis of large scientific datasets. Intl J Supercomput Appl 1992;50-68.

[178] Slotine JJ, Lohmiller W: Modularity, evolution, and the binding problem: a view from stability theory. Neural Netw 2001;14:137-145.

[179] Somogyi P, Kisvarday ZF, Martin KA, Whitteridge D: Synaptic connections of morphologically identified and physiologically characterized large basket cells in the striate cortex of cat. Neuroscience 1983;10:261-294.

[180] Sornborger A, Sailstad C, Kaplan E, Sirovich L: Spatiotemporal analysis of optical imaging data. Neuroimage 2003;18:610-621.

[181] Spath H. Cluster Dissection and Analysis: Theory, FORTRAN Programs, Examples. translated by J.Goldschmidt. 1985. Halsted Press, New York.
Ref Type: Generic

[182] Sperry RW: Some effects of disconnecting the cerebral hemispheres, Nobel Lecture, 8 december 1981. Bioscience Reports 2 1982;265-276.

[183] Spruston N, Johnston D: Perforated patch-clamp analysis of the passive membrane properties of three classes of hippocampal neurons. J Neurophysiol 1992;67:508-529.

[184] Stetter M, Schiessl I, Otto T, Sengpiel F, Hubener M, Bonhoeffer T, Obermayer K: Principal component analysis and blind separation of sources for optical imaging of intrinsic signals. Neuroimage 2000;11:482-490.

[185] Stone J: The naso-temporal division of the cat's retina. J Comp Neurol 1966;126:585-600.

[186] Stryker MP, Antonini A: Factors shaping the corpus callosum. J Comp Neurol 14-5-2001;433:437-440.

[187] Stryker MP, Harris WA: Binocular impulse blockade prevents the formation of ocular dominance columns in cat visual cortex. J Neurosci 1986;6:2117-2133.

[188] Swindale NV, Matsubara JA, Cynader MS: Surface organization of orientation and direction selectivity in cat area 18. J Neurosci 1987;7:1414-1427.

[189] Tasaki I, Watanabe A, Sandlin R, Carnay L: Changes in fluorescence, turbidity, and birefringence associated with nerve excitation. Proc Natl Acad Sci U S A 1968;61:883-888.

[190] Tettoni L, Lehmann P, Houzel JC, Innocenti GM: Maxsim, software for the analysis of multiple axonal arbors and their simulated activation. J Neurosci Methods 1996;67:1-9.

[191] Thomson AM, Bannister AP: Interlaminar connections in the neocortex. Cereb Cortex 2003;13:5-14.

[192] Toldi J, Wolff JR, Wiese UH: Functional consequences of modification of callosal connections by perinatal enucleation in rat visual cortex. Neuroscience 1989;33:517-524.

[193] Tonnelier A, Meignen S, Bosch H, Demongeot J: Synchronization and desynchronization of neural oscillators. Neural Netw 1999;12:1213-1228.

[194] Toyama K, Matsunami K, Ono T, Tokashiki S: An intracellular study of neuronal organization in the visual cortex. Exp Brain Res 1974;21:45-66.

[195] Tusa RJ, Palmer LA, Rosenquist AC: The retinotopic organization of area 17 (striate cortex) in the cat. J Comp Neurol 15-1-1978;177:213-235.

[196] Tusa RJ, Rosenquist AC, Palmer LA: Retinotopic organization of areas 18 and 19 in the cat. J Comp Neurol 15-6-1979;185:657-678.

[197] Varela F, Lachaux JP, Rodriguez E, Martinerie J: The brainweb: phase synchronization and large-scale integration. Nat Rev Neurosci 2001;2:229-239.

[198] Voigt T, LeVay S, Stamnes MA: Morphological and immunocytochemical observations on the visual callosal projections in the cat. J Comp Neurol 15-6-1988;272:450-460.

[199] von PK, Lundervold A, Duta N, Heiervang E, Klauschen F, Smievoll AI, Ersland L, Hugdahl K: Less developed corpus callosum in dyslexic subjects--a structural MRI study. Neuropsychologia 2002;40:1035-1044.

[200] Waxman SG, Bennett MV: Relative conduction velocities of small myelinated and non-myelinated fibres in the central nervous system. Nat New Biol 16-8-1972;238:217-219.

[201] Waxman SG, Wood SL: Impulse conduction in inhomogeneous axons: effects of variation in voltage-sensitive ionic conductances on invasion of demyelinated axon segments and preterminal fibers. Brain Res 27-2-1984;294:111-122.

[202] Weil H: Symmetry. 1952.

[203] Wiesel TN, HUBEL DH: EFFECTS OF VISUAL DEPRIVATION ON MORPHOLOGY AND PHYSIOLOGY OF CELLS IN THE CATS LATERAL GENICULATE BODY. J Neurophysiol 1963;26:978-993.

[204] Wiesel TN, HUBEL DH: Comparison of the effects of unilateral and bilateral eye closure on cortical unit responses in kittens. J Neurophysiol 1965;28:1029-1040.

[205] Wolfe JH: Pattern Clustering by Multivariate Analysis. Multivariate Behavioral Research 1970;5:329-350.

[206] Wree A, Kulig G, Gutmann P, Zilles K: Modification of callosal afferents of the primary visual cortex ipsilateral to the remaining eye in rats monocularly enucleated at different stages of ontogeny. Cell Tissue Res 1985;242:433-436.

[207] Yokoo T, Knight BW, Sirovich L: An optimization approach to signal extraction from noisy multivariate data. Neuroimage 2001;14:1309-1326.

[208] Zhou L, Chiu SY: Computer model for action potential propagation through branch point in myelinated nerves. J Neurophysiol 2001;85:197-210.

[209] Zufferey PD, Jin F, Nakamura H, Tettoni L, Innocenti GM: The role of pattern vision in the development of cortico-cortical connections. Eur J Neurosci 1999;11:2669-2688.